DIRECT SELECTIVE LASER SINTERING OF ALUMINIUM ALLOY POWDERS

By

Eyitayo Olatunde Olakanmi

B. Eng. (Mech.); M.Eng. (Mech.); MNSE; C.Eng. (COREN)

Submitted in accordance with the requirements for the degree of

Doctor of Philosophy

University of Leeds

Institute for Materials Research

Leeds, UK.

November 2008

The candidate confirms that the work submitted is his own and that appropriate credit has been given where reference has been made to the work of others.

DEDICATION

In most profound appreciation of my mother,

Madam Victoria Adewuni Abike Olakanmi

for bravely and persistently defying all odds to lay the solid foundation for all these blessings in my life unto God's glory.

And

My wife,

Eunice Eyitayo Olakanmi,

For continuing the good work of building on the solid foundation.

THESIS CONTAINS CD

ACKNOWLEDGEMENTS

All glory to my Lord and Saviour, Jesus Christ, for His faithfulness unto me and my family throughout this programme. My eternal gratitude goes to the people and the government of the Great Britain who offered me a scholarship, through the Commonwealth Scholarship of the UK, to study for PhD degree. May God continue to bless this land.

I am very grateful to my supervisors, Dr Cochrane and Professor Dalgarno, who had guided me with great patience in the course of the practical work and the preparation of this thesis. Thanks for being there always to listen and to give advice. I have benefited immensely from their wealth of knowledge on how to ask questions, express my ideas with supporting evidence, approach a research problem in a profoundly insightful manner, and persist to accomplish any goal. Special thanks to Mrs Cochrane, Mrs Joy Bielby, Mr John Harrignton, Dr Walshaw, Mr Ismail Abbass, Mr Tony Wiese, Mr Dave Wright, Dr Simon Strafford (Leeds Dental School) and the technical team at the Newcastle university mechanical worhop for their unalloyed co-operation while working in their various laboratories and workshops at Leeds and Newcastle.

To all my friends, brethren at St. Mathias Church of England, Burley, Leeds, Engr. & Mrs John Oseh family, Architect & Dr (Mrs) Theophilus Shittu family, Dr & Mrs Abiodun Adeniyi family, bro. Emmanuel Akanni, Deacon& Mrs Ayuba Paiko family, Dr & Mrs O. D. Jimoh, Inspector & Mrs Idowu Owohunwa, and Engr. Derrick Njobuenwu, thanks very much for all your moral, spiritual and financial support. You are all blessed.

My parents and siblings (Olanike, Olalekan and Omobola) have very been supportive to my family throughout this programme. Thanks very much for your moral and spiritual encouragement. May God bless you all tremendously. To my in-laws, the Oyebanjis, thanks be to God for all you have always been to me, may the good Lord reward you all in a deserving manner.

Lastly but not least, I am very grateful to my wife and children (Hannah, Samuel, and Elizabeth) for their loving support throughout this programme. May God bless you all.

ABSTRACT

The SLS/SLM of aluminium powder had been investigated by studying the effect of powder properties and laser processing parameters on the microstructures and properties of both single layer and multiple layer builds. On the basis of experimental evidence, the SLS/SLM of aluminium powders could be categorised into full melting (SLM) which was found to have occurred in both pure and pre-alloyed aluminium powders, and binary liquid phase sintering (SLS) which occurred in blended bimodal or trimodal powders. That successful disruption of the oxide film is possible is a significant result, as is the constitutional effect on this. The spheroidisation and oxide disruption phenomena in SLS/SLM processed aluminium powders are suggested to be mainly controlled by the amount of oxide on the as-received powder's surface, the degree of the uniformity of the distribution of the surface oxide film covering the aluminium particles as well as the nature of thermal mismatch existing between the oxide film and the parent aluminium particle which was dependent on the phase present in the oxide film (alumina, mullite, and spinel). It was discovered that the attainment of high sintered density and desirable microstructural properties in the blended aluminium powders is consequent upon the determination of the right processing conditions, appropriate choice of powders (in terms of particle size distribution, spherical particle shape, and component ratio). Moreover, it is now evident that chemical constitution of the blended aluminium powders only becomes influential in the determination of the properties of SLS processed parts when the choice of processing parameters and powder properties are correct. The choice of powder properties determines the thermal conductivity of the powder bed which in effect controls the sintered properties. This had been inferred from the relationship between powder tapping density on one hand, and selective laser sintered (SLS) density, dendrite spacing and fraction of primary phase on the other hand. In making smaller samples, it has been shown that the attainment of high sintered density (up to 90%) and a good microstructure are feasible. These are accompanied by reasonable hardness values, comparable to those of cast Al-12wt%Si castings. In fabricating larger sized parts for mechanical testing, defects such as delamination became more noticeable leading to poor mechanical properties in those samples. Thus, it is now clear that physical limitations of the sintering machine hinder the production of SLS/SLM processed parts having excellent structural integrity.

On the basis of this work, it is envisaged that the use of pre-alloyed Al-Si powders of uniform composition, but a wider particle size and size distribution, blended to optimise the bed density, offers the potential to produce light alloy components by SLS.

In conclusion, the specific laser energy input, the component ratio, and the particle size and size distribution of the powder were found to have strongly influenced the densification mechanism and the solidification process in a small sized aluminium powdered part fabricated by SLS/SLM process

TABLE OF CONTENTS

LIST OF FIGURES

LIST OF TABLES

NOTATION AND ABBREVIATIONS

A_s	The surface area of the new interface created by the solid nucleus and the liquid (m^2)
C1, C2,	Material constants
C_{FL}	Equilibrium liquid concentration at the end of equilibrium solidification and at the interface at T_S
C_{FSeq}	Equilibrium solid concentration at the end of equilibrium solidification and at the interface at T_S
C_L^*	Composition in the liquid along the solidus and liquidus lines
C_O	Nominal composition of the eutectic alloy
Cos	Initial concentration of solid
C_{Sav}	Line of average solid concentration
C_S^*	Composition in the solid along the solidus and liquidus lines
D_L^*	Complete mixing in the liquid phase
D	Initial diameter of unperturbed cylinder (μm)
D_L	Diameter of large spheres (m)
D_M	Diameter of medium spheres (m)
D_S	Diameter of small spheres (m)
D_S^*	Ideal diffusion in the solid phase
E	Thermal modulus of elasticity (GPa)
EDS	Energy Dispersive Spectrum
E_b	Modulus of elasticity in bending (MPa)
FSLB	First line scan balling
G	Temperature gradient (K/m)
G_L	Optimum composition in terms of weight fraction for large particles
HAZ	Heat Affected Zone
HIP	Hot Isostatic Pressing
HPGL	Hewlett Packard Graphics Language

K	Densification co-efficient
K_{IC}	Fracture toughness ($MPam^{1/2}$)
L	Span length (mm)
L_d	Distance between adjacent side branches on the longitudinal section of a primary dendrite
LPS	Liquid phase sintering
M	Mass of powder from the density cup (g)
MGB	Migrated Grain Boundaries
P	Laser power (Watts)
PECS	Pulse Electric Current Sintering
P/M	Powder Metallurgy
P_{max}	Maximum load at bending (N)
R	Solidification rate (μm/s)
R_1, R_2, R_3,	Radius of three existing large, medium and small disks (m)
S	Spreading co-efficient
SEM	Scanning Electron Microscopy
SLM	Selective laser melting
SLS	Selective laser sintering
SGB	Solidification Grain Boundaries
SSGB	Solidification Sub-Grain Boundaries
S (0)	Shape factor dependent on the contact angle (degrees)
T	Cooling rate (K/s)
T_E	Equilibrium eutectic temperature
T_L	Equilibrium liquidus temperature
T_S	Equilibrium solidus temperature
T_{Sneq}	Actual non-equilibrium solidus
V	Volume of density cup (cm^3)
V_B	Volume of binder particles (cm^3)

V_C	Volume of non-melted cores of particles (cm^3)
V_{OM}	Volume of space between the solid particles of the main component (cm^3)
V_S	Volume of nucleus (cm^3)
V^*_S	Volume of solid particles of raw powder (cm^3)
V_α	Volume fraction of the primary aluminium phase (cm^3)
X_i,	Dimensions of the sintered samples in the X, direction (mm)
Y_i	Dimensions of the sintered samples in the Y direction (mm)
W_a	Work of adhesion (N/m)
W_e	Weight fraction of the eutectic phase
W_α	Weight fraction of the primary phase
Z_i	Dimensions of the sintered samples in the Z direction (mm)
a_c	Half crack length (μm)
b	Specimen width (mm)
d	Layer thickness (mm)
f_i	Fraction of test points in the phase of interest
f_s	Fraction of solid
h	Specimen thickness (mm)
m_1	Mass of density cup and the powder shot (g)
m_2	Mass of the cup (g)
r*	Critical radius that promote heterogeneous nucleation (μm)
u	Scanning rates (mm/s)
v	Volume of the tapped powder (cm^3)
x_i	Number of points that fall on the primary aluminium phase
ΔG^*_{het}	Associated free energy barrier for heterogeneous nucleation (J)
ΔG^*_{hom}	Associated free energy barrier for homogeneous nucleation (J)
ΔG_v	Free energy change per unit volume associated with formation of nucleus (J/m^3)
ΔP	Load increament (N)

ΔT	Temperature change (^oC)
$\Delta\delta$	Deflection increament at mid-span (mm)
α	Thermal expansion co-efficient ($/^oC$)
α^*	Agglomeration factor
γ_{LV}	Surface tension of the liquid-vapour interface (N/m)
γ_{ML}	Interfacial energies between the substrate metal and the liquid (N/m)
γ_{SL}	Surface tension of the solid-liquid interface (N/m)
γ_{SL}	Interfacial energies between the solid nucleus and the liquid (N/m)
γ_{SM}	Interfacial free energy between the solid nucleus and the substrate metal (N/m)
γ_{SV}	Surface tension of the solid-vapour interface (N/m)
θ	Contact angle (degrees)
λ	Wavelength (m)
λ_d	Secondary dendrite arm spacing (μm)
μ	Viscosity of solid-liquid mixture (Nsm^{-2})
μ_o	Viscosity containing temperature terms (m^2/s)
μ^*	Population mean
Π	A constant (3.142)
ρ	Sintered density (g/cm^3)
ρ_a	Apparent density (g/cm^3)
ρ_{bed}	Bed density (g/cm^3)
ρ_e	Density of eutectic phase (g/cm^3)
ρ_L	Fractional packing density of larger particles
ρ_P	Fractional packing density at optimal composition
ρ_S	Fractional packing density of smaller particles
ρ_{st}	Saturation sintered density (g/cm^3)
ρ_α	Density of primary phase (g/cm^3)
б	Circumferential stress (MPa)

$б^*$	Theoretical fracture stress (MPa)
φ	Volume fraction of solids in liquid
φ_M	Critical volume fraction of solids above which the mixture has essentially infinite viscosity
ψ	Specific laser energy input (J/mm^3)

CHAPTER ONE BACKGROUND TO THE STUDY AND STUDY OVERVIEW

1.1 Introduction

This chapter describes, very briefly, the background to the study on layer manufacturing (LM) techniques including advantages, disadvantages, materials processed and a general overview of selective laser sintering/melting (SLS/SLM). A gap in the knowledge with respect to light alloys, (specifically aluminium), the desirability of SLS/SLM of these materials and a brief, 'uninformed', discussion of what potential problems might be in this, have been identified. This chapter ends with the description of the outline to this thesis and conclusion to this section.

1.2 Background to the Study

The observation made by Wang (2002) that global economy was facing the challenge of delivering new customised products more quickly in order to avoid business failure is still as relevant today. This could be attributed to the keenly competitive globalised business environment among manufacturers aiming at gaining more consumer markets for their products. Therefore, this challenge has led to the development of a range of manufacturing techniques known as Layer Manufacturing (LM) in the last two decades as presented in Table 1.1. These LM processes have been used to produce components in a variety of materials such as plastics, paper, sand, ceramics, polymers and metals (Karapatis *et al.* 1998, Kruth *et al.* 1998). These processes allow components to be fabricated without any part-specific tools being required. All of these processes produce components from 3-D CAD models and series of scans (e.g. CT scanner) by building 3-D objects a layer at a time (Dalgarno & Wright 2001, Hollander *et al.* 2006, Wang *et al.* 2006).

Table 01.1: Typical LM technologies (after Kruth et al. 1998).

Technique	Layer creation technique	Phase Change during layer solidification	Materials
Stereolithography (SLA)	Liquid layer deposition.	Photo-polymerisation.	Photo-polymers e.g. acrylates, epoxies, filled resins (glass, ceramic, metal) and colourable resins.
Laminated Object Manufacturing (LOM)	Deposition of sheet metal.	No phase change.	Paper, polymer, polymer foam, composites, ceramics and metals.
Fused Deposition Modelling (FDM)	Continuous extrusion and deposition.	Solidification by cooling.	Polymers, wax, filled polymers, metals with binders, ceramic with binders.
Selective Laser Sintering (SLS)	Layer of powder	Laser sintering / laser melting and re-solidification by cooling.	Polymers, metals with binders, pure metals, sand and ceramics.
3D Printing (3DP)	Layer of powder + Drop-on-demand binder printing.	No phase change.	Ceramic with binder, polymer with binder, and metals with binder.

These technologies have been developed to shorten the design and production cycle, and promise to transform many traditional manufacturing methods by engendering significant time and cost savings (Morgan *et al.* 2002). LM systems consist of a combination of a computer CAD system which controls a machine which performs the fabrication of the layers, an example of which is shown in Figure 1.1.

According to Wang *et al.* (2006), the working principles of LM can be described as follows:

(i) A 3-D CAD representation or series of scans of the part is created by a computer software package such as ProEngineer, Solid Works, AutoCAD, or IDEAS and converted to the standard STL format.

(ii) The computer representation of the part is then sliced into layers of a certain thickness, typically in the range of 0.02 to 0.25mm, and their two-dimensional (2D) profiles stored on the LM machine.

(iii) A layer of powder is spread on top of the building platform.

(iv) The powder particles are melted and fused together by the laser beam as it scans the geometry of the sintered part.

(v) The newly scanned layer is lowered to a depth equivalent to the specified layer thickness and a new layer of powder is spread over the building platform by the powder delivery mechanism.

(vi) Again, the newly deposited layer is scanned so that the powder particles can fuse together.

(vii) The process is repeated many times, building the part layer by layer until the component is fully fabricated.

(vii) The final step is removing the part from the machine, detaching support materials, and performing any necessary cleaning or surface finishing such as polishing, sealing and painting the parts in an attempt to improve their appearance.

However, in LM, a wider range of shapes can be achieved, including intricate geometries that would be difficult to fabricate by the conventional manufacturing processes. LM is gaining wide acceptance because it is a high-speed production technique for manufacturing tools such as specially shaped moulds, dies, and jigs

required for mass production by utilising an increasing variety of materials such as high speed steels, and stainless steel powders (Wang 2002).

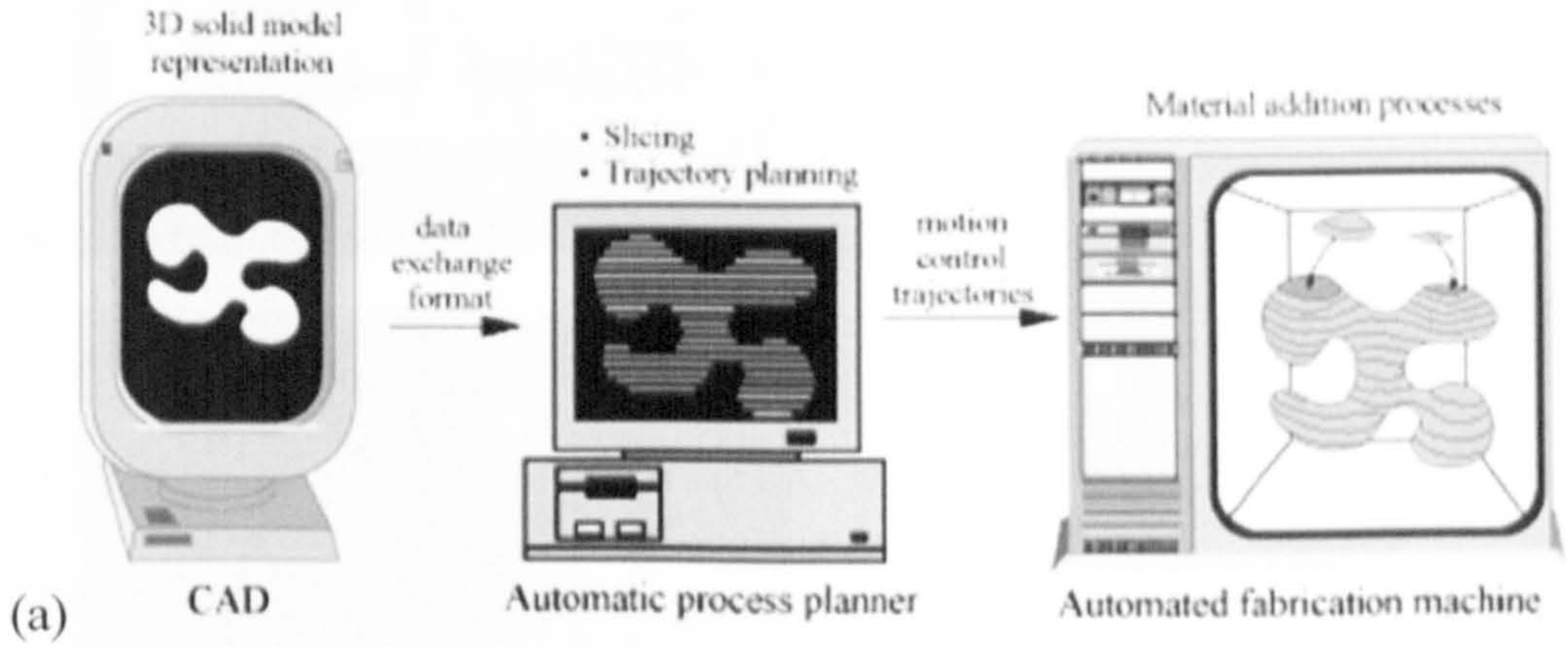

Figure 1.01: (a) A layered manufacturing (LM) paradigm (b) Generic fixturing (after Weiss 1997). Source (http://www.wtec.org/loyola/rp/02_01.htm)

According Levy *et al.* (2003) the following ranges of specified properties had been achieved for ferrous tooling parts manufactured via LM: surface quality (12.5 to 60 μm), dimensional accuracy (± 0.002 to ± 0.13 mm) and tensile strength (100 to 1400 MPa). A typical tooling part fabricated by LM is as shown in Figure 1.2. For some components, it can be economical to use LM to fabricate the final products themselves, sometimes in a matter of days instead of weeks or months (Wang 2002). LM techniques are typically not as fast as conventional mass production methods, but they eliminate tooling, set up and assembly processes (Wang 2002).

(a)

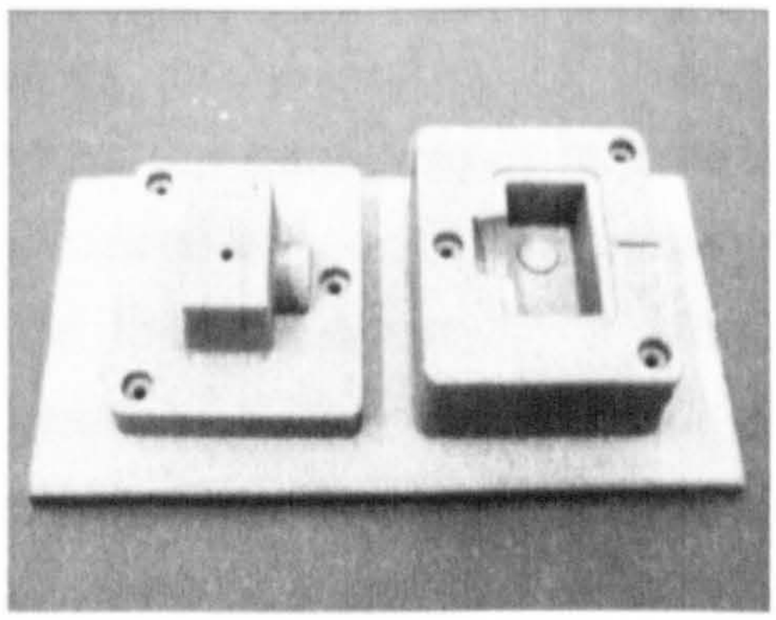

(b)

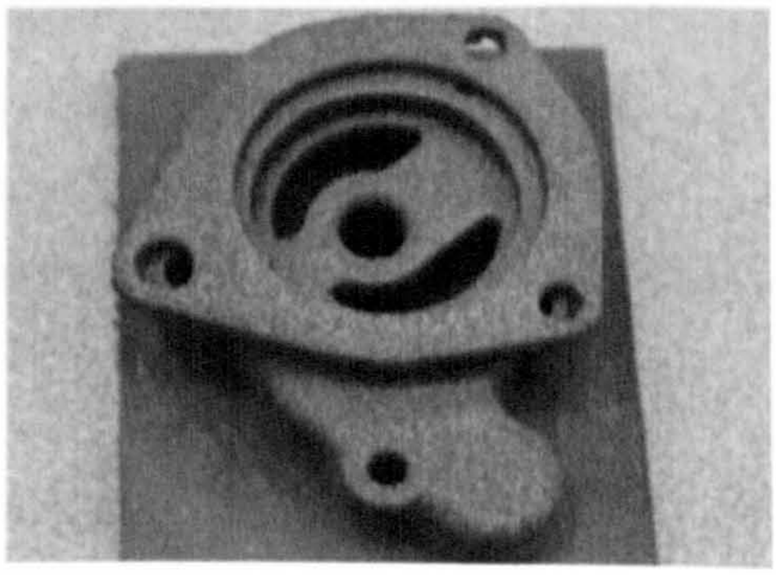

Figure1.2: Typical copper-based parts producible by LM (a) mould inserts (b) oil pump (Tang et al. 2003).

Consequently, LM can be ideal for making customised parts based on a customer's special requirements. Wang (2002) noted that an increasing number of manufacturers are adopting LM techniques for the following reasons:

(i) It allows parts of completely arbitrary 3-dimensional (3D) geometry to be produced, offering designers a new freedom to shape parts optimally without constraints imposed by forming, machining or joining.

(ii) The process utilises the computer description of the part's shape directly, and allows integration of the Computer Aided Design (CAD) with the Computer Aided Manufacturing (CAM) of the part.

In other words, LM allows a manufacturing cycle with seamless transition through the computer design, simulation, modelling and fabrication procedures. Moreover, the profiles used by the fabrication process are straightforward for the designers and customers to understand, thus facilitating technical communications. This is practicable with the fabrication procedure of a part which begins with the creation of prototype, in advance, with a view to demonstrating, evaluating, and testing the final product.

Fritz & Noorani (1999) demonstrated the cost saving benefit of LM technologies by investigating the application of SLA to the fabrication of tools for sheet metal forming. They concluded that for the most complex dies used in hydraulic and rubber pad

forming, manufacturing by hand machining took 96 hours while SLA was able to produce the same shapes in 2 hours, a time saving of 98%. The dies were ready to shape metal as soon as they cured. Another landmark application of LM by researchers at the Ibaraki University in Japan is the fabrication of porous bone substitutes as implants by SLS technique from titanium powder sheet (Hayashi *et al.* 2005). High quality and low cost metal dies for fabricating automobile deck parts were produced by LOM with a short production cycle (Song *et al.* 2002). With the expected rapid development and improvement in process capabilities of LM in the next decade, these examples buttress the fact that LM remains the technology of the future as human lives continue to depend upon the quality and ease of use of its products in the transportation, medicine, sports and electronics sectors.

The main drawbacks of LM techniques are poor surface quality, and dimensional accuracy, as well as material properties (microstructure and mechanical strength) that do not meet the pre-requisite for industrial applications. To address these demerits, post-processing treatments like polishing, painting, heat-treatment, and furnace-infiltration e.t.c. have been employed (Wang 2002). Again, these post-processing treatments also introduce the burden of elongating the production cycle and increasing the cost of production. Meanwhile, investigation of appropriate process and material parameters required for obtaining improved surface finish, dimensional accuracy, and mechanical strength of LM fabricated parts is also being undertaken with a view to eliminating these post-processing steps in order to shorten the lead time and production costs.

1.3 Project Overview

In agreement with Kruth *et al.* (2005, 2007), this study shall focus on the selective laser sintering/melting (SLS/SLM) because it is the most versatile of the LM techniques for processing metals. Meanwhile, SLS/SLM can be classified into various binding or consolidation mechanisms (Figure 1.3) which culminate in the formation of final parts having significantly different microstructure upon comparison with the starting material. This is effected via the manipulation of the original powder's properties and process parameters. Kruth *et al.* (2005, 2007) pointed out that SLS and SLM are different. For example, SLS is synonymous with the liquid phase sintering (LPS) which combines a structural material (high melting metal e.g. steel or Fe) remaining solid throughout the process and a binder material (low-melting metal e.g. Cu) being liquefied. According to Kruth *et al.* (2005), the structural and binder materials may be in the forms coated grains (Cu coated steel powders and nylon coated Al grains),

composites grains (WC-Co), and separate grains (e.g. stainless steel-Cu, and WC-Cu). Another variant of SLS is the partial melting which occurs in a mixture of different powders (multiple phases) having no distinct binder and structural materials (e.g. Fe-Fe_3P-Ni-Cu powder mixture), bimodal powders, or single phase material. SLM achieves fully dense parts in single component, single material powder (e.g. titanium); and single component, alloyed powder particles (e.g. stainless steel) (Kruth *et al.* 2005). SLM is able to impart full density into parts in a single step. Moreover, SLM requires careful process control in order to avoid difficulties such as part distortion, balling and dross formation in the melt pool that cause poor surface quality (Kruth *et al.* 2007). Apart from the properties of a material system, the choice of process parameters and the types of lasers used for consolidation also determine whether SLS or SLM would be obtained for a typical material system. This could be attributed to the duration of the laser-material interaction which controls the degree of consolidation that may be obtained in a material system. For example, high laser powers combined with low scanning rates would generate SLM whereas; high or low laser powers coupled with higher scanning rates would result in SLS. Although, all metals are candidate materials for SLM, significant variations associated with the ease of their processing due to variation in their laser absorption, surface tension and viscosity of the liquid metal; necessitate that experimental investigation is carried out for each new material in order to determine its process-window (Kruth *et al.* 2005). Verification of the appropriate process-window is important if scan track instabilities and part porosity are to be avoided and more commercialised SLS/SLM metal powders will be made available. Moreover, the fore-going discourse reveals the reservation associated with use of terminologies for describing SLS/SLM of metals among researchers due to lack of understanding of the consolidation mechanisms responsible for the process of SLS or SLM. It can be inferred that the classification of laser-based process as SLS or SLM is a function of the mechanism by which the solid is formed which is controlled by the material component system and the choice of laser processing parameters. While the products developed from the LPS and partial melting processes (SLS process variants) suffer from low mechanical strength and durability, they will require post-processing treatments such as furnace infiltration, and hot isostatic pressing (HIP) e.t.c. to achieve full density as noted earlier on. Meanwhile, the specifics of the variants of SLS/SLM and the application of LPS to SLS/SLM process will be discussed in sections 2.2 and 2.5 respectively.

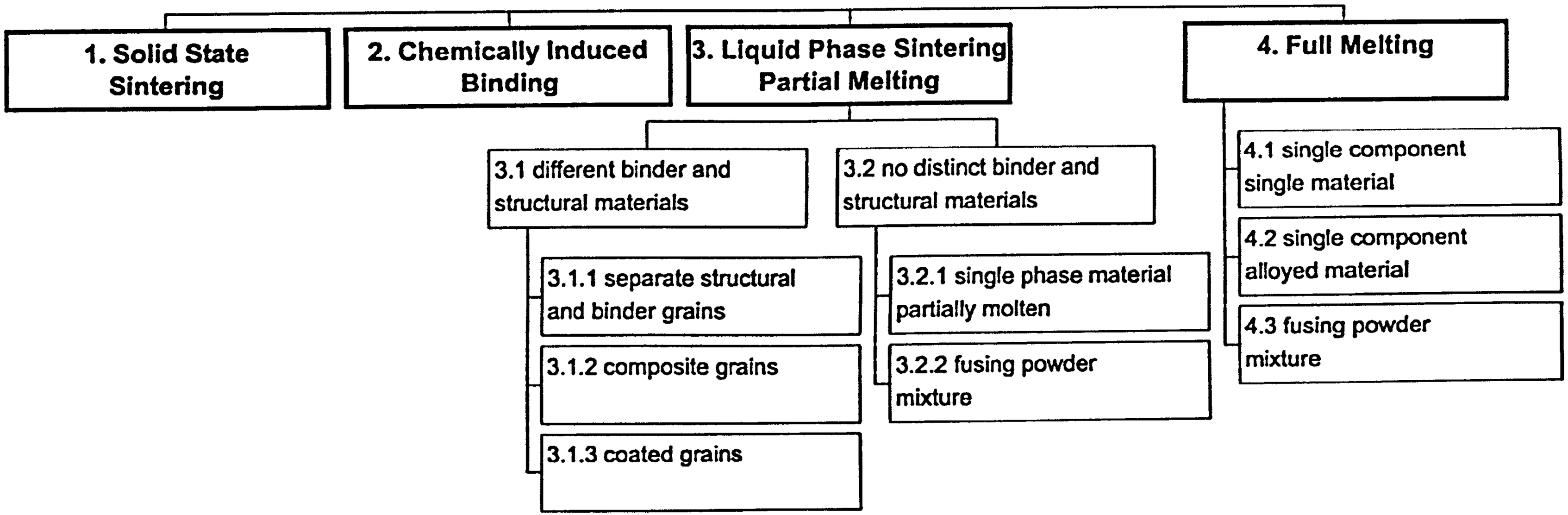

Figure 1.3: Classification of SLS/SLM according to binding mechanisms (after Kruth *et al.* 2005)

At Leeds University, the expertise in the field of LM is in SLS/SLM processing of metal (Hauser 2003, Dewidar 2003), polymers (Tontowi 2000) and bioceramics (Goodridge 2003, Xiao, 2007) powders. SLS processing of polymers is easier than that of metals because polymers undergo a softening phenomenon characterised by a strong temperature-dependent viscosity. On the other hand, since metals undergo a different bonding mechanism because they have a generally much higher melting temperature, a melting-solidification approach is usually adopted to describe the SLS/SLM of metals (Agarwala *et al.* 1995, Kruth *et al.* 2007). As pointed out in the preceding paragraph, SLS/SLM of metallic powders is bedevilled with complications such as balling, layer distortion, poor dimensional accuracy and surface roughness because of the oxidic contamination, non-uniform thermal gradient across the processed parts, and Marangoni convection which inhibit successful melt pool to substrate bonding in SLM or inter-particulate bonding in SLS across the layers (Kruth *et al.* 2007). It has been established that these difficulties result in components with undesirable microstructures giving rise to poor physical and mechanical properties. Therefore, research addressing these issues in direct SLS/SLM processed metallic parts is still on-going with a view to making available more commercialised powders.

The works of Das *et al.* (1998a, 1999), Dewidar *et al.* (2003), Zhu *et al.* (2005, 2006), and Rombouts *et al.* (2006), indicate that a lot of investigations had been conducted on ferrous (e.g. stainless and tool steels), and non-ferrous (e.g. Cu, bronzes, titanium alloys) materials with a view to overcoming these complications, whereas, there seems to be that no attention is being paid to address these issues in aluminium powders and its alloys. In an attempt to address the improvement of physical, microstructural and mechanical properties, the research described in this thesis focuses on the SLS/SLM of aluminium alloy powders. The choice of aluminium alloy powders for this research is premised upon the challenge of overcoming the anticipated attendant problems of balling which is likely to occur during its SLS/SLM processing. It is this balling problem which is thought to have made aluminium powders and its alloys an unattractive candidate material for investigation by SLS/SLM researchers. Meanwhile, it is expected that if this project is feasible, it will open the door of opportunities for producing commercial aluminium powders for fabricating automobile and aerospace components via SLS/SLM process. Therefore, this research aims to investigate the feasibility of overcoming the balling problems in SLM/SLS processing of aluminium powders with a view to producing fully dense parts with desirable physical, microstructural and mechanical properties. In supporting this research, both process parameters and powder properties that are likely to affect the performance of direct SLS/SLM processed aluminium alloy parts have been identified. The rationale is to

provide a detailed empirical study that investigates the appropriate processing window for aluminium and its alloyed powders with a view to determining a suitable powder that can generate a desirable sintering response for the direct SLS/SLM process. For the most appropriate processing window for SLS/SLM of aluminium powder, conditions where melt pool stability, repeatability, and reproducibility are optimised have been identified. The candidate aluminium powder was then taken for further improvement by blending it with other aluminium powders of varying particle sizes and distribution as well as in different component ratios. This allows for the effect of particle size distribution and component ratios on the powder bed thermal conductivity; which influences the development of densification mechanism and microstructure in SLS processed blended powders; to be investigated. Both the amounts of liquid phase present during SLS/SLM process as well as the variation in powder bed thermal conductivity have been identified as factors that influence the microstructural evolution in SLS/SLM fabricated components (Simchi 2004, Gu & Shen 2007a, b). Meanwhile, given that the SLS/SLM of aluminium powders may be feasible, the literature review section (chapter 2) seeks to determine the nature of materials, techniques and methodology that would be needed to maximise the chances of success in this investigation.

1.4 Thesis Outline

This thesis consists of nine chapters. Chapter one introduces the background of this study and the project overview of this research work. Chapter two starts with a brief summary of the literature survey. It then considers the application of powder metallurgy (P/M) and SLS/SLM process to various materials, as well as the assorted physical phenomena, processing parameters, and powder properties governing the sintering behaviour or the nature of the melt pool obtained in metallic powders processed by the direct SLS/SLM manufacturing technique. It also goes on to discuss how the physical mechanisms and processing parameters controlling the direct SLS/SLM process could affect the properties of components made in alloyed aluminium powders. It concludes by defining the key findings from the review of research publications with a view to outlining the aims and objectives of this research work. Chapter three gives a description of materials and experimental methods. This includes the procedure for powder blending, laser power calibration, material characterisation, operation of the sinter station for building both single and multiple components, as well as microstructural and mechanical characterisation of the samples. Chapter four presents and discusses the results of the preliminary investigation on the

single layers of the powders by examining the effect of the process parameters, powder particle shape and chemical composition on the surface morphology and spheroidisation phenomenon in SLS processed aluminium powders. Chapter five presents the results and analysis of the studies on the multiple layers of aluminium powders by examining the effect of the powder and process parameters on the sintered properties, oxide disruption, and liquid phase sintering development in the laser sintered aluminium powders. Chapter six looks into the effect of the component ratio and particle size of the bimodal additive binders on the processing condition, densification and microstructure of the suitable aluminium powder for the direct SLS process. Moreover, the influence of the trimodal powder particle distribution on the densification mechanism, microstructural and mechanical properties of the developed model powder for the direct SLS process is highlighted in chapter seven. Chapter eight discusses the implications of the results obtained so far for the direct SLS of aluminium powders. Finally, in chapter nine, inferences are drawn from the findings of this work and recommendations for future direction in the research of the direct SLS of aluminium are made.

1.5 Conclusion

The background to this study, project overview, and the thesis outline had been described. Reservations associated with use of terminologies for describing SLS/SLM of metals among researchers had been highlighted with the classification of laser-based consolidation mechanisms depending on the material component system and the choice of laser processing parameters employed. Aluminium alloy powders, a material bedevilled with problems of balling associated with its SLM/SLS processing had been chosen for investigation with a view to exploring the feasibility of producing automobile and aerospace components via SLS/SLM process.

CHAPTER TWO LITERATURE REVIEW

2.1 Introduction

This chapter primarily assesses the current prospects and challenges in the SLS/SLM processing of metal powders in order to identify a metal powder worth exploring for further research with a view to improving its processability and properties. This has been achieved by reviewing the available literature in the specialties SLS/SLM, pulse electric current sintering (PECS), and powder metallurgy (P/M) processing of ferrous and non-ferrous metallic powders as well as composites. The relevance of physical phenomena such as oxidation, wettability and epitaxial solidification in the direct SLS/SLM processing of metals has been considered. The effects of processing and material parameters in the densification mechanism and the development of microstructure in SLS/SLM processed parts have been presented. Finally, a summary of the key findings of this chapter is provided in an attempt to formulate the projects' aims and objectives.

2.2 Selective Laser Sintering (SLS)

The process of selective laser sintering (SLS) was developed at the University of Texas at Austin between 1987 to 1992. SLS allows the generation of complex 3-D parts by fusing together successive layers of powder material on top of bed of powder pre-heated to a temperature just below the material's melting temperature (Agarwala *et al.* 1995, Zhu *et al.* 2003b). Consolidation was obtained by processing the selected areas on the powder bed by using the thermal energy supplied by a focussed laser beam (Figure 2.1). Using a beam deflection system (galvano mirrors F), each layer is scanned according to its corresponding cross-section as calculated from a CAD model. Pre-heating the powder bed prior to laser scanning reduces thermally induced stresses that result in curling of layers, thereby improving inter-particle bonding or melting across the layers (Agarwala *et al.* 1995, Zhu *et al.* 2003b). Any portion of the powder bed that does not feature in the 2-D slice is not scanned by the laser beam. The unscanned area remains unconsolidated (A), thus acting as a natural support for overhanging features created on subsequent layers. When a layer is completed, the powder delivery mechanism (B and E) deposits fresh powder over the powder bed (A) and the process is

repeated with each newly deposited layer fusing upon the substrate layer. Having completed all the slices, the fabricated part is removed from the build chamber (C) and, thereafter, the unconsolidated powders are removed. The deposition of successive powder layers with a typical thickness of 50 to 200μm has been realised using a powder deposition system (Simchi & Pohl 2004). SLS machines vary, for instance, in the mode of powder deposition (roller or scraper), the sintering atmosphere (Ar or N_2) and in the type of laser they use (CO_2 laser, lamp or diode pumped Nd: YAG laser, disk or fibre laser). Table 2.1 gives details of some of the commercial machines in the market for fabricating parts using SLS/SLM technique. The feasibility of producing metal parts directly by SLS/SLM has been demonstrated in various metal systems such as copper-based powders (Zhu *et al.* 2005; Tang *et* al. 2003, Gu & Shen 2008c); iron-graphite powder mixtures (Simchi & Pohl 2004); alloyed-steel powder (Dewidar *et al.* 2003, Rombouts *et al.* 2006); iron powder (Simchi & Pohl 2003); and mixed iron-copper (Zhu *et al.* 2003b). Most of the SLS/SLM processed parts have been employed for applications such as medicine, transportation, sports, and tooling. Table 2.2 presents a summary of the merits and drawbacks that SLS/SLM processing of metals possesses over other conventional production techniques. With a brief overview of the SLS/SLM process already gained, its main process variants shall now be considered.

To build metal parts via SLS/SLM, both *direct* and *indirect* approaches have been adopted by various researchers. Before proceeding further, it should be noted that there is significant disparity between the definitions of each of these approaches adopted by different SLS/SLM specialists on the basis of the consolidation mechanisms (section 1.3). For instance, Uzunsoy & Chang (2005) agreed with Simchi *et al.* (2001) in regarding indirect SLS as sintering the base metal powder mixed with a polymeric binder with a low energy laser beam to produce a green part. After the sintering stage, the polymer is debinded and post-processed via infiltration in a furnace with a low–melting point alloy in order to enable the component produced attain full density. The main advantage offered by indirect SLS with a polymer binder, over SLM, is that it can be used to process any material. The demerit is that a post-processing step to remove the binder is always required, and that, prior to any further post-processing steps, the porosity is generally high (Dalgarno & Wright 2001). Dewidar *et al.* (2003), while agreeing with Simchi and co-investigators as well as Uzunsoy & Chang (2005) on the definition of indirect SLS, approached direct SLS of high-speed steels by directly heating the steel particles with the laser beam and thereafter infiltrated it with bronze in order to enhance the mechanical properties of the components. Furthermore, Tang *et al.* (2003) described direct SLS as sintering the metal powder directly by the high-energy laser beam to achieve 100% density in one step as opposed to indirect SLS where the

high melting point structural material is coated with a low melting point metal and, in reality; it is the coating material which is sintered by the laser beam thereby bounding the structural particles together. This use of a composite powder blend consisting of two or more immiscible alloys of different melting point has also been described as *binary* liquid phase SLS.

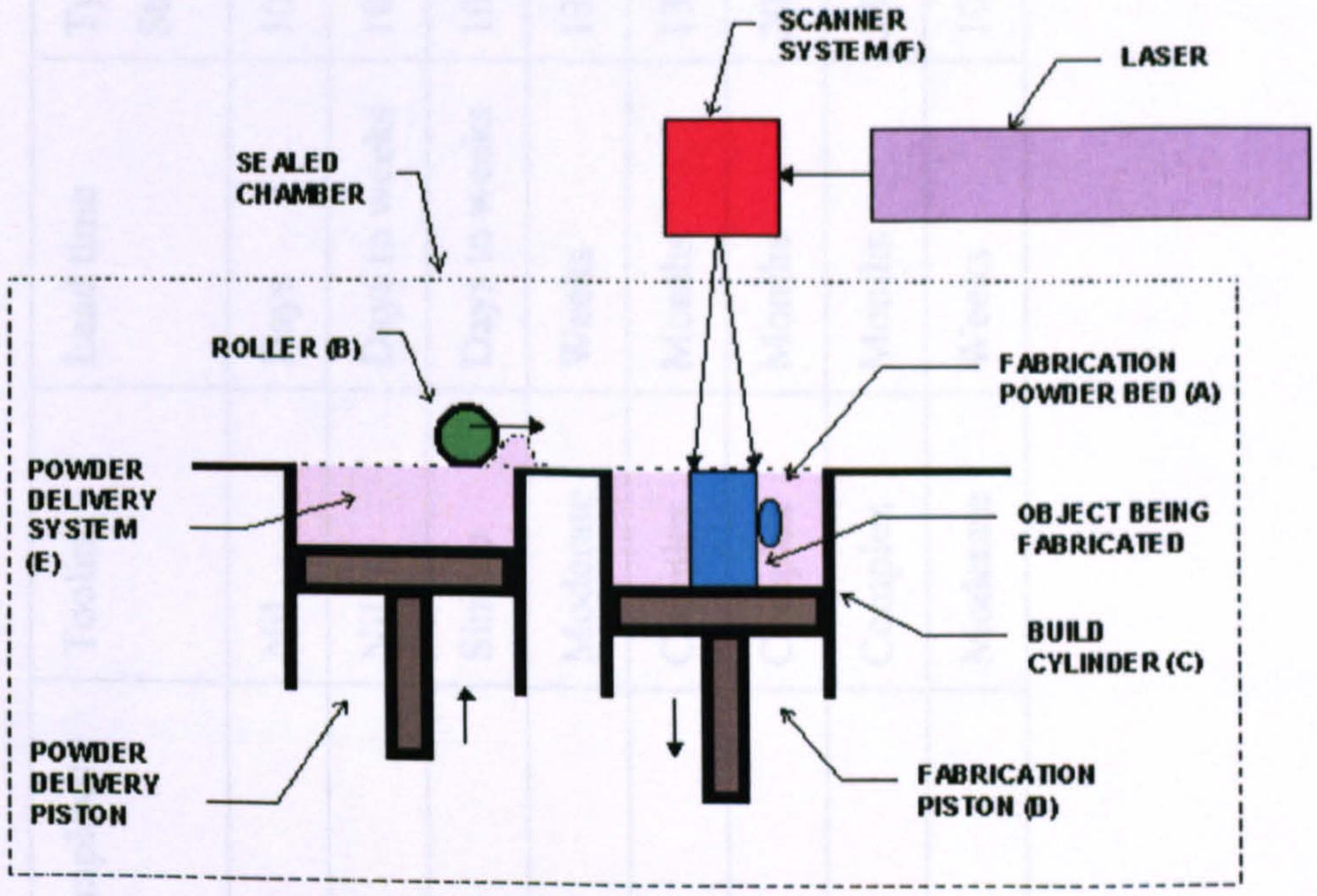

Figure 2.1: Direct selective laser sintering process. Source: Worldwide Guide to Rapid Prototyping (after http://home.att.net/~castleisland/sls.htm)

Table 02.1: Commercial Machines and Lasers for SLS/SLM of Metal Powders (after Santos et al. 2006).

Machines	Company	Process	Laser	Power
Sinter station 2000/2500	DTM	SLS	CO_2	50 W
EOSINT 250	EOS	SLS	CO_2	200 W
EOSINT 270	EOS	SLS	Ytterbium fibre laser	200 W
LUMEX 25C	MATSUURA	SLM	Pulsed CO_2	500 W
TrumaForm LF 250	TRUMPF	SLM	Disk laser	250 W
Realizer	MCP	SLM	Fibre	100 W

Table 02.2: Comparative analysis of parts fabricated by SLS/SLM and other traditional production processes (after ASM Specialty Handbook 1997; ASM Handbook. 1997; Schaffer & Apelian 2000; Kalpakjian & Schmid 2001).

Techniques	Min. mass (g)	Max. mass (g)	Min. section Thickness (mm)	Shape complexity	Tooling	Lead time	Typical Tensile Strength (M Pa)
SLS/SLM	5	5,000	0.5	5 Highest	Nil	Days	100- 230
Machining	1	No limit	0.1	4 High	Nil	Days to weeks	100- 600
Investment casting	5	30,000	0.5	4 High	Simple	Days to weeks	100- 280
Sand casting	50	No limit	3	3 Fair	Moderate	Weeks	130- 480
Powder metallurgy	1	1,000	1.5	3 Fair	Complex	Months	130- 400
Die casting	<50	50,000	1	2 Low	Complex	Months	200- 360
Closed die forging	10	No limit	3	2 Low	Complex	Months	330- 660
Extrusion	1,000	No limit	1	1 Lowest	Moderate	Weeks	100- 400

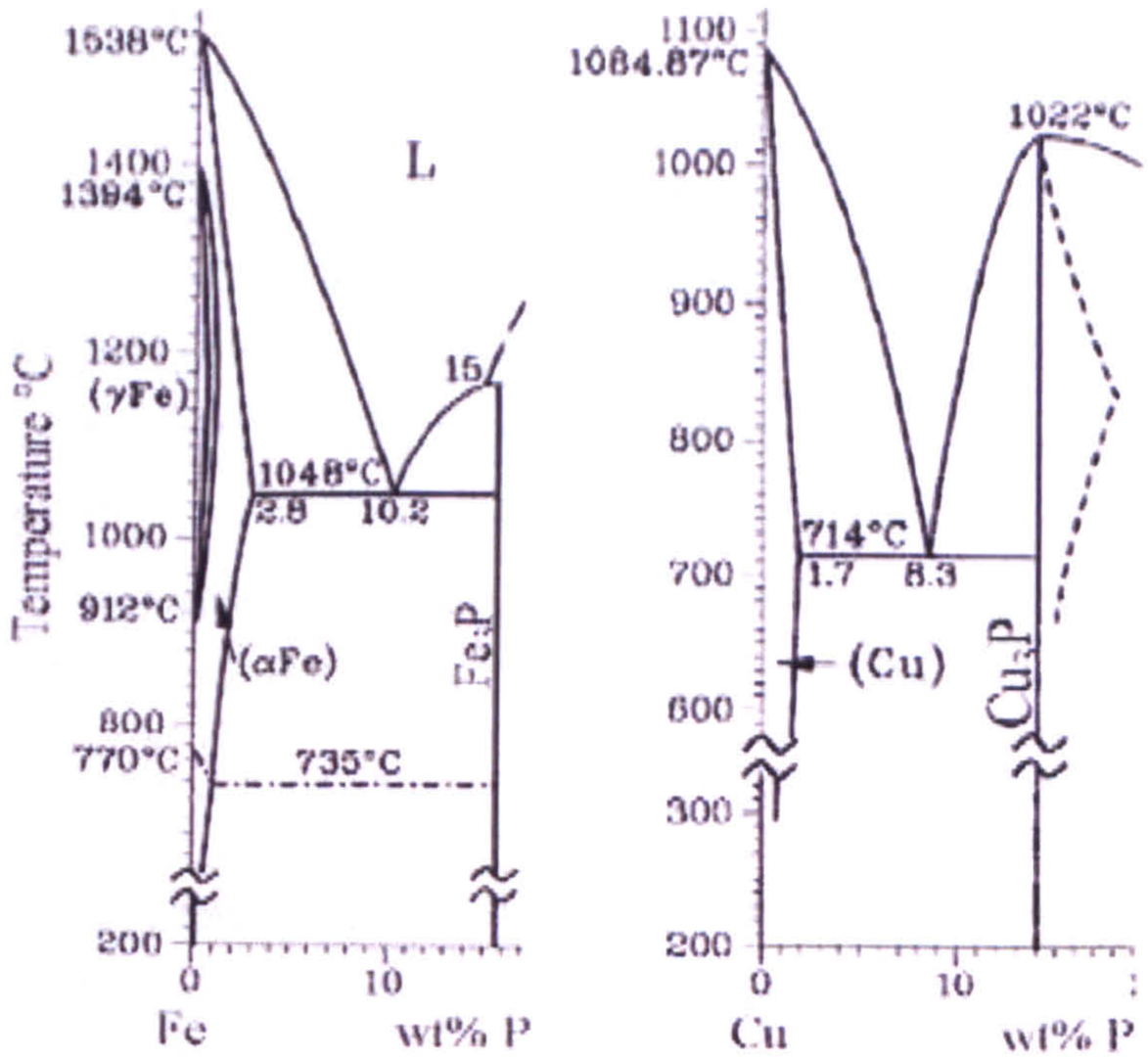

Figure 2.2: Phase diagrams of Fe-P and Cu-P showing the temperature lowering effect of the added P (after Kruth et al. 2003).

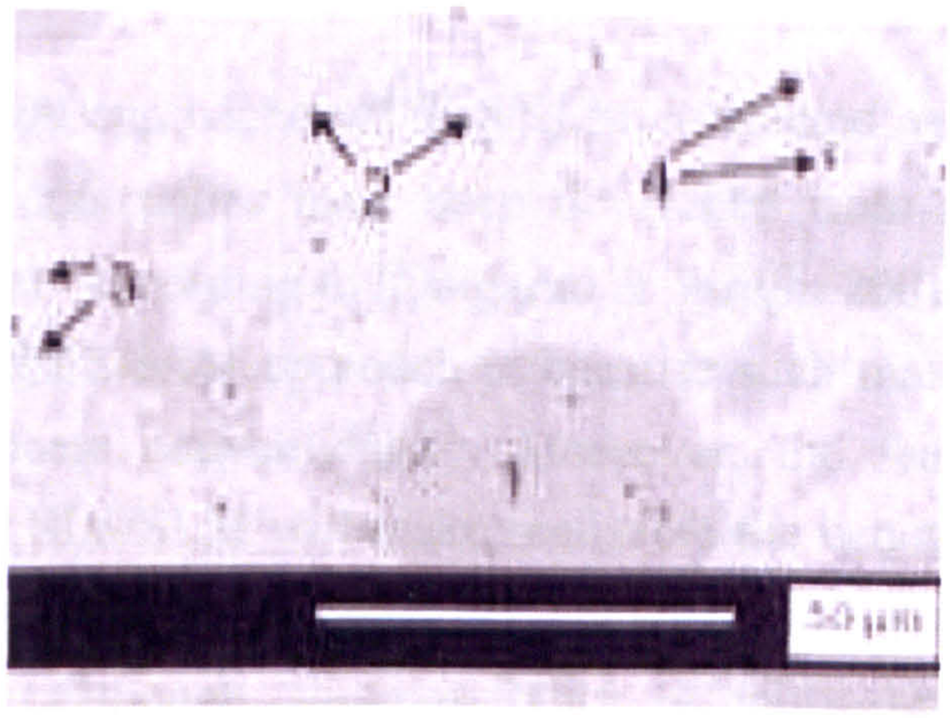

Figure 2.3: Micrograph of multiphase steel powder: (1) unmolten Fe powder particles, (2) a high melting P-poor phase, (3) low melting point P-rich phase (no. 3), and (4) porosities (after Kruth et al. 2003).

Figure 2.2 shows the application of the binary liquid phase to the SLS processing of a multiple phase steel powder (Fe-Fe_3P-Ni-Cu), having similar composition as DirectSteel 50V1 powder, with a view to attaining full density (Kruth *et al*. 2003). The lower melting point additive Fe_3P or Cu_3P improves the energy efficiency of the SLS process when added to the ferrous powder because it lowers the melting point of pure iron, thus requiring lower laser energy density. This is demonstrated by Figure 2.2 in which pure Fe has been alloyed with phosphorus (P). Consequently, the addition of P

lowered the melting point of pure Fe (1,538 °C) to the eutectic temperature of the Fe-P (1,048 °C). Furthermore, the dissolution of P in Fe is thought to have reduced the surface tension of the melt, thereby resulting in improved wetting behaviour (Figure 2.3). Micrograph of SLS processed Fe-Fe_3P-Ni-Cu suggests that not all the powder particles are molten (Figure 2.3). According to Kruth *et al.* (2003), the final sintered part consisted of some unmolten Fe powder particles (no.1), a high melting point phase with no significant amount of P (no. 2), low melting point P-rich phase (no. 3), and some porosity (no. 4). They concluded that the process could not be described as "full melting" or SLM; therefore, the name "LPS or partial melting" or SLS is preferred.

Although, selective laser melting (SLM) employs laser beam to consolidate metallic powders in an attempt to achieve 100% density (SLM) in one step, its demerit include the occurrence of balling which inhibit interparticulate melting as a consequence of the presence of the surface oxide film on the surface of powder particles which prevent wettability of the liquid metal with its solid form due to the initiation of Marangoni convection (Kruth *et al.* 2005, 2007). Another setback to SLM is the occurrence of part distortion or layer delamination due to high temperature gradients (Kruth *et al.* 2005, 2007).

In assessing the different approaches of SLS/SLM elucidated earlier on in this section, it is clear that some approaches have been developed from a desire to produce a specific material system. According to (Dalgarno & Wright 2001), the desire to process materials using direct SLS/SLM approach is because such materials may be difficult and expensive to process conventionally. Moreover, the feasibility of fabricating metallic parts in direct SLS/SLM will make realisable the benefits of time saving, and cost reduction over the SLS with a polymer binder by not requiring de-binding and post-processing steps. Although, the possibility of fabricating parts in SLS/SLM depends on fundamental materials issues, the processing conditions which allow direct SLS/SLM, and the size of the component which is to be fabricated; it had been noted that SLS with polymer binder is likely to continue to offer the processing of widest range of materials, because it concentrates on only using laser scanning to generate shape, with a wide range of subsequent processes available to generate strength and consolidate the part (Dalgarno & Wright 2001). In considering binary liquid phase SLS, removing the need for the debinding step requires the use of a low–melting point metal to act as a binder for a high melting point material. Therefore, on the basis of material component system (see section 1.2), SLS is applicable to different binder and structural materials (separate grains, composite grains, and coated grains); and no distinct binder and structural materials (single phase partially molten and fusing powder

mixture) whereas SLM is feasible in single component, single material powder; single component, alloyed powder particles; and fusing powder mixture (Kruth *et al.* 2005). In summary, direct laser sintering or full melting (SLM), binary liquid phase SLS, and indirect laser sintering incorporating polymeric binding and debinding stages followed by infiltration are hereby identified as the main process variant of SLS/SLM technique.

2.3 An Overview of Progress in Selective Laser Sintering/Melting of Metals

The primary aim of this section is to collate and analyse relevant information on the application of the SLS/SLM process to ferrous, wear resisting, composites and light metallic materials with a view to critically assessing the current prospects and challenges in the SLS/SLM processing of these engineering materials. This will identify areas worthy of further exploration in order to improve materials' processability and properties. Moreover, this analysis will be helpful in understanding the appropriate process variants of SLS/SLM which occur in each material component system.

2.3.1 Ferrous Materials

The specialty of rapid tooling has been identified as one of the most promising areas for the application of SLS/SLM (Asgharzadeh & Simchi 2005). High speed steels and stainless steels characterised by carbide structures, that provide improved hardness, strength, and wear resistance, are suitable materials for tooling applications such as cutting tools, fine blanking tools and dies (Bayer *et al.* 1998; Niu & Chang 2000). The traditional methods of manufacturing these materials such as casting and hot working have resulted in the problem of coarse grain structures and carbide coarsening at the grain boundaries as a consequence of low cooling rates associated with these processes (Niu & Chang 2000, Asgharzadeh & Simchi 2005). This problem reduces the strength of these steels thus causing premature failure under conditions in which parts are subjected to high stresses (Niu & Chang 2000). To address this challenge, a low cost powder metallurgy (P/M) sintering route had been employed to produce parts with improved mechanical properties (Brewin 1991; Wright *et al.* 1995; Gomes *et al.* 1995; Zhou *et al.* 1995). The main benefit which accrues from the P/M sintering route is the fine and homogeneous microstructure in which segregation is reduced to the minimal degree thereby resulting in improved hardness, strength and wear resistance (Pinnow & Stasko 1998).

In the P/M route, sinterability of high speed steel powders is strongly dependent on the sintering parameters, the powder properties and sintering atmosphere with full densification being obtained via the supersolidus liquid phase sintering in a vacuum atmosphere (Wright *et al.* 1995). In supersolidus sintering, the liquid forms within each particle of the pre-alloyed powder once above the solidus temperature, with each particle consequently undergoing fragmentation and re-packing thereby giving a homogeneous distribution of liquid (German 1985, 1998).

Meanwhile, SLS/SLM of high speed steel powders continues to generate considerable interest because of the advantages the process offers, as explained in Section 2.2. Studies on high speed steels (HSS) have been carried out by Niu & Chang (1998, 1999a, 1999b, 2000), Simchi *et al.* (2001), Morgan *et al.* (2002), Dewidar *et al.*(2003), and Sercombe (2003b), while Hauser *et al.* (1999a, 1999b), and O'Neill *et al.*(1999) investigated the processability of stainless steel powders using SLS. The role of laser sintering parameters, powder particle morphology, and the powder's oxygen content in the sintering response of laser sintered M3/2 and M2 high speed steel powders has been described by Niu & Chang (1998, 1999a, 1999b, 2000). Their studies revealed that the transition from solid phase sintering to liquid phase sintering to full melting/solidification occurred as laser power was increasing at low scanning rates during the SLM processing of these materials. Observation of the different surface morphologies (Figure 2.4) of the melted tracks at high laser power and low scanning rates suggested that the melt pool was affected by Marangoni flow as a consequence of variation in oxygen content and particle shape of the high speed steel powders (Niu & Chang 1998, 1999a, 1999b, 2000). For water atomised high speed steel powders containing irregularly shaped particles with high oxygen content, increased surface tension with increasing temperature induced radially inward fluid flow from the edge to the centre of the melt pool resulting in deep and narrow scan track (Figure 2.4a, b, and c) whereas, gas atomised powders containing spherical particles and having lower oxygen content formed a good bonding between the scan tracks as the fluid flow from the centre of the beam to the edge of the melt pool (Figure 2.4d). Furthermore, the agglomerate diameter increased with increasing laser power or decreasing scan rates. They observed that SLS of powder particles with diameter less than 38μm gave rise to low sintered density at low laser power range in which liquid phase sintering (LPS) occurred as a result of the high oxygen level.

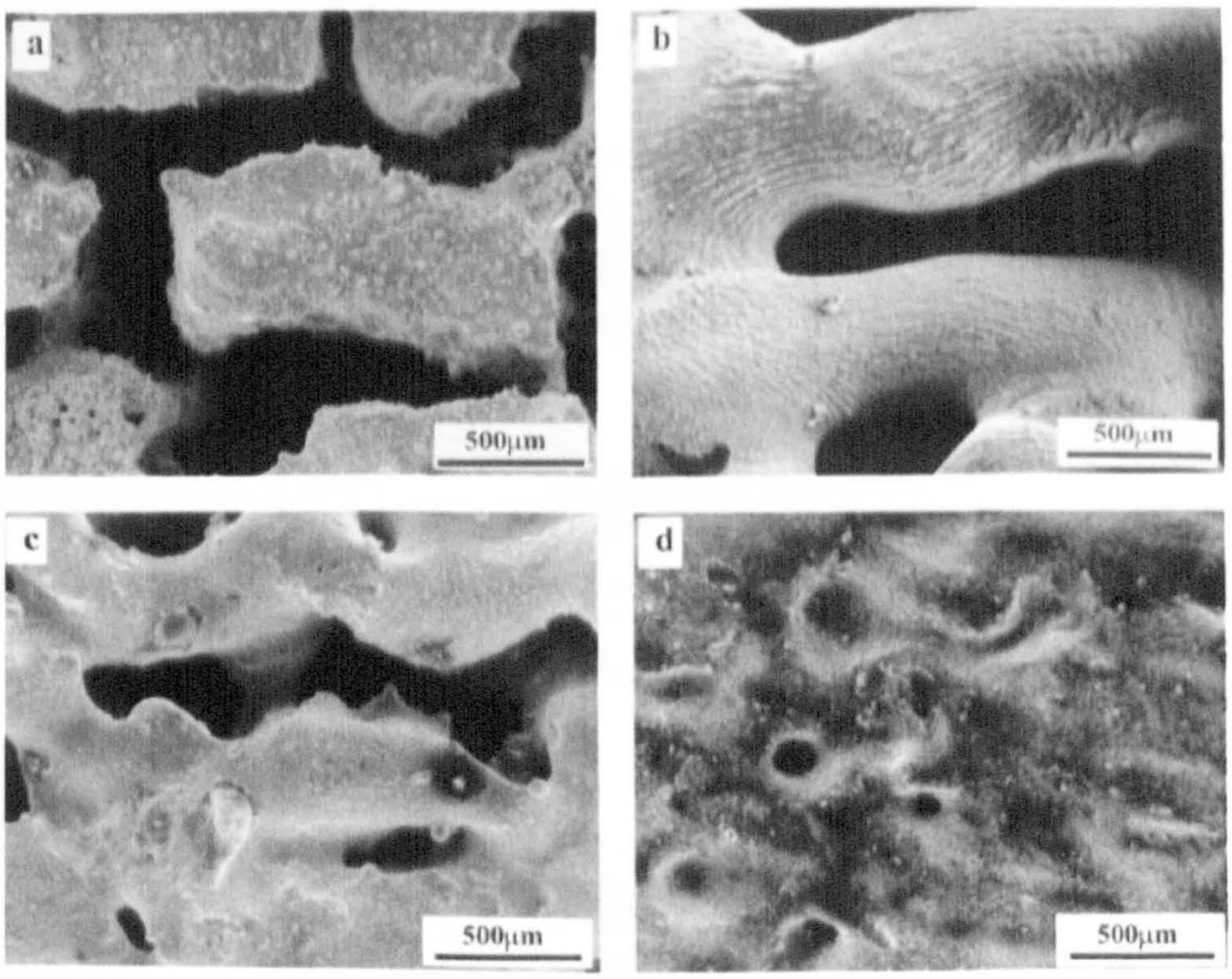

Figure 2.4: SEM images of laser sintered HSS surfaces using laser power of 30 W, scanning rate of 1.00 mm/s and scan line spacing of 0.15 mm: (a) as milled M3/2-11, (b) water atomised M3/2-32, (c) water atomised M3/2-100, (d) gas atomised M2-117 (after Niu & Chang 1999a).

They suggested that the surface tension gradient remained a significant factor causing the spheroidisation of the tracks or the break up of the liquid cylinder when single layers were constructed on the powder bed substrate. Childs *et al.* (2004) reported the effect of laser power and scan speed when a CO_2 laser beam was incident on beds made from M12 and H13 tool steels and 314S-HC stainless steel powders. Their results enabled boundaries between regions of different track formation to be explained in terms of melt surface temperature gradients, melt pool length to diameter ratio instabilities, and transitions from partial to complete melting. In conclusion, they elucidated that the resulting tracks from the rastered metallic powder bed are better understood in the context of selective laser melting build strategies.

Prior to the work of Childs and co-investigators, the effect of build strategies on the properties of laser re-melted steel powders had been explored by Morgan *et al.* (2002) who noted that the occurrence of porosity within the laser re-melted parts compromises the material's structural integrity and thereby its properties. In order to obtain components with more reliable structural integrity, and properties comparable to conventionally produced parts, they developed an odd-even knitting, normal consecutive layers scanning strategy (Figure 2.5) that produces laser re-melted stainless steel (316L) parts which have porosities of <1%.

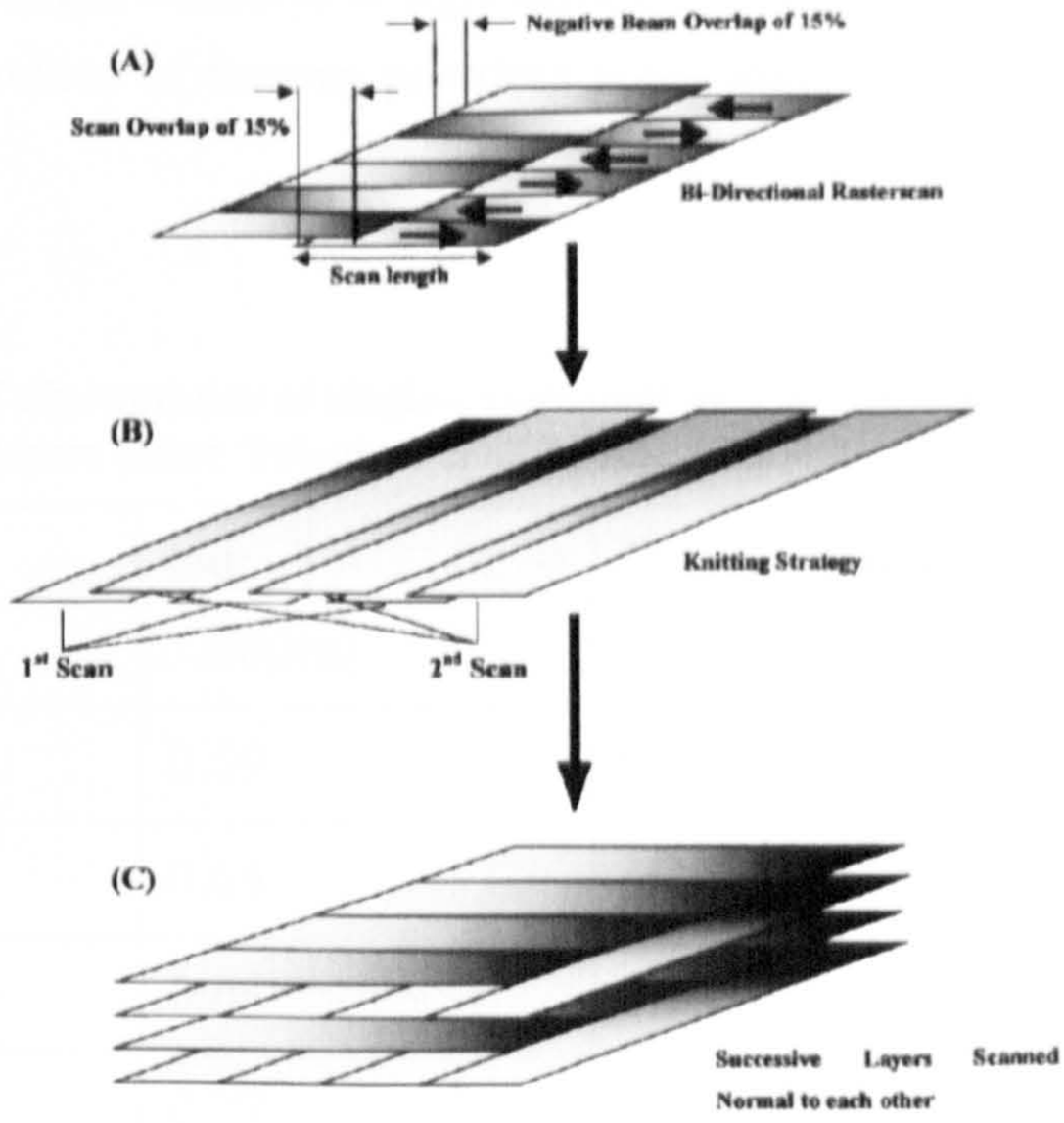

Figure 2.5: Development of the scanning strategy for the production of 99% dense 316L stainless steel. (A) bi-directional rasterscan strategy with changing beam direction and bean overlap, (B) the knitting strategy of the scan-units, and (C) how layers are scanned normal to each other to reduce porosity (after Morgan et al. 2002).

The studies of Hauser *et al.* (1999a, 1999b); Niu & Chang (1998; 2000), and Dewidar *et al.* (2003), have all used a CO_2 continuous wave laser beam, which generated fairly high densities (about 55-75% of the theoretical density) for single layer tracks. However, O'Neill *et al.* (1999) and Morgan et al. (2002) utilised a Nd-YAG laser with Q-switched nanosecond pulsing for fabricating multiple layers. This pulsing generates high power densities which can lead to rapid vapourisation of the powder material, generating extreme pressures and a recoil effect which acts to flatten and widen the spherical melt bead, thereby improving the cohesive structure of layers. Meanwhile, Dalgarno & Wright (2001) noted that proper controlling of the pulsing can result in densities of up to 90% of the theoretical density. These findings indicate that the type of laser employed for the SLS/SLM process determines to a very great extent, the behaviour of the powdered particles of ferrous materials during laser scanning. The basis for these findings could be attributed to the dependence of the laser absorptivity of the investigated material on the wavelength of the laser type in use (Table 2.3), as well as the resultant consolidation mechanism of ferrous materials being a function of the energy density delivered as a consequence of laser type and the laser mode. Both the material's laser absorptivity and the applied energy density determine the nature of

the melt pool size. Table 2.3 reveals that the absorptance of metallic materials increases with decreasing wavelength which is in agreement with the findings from the literature on the SLS/SLM behaviour of ferrous powders when laser scanned with either CO_2 or Nd:YAG lasers.

Table 2.3: Comparison of absorptance of single-component and two-component metallic powders using Nd:YAG and CO_2 lasers (after Tolochko *et al.* 2000).

Material	Nd: YAG (λ = 1.06μm)	CO_2 (λ = 10.6μm)
Cu	0.59	0.26
Fe	0.64	0.45
Sn	0.66	0.23
Ti	0.77	0.59
Pb	0.79	-
Cu-10Al (wt.%)	0.63	0.32
Fe-3C-3Cr-12V + 10TiC (wt.%)	0.65	0.39
Fe-0.6C-4Cr-2Mo-1Si + 15TiC (wt.%)	0.71	0.42
Fe-1C-14Cr-10Mn-6Ti + 66TiC (wt.%)	0.79	0.44

Murali *et al.* (2003) investigated the direct SLS of an iron-graphite powder mixture with a pulsed Nd-YAG laser while Asgharzadeh & Simchi (2005) employed a continuous wave CO_2 laser to process a M2 HSS/graphite mixture. Findings from both of these research groups revealed that the product of laser sintering of iron powder is significantly different from that obtainable via a conventional sintering technique. Both research groups confirmed that the addition of graphite to the ferrous powders exacerbated the heterogeneity of the microstructure as evident by its porous nature as well as the microhardness results obtained for the sintered specimen. Chen *et al.* (2004) noted that a high carbon content in direct laser re-melted M2 tool steel powders increased porosity. To address this problem, they introduced an alloying element, boron, into iron powders which increased the width of the scanned tracks for a given set of laser parameters. Thus the boron addition to iron reduces its melting point and

changes its surface properties. Consequently, they discovered that it reduced the tendency of the tracks to form balling, thus increasing the density of the part. Upon the addition of titanium, they found that there was improvement in the bonding of the sample to the substrate, although the extreme hardness of the laser remelted iron powder as well as its processability had been significantly compromised, thereby counteracting the effect of boron as evident by the reduction in the matrix hardness (see Figure 2.6 and Table 2.4).

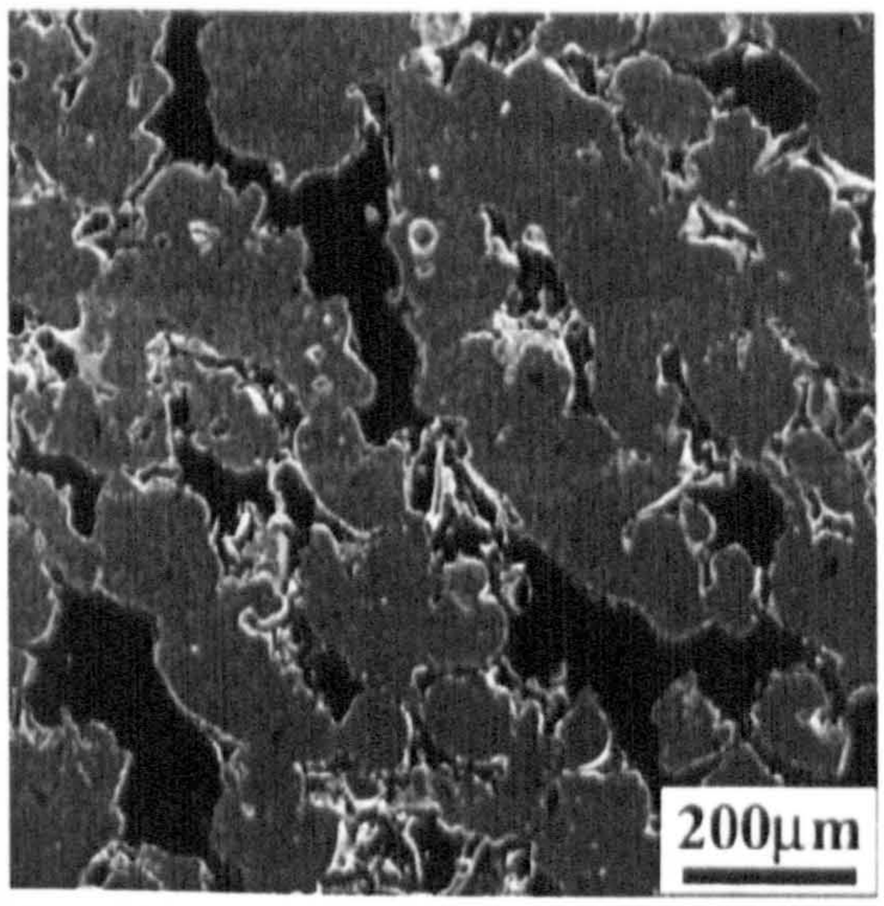

Figure 2.6: SEM image of Fe –4%B– 9%Ti scanned sample (after Chen *et al.* 2004).

Table 2.4: Vickers microhardness of laser remelted iron powder samples containing boron and titanium (after Chen *et al.* 2004)

	Microhardness ($HV_{0.98N}$)	
Phase	Fe-4%B	Fe-4%B-9%Ti
Matrix	838.2	610.0
Phase 1	1227.4	929.9
Phase 2	2074.3	2015.0

Further to this, Rombouts *et al.* (2006) extensively investigated the influence of carbon, silicon, titanium, and copper on the binding and melt pool stability in the selective laser melting (SLM) of ferrous powders. They discovered that the addition of carbon promotes the formation of spherical pores due to the entrapment of carbon monoxide (CO) or carbon dioxide gas bubbles while simultaneously reducing the oxygen content in the SLM processed parts. As a consequence the surface roughness was noted to have

improved for the single layer parts, whereas, it was exacerbated on the 3-D parts. The exacerbation of surface quality on the 3-D parts had been attributed to the entrapment of carbon monoxide (CO) or carbon dioxide (CO_2) gas formed by the oxidation of carbon. Although, the addition of silicon and titanium diminished the amount of spherical pores, while increasing the amount of irregular pores, nevertheless, it was noted to have produced an enlarged melt pool and increased its propensity to spheroidise, thus resulting in poor surface quality of parts. Their diminishing influence on the surface quality of parts is as a consequence of their predisposition to form oxides and carbides. It was discovered that copper had not significantly affected the melt pool behaviour of SLM processed ferrous powders. Copper also lowered the absorptivity of the ferrous powders as a consequence of its high reflectivity for Nd:YAG laser beam when added in its pure form, thereby reducing the densification of ferrous powders (Rombouts *et al.* 2006).

Simchi *et al.* (2001) observed that careful manipulation of the particle shape, diameter and size distribution as well as the chemical composition of the different powder constituents can increase the sintered density of powdered materials for the direct SLS process. They reported densities of 90-97% of theoretical for the SLS processed material, with the feasibility of attaining 99% theoretical density after a subsequent conventional sintering technique which homogenises the microstructure and removes residual stresses and porosity.

The available literature reviewed in this section suggests that a tremendous amount of improvement in the SLS/SLM technology of ferrous powders has been achieved. Nevertheless, it must be pointed out that the reported results in the cited literature are lacking in comparability as a consequence of various types of laser employed, powder properties, different heights of test samples, and alloy composition. It has been emphasised that the control of the surface tension gradient by both powder and processing parameters remains a significant factor influencing the spherodisation of the tracks or the break up of the liquid cylinder during the SLS/SLM of ferrous powders (Niu & Chang 1998, 1999a, 1999b, 2000). Moreover, the laser processing parameters, the chemical composition, particle size and size distribution of the powders, and the nature of atmosphere employed for laser sintering are among the factors influencing both the physical and mechanical properties of SLS/SLM processed ferrous powders. Nevertheless, at present, the SLS/SLM technique of ferrous powders could be said to be essentially dependent on empirical knowledge devoid of a strong theoretical metallurgical basis due to the tendency to interchange the word "sinter" and "melt."

The lack of a strong metallurgical understanding could be explained by the complex nature of SLS/SLM technique, which exhibits multiple modes of heat, mass and momentum transfer, in addition to chemical reactions. Perhaps, a lack of systematic investigations with model alloy systems is another consideration that hinders an insightful understanding of metallurgical processes controlling the SLS/SLM processing of ferrous metals. Therefore, significant research and development activity which adopts microstructural manipulation of the various steel alloys would be worth exploring for specific applications in order to obtain the full potential that SLS of ferrous materials offers. Table 2.5 summarises the results obtained for and comments on different SLS/SLM experiments of ferrous powders.

2.3.2: Wear Resisting Materials

Hard metals such as WC-Co and TiC-Ni are used as machining tools or abrasion-resistant parts because of their excellent tensile strength, hardness, wear resistance and elongation properties. Today, they are regarded as new materials for the SLS process (Das *et al.* 1998b; Wang, *et al.* 2002). Generally, hard metals are produced by a conventional P/M press and sintering method, which may require expensive and complex 3-D shaped tools e.g. die and punch. This technique is very productive and can achieve a fully dense structure but it is not suitable for short production runs and complex shapes. Hard metals are also used in thermal spray techniques to improve the wear resistance of a surface. It is very useful and effective in some applications, but the thickness is limited because of flaking and delamination of the hard coating. Some researchers have attempted the fabrication of 3-D objects by laser cladding but encountered problems of limited shapes and low productivity (Maeda & Childs 2004).

Deckard *et al.* (1993); Zhuoxing *et al.* (1999); Das *et al.* (1998b, 2000); Boivie (2000); Wang *et al.* (2002); Zhu *et al.* (2003a, 2003b); Murali *et al.* (2003); Kruth *et al.* (2004); and Zhu *et al.* (2004a, 2004b) have applied SLS to the manufacturing of wear resisting materials. For example, Das (1998b); and Deckard *et al.* (1993) employed binary liquid phase SLS in which a mixture of ceramics particles (WC) remain solid throughout the production cycle and the metal particles (Co) were melted by the laser beam. The sintered parts in which binary liquid phase SLS was employed could not attain full density because adequate quantity of liquid phase for filling up the inter-particulate pores could not be formed. As a result, post-infiltration of porous green parts was incorporated into the process. The findings revealed that properties such as density, hardness, impact toughness, and wear resistance of the laser sintered specimen are superior to the same materials which had been conventionally sintered. The laser

sintered hard materials are observed to have homogeneously distributed phases. The even dispersion of WC particles within the fluid cobalt phase could be ascribed to the re-arranging influence of the WC particles within the cobalt matrix in which significant densification result from particle re-packing concurrent with liquid formation. Moreover, the viscosity of the liquid cobalt phase and the wetting characteristics of the WC particles with the cobalt binder were noted to have been adequate for attaining near full density (~99%). With regard to the relationship between the energy input per unit area and the localised material densification, a higher sintered density was obtained by employing high scanning rates and increased laser power due to the formation of increased amount of liquid phase with sufficient viscosity. Maeda & Childs (2004) demonstrated the possibility of producing WC-Co-bronze hard metal by SLS and infiltration process. The functional property as a hard coating against abrasive wear had been achieved to the same level as high carbon steel with the possibility of increasing it further by optimising the SLS process conditions. Table 2.6 presents the summary of the key findings on SLS investigation of wear resisting materials. It could be inferred that binary liquid phase SLS incorporating post-infiltration is ideal for fabricating wear resistant materials rather than SLM. Binary liquid phase SLS is ideal for fabricating these wear resisting materials such as cermets because they are usually made up of multiphase material components system having different melting points.

2.3.3 Composites

SLS of composites may be achieved via the employment of two different powders corresponding to the matrix and reinforcement desired in the end product (Vaucher *et al.* 2002); *in-situ* chemical reaction (Leong *et a*l. 2002); and post-infiltration of SLS processed parts (Sercombe and Schaffer 2004a). The two-component powder method has been applied to metal matrix composites (Simchi and Godlinski 2008; Gu and Shen, 2008a); ceramic matrix composites (Laoui *et al.* 1999) and polymer matrix composites (Zheng *et al.* 2006). A survey of the available literature has pointed towards the fact that the sintered density and properties of the SLS processed metal matrix composites and ceramic matrix composites are not as good as are found in the laser sintered polymer matrix composites. This has necessitated the use of sintering additives or the incorporation of an infiltration stage in an attempt to achieve full density in laser sintered metal matrix composites and ceramic matrix composites.

Table 02.5: Summary of key findings from experiments on SLS/SLM of ferrous powders.

Materials	Key findings.	Comments
Steel powders	Transition from liquid phase sintering to full melting/solidification with increasing laser power at low scanning speed is the dominant mechanism of SLS/SLM in these materials.	SLS/SLM occurs in single component and alloyed steels powders dependent upon the adoption of low or high energy density.
	Boundary between regions of different track formation explained in ter mms of melt surface temperature gradients, melt pool length to diameter ratio instabilities, and transition from partial to complete melting.	Processing parameters influences the regions of formation of SLS/SLM processing map.
	The development of an odd-even knitting, normal consecutive layers scanning strategy produced laser re-melted part having porosities of <1%.	Appropriate build strategies aids in eliminating porosities.
	CO2 laser types achieved 55 – 75% theoretical density whereas Nd-YAG laser achieved 90% theoretical density with proper controlling of the pulsing.	Laser type, spot beam size, and the amount of energy dissipated on the powder bed influence the consolidation mechanism in steel powders with Nd:YAG attaining full density in one step.
Iron-graphite and M2 HSS/graphite mixtures.	The addition of graphite to SLS processed ferrous powders exacerbated the heterogeneity of the microstructure.	Binary liquid phase sintering SLS occurs in this material component system.
Ferrous powders.	Boron addition increased part density whereas combined addition of titanium and boron compromised the hardness and the processability of SLS processed iron powders. Carbon addition promoted the formation of spherical pores. On the contrast, the addition of silicon and titanium increased the amount of irregular pores. Copper was found to have no influence on the melt pool behaviour of laser melted ferrous powders.	Alloying addition and powder properties influence the microstructure of SLS/SLM processed parts by controlling the surface tension.
	Attainment of high sintered density (90-97%) due to careful manipulation of powder properties such particle size and distribution, shape, and composition..	

Table 2.6: Summary of key findings on SLS of wear resisting materials.

Materials	Key findings	Comments
WC-Co mixture	Density, hardness, toughness and wear resistance superior to conventionally sintered materials.	Post-infiltration of porous green part incorporated into liquid phase SLS to attain 99% density.
WC-Co-bronze hard metal	Wear resistance comparable to high carbon steel.	SLS/Post-infiltration.

For example, in order to attain full density and enhanced functional properties in direct laser sintered ultra-fine WC-Co particulate reinforced Cu matrix, La_2O_3, a sintering additive which lowers the surface tension of the melt and enhances its densification mechanism, was added to the composite (Gu *et al.* 2007b). Furthermore, Laoui *et al.* (1999) were able to achieve full consolidation in WC-9wt% Co by incorporating infiltration with bronze.

Laser-initiated chemical reactions that have been used to process composites are selective laser reaction sintering (Birmingham *et al.* 1995), and self-propagating high-temperature synthesis (Slocombe & Li 2001; Shi *et al.* 2004). The role of the applied laser is to ignite and provide sufficient thermal energy to overcome the activation energy barrier of the reactants thereby yielding adequate thermal energy to form chemical compounds. In addition, this technique is preferred to the two-component powder method as a result of its inherent benefits in giving rise to fine and uniform distribution of compounds, improved consolidation and the release of exothermic energy that promotes the sintering response of the reactants. Birmingham *et al.* (1995) investigated and reported on gas/powder reactions, powder/powder reactions, and precursor decompositions as forms of selective laser reaction sintering with the aim of manufacturing suitable components. They discovered that *in-situ* reaction synthesis combined with SLS opened a new door of opportunity to extend the capabilities of binary liquid phase SLS to process high melting point ceramic and intermetallic materials. Slocombe & Li (2001) applied self-propagating high-temperature synthesis (SHS) in combination with SLS process to manufacture TiC-Al_2O_3 composites. They pointed out that by varying the amount of diluents within the initial reactants, modification of SHS can be achieved through controlled solid state combustion during

SLS in a thin layer. Therefore, by controlling the SHS propagation wave, it was possible to produce a complex part manufactured from TiO_2, Al, and C synthesis utilising the SLS process. Shi *et al.* (2004) developed a new self-heating metallic powder material for binary liquid phase SLS process by controlling the amount of heat during the laser-material interaction. The results revealed that there exist an optimal blending ratio of constituent materials in the newly developed metallic powder material and an optimal set of processing parameters for which the release of large amount of thermal energy and the SHS reaction are controllable with the attendant benefits of reducing the price and running expenditure of an SLS machine, thereby widening its versatility. Composites fabrication via SLS/SHS processing is gaining wide acceptance because the processing speed is fast, the technology is simple, the time and energy of the preparation are saved and manufacturing cost is low (Shi *et al.* 2004).

In the light of above discoveries, SLS appears promising for the processing of composites being one of the methods to build near net shape parts of 3D complexity. From the point of view of the quality of part produced, the main drawback of the technique resides in the inherent high level of residual porosity which requires a post treatment such as re-sintering or infiltration. Additionally, the surface finish obtained is rougher compared to parts obtained by powder compaction.

Table 2.7: Key findings on the SLS fabrication of Composites

Material	Key findings	Comments
WC-Co particulate reinforced Cu matrix.	Sintering additive (La_2O_3) improves densification by lowering the surface tension.	Binary phase SLS incorporated with post-infiltration aids full consolidation.
WC-9Co (wt.%)	Achieved full consolidation via post-infiltration with bronze.	
TiC-Al_2O_3	Used SHS combined with SLS for fabrication of parts.	This process speed is fast, the technology is simple, the time and energy of the preparation are saved and manufacturing cost is low.

Future work needs to concentrate on developing a better understanding of processes such as selective laser pyrolysis, SHS/SLS, and SLS/Metal Infiltration in producing nanocrystalline ceramics, ceramic-ceramic composites, and ceramic-metal composites with a view to improving the density and mechanical properties of parts. Table 2.7 above presents the key findings of this section.

2.3.4 Light Metals

The demand for light metal, particularly from the automotive and aerospace industries, has propelled researchers to investigate the feasibility of manufacturing components from the light metals via SLS/SLM technique. At present, very little work has been reported on the SLS/SLM of the light metals. This brief review will only consider the limited body of information available on the laser processing of titanium and aluminium alloys from powder with the aim of applying this to understand the effect of the direct SLS/SLM technique on the properties of light metal components produced. Other sintering or consolidation techniques such as pulsed electric-current sintering (PECS) and conventional powder metallurgy (P/M), for these materials will be explored for aluminium powders with a view to gaining relevant insights that may be applicable to the SLS/SLM of aluminium powders. Meanwhile, both titanium and aluminium alloy powders are being considered together in this section because they are both very reactive and form very stable oxides. Therefore, they both require the use of high vacuum or high-purity inert gas atmosphere for their processing. Titanium, unlike many metals, is capable of dissolving its surface oxide at sintering temperatures. It is expected that insights to be gained from how processing and material parameters promote mechanism of oxide disruption for achieving good microstructural and mechanical properties in titanium powders could be helpful in understanding disruption mechanism of aluminium oxides as well as how processing and materials parameters favour this during laser processing.

Titanium parts are very costly to produce via conventional manufacturing methods due to complications which arise during its casting and machining. Some of these problems are wastage in lead time and material consumption and hinderance to the realisation of complex volumetric pore structures when producing titanium parts via traditional manufacturing techniques. Employing SLS/SLM processing of titanium alloy powders is able to eliminate these challenges, thereby, conferring the benefits as reported in section 1.2 of this thesis. Moreover, the capability of titanium to dissolve its own surface oxide at sintering temperatures accounts for its suitability as ideal candidate for SLS process. Das and co-investigators (1998a, 1999) demonstrated the feasibility of

fabricating Ti-6Al-4V components for defence applications by the SLS/HIP technique, while Stoodley *et al.* (1996); Hayashi *et al.* (2005) and Hollander *et al.* (2006) employed SLS/SLM to process pure titanium or alloy powders for medical purposes.

The SLS/HIP processed titanium alloys, for the defence applications, were characterised by equiaxed microstructure, high tensile strength (1,117 MPa) and a breaking elongation of 5% which are comparably equivalent to the conventionally P/M titanium parts. Das *et al.* (1999) recommended that further characterisation of structure/property relationships as well as optimisation of processing parameters for build speed, skin thickness, oxygen content and HIP cycle time needed to be explored.

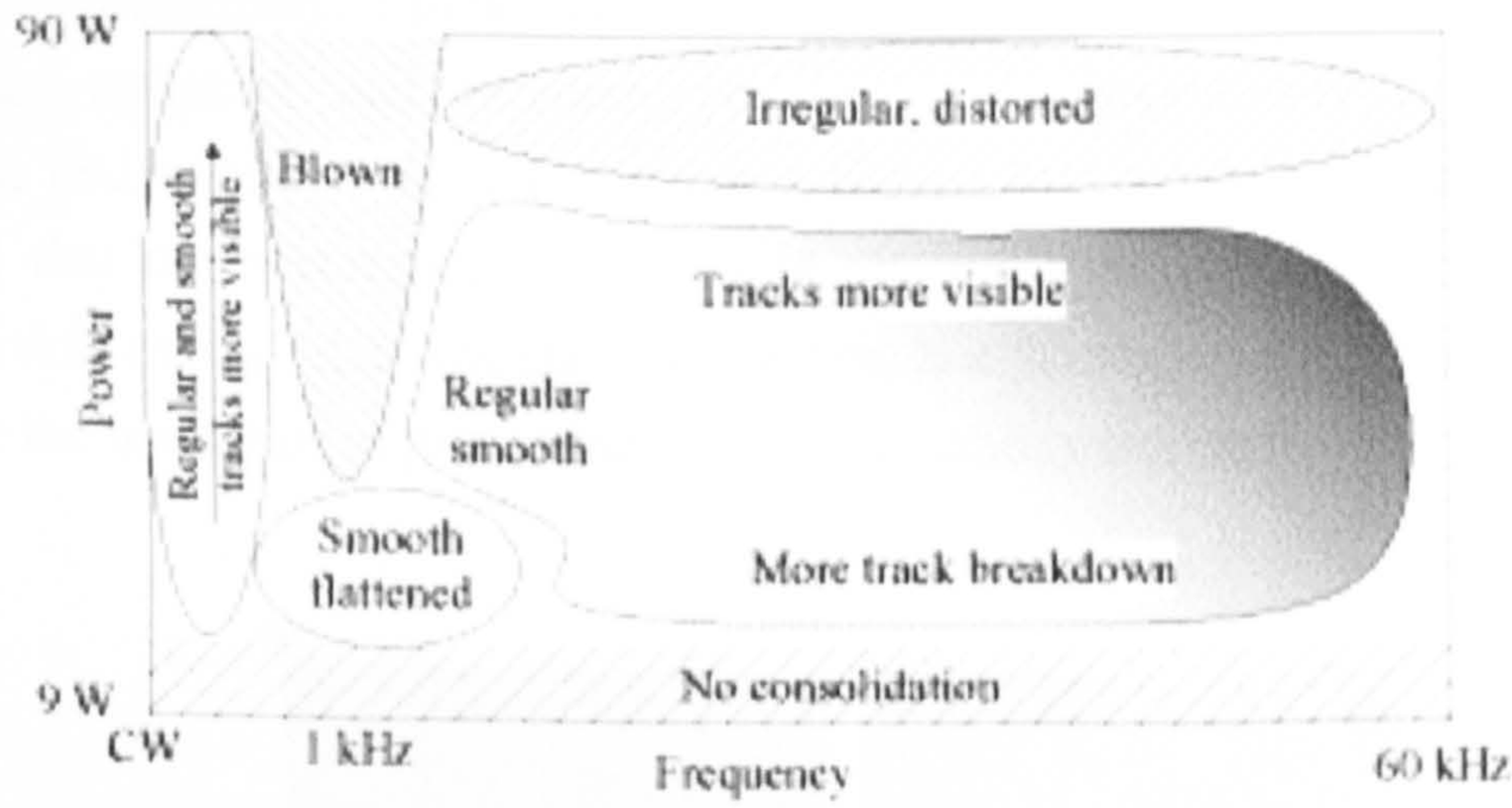

Figure 02.7: Powder bed process map for the Ti powder, melted by Nd:YAG laser at 40 mm/s (after Fischer et al. 2003).

In an attempt to investigate the SLS/SLM processing conditions of titanium powders, Fischer *et al.* (2003) described the energy exchange in the SLM of pure titanium powders between laser and material by applying the phenomenon of the gray body behaviour of granulated media. Figure 2.7 shows the three key repetition rate domains, namely the high domain, low domain and intermediate domain, which were identified with respect to pulse energy and heating effects. Figure 2.7 reveals that at low repetition rates, laser-melted titanium plates were obtained only at average powers between 10 and 15W. Below this range of laser power, no consolidation is obtained whereas the powder is blown away by the recoil pressure at higher laser powers. At intermediate repetition rates, laser-melted titanium plates were regular and smooth with increasing power resulting in increasing track visibility and presence of more track breakdowns. At high domain rates (laser power greater than 60W), the plates are distorted and irregular as a consequence of increased life time of the liquid formed as a

result of high thermal gradient. This ultimately results in balling. The surface pictures of laser-melted titanium plates obtained by scanning electron microscopy are shown in Figure 2.8.

Their finding imply that the intermediate domain characterised by fast and localised heating which minimises the plasma effect, constitutes the optimal processing window. Subsequent to this discovery, Fischer *et al*. (2005) investigated the influence of laser parameters on the properties of laser sintered titanium, steel micro-powder and amorphous PtCuNiP powders. They established that with the appropriate energy dissipation in the metallic powder layer, the degree of porosity, density as well as the crystalline microstructure can be controlled to meet the requirements of the finished work piece. Furthermore, Fischer *et al*. (2004a) investigated the interaction between pulsed laser radiation and titanium powders both theoretically (by calculation predictions) and experimentally (by using a pulsed Nd: YAG laser machine). They established that the occurrence of the liquid phase sintering (LPS) in an individual powder particle during SLS was spatially limited to a thickness of ~ 1μm of its surface layer while the main part of part of the material remaining unchanged.

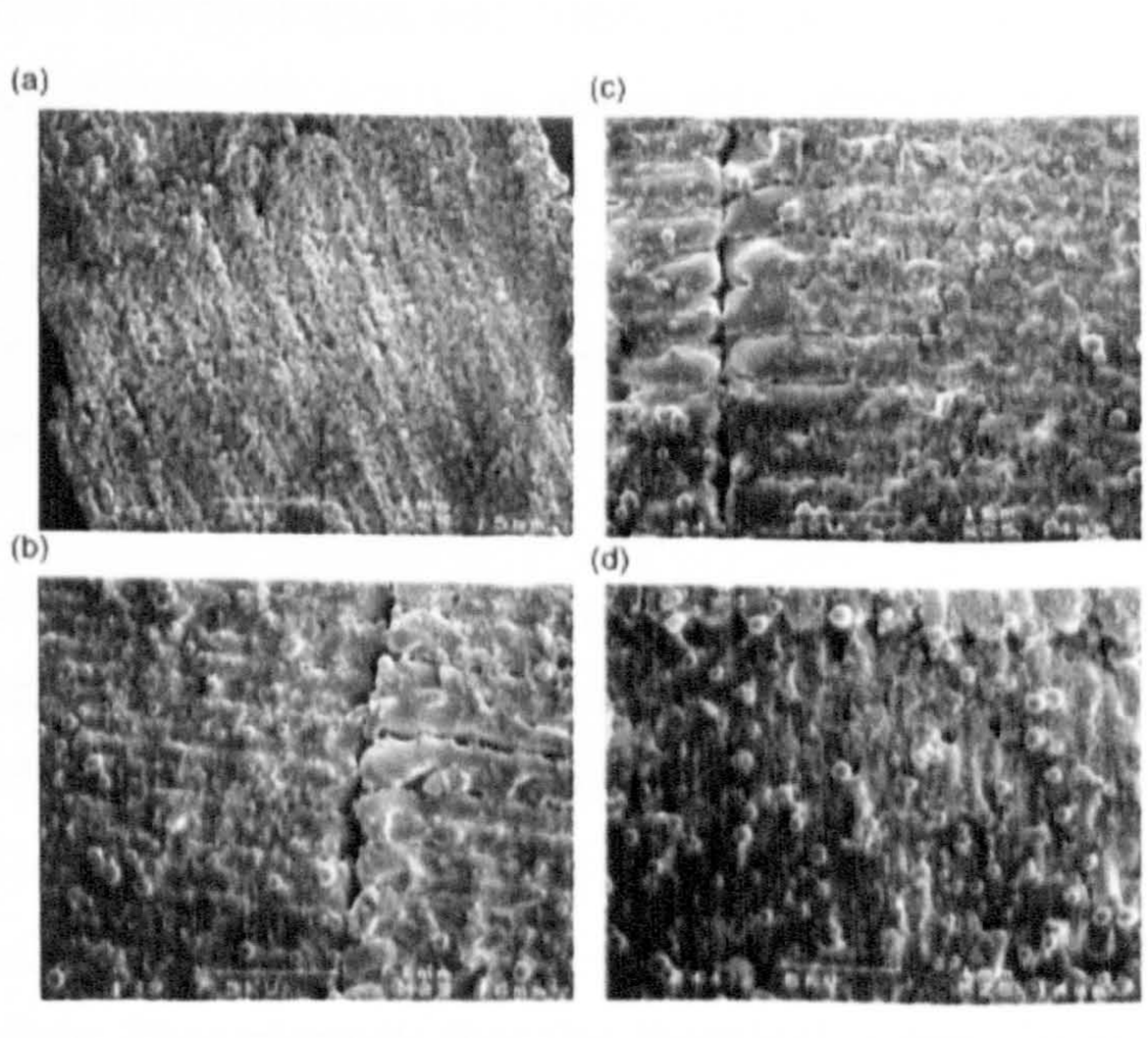

Figure 2.8: Surfaces of Ti plates, sintered in a powder a bed by a Nd:YAG laser of spot size 400 μm scanned at 40 mm/s, at (a) 1 kHz (b) 10 kHz, (c) 40 kHz (moderate energy per pulse at high repetition rate domain where v>vm) and (d) Continuous wave (CW). Experiments performed at 30 W, except (a) at 15 W (after Fischer et al. 2003)

This finding was attributed to the existence of a significant higher skin temperature during the SLS/SLM process which resulted in lower average temperature but stronger sintering. In another development, Fischer *et al*. (2004b) compared the temperature

measurements between the continuous wave sintering and pulsed sintering by verifying the predicted difference of skin and average temperature upon pulsed interaction. They discovered that the average laser power required to attain consolidation of the powder in pulsed sintering is 30% lower than that reported for continuous sintering. This implies that the consolidation of the powder particles due to melting is much more efficient and generates stronger inter-particulate bonding across the layers in the pulsed laser radiation at lower wave length (1μm) than in the continuous sintering operating at higher wave length (10μm). This observation has been attributed to the presence of the temporarily higher skin temperature which was attained through lower average laser power in the case of pulsed interaction. They pointed out the area of the temperature elevation during continuous sintering is much larger and the achieved peak temperature nearly 1000K higher than that during the pulsed interaction which scales quite well with the higher average power. Consequently, because no complete melting occurs during pulsed interaction, reduced thermal distortion, higher lateral precisions and low residual thermal stresses in the parts can be achieved. Srivastava *et al.* (2001) investigated the influence of process parameters and heat treatment on the microstructure of *direct laser fabricated* gamma titanium aluminide (TiAl) alloy samples. Their findings revealed that a variety of microstructures, ranging from cellular to columnar to dendritic morphologies and consisting of lamellar ($\alpha_2 + \gamma$), featureless (γ) and partially lamellar [$\gamma + (\alpha_2 + \gamma)$], is obtainable upon the variation of the laser power and scanning speed (Figures 2.9 and 2.10). Micro heterogeneous and finer microstructures were developed in direct laser fabricated titanium alloy samples by comparison with their conventionally processed counterparts due to high cooling rates (Figure 2.11). Subsequent heat treatment of the direct laser fabricated samples eventually resulted in the elimination of the compositional heterogeneity and microstructural refinement of the samples. Moreover, Wu and Mei (2003) employed direct laser fabrication to achieve good geometry control and surface finish for parts made of Ti alloys and hypereutectic Al-Si (SiAl) alloys. They observed that Ti burn-resistant alloy, Ti-25V-15Cr-2Al-0.2C (wt%) and the high SiAl alloy could have a large processing window in contrast with Ti-6Al-4V (wt%) alloy which has a very small processing window. This suggests that the chemical composition of metal powder determines to a very great extent the nature of the processing map that is likely obtained for laser-processing. They also concluded that the microstructure of the build is greatly influenced by the laser process parameters.

Wu *et al.* (2002) assessed the effect of the oxygen content on the microstructure of the burn-resistant alloys, Ti-25V-15Cr-2Al-0.2C (wt%), processed in air; using the argon carrier as protection, and in a glove box with an argon atmosphere with O_2 <5ppm.

They discovered that the microstructures obtained differed for each atmosphere with the alloy laser processed in air characterised by large titanium carbide dendrites while the carbides obtained in the argon processed atmosphere had finer and more uniformly distributed carbides. While Wu and co-investigators discovered that the atmosphere influences the microstructure obtained, they were not able to propose a mechanism responsible for this effect.

Having reviewed the available literature on the effect of laser processing on the microstructure of titanium alloyed powders, the next part of this section will look at the progress made so far in the laser processing, pulse electric-current sintering, and conventional powder metallurgy sintering of aluminium and aluminium alloy powders.

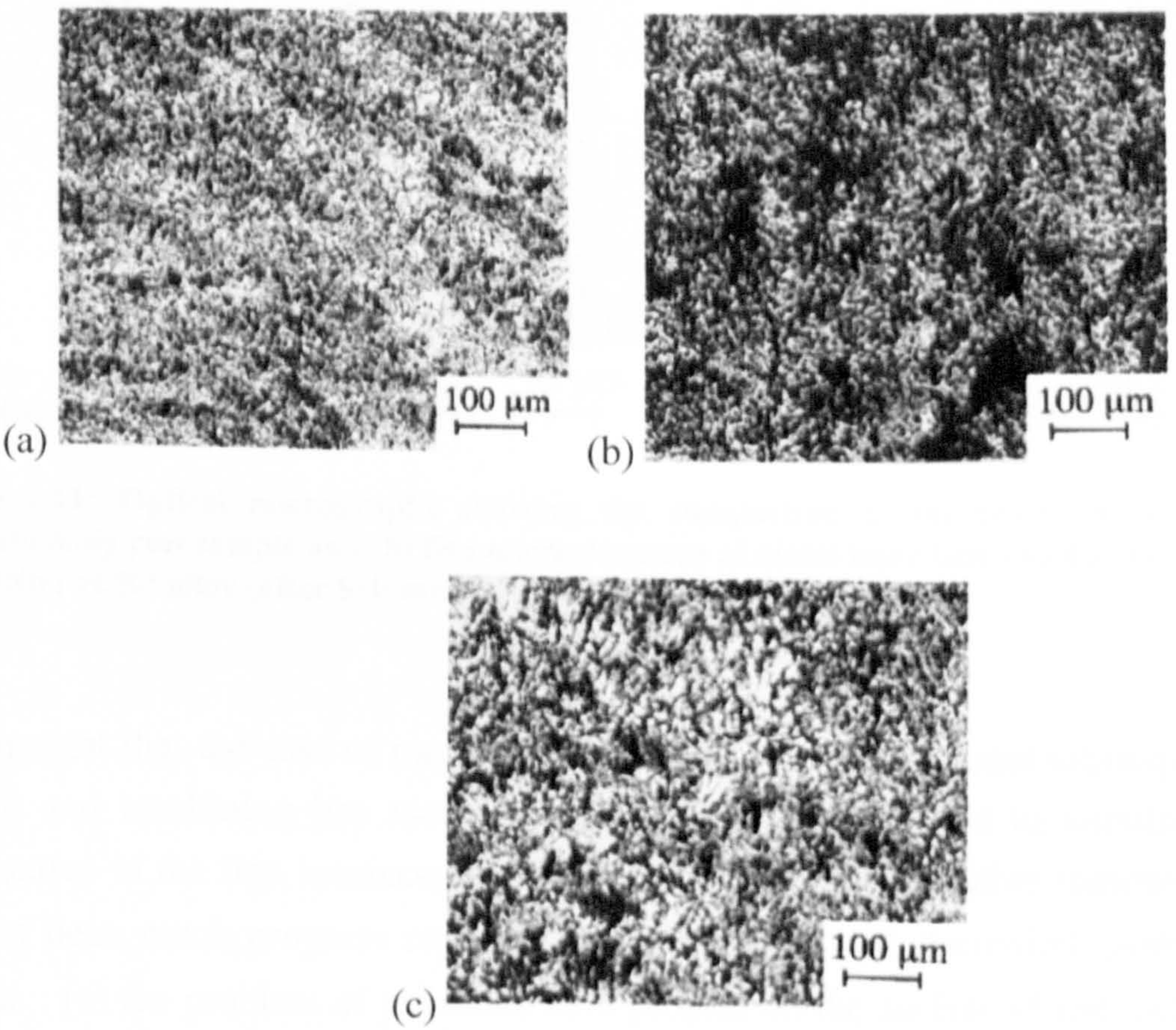

Figure 2.9: Optical micrographs showing the variation of microstructure of Ti-48Al-2Mn-2Nb (wt.%) alloy consisting of lamellar ($\alpha 2 + \gamma$), featureless (γ) and partially lamellar [$\gamma + (\alpha 2 + \gamma)$] and fabricated with laser power (a) 300W, (b) 360W, (c) 400W. (Scanning speed 8mm/s; powder feed rate 3g/min; z-increment 0.2mm; number of layers 20) (after Srivastava et al. (2001)).

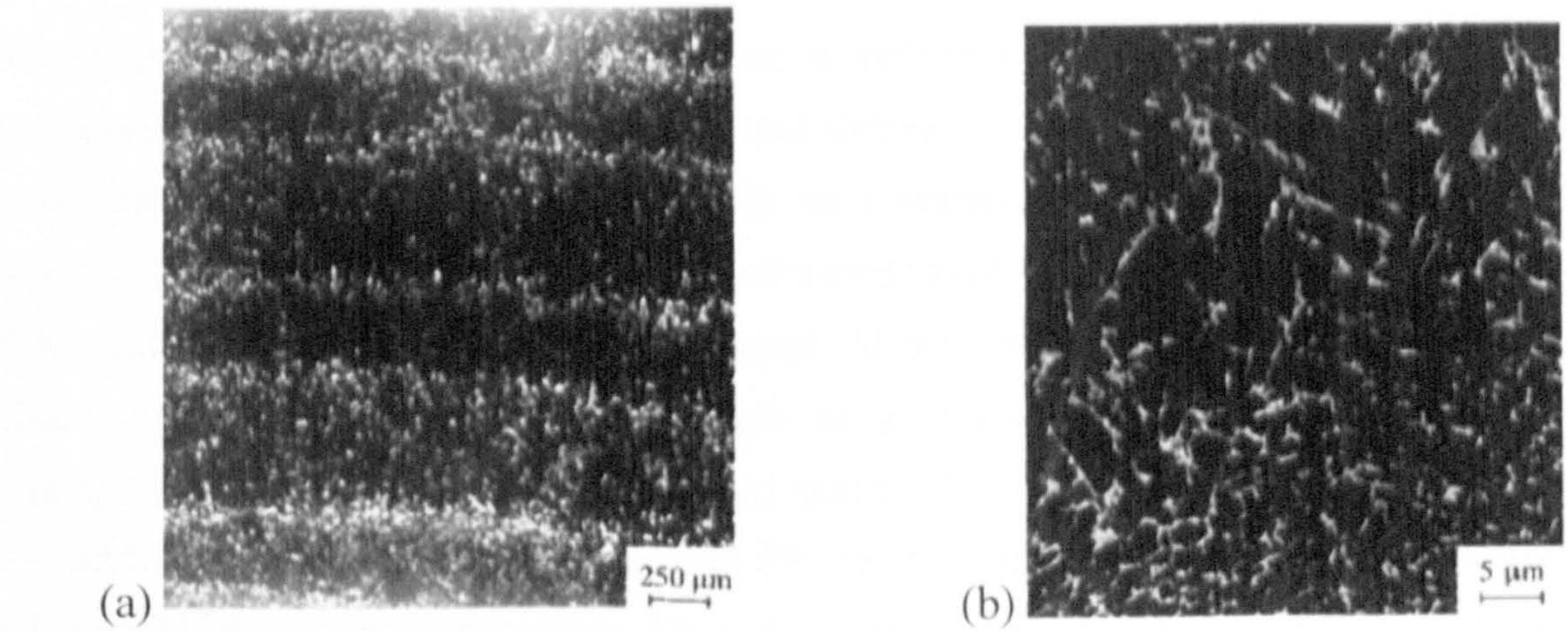

Figure 2.10: Optical micrographs showing the variation of microstructure of Ti-48Al-2Mn-2Nb (wt.%) alloy with scanning speed (a) 4mm/s, (b) 8mm/s (laser power 360W; powder feed rate 3g/min; z-increment 0.2mm; number of layers 20) (after Srivastava et al. (2001)).

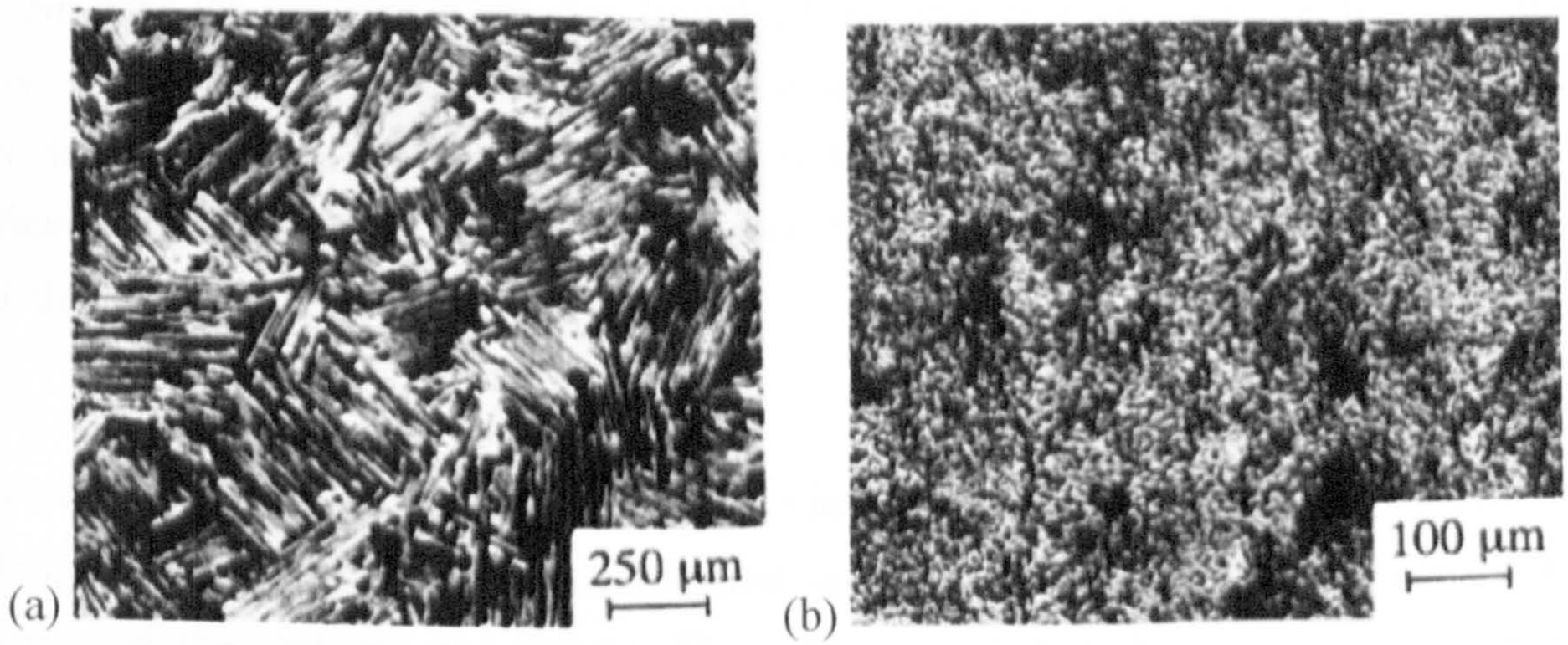

Figure 2.11: Optical micrographs showing the comparison of (a) coarse microstructure of conventionally cast sample and (b) fine microstructure of direct laser fabricated sample of Ti-48Al-2Mn-2Nb (wt.%) alloy (after Srivastava et al. (2001)).

It is thought that the ease of manufacture by low cost conventional techniques such as casting and machining has made the application of SLS/SLM to aluminium alloys unattractive in the first instance (Shellabear & Nyrhilä 2007). Other reasons why there has not been much progress reported in the SLS/SLM of aluminium powders might include : (a) the problem of the oxide film present on the surface of the metal powder, the thermodynamic stability of aluminium sesquioxide making it difficult to remove or avoid, and (b) the relatively low melting point of aluminium which makes it difficult to find a suitable lower melting point binder material that belongs to the group of light metals in order to generate sufficient amount of liquid phase for binary liquid phase SLS. Nevertheless, a number of notable efforts have been made in the indirect SLS production of aluminium components in an attempt to reduce the cost of production and the lead time as well as achieving improved tensile strength and dimension accuracy. For example, aluminium tooling has been produced from powder by extrusion free form fabrication (Sercombe *et al.* 1999) and indirect laser sintering (Sercombe 2003a).

These powder parts were fabricated as a polymer/aluminium composite and post-processed by burning out the polymer and thereafter, the remnant of the metal powder was sintered to full or near-full density in a manner similar to that used in powder injection moulding. Sercombe (2003a) demonstrated the feasibility of the conventional P/M sintering of uncompacted, pre-alloyed Al powder alloys. The parts obtained were characterised with low tensile strength as a consequence of the absence of any strengthening mechanism for the pure Al matrix. He went further to assess the effect of the addition of elemental Mg, Sn, and Pb on the sintering response of unpressed pre-alloyed 2124 and 6061 powders. They discovered, at a temperature above 500°C, that ~20 vol. % liquid phase was generated when polyethyl methacrylate (PEMA) resin was added to the aluminium powders with Mg facilitating the disruption of the oxide film, while Sn and Pb segregated to the liquid phase reducing the surface tension, thus improving the sintering process. The Sn or Pb segregates to the liquid phase as a result of its low solubility in the aluminium matrix thereby promoting wetting. The significance of this lies in the potency of Sn or Pb in reducing the surface tension of the liquid aluminium.

Xie *et al.* (2003) studied the behaviour of oxide films at the interface between pure Al powdered particles in pulse electric-current sintering (PECS) and its effect on the properties of the sintered specimens. They discovered that the occurrence of direct metal/metal bonding interfaces increase the mechanical properties of the sintered aluminium powder whereas the metal oxide film layer/metal bonding interfaces produced contrary effect on its mechanical properties. Xie and co-investigators concluded that by increasing the loading pressure at high sintering temperatures, or increasing the sintering temperature under loading pressure, the breakdown of the oxide film was promoted. Moreover, Xie *et al.* (2005a) investigated the reduction mechanism of the surface oxide film and microstructure of interfaces between powder particles in Al-Mg alloy specimens sintered by pulse electric-current (PECS) process. They established that nano-sized crystalline precipitates, which may be $MgAl_2O_4$, MgO, or both, were formed by the reduction reaction by magnesium and were observed in all of the Al-Mg alloy specimens which they studied. They attributed the type of crystalline precipitates formed to the variation in the Mg content in the alloy powder and the sintering temperature. Liu *et al.* (2007) showed that particle shape seems to be a significant factor controlling the P/M sintering response of uncompacted aluminium powder. In addition, they suggested that the differential thermal expansion between the aluminium particle and its oxide film may cause the oxide skin to fracture and that the fracture characteristics differ as a consequence of powder morphology. However, they elucidated that the oxide shell in irregularly shaped particles tend to crack and heal

more frequently than it will in the smooth, spherical shaped ones because of the tendency of the irregular particles to scanvenge more oxygen during heating process than spherical particles will. Furthermore, they posited that this eventually resulted in greater weight gain observed in the sintered irregular powder particles than the spherical particles due to the outer layers made from irregular particles providing a more effective autogenous gettering zone than the outer layers made up of spherical particles. It can be inferred from the findings of Xie and Liu research groups that the sintering mechanism of aluminium powders can differ on the basis of the sintering technique adopted, chemical composition, and particle surface morphology. Therefore, a mechanism elucidating the reduction of the surface oxide film during direct or indirect SLS processing of aluminium powders has not been established. This is necessary at this stage if the mechanism of disruption of the surface oxide film during SLS processing of aluminium alloyed powders is to be understood. Moreover, the associated factors that aid or inhibit the SLS sintering mechanism of aluminium powders will have to be discovered in an attempt to achieve this goal.

With regard to the indirect SLS route of aluminium parts' production in which they are processed as polymer/aluminium composites and then debinded/infiltrated with the a low melting point aluminium alloy in an attempt to achieve near full density; the main difficulty encountered is the poor dimensional accuracy observed during liquid phase SLS of the powder preform because of density gradients in the green parts and geometrical constraints. Although, SLS/SLM allows the incorporation of uniform shrinkage into the initial parts' design, however, it must be emphasised that non-uniform shrinkage is quite difficult to control and accommodate in the part's design. Consequently, the dimensional accuracy is highly relevant for a SLS/SLM processed parts, but the failure to precisely sinter large-sized parts is discouraging, thereby making the fabrication of only small-sized parts of ~1cm^3 feasible. Sercombe and Schaffer (2003) addressed the problem of dimensional instability by adopting an infiltration technique which involves the formation of an unconstrained, resin bonded aluminium powder part, the burning out of the resin, the partial transformation of the aluminium into a rigid aluminium nitride (AlN) skeleton, by reaction with the nitrogen atmosphere under a magnesium/alumina blanket, and the subsequent infiltration with a second lower melting point aluminium alloy. Moreover, they found out through another experiment that adding magnesium to the aluminium powder, or the infiltrant, is beneficial but not sufficient because full infiltration only occurs under an alumina blanket to which magnesium powder is added. AlN which forms due to partial transformation of the aluminium powder by reaction with a nitrogen atmosphere was

discovered to have aided wettability and facilitated spontaneous infiltration (Sercombe and Schaffer 2004a).

In an attempt to advance the understanding of the indirect SLS processing of aluminium for rapid prototyping applications, Sercombe and Schaffer (2004b) examined the role of tin, as an aid in the infiltration of pre-alloyed AA6061 by Al-13.8Si-4.7Mg (wt%), in controlling nitride growth. They discovered that if an insufficient quantity of nitride forms, then the dimensional stability is compromised during the infiltration step while cracking may occur as a result of excessive nitride formation which may result in the limitation of mechanical properties, particularly the tensile ductility. Therefore, tin slows the growth rate of the aluminium nitride by a mechanism which relates to the low melting point and low surface tension of tin, thereby increasing the subsequent rate of infiltration of the aluminium liquid into the nitride skeleton (Figures 2.12 and 2.13).

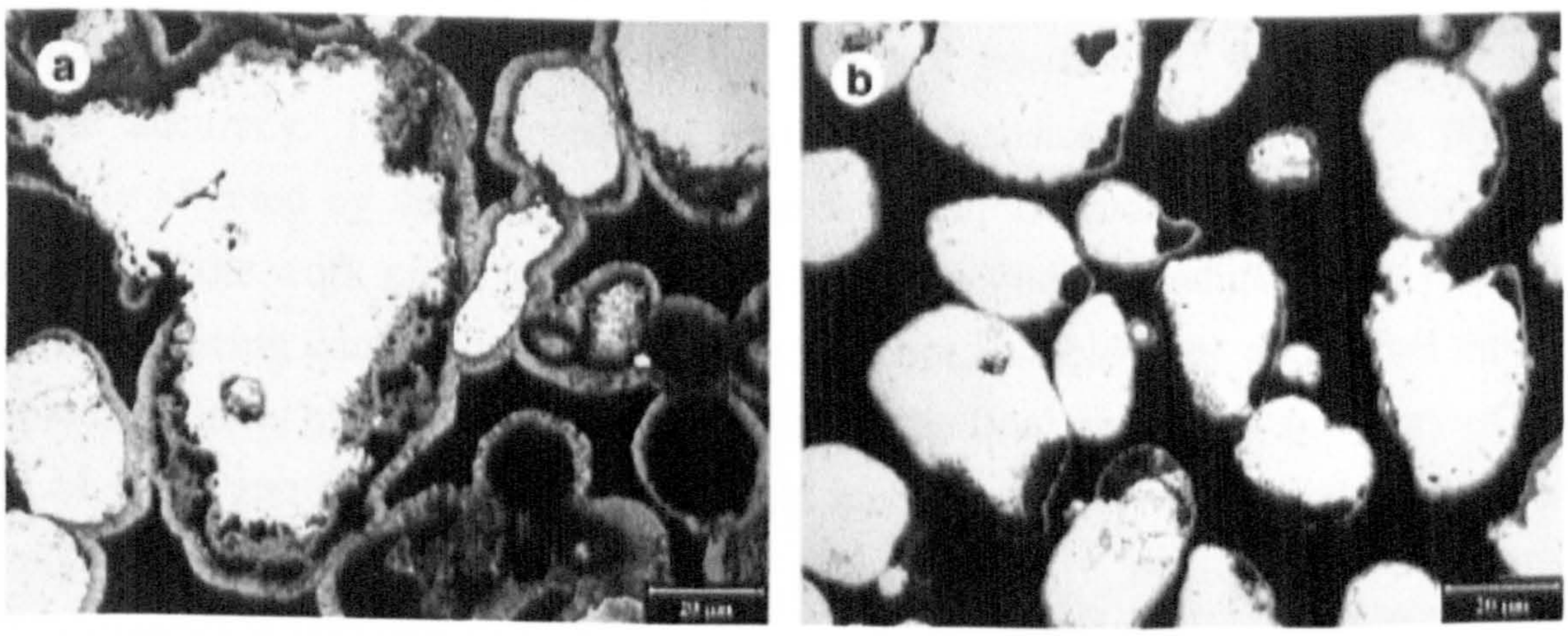

Figure 02.12: Optical microscopy of AA6061-2Mg (wt%) powder nitrided at 540oC for 6 hr. (a) without Sn and (b) with 2Sn (wt%) showing a significantly thinner nitride layer develops in the presence of tin (after Sercombe and Schaffer 2004b).

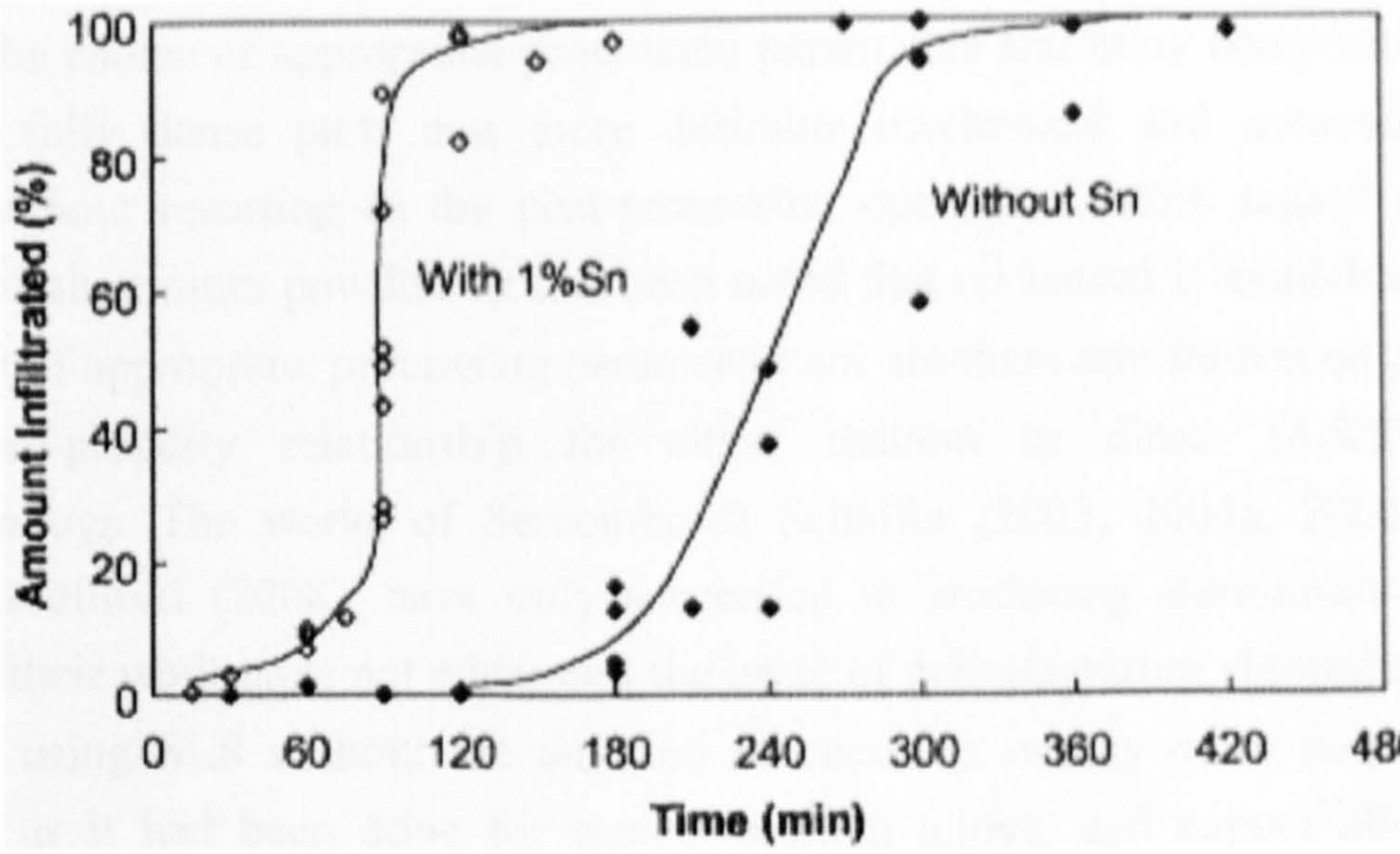

Figure 02.13: The effect of time on the percentage infiltration of 6061-2Mg (wt%) preforms by Al-13.8Si-4.7Mg (wt%) with and without 1% Sn. The presence of Sn decreases the incubation period and increases the amount of infiltration (after Sercombe and Schaffer 2004b).

Sercombe and Hopkinson (2006) investigated the shrinkage of indirect laser sintered aluminium alloys and the influence of the part bed position on the part size and achievable accuracy. They pointed out that the dimensional change of a part is significantly affected by the infiltration of the skeleton, the geometry of the part, and the location of the work piece within the part bed. The findings indicate that, within a rapid manufacturing context, it is appropriate to adopt suitable scale and offset values derivable from parts placed in the same position as the final parts. The summary of the SLS/SLM, P/M, and PECS processing of light metals is hereby presented in the next paragraph.

An extensive analysis of the available literature has shown, beyond reasonable doubt, that direct SLS/SLM of titanium and titanium alloy powders is feasible. In summary, the laser processing parameters, the chemical composition of the titanium powders, and the nature of the atmosphere under which the alloys are processed are hereby identified as the factors that determine the properties of laser processed titanium alloys. These factors are expected to be influential in the application of SLS/SLM to aluminium powders with a view to understanding how they could aid the dissolution or disruption of oxides in aluminium oxides for the attainment of good microstructural and mechanical properties. It worth noting that the laser processing technique has been applied to titanium powders to obtain engineering parts with good geometry control, surface finish, mechanical and microstructural properties, comparable to that obtainable via conventional processing methods. Thus, the current challenge for researchers is to

investigate the choice of appropriate processing parameters and alloy composition that could yield fully dense parts and more desirable mechanical and microstructural properties without resorting to the post-processing operations. With regard to laser processing of aluminium powders, it has been noted that no record is available on the development of appropriate processing parameters nor are there any studies on process-microstructure-property relationship for either indirect or direct SLS/SLM of aluminium alloys. The works of Sercombe & Schaffer (2003; 2004a, 2004b), and Simchi & Godlinski (2008), have only succeeded in producing aluminium-ceramic composites: their work have not addressed the issue of manufacturing aluminium alloy components using SLS without the addition of ceramics or any other non-metallic components as it had been done for steels, titanium alloys, and copper alloys etc. Although, the indirect SLS route of aluminium production addresses the problem of dimensional inaccuracy through the infiltration technique, it adds to the burden of production costs and increases the production cycle time. Likewise for aluminium, the incorporation of post-processing steps such as heat treatment and the application of hot isostatic pressing (HIP) is not desirable just as in the laser processing of titanium alloys

The lack of application of SLM to aluminium and its alloys has been attributed to the oxide film present on the surface of the metal powder which may likely engender spheroidisation phenomenon during laser-material interaction due to the initiation of Marangoni convection by the temperature gradient existing between the centre and the edge of the molten pool. Moreover, the relatively low melting point of aluminium which makes it difficult to find a suitable binder which can generate sufficient amount of liquid phase is another reason binary liquid phase SLS had not been employed to produce parts in aluminium or aluminium alloy powders. The application of the knowledge of effect of trace elements (see details in Section 2.7.2.4) on the disruption of the surface oxide film during the sintering phase of conventional P/M processing of aluminium alloys, as reported by Sercombe & Schaffer (1999a), and Schaffer *et al.* (2001a), seems to be likely solution that may improve wettability and inter-particulate melting during SLM of aluminium alloys. With regard to SLS, the issue of low melting point binder development for light metals such as aluminium, which applies binary liquid phase phenomenon, needs to be investigated by researchers. Key findings from SLS/SLM, P/M sintering, and PECS of light metals are presented in Table 2.8.

2.4 Sintering of Aluminium Alloys in Conventional Powder Metallurgy (P/M)

The conventional press-and-sinter P/M route presently offers the opportunity for net shape manufacturing. In an attempt to fabricate P/M functional parts, extensive research efforts had focussed on wrought alloy compositions (Schaeffer *et al.* 2001b). However, it was discovered that alloys for pressing and sintering significantly differ in composition from their wrought counterparts because the latter were not designed to be sintered (Schaffer *et al.* 2001b). Because liquid phase sintering (LPS) is the step in the P/M process that is most responsible for the development of strength and other functional properties, it is not surprising that current commercial wrought alloys do not meet the requirements of the direct SLS process. In order to understand why the available wrought aluminium alloy compositions are not able to meet the requirements for the ideal liquid phase sintering process, this section shall present the basic principles underlying the conventional P/M sintering process and define an ideal liquid phase sintering system as applicable to aluminium alloys.

To achieve this, it must consider the nature of the aluminium oxide and its influence on the sintering behaviour of aluminium powders, the requirements for the LPS to disrupt the aluminium oxide, the role of alloying elements in the LPS of aluminium powders, and the compositional design of aluminium alloys using binary phase LPS will be explored in this section. The insight gained from the available literature on these issues shall hopefully be employed in assessing the feasibility of developing aluminium alloys which could overcome the problems associated with the direct SLS.

Aluminium powder is usually covered by an oxide layer. The oxide has been described as usually amorphous and hydrated with an absorbed water layer (Schaeffer *et al.* 2001b). The thickness of the oxide, vary between 10 to 150Å, is dependent on the temperature at which it was formed and the atmosphere in which it is stored, particularly the humidity (Schaffer *et al.* 2001b). The oxide inhibits solid state sintering in aluminium as a consequence of the relative diffusion rates of its atoms through the oxide (Munir 1981, Higgins & Munir 1982, Guo *et al.* 1997). A more viable alternative to the solid state sintering in disrupting the ubiquitous aluminium oxide film is the adoption of LPS which contains the wetting liquid (Schaeffer *et al.* 2001).

.

Table 2.8: Key findings from SLS/SLM, P/M sintering, and PECS of light metals.

Materials.	Method	Key findings.	Comments.
Ti-6Al-4V (wt.%)	SLS/HIP	Mechanical and microstructural properties comparable to conventionally processed materials.	The need to eliminate post-HIP.
Titanium powders	SLS/SLM	Three key domains in the processing window namely low, intermediate and high domains were identified. Intermediate domain constitutes the optimal processing window. Consolidation of the powder particles due to melting is much more efficient and generates stronger inter-particulate bonding across the layers in the pulsed laser radiation at lower wave length (1μm) than in the continuous sintering operating at higher wave length (10μm).	CO_2 laser results in LPS whereas Nd:YAG results in melting of titanium particles.
Ti-alloys	SLM	Microstructures range from cellular to columnar to dendritic morphologies upon the variation of laser power and scanning speed. Good geometry control and surface finish obtained. Choice of atmosphere affects the resultant microstructure.	Processing parameters control the microstructure of SLM processed Ti-alloys.
Pre-alloyed Al powders	Uncompacted P/M sintering	Low tensile strength due to absence of any inter-particulate bonding mechanism for pure Al matrix. Addition of elemental Mg disrupted the oxide film while Sn and Pb reduced the surface tension.	Micro-alloying addition aided sintering, although, liquid phase was provided by the addition of polymeric binders.
Pure Al powders	PECS	Metal/metal bonding interface is associated with increased mechanical	Emphasises the need for oxide

		properties.	disruption for metal/metal bonding interface.
Al-Mg alloys	PECS	Crystalline precipitates $MgAl_2O_4$ and MgO contributed to the reduction reaction by magnesium in the Al-Mg alloy specimens.	Mg addition aids oxide disruption via chemical reaction.
Pure Al	Uncompacted P/M sintering	Particle shape and differential thermal expansion between Al particle and its oxide film control the sintering response of uncompacted Al powder.	Explains the mechanism for oxide disruption in the absence of Mg that facilitates chemical reaction.
Al-alloys	Indirect SLS incorporated with post-infiltration.	AlN which formed due to partial transformation of the aluminium powder by reaction with a nitrogen atmosphere aided wettability and spontaneous infiltration, thereby, improving dimensional stability.	Highlights the mechanism controlling infiltration of indirect SLS fabricated Al alloys.

According to Naidich (1981), and Dellanay *et al.* (1987), the wettability of a solid by a liquid (Figure 2.14) is dependent upon the work of adhesion W_a defined by equation 2.1 below.

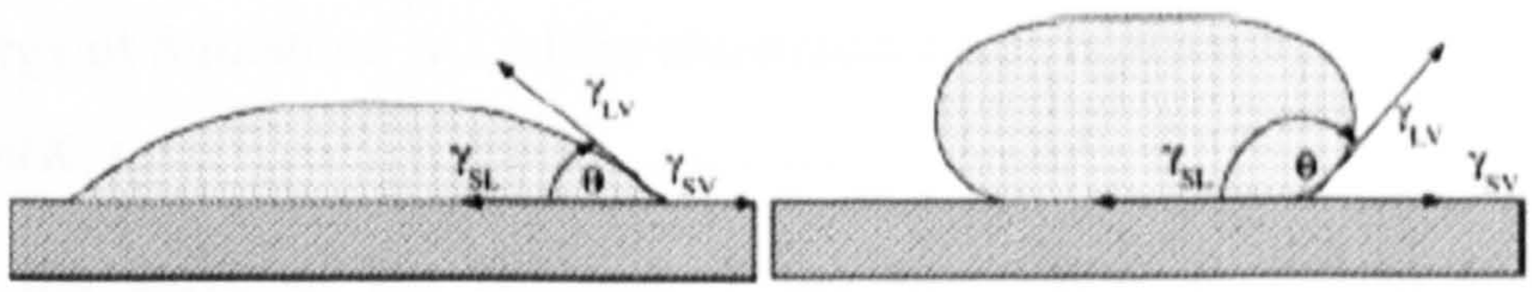

Figure 02.14: Three-phase equilibrium for wetting and non-wetting systems (after Das 2003).

Wetting of a solid particle by a liquid occurs provided $\cos\theta>0$. Aluminium oxide has a high melting point of 2,100 °C. Therefore, the oxide is expected to be poorly wetted by the liquid aluminium at a melting temperature of 660 °C. The only exception to this is when the temperature of liquid aluminium is above the wetting threshold of 2,100 °C, a temperature beyond which W_a increases very sharply (Naidich 1981). Moreover, it has been shown that the contact angle varies indirectly with processing temperature, but it must be emphasised that this is again a function of partial pressure of the oxygen and the presence of an oxide film on the molten metal (Schaeffer *et al.* 2001b).

$$W_a = (\gamma_{SV} + \gamma_{LV} - \gamma_{SL}) = \gamma_{LV}(1 + \cos\theta) \quad \text{.....(2.1)}$$

$$\cos\theta = (W_a / \gamma_{LV}) - 1 \quad \text{.....(2.2)}$$

where

γ_{LV} = surface tension of the liquid-vapour interface

γ_{SV} = surface tension of the solid-vapour interface

γ_{SL} = surface tension of the solid-liquid interface

θ = contact angle.

Furthermore, it had been pointed out that alloying addition of magnesium (Mg), cerium (Ce), and calcium (Ca) to molten aluminium had not effectively reduced the contact angle to produce wetting since the oxide on aluminium is a barrier to sintering and needs to be disrupted (Liu *et al.* 1992, Ip *et al.* 1993). Because the work of adhesion W_a of liquid metals on oxide surfaces increases with the free energy of formation of the metal oxide, Schaeffer *et al.* (2001b) suggested the use of conventional atmospheres in

reducing surface oxide films or the alloying elements that can initiate a chemical reaction with the oxide film, with a view to disrupting its deleterious activity.

The oxidation of aluminium can be represented as

$$4Al + 3O_2 \rightarrow 2Al_2O_3 \quad \text{.....2.3}$$

The free energy of formation, ΔG, of the aluminium oxide is given by

$$\Delta G = -RT\ln(K_1) \quad \text{.....2.4}$$

where R is the universal gas constant, T the temperature in Kelvin and K_1 the equilibrium constant given by

$$K_1 = (PO_2)^{-1} \quad \text{.....2.5}$$

where PO_2 is the partial pressure of oxygen when equation 2.3 is at equilibrium condition.

On the basis of equation of equations 2.4 and 2.5, Schaeffer *et al.* (2001b) proved that neither a dew point of -140 °C nor a PO_2 of 10^{-50} atmospheres required for the sintering of aluminium in conventional atmospheres was practically feasible. As a consequence of the non-feasibility of the suggestions above, magnesium, a highly reactive element with a more negative free energy of formation of its oxide than that of the oxide of aluminium was adopted for the P/M sintering of aluminium powder by Schaeffer *et al.* (2001b). Magnesium, therefore, has the potential to act as a solid reducing agent in this system according to the reaction below.

$$3Mg + 4Al_2O_3 \leftrightarrow 3MgAl_2O_4 + 2Al \quad \text{.....2.6}$$

The reduction reaction indicated by the presence of spinel crystallites (Figure 2.15) at bonding interfaces of elemental Al-Mg powder, may be facilitated during sintering by diffusion of the magnesium through the aluminium matrix and will be accompanied by a change in volume, creating shear stresses in the film, ultimately leading to the break up of the aluminium surface oxide film (Schaeffer *et al.* 2001b). This will propitiate diffusion, wetting and therefore sintering (Schaffer *et al.* 2001b). Schaffer *et al.* (2001b) observed that liquid tin only wets aluminium in the presence of magnesium, when the dihedral angle is very sharp whereas in the absence of magnesium, the dihedral angle is obtuse and the liquid is exuded during sintering (Figure 2.16). By promoting sintering, magnesium also affects the mechanical properties by increasing strength and ductility when 0.15wt% Mg was added to aluminium. This is an indication of enhanced inter-particulate bonding and densification following the disruption of its surface oxide films (Schaeffer *et al.* 2001b).

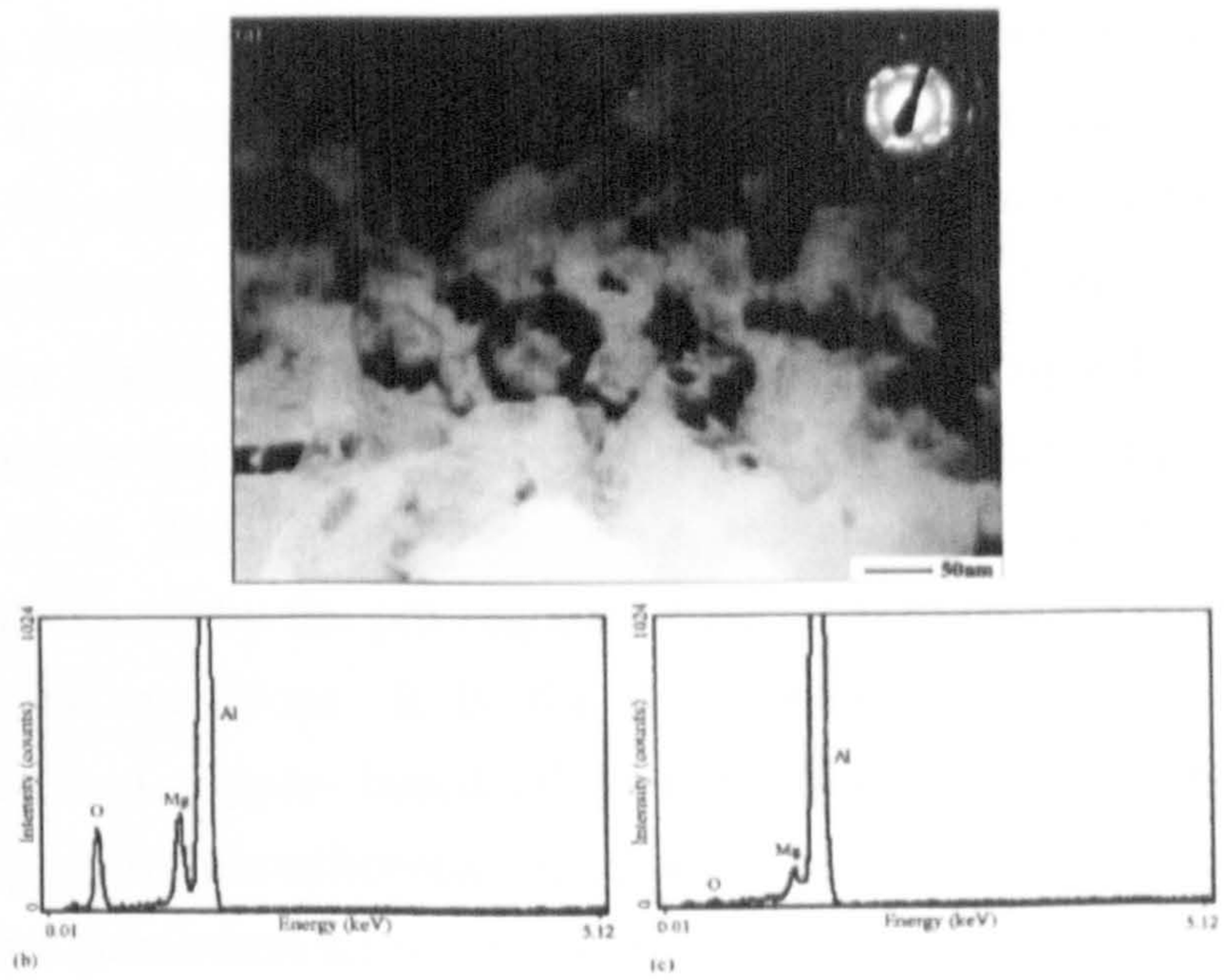

Figure 02.15: (a) Transmission electron micrograph of a sintered Al–2.5Mg (wt%) alloy, showing a multitude of spinel crystallites: the inset shows the selected area diffraction pattern from this region, which can be indexed to spinel. (b) EDS spectra from (a) showing that the fine crystallites contain significantly more magnesium and oxygen than does the aluminium matrix (c) (after Lumley et al. 1999).

The excess magnesium at concentrations above 0.15wt% remains in solution in the aluminium, causing expansion by the Kirkendall effect (an unbalanced diffusivity between the additive magnesium and the base aluminium which consequently results in the suppression of voids formed at the boundary interface) and solid solution hardening.

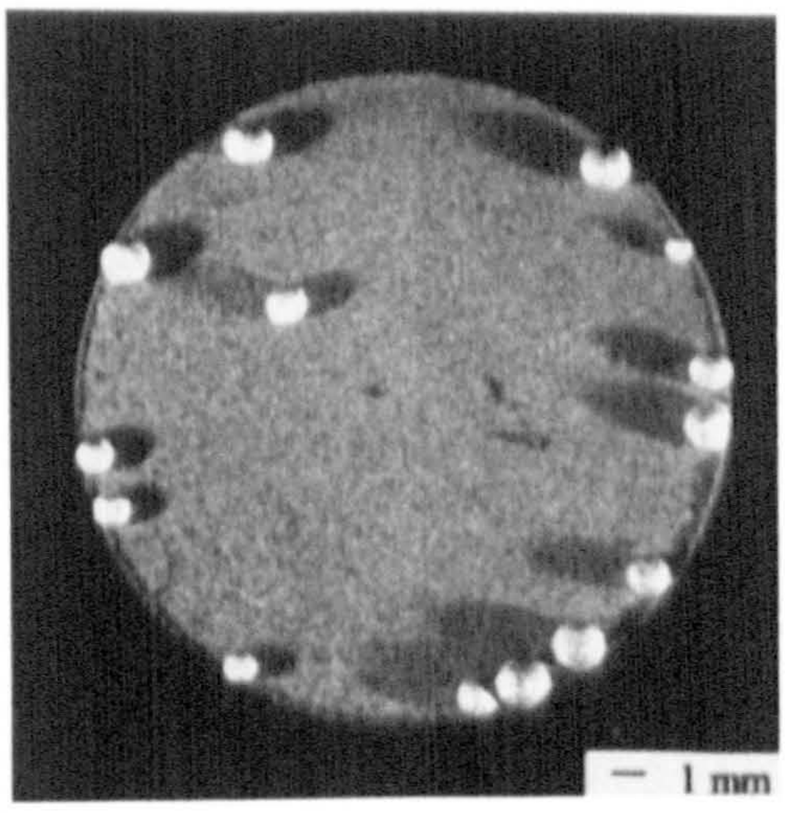

Figure 2.16: Exuded liquid on the surface of an Al–8Sn (wt%) alloy after sintering at 620 °C (after Schaffer et al. 2001).

Schaffer and co-workers (2001b), in their study on P/M liquid phase sintering of aluminium alloys, concluded that the oxide is not the barrier to the sintering of aluminium that it is conventionally considered to be since magnesium was found to have reacted with the oxide to form spinel, thereby disrupting the oxide and facilitating the sintering. Other factors, such as inappropriate alloy composition, must therefore be the cause of the poor sintering response. Alloys are generally designed to accommodate the manufactured goods made from them as much as the properties required of them in service (Schaffer *et al.* 2001b). In other words, the choice of alloying additions to parent metals is influenced by the pre-requisite functional properties of the parts made from them when in operations. It is for this reason that SLS processed steels (Sercombe, 2003b), and copper- based alloys (Zhu *et al.* 2005), for example, often contain boron, copper or phosphorous, in addition to carbon and nickel. Similarly, compositions of cast aluminium alloys are different to those of forging alloys which are different again to extrusion alloys. Meanwhile, press and sintered aluminium alloys of identical composition to their wrought counterparts are found to have exhibited poor sintering response as no consideration was given to the existence of the liquid phase for a short duration of time in their design (Schaffer *et al.* 2001b). Therefore, the compositions of aluminium alloys to be SLS processed need to be properly designed in order to obtain an enhanced sintering response which would result in the manufacturing of components possessing mechanical integrity that is comparable to that which is obtainable currently from other traditional production techniques. It is on this premise that the basics of liquid phase sintering phenomena (German 1985) will be applied to define the characteristics of an idealised binary liquid phase diagram which hopefully should assist in the design of aluminium alloys for the SLS technique.

The adoption of liquid phases in the SLS processing has the benefits of low sintering temperature, fast densification, homogenisation, high final densities, and microstructures that often possess improved mechanical and physical properties. An essential requirement for the effective liquid phase sintering is the transient wetting liquid (formation of sufficient liquid phase within short durations varying between 0.5 to 5ms) which promotes metallurgical bonding or inter-particulate melting across the layers of sintered components.

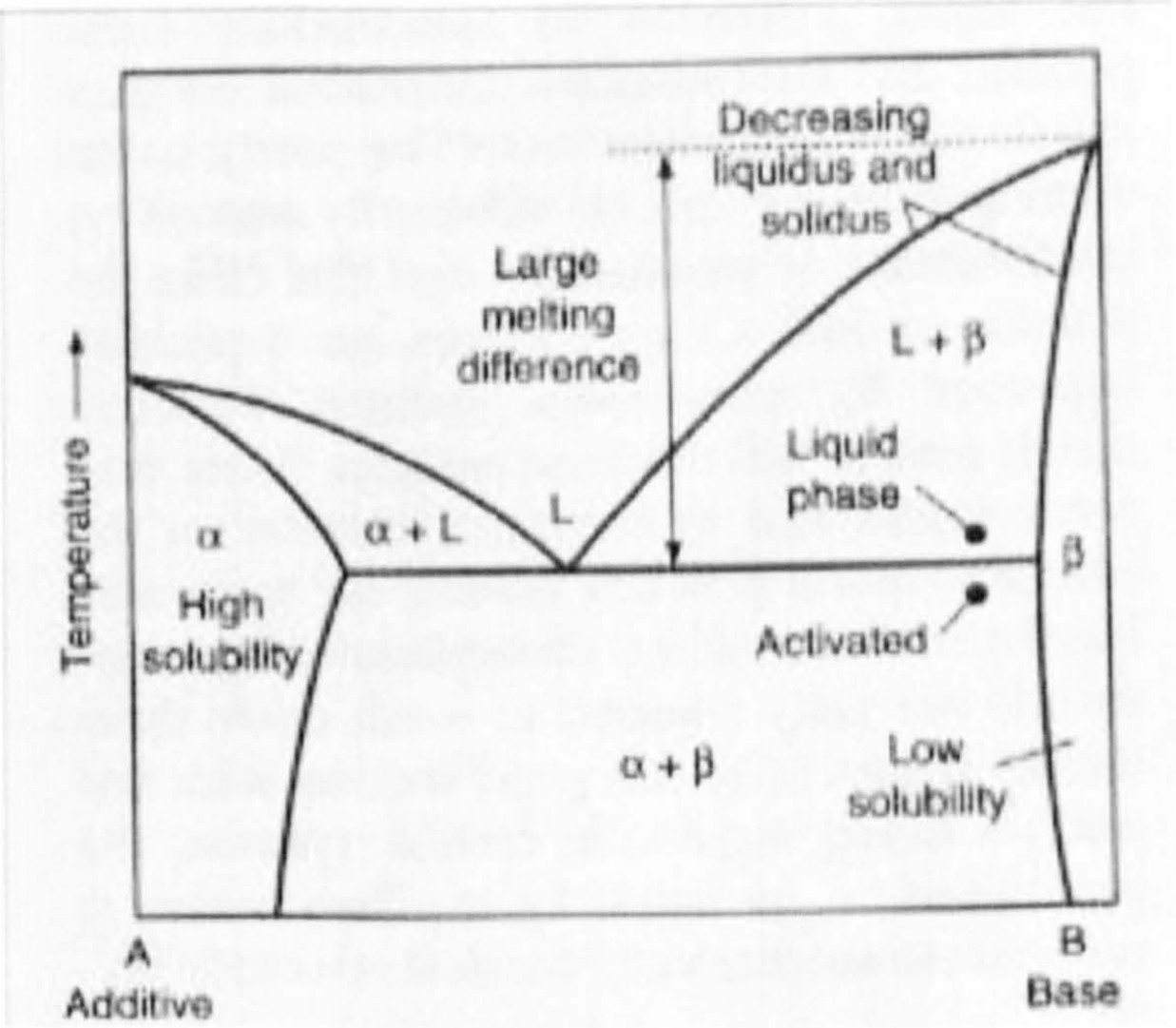

Figure 02.17: Phase diagram of an ideal system for LPS (Tandon & Johnson 1998).

German & Rabin (1985) and German (1985) considered the schematic binary phase diagram shown in Figure 2.17 and suggested the key features of an ideal liquid phase sintering system to be:

(1) The additive A should have a lower melting point than the base B. The alternative is a low melting point eutectic which does not form liquid phase on spontaneous heating.

(2)The solubility of the additive A in the base B should be low for the additive to remain segregated to particle boundaries. This increases the liquid + solid range and the volume of liquid for a given amount of the second added component.

(3) The base should be soluble in the liquid and it should also have a high diffusivity in the liquid in order to ensure high rates of mass transport and therefore rapid sintering.

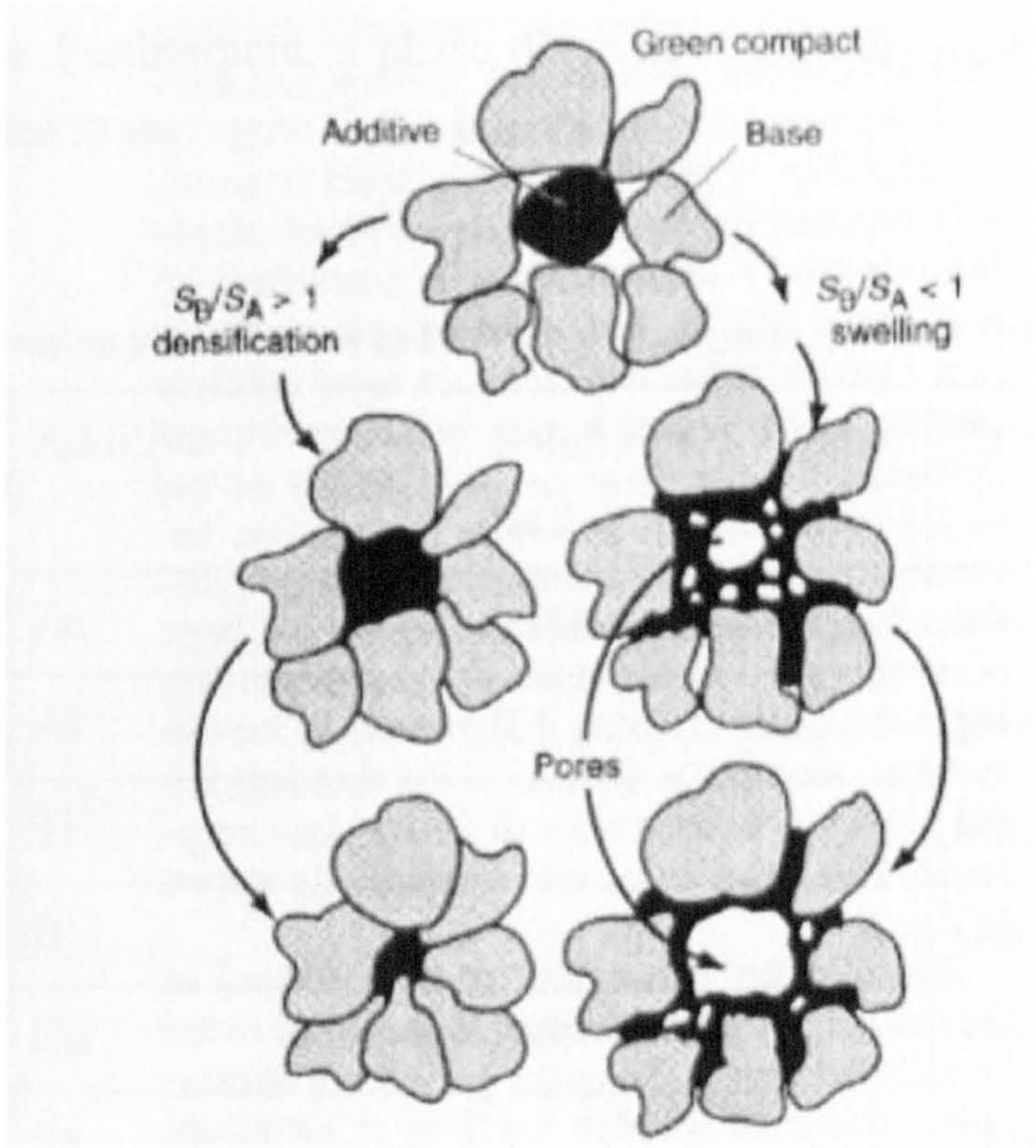

Figure 2.18: A schematic diagram contrasting the effects of solubility on densification or swelling during LPS (Tandon & Johnson 1998).

Solubility of the solid in the liquid is a necessary pre-requisite for successful LPS with regard to systems having more than 65vol% solid (Tandon & Johnson 1998). Solubility promotes solubility re-precipitation and increased efficiency in particle arrangement thereby leading to increased sintered density. As noted earlier on, solubility of the liquid in the solid is not preferred due to occurrence of swelling as the liquid which diffuses into the solid grains leads to formation of porosity which is difficult to remove upon subsequent sintering. Figure 2.18 suggests that transient liquid phase can be controlled to produce desirable properties as exemplified in Cu-Sn and Cu-Zn systems. The solubility parameter (S), which determines whether swelling or shrinkage occurs during LPS, is the ratio of the solid solubility (S_B) in the liquid to the liquid solubility in the solid (S_A). Table 2.9 presents the solubility effects on densification in LPS for various material systems.

The actual amount of dimensional change is a function of the processing conditions. Phase diagrams are useful in identifying solubility parameters and other features that promotes LPS (Tandon & Johnson 1998). A study of an ideal phase diagram for LPS (Figure 2.17) reveals that a deep eutectic is preferred due to significant reduction in sintering temperature with the formation of liquid phase. The formation of intermediate compound is generally unfavourable. High-temperature phases can reduce diffusion rates, while brittle intermetallic phases that form during cooling can degrade

mechanical properties. Furthermore, a phase diagram reveals the tendency of alloying elements and impurities to segregate to the interfaces.

Table 2.9: Solubility effects on densification in LPS (after Tandon & Johnson 1998).

Base	Additive	Solubility ratio, (at.%)	Behaviour
Al	Zn	0.004	Swell
Cu	Al	0.1	Swell
Cu	Ti	4	Shrink
Fe	B	7	shrink
Fe	Cu	0.07	Swell
W	Fe	5	Shrink

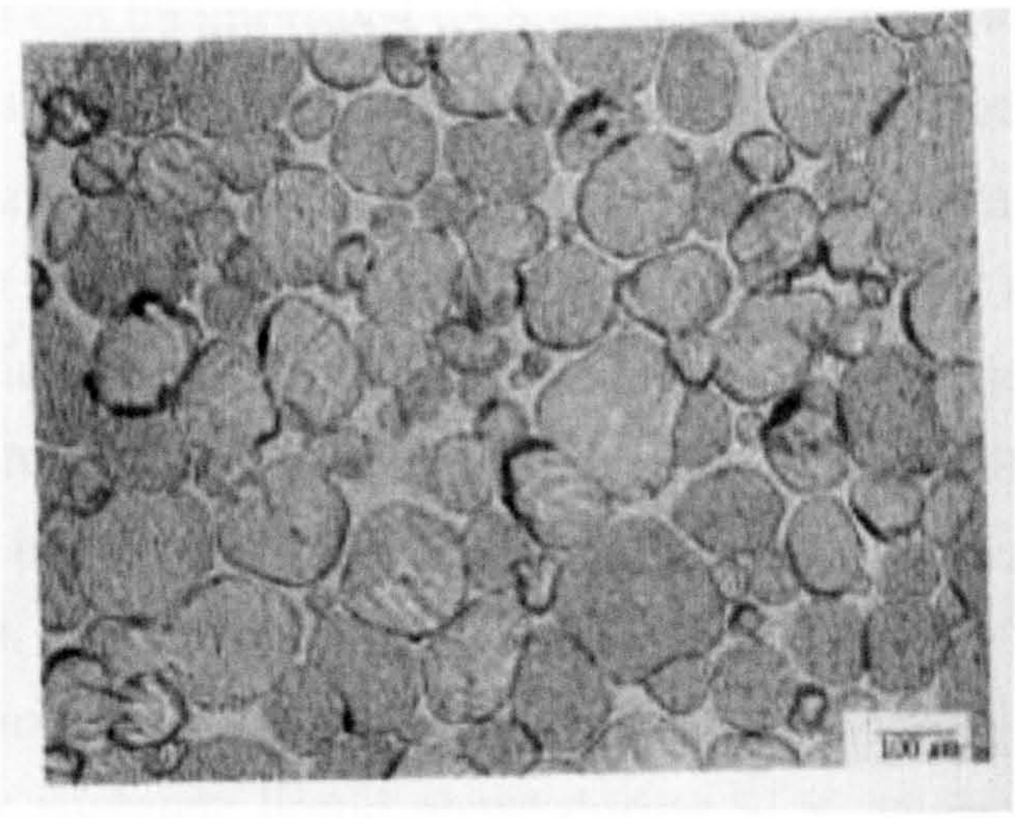

Figure 2.19: Typical microstructure of a LPS system with the phase diagram characteristics shown in Figure 2.17 (Tandon & Johnson 1998).

A downward sloping liquidus and solidus indicates a propensity for solute segregation and lower surface energies (Tandon & Johnson 1998). Therefore, a sintering temperature just above the eutectic temperature is optimal for a composition in the L + β region. A typical LPS microstructure is shown in Figure 2.19 which consists of relatively large, rounded grains suspended in a liquid matrix, with the degree of grain contact governed by the dihedral angle. In a system that lack solubility of the solid in the liquid phase, a rigid skeletal structure is expected with densification controlled by solid state diffusion. Use of extremely fine starting powders or segregating activators

that promote solid-state sintering in the presence of the liquid ensures high sintered densities are obtained.

Schaffer and co-workers (2001b) examined the behaviour of a number of likely candidate alloys and discovered that Al-Sn, which follows very closely the ideal characteristics described in Figure 2.17, had a much more desirable sintering response than either Al-Cu or Al-Zn, both of which have at least one ideal characteristic. On this ground, they designed the Al–Sn–Mg system for uncompacted sintering and were able to achieve near full theoretical density. However, the tensile strength of the Al–Sn system was poor because tin could not provide much strengthening whereas Mg addition in Al–Sn–Mg system improved its tensile strength. This confirms the potency of Mg in disrupting the surface oxide film of aluminium, thus, promoting metal/metal bonding. Meanwhile, it is hereby speculated that the addition of tin could have reduced the strengthening effect of magnesium in the Al-Sn-Mg powder.

P/M aluminium alloys can be improved without recourse to hot working or master alloy powders if their design is based on an understanding of the underlying sintering processes and the characteristics of an ideal liquid phase sintering system (Schaeffer *et al.* (2001b). However, this idea can be applied to the design of suitable aluminium alloys for the fabrication of parts in direct SLS process with a view to ensuring that the oxide phase of the aluminium powders is disrupted in order to make allowance for effective interparticle bonding/melting across the layers so as to achieve the production of full density parts. This entails the determination of the appropriate chemical composition of aluminium alloys that make allowance in their thermal cycle for the transient nature of the adequate liquid phase during SLS. Moreover, there is an urgent need to establish whether there exist appropriate alloying elements that will effectively disrupt the surface oxide of the aluminium powder under the direct SLS process and, if so, the necessary concentration. To do this, the mechanism of disruption of the surface oxide film in aluminium powders via the direct SLS process need to be understood as noted in Section 2.3.4. Thus, an investigation is necessary to ascertain if alloys of the same composition as those employed in the press and sinter technique could give equivalent or a better sintering response during direct SLS without the application of hot working processes. If this is not the case, alloys that would give desirable response to direct SLS need to be designed.

Having investigated the sintering of aluminium powders in the P/M technique, specifically, the disruption of the surface oxide film of aluminium, liquid phase sintering and alloying design, the fundamental principles of the LPS in direct SLS technology, as well as its effect on the properties of sintered components, is developed, in the following section.

2.5 The Application of Liquid Phase Sintering to Direct SLS

Kruth *et al.* (2005) classified the binding mechanisms for SLS processes as shown in Figure 1.3. The most applicable of all the binding mechanisms to direct SLS is the liquid phase sintering/partial melting (LPS) which incorporates the melting of the binder material of lower melting point thereby binding together the particles of the structural components of the system. Agarwala *et al.* (1995) described the application of LPS to SLS of metals as follows: "sintering or bonding between particles during SLS occurs by raising the temperature of the powder above the softening temperature by a laser beam heat source." The process is similar to other laser assisted material processing techniques in the sense that its success depends strongly on the adequate coupling of the laser energy. From the point of view of the conventional powder metallurgy sintering process in which bonding between particles is achieved by compaction; when sintering between solid particles occurs via the incident laser energy, it is accompanied by the formation of a neck between individual particles (Figure 2.20). The phenomenon of necking during the sintering process has been attributed to the diffusion of atoms, through the liquid phase, along the surface, grain boundaries or other paths at elevated temperature (Agarwala *et al.* 1995). Because solid state sintering is very slow and requires an extremely long time (hours) for completion, a more rapid form of sintering is liquid phase sintering has been suggested to elucidate the concept of necking in SLS. LPS, illustrated schematically in Figure 2.21, is such that a low melting point additive component of the material system is in liquid phase (LP) during the sintering process (German 1985). The LPS phenomenon, as applicable to SLS, involves only the re-arrangement phase. Presence of the liquid phase results in rapid sintering process since mass transport can occur by liquid flow and particle re-arrangement. During this stage, diffusion is significantly faster.

During SLS, the entire thermal cycle is very short. The duration of the laser beam on any powder particle is typically between 0.5 and 5ms so bonding or sintering must occur speedily, in the order of seconds. This is achieved by viscous flow or by melting. As noted earlier on, because metals do not have a softening phenomenon but rather a generally high melting temperature, a melting-solidification approach is used for the

description of the SLS processing of metals. From the early experimental evidence gathered by Agarwala *et al*. (1995), Tolochoko *et al*. (2003), Zhu *et al*. (2003a, 2003b), and Zhu *et al*. (2005), it can be deduced that the SLS of metals is similar to liquid phase sintering which employs a material system that has a mix of the higher melting point structural materials and lower melting binding materials such that the lower melting phase melts while the higher melting phase remains solid and is bonded together by the melt.

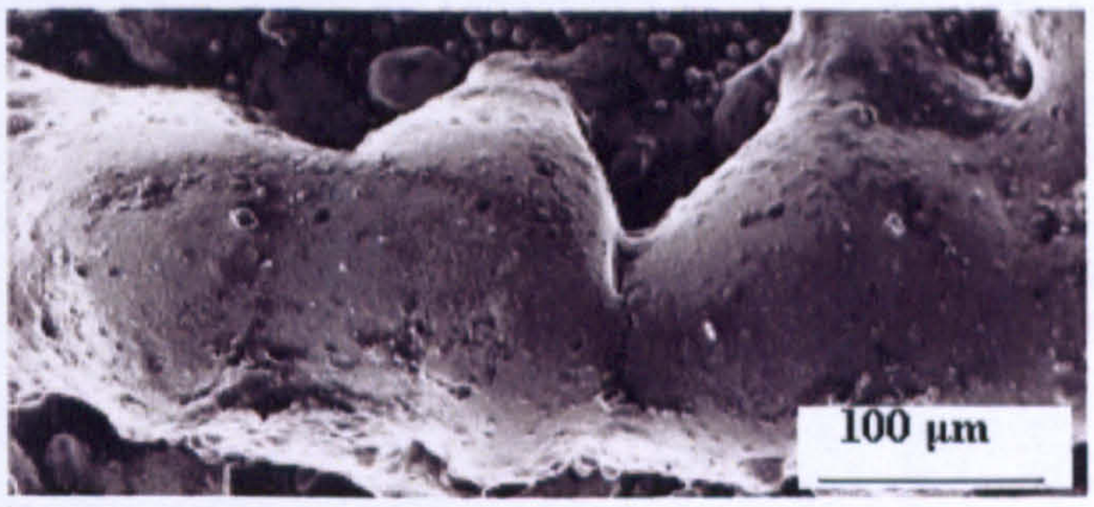

Figure 20.20: SEM micrograph showing formation of a neck between individual particles (Gu &Shen 2007c).

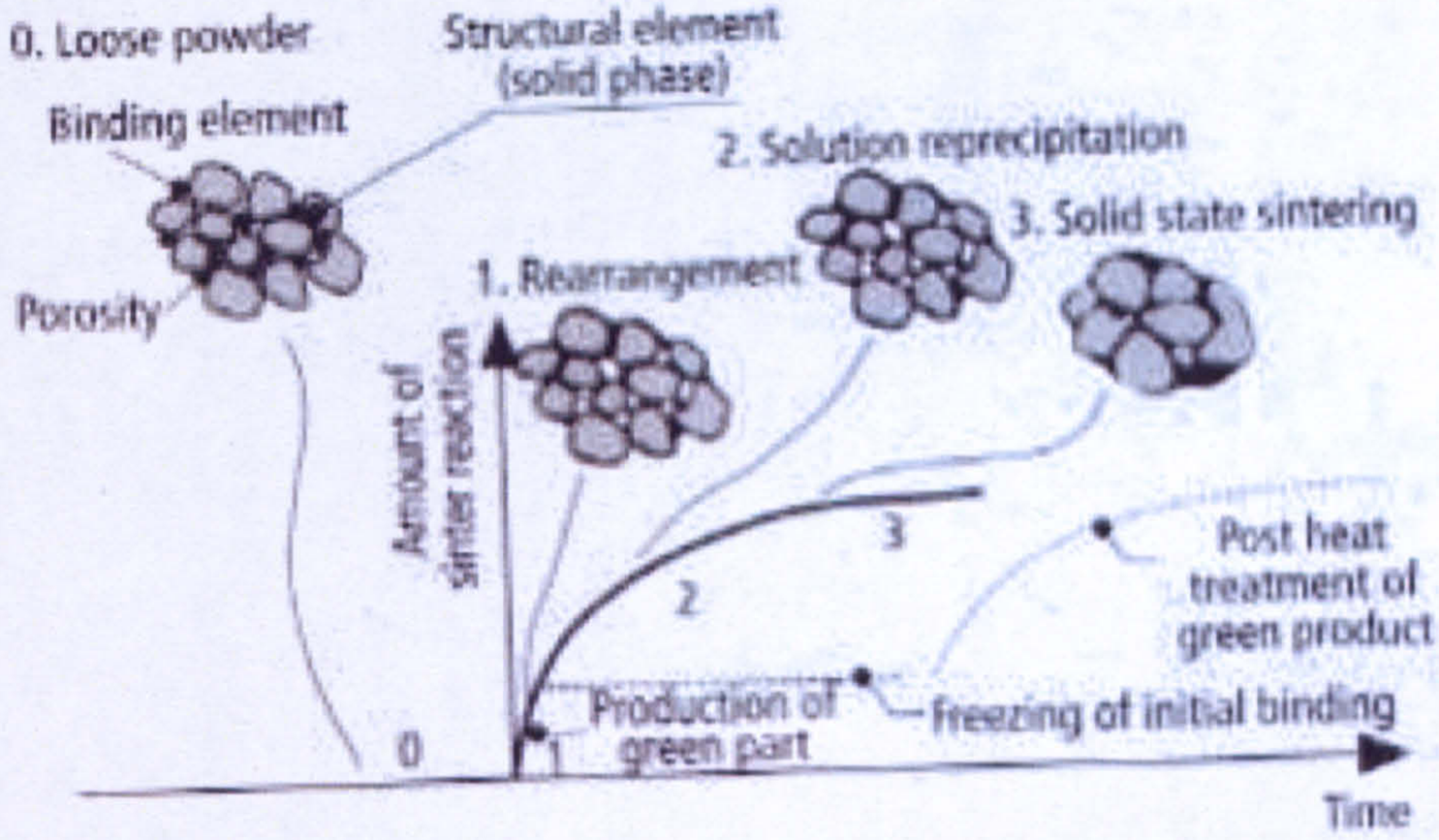

Figure 2.21: Mechanism of Liquid Phase Sintering (LPS) as applied to SLS (after Kruth et al. 2005).

Moreover, it can be concluded from the results of literature cited earlier that the improvement obtained in the mechanical and microstructural properties of laser sintered components depends on the success or otherwise of the LPS with regard to the amount of liquid phase present.

Tolochoko *et al.* (2003) elucidated that a pre-requisite for obtaining components of improved mechanical integrity via direct SLS is the attainment of low porosity in the sintered parts. To achieve this goal, a condition of an absolutely pore-free structure in which the volume of space between the solid particles equals the volume of the liquid phase at the end of the particles' re-arrangement process must be obtainable. However, if an excess amount of liquid phase is present over a long period of time, balling results. If the liquid phase quantity is insufficient to fill all interparticulate pores completely, this results in the sintered part being characterized by excessive porosity. Furthermore, Tolochoko and co-workers applied this theory to the SLS of single-component powders during which partial (surface) melting of particles occurs. Mathematically, the volume fraction (γ_L) is hereby expressed as

$$\gamma_L = (V_s^* - V_c)V_s^* \quad \text{.....2.7}$$

Where V_s^* = volume of solid particles of raw powder and V_c = volume of non-melted cores of particles.

They also considered the SLS of two-component powders in which complete melting of binder particles is assumed while the main component particles remain solid (this is particularly true when the difference in the melting points of the structural and binder component particles is significantly high). By considering a condition in which the binder particles melt completely, Tolochoko *et al.* (2003) described their observation according to equation (2.8) below:

$$\gamma_L = V_B / V_{OM} + V_B \quad \text{.....2.8}$$

where V_{OM} = volume of space between the solid particles of the main component and V_B = volume of binder particles.

To achieve a low porosity component, the amount of available liquid phase should be such that it may act as lubricant for the re-arrangement of the particles. Therefore, the amount of available liquid phase in the sintering pool controls the densification mechanism and the resultant microstructure of the SLS processed parts by altering the thermokinetic and thermocapillary properties such as viscosity, wettability, and

rheological properties (Bourell *et al.* 1992, Agarwala *et al.* 1995, Zhu *et al* 2004). The mobility of a solid-liquid mixture and degree of interfacial bonding are functions of the amount and viscosity of the melt. The viscosity μ of the solid-liquid mixture is defined as shown below according to Agarwala *et al.* (1995), and Tolochoko *et al.* (2003).

$$\mu = \mu_o(1-(\varphi/\varphi_M))^{-2} \quad \text{.....2.9}$$

Where μ_o is a base viscosity that contains no solid particles, φ, the volume fraction of solids in liquid, and φ_M, a critical volume fraction of solids above which the mixture has essentially infinite viscosity.

The inter-particulate bonding across layers is controlled by the base viscosity, μ_o, which decreases with increasing powder bed temperature. The base viscosity must be sufficiently reduced such that liquid completely surrounds the solid particles. Also, the mixture viscosity, μ, must be low enough during SLS. Moreover, the viscosity of the mixture must be sufficiently high to prevent balling and this condition can best be attained by manipulating an appropriate solid-liquid ratio (Agarwala *et al.* 1995, Zhu *et al* 2004). This can be achieved by the combination of low μ_o and regulated μ if parts having desirable sinterability are to be obtained. According to Zhu *et al.* (2004), in LPS, the relative shrinkage of the powder bed is described mathematically by equation 2.10.

$$(\Delta L/L_o) = (k\gamma_{lv}t)/D\mu \quad \text{.....2.10}$$

Where γ_{lv} is the liquid-vapour surface energy, t, the sintering time, D the particle diameter, and k is a constant. The sintered density ρ for a powder bed having initial tapping density ρ_t is described in equation 2.11 by German (1990).

$$\rho = \rho_t(1-(\Delta L/L_o))^{-3} \quad \text{.....2.11}$$

Defining a non-dimensional parameter α according to equation 2.12,

$$\alpha = ((k\gamma_{lv}t)/D\mu_o) \quad \text{.....2.12}$$

The final sintered density ρ is obtained by combining equations 2.10, 2.11, and 2.12 according to German (1990).

$$\rho = \rho_t(1-\alpha(1-(\varphi/\varphi_M))^2)^{-3} \quad \text{.....2.13}$$

Equation 2.13 suggests that the densification of the SLS processed powders is directly proportional to its tapping density (ρ_t). Moreover, it is evident from equation 2.13 that in order to attain the ideal condition during SLS in which the amount of liquid phase is exactly equal to the volume of pore spaces between the powder particles, the right choice and correct amount of binder material must be made coupled with the determination of the appropriate processing parameters (see Section 2.7.1). Powder properties such as the size, and shape of the powder particles, as well as particle arrangement play an important role in determining the ideal SLS liquid phase condition. If the processing and powder parameters are poorly controlled, difficulties such as balling, microstructural agglomeration, layer delamination and porosity are bound to be encountered during the SLS of metals due to the initiation of Marangoni convection, and uneven thermal gradient on the powder bed. These problems may also arise as a result of improper arrangement of the powder particles on the sintering bed. While the role of component ratio of binder material in the SLS of metals will be presented in this section, the roles of processing parameters as well as powder properties will be discussed in sections 2.7.1 and 2.7.8 respectively.

An appropriate choice of the amount (measured in weight percentage) of binder materials (which represents the amount of liquid phase formed if complete melting of the binder is assumed) has been shown to overcome some of the SLS challenges highlighted in the preceding paragraph. Gu & Shen (2006a, 2007a, 2007b, 2008b) demonstrated that there exist optimal component ratios; for each of WC-Co particulate reinforcing Cu matrix composites; multi-component Cu-based metal powder; and sub-micron W-Cu / micron Cu powder mixture systems. At the binder's optimal component weight ratio, high densification and homogeneous sintered microstructure are obtainable as a consequence of favourable viscosity of liquid-solid mixture and the sufficient re-arrangement of binder and structural particles. However, they noted that when binder content falls below its optimal component weight ratio for each of these

systems, severe particulate aggregation occurs due to limited liquid formation and the resulting high liquid viscosity due to high solid fraction and reduced Marangoni effect.

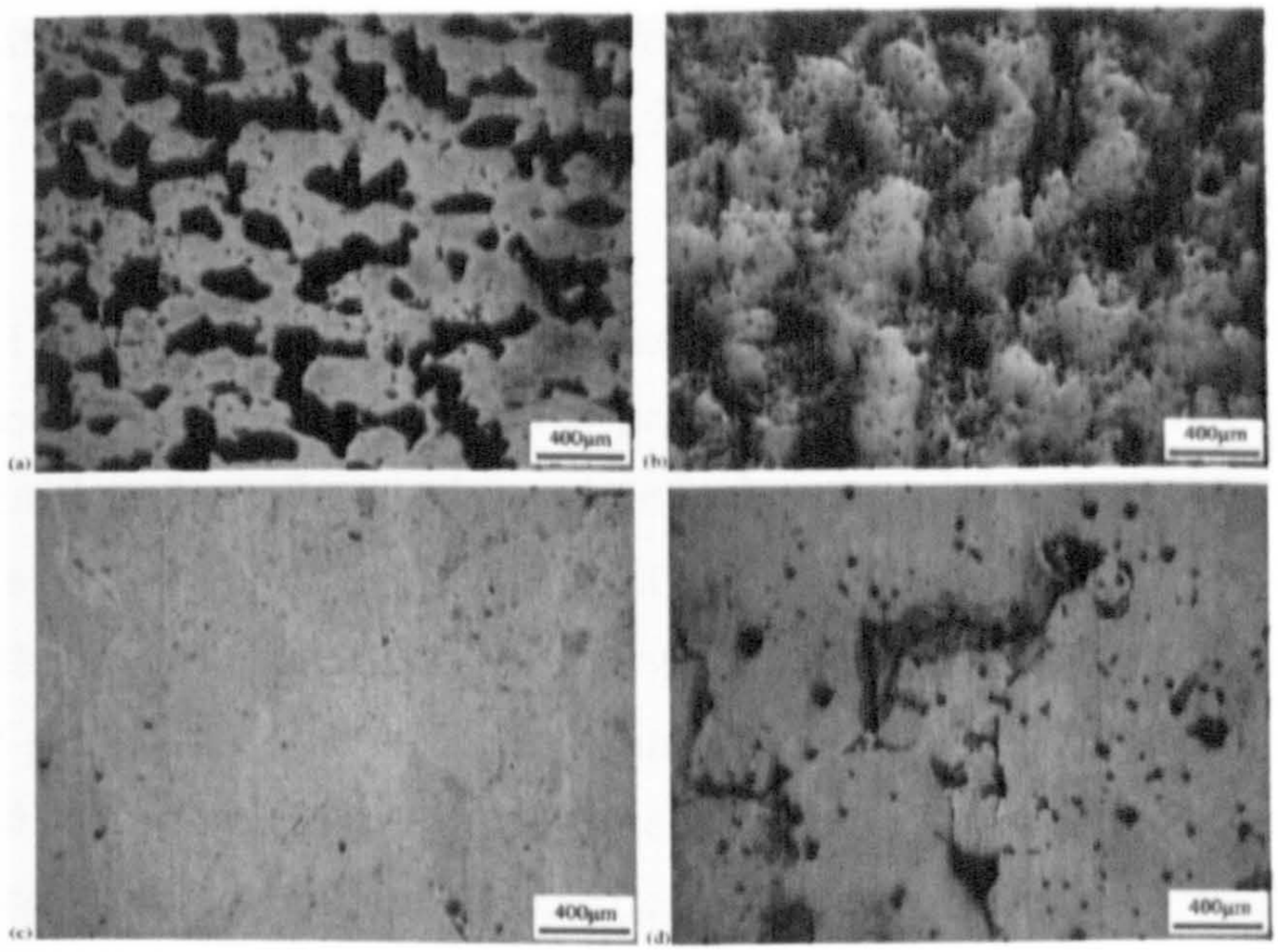

Figure 02.22: Optical images of the polished sections of the laser sintered multi-component Cu-based metal powder with varying contents (wt%) of binder CuSn in the samples (a) 20 (b) 35 (c) 50 and (d) 65 (after Gu & Shen 2007a).

Table 2.10: Fractional amount of liquid phase generated in various SLS processed metal systems.

Material	Binder material	Fractional liquid phase.	Author (s)
Fe-Cu system	Cu	. 0.3	Zhu *et al.* 2003b
multi-component Cu-based metal powder	CuSn	0.5	Gu & Shen 2007a
sub-micron WC-Cop / Cu bulk metal matrix composites	Cu	0.7	Gu & Shen 2007b
sub-micron W-Cu / micron Cu powder mixture	Micron Cu powder	0.6	Gu & Shen 2008b

With the binder content increasing beyond its optimal component ratio, the laser sintered densities of the parts made in each of these powder systems deteriorates

because of the initiation of the balling phenomenon and uneven thermal gradient. Their experimental evidence has revealed that the fractional amount of liquid phase yielding optimal densification and homogeneous microstructure (Figure 2.22) for the SLS of various powder systems are as shown in Table 2.10.

In conclusion, all these studies attest to the fact that the determination of the optimal liquid phase amount for SLS, for which a pore-free microstructure is obtainable, is complex and significantly influenced by chemical composition and component ratio which in turn is affected by the packing density of the blended powder bed as well as the viscosity of the laser sintered powders powder systems. It is now evident that the fraction of liquid phase available in the sintering pool of SLS of metals determines the densification and microstructure of the laser processed parts by influencing the thermokinetic and thermocapillary properties such as viscosity, wettability and rheological characteristics (Agarwala *et al.* 1995). Table 2.10 suggests that provided appropriate processing parameters are used, the optimal liquid fraction existing at the binder's optimum component ratio is dependent on the energy gain of the powder and is partly controlled by the weight fraction of the binder in the powder mixture.

With the background knowledge of the application of LPS to the direct SLS clearly laid out in the above paragraphs, the stage is now set for the understanding of the various physical phenomena underlying direct SLS of metals, with regard to laser-material interaction as well as some complications that accompany this process. In the following section, an attempt is made to examine how various workers in this field have overcome these difficulties.

2.6 Selective Laser Melting of Metals (SLM)

Das (2003) carried out a comprehensive review of SLM of metals by identifying and presenting an understanding of the important physical mechanisms affecting the process. The relevant physical mechanisms to be considered are oxidation, "homologous wetting", and epitaxial solidification. Some of these issues will be discussed in this section in order to determine their relevance to the SLM process.

2.6.1 Oxidation, Wettability, and Mechanical Properties

Metallic powders have a higher degree of contamination by moisture, organics, adsorbed gases, oxide and nitride films on particle surfaces due to their much higher surface area per unit volume when compared to cast or wrought components (Das 2003). These contaminants not only inhibit successful wetting, which promotes interlayer bonding and densification of the melted powder, but also degrade the mechanical properties and part geometry of the consolidated component during SLM (Das 2003). For this reason, SLM of metals is considered to be far more difficult than the laser sintering of polymers, direct or indirect SLS of metals because of the oxidation, balling and uneven thermal gradient across the layers which may cause poor interlayer bonding, low density, weak strength and rough surface of the SLM processed part (Das 2003, Tang *et al.* 2003, Gu & Shen 2007c).

In an attempt to mitigate the deleterious effect of oxidation as well as ensuring good wetting and successful layer- by-layer consolidation in direct laser sintering of metals, various approaches have been adopted by SLM investigators: sintering in an inert atmosphere like argon, neon, and nitrogen which renders the oxidation process inactive or slows it down; disruption of the surface oxide film by alloying addition; determining the optimal processing parameters that allows minimal balling; remelting of the underlying substrate in order to break down the surface contaminants to ensure a clean surface at the atomic level between the solid and the liquid; ad incorporation of fluxing additives (Niu & Chang 1998, 1999a, 1999b, 2000; Schaffer *et al.* 2001a, 2001b; Das 2003; Zhu *et al.* 2004; Zhu *et al.*2005; Gu & Shen 2007c). Therefore, the disruption of surface oxide films in metals and their alloys is of paramount importance during their SLM processing in order to develop high performance components with improved mechanical properties at elevated temperatures (Das 2003). The condition of attainment of effective disruption of the surface oxide film with a view to ensuring inter-particulate melting or coalescence requires an understanding of the wetting mechanism of a molten liquid on a substrate of its own kind, i.e. of identical chemical composition. Schiaffino and Sonin (1997a, 1997b, 1997c) designated this mechanism as "homologous wetting." They described "homologous wetting" as an inherently non-equilibrium phenomenon involving heat transfer, fluid flow and solidification.

Furthermore, Das, (2003) explained the poor wetting of a substrate by a liquid metal by investigating the balance between the interfacial energies involved in wetting and non-wetting systems as illustrated in Figure 2.14. At equilibrium, the wetting angle, 0, is determined by the interfacial free energies according to equations 2.1 and 2.2. As noted

earlier on, the liquid will completely wet the substrate as cos (θ)→1 or equivalently, if $\gamma_{sv} - \gamma_{sl} > \gamma_{lv}$. This corresponds to the case shown on the left in Figure 2.14. This idea had been applied to gain an understanding of the effect of surface oxide on aluminium sintering by Schaffer *et al.* (2001b). Das (2003) extended the application of this principle in describing the phenomena of homologous wetting (wetting behaviour of a molten liquid on a substrate of its own kind i.e. the identical chemical composition) and epitaxial solidification in an attempt to surmount the challenge of oxidation in the direct SLS of titanium alloy powders. Both homologous wetting and epitaxial solidification will now be explained in the next paragraph.

In order to understand the wetting behaviour of a metal on a substrate of its own kind, Das (2003) conducted two types of experiments in which a stainless steel powder placed on the stainless steel substrate (having the same composition as the powder) was melted by a stationary Nd: YAG laser beam incident on the powder at first and another one in which a 1x4mm strip of stainless steel was placed on the same composition substrate and melted by the same laser beam. The same conditions of vacuum atmosphere (10^{-6} Torr) with no substrate preheat, 350°C preheat and 900 °C preheat were applied to investigate the influence of substrate preheating on wetting behaviour. The dynamics of melting, droplet formation, wetting and solidification were captured by video microscopy during the investigation. The results of the experiments revealed that after melting and droplet formation, the molten metal showed no tendency to spread and wet the underlying substrate because the droplet stopped the substrate from heating sufficiently. Instead it formed a nearly spherical droplet having a point like contact with the substrate (Figures 2.23).

Figure 2.23: Homologous wetting experiment at 37 s, 50 s, and 54 s (after Das 2003).

The solidified droplets were easily detached from their respective substrates. In addition, the substrates did not exhibit any evidence of melting at the droplet/substrate

interface. This result implies that the impact of preheat temperature on the wetting behaviour was minimal as shown in Figure 2.23.

Figure 02.24: Solidified droplets in "powder on plates" experiments (after Das 2003).

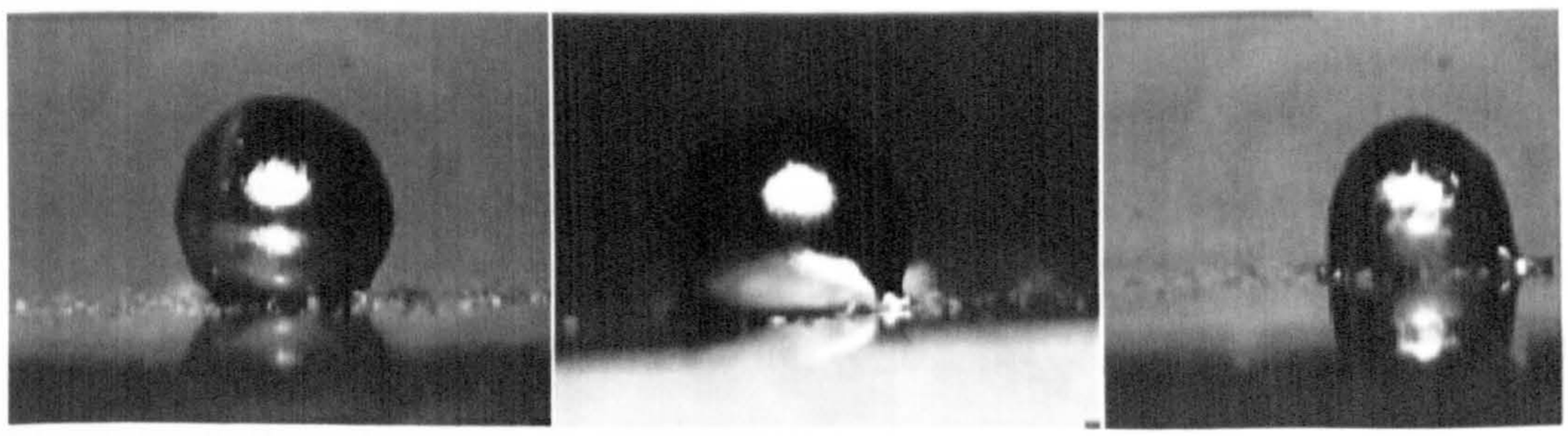

Figure 02.25: Solidified droplets in "strip on plates" experiments (after Das 2003).

Moreover, the shape of the solidified droplets obtained for the "powder on plate" experiment was noted to have been characterised by an elongated peak feature at the top and a finite contact area with the plate (Figure 2.24) whereas that of the "strip on plate" experiment exhibited a greater degree of sphericity and a very small area of contact with the plate (Figure 2.25). In conclusion, despite the fact that the vacuum atmosphere was used during the experiment (10^{-6} Torr), poor wetting observed in these experiments was attributed to a lack of substrate remelting. This led Das to consider the idea of remelting the underlying substrate (as will be described in the next section) in order to weaken and/or disrupt surface contamination such as oxide films so as to provide a clean interface at the atomic level between the solid and the liquid.

2.6.2 Epitaxial Solidification in SLM

According to Nelson *et al.* (1999) and Das (2003), SLM of metals could be likened to fusion welding. In fusion welding, the base metal and the weld metal may have similar but not necessarily the same composition, while in SLM of monolithic metallic materials, the substrate layer and the new layer of metallic powder to be melted are the same in composition. Meanwhile, it has been established that dilution of the base metal occurs in all types of fusion welding. Dilution is the partial localised remelting of the base metal which provides a continuous interface free of oxide films or other contaminants between solidifying liquid weld metal and the base metal. Dilution is a pre-requisite for good weld integrity. During dilution, or "melt back", grain growth occurs at the solid-liquid interface between the base metal and the liquid in contact with it. Due to the significant similarities between fusion welding and SLM, it is instructive to understand the implication of epitaxial solidification on SLM process control.

In fusion welding, it is generally agreed that the liquid weld metal completely wets the partially melted substrate at the fusion boundary. Meanwhile, by likening the epitaxial solidification mechanism in SLM to the formation of a nucleus of solid from its melt in contact with a substrate as it occurs in the fusion welding process (Figure 2.14), the free energy required for the initiation of nucleation is a function of the wetting angle (0) between the substrate and solid formed. Therefore, the relationship between wetting angle and interfacial energies is illustrated in Figure 2.14, equations 2.1, and 2.2. During epitaxial solidification, both the contact angle, (0), (equation 2.2) and free energy ΔG^*, become zero (equation 2.16), and consequently, growth of the solid initiates at the fusion boundary without difficulty (Savage *et al.* 1976). As a result, it can be argued that little or no nucleation barrier in solidifying weld metals exists during fusion welding or SLM.

$$\Delta G_{het} = S(\theta) * (-V_S \Delta G_v + A_S \gamma_{SL}) = S(0) * (-4/3\pi r^3 \Delta G_V + 4\pi r^2 \gamma_{SL}) \text{.....(2.14}a\text{)}$$

$S(0) =$

ΔG_v = the free energy change per unit volume associated with formation of the nucleus,

V_S = The volume of the nucleus.

A_S = The surface area of the new interface created by the solid nucleus and the liquid,

S (0) = Shape factor dependent on the contact angle

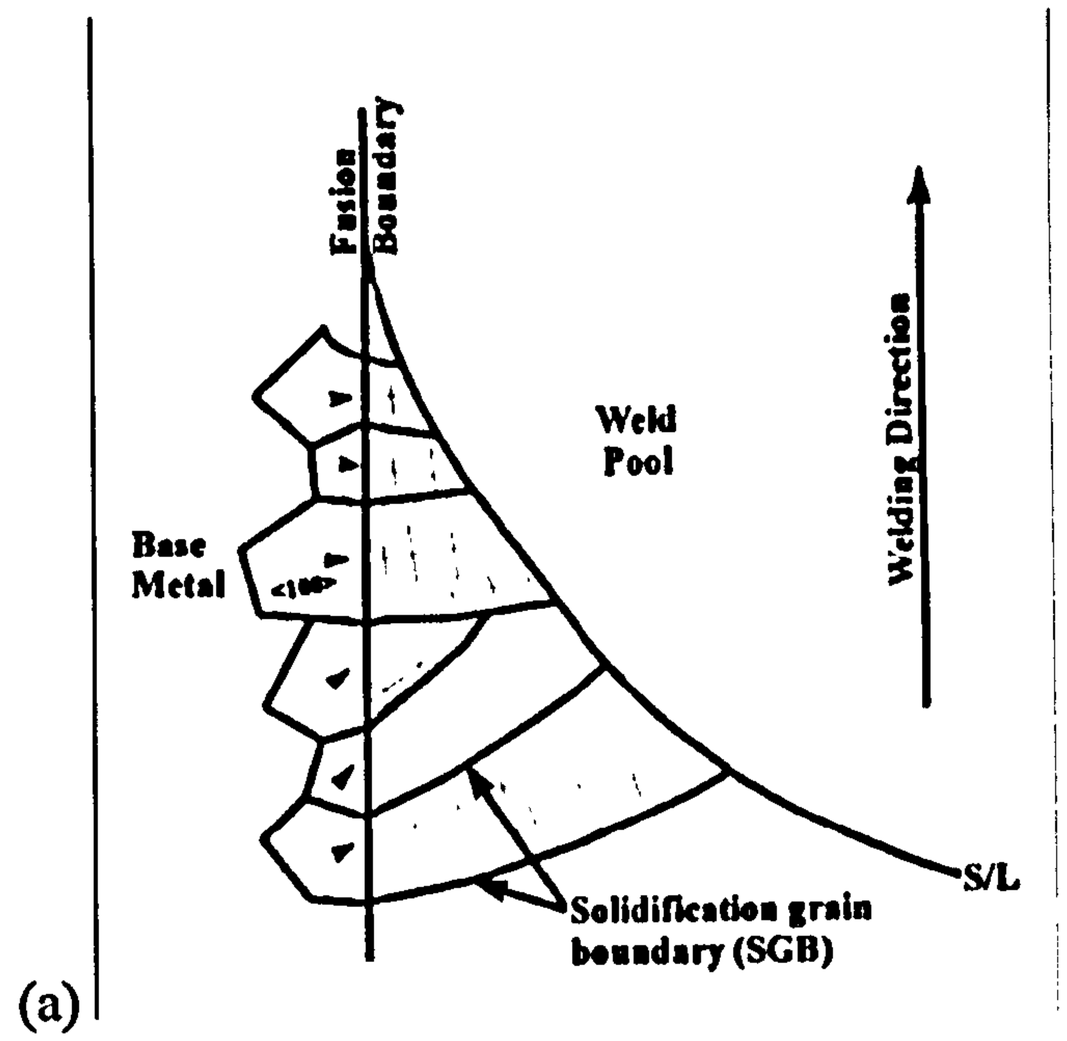

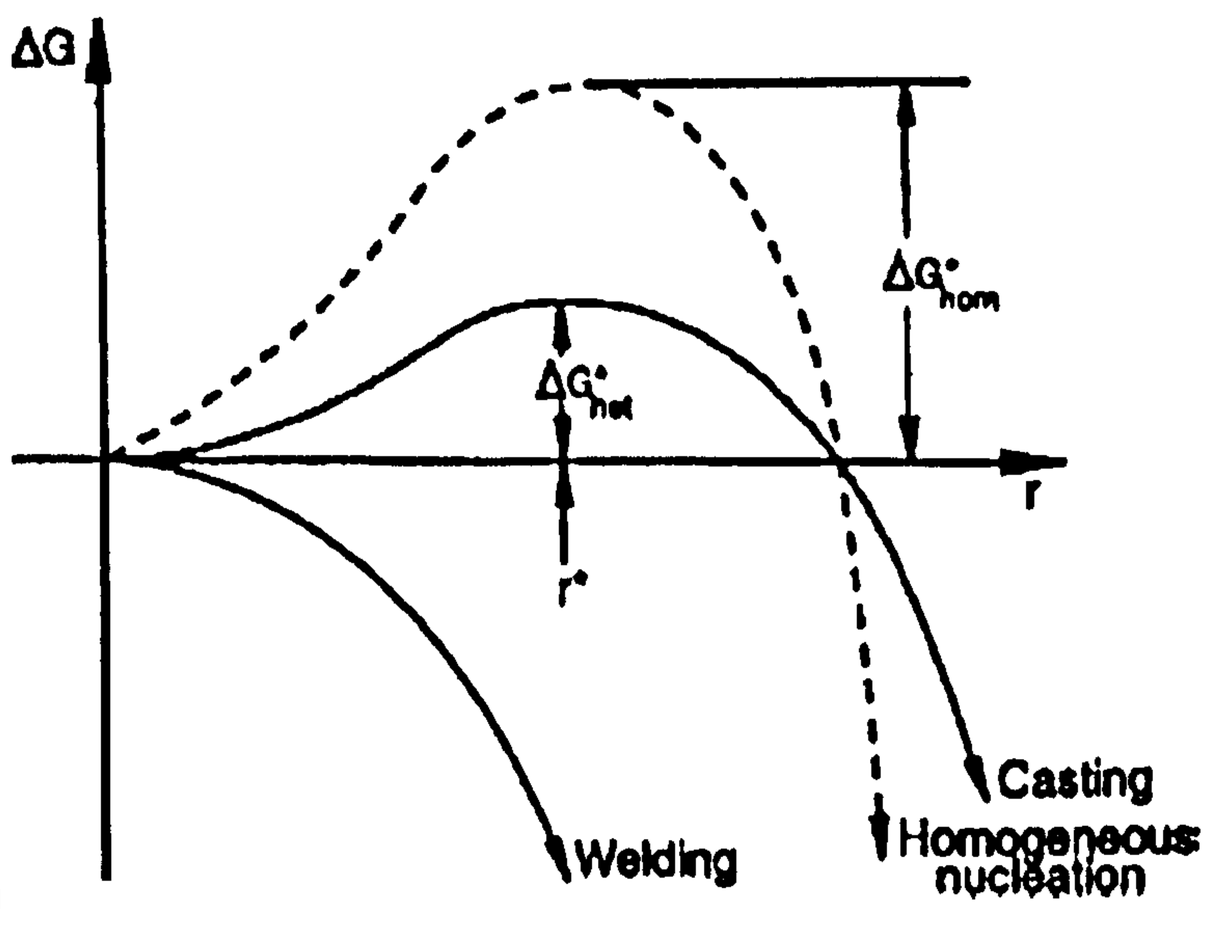

Figure 2.26: (a) Illustration showing the epitaxial nucleation and competitive growth in the weld fusion zone (after Nelson *et al.* 1999), (b) Schematic of free energy change associated with heterogeneous nucleation in casting and welding juxtaposed with free energy change in homogeneous nucleation (after Grøng 1994).

The critical radius r^* for heterogeneous nucleation is obtained by setting the first derivative of equation (2.14a) to zero.

$$r^* = (2\gamma_{SL}) / \Delta G_V \quad \text{.....2.15}$$

The associated free energy barrier ΔG^*, for heterogeneous nucleation is derived by substituting the expression for r^* r* into (2.14a):

$$\Delta G^* = 16\pi\gamma_{SL}^3 S(\theta)/3\Delta G_V^3 \quad \text{.....2.16}$$

According to Kou (1987) and Savage (1980), growth of the solid in a fusion welding is perceived as being initiated by epitaxial growth from the substrate and proceeds by competitive growth toward the center line of the weld. At the fusion boundary, since the substrate is assumed to be completely wetted by the weld metal, grain growth is initiated in the weld by arranging atoms in the liquid phase on the existing crystalline substrate, thus extending the solid without altering the crystallographic orientation (Savage, *et al.* 1965, 1972; Savage & Aronson 1966).). Moreover, Savage & Aronson (1966) noted that solidification by epitaxial growth in fusion welding results in nearly complete continuity of the crystallographic orientation and grain boundary mis-orientation between base and weld metal grains adjacent to the fusion boundary. Therefore, Nelson *et al.* (1999) reported that once solidification by epitaxial growth is initiated, it proceeds toward the weld center-line in a competitive-type growth mechanism illustrated in Fig.2.26a above. This implies that grains with growth direction oriented most preferentially along the heat flow direction gradient tend to crowd out those grains whose growth directions are not as suitably oriented (Figure 2.26a). Whereas, the predominant mechanism of solidification in fusion welding is the competitive growth in the weld fusion zone, Kou (1987) identified and discussed the details of other mechanisms such as dendrite fragmentation, grain detachment, heterogeneous nucleation and surface nucleation that may tend can interrupt and/or dominate the solidification structure in fusion welding. Moreover, Nelson *et al.* (1999) noted that it is unlikely that dendrite fragmentation, grain detachment, heterogeneous nucleation and surface nucleation would occur in fusion welding. In addition, Lippold *et al.* (1992), defined the nature of the various boundaries observed in single-phase weld metal as solidification grain boundaries (SGB), solidification sub-grain boundaries (SSGB) and migrated grain boundaries (MGB). It is now understood that the nature of epitaxial growth in fusion welding metals described in this section produces a network of grain boundaries in the fusion zone (Figure 2.26a). This network of grain boundaries in the fusion zone consists of the solidification grain boundary (SGB) network which is an extension of the heat affected zones (HAZ) grain boundaries at the fusion boundary. Nelson *et al.* (1999) and Das (2003) noted that the fusion boundary morphologies observed in the fusion welding of homogeneous or

single-phase metal are in contrast to that observed in the welding of heterogeneous substrate and weld metals and traditional casting processes because the energy barrier in the latter processes are finite in nature (Figure 2.26b).

For epitaxial solidification to take place in SLM, the substrate must be partially melted back (solidification regrowth) to promote growth from the prior grains of the substrate. For solidification regrowth to occur, the amount of material constituted in the layer thickness of metal powder to be melted over the substrate metal must be commensurate with the laser energy intensity of the chosen processing parameters (laser power and scan rates e.t.c.). This strict control of laser-metal powder interaction is essential in order to obtain stronger interlayer bonding which results in full density components. Evidence of epitaxial solidification is usually confirmed by microstructural examination of cross-sections of SLM processed material encompassing several layer thicknesses as demonstrated by Das (2003) and reproduced in Figure 2.27. Figure 2.27a is an example of incomplete homologous wetting and solidification whereby the melt front from the laser-melted powder layer above propagated down to barely contact the surface of the previous layer. The non-uniformity of layer thickness is especially notable. In contrast, layers in the cross-section of specimen fabricated at a higher laser power density, shown in Figure 2.27b, completely indistinguishable indicating continuous grain growth across the layers. This result indicates sufficient remelt of the previous layer took place to induce epitaxial solidification. It should be noted that these micrographs traverse approximately three layer thicknesses.

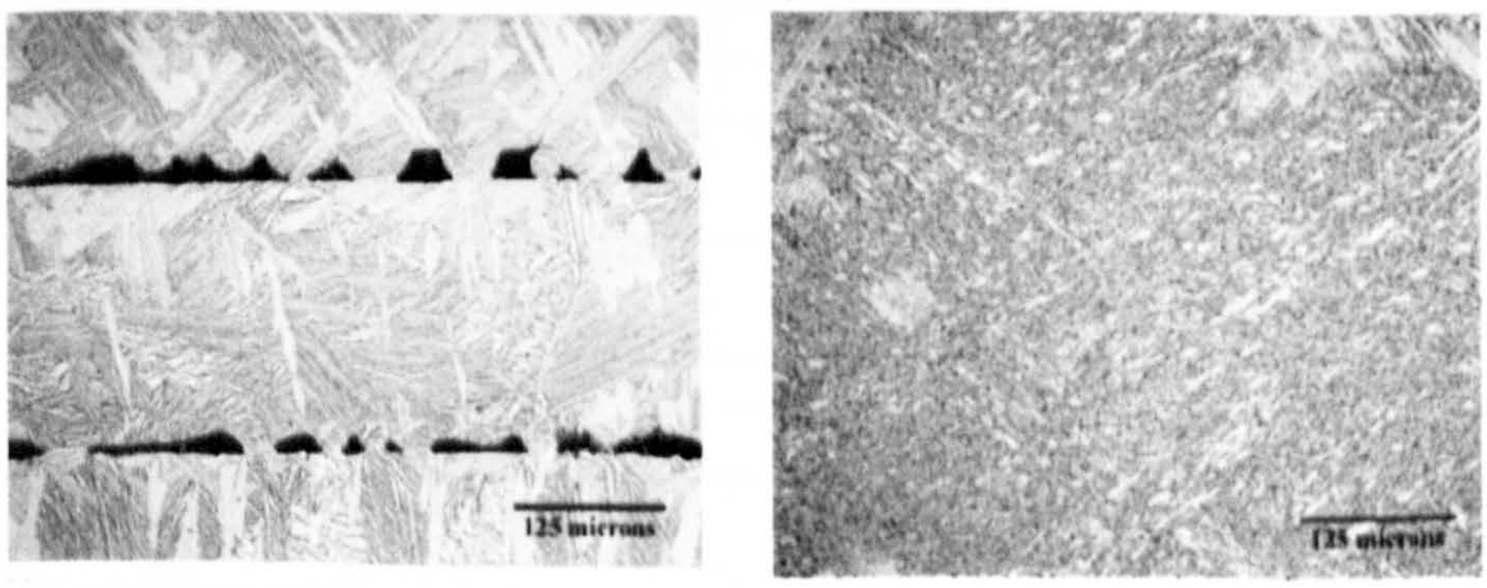

Figure 02.27: (a) Microstructure of SLM processed Ti-6Al-4V exhibiting porosity and insufficient substrate remelts and (b) Etched microstructure of fully dense Ti-6Al-4V specimen (after Das 2003).

Since SLM is a localised solidification process which occurs via epitaxial growth, evidence from Figure 2.27 confirms that it can impart finer and more uniform grain size to processed parts when compared to traditional casting processes. Consequently, this results in better mechanical properties. In summary, the mechanism for "good wetting"

is ensured by partial remelting of the previous layer in SLM giving rise to epitaxial solidification. Remelting the previous layer removes surface contaminants, breaks down oxide films, provides a clean solid-liquid interface at the atomic level and allows epitaxial solidification. Laser processing parameters in SLM should be chosen so as to ensure that sufficient remelt of the previous layer takes place and continuity of the solid-liquid interface under the impingement of the laser beam is maintained. From the above discourse, having examined the physical mechanisms governing the SLM process, the role of the various process parameters and materials properties as they affect the properties of sintered components made of steels, iron-graphite mixture, and tin-bronzes reported in the literature will be presented and discussed.

2.7 Effects of Process Parameters and Powdered Characteristics on the Properties of SLS/SLM Fabricated Components

2.7.1 Typical SLS/SLM Fabrication Parameters and Materials Properties

It has been established that the qualities of SLS/SLM processed components are strongly influenced by the sintering/molten pool sizes and residual stresses, which are mainly controlled by the laser energy input (Beuth & Klingbeil 2001).

Table 2.11: Process variables and material properties which affect sintering and densification of SLS/SLM-processed parts (after Agarwala et al. 1995).

Processing Parameters	Material properties
Laser power	Viscosity
Scan rates	Surface tension
Atmospheric control	Particle size and distribution
Gas flow	Particle shape
Heaters (bed temperature)	Absorptivity/reflectivity
Laser type	Thermal conductivity
Scan radius	Specific heat
Scan vector length	Emissivity
Scan spacing	Melting temperature.
Thickness of layers	Component ratio
Machine (specific type)	Chemical composition.

Previous researchers have described SLS/SLM as a very complicated process, and have suggested that several parameters influence the densification mechanism and the attendant microstructural features of materials processed by SLS/SLM. The main process parameters that determine the quality of a component fabricated by SLS/SLM technique are as listed in the first column of Table 2.3 whereas the characteristics of powder material which are of special concern are listed in its second column. The objective of this section is to determine from the available literature, the definitive effects of the SLS/SLM processing parameters on the properties of laser sintered components produced from materials like steel, iron, copper, and titanium powders.

2.7.2 Density of SLS/SLM Processed Components

This section considers the influence of processing and material parameters on the density of SLS processed materials.

2.7.2.1 Effect of SLS/SLM Parameters on the Density of Components

Dewidar *et al.* (2003) investigated the density of single layer parts over a range of SLS processing conditions for a pre-alloyed high-speed steel powder. Their results, reproduced in Figure 2.28, establish that density increases as the laser power increases and as the scan speed and scan spacing reduce. Figure 2.29 shows the effect of SLM laser processing parameters on the sintered density of multiple layer parts made in iron powder as investigated by Simchi & Pohl (2003). At constant laser power (P=215W), an increase in scan velocity or scan line spacing decreased the part's density (Figure 2.29a). When scan line spacing was held constant (h=0.3mm) the sintered density reduced with increasing scan velocity or decreasing laser power (Figure 2.29b). Using increasing layer thickness resulted in a lower attainable density (Figure 2.29c). Simchi & Pohl (2003) inferred that intensifying the laser energy input (increasing laser power, decreasing scan velocity, a thinner layer thickness, and overlapping of scan lines) leads to higher densification. In their investigation, a scan velocity of 150mm/s was found to be a critical speed, above which a sound part was not obtained. Therefore, it can inferred that the findings from the works of Dewidar *et al.* (2003), Niu & Chang (2000), and Simchi & Pohl (2003) corroborate the assertion that densification is improved as the laser power increases and as the scan speed, layer thickness and scan spacing decrease. This assertion is also found to be true for other materials (Table 2.12) such as Ni-Sn and Cu-Solder (Pb-Sn) (Agarwala *et al.* 1995), and Ni-alloy-Cu and Fe-Cu (Tolochko, *et al.* 2003).

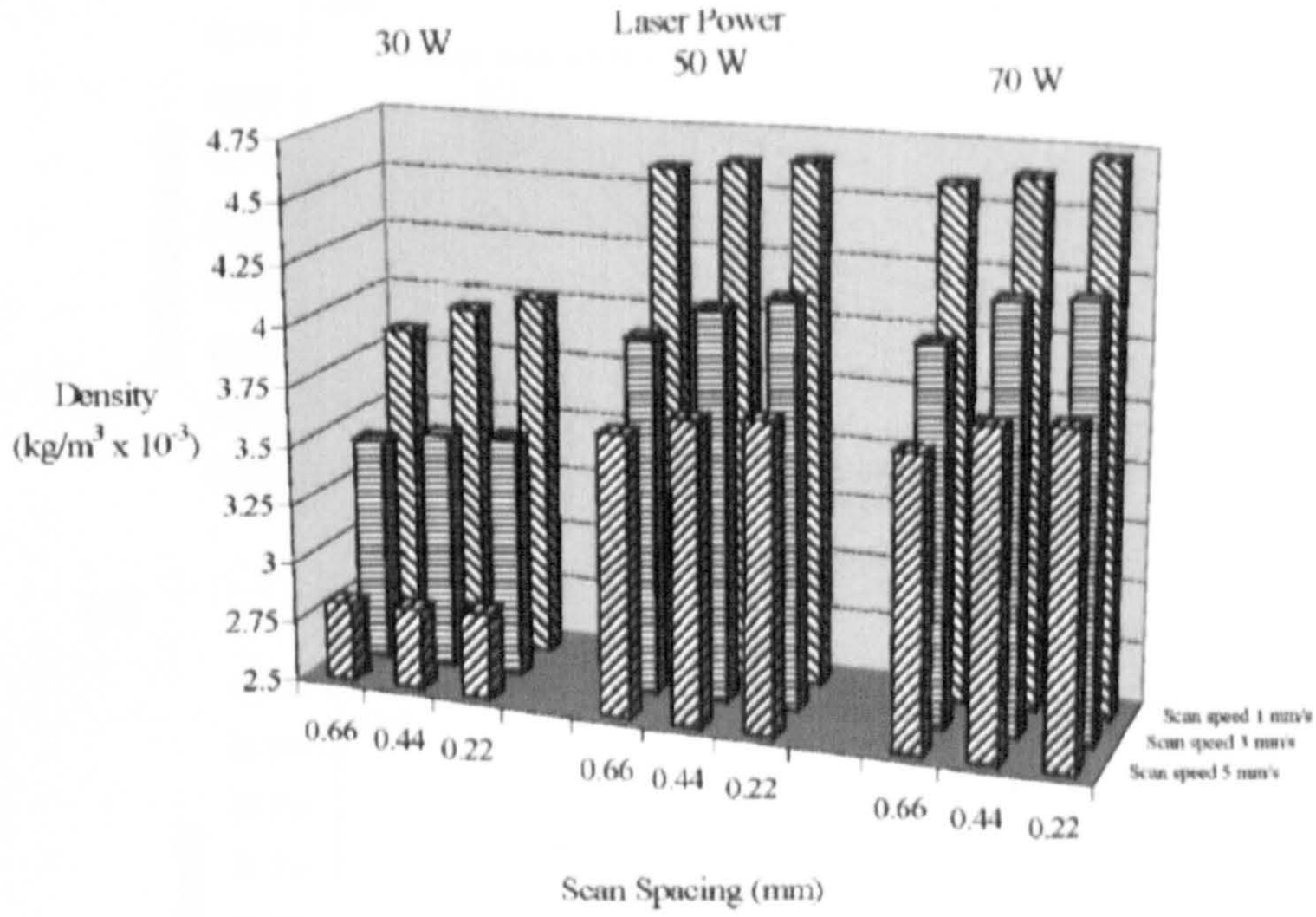

Figure 2.28: Effect of SLS processing conditions on the density of single layers of high-speed steel powder (after Dewidar et al. 2003).

Table 2.12: Summary of application of SLS/SLM to metal systems.

Material	Key findings	Comments
High speed steels	Partial melting (SLS) incorporated with post-infiltration to achieve full densification.	Partial melting indicates the choice of energy density is not sufficient to cause full densification.
Iron powder	Full melting (SLM) resulted in densification.	Applicable to single component, single material (e.g. Fe) in which adequate energy density is supplied to the powder bed.
Ni-Sn	Binary liquid phase SLS employing high and low melting point materials to attain densification. Low melting point materials melt and bind the particles of the high melting point materials together.	Applicable to two-component material system having different melting points.
Cu-Solder		
Ni-alloy-Copper		
Fe-Cu		
Bronze-nickel		Fractograph suggest that bronze melts and wets the nickel particles which do not exhibit any melt.

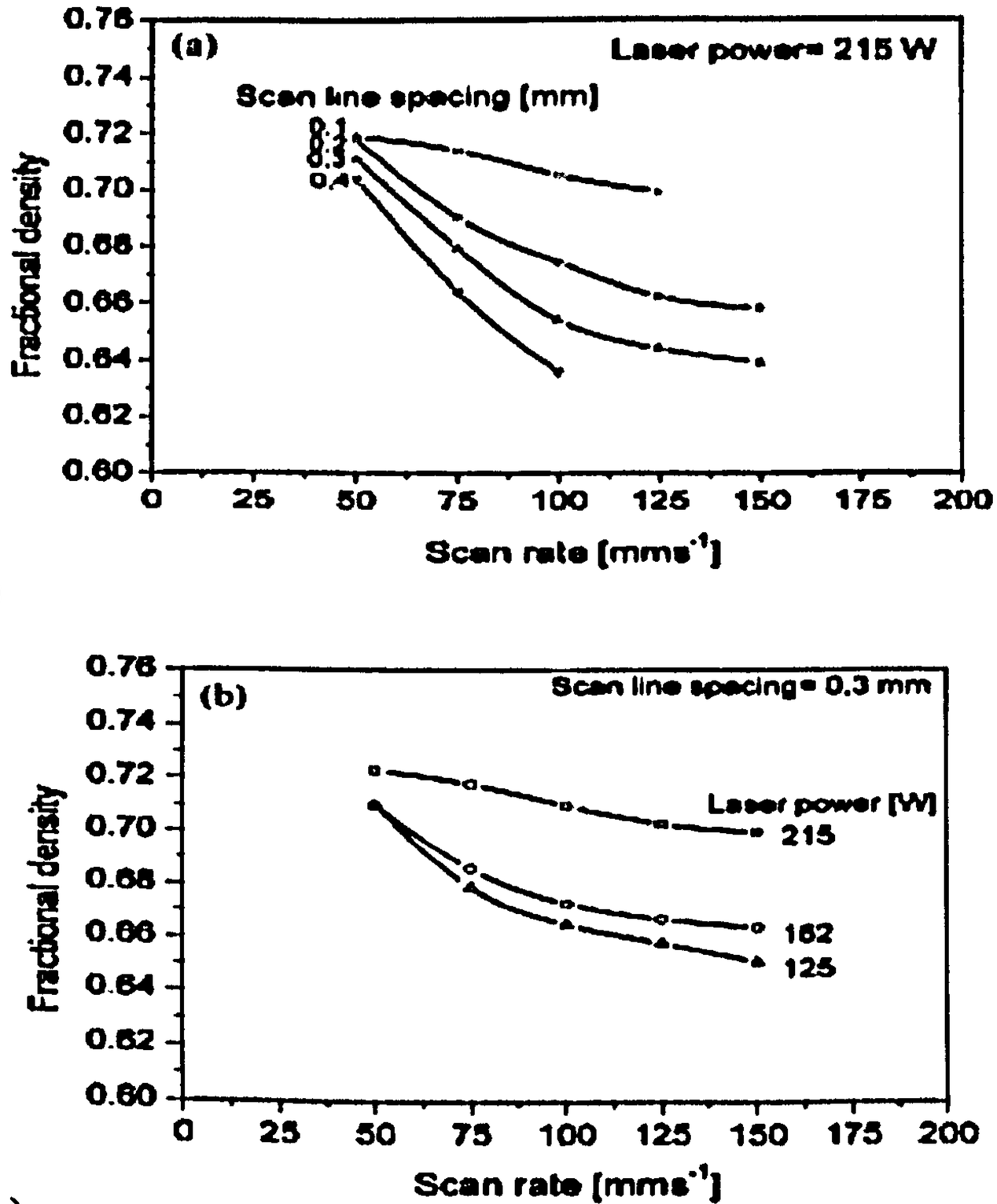

Figure 02.29: Effect of processing parameters on the density of laser sintered iron powder: (a) Scan line spacing (P=215W, d=0.05mm); (b) Laser power (h=0.3mm, d=0.05mm); (c) Thickness of layer (P=215W) (after Simchi & Pohl 2003).

The implications of these findings with regard to how variation in processing parameters influences the occurrence of densification mechanism either through full melting (SLM), partial melting or binary liquid phase sintering (SLS) of metals (see Table 2.12) will now be considered.

It is an established fact that high temperature in SLS/SLM leads to a low contact angle and viscosity and high Marangoni flow thus improving densification (German 1985). Marangoni flow (Figure 2.30) can be described as the initiation of thermocapillary forces for fluid flow as a consequence of the temperature gradient in the melt pool which gives rise to a corresponding differential surface tension between the edge and center of the melt pool.

Zhu *et al*. (2004, 2005), Gu & Shen (2006b) and Gu *et al*. (2008) related the observations made by Dewidar *et al*. (2003), Niu & Chang (2000), and Simchi & Pohl (2003) to the volume fraction of the liquid phase formed during SLS/SLM processing. They observed that at processing parameters combining low scan speed and relatively low laser power, the resultant input energy is insufficient to generate adequate liquid phase that binds the particles together. Therefore, the outcome is partial melting (SLS) resulting in poor densification. As the laser power increases at low scan rates, the increasing incident laser energy increases the temperature of the powder bed thereby causing a significant amount of powder's interparticulate melting as a consequence of the occurrence of adequate liquid phase. This condition culminates in higher densification due to the instability of the liquid cylinder which occurs as the surface free energy is minimised. Therefore, it can be inferred that appropriate increment in the laser energy input leads to high working temperature which eventually reduces both melt viscosity and surface tensions. Furthermore, at high temperature, the material transport during laser sintering process is enhanced as a consequence of the formation of connective streams within the molten pool during SLS.

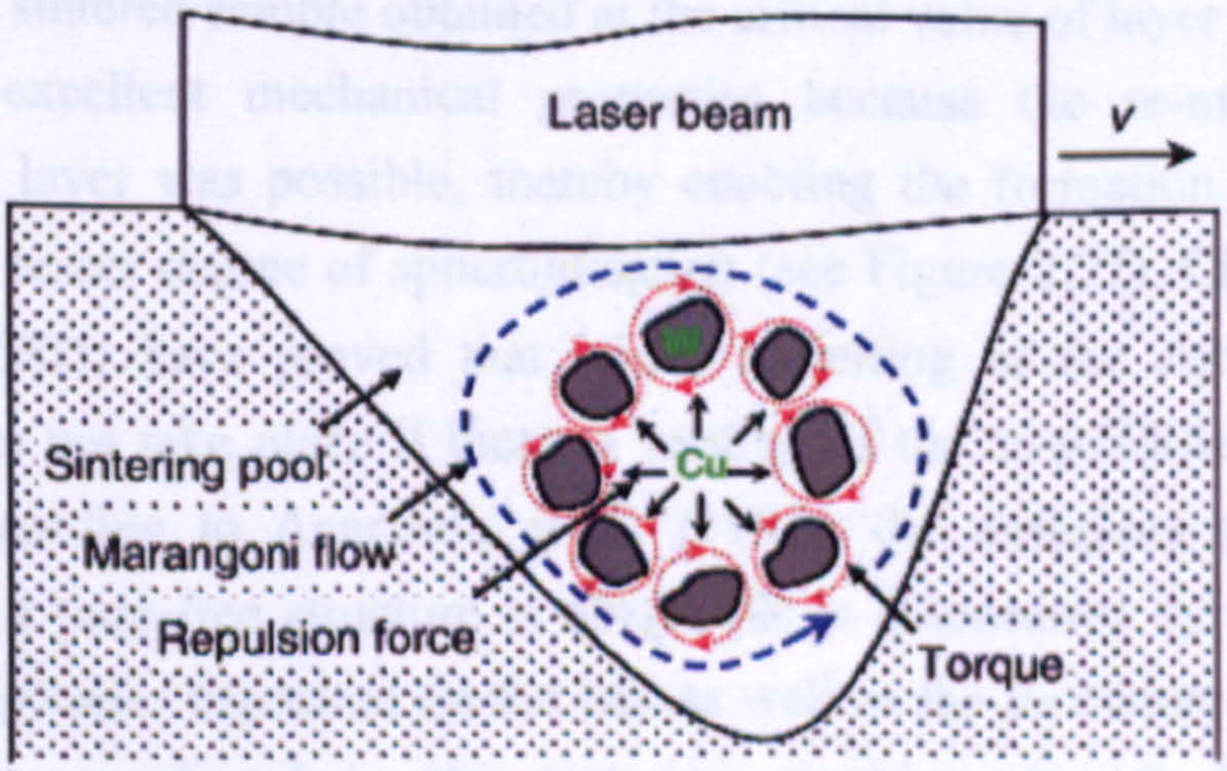

Figure 2.30: A schematic illustration of Marangoni flow as applied to the direct SLS of W-Cu 2-phase direct SLS (after Gu et al. 2008).

This results in the reduction of the amount and sizes of inter-agglomerate pores, thereby, obtaining fully dense parts. Moreover, the wetting characteristics and the attendant re-arrangement force of solid particles in the liquid phase increase as the amount of liquid phase increases provided the energy density increases appropriately. The implication of this finding is that there exists an optimal laser energy density combining relative high laser power with low scan speed, at which the solid-liquid wettability is most successful such that the structural particles in the liquid are most suitably re-arranged with a view to achieving higher sintered density. Further increment in laser energy density leads to reduced sintered density. In this condition, the higher laser power generates increased quantity of liquid phase, but the reduced scan speed causes substantial increament in its lifetime, thereby promoting spheroidisation and breakdown in the melt pool. The reduced sintered density in this case is attributed to the significant aggregation of the structural particles.

Successful SLM processing of metals demands that an appropriate layer thickness is established for the other processing parameters which are employed. For instance, if the powder layer thickness is very high, complete melt down of particles will be impossible to achieve due to insufficient laser energy penetration into the powder bed. Consequently, large and interconnected pores are formed in the sintered structure which reduces the density of the SLM fabricated sample. During SLS processing of WC-Co particulate reinforced Cu matrix composites, Gu & Shen (2006b) discovered that there exists a critical value for layer thickness at which most of the gas bubbles in the powder bed are able to move up to the layer's surface, and collapse when the molten liquid solidifies rapidly to form finer grains and produces a pore-free sintered part. This pore-free sintered sample obtained at the critical value of layer thickness was noted to possess excellent mechanical properties because the re-melting of the previously sintered layer was possible, thereby enabling the formation of coherently bonded layers with lesser degree of spheroidisation (see Figure 2.27). Chatterjee *et al.* (2003) and Das (2003) have proved that where remelting of the substrate occurs, spheroidisation does not take place if there is wetting of the as-solidified material by the melt pool. According to Agarwala *et al.* (1995), the minimum possible layer thickness at which a pore-free structure is obtainable is determined by the maximum particle size of the powder deposited on the bed as well as the precision of the powder delivery mechanism employed in the sintering machine. Gu & Shen (2006b) established that lowering the layer thickness below the minimal permissible layer thickness for a powder system would create complications in spreading homogeneous layers of fresh powders with the previously laid layers being displaced and the surface

roughness of the sintered samples exacerbated. This consequently hinders inter-particulate bonding or melting.

It must be emphasised that the most significant parameter SLS/SLM parameter influencing the densification of parts is the laser energy density which is defined by the relationship shown in equation 2.17. This shows that the energy density for the SLS/SLM process increases with increasing laser power, and decreasing scanning rates, scan spacing and layer thickness.

$$\psi = P/(uxhxd) \quad \text{.....2.17}$$

Where ψ = Specific laser energy input (J/mm^3); P = Power (W); u = Scanning rates (mm/s); h = scan spacing (mm); d = layer thickness (mm).

Simchi & Pohl (2003) and Sanz-Guerrero & Ramos-Grez (2007) established that the resultant fractional sintered density is in direct relationship with the specific laser energy input incident on a powder bed for iron powder and copper-titanium powder mixtures. They pointed out that the fractional density, ρ, of these powders is an exponential function of the specific laser energy input (ψ) of as shown in equation 2.18.

$$\rho = C_1 - C_2 \exp(-K\psi) \quad \text{.....2.18}$$

where C_1, C_2 and K (densification co-efficient) are material constants of the specific powders under investigation.

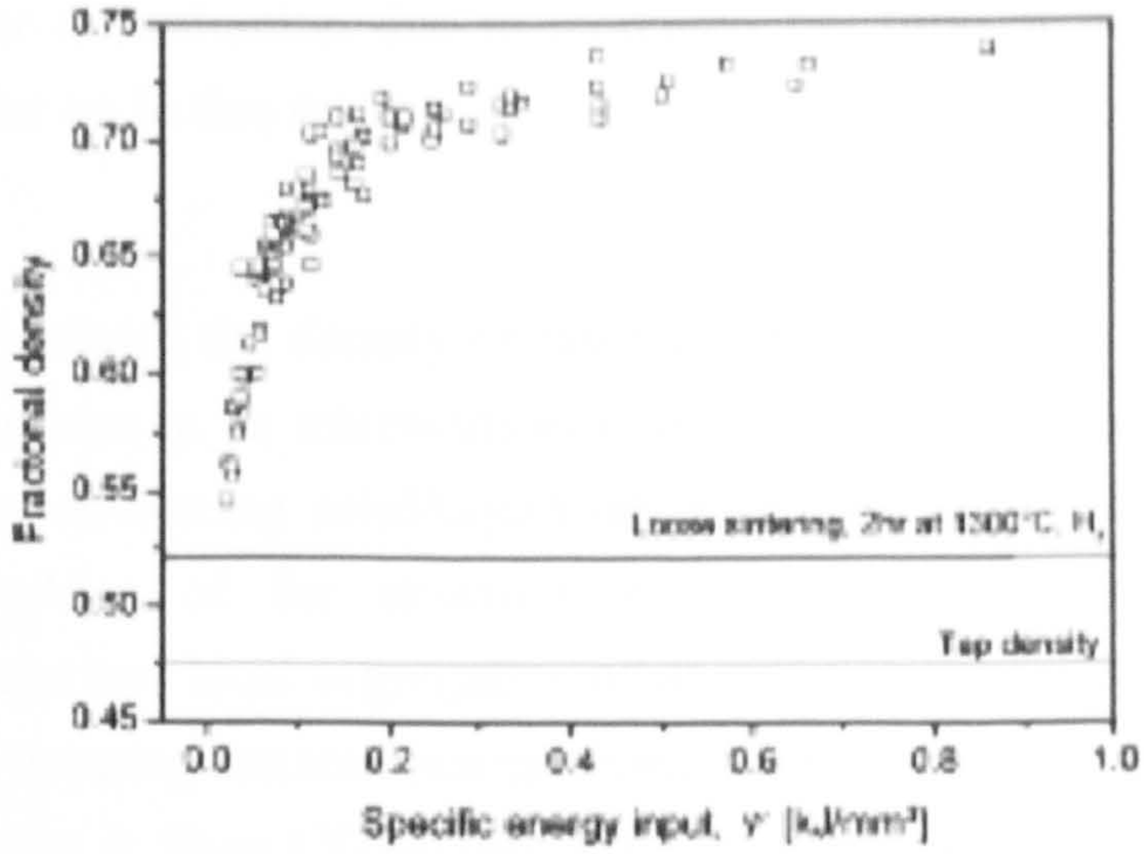

Figure 2.31: Fractional density vs. the specific energy input (ψ) for sintered iron using different processing parameters (after Simchi & Pohl 2003).

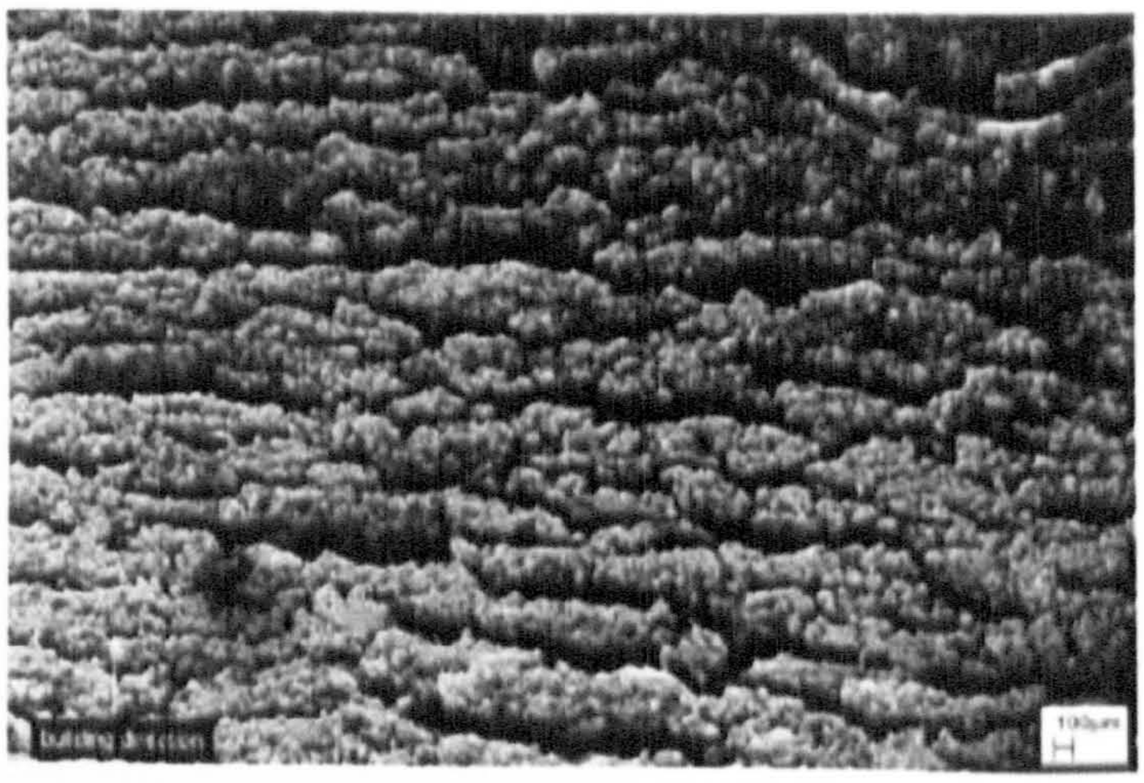

Figure 2.32: SEM image of SLS/SLM processed iron powder at the excessive delivery of specific laser energy input of 0.8 kJ/mm^3 showing the occurrence of layer delamination as a result of increased life time of the generated liquid phase (Simchi & Pohl 2003).

Figure 2.31 illustrates that the fractional density increased with the specific laser energy input, for an iron powder, up to a maximum of 0.74 at the saturation specific laser energy input and at ψ=0, the density approaches to the tap density of the powder material (Simchi & Pohl 2003). Moreover, when the experiment data were fitted according to equation 2.18, C_1=0.719, C_2=0.214, and K=14.82 at a ψ<0.8 kJ mm^{-3}. Beyond the saturation specific laser energy input of 0.8 kJ mm^{-3}, the maximum fractional density remained constant irrespective of the amount of specific laser energy incident on the powder bed. Observations from Figures 2.31 and 2.32 imply that excessive delivery of the energy density at very high laser power and low scan rates (i.e. above the saturation specific laser energy input) will result in complications such

as balling and layer delamination due to increased life time of the generated liquid phase as noted earlier on in this section.

Wu & Chen (1999) related the density of laser sintered parts to the micro-distribution of the structural particles in its microstructure, by considering the interaction between the particles and the advancing solid/liquid interface (pushing versus trapping). They discovered that pushing of the structural particles by the solid/liquid interface culminated in pile-ups and local segregation of particles to the region of the last liquid to solidify whereas trapping causes homogeneous distribution of the structural particles in the sintered part. Gu & Shen (2006b) employed this idea in their work (Figure 2.33). They identified a critical scan speed corresponding to the transition from pushing to trapping of the structural particles by the advancing solid/liquid interface.

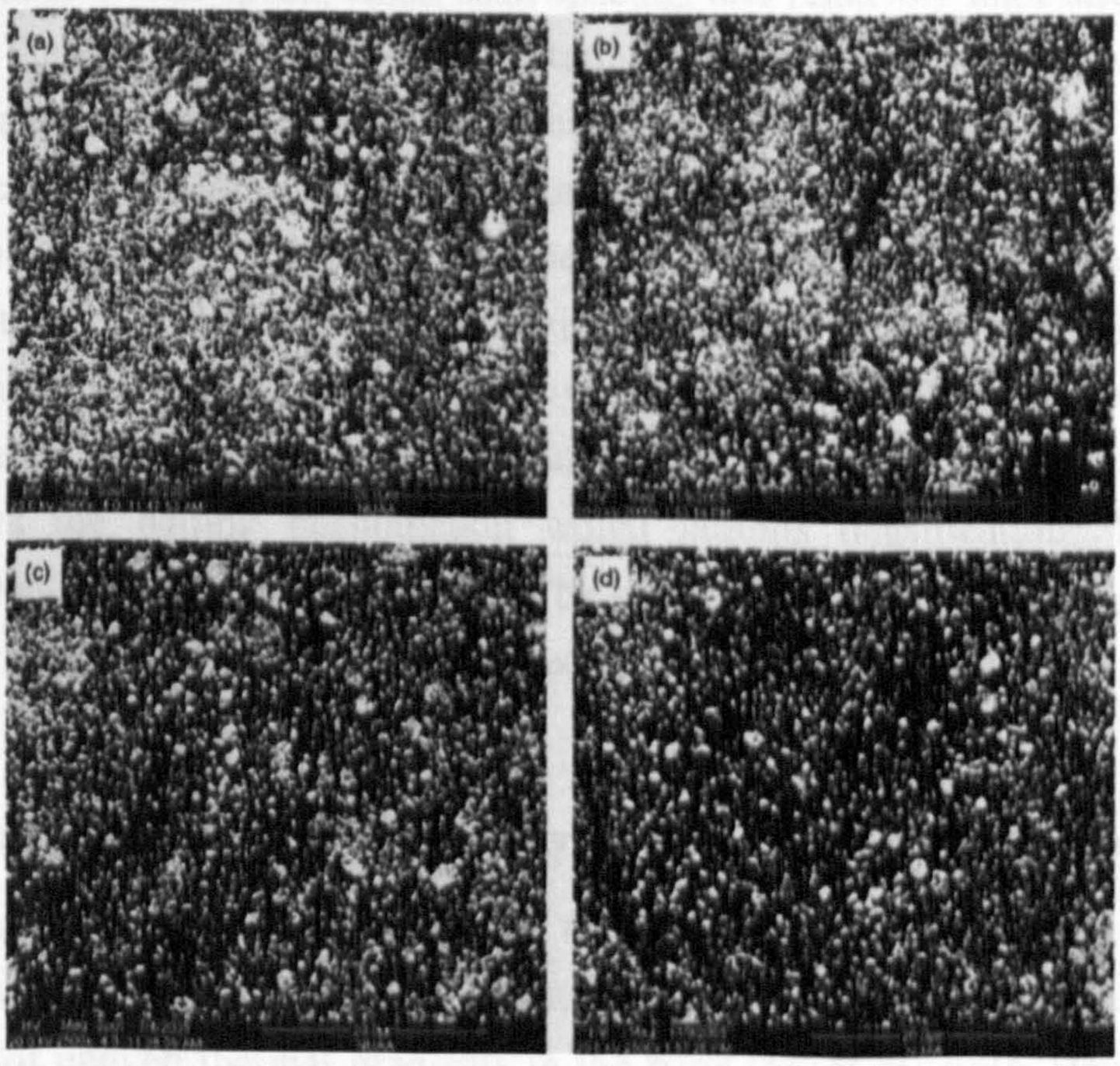

Figure 2.33: SEM (BSE mode) images showing microstructure of laser sintered Cu matrix composite samples with variation of scan speeds: (a) 0.02m/s; (b) 0.03m/s; (c) 0.05m/s; (d) 0.06m/s. Other processing parameters were fixed: laser power of 700W; layer thickness of 0.20mm (after Gu & Shen 2006b).

Beyond the critical scan speed, they discovered that trapping occurred due to what Gåård *et al*. (2006) explained as the rapid infiltration rate of the liquid into the powder bed, thereby, promoting the introduction of fresh melts into the inter-particle regions

and consequently forming a continuous infiltration front to fill the voids between the structural particles. Therefore, the structural particles ceased to be pushed to the microstructural interface, but are trapped and consequently wetted and incorporated into the matrix in order to obtain a homogeneous distribution of particulates without the apparent segregation. The densification mechanism which has just been described is applicable to the binary liquid phase SLS. In the case of single phase powders such as copper (Pogson *et al.* 2003), and 316L stainless steel powders (Morgan *et al.* 2004), the density of SLM processed parts was related to the optimal specific laser energy input below which lesser quantity of powder particles consolidated into smaller size of the melt bead, hence resulting in high porosity level in the laser melted parts. At the optimal specific laser energy input, the recoil compression effects associated with the low pulse rates served to deform the circular section beads into flatter shapes, thereby widening the melt beads and allowing adjacent beads to bond into a dense layer.

In conclusion, at low scan speed, small scan spacing, and relatively high laser power, the amount of liquid phase is higher and sintering time is longer, thereby promoting higher densification. Meanwhile, at a low volume fraction of liquid and short sintering time obtainable by using a high scan speed and scan spacing and low values of laser power, the liquid phase is not enough or has not sufficient time to enhance wettability. There appears to be a maximum sintered density which may be achieved in SLS/SLM at a critical value of the specific laser energy input. Above this critical value, it is unable to increase densification further because the increased lifetime of the liquid phase promotes the balling phenomenon which inhibits densification. The only exception is when substrate wetting occurs. The effect of the scanning strategy on the density of laser-sintered parts will be considered in the next section.

2.7.2.2 Effect of Scanning Pattern on Density of Laser Sintered Components

Porosity, residual stresses, and cracking as a consequence of hot shortness, and poor surface finish are among the problems associated with SLS/SLM process as a result of the generation of uneven thermal gradients in the parts (Su *et al.* 2003, Hauser *et al.* 1999a, 2003). To control the thermal gradient during powder heating and cooling and thereby fabricated unwarped and uncracked layers, Su *et al.* (2003); and Hauser *et al.* (1999a, 2003) have investigated the relationship between scanning strategies and the properties of SLS/SLM processed steel powders.

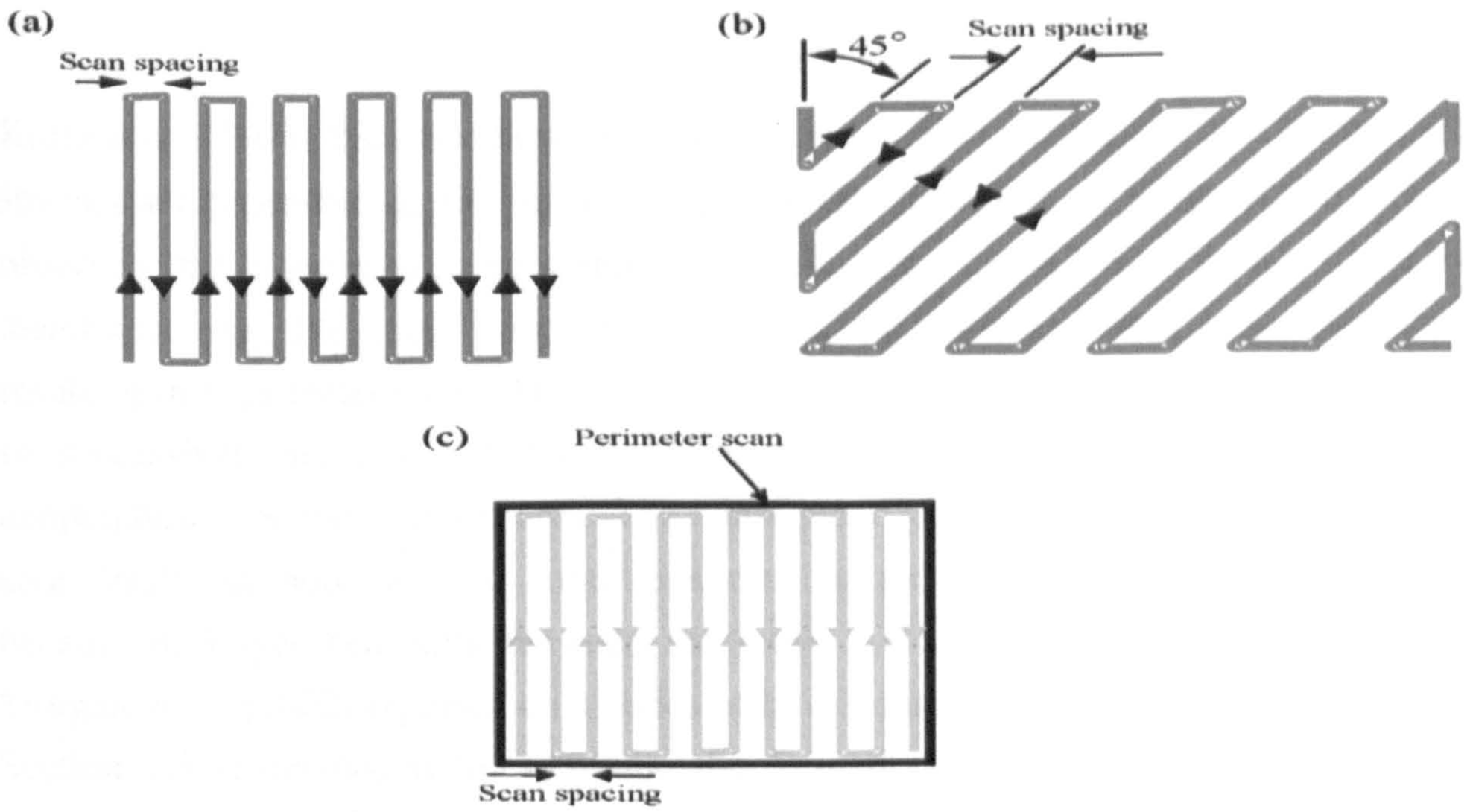

Figure 2.34: SLS/SLM scanning strategies (a) Standard (b) Diagonal and (c) Perimeter (Dewidar *et al.* 2003).

	Pattern 1	Pattern 2	Pattern 3	Pattern 4
	1 2 3 4 5	1 2 3 4 5	1 4 2 5 3	1 4 2 5 3
Travel time		minimum	maximum	

Figure 02.35: Four different scanning strategies adopted in the direct laser sintering of tool steels using a Nd: YAG laser machine. The numbers indicate the scanning sequence while the arrows represent the scanning directions (after Su et al. 2003).

Dewidar identified standard, diagonal and perimeter scanning strategies (Figure 2.34) for producing single layers whereas Su *et al.* (2003) tested the influence of four types of scanning patterns (Figure 2.35) and various scan spacings on the building of overlapped beads of laser sintered tool steel powders. Although, Dewidar *et al.* (2003) discovered that perimeter scan approach was less successful while the standard and the diagonal scan strategies gave very similar results for high speed steel fabricated by direct SLS, Su and co-investigators concluded that the adoption of different scanning patterns culminated in different processing times which affected the nature of the microstructure obtained for the laser sintered parts. Hauser *et al.* (1999a) reported on the scanning routines for successful small scale direct SLS of stainless steel powders processed at room temperature. It was established that single layer shape affect warping but the heights of test samples did not.

Kruth *et al.* (2004) discussed how the temperature gradient mechanism induced internal stresses are dependent on the part geometry and the scan strategy being adopted. They observed that if the area to be scanned is small, a short scan length normally occurs thereby leaving little time for the surface to cool before the next track is scanned, thus resulting in high temperature. For larger areas, the laser beam travels a longer distance so successively scanned tracks have more time to cool down resulting in a lower temperature over the scanned area. The consequent lower temperature of the scanned area results in poor wetting conditions causing reduction in the material density because of larger heat sink between the loose powder and the solidified material. Morgan *et al.* (2002) reported on a series of knit-scanning strategies (see Figure 2.5 in Section 2.3.1) developed to overcome the formation of the surface roughness and porosity in laser melted parts, and hence removed the associated porosity within the 316 stainless steel material in order to achieve full density. The effect of scanning pattern on the sintered density of iron powder is presented in Figure 2.30 as investigated by Simchi & Pohl (2003). The dependence of the densification of iron powder on the scanning pattern is apparent and it is noticeable that the effect is less pronounced for specimens with dimensional ratio X/Y (the scan line distance in X- and Y- directions) approaching unity. Furthermore, lower sintered density resulted from "Sorted" scanning pattern in Y-direction (long scan vector) than in the X-direction. Xie *et al.* (2005b) proposed a modified knit-scan strategy to obtain increased density (84% of its theoretical density) for H13 tool steel by optimising the line spacing and scan speed.

2.7.2.3 Effect of Atmospheres on Density of SLS/SLM Processed Components

During the SLS/SLM of metal powders, the presence of oxygen in the operating atmosphere and as a form of passive layer of oxide on the powder surfaces does exacerbate the balling phenomenon during the SLS/SLM process due to the initiation of Marangoni convection. The major concerns arising from this are the significantly high absorption of laser energy on the sintering/melt pool and the liquid-metal surface tension which increases the wetting angle between the solid and liquid phases that can inhibit interparticulate bonding/melting between rastered lines and individual layers (Hauser *et al.* 1999b). Therefore, the use of controlled atmosphere during SLS/SLM of metals is very important because it prevents undesirable reactions, sweeps deleterious reaction products from the sintering chamber, initiates desirable reactions as demonstrated in the use of nitrogen atmosphere to form AlN (aluminium nitride) which improves the dimensional stability of sintered aluminium parts, and reduces oxide

present on the metal surfaces as exemplified in iron through dissociated ammonia (Schaffer *et al.* 2006).

From the available literature, very limited experimental evidence could be gathered on the effect of sintering atmospheres on the density of materials fabricated via SLS. Asgharzadeh & Simchi (2005) investigated the role of argon and nitrogen sintering atmospheres on the laser sintering of M2 high-speed steel (HSS) powder. Their findings showed that laser sintering under argon atmospheres yielded better densification in comparison to nitrogen atmospheres especially at higher scan rates. This behaviour was also observed by Simchi & Pohl (2003) for iron powder (Figure 2.37). Das *et al.* (2000) evaluated the effect of a wider range of atmospheres (rough vacuum of the order of 30mtorr, rough vacuum purged with argon, high vacuum < 5 x 10^{-5} torr, and high vacuum followed by argon-2% hydrogen backfill) on the fabrication of superalloy cermet abrasive turbine blade tips via the direct SLS process.

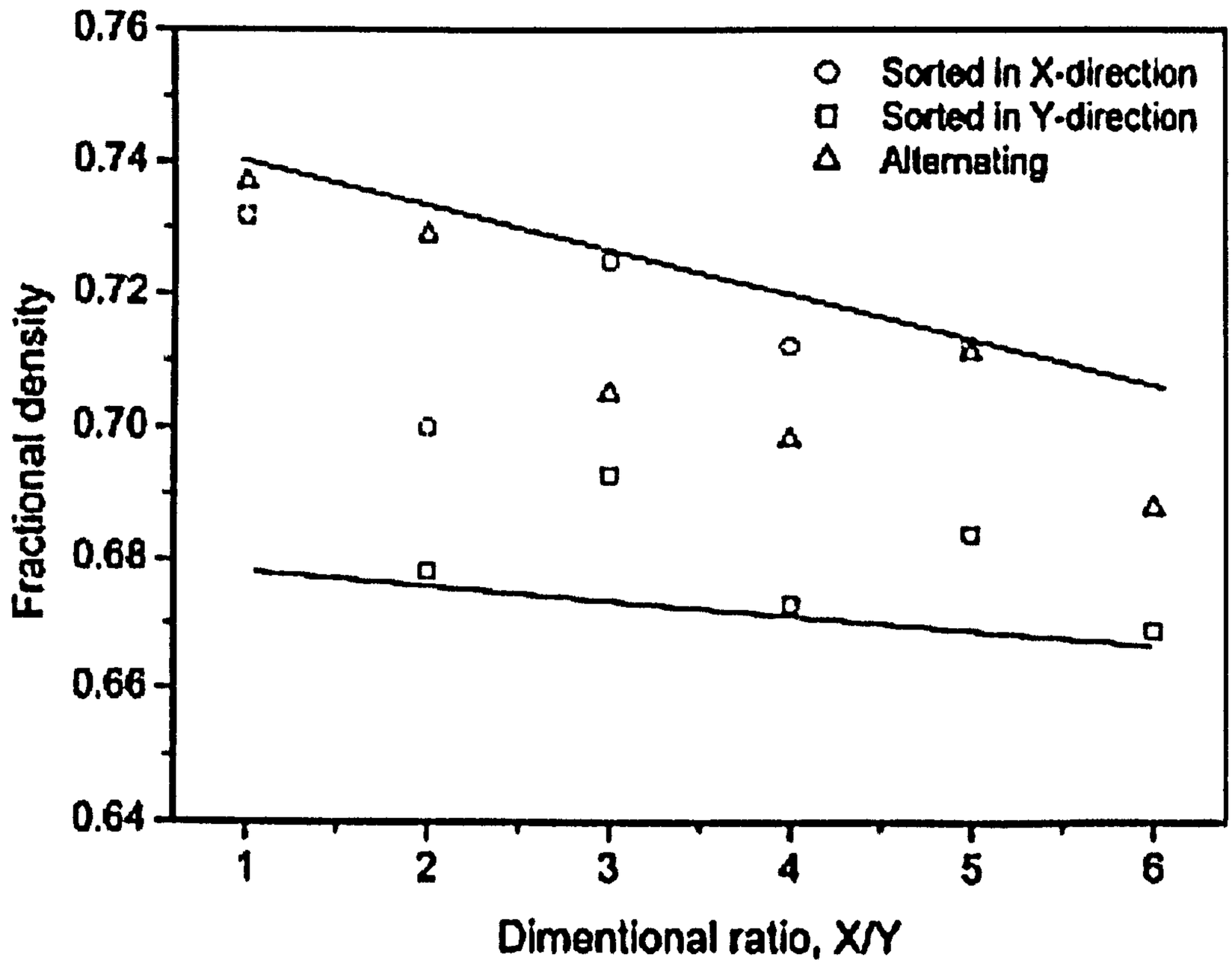

Figure 02.36: Dependence of sintered density of iron powder on scanning pattern for various dimensional ratios; P = 215 W, v = 100 mm/s, h = 0.3 mm, N2 atmosphere, ambient powder temperature. Note that dimensional ratio X/Y is the scan line distance in X- and Y- directions. (after Simchi & Pohl 2003).

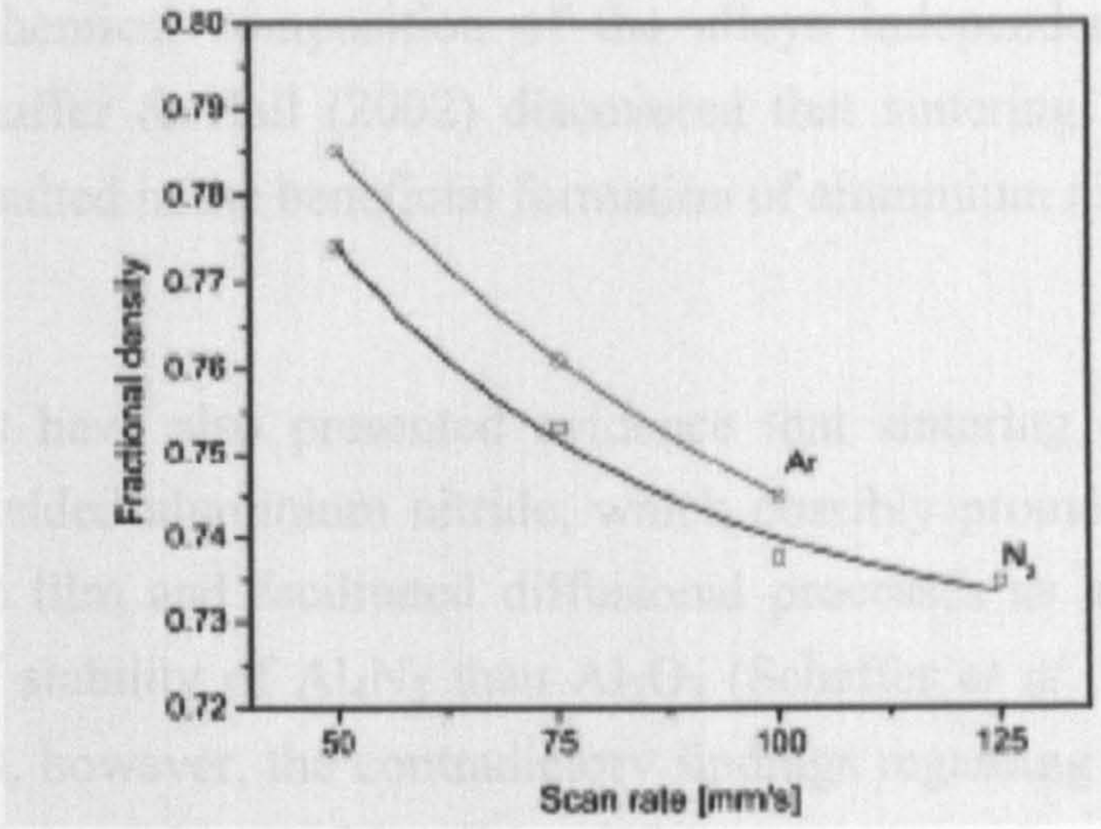

Figure 2.37: Effect of sintering atmosphere on the density of iron powder as a function of laser scan (after Simchi & Pohl (2003)).

Their results revealed that both rough vacuum and the purged argon contained sufficient oxygen to oxidize the molten superalloy matrix thereby causing balling, separation, and tearing due to surface tension effects. They concluded that a high vacuum atmosphere resulted in relatively uniform surface features, with no cracking, tearing, or separation when the investigation was conducted within an acceptable window of processing parameters.

All the literature reviewed in this section so far are in concurrence with the observation made by Hauser *et al* (1999b) that the amount of oxygen presents during heating, melting and fusing of metal powder strongly inhibits the effectiveness of laser power and scanning rates for successful SLS processing. However, no previous studies have been made of the effect of atmosphere on the direct SLS of aluminium alloys. It would seem, on the other hand, instructive to examine the effect of atmospheres on the sintering response of aluminium and its alloys in the powder metallurgy route. Schaffer *et al*. (2006) carried out an extensive literature survey on the effect of atmosphere on the sintering of aluminium and its alloys. They identified nitrogen, vacuum, argon and hydrogen gases as atmospheres that had been utilised for the conventional sintering of aluminium and its alloys. The outcome of their review suggested the effects were quite complex. For instance, Martin & Castro (2003) found that nitrogen was more effective than vacuum for an Al-1Mg-0.5Si-0.2Cu (wt%) alloy while an improved sintering response was obtained for Al-4.5Cu-0.5Mg-0.2Si (wt%) alloy under vacuum. They pointed out that the differences noted in the sintering responses of the alloys under the two atmospheres under consideration were a result of varying cooling rates after sintering. It is worth noting that Martin & Castro (2003) had not investigated the effect

of the varying chemical composition of the alloys independently of the sintering atmospheres. Schaffer & Hall (2002) discovered that sintering of aluminium alloys under nitrogen resulted in the beneficial formation of aluminium nitride.

Other researchers have also presented evidence that sintering of aluminium alloys under nitrogen yielded aluminium nitride, which possibly promoted the disruption of the surface oxide film and facilitated diffusional processes as a consequence of the greater degree of stability of Al_4N_3 than Al_2O_3 (Schaffer *et al.* 2006). The available literature presents, however, the contradictory findings regarding the role of hydrogen in the sintering of aluminium and its alloys. While some investigators have claimed that hydrogen had little influence on the sintering of aluminium and alloys, others have shown that it has a deleterious effect on its sinterability with the explanation that water vapour associated with hydrogen acts as a stabiliser of hydrated alumina thus inhibiting shrinkage (Schaffer *et al.* 2006). While no convincing inference could be drawn from the available literature on the effect of atmospheres on the sintering response of aluminium and its alloys, Schaffer and co-workers noted that anecdotal evidence from the industry indicates that nitrogen is always the preferred atmosphere for the sintering of aluminium and its alloys because of its cheap cost. Schaffer and co-investigators examined the sintering of aluminium alloys of varying compositions in vacuum, argon, wet and dry nitrogen, nitrogen-5%hydrogen and argon-5%hydrogen mixtures and proffered explanations as to why moisture is deleterious and the formation of aluminium nitride is essential. Figure 2.38 presents the results of this investigation. The solid line represents no change in density between the green and sintered state. Hence, points above and below the line confirm the occurrence of net shrinkage and net expansion of the sintered parts respectively. It can be seen that shrinkage only occurs for all green densities under nitrogen atmosphere, whereas volumetric expansion of sintered parts occurred when 5% H_2 was added to either a nitrogen or argon atmosphere.

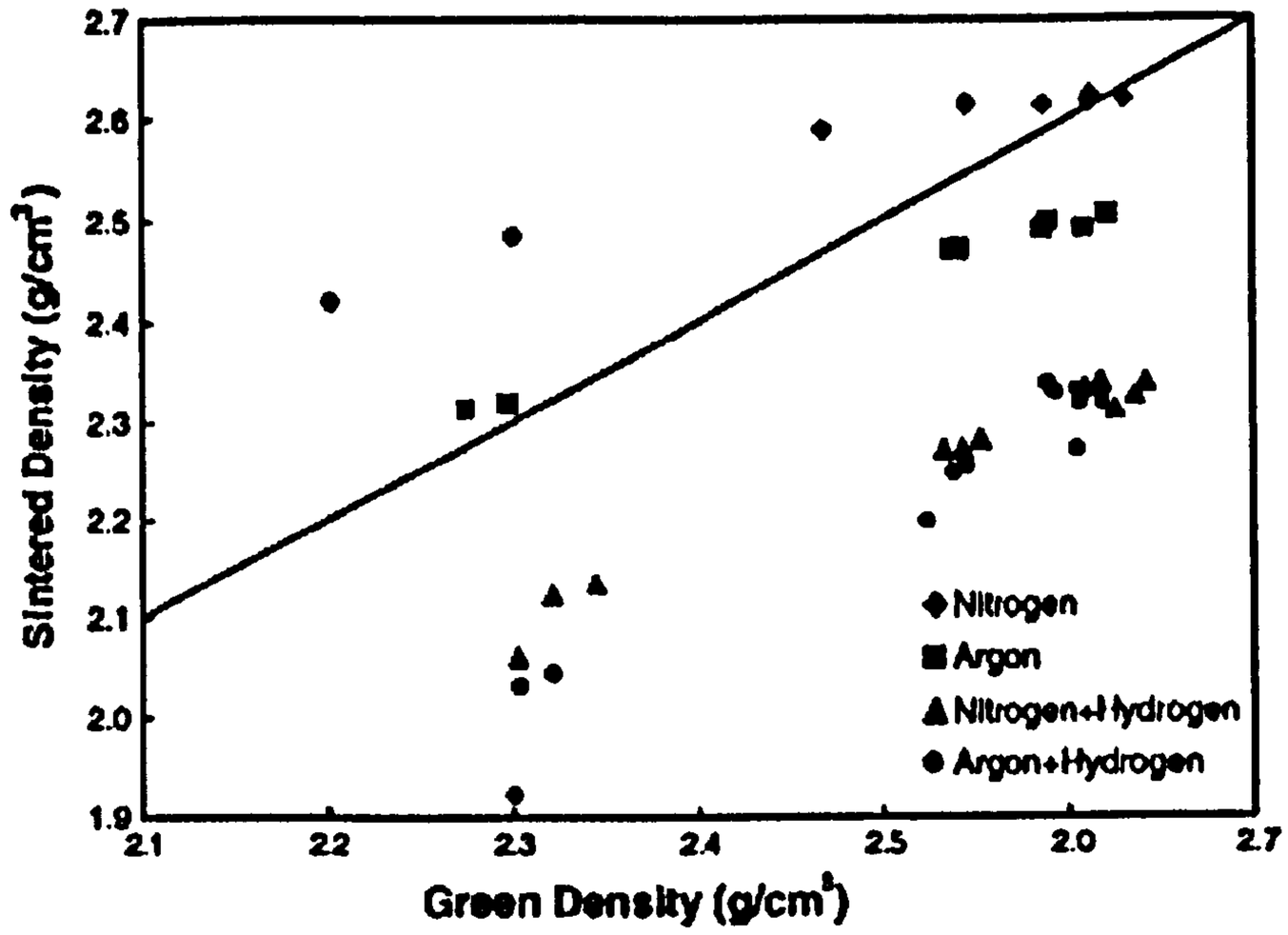

Figure 02.38: The effect of the sintering gas on sintered density for Al–3.8Cu–1Mg–0.7Si (wt%) samples were sintered for 1 h and air cooled (after Schaffer et al. 2006).

Therefore, Schaffer *et al.* (2006) showed that dry nitrogen is the most efficacious atmosphere for the sintering of aluminium alloys while hydrogen (moisture) is extremely prejudicial to sintered density. It was explained that aluminium nitride formation was beneficial in the reduction of the pressure in the pore spaces thereby inducing pore filling at particle sizes that are smaller than those required for the sintering in inert atmospheres. Since the processing conditions of the conventional powder metallurgy sintering differ from that of the direct selective laser sintering, it will be good to explore whether changing from argon to nitrogen atmospheres enhance sinterability of aluminium alloys in direct SLS/SLM

2.7.2.4 Effect of Additives on the Density of Laser Sintered Components

To fabricate components using the binary liquid phase SLS, sintering from a low green density to a high final density is required. To achieve this aim, the use of additives that promote the formation of liquid phase and improve the wettability is a simple and inexpensive technique that is feasible. Many researchers have expended significant efforts in attempting to increase the densification by improving the wettability in direct laser sintering. Among numerous approaches adopted by various research groups are the use of *in-situ* deoxidiser or fluxing agent, alloying additions and a pre-heated powder bed. This section is devoted to a review of the literature on the use of fluxing agents and alloying additions to enhance the densification mechanism in SLS processed powders.

Fluxing agents which are used in brazing and soldering can improve wetting effectively during sintering due to their abilities to de-oxidise and reduce the surface tension of the solid-liquid-vapour interface (Zhu *et al.* (2006). Agarwala *et al.* (1995) examined the exact chemical role of phosphorus in SLS of bronze (Cu-10wt%Sn)-nickel powder. They were able to determine an optimum processing window for which a density of around 70% was obtained without any significant curling. Zhu *et al.* (2005) found the formation of Cu_2O in a copper-based powder (Cu-40%wtSCuP) to be sensitive to the scan spacing as a consequence of a lack of Cu_3P protection under the re-heating condition if small scan spacing was used. Moreover, they discovered that atomic concentration diffusion was the densification mechanism at fast scan speed and high scan spacing whereas solute-reprecipitation was noted to be the predominant mechanism for densification at low scan rates and small scan spacings. Although, Zhu and co-workers (2005) did not elaborate on the role of Cu_3P in improving wetting between sintered layers and enhancement of densification, Zhu *et al.* (2006) investigated the influence of varying contents of brazing flux on the wettability and densification in the direct laser sintering of Cu-based metallic powder (Cu-40%wt.SCuP). Their findings revealed that small amount of flux increased the densification and sinterability. A large amount of flux additive had a negative effect, however, with balling taking place and a residual covering of flux on the surface leading to a deterioration of adhesion between the sintered layers (Zhu *et al.* 2006).

Furthermore, the densification kinetics of iron, by SLS, was found to be enhanced by the addition of graphite powder (an increase of ~15% theoretical density) and this enhancement was influenced by the scanning rates as shown on Figure 2.39 (Simchi & Pohl 2004). The critical scan velocity, however, increased from 150 mm/s for iron powder, to 600 mm/s for the iron-0.8%wt.graphite powder mixture. Chen *et al.* (2004) showed that boron addition to iron reduced the tendency to spheroidise and increased to some extent component density for a given set of conditions.

On the basis of the characteristics of phase diagrams of ideal sintering systems, alloying elements have been used to enhance the sintering behaviour of metallic systems (see Figure 2.17 in Section 2.4). In these systems, the mechanism of enhancement is the formation of eutectic liquid phase and, since the solubility of the additive in the structural metallic component is low, the liquid remains segregated to particle boundaries. Sercombe (2003b) added boron to maraging steels with the aim of producing high hardness rapid tooling. His findings showed that the reaction of 0.4% boron with the alloying elements in the maraging steel resulted in the formation of Mo-

and Ti- rich borides, thereby providing a liquid phase for enhanced sintering to produce a near full density component. Chen *et al*. (2004) found that the inclusion of titanium in steel samples improved the bonding of the sample to the substrate and reduced the extreme hardness of the material. A search of the literature on the effect of alloying elements on the densification mechanisms of SLS/SLM processed aluminium powders has yielded no result. Hence, in order to gain an understanding of the role that alloying additions play in the sintering/melting of aluminium powders, results from conventional powder metallurgy must be considered.

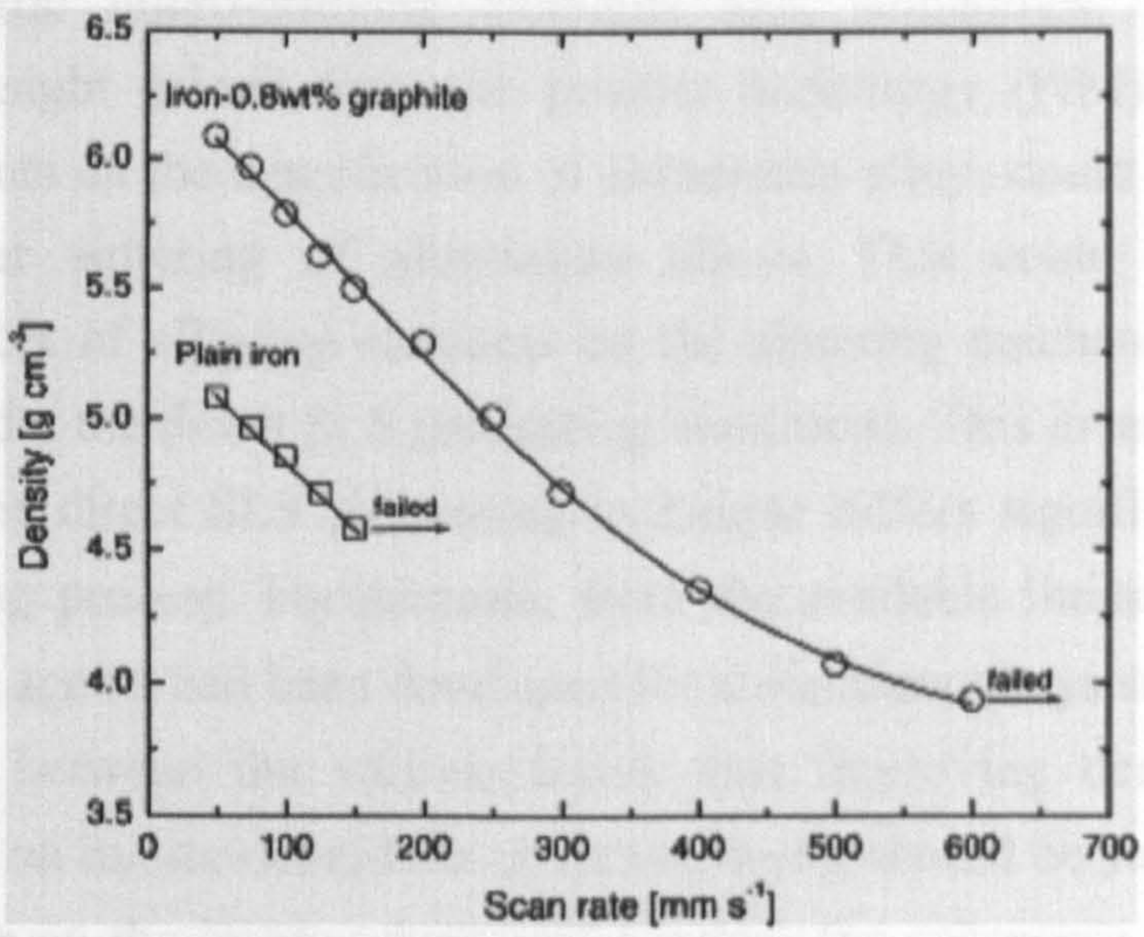

Figure 2.39: Effect of laser scan rate on the sintered density of iron powder and iron-0.8 wt. % graphite powder mixture processed at laser power of 215W, scan line spacing of 0.3mm, and layer thickness of 0.1mm (after Simchi & Pohl 2004).

It is an established fact that trace elements facilitate the sintering of aluminium and its alloys by the formation of liquid phase. This initiates a change from the solid state to liquid phase sintering with corresponding increase in sintering rates. Sercombe & Schaffer (1999a, 1999b) had observed that trace additions (0.1 wt%) of Sn, Pb, Bi, and Sb enhanced densification during sintering of aluminium alloys and dramatically improved their tensile properties. This observation could be attributed to the high vacancy binding energy of the trace elements used as well as their insolubility. Schaffer *et al*. (2001a) proposed a mechanism by which as little as 0.07wt% lead, tin, or indium promotes sintering in an Al-Zn-Mg-Cu alloy. They stated that the sintering enhancement was as a result of the segregation of the micro-alloying additions to the liquid-vapour interface thereby lowering the effective surface tension of the oxides. McPhee *et al* (2003) discovered that the segregation of iron into the inter-granular liquid pools retards the liquid film migration rate in aluminium alloys while alloys with low iron levels develop few intergranular pools and have higher sintered densities.

Delgardo *et al.* (2005) examined the effect of the second liquid phase coming from the addition of eutectic Al-Si on the super solidus liquid phase sintering (pre-alloyed powder) and liquid phase sintering (pre-mixed powders) of Al-Cu 2XXX series. Their result showed an improvement in AA2014 (Al-4.4wt%Cu-0.7wt%.Si-0.4wt%Mg) densification and mechanical properties but the product was noted to have been bedevilled with porous microstructure while Alumix 123 (Al-4.4%wt.Cu-0.6%wt.Si-0.5%wt.Mg) densification and microstructure improved by having lower amount of porosity but had lower bending strength. Therefore, it can be deduced from the foregoing discussions, that the sintering mechanisms of various aluminium alloys differ depending on specific micro-alloying elements and, sometimes, the bulk alloy composition. The insight gained from the powder metallurgy (P/M) studies on the effect of trace elements on the densification of aluminium alloys could be useful in the direct selective laser sintering of aluminium alloys. This could be applied by investigating the effect of alloying elements on the sintering mechanisms of various aluminium alloys under the direct SLS processing conditions. This investigation is very important because the direct SLS processing technique differs significantly from the conventional sintering process. Furthermore, from the available literature, no in-situ-deoxidiser or fluxing agents had been developed for aluminium alloys such that it could promote wettability between the various layers thus improving densification. The requirement for such an in-situ-deoxidiser or fluxing agent should be such that it would not leave any residue on the layers which could impair the coherence of the layers of the components being formed.

2.7.3 Surface Morphology of Laser Sintered Components

The impact of various processing parameters on surface morphology of a variety of SLS/SLM processed engineering materials has been investigated by several researchers. These results are summarised and discussed in this section. Simchi & Pohl (2003) employed SEM to determine that the surface morphology of laser sintered iron was strongly influenced by scan line spacing (h), whereas other parameters were less effective. Figure 2.40 reproduces the observations of the surface morphology of laser sintered iron processed at various scan spacings (h =0.1, 0.3, and .0.4 mm) in a N_2 atmosphere at fixed processing parameters (P = 215 W, u = 50 mm/s, d=0.05 mm) and bed temperature of 80 °C. At h = 0.4 and 0.3 mm, the solid particles were bonded together to form a network of columnar agglomerates parallel to the scan direction (Figure 2.40(a) and (b)) with the columns separated by longitudinal gaps. Decreasing the scan spacing resulted in a lower gap width, as a comparison of Figure 2.40(b) and (c) indicates. However, a relatively smooth and almost fully dense sintered surface was

obtained for specimens processed at h = 0.1mm (Figure 2.40(c)). Zhu *et al.* (2005) showed that for a Cu powder blended with pre-alloyed with SCuP, decreasing the scan speed also leads to a dense surface. The surface of the sample sintered at scan speed of 500 mm/s consisted of small randomly oriented, loose equiaxed agglomerates. The average size of the agglomerates was only about 100 μm, as shown in Figure 2.41(a). A large amount of small pores with almost the same shape and size were inter-connected suggesting insufficient densification during the SLS process. As the scan speed was decreased to 300mm/s, as shown in Figure 2.41(b), the surface consisted of larger agglomerates, approximately 150 μm diameter, which were connected by bridges. Moreover, the sizes of the pores were larger, their shape became more irregular and they became more inter-connected. Further reduction in the scan speed to 100 mm/s resulted in surface morphologies consisting of large, highly dense agglomerates and isolated pores with a nearly spherical shape (Figure 2.41(c)). An almost fully-dense sintered surface could be obtained when scan speed of 20 mm/s was used (Figure 2.41(d)). Niu & Chang (2000) carried out qualitative analysis of the effect of laser processing parameters on the sintering response of gas atomised M2 high speed steel powder by observing the SEM images of the surface morphology and internal microstructure of single layer parts. They discovered that with increasing laser power, the sintered surface varied from open/closed pores to a fully dense structure (Figure 2.42). Large lateral pores on the sintered surface of samples were found to result from the usage of high scan rates. The results obtained by Zhu *et al.* (2005) though in agreement with the work of Niu & Chang (2000), contradict the findings by Simchi & Pohl (2003) that all SLS parameters, with the exception of scan spacing, have little or no effect on the surface of parts. It seems likely that this disagreement could be attributed to the variation in the properties of each material.

The remaining part of this section will be devoted to the examination of the reported effects of laser processing parameters on the microstructure of laser-sintered multiple-layer parts.

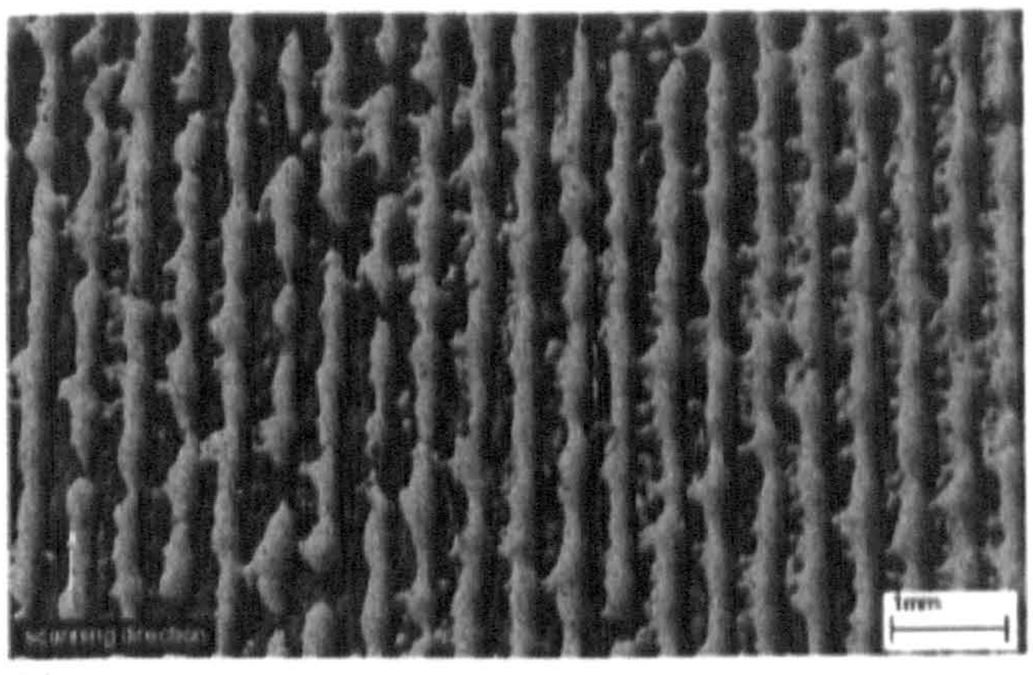

(a)

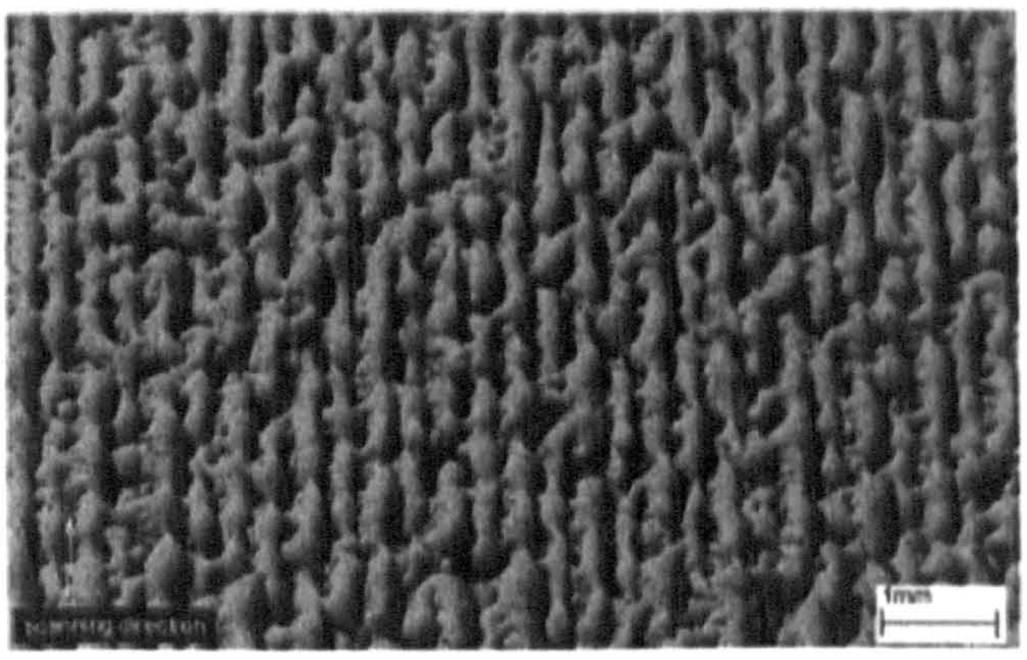

(b)

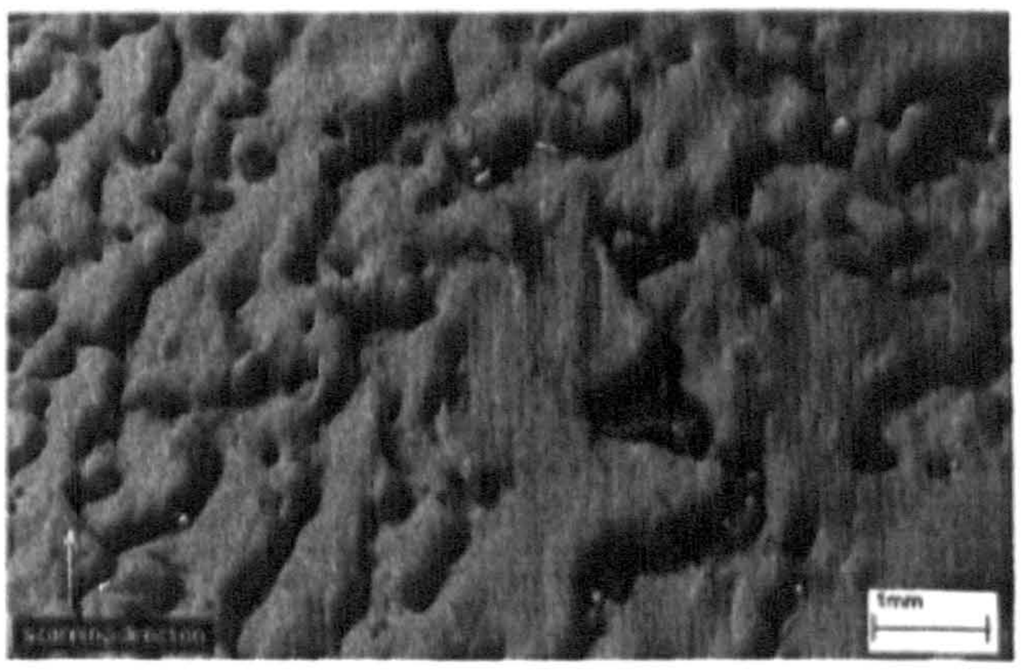

(c)

Figure 2.40: SEM images of laser sintered iron surfaces using different scan spacings: (a) 0.4 mm; (b) 0.3 mm; (c) 0.1 mm (after Simchi & Pohl 2003).

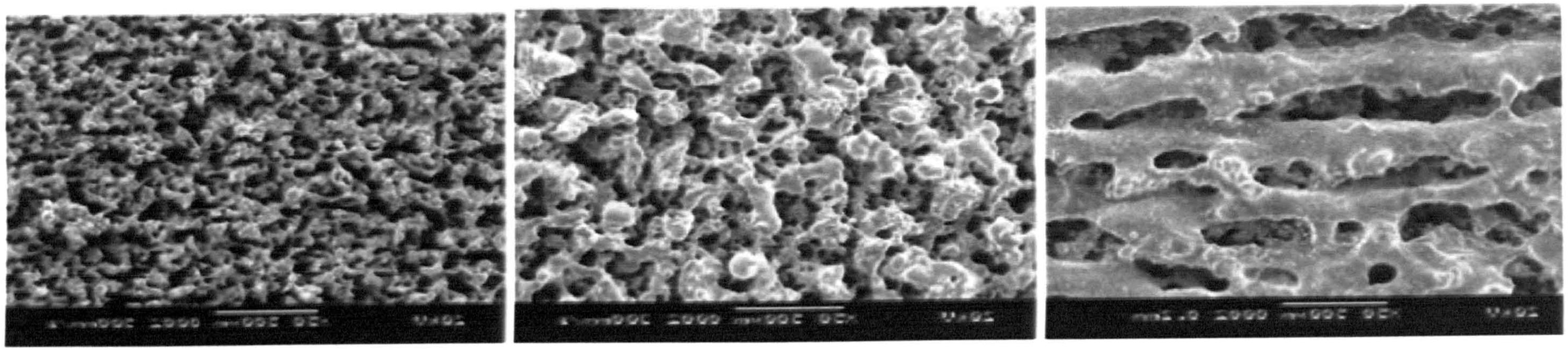

(a) 500mm/s, 0.1mm

(b) 300mm/s, 0.1mm

(c) 100mm/s, 0.2mm.

(d) 20mm/s, 0.1mm

(e) 100mm/s. 0.1mm

(f) 100mm/s, 0.3mm.

Figure 2.41: SEM images of surface morphologies of laser-sintered Cu-based samples at a fixed laser power of 100W, and different values of scan spacing and scan rate (after Zhu et al. 2005).

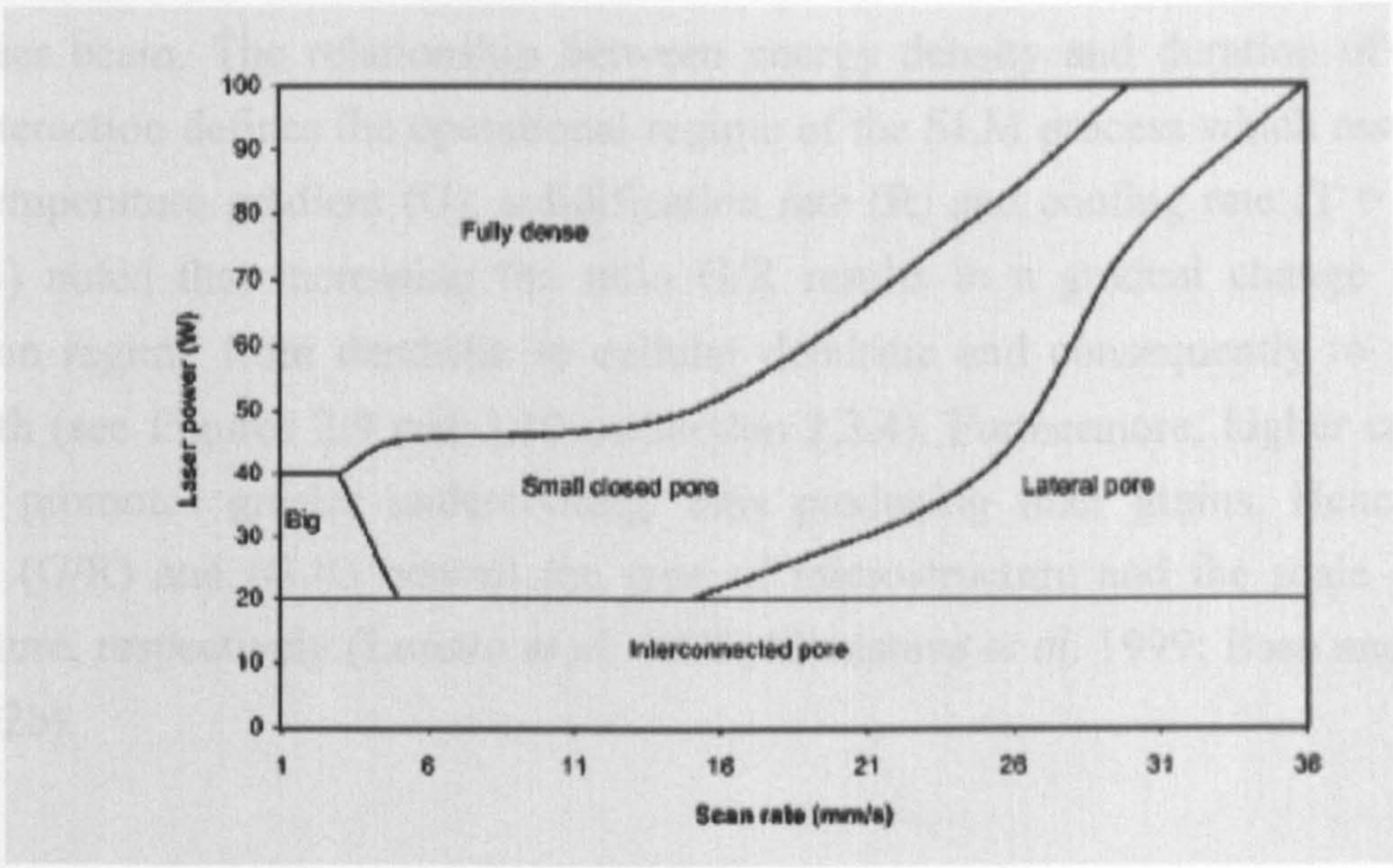

Figure 2.42: A processing map for M2 HSS showing the variation of porosity morphologies with scan rates for various laser powers and a constant scan spacing of 0.15 mm (after Niu & Chang 2000).

2.7.4 Microstructure of SLS/SLM Processed Components

Zhuoxing *et al.* (1999) demonstrated the feasibility of laser-sintered Cu-Sn-C system to produce intermetallics/phases such as α-Cu, $Cu_{31}Sn_8(\delta)$, $Cu_3Sn(\varepsilon)$ and $Cu_6Sn_5(\eta)$ in Cu-Sn-C systems. They were found to have a more enhanced homogeneous distribution than conventionally sintered materials as a result of improved flowability of the melt brought about by a relatively high sintering temperature. Furthermore, Niu & Chang (2000) reported that the SLM of M2 HSS powder resulted in the formation of fine grains with the microstructure consisting of a ferritic matrix with grain boundary carbides of M_6C and M_4C_3. These examples depict the benefits which may accrue from the application of SLS/SLM to the fabrication of metallic alloy components. These are generally, the ability to employ the transient cooling patterns to control grain sizes and shapes, phase percentages, and phase compositions in order to promote desirable mechanical properties during SLM. An extensive search of the literature has revealed that an accurate interpretation of the complex microstructure of laser sintered/melted samples requires a knowledge of the thermal history during the process resulting from building a range of laser sintering processing conditions. For example, the laser processing technique is capable of generating typical cooling rates ranging between 10^3 to 10^{11} K/s ((Ion 2005; Steen 2003; Basu and Date 1992a, 1992b). The fine microstructure usually observed in materials processed by SLS/SLM is a consequence of the high cooling rate ((Steen 2003; Basu and Date 1992a, 1992b). The nature of the microstructure obtained when laser power, scanning rates, scan spacing and layer thickness are varied is dependent on the duration of the interaction between the powder

and the laser beam. The relationship between energy density and duration of laser-material interaction defines the operational regime of the SLM process which results in a unique temperature gradient (G), solidification rate (R) and cooling rate (T = G.R). Steen(2003) noted that increasing the ratio G/R results in a gradual change in the solidification regime from dendritic to cellular dendritic and consequently to planar front growth (see Figures 2.9 and 2.10 in Section 2.3.4). Furthermore, higher cooling rate (G.R) promotes greater undercooling, thus producing finer grains. Hence, the parameters (G/R) and (G.R) control the type of microstructure and the scale of the microstructure, respectively (Loretto *et al.* 1998; Srivastava *et al.* 1999; Basu and Date 1992a, 1992b).

Longer laser-material duration or a higher energy density, during SLM, as a consequence of lower scanning rates and/or higher laser power lead to the formation of a superheated melt pool and high surface temperature (Ion 2005; Steen 2003). Under these conditions, it takes longer for the liquid to start solidifying and the temperature of the base material becomes higher, thus lowering both the temperature gradient at the interface and the cooling rate. A coarse microstructure may result in this case. When low laser power and/or faster scanning rates are employed, superheating is not pronounced and the average temperature gradient at the interface is sufficiently high to give a faster cooling rate thereby leading to the formation of finer microstructure. The geometry of the melt bead in the SLM process is dependent on the laser processing parameters. For example, provided the energy density is less than a critical value, when the heat input is just sufficient to melt the powder, this will result in the melt pool having a cylindrical geometry due to high surface tension. The contact area between two such layers will be smaller resulting in poor heat conduction and a low cooling rate.

For a multiple-layer part fabricated by the SLM process, where the substrate layers are pre-heated or partially melted in the subsequent deposition, both the cooling rate and the microstructure are affected (Steen 2003). The degree of formation of the heat affected zone (HAZ) in the deposited layer is a function of laser processing parameters. This could be responsible for the observed variations between the morphology and microstructure of individual laser deposited layers.

The following sections present various examples of how varying SLS/SLM process parameters and additives affect the microstructure of laser sintered metallic materials.

2.7.4.1 Effect of Processing Conditions on the Microstructure of Laser Sintered Components

Zhu *et al.* (2005) investigated the influence of SLS processing parameters on the microstructure of a Cu-based powder blended with pre-alloyed SCuP (Cu-40wt%SCuP) by varying scan speed and scan spacing as shown in Figures 2.43 and 2.44 respectively. These figures reveal that the grain size of the samples after laser sintering is much finer than the original particle size. They suggested the following reasons for this behaviour. The first possibility was that the Cu particles reacted with the melting binder (SCuP) and melted or partially melted. Consequently, as the laser beam moves away, molten Cu solidifies first because of its higher melting point (epitaxial growth). Therefore, the re-solidified Cu grains could be finer because of the high cooling rate. However, the laser energy in this experiment could not melt Cu completely, especially in the sample with the highest scan speed of 500 mm/s and a large scan spacing of 0.3 mm. Another possibility that may explain the occurrence of finer particle size is the mechanism of re-arrangement. Generally, the re-arrangement in liquid phase sintering (LPS) include two stages: the first stage in which the liquid flows into pores inducing the sliding, rotating and re-arrangement, of solid particles and the second stage in which the liquid penetrates along the grain boundary of the solid thereby making the particles size to be finer. Since the growth of Cu particles is temperature and time dependent, the decrease in the scan velocity and scan spacing may lead to coarsening. There are three overlapping stages associated with classic LPS: re-arrangement, solution-reprecipitation and solid-state sintering. Among these stages, solution re-precipitation and solid state sintering are responsible for microstructural coarsening. The contribution of the third stage is very limited because of the short duration of interaction between laser and metal powder. Therefore, it is the second stage, solution-reprecipitation, that is likely to be the main mechanism which promotes microstructural coarsening.

Simchi & Pohl (2003) examined how the connectivity and orientation of the pores in the microstructure of SLM processed iron powder depended on the processing conditions. They observed that for a laser power of 215 W, scanning velocity of 50 mm/s, scan spacing of 0.1 mm, and layer thickness of 0.05 mm the pores are elongated horizontally, almost perpendicular to the building direction (Figure 2.45(a)). The length of the pores was of the order of millimeter, and the width was about 0.1 mm. The agglomerates were fully dense and consisted of elongated ferrite grains oriented parallel to the building direction (Figure 2.46(a)).

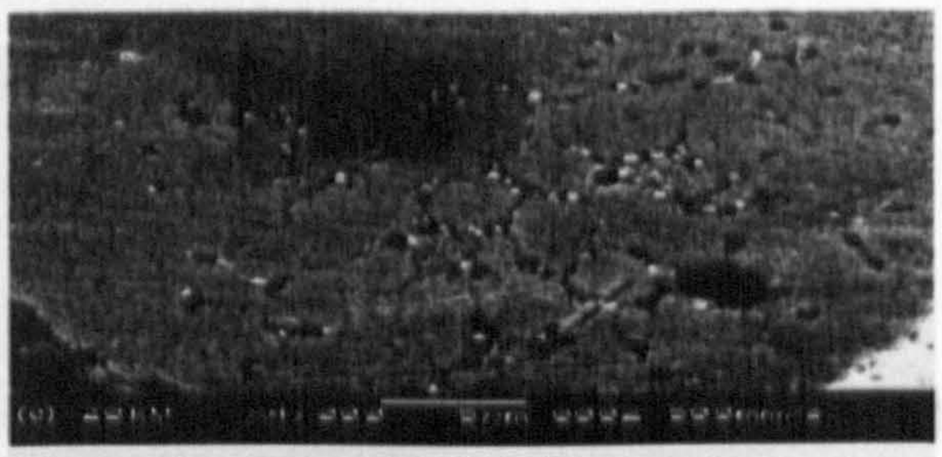

(a) 500mm/s

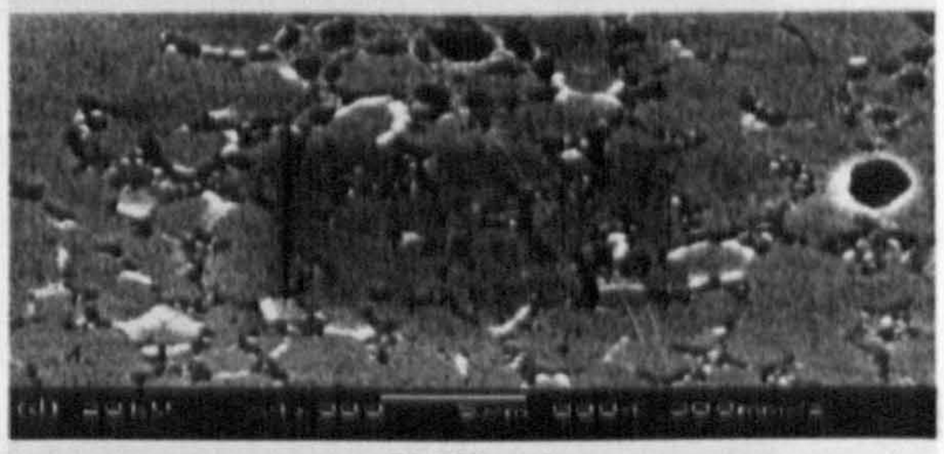

(b) 300mm/s

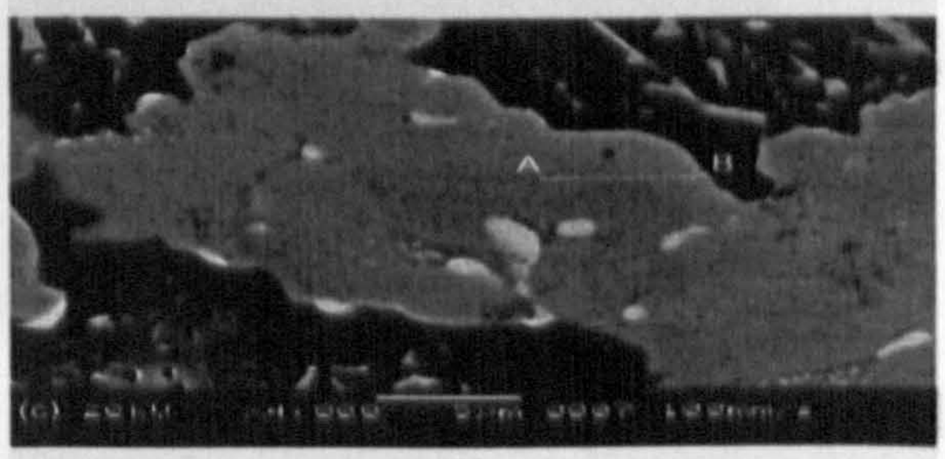

(c) 100mm/s

Figure 02.43: Microstructures of the laser sintered Cu-based samples using different scan speeds (after Zhu et al. 2005).

Increasing the scan spacing to 0.3 mm, resulted in the orientation of the pores becoming parallel to the building direction (Figure 2.45(b)). Again, the inter-agglomerates were fully dense, elongated ferrite grains oriented in the same direction as the pores (Figure 2.46(b)). However, the pore sizes in the two cases (h = 0.3 and 0.1 mm) were comparable and the fractional sintered density was almost equal (~0.74). On the other hand, increasing the scan velocity or decreasing the laser power increased the connectivity of the pores (Figure 2.45(c)). Furthermore, the pores became less oriented. Similar results were obtained for higher layer thickness but the pore channels were considerably bigger (Figure 2.45(d)).

The influence of laser processing parameters on the microstructural transition of laser processed metal powders from cellular to columnar to dendritic morphologies had been highlighted in sections 2.3.4 and 2.7.1.3 (see Figures 2.9 and 2.10). It had been emphasised that columnar regrowth occurs under the condition of low interfacial undercooling.

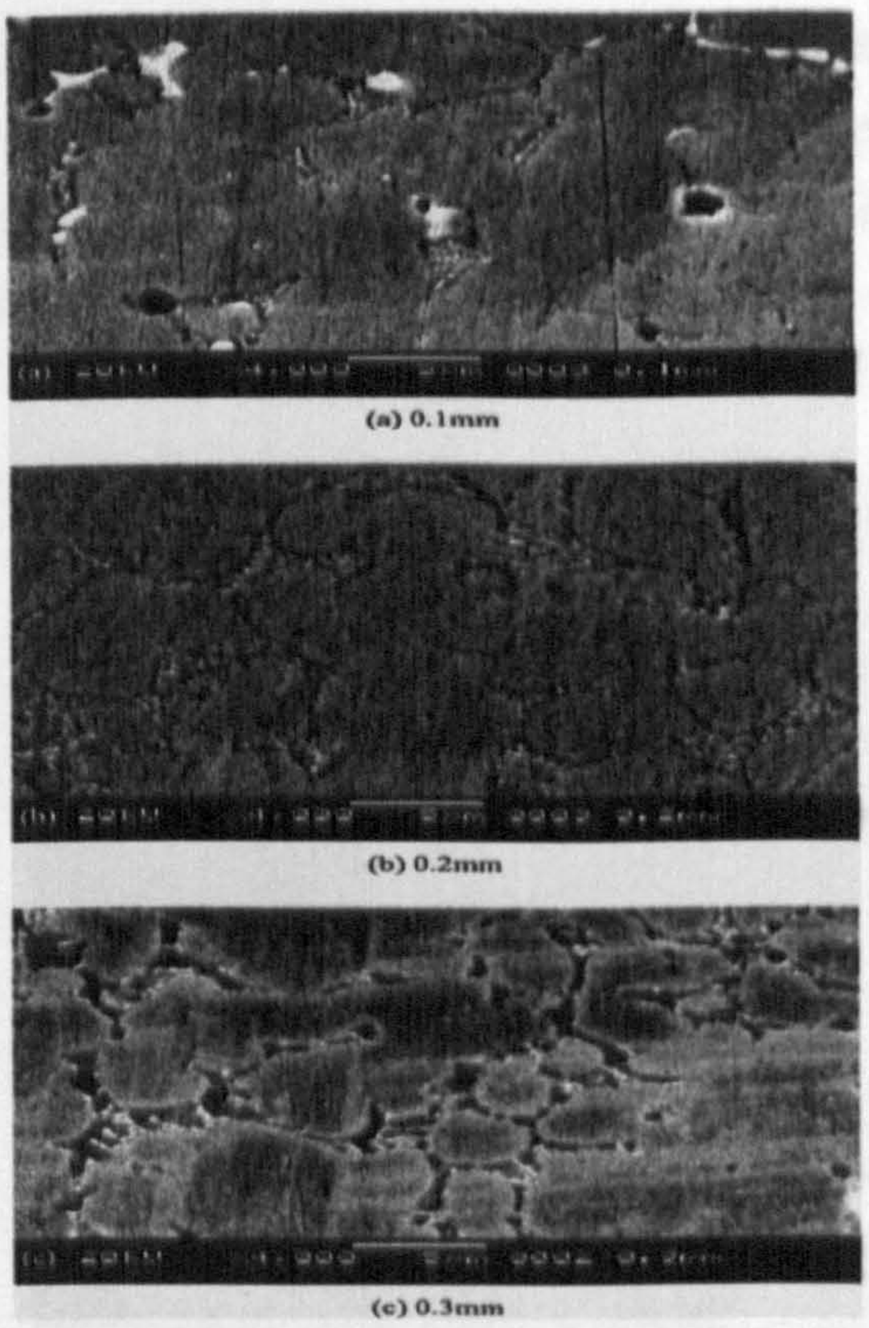

Figure 2.44: Microstructures of Cu-based laser-sintered samples using different scan spacings (after Zhu et al. 2005).

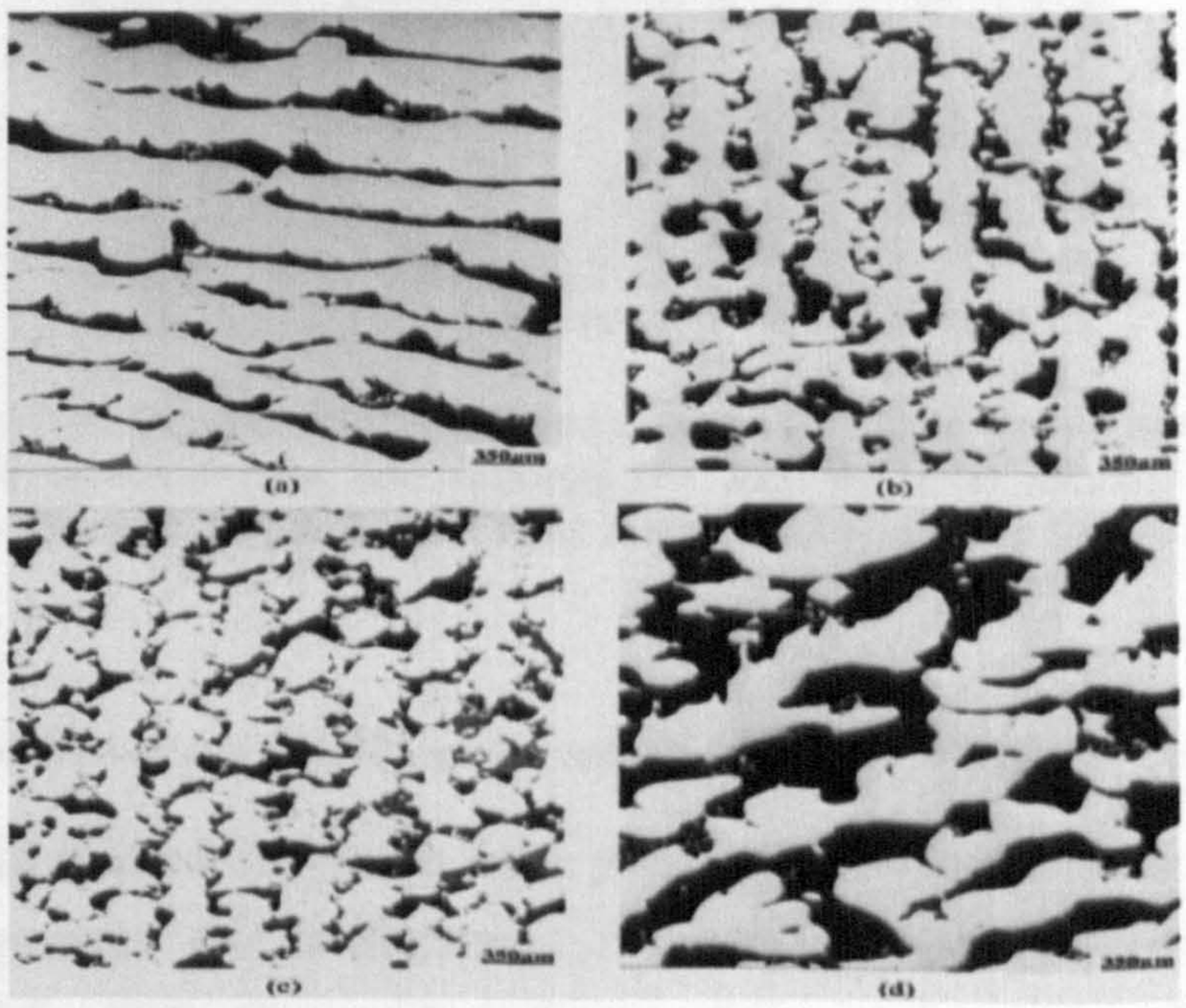

Figure 02.45: Polished section of laser sintered iron showing the pore structures on a section cut parallel to the building direction (N2 atmosphere and 80 oC powder bed temperature) and processed at the laser of 215 W: (a) u=50 mm/s, h=0.1 mm, d=0.05 mm; (b) u=50 mm/s, h=0.3 mm, d=0.05 mm; (c) u=100 mm/s, h=0.3 mm, d=0.05 mm; (d) u=50 mm/s, h=0.3 mm, d=0.2 mm (after Simchi & Pohl 2003).

For high laser scan speeds, the lag of the solidification front behind the liquidus isotherm may be quite significant, thus making the nucleation of new grains within the undercooled liquid a possibility. Ultimately, under extreme processing conditions and with the right alloy constitution, the formation of new grains will be inhibited by the onset of glass formation.

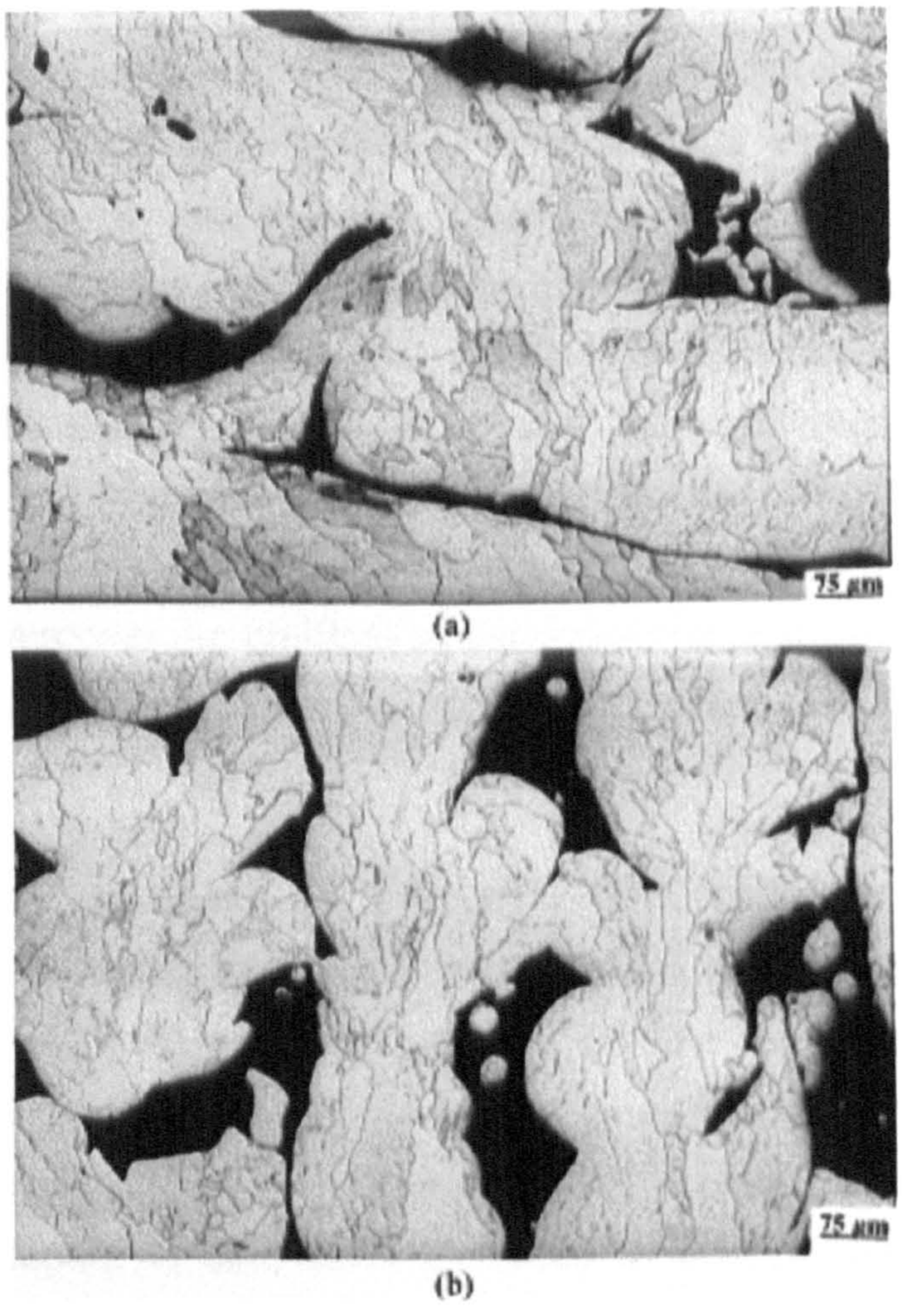

Figure 2.46: Characteristic microstructures of laser sintered iron on a section cut parallel to the building direction for different scan line spacings (P= 215 W, u=50 mm/s, d=0.05 mm, N2 atmosphere, 80 oC powder bed temperature): (a) 0.1 mm; (b) 0.3 mm (after Simchi & Pohl (2003)).

2.7.4.2 Effect of Additives on the Microstructure of Laser Sintered Components

It is widely believed that additives can have profound effect on the microstructure of laser-sintered components: this is illustrated in the following examples. Murali *et al.* (2003) investigated the SLS of a powder mixture of iron and graphite (99.22wt.% and 0.78wt.%. respectively) using a pulsed Nd: YAG laser and observed the laser sintered iron-graphite parts to be porous with a microstructure and mechanical properties substantially different from the same parts fabricated from the same powder mixture via conventional P/M. Moreover, they discovered that the carbon content in the sintered samples was as low as 0.3wt%. They concluded that in order to achieve a target carbon

content, a powder mixture of higher graphite content must be used. Simchi & Pohl (2004) followed up this suggestion by varying the graphite content between 0.4 to 1.6wt% in direct laser sintering. They found that with the addition of graphite (0.4wt% to 0.8wt%) to the iron powder, the continuous network of pore channels was eliminated and irregular shaped pores surrounded by a fully dense iron matrix were formed (Figures 2.47(b) and (c)). The microstructure consisted of small, spherical pores with no degree of orientation. With increasing graphite content (1.2wt%), the total porosity decreased steadily, and more pores were found in the microstructure (Figure 2.47d). Finding by Simchi & Pohl (2004) clearly demonstrates that the heterogeneous distribution of carbon in the iron matrix (Figure 2.48 and Table 2.13) leads to the formation of different phases as corroborated through the work of Murali *et al.* (2003). Similar results were obtained for the other sintered parts, although heterogeneity is more pronounced in the case of samples having higher graphite content. The work of Simchi & Pohl (2004) and Murali *et al.* (2003) once again have directed attention to the issue of altering the starting powder composition and making the correct choice of alloy addition in order to overcome the problem of heterogenous distribution of phases with the resultant poor mechanical properties, as pointed out earlier in Section 2.5.

Prior to these findings, Tang *et al.* (2003) described how microstructural features such as porosity, pore size and shape, the agglomerate size, and grain shape of laser sintered copper alloy (Cu and Cu_3P)are associated with the variation of the amount of *in-situ* - deoxidiser (SCuP). They noted the existence of a large amount of pores at a low SCuP level (25vol%) with small agglomerate sizes (200-300 μm) of ball-like shape (Figure 2.49(a)). When the amount of deoxidiser increased to 40vol%, more molten binder flowed and infiltrated into pores between the copper particles, thereby forming big agglomerates and a denser microstructure, but the pore sizes became larger (Figure 2.49(b)). However, at higher fractions of SCuP, the re-arrangement force is higher and the viscosity of the mixture was lower, leading to faster re-arrangement of Cu particles and spreading of the binder (Figure 2.49(c)). The molten binder spreads and wets the Cu particles well. The copper particles are pulled together by the liquid towards the center of a laser scan path, thus forming long bar shaped tracks. Tang *et al.* (2003) concluded that high porosity was still left in the microstructure due to the short transient interaction duration (0.1 to 1s) between laser and metal powder. The porosity could be eliminated by the appropriate choice of the laser processing parameters which allows sufficient laser-material interaction duration that eliminates porosity and balling. The findings in this section corroborate the results obtained from the investigation on the effect of component ratios on the attainable liquid phase which determines, to a very great extent, the nature of microstructural features and densification mechanisms

of direct laser sintered powders (see Section 2.5). Therefore, the right choice and correct amount of the appropriate additive for microstructural improvement in a typical SLS powder system is very important.

Table 02.13 : The local carbon concentration measured by X-ray photoelectron spectroscopy (XPS) method and microhardness values of marked areas in Figure 2.42 (after Simchi & Pohl 2004).

Area	Possible phases	Carbon content (wt.%)	Hardness ($HV_{0.025}$)
I	Ferrite	0.1	137
II	Tempered Martensite	1.6	463
III	High Carbon Austenite	1.9	476

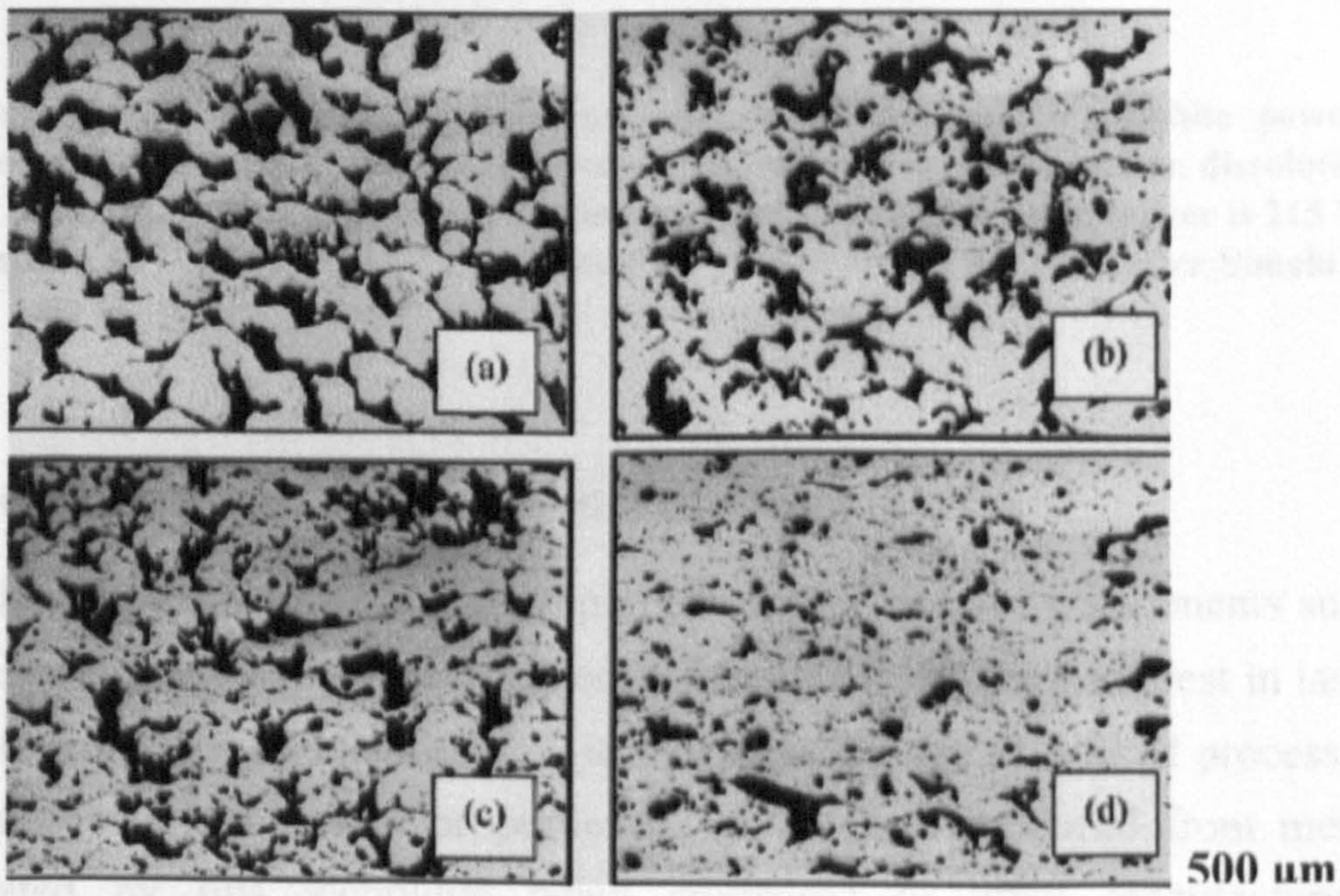

Figure 2.47: Polished section of laser sintered parts shows the effect of graphite addition on the pore structures on a section cut parallel to the building direction; laser power is 215 W, scan rate is 75 mm/s, scan line spacing is 0.3 mm, and layer thickness is 0.1 mm (a) 0% C (b) 0.4% C (c) 0.8% C (d) 1.2% C (after Simchi & Pohl 2004).

There appears to be no literature dealing with the effect of sintering atmospheres and alloying additions in the SLS/SLM of aluminium or its alloys. Reports on the indirect SLS of aluminium alloys carried out at the University of Queensland in Australia, document the effects of nitrogen sintering atmospheres and alloying addition but only as they affect the dimensional stability of the components, (Sercombe 2003a; Sercombe & Schaffer 2004a, 2004b, Sercombe & Hopkinson 2006) no mention is made of their effect on microstructure. Therefore, the effect of the various additives or alloying

contents on the microstructure of direct SLS fabricated aluminium components is an area worthy of investigation.

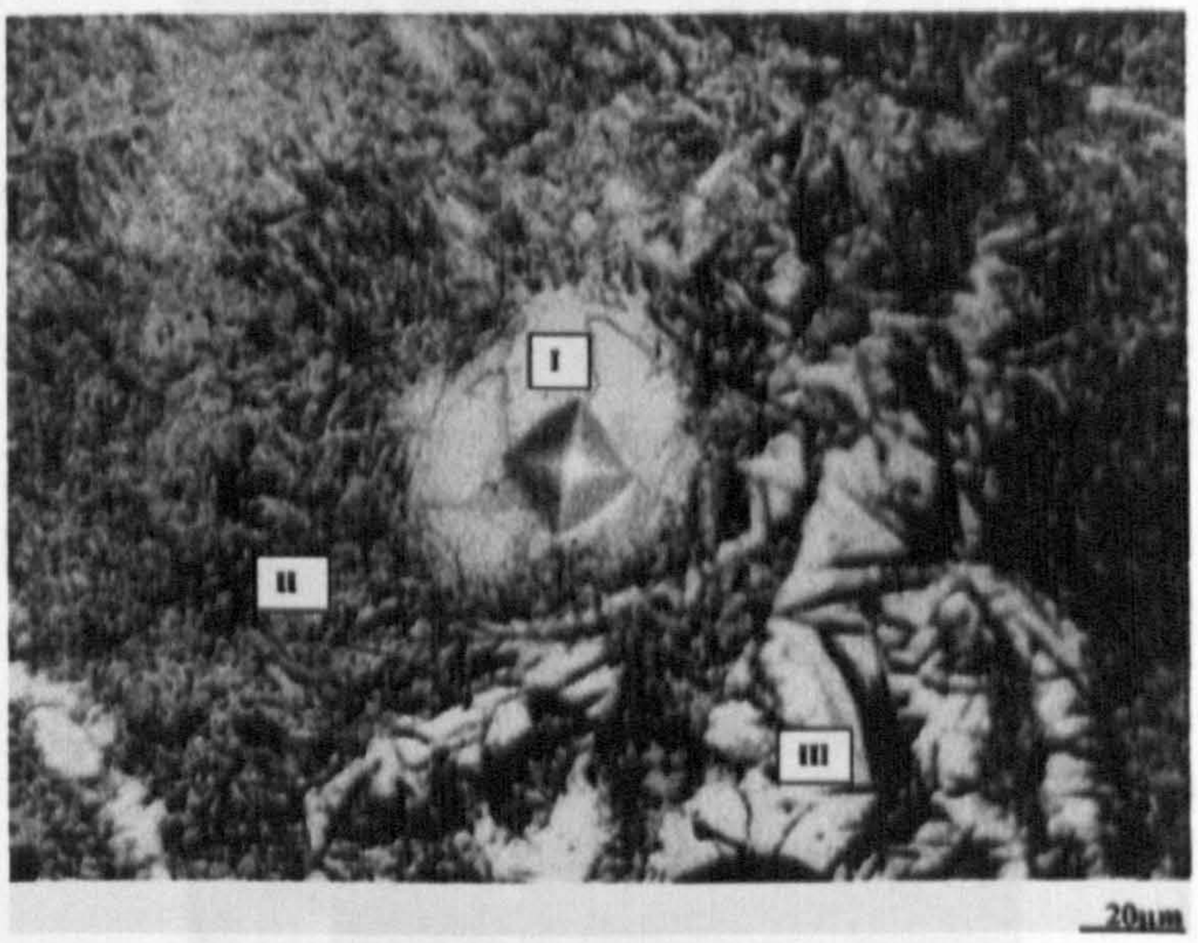

Figure 02.48: Characteristic microstructure of laser sintered iron-1.2 wt.% graphite powder mixture on a section cut parallel to the building direction shows heterogeneous carbon dissolution in the iron matrix resulting in the varying local hardness values (Table 2.4). Laser power is 215 W, scan rate is 75 mm/s, scan line spacing is 0.3 mm, and layer thickness is 0.1 mm (after Simchi & Pohl 2004).

2.7.5 Mechanical Properties of Laser Sintered Components

This section is devoted to the mechanical properties of laser sintered components such as hardness, strength, ductility, and impact energy. Strength is of major interest in laser sintered parts. From Table 2.2 in Section 2.2, it is evident that the SLS/SLM process is able to impart adequate mechanical properties to components produced from metal powders fabricated by this technique when compared to other manufacturing techniques. Moreover, mechanical properties "which are primarily dependent on fractional density" exhibit similar trends to the variation of sintered density with respect to scan speed and laser power (Figure 2.50). Besides the fractional density, the strength of porous sintered samples also depends on various powder characteristics such as particle size and distribution, and particle shape. To understand how mechanical properties of laser sintered parts vary with the fractional density, the effect of pores (porosity and pore shape) on the structural integrity (impact energy, fracture toughness, and fatigue strength) of parts will be discussed briefly. Furthermore, it is pertinent to note that although a sintered sample may attain full density, it may possess inferior mechanical properties as a result of microstructural defects, such as the presence of inclusions such as oxides (Figure 2.51).

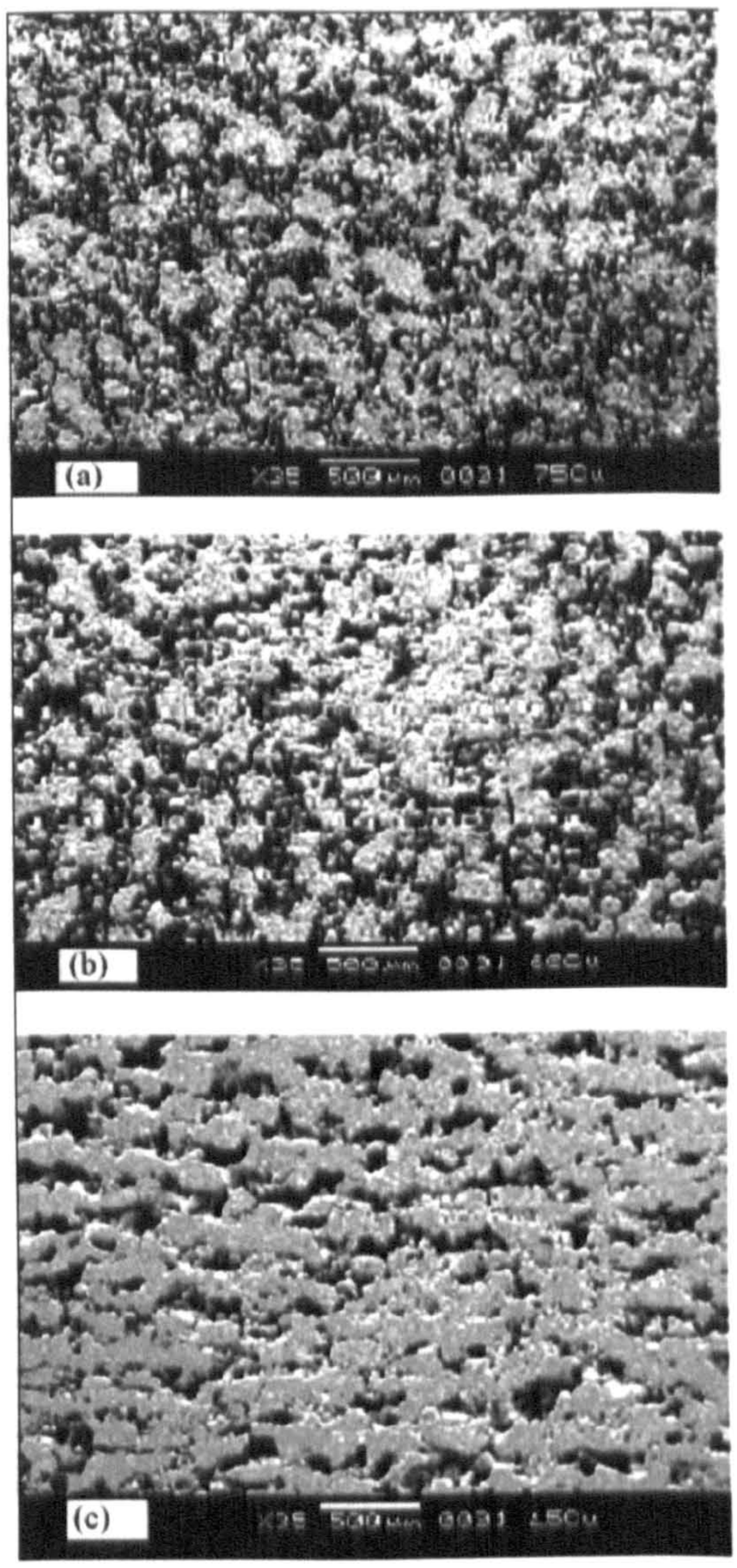

Figure 2.49: SEM images of sintered Cu-Cu3P samples using different amount of binder: (a) 25 vol% SCuP; (b) 40 vol% SCuP; (c) 55 vol% SCuP (after Tang et al. 2003).

Pores reduce the effective load carrying capacity of a material and act as stress concentrators and effective crack initiation sites which affect hardness, tensile properties and ductility. Therefore, a sample with residual microstructural porosity would be expected to be weaker than fully dense bulk material. Interestingly, mechanical properties of sintered parts are sensitive to pore shape and placement. Smooth pores at large spacings are noted to be less detrimental than small, closely spaced pores (Figure 2.52). The undesirable influence of pores on ductility is as a consequence of crack initiation at the pores. Therefore, aside from the effect of pore volume on ductility, there is a further sensitivity to pore shape. On the basis of the above discourse, German (1998) and Grayson *et al.* (2004) inferred that the shape, spacing, size, and placement of pores contribute to the significant variation in ductility

observed in P/M materials. German (1998) noted that with a porosity level greater than 15%, ductility is often negligible.

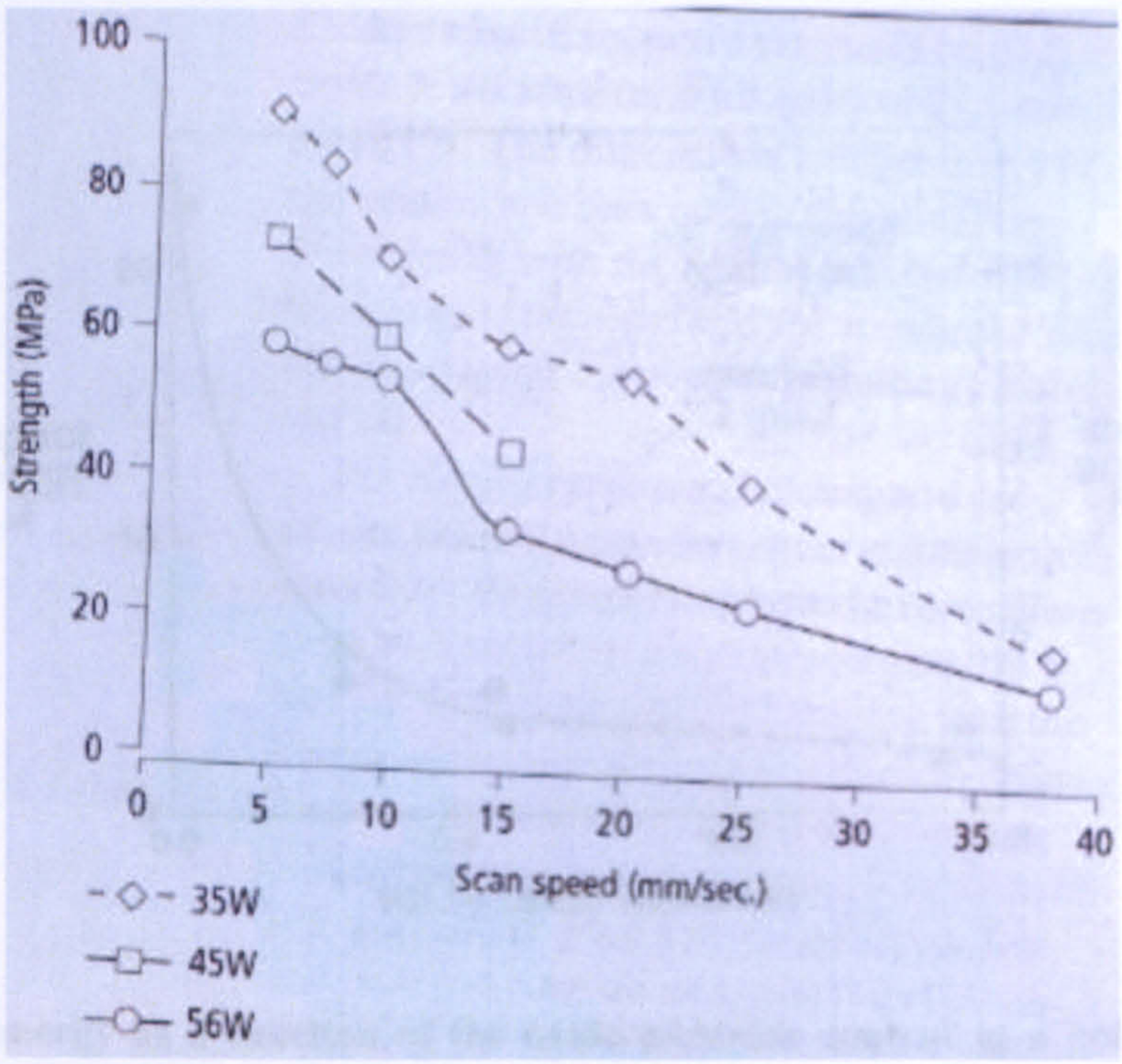

Figure 2.50: Ultimate tensile strength of SLS-processed bronze-nickel parts as a function of scan speed and laser power (after Agarwala et al. 1995).

Grayson *et al*. (2004) characterised the fatigue behaviour of unreinforced pressed and sintered aluminium alloys by examining aspects of crack initiation and growth. They discovered that crack initiation occurred at surface or sub-surface pores and pore clusters with the veins of oxide observed on fatigue fracture surfaces. The presence of the veins of oxide was attributed to pre-existing microstructural features arising from the residue of the alumina coating on the aluminium powder particles. Moreover, Upadhyaya (2000) established that, for a common P/M alloy (201 AB), the tensile strength for a compaction pressure of 110 MPa and sintered density of 2.53 g/cm^3 (approximately 9vol% porosity) was 169 MPa.

When the sintered density was increased to 2.70 g/cm^3 (6% higher density), the tensile strength increased by ~25% to 209 MPa. Furthermore, German (1998) highlighted the role of porosity in low-alloy (Ni-Mo-C) steels; for instance, the fatigue endurance strength for hot forged material having 0% porosity is 650 MPa, whilst the value for the same alloy produced by metal injection moulding (3% porosity) is 575 MPa and die compaction (12% porosity) is 390 MPa. In the formation of fatigue cracks and their propagation through the microstructure, pores play a significant role. Given the

condition of dynamic loading, the crack grows ever so slightly on each stress cycle, eventually reaching a point where fracture takes place (German 1998). The nature of the final failure may be ductile or brittle.

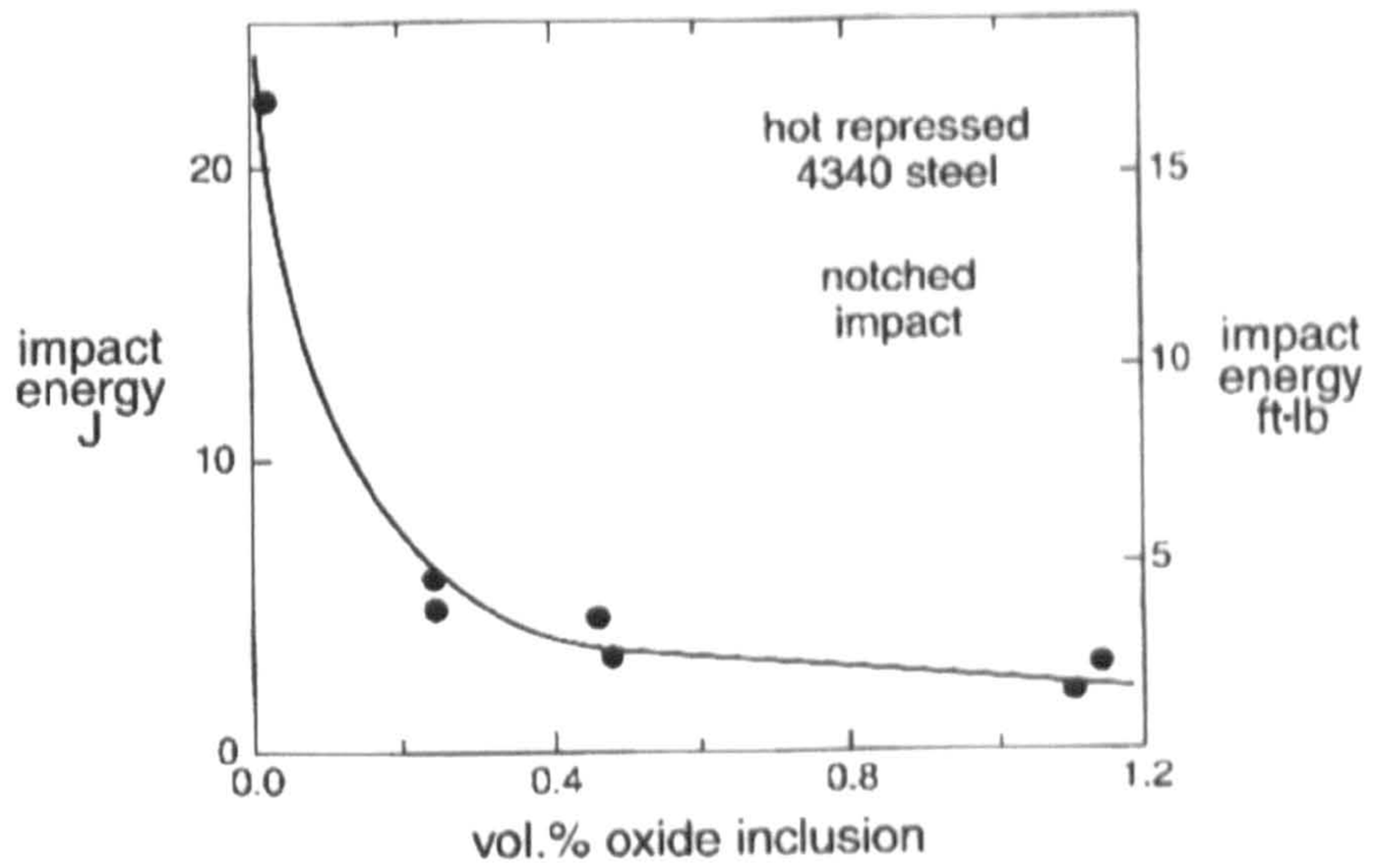

Figure 2.51: Impact energy as a function of the oxide inclusion content in a hot-repressed 4340 steel, showing the detrimental effect of a small level contamination (after German 1998).

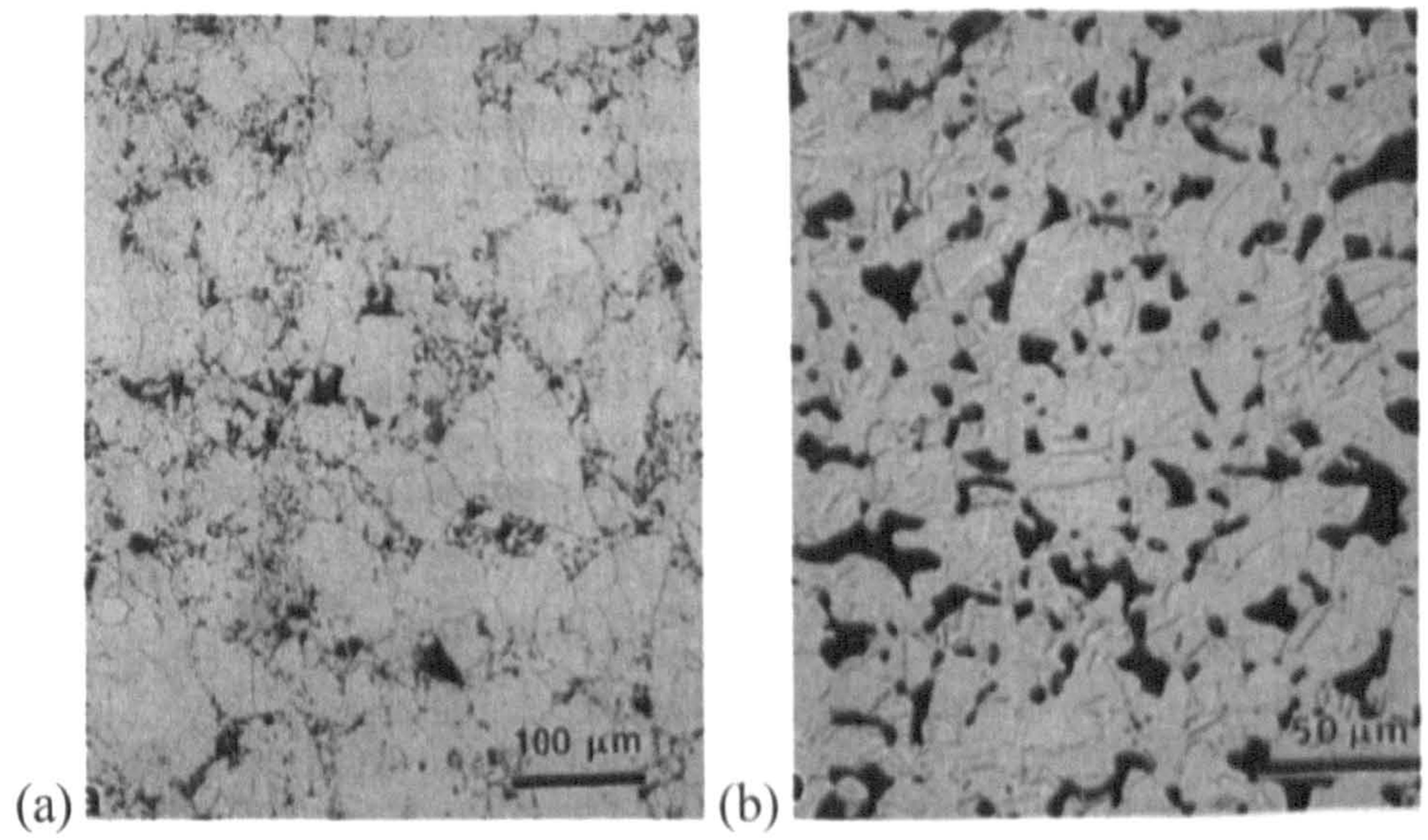

Figure 2.52: The pores (dark spots) in these two sintered steels vary in shape and size, largely due to differences in sintering cycles. The arrangement of pores outlining the particles in (a) is detrimental to final properties, while the smooth pore structure evident in (b) is more desirable (after German 1998).

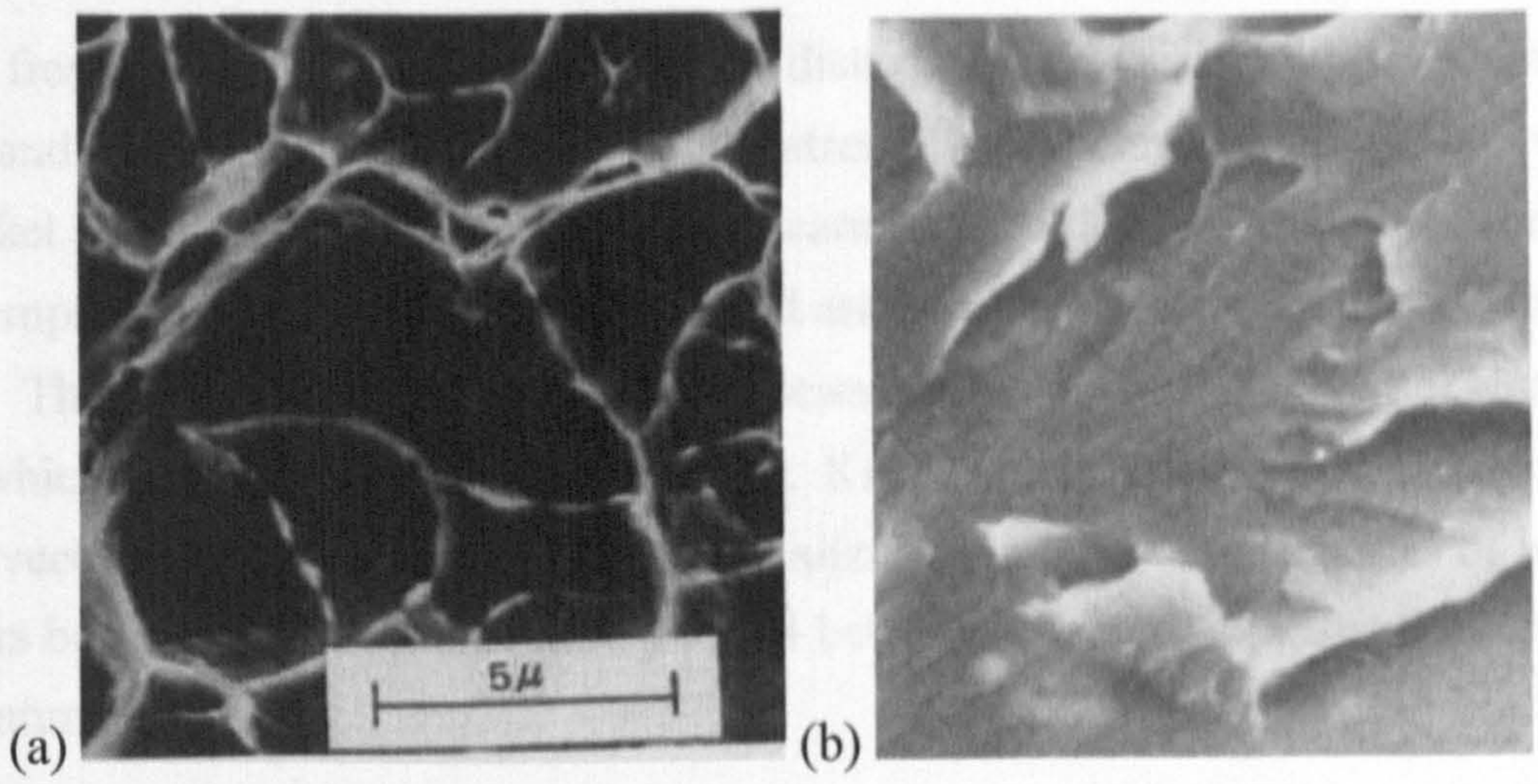

Figure 02.53: Fracture Surfaces obtained by scanning electron micrograph showing (a) dimple region, an indication of ductile fracture and (b) the cleavage characteristics 3500x (Callister 2007).

An understanding of the nature of the failure demands an accurate interpretation of the microstructure and of the fracture surface (Callister 2007). The presence of dimples on the SEM fractured surfaces is an indication of ductile failure while brittle fracture is characterised by cleavage with each fractured grain flat and differently oriented, thereby giving a "crystalline" or "rock candy" appearance (Figure 2.53) to the fracture surface (Callister 2007).The impact energy and fracture toughness are also sensitive to pores. The impact energy is the energy needed to fracture a sample, while the fracture toughness indicates the energy required for the crack growth in an already defective structure (German 1998). Porous P/M parts are poor in impact toughness and fracture toughness tests.

As observed in other studies, higher SLS/SLM part densities were obtained by using a lower layer thickness (Simchi & Pohl 2003; Agarwala *et al.* 1995). However, the minimum layer thickness that can be successfully employed is determined by various factors and most importantly by the maximum particle size in the system, as discussed in section 2.7.2.1. Below a certain layer thickness, the roller mechanism tends to displace the previously sintered layers from their predetermined position, thus disturbing the geometry of the component. (Agarwala *et al* 1995). This problem is particularly serious during the early build up of the component. In a study carried out by Agarwala *et al* (1995) on bronze (Cu-10%wt.Sn)-nickel powders having agglomerate particles as large as ~150 μm, it was discovered that lowering layer thickness from 500 μm to 250 μm resulted in an increase in ultimate tensile strength from approximately 35MPa to 60 MPa, irrespective of laser power or scan speed. The lower layer thickness resulted in improved sintering between layers thus advancing the part density. However, lowering the layer thickness to 125 μm resulted in difficulty in

spreading fresh layer of powders without disturbing previously sintered layers. Agarwala and co-investigators observed that strength was considerably lower when bronze-nickel specimens were oriented and scanned in a longitudinal direction (40 MPa) in comparison to when they were oriented and scanned in the transverse direction (60 MPa). This is as a result of the short scan vector in the transverse scanning direction which resulted in better sintered part. Kruth *et al.* (2004) demonstrated that short scan vectors cause the receipt of more localized net energy than a series of longer scan vectors because of the shorter time interval between successive pulses, minimising the temperature decay.

Dewidar and co-workers (2003) adopted infiltration with bronze to improve the mechanical properties of high speed steel components fabricated via direct SLS. Uzunsoy & Chang (2005) carried out a comparative evaluation of the microstructure and mechanical properties of laser sintered low carbon stainless steel (316L) processed using three different copper alloy infiltrants. They found the tensile fracture strength increased in the order of high tensile brass< bronze < cast aluminium manganese bronze. The alloying effect on the mechanical properties of conventional P/M processed samples is less clear because, in most cases, alloying elements induce different density which is at variant with microstructure.

Liu *et al.* (2006) investigated the effect of iron (Fe) and molybdenium (Mo) contents on the tensile properties of P/M binary titanium alloys at room temperature (Figure 2.54). For Ti-Fe alloys, Ti-3wt%Fe had the highest yield strength but poor elongation (1%). They had ductility larger than 2% when the Fe content was below 2wt% whilst the Fe content was above 3wt%, the strength reduced as a result of its poor ductility. Liu *et al.* (2006) attributed the observed reduction in tensile strength and poor elongation to the promotion of the coarse, primary β-grains by Fe and the formation of TiFe intermetallic phase during cooling. Therefore, the existence of TiFe intermetallic phase was noted to have deteriorated the ductility and the tensile strength. For Ti-Mo alloys, the microstructural refinement effect of Mo and the stabilisation of ductile β-phase lead to the rapid increase in strength of P/M Ti-Mo alloy and good ductility. Moreover, the reduction in elongation of P/M Ti-Mo alloys at Mo content above 3% could be ascribed to their low density, which decreases with the Mo content.

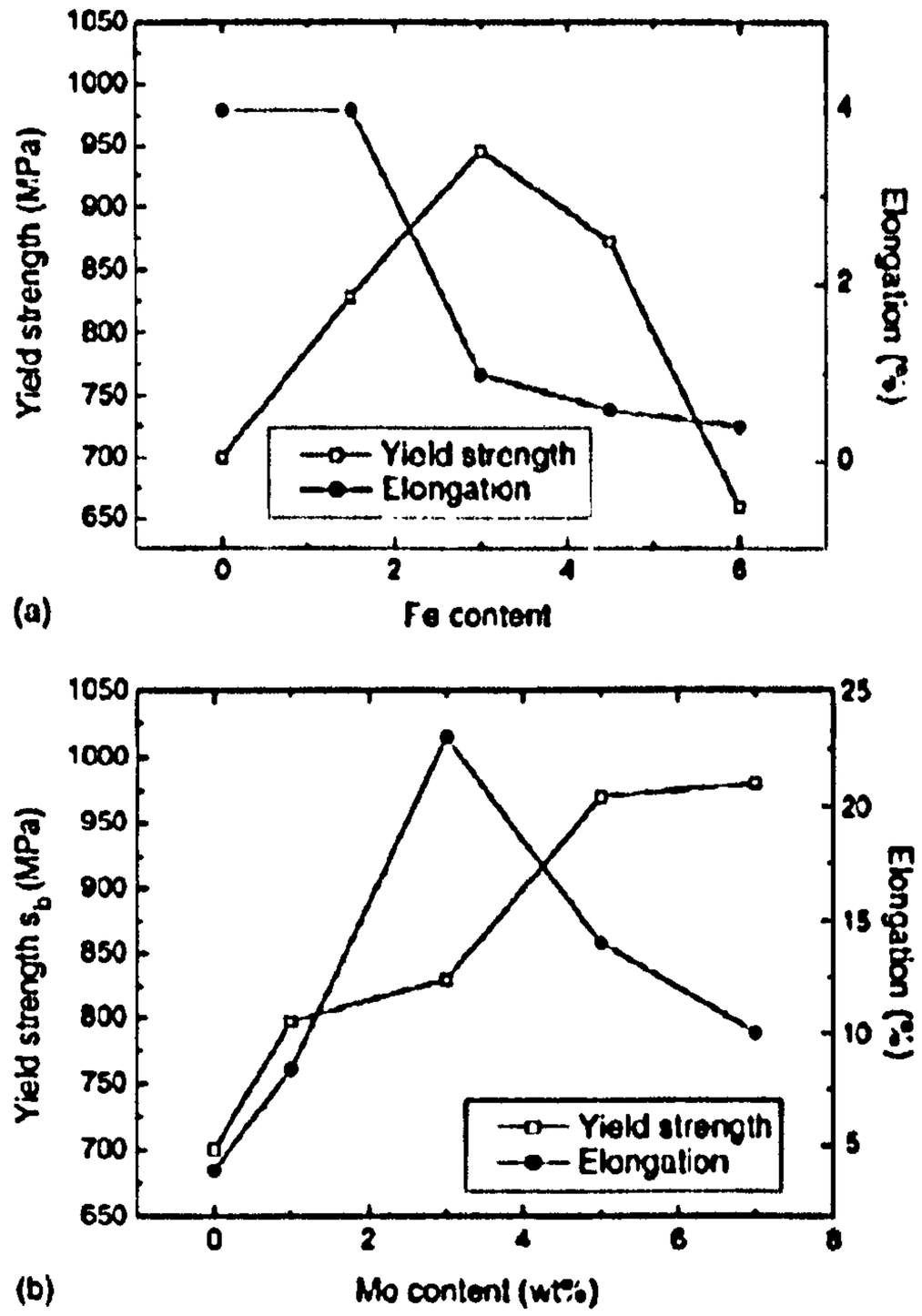

Figure 2.54: Effect of alloying elements on the tensile properties of binary P/M Ti alloys at room temperature: (a) Fe content (b) Mo content (after Liu et al. 2006).

2.7.6 Dimensional Accuracy of Laser Sintered Components

Despite continued improvements that have been recorded in the field of SLS/SLM over the past few years, achievable dimensional accuracies remain limited when compared to the CNC machining technique. Although, the SLS/SLM process has claimed accuracies of ± 0.05 mm (Pham *et al.* 1998), achieving this demands a thorough understanding of the process and the long term experience of the machine operator. Reports from the available literature have shown that unfinished prototypes made by SLS/SLM and other rapid prototyping processes are characterised by oversize in the X, Y, and Z directions with the least accuracy noted for the Z build direction (Dunne *et al.* 2004).

The beam quality, powder granularity, shrinkage, CAD model, slicing algorithms, data transfer, and device motion resolution have been identified as critical process parameters and powder properties affecting the dimensional accuracy of components fabricated by LM processes (Karapatis *et al.* 1998). The mode or quality of the laser beam has been found to play a crucial role in SLS/SLM produced components.

Karapatis *et al.* (1998) observed that Nd: YAG (λ = 1.06 μm) lasers have better absorptivity on powders than CO_2 lasers (λ = 10.6 μm) while they noted the CO_2 lasers are of higher quality than the Nd: YAG lasers. They elucidated that the absorption of laser energy affected the accuracy of parts made by the SLS/SLM process because thermal gradients cause residual stresses in the parts and thermal diffusion induces sintering of particles not situated directly under the beam. In order to maintain excellent dimensional accuracy in SLS/SLM manufactured parts, powder particles sizes must not be too fine, to ensure the powder flowability under the delivery device, while proper wetting behaviour between the structural material and the binder is very critical. The remaining unfused powder holds the parts thereby promoting structural rigidity during the process. With regard to the CAD model, slicing algorithms and data transfer accuracy, dimensional accuracy is dependent on computer power and programming. Lewis (1995) observed that CAD software is at present of high precision with the slicing algorithms allowing a good layer representation of parts. Moreover, infiltration has been adopted to improve the dimensional accuracies of indirect SLS processed aluminium alloys (see section 2.3.4).

2.7.7 Effect of Laser Types on the Properties of Laser Sintered Components

The type of laser (see Table 2.1) used for sintering has been identified as one of the factors affecting the properties of laser-sintered components. For instance, Lauwers *et al.* (1999) explored the comparative fabrication of components made in Fe-Cu and WC-Co powders by CO_2 and Nd: YAG lasers. They inferred that with the Nd: YAG laser, components of higher density, a deeper sintering depth, and a larger processing window are obtainable, given the same laser energy density for both laser types. Abe *et al.* (2001) employed a dual laser scanning system combining a pulsed Nd: YAG, with a mean power of 50W and a maximum peak power of 3kW, and a CO_2 laser, to fabricate 3-D components from nickel, aluminium, iron, copper, stainless steel, chromium and nickel-base alloys. Their findings showed that reheating by CO_2 after initial heating by Nd: YAG improved the material's properties, the elimination of residual stress and ductility improvement being attributable to the reheating after melting. Steen (2003) noted that in order to attain effective bonding between the layers, the depth of penetration should be of the order of the layer thickness with the aid of pulse lengths of a few milliseconds for layer thickness varying from 20 to 100 μm. Morgan *et al.* (2001) achieved porosities less than 1% with a continuous wave (CW) Nd: YAG laser when fabricating stainless steel 316L powders. Although many of the commercial SLS machines are equipped with CO_2 lasers, Nd: YAG lasers are well known to offer enhanced absorption characteristics for metallic powders (Lauwers *et al.* 1999;

Tolochoko *et al.* 2000). CO_2 lasers are associated with high efficiency, low price and ease of maintenance. These reasons could be responsible for the increasing popularity of CO_2 laser systems when compared to the Nd: YAG systems, especially for powers greater than 5kW (Steen 2003). Recently, a new generation of machines which employ lasers of enhanced beam quality are being developed (Santos *et al.* 2006). Among such machines are EOSINT 270, TrumaForm LF 250, and Realizer. Even though machines using diode lasers are more cost effective than those employing CO_2 or Nd: YAG lasers but they have the limitation of poor beam quality as a result of the high beam divergence which needs to be improved upon (Santos *et al.* 2006). Meanwhile, a comparative processing test would be necessary for both CO_2 and Nd: YAG machines in order to observe the sintering behaviour of aluminium alloys and make conclusions regarding any of the machines that may yield a more acceptable processing window and improved functional properties for processing aluminium alloys.

2.7.8 Powder Bed Behaviour and its Effect on the Properties of Laser Sintered Components

This section considers the property requirements of powders that may be deemed suitable for the direct SLS process as well as their role in the development of the properties of laser sintered parts.

2.7.8.1 Powder Properties

Many researchers working in the specialty of conventional powder metallurgy have emphasised the importance of controlling specific powder properties to achieve increased efficiency during powder handling, packing and compaction with a view to obtaining substantial improvements in the density and mechanical properties of the sintered components (Thümmler & Oberacker 1993; German 1991). Of special interest are the properties of individual particles, such as size and shape, and the bulk properties, such as packing density and flowability. The customisation of these properties can lead to changes in melt pool behaviour, sintering kinetics and laser absorptivity in SLS/SLM (Van der Schueren & Kruth 1995; Niu & Chang 1998). Powder metallurgy techniques generally deal with powder particle sizes that vary from less than one μm to several hundred μm. The powders are often available in different shapes and sizes which are determined solely by the production parameters and methods (Thümmler & Oberacker 1993). Due to the fact that it is difficult to quantify every particle shape, qualitative descriptors are frequently used, examples of which are shown in Figure 2.55. A brief overview of how particle shape, size and distribution

affect the powder properties and the density of functional properties of sintered parts is given in the following sections.

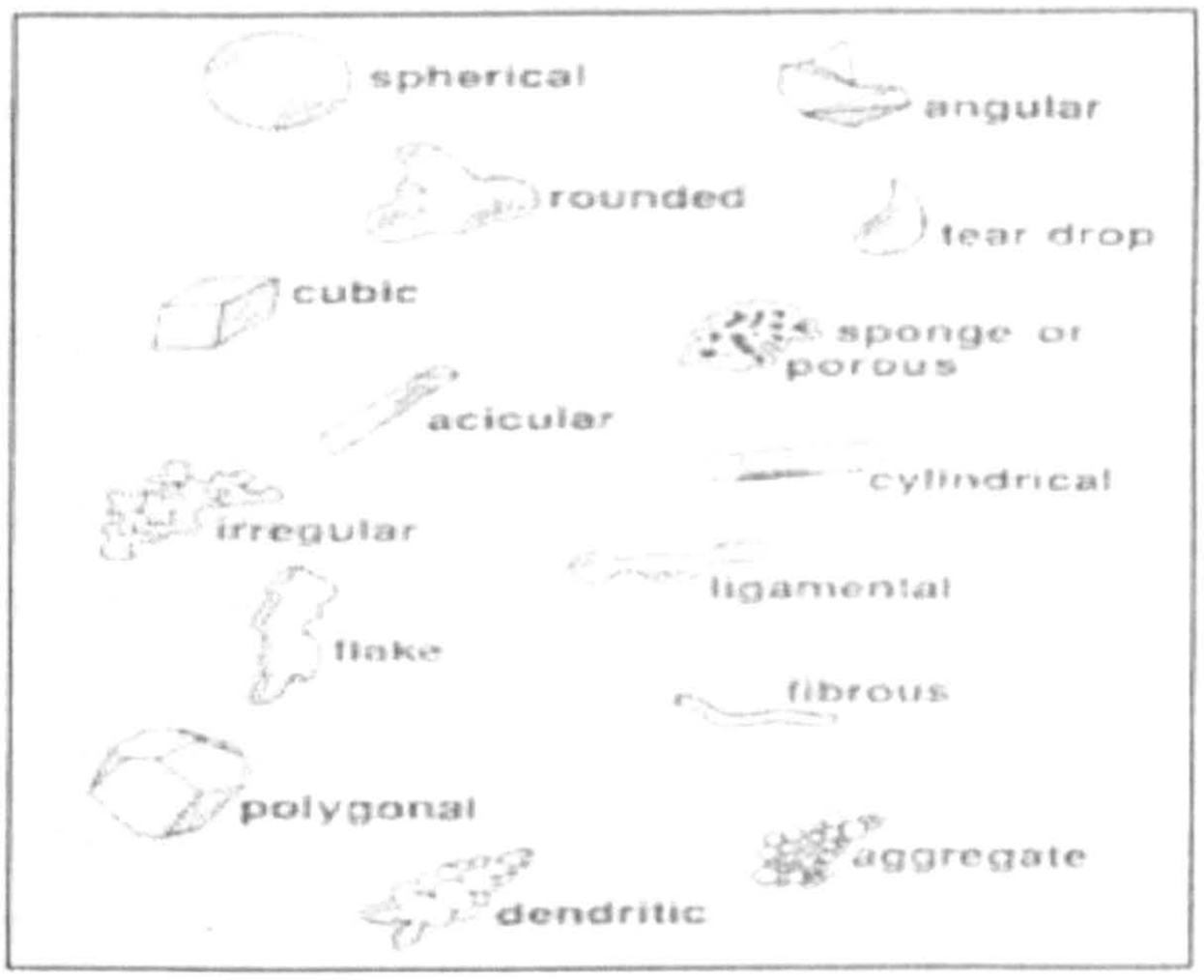

Figure 2.55: A qualitative description of powder particle shape (after German 1994).

2.7.8.2 Effect of Particle's Shape, Size and Distribution on the Powder Properties

Among the pre-requisites that metallic powders must fulfil in order to become suitable candidate materials for SLS process are that they must have a narrow range of particle sizes, small average particle size, and regular particle shape (Zhu *et al*. 2007). Powders possessing these attributes are known to be characterised by small interparticle friction, good flowability, in addition to large apparent and tap density (German 1998). These characteristics enhance smooth powder transportation and deposition in the form of a thin layer during the direct SLS process. This implies that the control of the properties of the powders (flowability, packing density e.t.c.) is a determining factor in obtaining components of excellent mechanical integrity in direct SLS (Zhu *et al*. 2007). In this process, the loose apparent density of the metallic powder is regarded as the equivalent of the green density of a component processed by the conventional furnace liquid phase sintering (LPS) (Zhu *et al*. 2007). German (1985) discovered that a high green density inhibits re-arrangement but it increases the subsequent sintered density of the part. Therefore, the expectation is that the final density obtained via the direct laser sintering process increases with the apparent density of the deposited loose powder. However, the maximum density from close random packing of monosized spherical powders is approximately 60%. Findings from a survey of the literature reveal that an effective

way to increase the bed density of a powder is to fill in the interstices between the large particles with smaller particles (Zhu *et al.* 2007). The expected trend is that smaller powder particle sizes generate lower packing density as a consequence of high interparticulate friction. Interestingly, packing of spherical powder particles yields higher density than other shapes (Zhu *et al.* 2007). The employment of irregular shaped powder particles with high surface roughness also reduces the packing density. It has been established that the distribution of particle sizes significantly impacts on the apparent density of a powder. Therefore, the relative amount of coarsest and finest particles as well as the percentage of particles between the two extremes, needs to be considered in order to develop a powder blend that would achieve the optimum apparent density (German 1998). German (1999) proposes four likely possibilities for the blending of varying sizes of powders, where D_L, D_M, and D_S represent the diameters of the large, medium and small spheres respectively. These are illustrated schematically in Figure 2.56. An observation of Figure 2.56 suggests that the highest packing density is obtainable by the tri-modal arrangement (Figure 2.56(c)) while the mono-sized particles (Figure 2.56(a)) yield the lowest packing density. It is possible to make an idealized quantitative analysis of the tri-modal particle arrangement in which all the particles are in contact (Figure 2.57).

German (1999) employed his proposition in the last paragraph to estimate the proportional ratio of blending together the particles of different sizes in Figure 2.57 to achieve the highest possible packing density. By assuming the three large disks in Figure 2.57 have equal radii of $R_1 = R_2 = R_3 = D_L/2$, the radius of the medium filling powder size is $D_M/2$ and the radius of the smallest filling powder size is $D_S/2$; and using geometry on the inscribed square, German (1999) determined D_M and D_S according to equations 2.19 and 2.20:

$$D_M = \sqrt{2}D_L - D_L = (\sqrt{2} - 1)D_L \quad \text{.....2.19}$$

$$2/D_S = 2/D_L + 2/D_L + 2/D_M + 2(4/(D_L^2) + 4/(D_L D_M) + 4/(D_L D_M))^{1/2} \quad \text{.....2.20}$$

From these equations, it can be deduced that:

(a) $D_L : D_M = 2.41:1$ and (b) $D_L : D_M : D_S = 9.23 : 3.83 : 1$.

Therefore, if the proportion of particles is 1:1:4, the maximum achievable packing density is 95.7%.

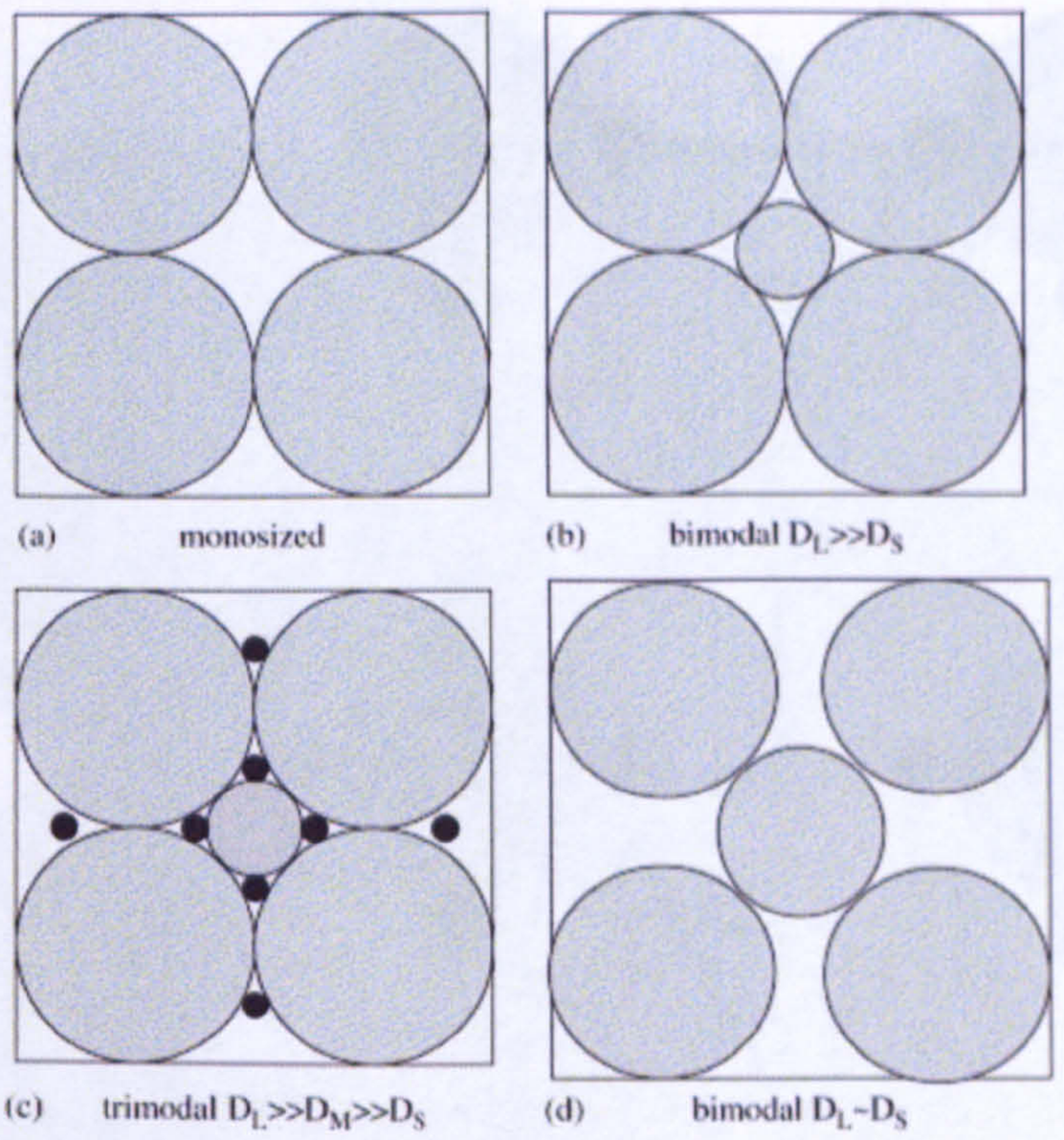

Figure 02.56: Four different ordered powder particle packing arrangements (after German 1999).

Zhu *et al.* (2007) envisaged that the composition of a mixture according to the geometrical relationship considered above would not be feasible. They based this assertion on two main reasons, namely: the impossibility of having metal powders consisting of purely mono-sized particles; the fact that the size of the working powder for direct SLS is controlled by factors such as layer thickness, flowability, deposit characteristic and cost.

It has been noted previously (sections 2.7.2.1 and 2.7.5) that the biggest size of a metal powder should be less than the layer thickness, usually in the range of 50 - 200 μm. If this sets the value for D_L, then $5.4 < D_S < 21.7$ μm. Having a metal powder with such a high amount (66 %) of such a fine particle size would have a deleterious effect on the apparent density because its flowability is likely to be low and it can easily agglomerate upon the interaction of the laser beam with the powder. Moreover, metal powders with fine particle size are not desirable for SLS/SLM because they are highly flammable and potentially hazardous to human health during handling.

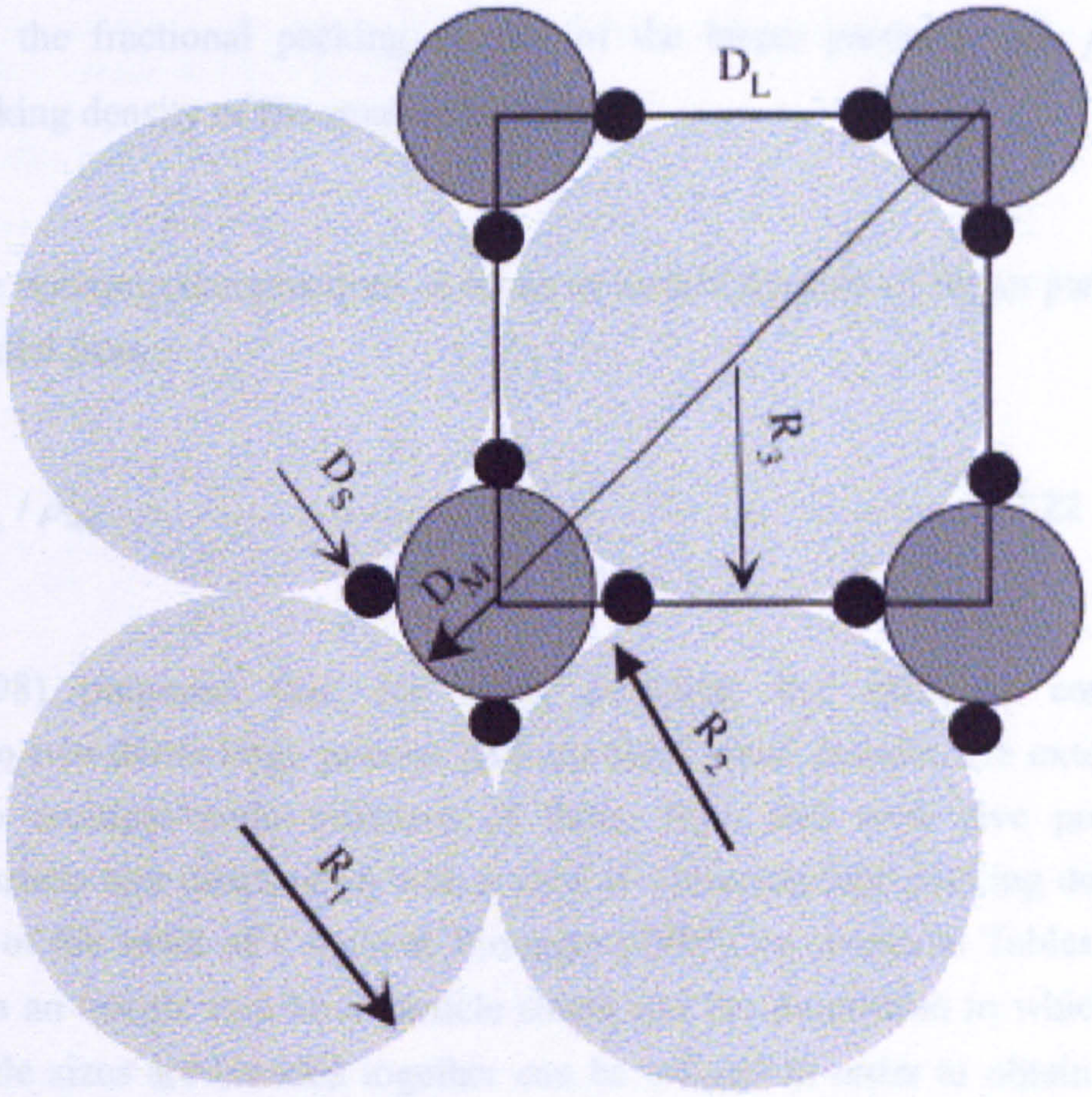

Figure 02.57: The plain tri-modal of powder packing. (after German 1999).

In order to overcome the challenge of making appropriate choice of powder particle size and distribution, Powell (1980) recommended that to improve the powder packing density, it is necessary to increase the particle size dispersion. Nevertheless a very wide power particle size distribution increases the net surface area and therefore deteriorates its packing characteristics by reducing its flowability. With regard to the 2-phase SLS process, the working powder always consists of a blend of several powders of varying particle sizes. Therefore, it is a condition that particle size of the binder material is usually smaller than that of structural metal powder. The determination of the exact size of the interstices or porosities present in the compacted blend is a very challenging task. To solve this problem, German (1998) proposed an empirical formula for the powder packing of a powder mixture with two kinds of powder with different particle sizes. He reasoned that if the smaller particles fill the voids formed by the larger particles, the bed or packing density ρ_{bed} at optimal composition, can be estimated by equation 2.21:

$$\rho_{bed} = \rho_L + \rho_S /(1 - \rho_L) \quad \text{.....2.21}$$

where ρ_L is the fractional packing density of the larger particles and ρ_S is the fractional packing density of the smaller particles.

Therefore, the optimum compositions in terms of weight fraction of larger particles, G_L can be calculated from :

$$G_L = \rho_L / \rho_{bed} \quad \text{.....2.22}$$

German (1998) proposed that, for many powders, the optimum composition corresponds to two-thirds large powder and one-third small powder. He extended this same idea to multiple-mode mixtures of three, four, and even five powders of continuous particle size distribution with a view to obtaining high packing densities. A careful study of the work of Carson & Pittenger (1998), as shown in Tables 2.14 and 2.15, provides an insight into how particle shape and the proportion in which varying powder particle sizes are blended together can be utilised in order to obtain optimum powder apparent density. They compared the effect of the addition of three different shapes (spherical, irregular, and flake) of -45 μm powder to + 45 μm powder particle distribution on the apparent density of 316L stainless steel powder. Their results showed that the addition of fine spherical powder significantly increases apparent density, while the converse was observed for flake powders (Figure 2.58).

Table 2.14: Effect of mixture of coarse and fine spherical stainless steel particles on apparent density (after Carson & Pittenger 1998).

Particle size (μm)	Particles (wt.%)					
-150 + 90	100	80	60	40	20	0
-45	-	20	40	60	80	100
Apparent Density, (g/cm^3)	4.50	4.90	5.20	4.80	4.60	4.30

Table 02.15: Apparent densities and flow rates of electrolytic iron powders of three particle size distributions (after Carson & Pittenger 1998).

Particle size (μm)	Particles (wt.%)		
	Powder A	Powder B	Powder C
+ 150	4	3	15
- 150 + 90	11	26	10
- 90 + 75	18	18	30
- 75 + 53	16	6	25
- 53 + 45	18	16	5
- 45	33	31	15
Apparent Density, (g/cm^3)	2.6-2.8	3.2-3.4	3.8-3.9
Flow rate, s/50g	29	24	20

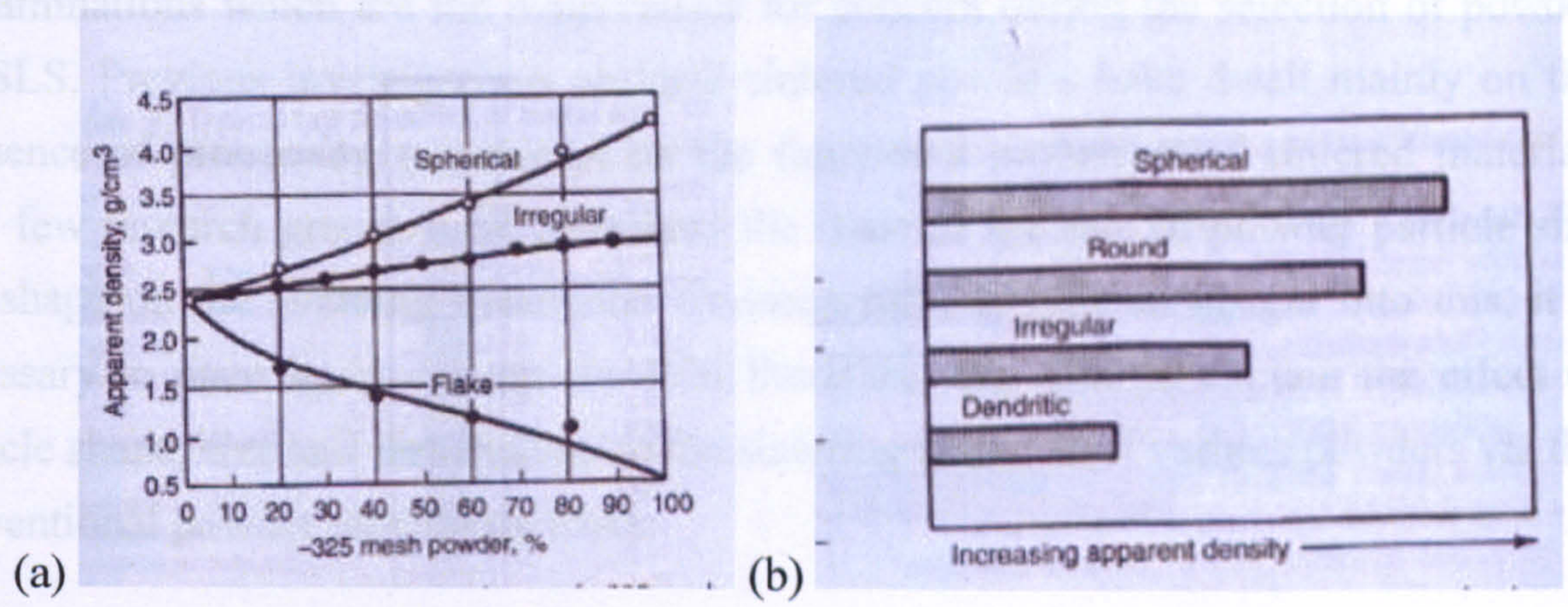

Figure 02.58: Effect of particle shape on the apparent density of powders (after Carson & Pittenger 1998).

Table 2.14 shows that for spherical stainless steel powders, the optimal apparent density was obtained when a mixture of 60 % coarse and 40 % fine spherical particles were blended together. Table 2.15 extends this to a mixture of six different particles sizes in which both apparent density and flow rates of the blended powders are seen to vary as different fractions of powder sizes were mixed together. They reported that in the case of atomised aluminium powders, the proportion of particles from the + 45 μm size fraction should be at least 75% when blended with -45 μm fraction in order to attain an apparent density of 1.25 g/cm^3.

2.7.8.3 Effect of Particle Shape, Size and Distribution on the Sintered Density, Surface Morphology and Microstructure of Laser Sintered Components

In SLM, the effect of powder's particle sizes and distribution is considered to be of no avail because all particles undergo melting. Meanwhile, German (1993, 1996) noted that chemical composition, particle shape, surface morphology, and the particle size distribution are among the factors that have tremendous influence on the sintering response of metallic powders. From the available literature, mean particle sizes of the bulk metallic powders that have been adopted in various SLS experiments vary from 0.6 μm up to 400 μm and are more often produced by gas atomisation methods. This manufacturing technique yields spherical shaped particles with smooth surfaces and, when inert gases are employed, the powder often has low levels of residual oxygen and surface oxidation (German 1998).

These characteristics provide for ideal flow properties and reduced surface contaminations which are the main causes for concern during the selection of powder for SLS. Previous investigations on laser sintered powders have dwelt mainly on the influence of processing parameters on the functional properties of sintered material; very few research groups have addressed the issue of the role of powder particle size and shape on the sintering behaviour. Consequently, to gain an insight into this, it is necessary to once again consult the P/M literature, this time to explain the effect of particle shape, size and distribution on the sintering response of various powders via the conventional powder metallurgy route.

Stevens *et al.* (1999) employed his investigation on the role played by particle size distribution in the sintering response of fine titanium powders to provide a basis for process control. Liu *et al.* (2007) discovered that particle size and size distribution, the tap density, the oxide film thickness, the surface chemistry, and impurity concentration had little effect on the sintering behaviour of aluminium powders whereas particle shape was noted to have contributed significantly to differences in sintering response. They suggested that the differential thermal expansion between the aluminium particle and its oxide film might have caused the oxide to fracture and that the fracture characteristics are different for spherical and irregular particle shapes. Moreover, in a system having substantial solid solubility of the additive in the base metal and/or exhibiting preferential diffusive flow from the additive to the base metal during sintering, Lumley & Schaffer (1996) found that the use of fine additive powders resulted in a greatly reduced quantity of liquid phase formed whereas coarse powders

increased the amount of liquid phase that formed and prolonged its existence. They concluded that where there is no mutual solid solubility, particle size is unimportant in liquid development. Lumley & Schaffer (1996) did not consider the effect of fine particles sizes on the thermal conductivity of a packed powder since this is unlikely to be a significant factor in P/M sintering. However, this is an important consideration in SLS and, as noted earlier, is likely to influence the liquid formation in the laser sintered part. They also explored the nature of the influence of the additive particle sizes on the properties of sintered aluminium-copper alloys. They showed that bulk density and pore sizes might not be accurate indicators of the strength of sintered parts. They established that particles of intermediate size sintered at slow heating rates and fine particles sintered at fast heating rates (Figure 2.59). This tended to promote the formation of an extensive, well distributed liquid phase, from which a well sintered matrix develops.

In the case of SLS, the powder particle size and size distribution play a key role in the manipulation of sintering response given that the powders are highly uniform in composition, shape and surface morphology. Theoretically, there ought to exist a relationship between the sintered properties and the particle size distribution of a candidate powder for the SLS process. A comparison of the SLS process with the conventional P/M sintering process, suggests the following features of such a relationship: (1) smaller sized powder particles tend to sinter more quickly since the sintering stress is inversely related to particle diameter; (2) powder particle densification should take place through neck formation at points of contact between particles. The consequence of this is that with a higher packing density of similarly sized particles in a powder, the tendency should be for a faster sintering rate to be obtained.

In order to improve the packing density of the powder bed during SLS, it is necessary to blend together powders of different particle size distributions as noted in Section 2.7.8.2. It is clear, however, that the introduction of fine particles to a powder can be significantly influential in increasing its sintering response. Furthermore, while the introduction of smaller particles into the interstices of larger particles which also increases packing density could lead to enhancement of the sintering process, it must be noted that the addition of smaller particles could result in the formation of defects in the laser sintered samples. This could be ascribed to the sintering stress encountered by the small particles which is much higher than that experienced by the larger particles. This means the larger particles are able to constrain the shrinkage of the smaller particles,

thus resulting in circumferential cracking defects around large particles (German 1996; German & Bulger 1992).

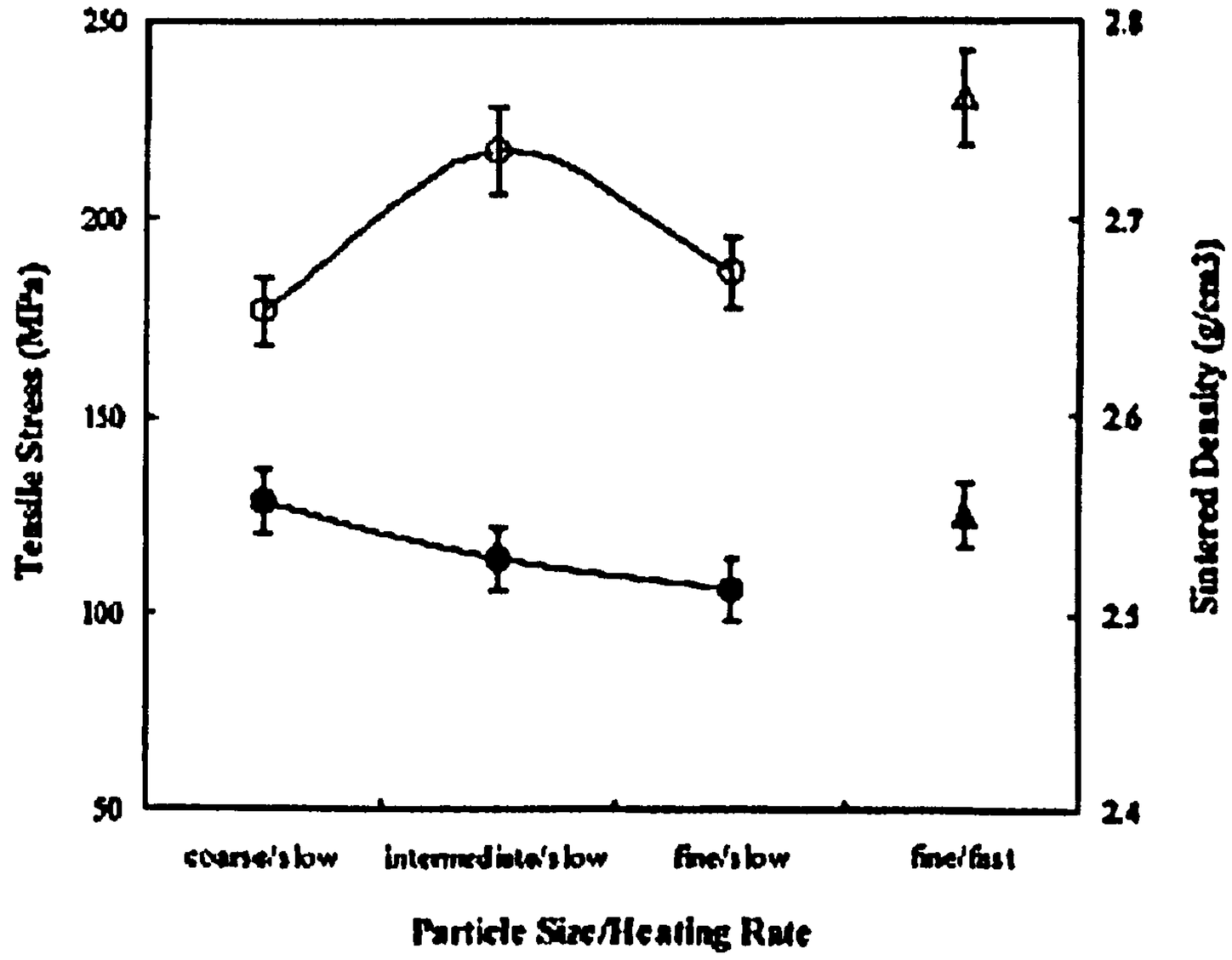

Figure 2.59: The effect of particle size and heating rate on the sinter density (solid symbols) and tensile strength (open symbols) of P/M sintered Al-4wt%Cu alloy (after Lumley & Schaffer 1998).

The available literature on the effects of particle size and shape on the surface morphology and microstructure of SLS processed components is very scarce, especially on aluminium alloy powders. In the case of steel powders, it has been generally restricted to powder contamination issues rather than actual particle size effects on surface morphology and microstructure. Meanwhile, the available results from some of the studies which have addressed the effects of particle size and shape on the laser sinterability, surface morphology and internal microstructure have not been able to clearly, quantitatively define what direct consequences the choice of particle size and shape has on the surface morphology, microstructure and mechanical properties of laser sintered components. For instance, Niu & Chang (2000) observed that SLS of gas atomised M2 HSS powder yielded a highly porous structure when the particle size was small <38 μm) or coarse (>150 μm) but discovered that laser sinterability was better for particle sizes ranging between 53 and 150 μm as evidenced by a smooth, dense surface of the single layer part (Figure 2.60). They attributed the behaviour of finer particle sizes under SLS to oxidation, which is more dominant when heating powder of smaller particle sizes: the porous structure might have been as a consequence of incomplete wetting rather than some other phenomenon being governed only by particle size.

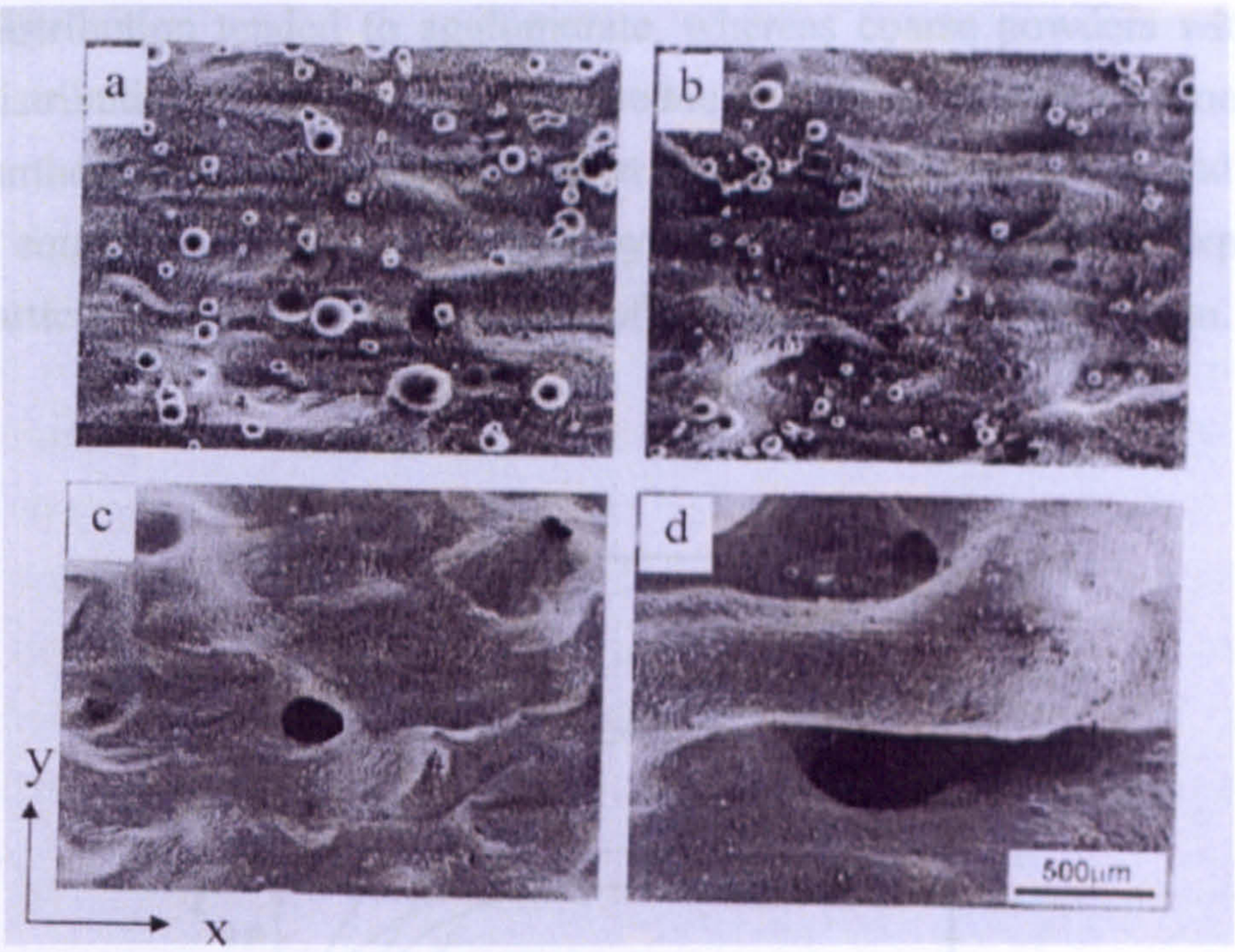

Figure 2.60: SEM images of laser sintered high speed steel powders using laser power of 50 W and a scan rate of 5.0 mm/s and a scan line spacing of 0.15 mm. Particle sizes were: (a) as supplied from atomiser (full range), (b) 53 μm – 150 μm, (c) >150 μm and (d) <38 μm (after Niu & Chang (2000)).

Niu & Chang (1999a) explored the differences in the sintering response of both angular, water atomised and spherical, gas atomised high speed steels powders. Their findings showed that SLS of gas atomised powder yielded a homogeneous, dense single layer. Agglomerates and inter-agglomerate pores obtained for water atomised powders which they believed to be caused by a combination of irregular shape and high oxygen content in the powder particles. Niu & Chang stated that large particles (>100μm) required higher laser power for melting since heat transfer into the powder layer was lower. Therefore, for a given energy density, the structure produced tended to be more porous than a structure produced using smaller particle sizes. The observations of Niu & Chang are only indicative: to ascertain the actual impact of the particle size and shape on the microstructure and mechanical properties, multiple layer experiments need to be carried out.

Simchi (2004) investigated the effect of powder particle size on the densification and microstructure of direct laser sintered iron powder. He discovered that the maximum attainable sintered density (saturation density), which was obtained at the optimal specific laser energy input, was optimised when a mean particle size of iron powder

was 29.2 μm (Figure 2.61a and b). He pointed out that fine powder with a narrow particle size distribution tended to agglomerate, whereas coarse powders with broad particle size distribution tended to segregate: reduced sintered density obtained in the both cases. Furthermore, a material-dependent factor, K, (Figure 2.62a and b) was defined using equation 2.18 and employed by Simchi in an attempt to explore the influence of particle sizes and oxygen content of iron powders on densification.

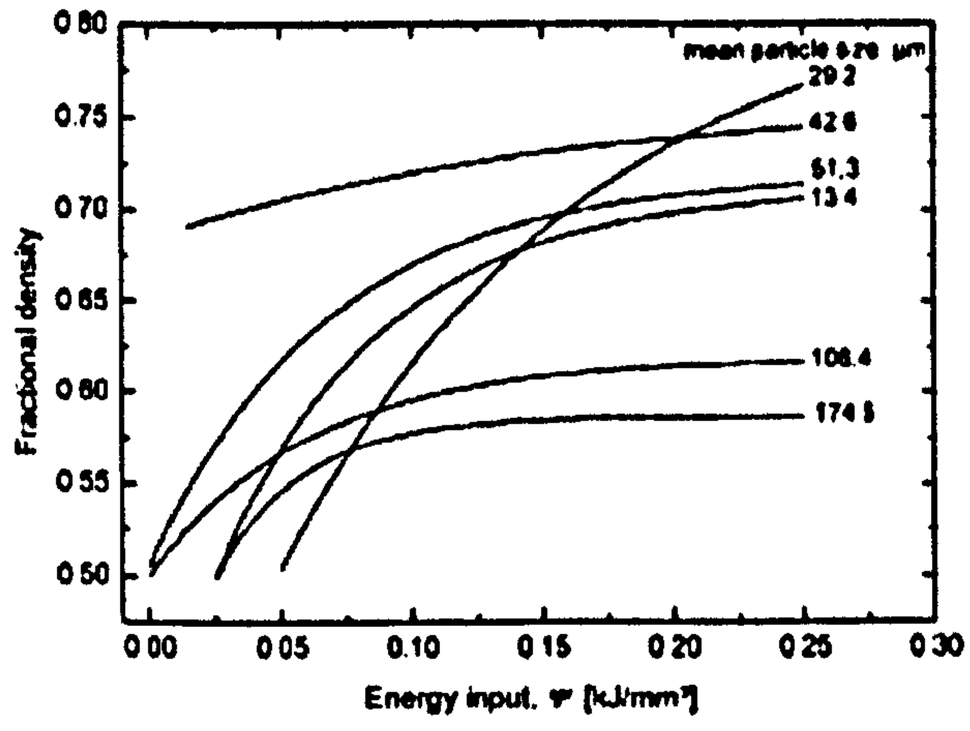

(a)

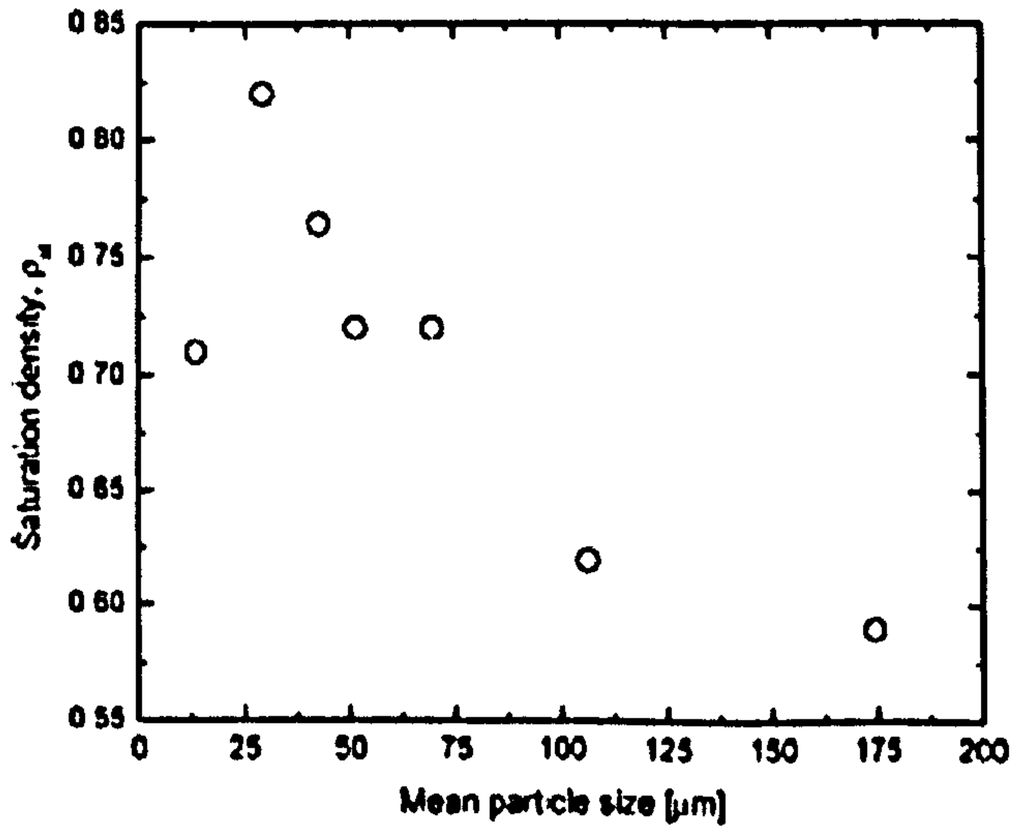

(b)

Figure 02.61: The variation of (a) fractional density with specific energy input (ψ) for iron powders of varying particle sizes; (b) saturation density with the mean particle sizes of iron powders (after Simchi 2004).

It was established that this material-dependent factor K increases as the particle size of iron powder increases. Since the degree of densification is inversely related to K, this indicated that coarser powder particles are susceptible to lower densification during laser sintering. He concluded that at higher oxygen concentrations, the iron melt pool is

solidified to agglomerates, and formation of pores oriented towards the building direction is more likely to occur (Figure 2.63).

However, a careful scrutiny of the results obtained by Simchi (2004) for the densification co-efficient of direct laser sintered iron powders seems to conflict with his claim that iron powders of poor sinterability tend to have a higher densification co-efficient. In assessing the densification co-efficient of iron powders of varying particles presented in Figure 2.62 (a), it should be noted that the processing conditions he used were not uniform for all the powders. Therefore, non-uniformity of the processing conditions he used could be responsible for his claim that iron powders with higher densification co-efficient exhibit poor sintering behaviour. Had he used the same processing conditions for all the powders, he would have discovered that the contrary is true (see Figure 2.64).

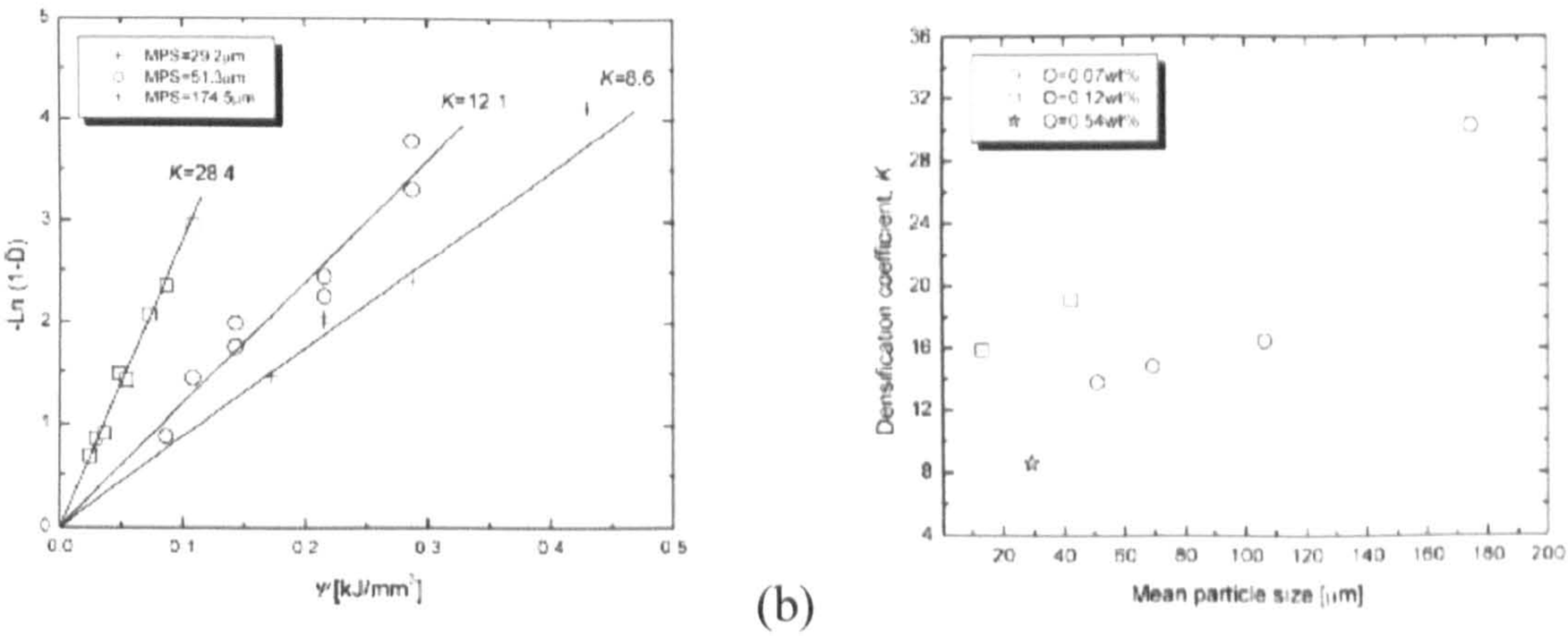

Figure 2.62: The variation of (a) the densification (D) with the specific energy input (ψ) for iron powders of different particle sizes; (b) the densification co-efficient (K) with the mean particle size of iron powders at different oxygen concentrations (after Simchi 2004).

Figure 02.63: Polished sections showing the pore structure on a section cut parallel to the building direction for iron powders as a function of varying particle size and oxygen concentration (after Simchi 2004).

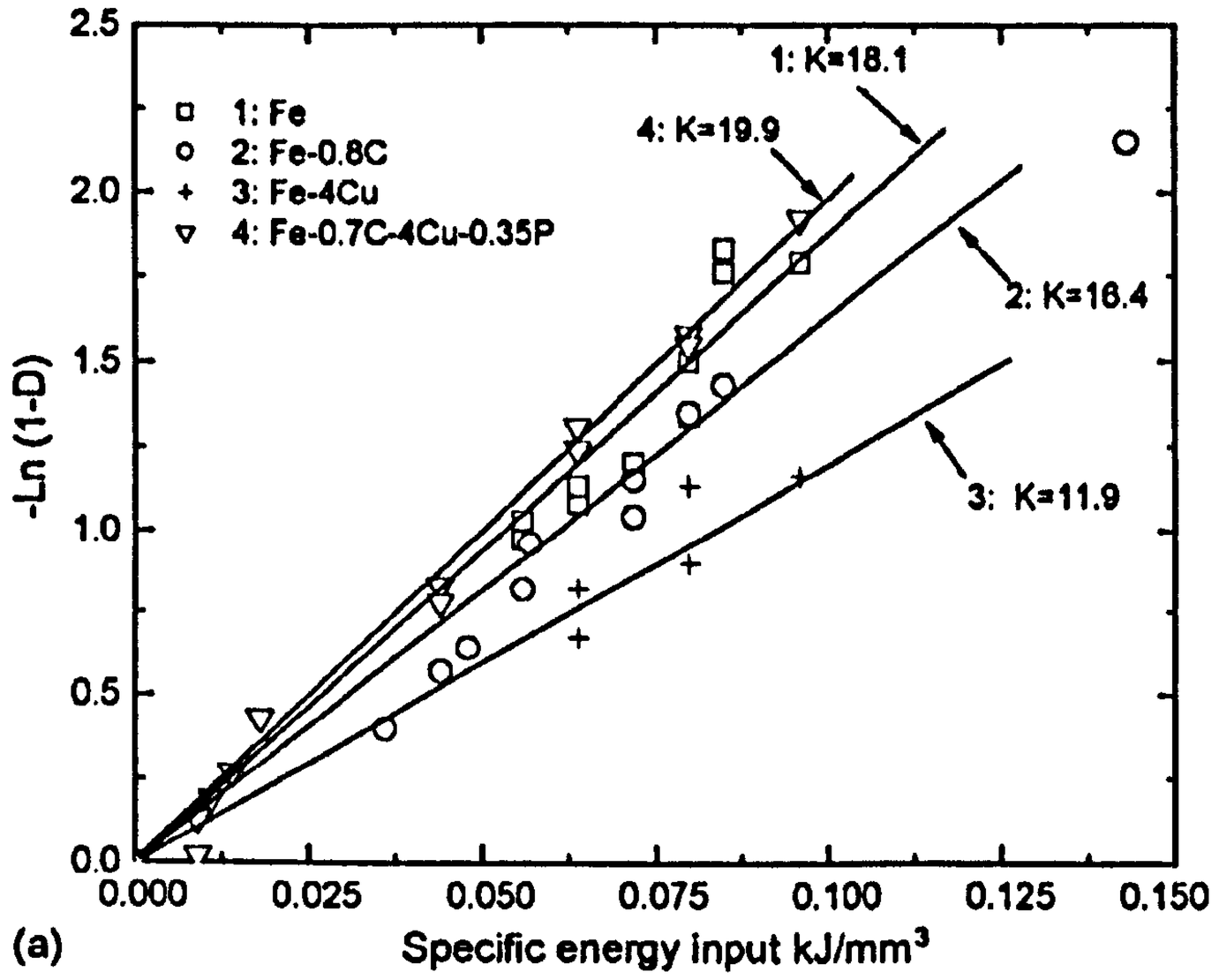

Figure 2.64: The variation of the densification (D) with the specific energy input (ψ) for iron-based powders of varying chemical composition under the same processing conditions (after Simchi 2006).

2.7.8.4 Effect of Powder Properties on the Surface Roughness of Laser Sintered Components

Surface roughness is another critical property of components fabricated by SLS/SLM that affects their performance. It is particularly dependent on the powder granularity and laser process parameters. Das *et al.* (1999), and Karapatis *et al.* (1998) have established that particle sizes often determine the surface roughness of the fabricated component. As a result of the local heat transfer, surrounding particles tend to fuse to the molten region and hence the surface roughness is often found to be a direct function of particle size, indicating that finer particle sizes will produce improved surface finish given an ideal melting condition. Van der Schueren & Kruth (1995) observed that these results emphasised the overriding influence of the flowability of the bulk powder on surface quality. If the particle size is too small and the shape is very irregular, the smooth deposition of layers is impeded due to the initiation of inter-particulate friction between the particles. This in turn influences the quality of the irradiated layer. However, with careful control of the process parameters, it is possible to attain an acceptable raw surface quality. Rombouts *et al.* (2005) studied the influence of process and material parameters on the behaviour of the melt pool during laser melting of iron based powders. Their findings revealed that all processing parameters, with the exception of laser power have a significant effect on surface roughness. Lower values of surface roughness were obtained with smaller scan spacing, higher scan speed, and higher preheating temperature for layers scanned in a loose powder bed. With regard to

alloying effects, Cu, P, and C led, in contrast to Si, to a more stable melt pool in the concentration range investigated. Karapatis *et al.* (1998) noted that post-processing steps, such as infiltration and surface finishing techniques, can smoothen out the surface by filling the voids between the attached particles.

2.7.8.5: Effect of Powder Flowability, Deposition and Spreading on the Properties of Laser Sintered Components

Powder deposition and spreading is a very important step in the SLS/SLM process because the morphology and density of the melted layers together with the fusion bond between the deposited layers is primarily determined by the uniformity, packing efficiency and smoothness of every deposited powder layer (Lee *et al.* 1995, Van der Schueren & Kruth 1995, Hauser 2003). This implies that any surface irregularities in the deposited powder layer will be reproduced in the sintered surface. Thus, the choice of the deposition mechanism and the efficient fluidity of the powder play a decisive role in the SLS process. Powder flowability is defined as the ease of flow and relates to the change of mutual position of individual particles forming the powder bed (Yokoyama 1991). It is expressed as the time required for a 50 g powder sample to be discharged by the gravitational force through a Hall flow meter (Yokoyama 1991). Short flow times indicate free flowing powders while long flow times are suggestive of the presence of high interparticle friction between the powder particles. The friction between particles is dominated by particle shape, surface area, surface roughness and surface chemistry. As the surface roughness and surface area increases, or the particle size decreases, the amount of friction within the powder mass will increase.

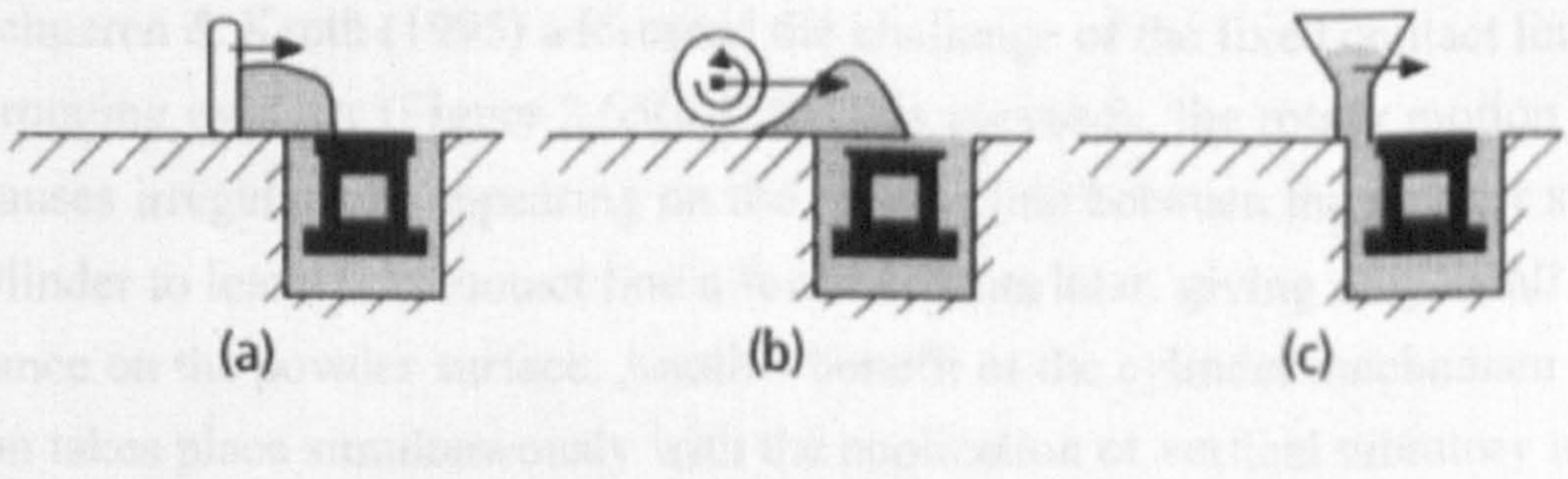

Figure 02.65: Three solutions for powder deposition and spreading during SLS, based on (a) scraper blade, (b) counter rotating roller and (c) slot feeder (after Van der Schueren & Kruth 1995).

The powder flowability may be improved by changing its physical properties, such as moisture content and particle size and shape, by means of drying, classification, additives and granulation. A bulk powder consisting of spherical particles greater than

45 μm diameter can usually be considered as free flowing, but there will exist an inherent resistance to de-agglomeration up to particle sizes of 100 μm (German 1994).

Van der Schueren & Kruth (1995) proposed three powder deposition mechanisms namely the scraper blade, counter rolling cylinder and slot feeder, for fabrication of components via SLS. The first is founded on the use of a scraper blade which sweeps the powder across the build zone, thereby spreading and levelling in one operation (Figure 2.65(a)). Although the design is capable of depositing a layer of material, nevertheless, it is bedevilled with some of the problems outlined below:

(1) The quantity of powder required is not regulated during each sweep as surplus powder is needed to ensure complete coverage of the newly built layer in the build cylinder. The surplus powder consequently increases the weight of the powder shot, hence causing an increase in friction between the moving powder heap and the underlying melted layer: this can cause shearing and displacement leading to misalignment of layers.

(2) A fixed contact line between the scraper blade and the surface of the powder bed can cause irregularities in the powder material which will be swept over the surface and trace lines on the new powder surface thereby raising concerns on the smoothness of the layer.

(3) This approach offers no direct means of compacting the powder after deposition.

Van der Schueren & Kruth (1995) addressed the challenge of the fixed contact line with a counter rotating cylinder (Figure 2.65(b)). By this approach, the rotary motion of the cylinder causes irregularities appearing on the contact line between the powder surface and the cylinder to leave this contact line a few moments later, giving only small traces of disturbance on the powder surface. Another benefit of the cylinder mechanism is that compaction takes place simultaneously with the application of vertical vibratory motion during deposition thereby yielding a high tap density in the newly deposited layer.

Van der Schueren & Kruth (1995) addressed the demerits of scraper blade and counter rolling cylinder mechanisms by incorporating a slot feed mechanism which minimises friction between the newly deposited powder layer and the substrate upon which a new layer is being deposited (Figure 2.65c). Unlike the first two techniques, this third

system continually deposits powder during transit rather than pushing a heap of powder across the build cylinder, thus reducing the interaction between powder and melted layer. The outflow from the hopper acts as a natural blade to deliver a final levelling action. There is no tapping operation to increase powder density but this technique often proves successful in minimising layer displacement. Since no single system fulfils all the deposition requirements imposed by SLS, Van der Schueren & Kruth (1995) planned a two phase deposition, spreading and compacting mechanism which combines a slot feeder and a rotating roller. They proposed a four stage deposition cycle (Figure 2.66) as follows:

(1) The build cylinder piston lowers to a depth just below the required layer thickness.

(2) The slot feeder deposits a layer of loose, uncompacted powder.

(3) The piston rises up to the required layer thickness.

(4) A roller, traverses across the powder bed and compacts the projecting powder layer.

Van der Scherer & Kruth speculated that such a cycle should achieve a powder bed density that approaches the powder tap density. This theory was supported by Lee *et al.* (1995) through evidence from their work on the compaction of alumina powder layers with a rotating roller. They discovered that the tap density for irregularly shaped particles could be reached by this method (40% of theoretical density). However, Lee *et al.* (1995) also reported that powder layer compaction, which is difficult to achieve consistently due to the irregular distribution of particles, can cause previously melted layers to displace vertically from their suspended positions and thus that object dimensional accuracy could not be guaranteed during compaction.

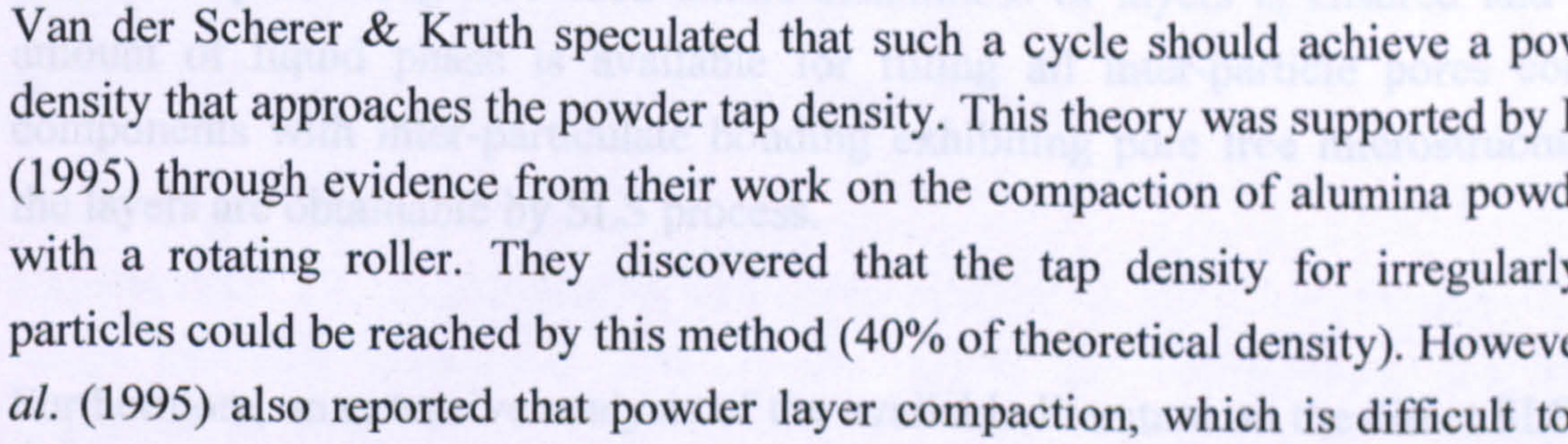

Figure 2.66: A four stage deposition cycle (after Van der Scherer & Kruth 1995).

2.8 Summary of the Literature Review

Consolidation regimes associated with SLS/SLM of metallic materials have been identified. Binary liquid phase sintering, partial melting, full melting (SLM) and indirect SLS incorporated with polymeric debinding and post-process infiltration with a low melting point infiltrant alloy are the variants of SLS/SLM of metals. The variants of SLS/SLM process have been categorised on the basis of material component system, type of laser employed for consolidation, and the intensity of the specific laser energy input dissipated on the powder bed. An analysis of the available literature on the SLS/SLM of metallic materials has revealed the research in the field of light metals is the least developed. Aluminium, an engineering material in very high demand but which has not been extensively investigated by the SLS/SLM manufacturing method; is hereby chosen in order to explore the possibilities it offers for engineering applications. Available literature on SLS/SLM, powder metallurgy (P/M) sintering, and pulsed electric current sintering (PECS) of aluminium and its alloys were evaluated with a view to gaining useful insights especially in the aspect of alloying effect in disrupting the surface oxide film barrier to sintering or melting; liquid phase sintering (LPS); and alloying design suitable for the SLS/SLM process of aluminium powders. This led to highlighting the importance of oxidic cleanliness of metals and their alloys during their SLS/SLM processing. Provided oxidic cleanliness of layers is ensured and adequate amount of liquid phase is available for filling all inter-particle pores completely, components with inter-particulate bonding exhibiting pore free microstructure across the layers are obtainable by SLS process.

Furthermore, an extensive analysis of the available literature on the direct SLS/SLM of metals has led to the recognition of the influential process parameters (processing atmospheres, laser processing parameters, layer thickness, and type of lasers employed for the sintering process) and material properties (powder particle size and distribution, powder particle shape, apparent and tapping densities, powder's flowability, chemical composition, and liquid phase forming additives). All the process and powder parameters reported above have been implicated throughout the literature as having strong influences on the properties of metallic powdered parts fabricated via SLS/SLM with their effects being linked to what impact each has over the wetting conditions between the layers, density, surface roughness, dimensional accuracy, surface morphology, microstructure and mechanical properties. For instance, a typical sintering/melt pool resulting from SLS/SLM processed powders does undergo significant variation in shape, volume and flowability as a consequence of variation in process and material parameters. Therefore, the preliminary aim of the research is

geared towards establishing an understanding of the laser sinterability/melting of aluminium powders as well as the determination of optimum processing conditions that favours the fabrication of continuous surface of sintered samples made in aluminium powders. The insight already gained from the effect of the processing parameters on the sintering response and densification of various materials is expected to assist greatly in constructing the processing maps for predicting the behaviour of aluminium alloy powders under varying SLS/SLM processing conditions. However, the relevance and influence of these parameters, both individually and when in combination with each other need to be clearly understood with regard to the application of SLS/SLM process to aluminium powders. This is very important as the aluminium powder is known to be uniquely bedevilled with the tenacious surface oxide film (due to the thermodynamic stability of aluminium sesquioxide) which is difficult to remove or avoid. The tenacity of the surface oxide film inhibits metallurgical bonding across the layers during laser processing and this consequently leads to initiation of balling process due to the initiation of Marangoni convection. Therefore, on-going studies on the sintering of aluminium and its alloys are debating whether the oxide film is the barrier to the SLS/SLM of aluminium or if factors do exist which need to be identified in order to fabricate parts in powders of aluminium and its alloys via SLS/SLM. Nevertheless, it is now clear that laser sintered metal powders need to be designed differently from the conventional powder metallurgy alloys which have no consideration for the existence of the liquid phase for a short duration in their design.

Experimental evidence obtained from investigation of SLS/SLM processed materials reveal that they have their own peculiar porous and heterogenous microstructures characterised by interlayer porosity and pore clusters, and a mixture of different phases which make them distinct from the conventional P/M processed parts (Wang *et al.* 2006a, 2006b). Consequently, the mechanical properties of laser sintered materials are likely to have features which may be absent in the conventional P/M materials. On the basis of the available literature, it is clear that the effect of porosity and microstructure on the mechanical properties of SLS/SLM processed aluminium powders has not been investigated. This requires further investigation to develop a better understanding of the process -microstructure-property relationship for the SLS/SLM of these materials. Furthermore, with regard to microstructural properties of SLS/SLM processed parts, a consideration of the competition between re-solidification by substrate regrowth (see section 2.6.2) and nucleation within an undercooled melt zone (see sections 2.7.4) has helped in gaining an understanding of the importance of differentiating between external parameters and internal kinetic parameters that determine the nature of the re-solidification microstructure obtained in direct SLS/SLM. External parameters are the

controllable processing variables, the powder' particle size distribution, component ratios, whereas factors such as the solidification velocity, degree of undercooling, nucleation site density, nucleation rate, metastable phase selection options, microstructural scale and morphology make up the internal kinetic parameters. A review of the available literature reveals that limited work has been carried out detailing the investigation on the roles of external parameters in the development of nucleation controlled microstructures during the SLS/SLM process of aluminium alloys. It is necessary at this stage that the investigation is extended to SLS/SLM of aluminium powders in order to gain a holistic understanding of the microstructural evolution that accompanies its processing via the SLS/SLM technique. Moreover, a more complete metallurgical control of laser sintered microstructures entails the need for an in-depth understanding and analysis of the internal kinetics parameters.

In this research work, the approach to be adopted is the SLS/SLM process in which the powder's particles are directly heated by the laser beam. The post-processing step which entails infiltration will not be adopted since it is expected that with the appropriate choices of materials and process parameters designed to accommodate the transient liquid phase sintering, improved properties of the components can be obtained. From this, the definite contribution of the alloying elements in generating adequate sintering/melting pool needs to be clearly investigated under the SLS/SLM process since the polymeric binder will not be used to generate the liquid phase for sintering/melting in this context. Moreover, while the qualitative description of the properties of single layer parts (density, porosity, surface morphology and surface roughness) could not be said to wholly represent the quantitative measurements of these properties; it provides a basic understanding of the sintering response of the powder which is necessary in order to determine appropriate processing map for the processing of multiple layer parts. Therefore, the approach entailing initial qualitative observation of the sintering response of the single layer parts produced in aluminium powders after which multiple layer parts' properties are subjected to quantitative measurements shall be adopted in this research work.

2.9 Aims and Objectives of the Thesis

The outcomes of the reviewed literature in this section connote that if fully dense parts are to be obtained via the SLS/SLM processing of aluminium powders, careful consideration must be given to investigating the appropriate choice of processing parameters and materials properties with a view to minimising the problem of curling

or delamination. The aims and objectives of this study shall now be formulated on the premise of the literature review conducted in this chapter. In summary, this thesis focuses on the study of SLS/SLM processing of aluminium and its alloy powders. The idea is to develop an understanding of the dependence of the sintered properties of aluminium and its alloys on the processing parameters and powder properties. Results of sample powders having the most desirable properties obtainable from this work will then be used for the development of model alloys and thereafter mechanical test specimens will be produced for further investigation. To achieve this goal it was decided in collaboration with my supervisors that the following research objectives should be met:

(1) Determination of the appropriate single layer processing windows for the SLS/SLM of pure aluminium and its alloyed powders.

(2) Determination of the effects of SLS/SLM process parameters and powder properties on the surface morphology of sintered pure aluminium and its alloyed powders.

(3) Understanding of the spheroidisation and oxide disruption phenomenona in the SLS/SLM processed aluminium powders.

(4) Determination of the suitable aluminium powder for the SLS/SLM process through the fabrication of multiple layer samples.

(5) Effect of the process parameters on the densification mechanism and microstructure of the suitable aluminium powder for the direct SLS process.

(6) Effect of the additive powder's component ratio on the densification mechanism and microstructure of the suitable aluminium powder for the direct SLS process.

(7) Effect of the additive powder's particle size and distribution on the densification mechanism and microstructure of the suitable aluminium powder for the direct SLS process.

(8) Development of a model tri-modal aluminium alloyed powder blend fabricated via direct SLS.

(9) Microstructural, mechanical and morphological characterisation of direct SLS processed trimodal aluminium powders.

It is expected that the exploration of these possibilities, if eventually successful, shall open the door of opportunity for the commercialisation of aluminium alloy production via the SLS/SLM route.

2.10 Conclusion

The application of direct laser sintering technique to the fabrication of aluminium and its alloys has been an omission in the literature. The effect of the SLS/SLM process and powder parameters on the physical, mechanical and microstructural properties of aluminium powders and its alloys are yet to be proven. It is this lack of understanding of the effect of process and powder parameters on the sintering behaviour of aluminium powders processed via direct SLS that has led to the formulation of this research.

CHAPTER THREE MATERIALS AND METHODOLOGY

3.1 Introduction

This chapter describes the experimental methodology adopted and the materials and techniques employed in order to achieve the aims and objectives of this research work outlined in chapter 2, section 2.9 of this thesis. The first part of this chapter describes the as-received powders used in the research and outlined the storage, usage, preparation, handling, and finally, measurement of the physical properties of the bulk powders. At this juncture in the research, careful thought was given to the necessity of establishing a reliable degree of consistency within and between the deposited layers of powders. This required calibration of the mixing time to obtain a homogeneous particle distribution in the powder following storage and before deposition. The results of this calibration for both monosized and bimodal powders are presented in chapter 4. A detailed description of the microstructural characterisation techniques employed and the preparation of suitable specimens for these form the main focus of section 3.3.

The Leeds sinter station, a Synrad 240 W CO_2 laser machine, employed for all scanning experiments is described in the first part of section 3.4. Prior to conducting single layer experiments, the calibration of the laser power output and the presentation of its results were carried out. Thereafter, single layer scanning experiments were carried out on the sintering plates for the first batch of the monosized aluminium powders AL-1, AL-2, AL-3, AL-4, and AL-5 (see detailed description in Table 3.1). These powders have the same powder particle distribution (+45 to -75 μm), varying particle shapes and chemical composition. The aim of single layer scanning experiments was to determine the appropriate processing window for each powder that would favour the subsequent development of multiple-layer parts.

Table 3.1: Particle sizes and distribution of the experimental monosized aluminium powder according to the supplier's specification

Name of Powders.	Supplier	Designation	Size Fraction (μm)	Production Method	Particle Shape
Pure Aluminium 1	ALPOCO	AL-1	+45 to -75	Air atomised	Irregular
Pure Aluminium 2	ALPOCO	AL-2	+45 to -75	Inert gas atomised	Nearly Spherical
Al-6Mg	ALPOCO	AL-3	+45 to -75	Water atomised	Irregular
Al-7.9Mg	ALPOCO	AL-4	+45 to -75	Water atomised	Irregular
Al-12Si	ALPOCO	AL-5	+45 to -75	Inert gas atomised	Spherical
Pure Aluminium 3	ALPOCO	AL-6	+10 to -45	Inert gas atomised	Irregular/Spherical
Pure Aluminium 4	Alfa Aesar	AL-7	+17 to -30	Inert gas atomised	Spherical
Pure Aluminium 5	Alfa Aesar	AL-8	+10 to -14	Inert gas atomised	Spherical

Table 03.2 : Chemical composition of the experimental monosized aluminium powders according to the supplier's specification

Name of Powders.	wt% Al	wt% Si	wt% Mg	wt% O_2	wt% Fe	wt% Cu	wt% (Others)
Pure Aluminium 1	N/A	-	N/A	N/A	N/A	N/A	N/A
Pure Aluminium 2	99.70	0.05	-	-	<0.05	<0.05	<0.05
Al-6Mg	94.92	0.05	5.90	-	0.13	-	-
Al-7.9Mg	92.00	0.05	7.86	-	-	<0.05	<0.05
Al-12Si	88.40	12.10	-	-	0.36	0.08	<0.05
Pure Aluminium 3	99.82	-	-	-	0.17	-	<0.05
Pure Aluminium 4	99.87	-	-	-	0.12	-	<0.05
Pure Aluminium 5	99.84	-	-	-	0.15	-	<0.05

N/A: Not available.

Moreover, it provided an opportunity to investigate the effect of varying particle shape and chemical composition on the SLS/SLM processability of each powder. Scanning electron microscopy (SEM) was used to study surface morphology and the development of the agglomerates on the single layers of each powder when laser power, scan rates and scan spacing were varied under an argon atmosphere. Comparative studies between the different powder batches and the microscopic studies of the variations in the solidification microstructure between the sintered samples were also carried out.

Multiple-layer experiments were carried out for each of the monosized powdered samples AL-1, AL-2, AL-3, AL-4, and AL-5 at a constant 150W laser power, 0.1mm scan spacing and 0.25mm layer thickness, but with scan speeds varied between 80 and 200mm/s under an argon atmosphere. The mass and dimensions of each sintered sample were measured in order to determine the sintered density. This stage of the research helped in assessing the sintering response of each powder by evaluating the sintered density as well as observing the microstructure of each sample through the optical and scanning electron microscopy studies. Microhardness of the sintered samples was also determined. The aluminium powder sample found to have the most desirable sintering response on the basis of the sintered density, microhardness, and observed microstructure was taken further with the aim of developing its properties by optimising the processing parameters. This entailed processing AL-5 powder at varying processing conditions (100-200 W laser power, 80-200 mm/s scan rates, 0.1mm-0.5 mm scan spacing, and 0.25 mm-1.0 mm layer thickness). This enabled the effect of each of the processing parameters on the sintered density, microhardness and microstructures of SLM processed AL-5 powder to be evaluated. Eventually, AL-5 was found to have been optimised at laser power of 200 W, 120 mm/s scan rate, 0.1 mm scan spacing and 0.25 mm layer thickness. Microstructural observation of the SLM processed AL-5 samples was carried out in an attempt to investigate the effect of the variation in the processing parameters on the orientation and sizes of the pore structure, and the development of agglomeration, the morphology of the dendritic microstructure and the fraction of primary phase in the multiple layer samples.

With the optimisation of the processing parameters for the SLM processed AL-5 powder already achieved, it was thought that the only means remaining to take the sintered density of AL-5 to full or near full sintered density was to improve on the apparent and packing densities via bimodal powder blending. This entailed blending pure aluminium powders of varying particle sizes and distribution with AL-5 with a

view to filling up the interstices in the AL-5 powder. According to Lumley & Schaffer (1996, 19998), powders of smaller particle sizes and distribution tend to sinter at a faster rate than larger sized particles. Therefore, additive particles of smaller sizes and distribution are expected to melt at a lower temperature than 660 °C. Again, it is speculated that AL-5 particles will melt completely due to its low melting temperature of 577 °C. Therefore, complete melting of the mixed powders is expected. Furthermore, due to the mis-allignment in the particle packing arrangement of the blended powders, occurrence of porosity is expected due to inappropriate choice of component ratio, particle size and distribution and particle shape of SLS powders. Consequently, this is likely to affect the thermal conductivity of powder particles across the layers on the powder bed which in turn influence the amount of melt pool or sintering pool available for densification. Therefore, blended powder particles may likely sinter or melt depending on the its particle packing arrangement. Four pure aluminium powders of varying particle sizes and distribution, designated AL-2, AL-6, AL-7, and AL-8 were added to AL-5 in varying proportions. These four powders were either smaller or equal in particle size and distribution to AL-5 and were either spherical or irregular in particle shape. With each of the additive powders properly blended together with AL-5, the optimum ratio of the two powders was determined by directly laser sintering the powder mixtures using the optimum processing parameters already developed for AL-5 powder. Thereafter, SLS processing conditions for the blended powders were adjusted to optimise the properties of the built deposit. This step was necessary because the introduction of the additive powders was expected to have altered the laser absorptivity of AL-5 and the thermal conductivity of the powder bed, thereby modifying the processing window.

The blending of the additive powders with AL-5 provided an insight into the effect of powder constitution and particle size distribution on the powder properties, sintered density and microstructural properties. For the bimodal powder blends, the powder and sintered properties of the 75wr% AL-5 and 25wt% AL-7 blend were the most desirable. This optimum composition of the bimodal powder blend was developed further into a trimodal powder blend by varying the ratios of AL-7 and AL-8 additive powders while the proportion of AL-5 was held fixed at 75wt%, again adjusting the processing window to optimise for this blend. Eventually, a trimodal powder blend with composition 75wt% AL-5, 20wt% AL-7 and 5wt% AL-8 was found to give the optimum sintered density. In addition to microstructural studies, the design and fabrication procedure for the mechanical test parts as well as an investigation of the mechanical properties of the trimodal blended samples were described. Finally, section 3.5 describes the procedure adopted for the determination of the sintered density,

microhardness, mechanical properties and dimensional accuracies of the multiple layer parts.

3.2 Experimental Powder

Eight aluminium and aluminium alloy powder samples, designated as AL-1, AL-2, AL-3, AL-4, AL-5, AL-6, AL-7, and AL-8 used in this study were supplied by ALPOCO (Aluminium Powder Company) and Alfa Aesar.

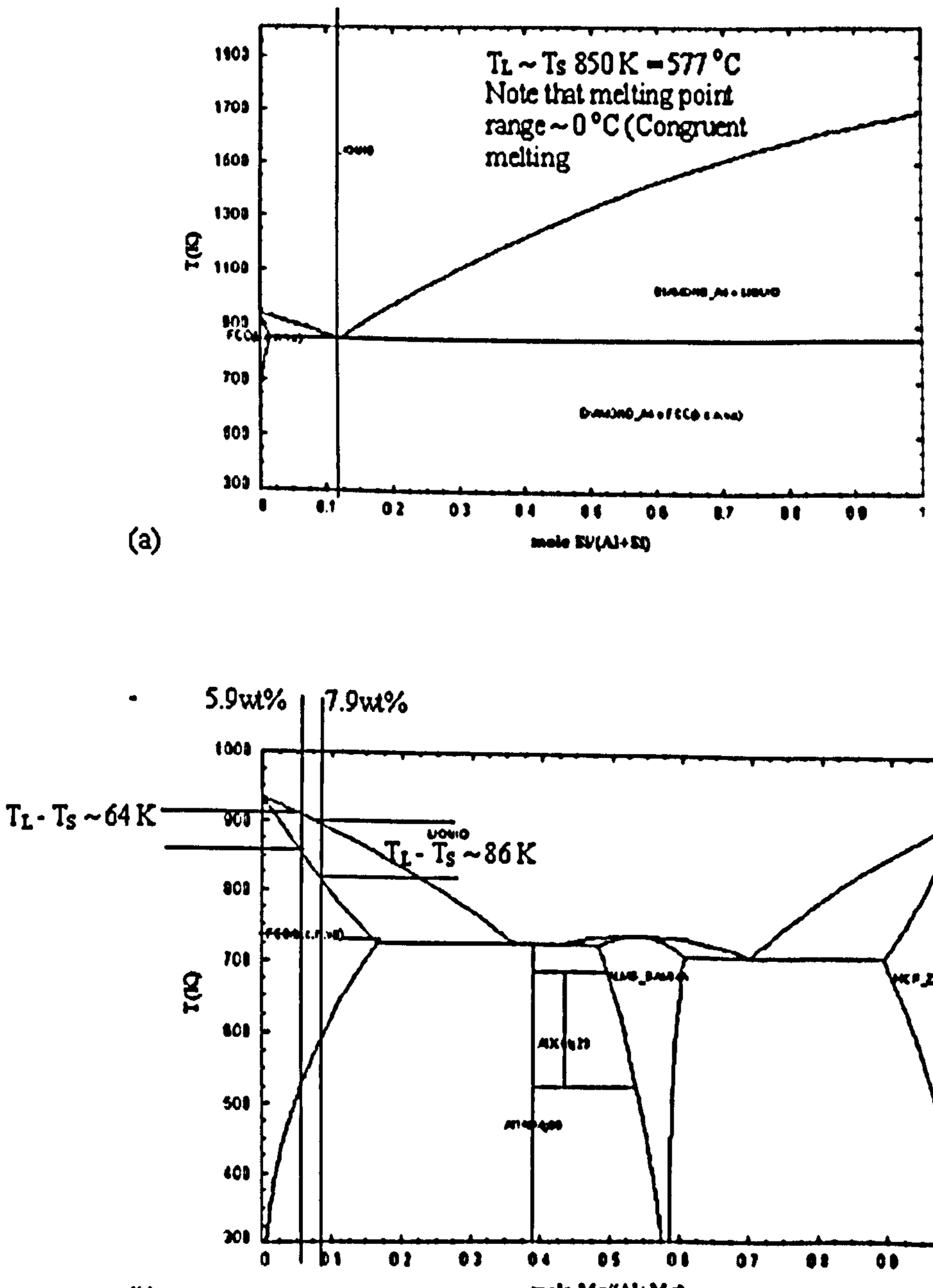

Figure 3.1: Binary phase diagrams of (a) Al-Si and (b) Al-Mg indicating liquidus/solidus temperatures of alloys (BINARY (SGTE) www.crct.polymtl.ca/.../BINARY/BINARY_Figs.htm).

The powders were produced by air, water or argon atomisation and had different particle sizes, size and distributions, particle shapes, and chemical composition (see Tables 3.1 and 3.2). Particle sizes ranging from +10 to -75 μm were chosen because they were the same as those typically encountered in the SLS literature for other powdered materials (Dewidar *et al.* 2003, Murali *et al.* 2003, Zhu *et al.* 2006, Mumtaz *et al.* 2008). For aluminium powders in particular, this range of particle size is known to promote the formation of an extensive, well distributed liquid phase, from which a strongly sintered matrix may develop at a fast heating rate (Lumley & Schaffer 1998). Furthermore, the choice of this range of particle sizes was expected to minimise the formation of balling during the beam-powder interaction. The use of larger particle sizes is reported to exacerbate the development of large-sized agglomerates which inhibit strong metallurgical bonding across the layers of the laser sintered parts. The choice of spherical and irregular shaped powder particles was made specifically to allow for the investigation of the role of particle shape in the liquid phase sintering of laser sintered aluminium powders. Pre-alloyed powders were chosen because their usage eliminates the problems of inhomogeneous distribution of the melt, and segregation of powder particles when deposited in the build chamber which are associated with coated and mixed powders respectively. Elements such as magnesium and silicon had been pre-alloyed in varying quantities with some of the powders. Binary phase diagrams of Al-Si and Al-Mg alloys indicating their respective liquidus/solidus temperatures are presented in Figure 3.1. It is evident from Figure 3.1a that Al-12Si (AL-5) alloy undergoes congruent melting because its melting point range is approximate 0 °C. Figure 3.1b shows that the non-equilibrium freezing range for Al-Mg alloys (AL-3 and AL-4) could be much greater, up to 186/171 °C. The choice of these alloying elements was informed by their roles in the disruption of aluminium surface oxide film and their liquid phase forming tendency during the P/M sintering process, respectively (section 2.4). The variation in the chemical composition of the powders provides the basis for the determination of the likely candidate aluminium alloy powder to be taken further for development into a suitable powder for direct laser sintering process. The melting temperature of the pure aluminium powder is 660°C.

3.2.1 Powder Storage and Use

The powders were supplied in 5.0 kg and 2.0 kg capacity self–sealing containers. The containers were also used for storing the powders. Used powders were sieved to remove solidified melt debris and then stored separately.

3.2.2 Powder Preparation

The powders were used in their 'as supplied state' without the application of heat treatment or fluxes addition to the powders. However, the powders were consistently degassed by the flow of argon gas through the bed before and during the laser sintering process throughout the period of this research.

3.2.3 Powder Handling

To ensure minimal adsorption of contaminants from the atmosphere onto the powders and to maximise the reproducibility of the results, powders were handled carefully. The lids of the storage containers were only removed when the powder was to be used and the pouring height of the powder from the container to the build tray and hopper were kept a minimum to limit the aeration of the powder.

3.2.4 Powder Mixing Procedure Calibration of the Mixing Time; and Determination of the Powder Bed Density

In order to ensure that the powders employed in this research were properly blended together, a V-cone mixing device (Figure 3.2), fabricated and described by Hauser (2003), was employed. The device consists of five unit shells. All the five V-cones, each containing 400g of one of the five different monosized or four blended powders, were attached together on a cylindrical bar and turned on Harrison lathe at 125 rpm for a specific time. The 400g of powder in each V-cone-mixer corresponded to 30% of the fill capacity. This procedure is in conformity with German's (1994) finding that a powder volume between 20% and 40% of the mixer's capacity should give optimal blending. The blending time was adjusted for each monosized or blended powder to give the required blending for that powder. The rotational speed was that which was found by Hauser (2003) to give the best mixing.

The procedure adopted for the determination of the appropriate time for optimal blending of each of the monosized powders AL-1, AL-2, AL-3, AL-4, and AL-5 as well as blended powders containing 50% AL5 and 50% of each of AL-2, AL-6, AL-7, and AL-8 additive powders was to compare the variation in the powder bed density with the mixing time (Hauser 2003).

Figure 3.2: A V-shell Mixing Device for blending the powders attached to the centre-lathe machine during mixing operation

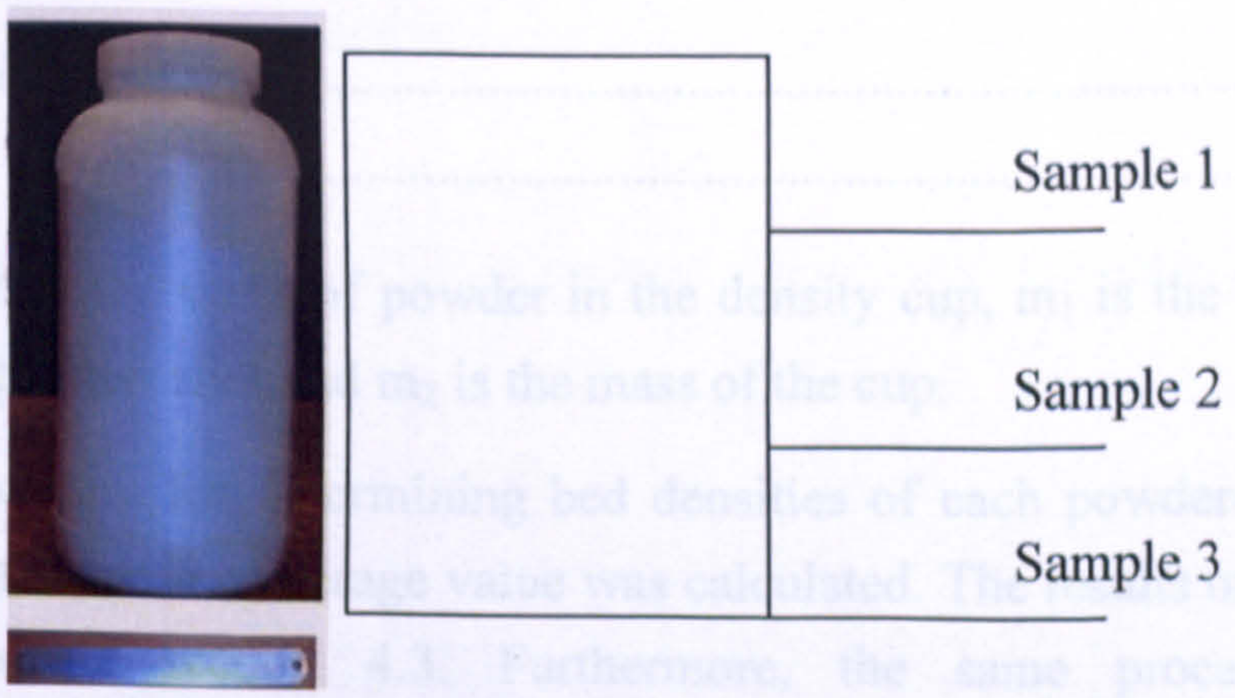

Figure 3.3: Relative position and sub-sample identity numbers of powder samples drawn from the main the sample kept in a typical storage container for mixing calibration

Each batch of powder was divided into four samples by the cone and quartering method. Thereafter, each of the four main samples was kept in storage containers A, B, C, and D (Figure 3.3). Each of the four samples was further sub-divided into three smaller samples, taken from the different heights in the containing vessel, thereby giving a total of twelve samples for a batch of powder (Figure 3.3). Powder samples were taken from different heights in the containing vessel with a view to controlling the effects of particle segregation. Each sample number in Figure 3.3 corresponds to the height at which it was taken. For control purposes, a small quantity of powder was removed from each of the twelve samples drawn from each batch of the powder before blending. Each of the twelve sub-samples drawn from one of the initial main samples was placed into separate v-cone mixers and blended for 10, 20, 30, 40, 50, and 60 minutes at a fixed rotational speed of 125 rpm. The times taken for the blending

process was cumulative, therefore, at the termination of each time segment, the mixer was stopped and a small quantity of powder was taken for density measurements. It was ensured that the volume of the powder remaining in each of the five mixers at the end of one hour was more than the minimum mixing efficiency of 20% of the overall mixing volume. At the end of each mixing stage, a small quantity of powder taken from each cone-mixer was deposited into a machined nylon cup, 44.75 mm deep and 26.66 mm inner diameter. The nylon cup was placed in the build zone within the process chamber of the Leeds sinter station machine. Thereafter, powder sample was poured into the hopper and the powder shot placed in front of the wiper blade was spread across the build zone thereby filling the nylon cup. The mass of the powder, m, was obtained using an electronic balance (model WPS2100/C1) with 0.01gram precision. Digital vernier calliper was employed for the measurement of the volume, V, of the density cup. The bed density (ρ_{bed}) of each shot of powder was calculated as follows:

$$\rho_{bed} = (M)/V \quad \text{.....3.1}$$

$$M = m_1 - m_2 \quad \text{.....3.2}$$

where M is the mass of powder in the density cup, m_1 is the mass of the density cup and the powder shot and m_2 is the mass of the cup.

The procedure for determining bed densities of each powdered sample was repeated three times and the average value was calculated. The results of the calibration tests are presented in section 4.3. Furthermore, the same procedure adopted for the determination of bed density in this section was used later on for the measurement of bed densities of monosized, bimodal and trimodal powders. Detailed measurements of both the calibration mixing time and the bed densities of powders are presented in Appendix B.

3.2.5 Sampling of the Experimental Powders

The MPIF Standard 01 method for sampling finished lots of metal powders was adopted. Each powder after mixing, as described section 3.2.4, was passed through a sample splitter (Figure 3.4) to form a number of test samples. These test samples were then used to supply the test portions for subsequent testing.

Figure 3.4: Sample Splitter used in this research.

3.2.6 Determination of the Physical Properties of the Bulk Powders

The experimental procedures used for the determination of the flow rate, apparent density, sieve analysis and tapping density of the powders is described in this section.

3.2.6.1 Determination of Flow Rate of Aluminium Powders Using the Hall Apparatus

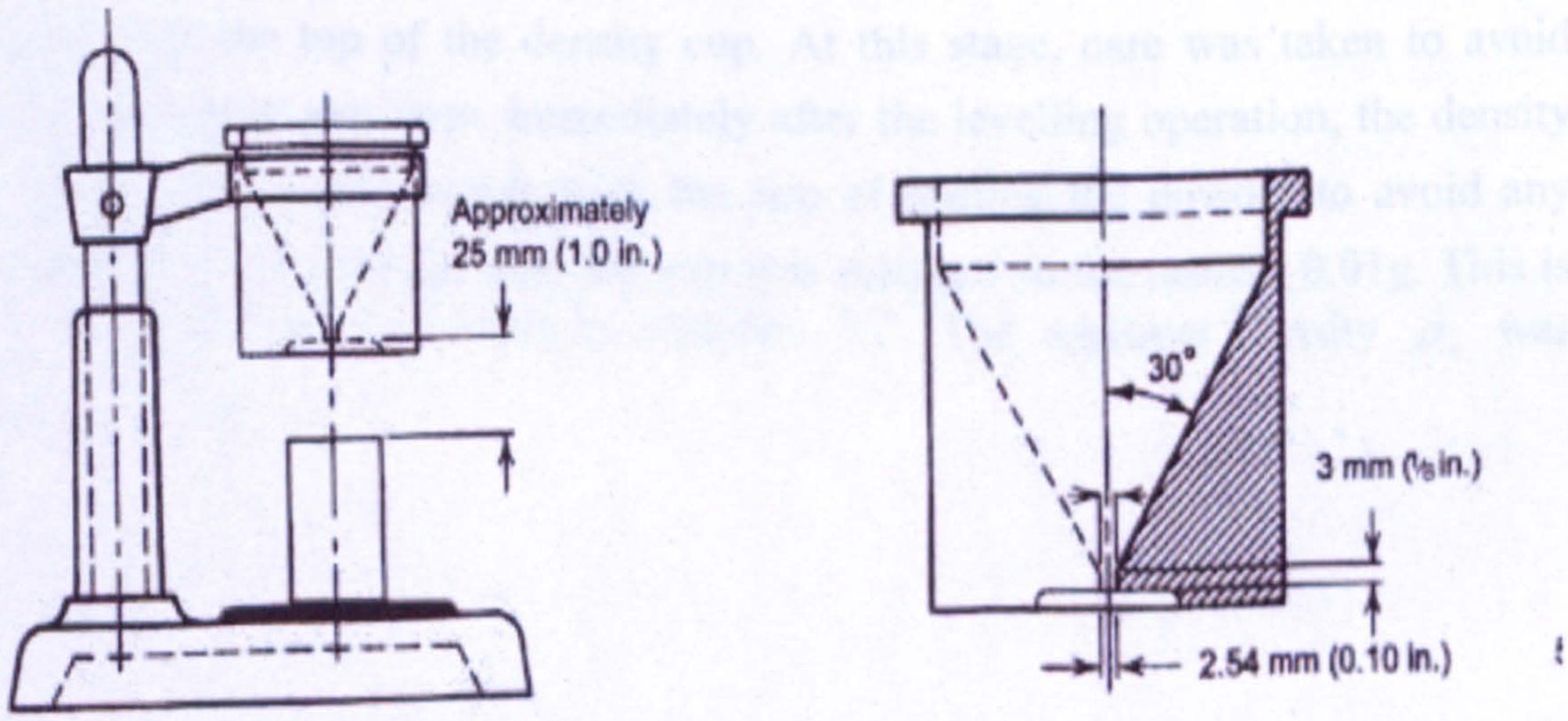

Figure 3.5: Hall apparatus for the measurement of the apparent density of aluminium powders. (a) Equipment assembly (b) Hall funnel (after Carson and Pittenger 1998)

MPIF Standard 03 was employed for this purpose. A 50 g powder test specimen was obtained in accordance with MPIF Standard 01, (section 3.2.5). The experimental arrangement and dimensions of the Hall funnel used in this research are as shown in Figures 3.5a and b respectively. The test specimen was carefully loaded into the

flowmeter funnel while keeping the discharge orifice at the bottom of the funnel closed by placing a dry finger under it (Figure 3.5). Adequate care was taken to ensure that the short stem of the funnel was filled. Just as the finger was removed from the discharge orifice, the stopwatch was started, and it was stopped immediately the last of the powder left the funnel. The elapsed time in seconds was recorded. This procedure was repeated five times for the original and the blended powdered samples and the average value was calculated for each powdered sample. The flow rate of the powders is reported in s/50g to the nearest second.

3.2.6.2 Determination of Apparent Density of Aluminium Powders Using the Hall Apparatus

The test specimen consists of a volume of 25 cm^3 of powder obtained in accordance with MPIF Standard 01 method (see section 3.2.5). The entire test specimen was carefully loaded into the flowmeter funnel and permitted to flow through the discharge orifice into the centre of the density cup (Figure 3.5) ensuring that the testing apparatus was not moved during the filling. When the powder completely filled and overflowed the periphery of the density cup, the funnel was rotated approximately 90° in a horizontal plane so that the remaining powder fell away from the cup. A non-magnetic spatula with the blade held perpendicular to the top of the cup was used to level off the powder flush with the top of the density cup. At this stage, care was taken to avoid jarring the apparatus at any time. Immediately after the levelling operation, the density cup was lightly tapped on the side with the aim of settling the powder to avoid any spillage in transfer. The powder with the cup was weighed to the nearest 0.01g. This is the mass M determined according to equation 3.2. The apparent density ρ_a was calculated as follows:

$$\rho_a = M / V \quad \text{.....3.3}$$

where:

M = mass of powder in the density cup.

V = the volume of the density cup.

This procedure was repeated five times for the main and the blended powdered samples and the average value determined.

3.2.6.3 Sieve Analysis of the Aluminium Powders

Sieve analysis of the aluminium powders was carried out according to MPIF Standard 05. A mass of 60g of the each test specimens obtained in accordance with MPIF Standard 01 was used in this section because the apparent density of each of the powders was less than 1.50g/cm^3. A set of 100 mm diameter calibrated sieves was selected on the basis of the mesh size of aluminium powders (45-75 μm) being evaluated. The group of sieves selected was assembled in consecutive order depending on the size of openings, the sieve having the largest opening being placed at the top. The assembly was completed by a solid collecting pan placed below the bottom sieve. The test specimen was placed on the top sieve, thereafter, the assembly was closed with a solid cover, fastened securely in a AS 200 basic mechanical sieve shaking device which was operated for a constant time of 15 minutes. The sieved fractions were removed from the nest of sieves using the following procedure. The coarsest sieve was removed from the nest, its contents were gently tapped to one side and poured on a glazed paper. Any material adhering to the bottom of the sieve and frame was brushed with a soft brush into the next finest sieve. The sieve just removed was then tapped upside down, on the paper containing the portion that had been retained on it. This fraction was weighed to within 0.1g. This step was repeated for each sieve in the nest, the fraction collected in the pan was removed and weighed. The sum of the masses of all the fractions was recorded. The sum of the masses of individual fractions was the total sample mass added to sieve track. If the sum of the fractions is not less than 99% of the original sample mass, the result was recorded. Otherwise, a check was made for weighing errors, pin holes and the test was repeated. The masses of the fractions retained on each sieve and the mass of the fraction collected in the pan were expressed as percentages of the test specimen mass to the nearest 0.1%. Powder fractions whose mass fraction were less than 0.1% was reported as 'trace.' The results are presented in Table 4.1). This procedure was not used for powdered samples AL-6, AL-7 and AL-8 because the appropriate sieve sizes for samples were not available.

3.2.6.4 Determination of Tap Density of Aluminium Powders

MPIF Standard 46 was employed for the purpose of the determination of the tap density of aluminium powders. Firstly, the inside of a 50 ml graduated cylinder was thoroughly cleaned and dried with cloth. A standard 50 g weight of the test sample was poured into the graduated cylinder from a height of 5 mm in order to limit aeration of powders, care being taken to ensure that a level surface of powder was obtained. The base of the filled cylinder was tapped squarely with hand onto a hard rubber slab (Figure 3.6) until no further decrease in volume took place. The cylinder was given

only a gentle tapping toward the end of the procedure to avoid loosening the surface layers of powder.

Figure 03.6: Apparatus for the measurement of the tap density of the aluminium powders

The volume of the powder was read to the precision of 0.5 ml and the tap density calculated as:

$$\text{Tap Density } \rho_t = M / v \quad \text{.....3.4}$$

where:

M = mass of powder from the density cup in grams.

v = the volume of the tapped powder.

This procedure was repeated five times for the original and blended aluminium powdered samples and the average value reported for each powdered sample.

3.3 Microscopic Inspection of Powders and Processed Samples

The purpose of microscopic inspection of the powders and laser sintered samples was to establish the particle shapes, powder microstructures, presence and amount of alumina oxide phase, the solidification mechanism, as well as qualitative and quantitative description of the elemental composition of the test samples. The characterisation of materials was carried out by optical microscopy (OM), Scanning

Electron Microscopy (SEM), Energy Dispersive X-ray analysis (EDX) and X-Rays Diffraction (XRD). In order to observe representative microstructures, the materials need to be prepared properly. All powder, single layer and multiple layer samples were properly labelled and kept separately in order to avoid any mix-up of the samples. General housekeeping rules were strictly observed when carrying out all procedures in this section.

Each of the characterisation techniques, the corresponding materials preparation route is described in this section.

3.3.1 Optical Microscopy

Optical microscopy was employed to observe the solidification microstructure of the powder and multiple layer samples, the powder samples being included to provide a basis for comparison between the as-supplied and processed powders. A Leitz (Leica) Laborlux optical microscope, fitted with a micrometer-adjustable XY-stage and an Olympus Camedia 5050 digital camera was used for the capture of the micrographs via Photograb-300Z software.

3.3.1.1 Preparation of Multiple layer Samples

Sections perpendicular to the direction of the laser scan were prepared from multiple layer samples by cutting them with a Struers Accutom 5 circular cutting machine equipped with a 356CA circular cutting wheel made of aluminium oxide having a hardness of 500 HV. The specimens were then hot mounted in Bakelite using a Buehler Simplimet 3 mounting press. Care was taken to ensure that samples did not topple over when the Bakelite was added. The machine was set at a temperature of 150 °C and pressure of 250 bar and the cycle was completed after ten minutes. Samples were ground with a Metaserve 2000 grinding wheel using progressively finer grinding silicon carbide papers (P400, P800, P1200, and P2500). Thereafter, in order to remove the scratches on the samples as a result of grinding, they were polished on Metalo polishing cloths using 0.05 μm colloidal silica solution. The polished specimens were etched by placing them face down in dilute Keller's reagent for a period of twenty seconds and their solidification microstructure observed under the optical microscope.

3.3.1.2 Microstructural Observations and Quantitative Microscopy

The solidification behaviour across the layers of each sample was observed under the optical microscope at different magnifications. Micrographs of the cross-section of each sample taken at 50x magnification were combined together to form a montage which assisted greatly in studying the influence of both materials properties and processing parameters on the microstructure of direct laser sintered aluminium powdered parts. Within the range of processing and powder parameters employed, the dendrite morphology of each sintered sample was also observed.

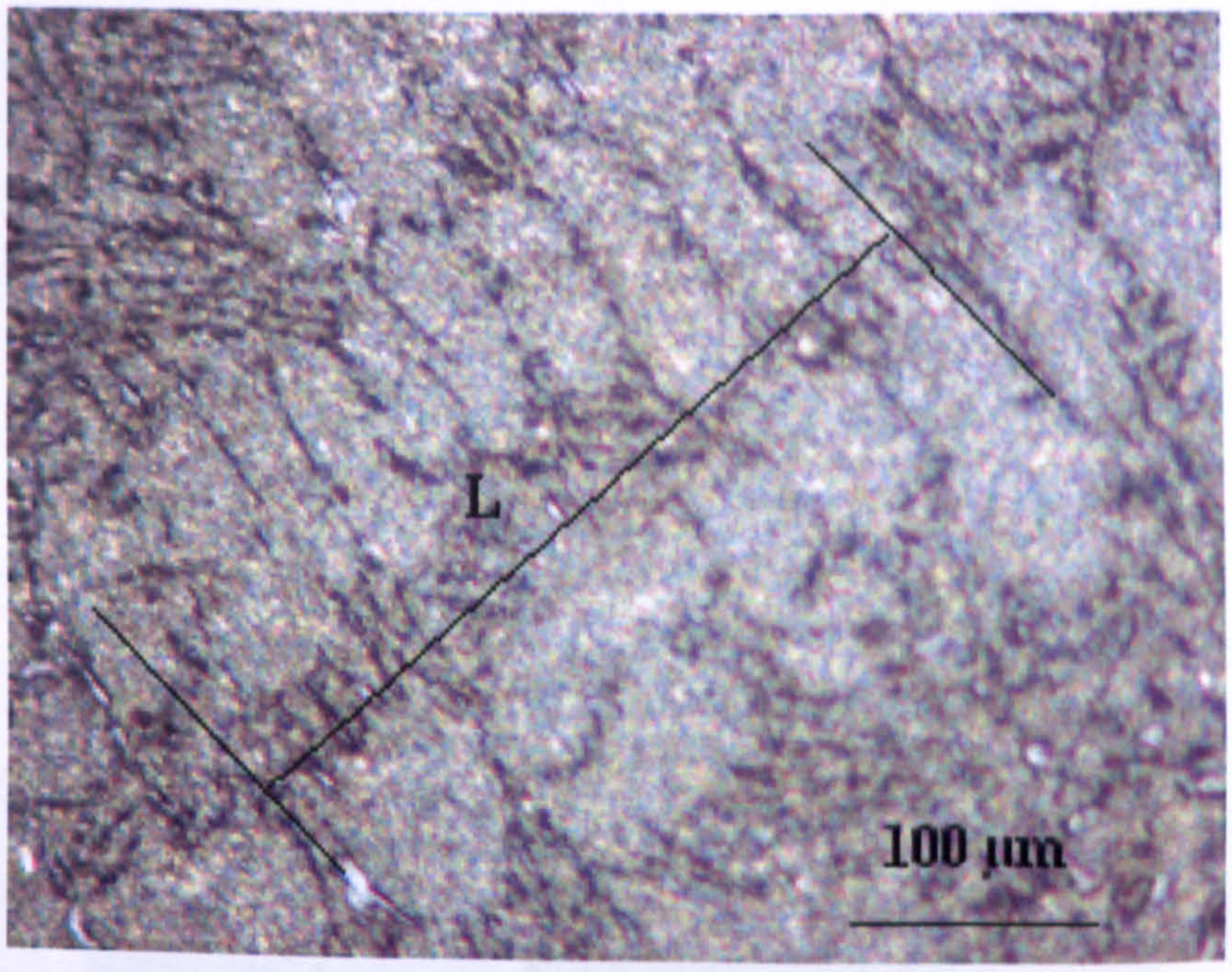

Figure 3.7: Measurement of dendrite arm spacing.

From Figure 3.7,

$$\lambda_d = L_d /(n-1) \quad \text{.....3.5}$$

The secondary dendrite arm spacing (λ_d determined from equation 3.5) was determined by averaging the distance (L_d) between adjacent side branches on the longitudinal section of a primary dendrite according to Toloui & Hellawell (1976), Grugel & Kurz (1987), Gündüz & Cadirli (2002) as shown in (Figure 3.7). Each of the dendrite spacings reported in this study is the average values from 25 to 35 measurements made on each specimen. The details of measurements for the secondary arm dendritic spacings of SLS/SLM processed aluminium alloy powders are presented in Appendix F.

The volume fraction of the primary aluminium phase in the laser sintered samples was determined by the systematic point counting method because it requires the least effort per observation (Brandon & Kaplan 1999; Gokhale 2004). This method is based on the premise that the average fraction of points which fall on grains of a given phase is equal to the area fraction of the phase in the microstructural field section and this consequently equals the volume fraction of the phase. An 80 square array of points as selected and overlaid at regular intervals in the metallographic plane rather than at independent random locations.

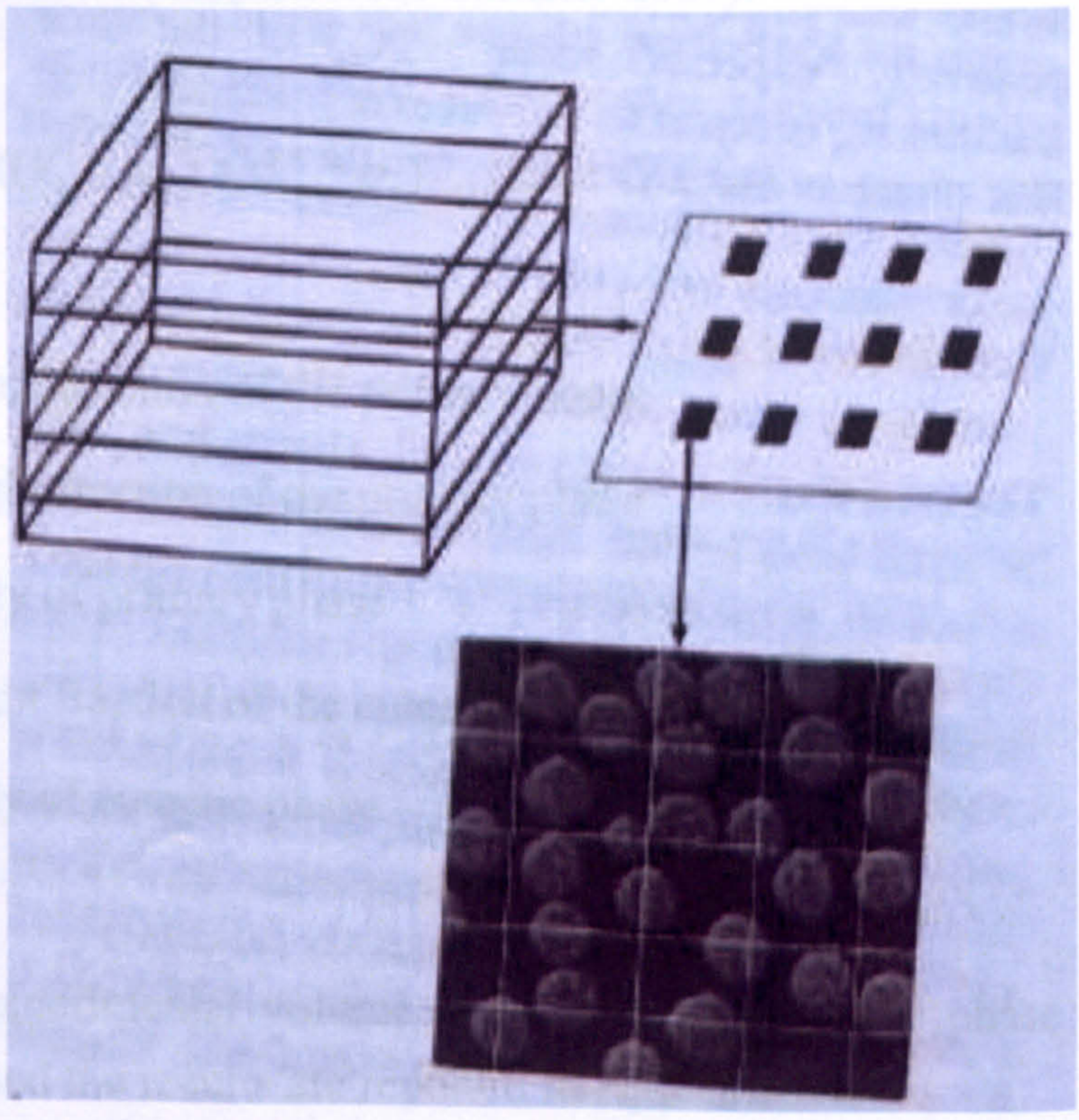

Figure 3.8: A typical multilevel system sampling (after Gokhale 2004).

The points that fell only on the well developed trunks of primary dendrite phases were counted and recorded as exemplified in Figure 3.8. This procedure was repeated fifteen times for each sample with fifteen sampling planes at different locations at fixed distance intervals in the specimen of interest. The volume fraction of the primary dendrite phase (V_α) of the test samples is calculated from the population of average value of point fraction (f_i) according to equation 3.6:

$$V_\alpha = \sum_{i=1}^{n} ((f_i)/n) \quad \text{.....3.6}$$

where the fraction of test points in the phase of interest $f_i = (x_i) / 80$, x_i is the number of points that fell on the primary dendrite phase, and n = 15. Finally, the standard deviation and the confidence interval for each measurement were computed The theoretical weight fraction of the primary phase at the corresponding silicon content in the additive powders was determined by Lever's rule from the Al-Si phase diagram. The experimental volume fraction of the primary aluminium phase was used to estimate the corresponding weight fraction of the primary phase by using equation (3.7). Since density values for both primary aluminium phase and eutectic phase are approximately equal to 2.7 g/cm^3, therefore, the weight fraction (W_α)of the primary aluminium phase was estimated to be equal to its volume fraction (V_α) by employing equation 3.7 as follows (adapted from Callister 2007):

$$W_\alpha = (V_\alpha * \rho_\alpha) / ((V_\alpha * \rho_\alpha) + (V_e * \rho_e)) \quad \text{.....3.7}$$

where

V_α = Volume fraction of the primary phase

W_α = Weight fraction of the primary phase

ρ_α = Density of primary phase

W_e = Weight fraction of the eutectic phase

ρ_e = Density of eutectic phase

On this basis, experimental volume fraction of the primary phase was converted to weight fraction and the results are reported in Appendix G.

3.3.2 Scanning Electron Microscopy

In this section, the methods of material preparation and observation for SEM are presented.

3.3.2.1 Materials Preparation for Scanning Electron Microscopy

To prepare powder specimens for SEM observation, a small sample of powder was taken and independently mounted on an aluminium stub using a graphite paste. The specimen was cleaned by spraying with pressurised air before it was placed in the SEM chamber. Powder samples for SEM observation were prepared in two groups. The first group consisted of samples taken from the as-received powders AL-1 to AL-8, whereas

the second group was the blended mixtures of AL-5 powder with the additive powders AL-2, AL-6, AL-7, and AL-8. The second group of samples provided the basis for the analysis of how the particles of the additive powders had blended with the particles of AL-5 powders.

The sintered single layer specimens were mounted on a stub using a graphite paste and, thereafter, they were placed into the SEM chamber for observation. Again, prepared samples were thoroughly cleaned using pressurised air before they were placed in the SEM chamber. Multiple layer samples for SEM observation were prepared as described in section 3.3.1.1. The hot mounted samples were carbon-coated using a sputter coater in order to prevent electron charging. Fractured surfaces of multiple layer parts were observed by mounting on a stub using graphite paste.

3.3.2.2 Observation of Samples with Scanning Electron Microscopy

A Philips XL30 ESEM Scanning Electron Microscope (SEM) with Link Systems EDS (operating voltage of 20 keV) and image capture accessories was employed to observe the particle size and shape, chemical composition and homogeneity, surface morphology and microstructure of the starting powders and the sintered samples. Working distance was maintained at approximately 12mm for all studies, and for most, spot size was set to 6. Topography was imaged at 20keV. Powdered and processed samples were mounted on stubs using double-sided carbon paste tape and examined uncoated. Again, the powder samples were included to provide a basis for comparison between the as-supplied and processed powders.

The measurement facility within the FEI XL microscope control v.6.0 software was used to measure the size of individual powder particles (Figure 3.9a) in either x or y direction depending on the orientation of the particle. Only ten measurements could be taken at once in a particular region of the particles at 200x magnification. The measurements were repeated three times for each of five different regions of interest chosen on the same sample. Average particle size was determined from these measurements for each sample, with the standard deviation about the mean value also recorded.

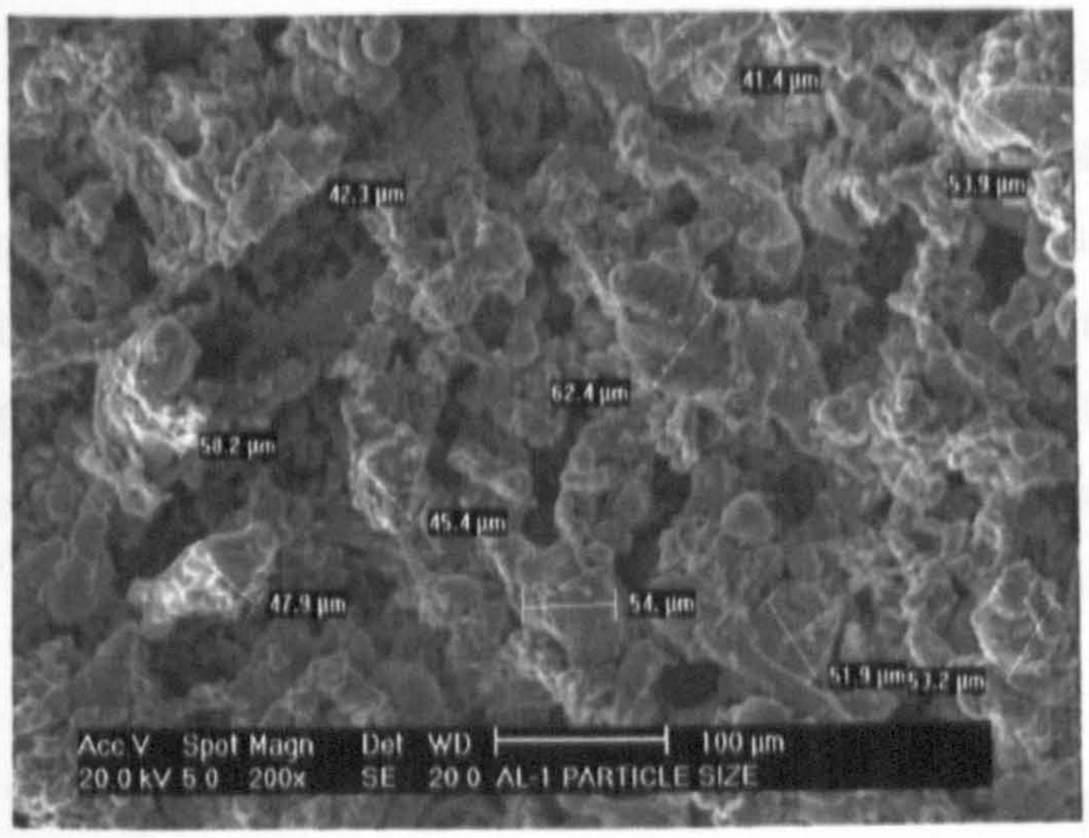

(a)

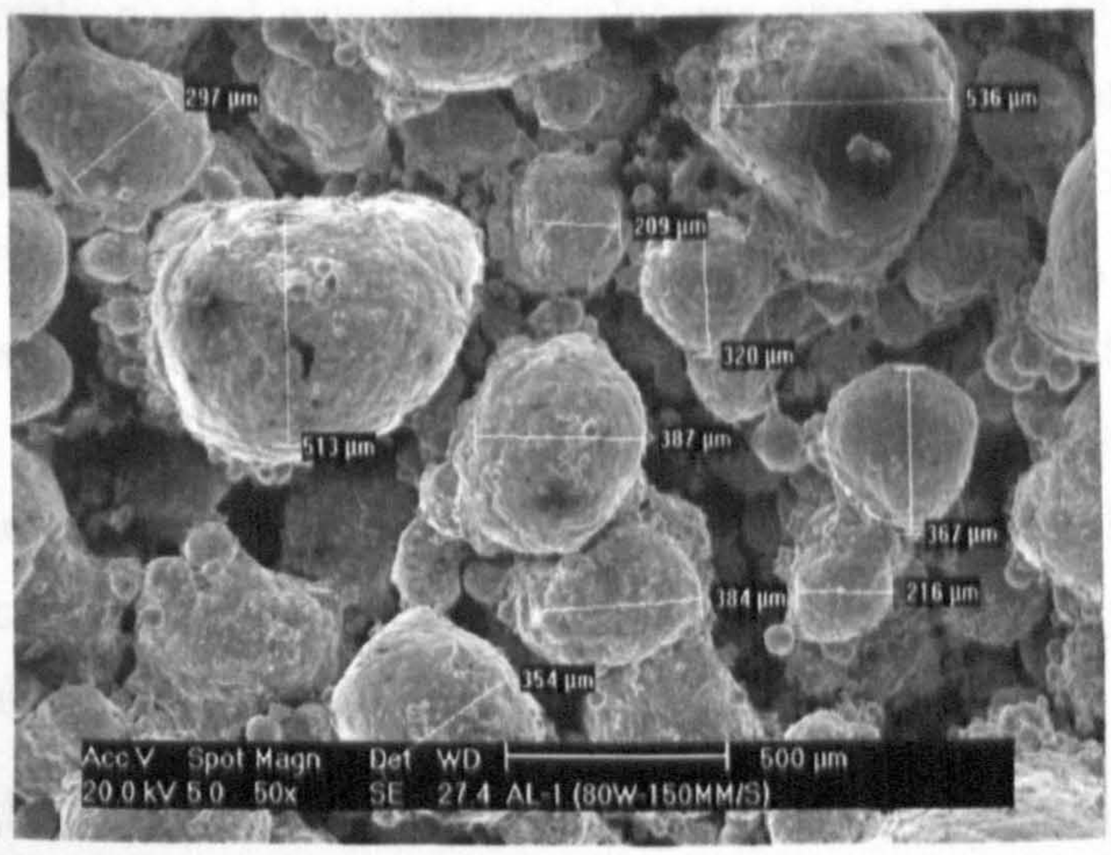

(b)

Figure 03.9: (a) Measurement of particle sizes (b) Measurement of agglomerate sizes.

Powdered and SLS/SLM processed samples were also analysed for surface composition using the energy dispersive X-ray microanalysis (EDS) apparatus with the SEM. Images obtained for each location were analysed, and the resultant spectra also recorded as bitmap image files (Appendix H). Three fields were selected arbitrarily for analysis: the centre of each disc and 5mm to either side of this. Providing the surface appeared relatively uniform, only a small area was analysed within each field, to reduce scanning time. The only limiting criterion was to avoid scanning what appeared to be surface contamination, unless this was uniformly spread over the surface, or was the specific target of analysis. This characterisation used a lower beam power – 10kV (spot size 5.0) – in an attempt to increase surface specificity, while still producing a significant "signal". The FEI XL microscope control v.6.0 software was used to identify the most likely elements corresponding to the peaks on the spectra. Images were recorded with these reference peaks displayed. The "quantify spectrum" function provided approximate values of the proportions of aluminium, oxygen, and other

alloying elements such as silicon, and magnesium, present in the sample. Carbon had been examined due to its near-ubiquitous surface contaminating nature; and grinding may result in contamination from the silicon carbide grit and/or residual material from previous grinding processes using the equipment. To determine any major effects of processing conditions on surface composition and/or contamination, the EDX study included samples fabricated at different processing conditions. This was intended as a basis for comparison of the surfaces used in the present study with the starting powders.

According to Exner & Weinbruch (2004), readers must note that the quantification of x-ray micro microanalysis necessitates the measurement of standards (sample with known chemical composition) and complex calculations with a view to correcting the matrix effects that arise due to the variation in chemical composition between the unknown sample and the standards investigated. To compensate for matrix effect, ZAF-correction (where "Z" represents atomic number, "A" absorption, and "F" for fluorescence), a most widely used algorithm (EDS INCA microanalysis suite, version 4.08), was used in this research. Since quantitative chemical analysis usually requires flat and polished samples with dimensions larger than the interaction volume; for small particles, rough surfaces, stratified samples and depth profiles employed in this research, ZAF special algorithm had been used.

Nevertheless, because this procedure may lead to large errors that cannot be recognised without measuring standards, the uncertainty in reporting EDS chemical analysis of samples is hereby reported with a view to informing the readers of this thesis.

SEM of the sintered single-layer samples was undertaken with the aim of determining the agglomerate sizes, and describing the shapes of agglomerate, and pores, and observing the solidification microstructure. To measure the agglomerate sizes, the same procedure used for the measurement of particle sizes was adopted (Figure 3.9b).

For the multiple layer samples, SEM observation was carried out with the aim of determining the degree of inter-particulate bonding and particulate aggregation or segregation, the solidification mechanism, the mode of fracture across the interfaces, the chemical homogeneity, and describing the porosity in the sintered samples.

3.3.2.3 Analysis SEM Qualitative Surface Topographic Information of Samples and EDS Results

Qualitative surface topographic information of samples provided by scanning electron microscopy are shown in Figures 4.1, 4.18 to 4.22, 4.27, 6.1 to 6.3, 6.23, 6.43, 7.1, and 7.21 whereas Tables 4.2, 6.1 to 6.3, and 7.1 summarise approximate quantitative measurements of the elements detected in each of the powders. It must be emphasised that no oxygen was detected in the "natural" oxide surfaces because the depth of the natural oxide layer is negligible compared to the "sampling depth" of the EDX technique. Furthermore, statistical analyses were not performed, due to the approximate nature of the measurements. Meanwhile, these EDS results must not be regarded as conclusive since each surface preparation was represented by a single sample. Carbon was not detected on any of the samples examined. Other contaminants in the pure aluminium powders such as copper and iron were frequently identified by automatic peak fitting, but were not clearly visible in the spectra (occurring amidst "noise" in the spectrum). A more surface-specific technique would be required to quantify these with any confidence.

As noted earlier on, EDS results must be taken as preliminary because each surface preparation was represented by a single sample. Moreover, it is generally accepted that EDS is not a highly surface-specific technique, with measurements obtained from the outer 1–5 μm of the surface (Brandon & Kaplan 1999, Exner & Weinbruch 2004). Consequently, quantitative results from this technique must also be regarded with caution as such measurements require flat, homogeneous surfaces for accuracy. In contrast, electron spectroscopy for chemical analysis (ESCA) or X-ray photoelectron spectroscopy (XPS) measures only from the outermost 1–10 nanometer (nm) (Brandon & Kaplan 1999, Exner & Weinbruch 2004). Both Brandon & Kaplan (1999) and Exner & Weinbruch (2004) reported that analysis employing ESCA or XPS is bedivilled with ubiquitous contamination from adsorbed atmospheric hydrocarbons; therefore, non-usage of these techniques in this study is most likely due to the lack of surface specificity of EDS. This reason could probably elucidate the failure to detect, with confidence, contamination on autoclaved surfaces according to Exner and Weinbruch (2004). EDS spectra were dominated by aluminium peaks in all samples, with a significant increase in oxygen content (approximately 10–20% by weight) for pure aluminium sample AL-1. Other contaminants/impurities identified by peak fitting did not appear to be clearly distinct from noise in the spectra, and are therefore considered unreliable. Because only the outermost layer forms inter-layer contacts during

SLS/SLM, it is recommended to carry out XPS to analyse the surface chemistry and contamination. Backscattered electron imaging in scanning electron microscopy can also reveal contamination, by showing variations in atomic number as contrasts in brightness (Brandon & Kaplan 1999, Exner & Weinbruch 2004).

Moreover, it was thought that oxide thickness would be the principal basis for minimising variations in surface microstructure (i.e. distortions of crystal structure) due to the different degrees of grinding during preparation. The EDS measurements suggest significantly increased oxide thickness for AL-1 powder. Meanwhile, the variations in oxide thickness could indicate uneven heat distribution and/or cooling rates during SLS/SLM of aluminium powders. This has yet to be investigated. Variable oxide thickness may account for the significant differences in oxygen content measured by EDS on all the powdered samples.

3.4 Selective Laser Sintering

In this section, the SLS equipment and its accessories are described. Procedures adopted for laser power calibration, fabrication of single and multi-layer coupons in aluminium powders, and the variability studies are presented.

3.4.1 Selective Laser Sintering Equipment

The sintering of the pure and alloyed aluminium powders reported in this thesis was carried out using a research SLS machine (Leeds Sinter Station) which is shown schematically in Figure 3.10. The machine consists of the following parts: laser and focussing optics, X-Y scan head, process chamber, powder handling apparatus, vacuum pump, power output control, motion control table and Pentium PC which runs the various software for controlling the process. A detailed description of the apparatus has already been given by Hauser (2003). The scan head directs the laser beam over the powder bed. The functions of the build cylinder are to house the piston assembly and store the deposited powder and the sintered components during multiple layer construction. The piston head is moved by the motion control table. The storage, deposition, and levelling of powder over the build zone is accomplished by using a hopper and a wiper blade which ensures smooth passage of the cradle and blade when traversing across the build zone. The motion control table was controlled by a DOS-based software programme called talk2bus.

3.4.2 Laser Power Calibration Procedure and Results

Before carrying out direct laser sintering for building parts, either single layer or multiple layer, careful consideration was given to laser power output calibration. The aim, procedure and results for the laser power output calibration are hereby described.

In order to ensure that the laser power output remained consistent throughout the period of this research, it was thought necessary to carry out the calibration of the laser power output using a laser power probe (POWERMAX 5200). The procedure adopted was the same as that developed by Hauser (2003). To calibrate the laser power, the heat sink of the laser power probe was placed in the path of the laser beam at a distance of 150 mm above the build zone. According to Hauser (2003), this position was sufficiently far away from the focal point of the laser to avoid the accuracy of the probe being compromised by a high heat intensity damaging the surface coating on the heat sink. The laser power was measured every 50^{th} unit on the dial.

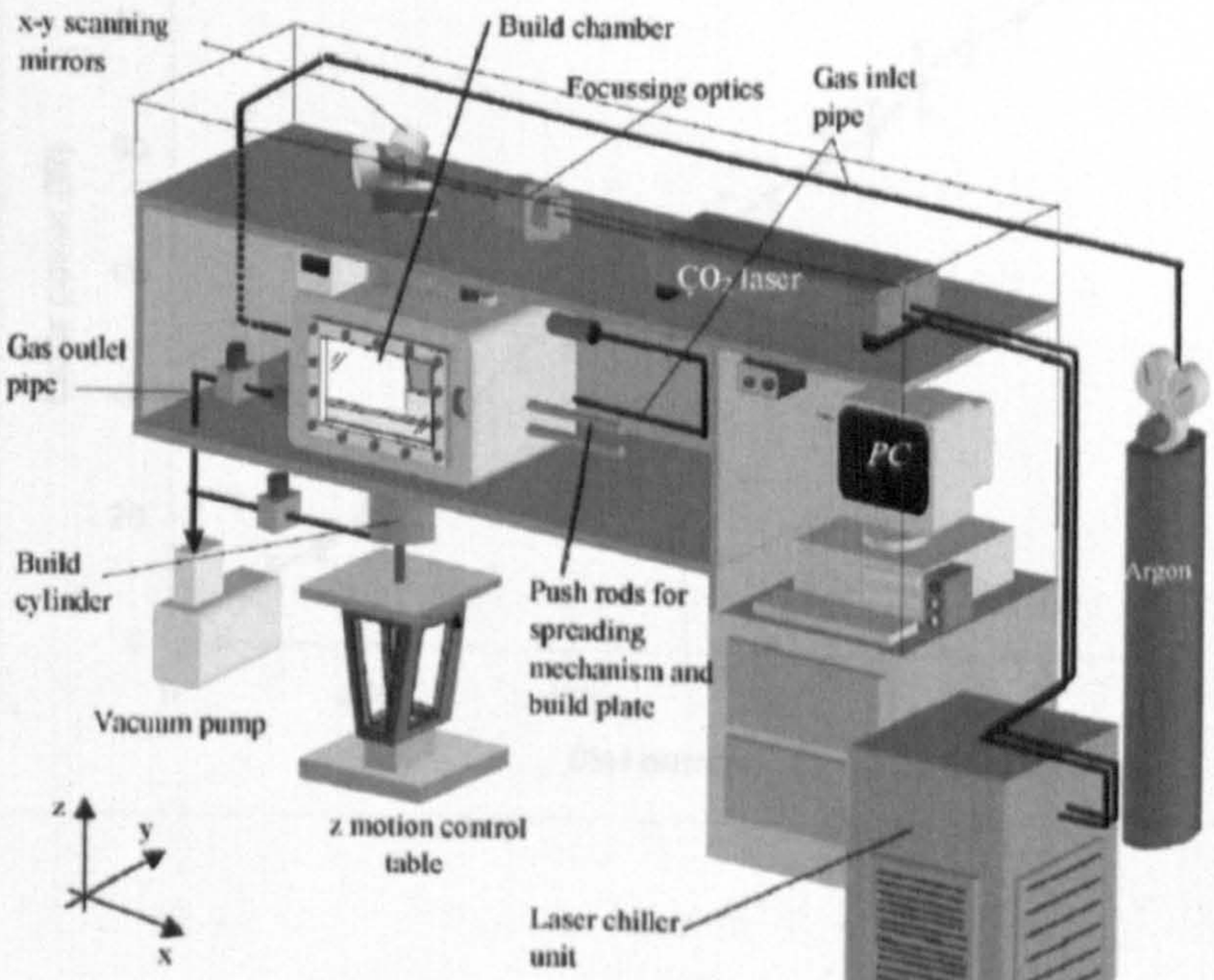

Figure 03.10: Schematic diagram of SLS experimental machine (after Hauser 2003).

The relationship between the dial setting and the power output from the laser is presented in Figure 3.11.

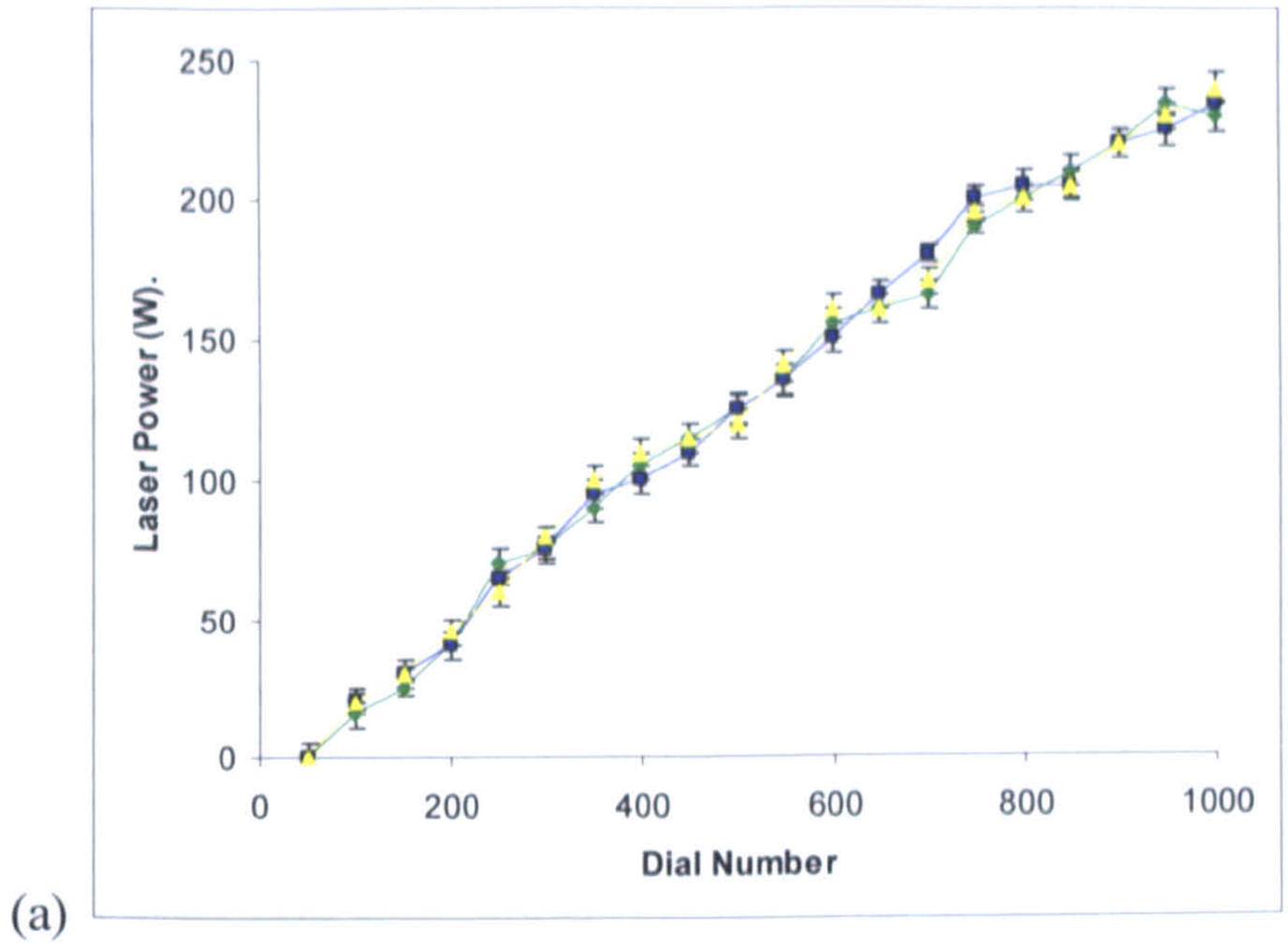

(a)

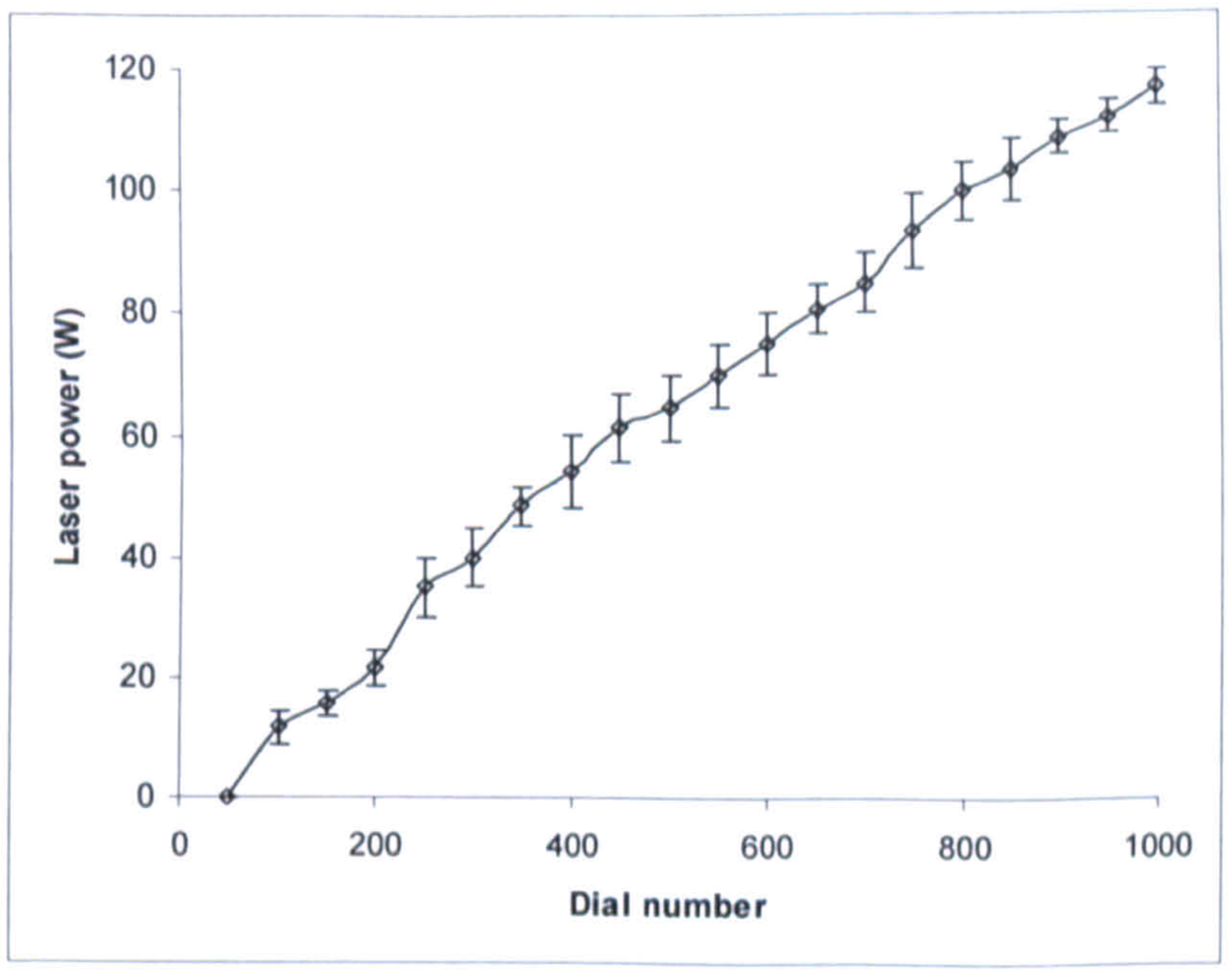

(b)

Figure 3.11: (a) Calibration graph showing comparison in the laser power versus dial setting over the two year period of this research at Leeds University. (b) Calibration graph for the manual laser power modulation for the machine while at Newcastle university.

The calibration procedure was repeated several times over a period of two years in order (while situated at the university of Leeds) to ensure consistency of experimental procedures. Figure 3.11a shows that the results obtained from several trials carried out over the period of two years, at Leeds University, fall within the experimental error values of 5% for a single calibration. This confirms that the laser power output had remained consistent throughout the period of this research. Furthermore, it was re-calibrated again one year after the sinter-station was moved to the Newcastle

University when the maximum laser power available was found to have fallen to 115 W (Figure 3.11b) because only one of the two laser power sources was found to be functioning properly.

3.4.3 Deposition Procedure

The procedure adopted for the preparation of single layer and multiple layer specimens are described in this section. All experiments were carried out using an argon atmosphere having 99.9% purity.

3.4.3.1 Single Layer Scanning Conditions

The purpose of carrying out single layer scanning experiments was to gain an indepth understanding of the sintering behaviour of aluminium powders under varying processing conditions and powder properties as well as establishing the favourable processing condition for the fabrication of multiple layers specimen. All single layer experiments were carried out using a Synrad 240 W CO_2 laser of beam diameter 0.6 mm, and Gaussian profile, with a wavelength of 10.6 μm. A range of scanning rates from 10 – 500 mm/s and laser power 10 – 200 W was used during the investigation. The notional size of each single layer build was 15 mm x 15 mm, and they were scanned in the build tray (170 mm x 140 mm x 10 mm) on a stainless steel plate with a machined pocket of dimensions 140 mm x 130 mm x 7 mm. To build single layers, a sample of powder was initially deposited on the tray and levelled by a metre rule prior to the build plate's insertion into the build chamber. With the sintering chamber locked securely, an argon (99.9% purity) rich atmosphere was established by evacuating the build chamber (via the vacuum pump) to approximately 50 mbar pressure and back-filling with argon to atmospheric pressure. Evacuation was found to be necessary in order to improve the consistency of results. This step was repeated twice before balancing the flow rate of argon through the build chamber to give a slight positive overpressure (50 mbar). Because flow gauges were not available, to maintain consistency the flow rate was balanced at the maximum pumping speed of the vacuum pump. Immediately the flow rate through the build chamber was balanced, it was left to settle for fifteen minutes before the laser was fired. During this period, scanning parameters (such as scan speed, scan spacing, beam diameter, build shape and dimensions) were entered into the computer using HPGL (Hewlett Packard Graphics Language) commands. These conditions were maintained throughout the duration of the single layer experimental tests and during a five minute cooling period at the end. The total cycle time for a single layer build on a plate was forty-five minutes, including

the conditioning and sintering of the powder. It is essential to note that trace elements of other gases like oxygen did reside within the chamber. The presence of oxygen in trace amounts is expected to influence the sintering response of the powders as it may increase the surface tension, thereby promoting balling (Hauser 2003, Simchi & Pohl, 2003, 2004). To maintain good repeatability of results and impose safe handling, the number of coupons built on a tray in a cycle was restricted to a maximum number of twenty-eight. After cooling, the sintered coupons were taken out of the chamber and were thoroughly cleaned with liquidised air. Images of the samples arranged as-sintered in the build trays were taken with a Leitz (Leica) Laborlux microscope equipped with an Olympus Camedia 5050 camera as soon as they were removed from the build chamber. This procedure was repeated for building of single layers in powder samples AL-1, AL-2, AL-3, AL-4, and AL-5.

3.4.3.2 Multiple Layers Scanning Conditions

Multiple layers were produced using the same laser used for single layer samples with the first layer built on the powder bed. The following ranges of processing parameters were employed: laser power (150 W), scan rate (80-200 mm/s), scan spacing 0.1 mm, and layer thickness 0.25mm. With the powder bed lowered initially to a depth of 5mm, the powder was simultaneously spread and levelled over the bed by using a hopper and wiper blade, the motion of which was controlled by push rods. With the sintering chamber locked securely, an argon atmosphere was established in the chamber using the procedure described in section 3.4.3.1. and the first sintered layer was deposited. To fabricate subsequent layers, the powder bed was lowered by the specified layer thickness and the powder again simultaneously spread and levelled over the bed. In fabricating multiple layer parts, the scan direction was altered between the layers. The scan direction was in the x-direction of the first layer, the y-direction for the second layer, and this sequence was repeated for as many layers as the part contained. The sintered multilayered coupons were taken out of the chamber and were thoroughly cleaned with liquidised air for microstructural characterisation and density measurements. An image of each sample was taken with a Leitz (Leica) Laborlux equipped with an Olympus Camedia 5050 camera. The procedure outlined above was used to build multiple-layers parts in each of the powders AL-1, AL-2, AL-3, AL-4 and AL-5.

These experiments were used to determine which of the five powders AL-1 to AL-5 was the most likely candidate for the direct laser sintering process. Once this powder (AL-5) had been selected, the procedure was repeated for powdered sample in order to

optimise the process parameters but with a wider range of process parameters: laser power (80-200 W), scan rates (80-200 mm/s), scan spacing (0.1 mm to 0.5 mm), and layer thickness (0.25 mm to 1.00 mm).

The effect of variation in composition and particle sizes and distribution on the sintered properties of AL-5 powder was also explored. AL-5 powder was blended, initially, with each of the powdered samples AL-2, AL-6, AL-7, and AL-8 for 20 minutes at 125 rpm as described in section 3.2.5. Each of the additive powders was blended with sample AL-5 in the following proportions: 0wt%, 10wt%, 20wt%, 25wt%, 30wt%, 40wt%, 50wt% and 100wt%. The additive powders were either of the same or smaller/narrower particle sizes and distribution than those of AL-5 powder. The optimal composition for each type of powder mixture was investigated at this stage by employing the optimal processing condition developed initially for powder AL-5. Having determined the optimum composition for each powder blend, the optimal processing conditions for these groups of powder blends were investigated.

Furthermore, optimum composition obtained for the blended trimodal mixture of AL-5, AL-7, and AL-8 was investigated further. This was achieved by determining how much of varying the proportions of AL-7 and AL-8 ranging from 0wt% to 25wt% that should be mixed with 75wt% of AL-5 powder. The optimum process parameters were again determined for the trimodal blend optimum composition. Thereafter, the sintered specimens were taken for microstructural and mechanical characterisation. Overall, two samples were fabricated for each processing condition either for monosized or blended powders.

3.4.3.3 Procedure and Results of Variability Studies

In order to ensure consistency in results obtained from the sintered/melted tracks for all single layer and multiple layers builds at any time and to provide a basis for comparisons between the required tests, variability test was conducted. To achieve this aim, twenty-five multiple layer samples were fabricated as described in Section 3.4.3.2. The multiple layer parts were made in powder sample AL-4 using the following processing conditions: laser power (200W), scan rate (120mm/s), scan spacing (0.1mm), layer thickness (0.25mm). The sintered samples produced varied in the number of layers from 5 to 12. The dimensions X_i, Y_i and Z_i of the sintered samples were measured on three different days in order to determine the variability in the calculated density of the sintered parts (where i denote the day (1, 2, and 3) on which

the reading was taken). The results of the variability studies are presented in the next paragraph.

The sintered densities of twenty five multiple-layer sintered samples made in AL-4 powder with the following processing parameters: laser power (200W); scan rate (120mm/s); scan spacing (0.1mm); and layer thickness (0.25mm) were determined. The sintered samples varied in the number of layers from 5 to 12. The dimensions X_i, Y_i and Z_i of the sintered samples were measured on three different days in order to quantify the variability in the calculated sintered density of the sintered parts (X_i, Y_i and Z_i denote the number of different measurements made in different days in which the reading was taken 1, 2, and 3). The mean for each of the three days was calculated to be 1.5318, 1.54, and 1.54 g/cm^3 respectively while the sample mean sintered density for AL-4 was calculated to be 1.53 g/cm^3. The standard deviation was 0.015 g/cm^3 or 1% of the mean. Analysis of the empirical rule was applied to the variability studies on aluminium powders while both 95% and 99% confidence limits were determined for the sintered density population. Although, the proportion of the sintered densities population was noted to have laid in the interval that is very close to that specified by the empirical rule, nevertheless only 64% and 80% of the sintered density population were noted to have enclosed the true parameter value $\mu^* = 1.5338$ (population mean) for 95% and 99% confidence limits, respectively. While the empirical rule analysis indicates that the variability in the sintered density is negligible, the application of the confidence limits reveals the contrast.

Furthermore, the test was repeated for other monosized and blended powders over the period of three years. The range of processing conditions used for variability test was noted to have varied depending on the powder in use. Moreover, to ensure that data generated from this work are reproducible, control charts (Figures 3.12 and 3.13) were drawn at four intervals over the three year period. On the basis of the control data generated, it could be concluded that the impact of the error due to machine setting, operator, different powder batches in use and environment on the readings is minimal. The distribution of the sintered density could be described as being closed to the normal curve as shown in Figure 3.12 below. Moreover, the averages of the 25 samples of the sintered density are in control with the exception of sample number 5 while all the sample standard deviation values are found within the upper and lower limit boundaries of the control chart as shown in Figure 3.13.

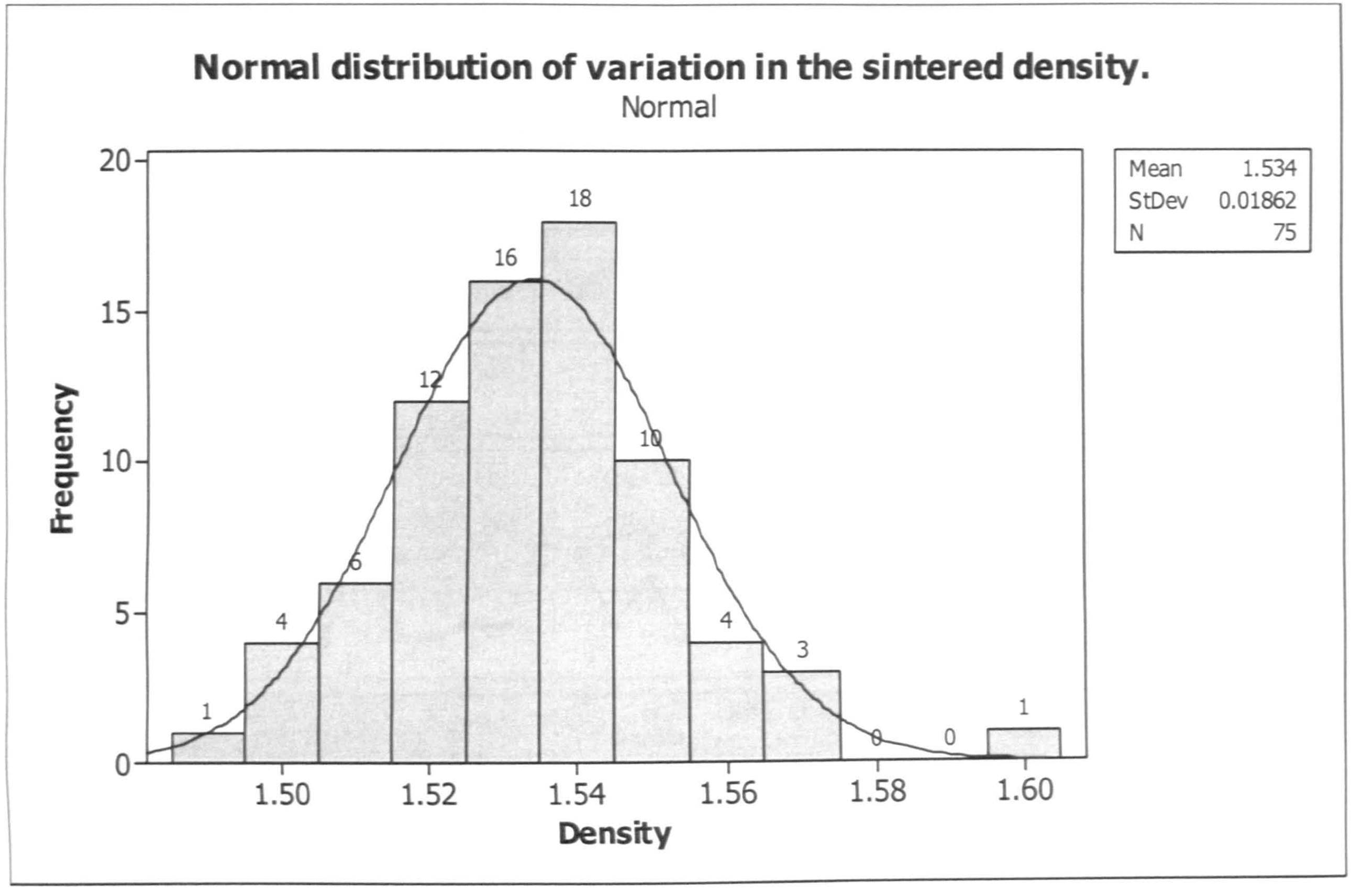

Figure 3.12: Normal distribution of variation in the sintered density.

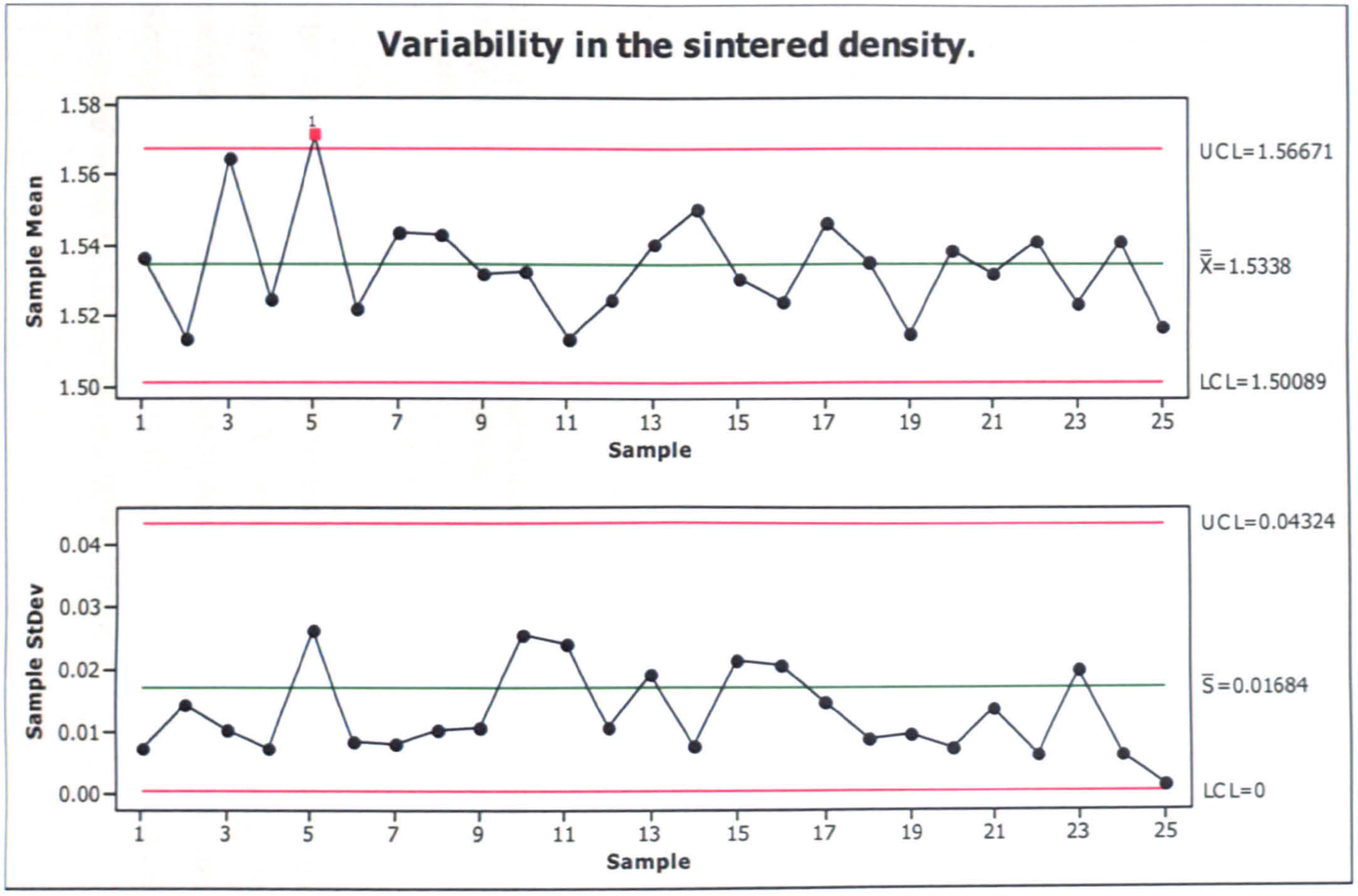

Figure .3.13: Control charts illustrating the degree of variability observed in the sintered density.

3.5 Determination of the Density and Mechanical Properties of the Multiple Layer Parts

3.5.1 Measurement of Density of Multiple Layer Parts

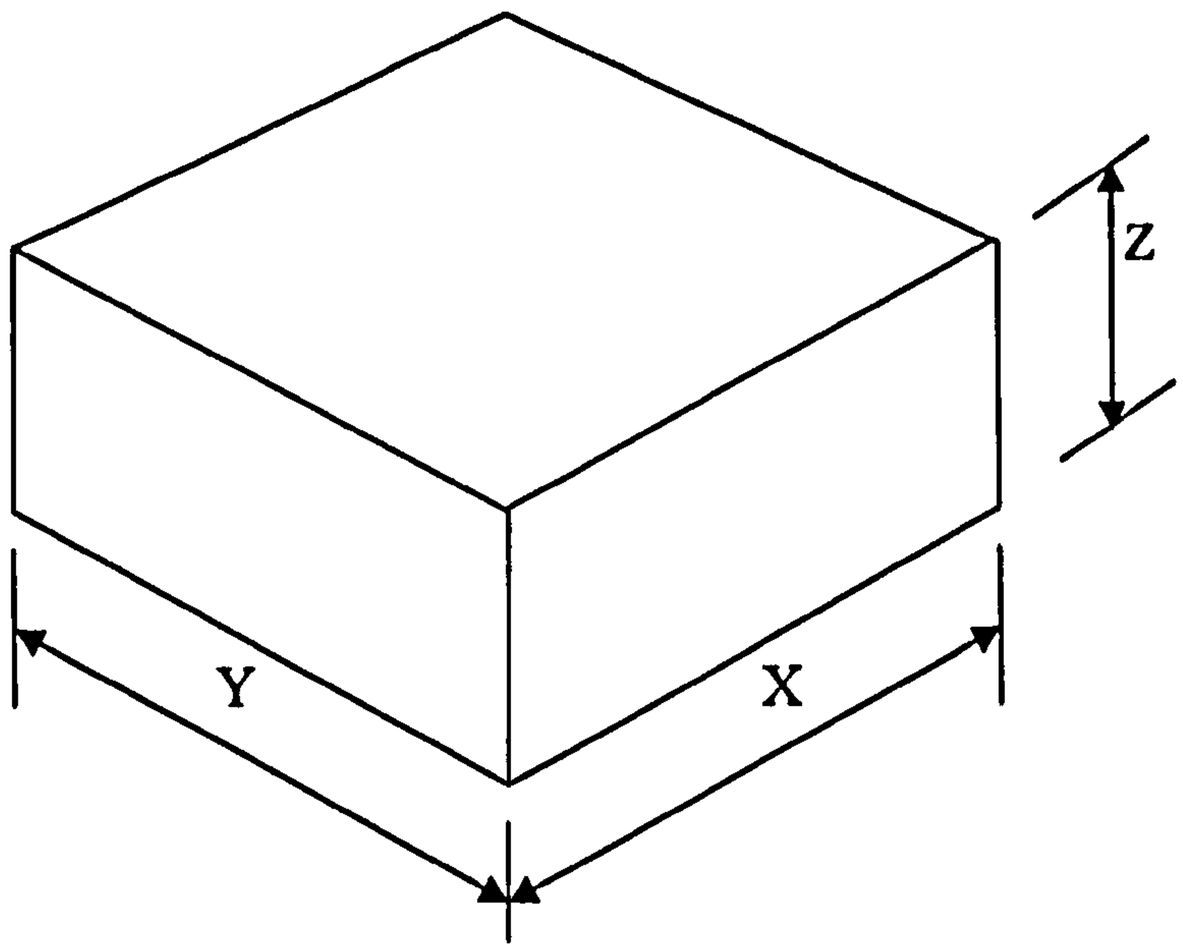

Figure 03.14: Dimensions of a typical direct laser sintered aluminium powder specimen length X ≈ 15mm, width Y ≈ 15mm, and depth Z ≈ 4mm for the determination of the part's sintered density (↔ scan direction).

The approximate volume of the multiple layer parts was calculated on the basis of measurements of the length Y, width X, and depth Z of the coupons in order to compute the density of the components (Figure 3.14). Each dimension was based on an average of five measurents with a vernier calliper. The mass of each coupon was measured using a balance (model WPS 2100/C1).

3.5.2 Determination of the Mechanical Properties of the Multiple Layer Parts

Mechanical testing of the parts made from the blended trimodal powdered samples was carried out in order to determine the mechanical properties of the materials. The tests carried out were tensile, bending, and un-notched impact energy tests according to ASTM standards E8, E855, and MPIF40 respectively.

3.5.2.1 Design and Fabrication of the Mechanical Test Specimens

Figures 3.15, 3.16, and 3.17 show the design of the tensile test, bending test and impact test samples, respectively, with their standard dimensions indicated on the drawings. The geometry of the test specimens were defined using HPGL. All the specimens were produced using the Synrad 240W CO_2 laser of 0.6 mm beam diameter with the following processing parameters: laser power (115 W), scan rate (30.5 mm/s), scan spacing (0.1 mm), layer thickness (0.25 mm) which generated an energy density of 150 J/mm^3.

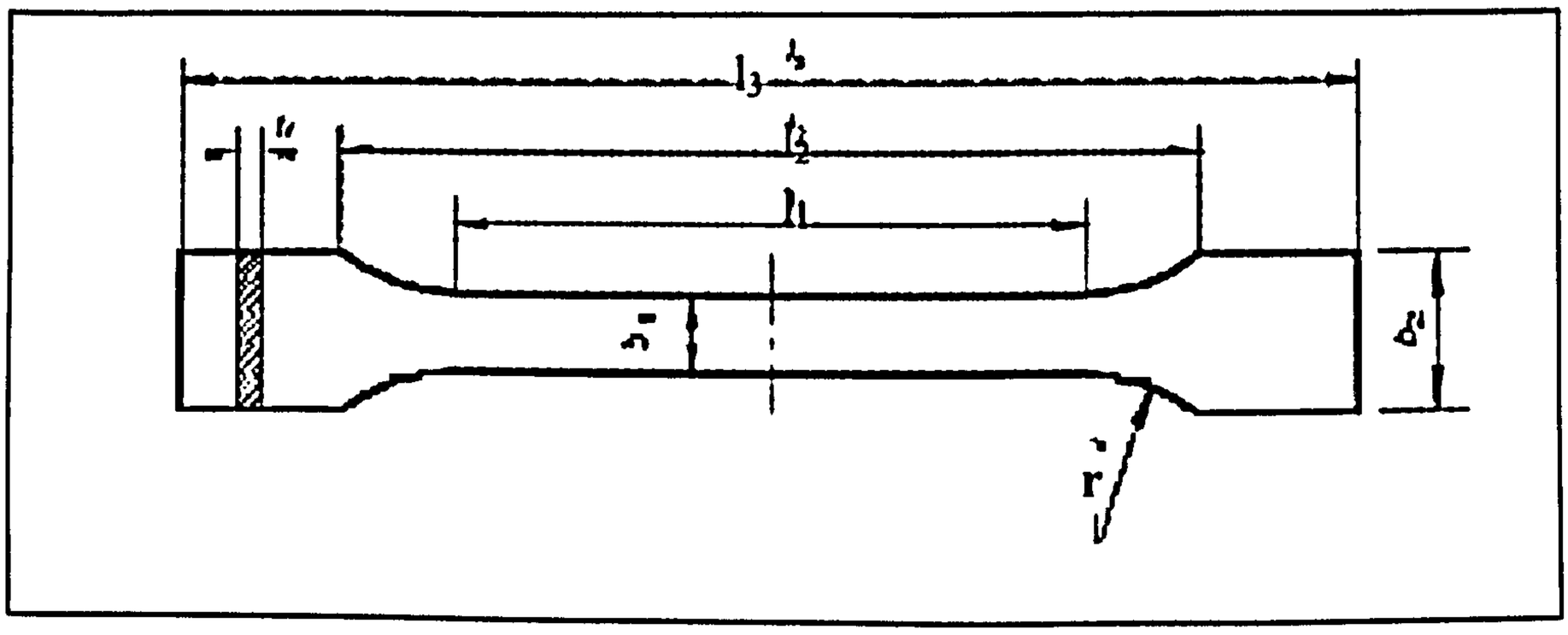

Figure 3.15: The design of the tensile test specimen used in the experiment.

The dimensions of the test specimen are as follows:

$l_1 = 16.00$ mm

$l_2 = 26.00$ mm

$l_3 = 45.00$ mm

$b_1 = 4.00$ mm

$b_2 = 8.00$ mm

h = 2.00 mm

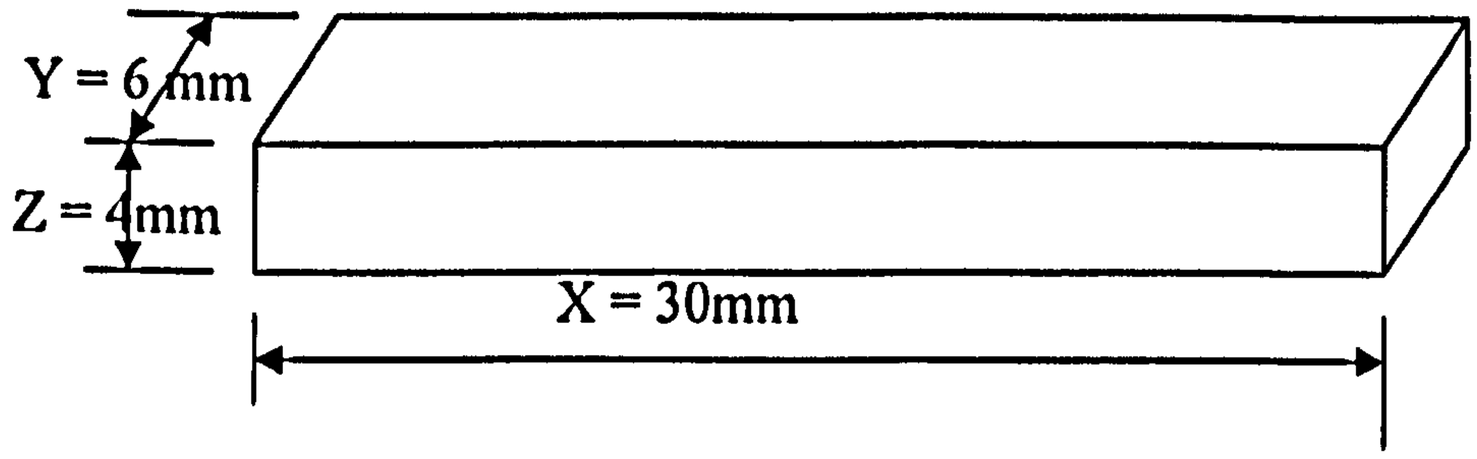

Figure 3.16: The design of the three-point bend test specimen used in the experiment.

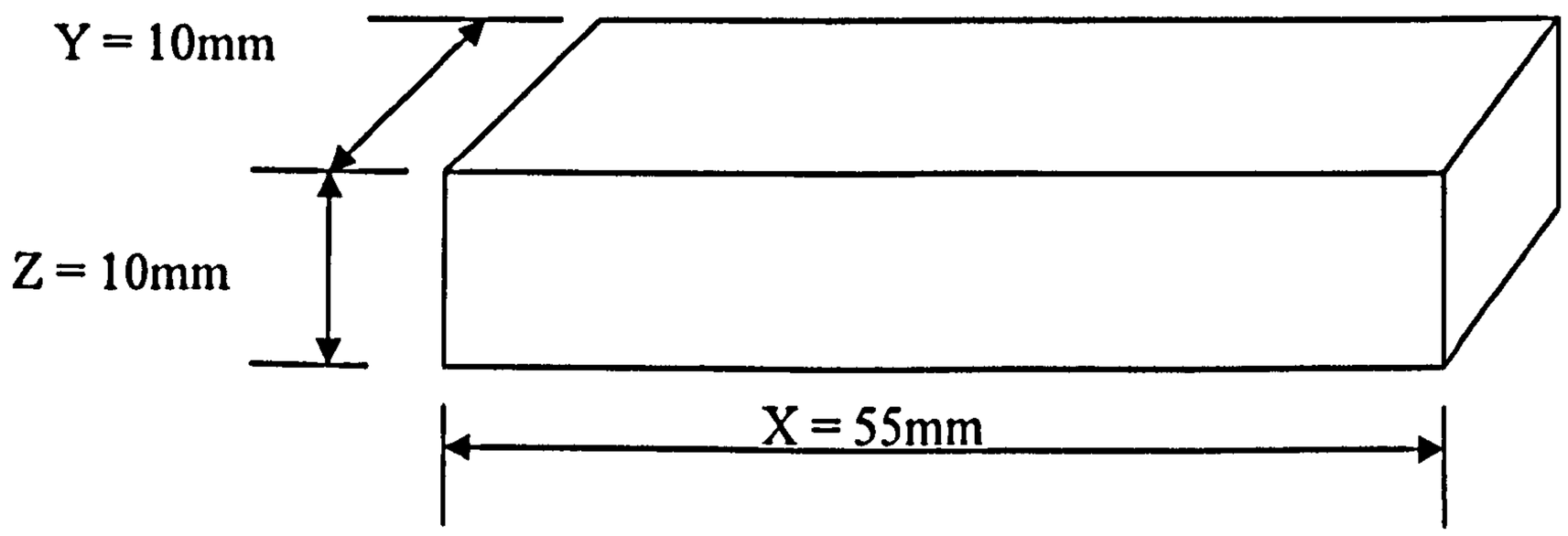

Figure 03.17: The design of unnotched impact test specimen.

3.5.2.2 Determination of Bend Strength of the Multiple Layer Components

In order to determine the modulus of elasticity in bending and the bending strength of the parts made by direct SLS, a 3-point bending test was carried out using grips (Figure 3.18) developed for a JJ universal tensile testing machine by a former researcher at the Institute for Materials Research, University of Leeds. The 3-point bend test specimen consisted of a simple 30mm x 6mm x 4mm rectangular beam resting on two supports and point loaded mid-way between these two points equally spaced from each support (Figure 3.19). The cross-head speed was at 6 mm/s. A 100N load cell was used and the test was carried out at room temperature. Values of load versus deflection at the loading point were recorded on a computer. After testing, selected test pieces were chosen for SEM fractographic examination.

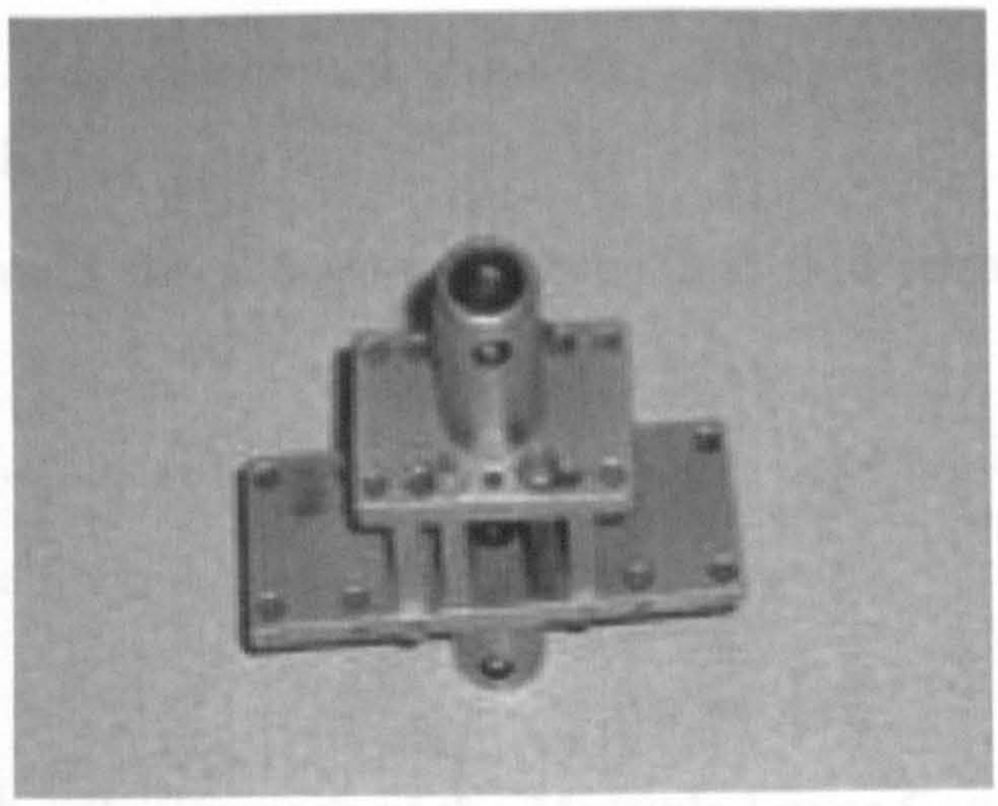

Figure 03.18: The grip used in the 3-point bending test.

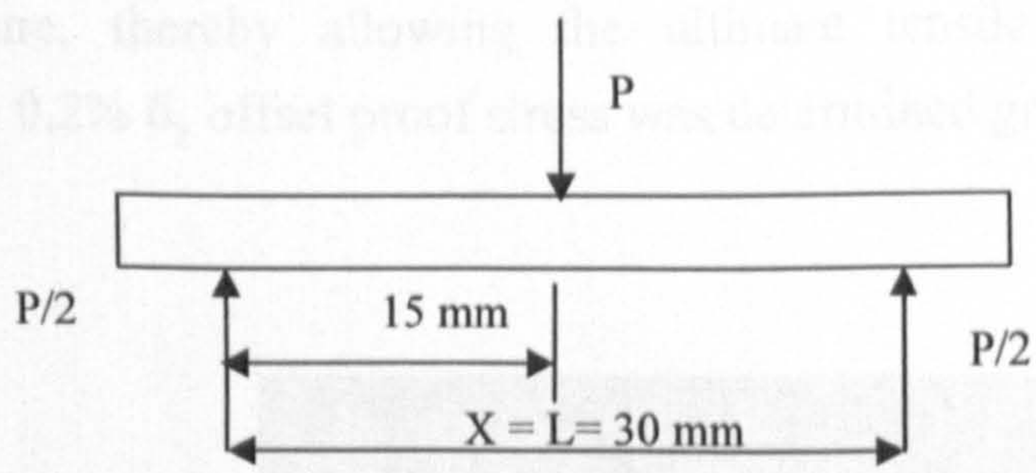

Figure 3.19: Loading diagram for 3-point bending test.

The modulus of elasticity in bending was calculated from this data using Figure 3.16 and equation (3.8) adapted from Guha (2004):

$$E_b = (X^3 \Delta P)/(4YZ^3 \Delta \delta) \quad \text{.....3.8}$$

where

E_b = Modulus of elasticity in bending (MPa)

ΔP = Load increment (N)

X = Span length (mm)

Y = Specimen width (mm)

Z = Specimen thickness (mm)

$\Delta \delta$ = Deflection increament at mid-span (mm)

The parameter $\Delta P/\Delta\delta$ was determined from the slope of the load (N) versus displacement (mm) graph.

Moreover, flexural strength for a three-point bend test is determined according to equation 3.9:

$$\sigma_b = (3P_{\max} X)/(2YZ^2) \quad \text{.....3.9}$$

$P_{\max}$ = load (force) at the fracture point

3.5.2.3 Measurement Tensile Strength of the Multiple Layer Components

A JJ universal tensile testing machine (Figure 3.20) was used to determine the tensile properties of the specimens at a fixed cross-head speed of 6 mm/s using a wedge grip. The specimen used for the test was an ASTM type V sample (Figure 3.15). A 100N load cell was used and the test was performed at room temperature. The samples were tested to fracture, thereby allowing the ultimate tensile strength (UTS) to be determined. The 0.2% $б_y$ offset proof stress was determined graphically from the stress-strain graph.

Figure 3.20: The JJ Universal Tensile Testing Machine.

3.5.2.4 Determination of Impact Energy from Charpy-type Test

The purpose of carrying out the impact test of the fabricated parts was to determine the impact energy of the materials. Energy required to fracture the fabricated test parts

under the impact loading condition was measured. The test was carried out on a Avery charpy impact testing machine using a 150J pendulum.

3.5.3 Determination of the Microhardness of the Laser-Sintered Parts

A Struers Duramin micro-hardness tester was employed to determine the Vicker hardness of all laser sintered parts. A load of 0.1 kgf and an indentation time of 15 s was used for all tests. Test samples were hot mounted in Bakelite, ground, polished and etched, as described in Section 3.3.1.1, in order to reveal the phases present. The specimen was placed normally to the axis of the indenter on a flat and hard surface. Having located a representative location on the specimen for testing, the indentations were spaced so that the distance between indents or a free surface was at least twice the shorter diagonal or twice the extent of any deformation that appeared on the surface of the specimen. The indentation was observed at 500x magnification for possible defects and only results where the two sections of each diagonal agreed within 20% of each other were recorded.

3.6 Conclusion

This chapter outlines the testing of the materials' bulk properties and its preparation for microstructural characterisation, description of SLS equipment, experimental procedures, mixing time and laser power output calibration procedures as well as the methods of design, fabrication and measurement of properties of the mechanical test specimen.

CHAPTER FOUR FABRICATION OF ALUMINIUM POWDERS IN SINGLE LAYERS

4.1 Introduction

The main focus of this chapter is the presentation of results detailing the microstructure and properties of the as-received monosized powders (AL-1, AL-2, AL-3, AL-4 and AL-5) and their sintering response in single layer coupons. The effects of varying composition, powder properties and laser processing conditions on the laser sinterability, liquid phase sintering, surface morphology and spheroidisation of aluminium powders is hereby presented. The results and analysis of the measurement of the physical properties, and chemical composition of the as-received powders is presented first (section 4.2). This is followed by the results of the powder mixing time calibration for the same set of five powders (section 4.3). Thereafter, results of the observation of the surface morphology and measurements of agglomerate sizes for single layer samples and its implications for the single layer scanning are also presented in section 4.4. This gives the detailed description of the processing maps for each aluminium powder, effects of the processing parameters, powder's shape and chemical composition on the surface morphology, agglomerate development and laser sinterability of aluminium powders.

4.2 Properties of the As-received Powders

The results of the flowability tests, apparent and tapping densities measurements, and sieve analysis of the powders are presented in this section.

4.2.1 Sieve Analysis and Particle Size Measurement of Powders AL-1 through AL-5

The particle size distribution of the as-received monosized powders obtained by sieving is presented in Table 4.1. This reveals that the particle size distribution of all the powders falls within the range of +45 to-75 μm as expected.

Table 4.1: Particle distribution of the as-received aluminium powders.

Powder Designation	+90 (μm)	+75 (μm)	+63 (μm)	+53 (μm)	+45 (μm)	-45 (μm)
	% Distribution					
AL-1	0.40	0.40	33.50	62.30	3.10	0.30
AL-2	0.20	0.20	43.70	52.70	3.00	0.20
AL-3	0.10	0.10	63.80	33.00	2.90	0.10
AL-4	0.10	0.10	81.70	16.00	1.80	0.30
AL-5	0.10	0.10	38.90	59.30	1.50	0.10

4.2.2 Scanning Electron Microscopy (SEM) Observation of Aluminium Powders Particle Shape

SEM images of the aluminium powders are presented in Figures 4.2a-e. It can be seen that samples AL-1, AL-3, and AL-4 (Figures 4.1a, c and d) have irregular particle shapes, AL-2 powder has near spherical particles (Figure (4.1b) while sample AL-5 (Figure 4.1e) consists mainly of spherically shaped particles. Moreover, a careful observation of samples AL-1, AL-2, AL-3 and AL-4 suggests the presence of oxide clumps or islands on the surfaces of the particles of these powders (see the arrows in Figures 4.1a to d). In contrast, the surfaces of the particles of AL-5 are noted to be smooth. It is hereby speculated that the thickness of the oxide films present on the AL-5 powder is more uniform and is likely to have lesser content of oxygen than other powders. The implication of the nature of the oxide film on sintering behaviour will be discussed later in section 5.3.

4.2.3 Chemical Composition of the As-received Powders

The energy-dispersive spectrum acquired in area scan mode for each powder sample AL-1 to AL-5 is shown in Appendix H. Only elemental aluminium (Al) and oxygen (O) were detected in samples AL-1 and AL-2; Al, magnesium (Mg) and O were detected in samples AL-3 and AL-4 while Al, silicon (Si) and O were detected in sample AL-5.

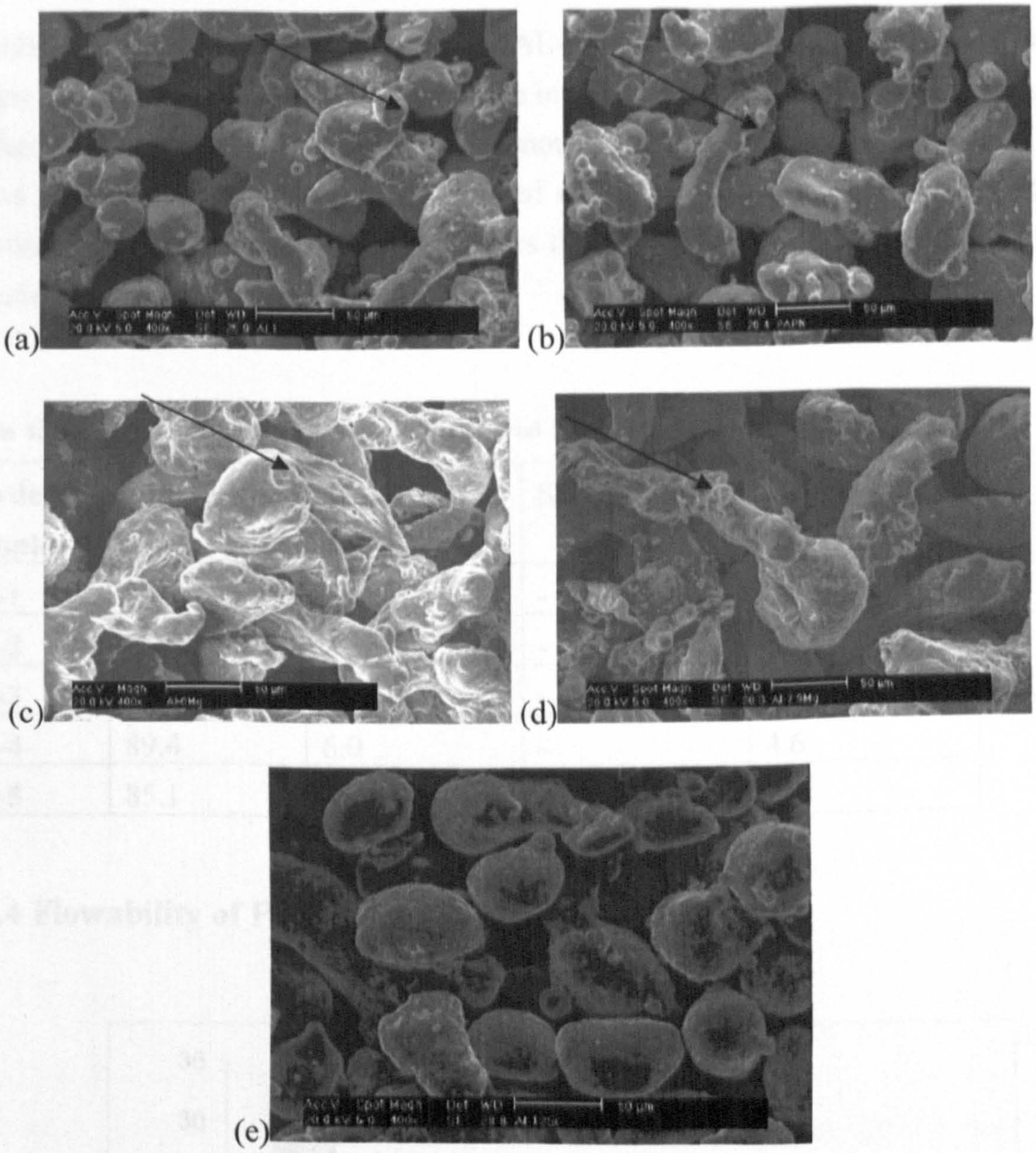

Figure 4.1: SEM images showing the particle shapes of the as-received monosized aluminium powders: (a) AL-1; (b) AL-2; (c) AL-3; (d) AL-4 and (e) AL-5. Oxide islands on the surfaces of particles of AL-1, AL-2, AL-3 and AL-4 are identified by the arrows.

The EDS spectra for the major elements in each of the powder correlate with the major elemental composition indicated by the suppliers. Note that the failure to detect Fe, Cu, and other minor elements in the energy-dispersive spectrum (see Table 3.2) taken is because the total amount of these elements is below the detection limit of the EDS technique. Moreover, the non-inclusion of the oxygen content in the manufacturer's powder's composition and the variation in the Mg content in AL-4 when investigated by EDS could probably be attributed to the wet analytical technique (atomic absorption spectrometry AAS) employed by the powder's manufacturer. As explained in section 3.3.2.3, due to ZAF correction factor of ±16wt% great caution needs to be exercised with the quantitative oxygen values reported in this study. Meanwhile, Table 4.2 confirms the earlier speculation (section 4.2.2) that the presence of oxide clumps or

islands on the particles of AL-1, AL-2, AL-3 and AL-4 suggests the tendency for higher oxide contents in these powders than in AL-5 particles observed to have smooth surface. The presence of a much higher amount of oxygen in sample AL-1 than that found in the other samples should be noted as the amount of oxygen present in the powders is expected to be one of the factors that influence both the properties and the sintering response of the powders.

Table 4.2: Elemental Composition of the Powdered Samples by EDS Analysis (weight %).

Powdered Samples	Aluminium	Magnesium	Silicon	Oxygen
AL-1	84.1	-	-	15.9
AL-2	93.5	-	-	6.5
AL-3	89.3	5.7	-	5.0
AL-4	89.4	6.0	-	4.6
AL-5	85.1	-	12.1	2.8

4.2.4 Flowability of Powders AL-1 through AL-5

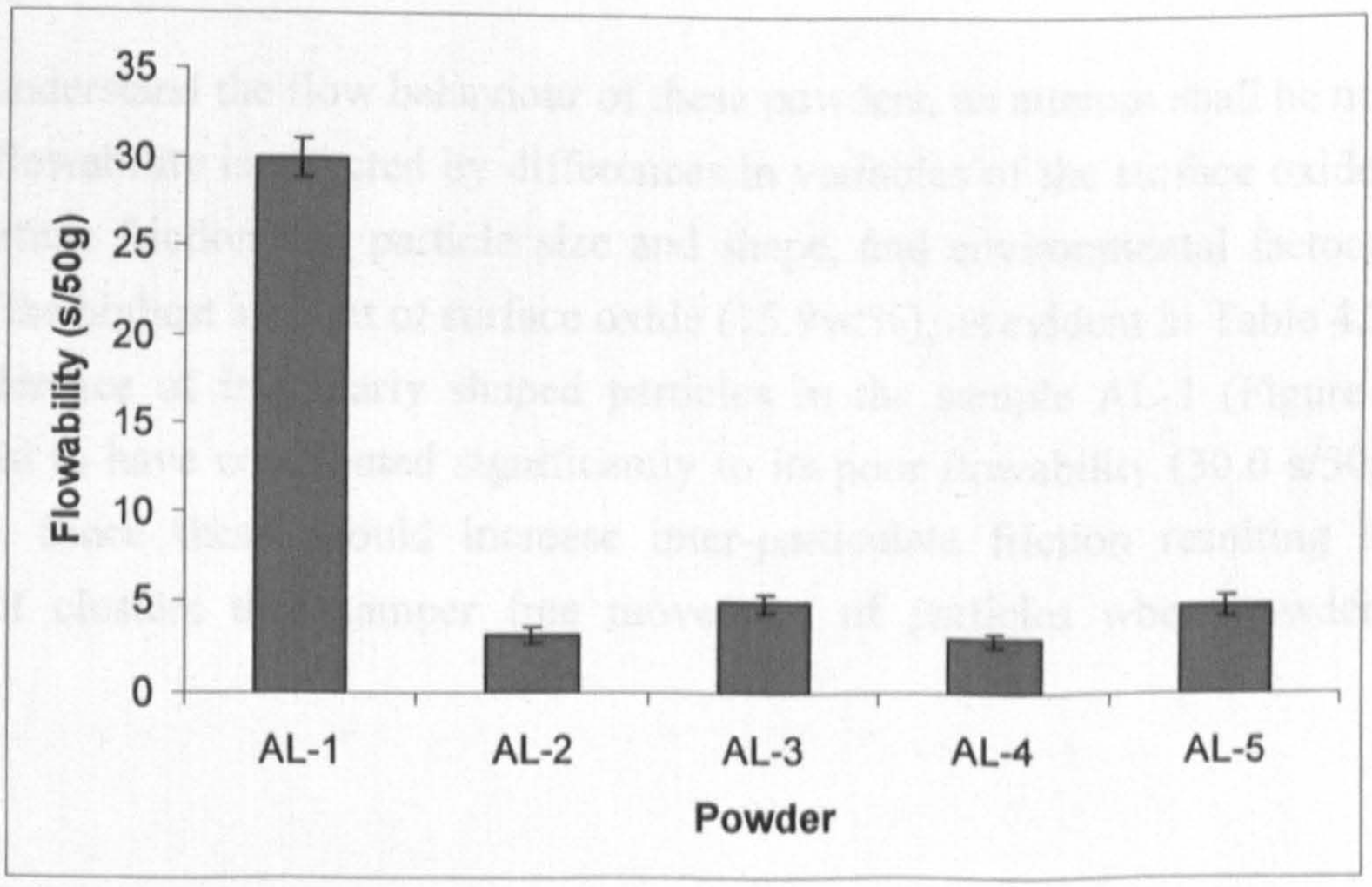

Figure 04.2: Flowability of the original aluminium powders.

Flowability results for the aluminium powders AL-1 through AL-5 are presented in Figure 4.2. The standard deviation based on five measurements varies between 3.59 % and 14.39 % and these are shown as error bars in the Figure 4.2. All the powders, with

the exception of AL-1, could be described as free flowing since their flowability is 5 s/50g or less. The details of experimental records taken for flowability of the original powders are presented in Table A1 (Appendix A).

4.2.5 Apparent Density and Tap Density of the Powders through AL1 to AL-5

The apparent densities of the powders are presented in Figure 4.3 together with the standard deviation, which varied from 3.50 % to 8.50 %. The apparent densities of these powders range from 38.62 % to 52.68 % (1.04 g/cm^3 to 1.42 g/cm^3) of the density of wrought aluminium. The details of experimental records taken for apparent densities are presented in Appendix A. Meanwhile, the results of the tapping density of the powders are presented in Figure 4.4. Error bars are included which represent the standard error in mean over five measurements. The details of the experimental records taken for tapping densities are presented in Appendix A.

4.2.6 Effect of Powders' Characteristics on the Physical Properties of the Powders

In order to understand the flow behaviour of these powders, an attempt shall be made to relate how flowability is affected by differences in variables of the surface oxide film, the inter-particle friction, the particle size and shape, and environmental factors. The presence of the highest amount of surface oxide (15.9wt%), as evident in Table 4.2, and the preponderance of irregularly shaped particles in the sample AL-1 (Figure 4.1a) could be said to have contributed significantly to its poor flowability (30.0 s/50g, see Figure 4.2). Since these should increase inter-particulate friction resulting in the formation of clusters that hamper free movement of particles when powders are flowing.

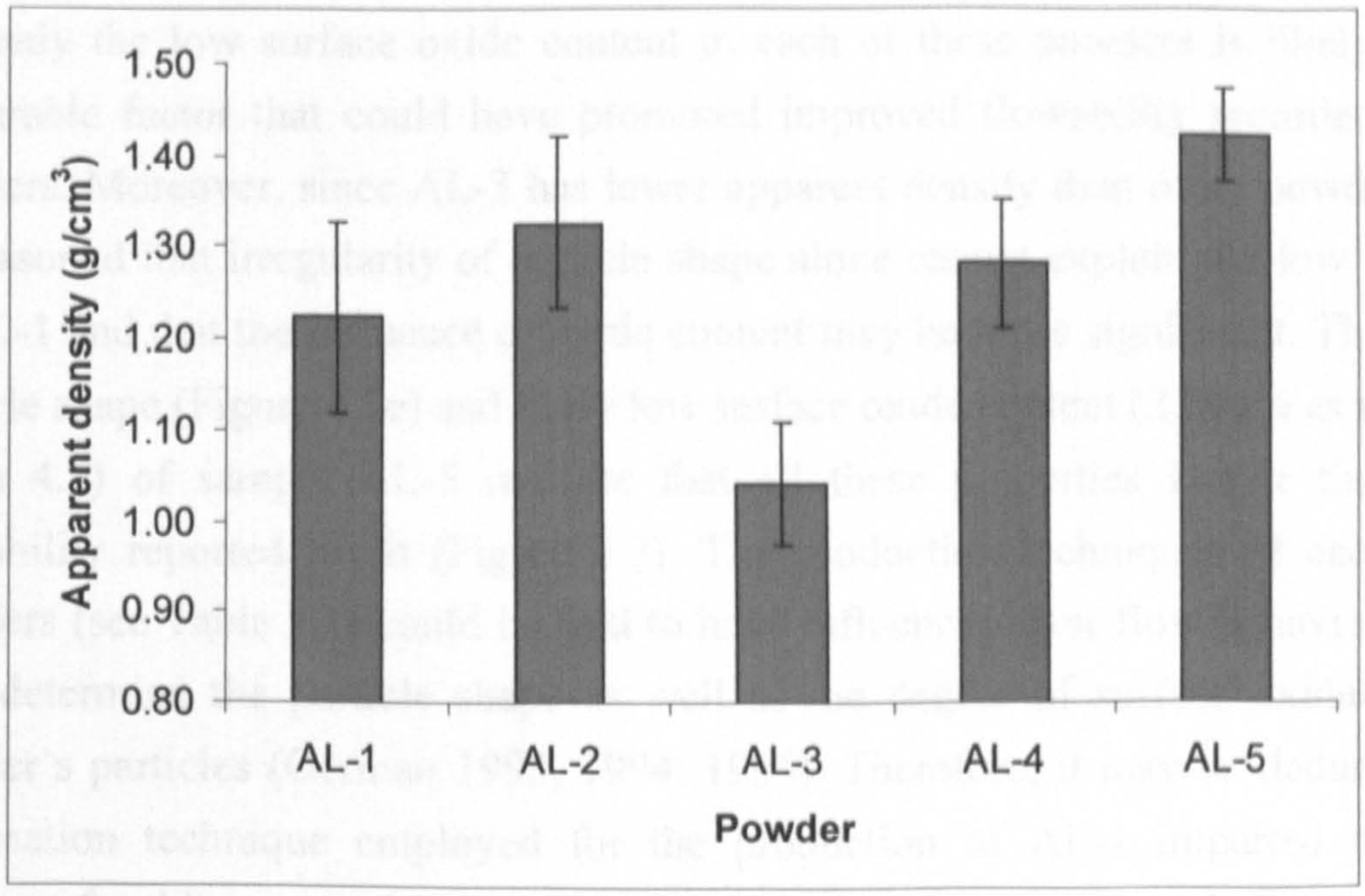

Figure 4.3: Apparent density of the original aluminium powders.

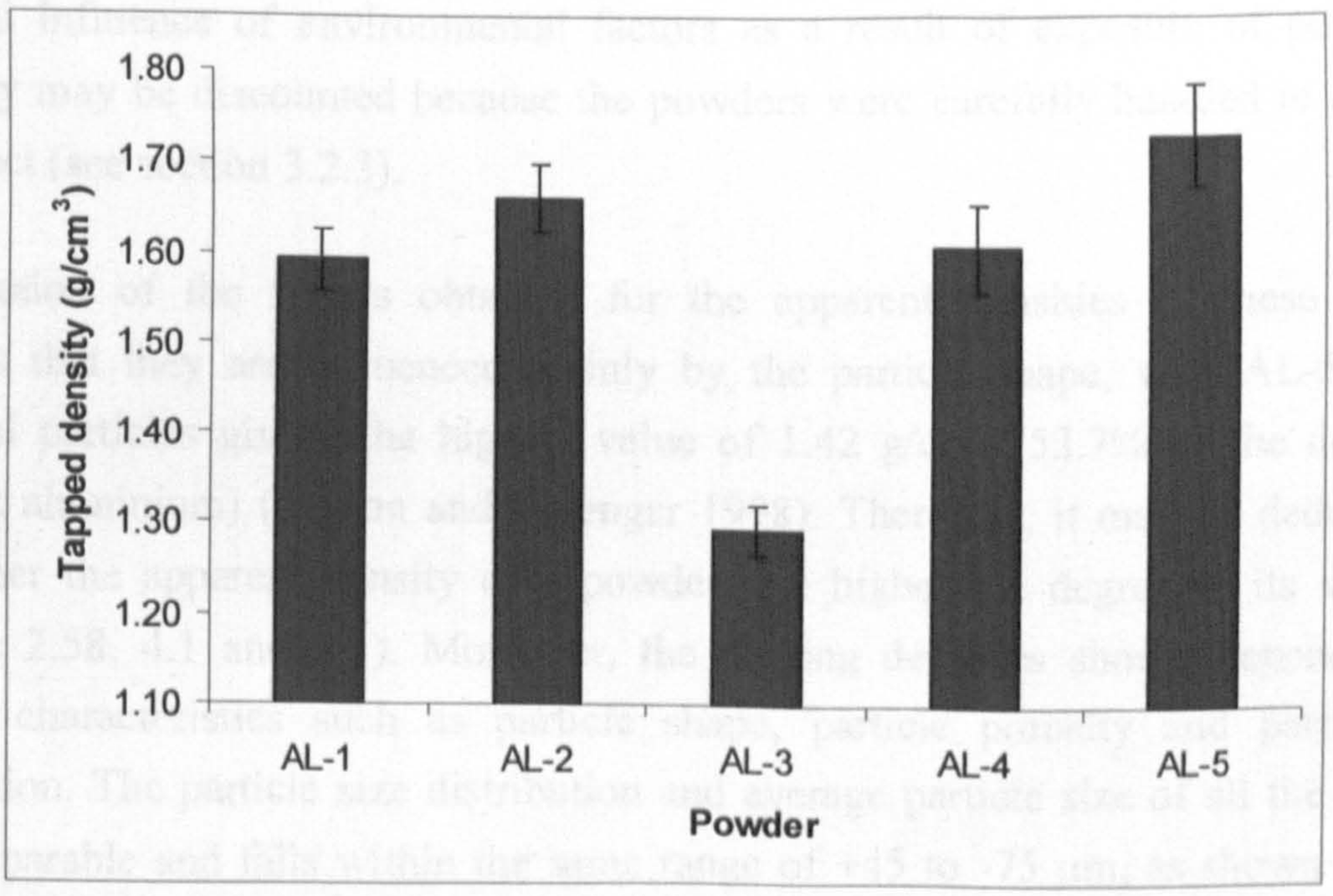

Figure 4.4: Tapping density of the original aluminium powders.

In contrast to the poor flowability of AL-1, the excellent flowability of samples AL-2, AL-3, AL-4 and AL-5 could be explained as a consequence of lower amount of surface oxide film (see Table 4.2) present on the surfaces of the particles and of their sphericity. For example, samples AL-2, AL-3, and AL-4 have irregularly shaped powder particles (Figures 4.1b, c, and d), and very low surface oxide present (6.5wt%, 4.6wt% and 5.0wt% respectively as presented in Table 4.2). Perhaps, the rationale is

that only the low surface oxide content in each of these powders is likely to be the favourable factor that could have promoted improved flowability recorded for these powders. Moreover, since AL-3 has lower apparent density than other powders, it may be reasoned that irregularity of particle shape alone cannot explain the low flowability of AL-1 and that the influence of oxide content may be more significant. The spherical particle shape (Figure 4.1e) and fairly low surface oxide content (2.8wt% as recorded in Table 4.2) of sample AL-5 indicate that all these properties favour the excellent flowability reported for it (Figure 4.2). The production techniques of each of these powders (see Table 3.1) could be said to have influenced their flow behaviour because they determine the particle shape as well as the degree of surface oxidation of the powder's particles (German 1993, 1994, 1996). Therefore, it may be deduced that air atomisation technique employed for the production of AL-1 imparted the highest amount of oxidic contamination on its particles when compared with water (AL-3 and AL-4) and gas (AL-2 and AL-5) atomisation techniques. In conclusion, these findings suggest the most predominant factor controlling the flowability of aluminium powders is the amount of surface oxide present on the particle's surface in the powder. The potential influence of environmental factors as a result of exposure of powders to humidity may be discounted because the powders were carefully handled to minimise this effect (see section 3.2.3).

Examination of the results obtained for the apparent densities of these powders suggests that they are influenced mainly by the particle shape, with AL-5, having spherical particles giving the highest value of 1.42 g/cm^3 (52.7% of the density of wrought aluminium) (Carson and Pittenger 1998). Therefore, it may be deduced that the higher the apparent density of a powder, the higher the degree of its sphericity (Figures 2.58, 4.1 and 4.3). Moreover, the tapping densities should depend on the powder characteristics such as particle shape, particle porosity and particle size distribution. The particle size distribution and average particle size of all the powders are comparable and falls within the same range of +45 to -75 μm, as shown in Table 4.1, so this may be excluded. Figure 4.5 reveals that as the apparent density increases, tapping density also increases whereas Table 4.3 shows that the lower the apparent density, the higher the percentage increases in density on tapping. These findings imply that irregularly shaped powder particles found in samples AL-1 to AL-4 which have lower apparent and tapping densities do bridge or arch during loose packing. Upon tapping, re-arrangement of particles can overcome this, leading to a significant reduction in porosity. In the case of sample AL-5, a smaller percentage increase in density was obtained upon tapping. This is easily explained by the fact that its spherical particles pack more closely, without bridging or arching, as the particles move easily

past each other because of their smooth surfaces as observed in the high flowability values (see section 4.2.4).

Table 4.3: Comparison of Density Increases for the Original Powders.

Powder Designation	Apparent Density (g/cm^3)	Tap Density (g/cm^3)	% Increase
AL-1	1.22	1.59	30.20
AL-2	1.32	1.66	25.42
AL-3	1.04	1.30	24.26
AL-4	1.28	1.61	25.53
AL-5	1.42	1.73	21.75

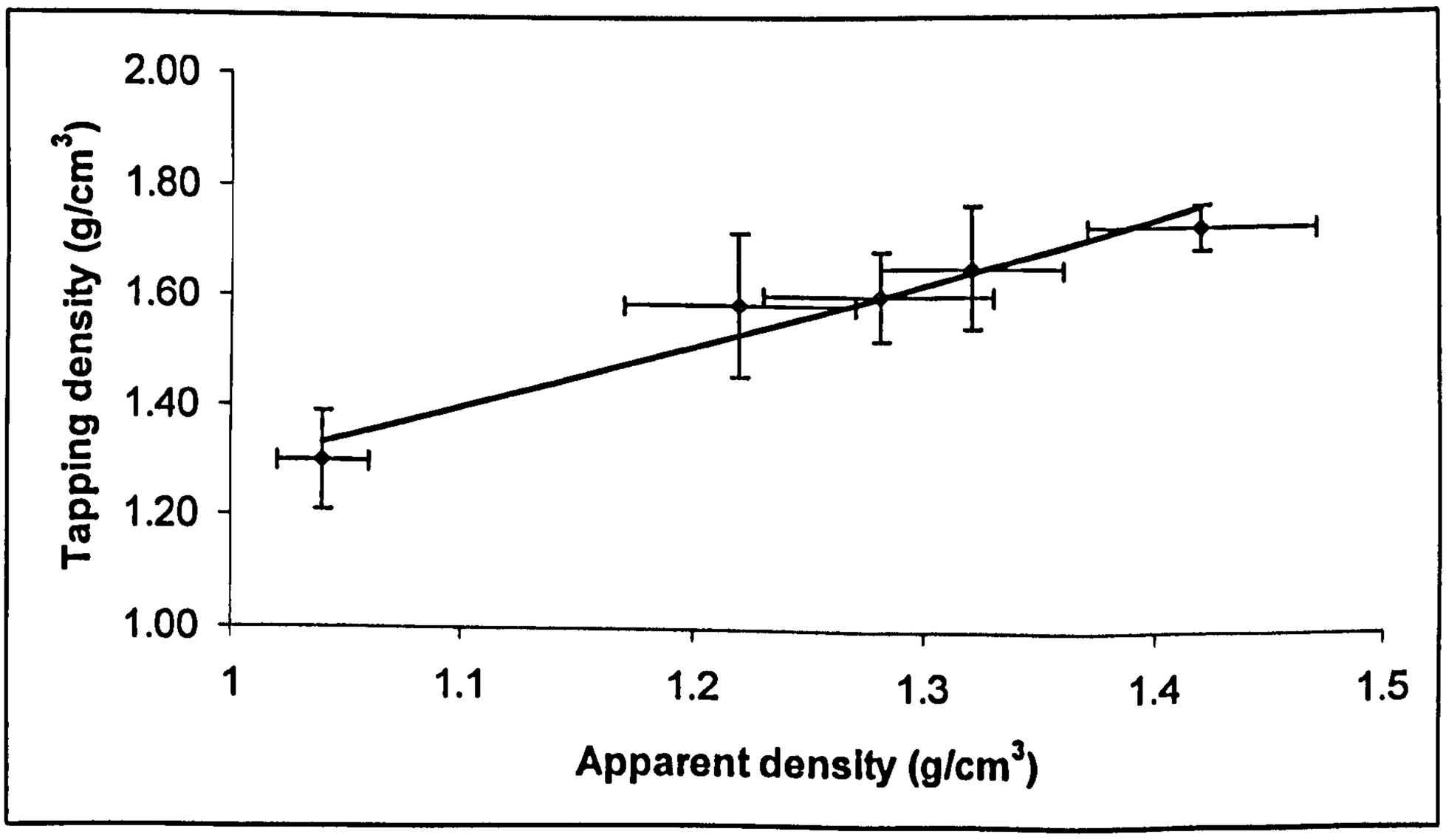

Figure 4.5: Comparison of apparent and tapping densities of the original powders.

4.3 The Results of Powder Mixing Time Calibration

All the individual measurements made to ensure calibration of powder mixing time are presented in Tables B1 to B9 (Appendix B). The results showing the variation in the average bed density with the duration of mixing for each of the five monosized as-received aluminium powders, and the blended bimodal powders are shown in Figures

4.6 and 4.7 respectively. The length of the error bars represents the variability in the results for all samples, including those taken from different depths within the storage container. It is clear from Figure 4.6 that the results for each of the as-received aluminium powder batches are similar, revealing a peak in the average powder bed density, and a minimum in density variation, after ten minutes of mixing. By contrast, Figure 4.7 shows that the bed density for the bimodal powder mixtures peaks at a mixing time of 20 minutes. Although, the powder bed density decreases as the mixing time increases beyond the peak, this fall is not as sudden as the initial increment between the starting time and the peak time. It would appear that the longer mixing time required for the bimodal powder mixtures is a result of the difficulty encountered by the smaller particles added in percolating through the available interstices of the parent powder, AL-5. These results differ from the findings of Eane (2002) who reported that the bed density of both monosized and bimodal stainless steel powders peaked at the same calibrated mixing time of 15 minutes. However, critical examination of Eane's work reveals that the monosized and bimodal powders which he studied both had a wider particle size distribution than the aluminium powders used in this research.

The maximum variation in bed density occurs in as-received samples and generally rises with mixing time for both monosized and bimodal powders. The maximum noted for the unmixed powders could be attributed to particle segregation as a consequence of transportation and prolonged storage. The continuing increase in variation up to 60 minutes could be ascribed to over mixing, which triggers particle re-segregation. These findings are strongly supported by German (1998) and Hauser (2003) who both claimed that, provided the mobility and density of powder particles vary as a consequence of their forms and sizes, the influence of external forces may cause segregation.

In addition, Figure 4.6 shows that the average powder bed density recorded at each mixing time interval decreases as the particle shape of the powder becomes less spherical, but the variation decreases. According to Hauser, (2003), the variation in powder bed density increases as the average powder bed density decreases for corresponding mixing time as the batch powder sizes decreases. The discrepancy between the relationship of the variation in the powder bed density with average powder bed density for powders of varying particle shapes employed in this research, and that of Hauser (2003) could be attributed to problems of powder deposition. A cursory look through Tables B1 to B5 in Appendix A shows that values obtained for powder bed density at some instances for all the powders are only slightly higher than their reported apparent densities. In these cases, it is suspected that the powder

deposition mechanism might have not properly delivered the powder to enable efficient packing across the powder bed. Therefore, it may be suggested that the improper and inconsistent delivery and packing of powder's particles across the powder bed appears to have affected the variations obtained in the powder bed density such that no definite relationship could be established between the variation in the powder bed density and the average powder bed density of the experimental powders. It is now evident that the discrepancy between the relationship of the variation in the powder bed density with average powder bed density for powders may be explained by the differences in the powder packing behaviour in the bed as a consequence of lesser degree of powder's particle sphericity and increasing surface oxide content of the powders. For AL-1, the combined effects of lower degree of particle sphericity (section 4.2.5) and highest oxide content (section 4.2.3) are responsible for non-existence of a relationship of the variation in the powder bed density with its average powder bed density. In the case of AL-3, its lowest degree of particle sphericity as evident by its apparent density (see section 4.2.5) could explain the same behaviour it had displayed as AL-1. It is now clear that the higher the sphericity of the particle shape of a powder, the higher the likelihood of the increased variation in the powder bed density with average powder bed density as seen in the case of AL-2, AL-3 and AL-4. This is because higher degree of sphericity of powder's particle provides for close packing of the particles in bed without arching or bridging, during powder deposition.

In the case of the bimodal powders (Figure 4.7) containing a preponderance of spherically shaped powder particles (AL-5), it can be seen that the average powder bed density increases as the average particles sizes of the additive powder reduces (AL-5/AL-2 > AL-5/AL-6 > AL-5/AL-7 > AL-5/AL-8) and the variation in the powder bed density decreases. This finding again contradicts the outcome of similar studies carried out by Hauser (2003), reported in the last paragraph. The introduction of the additive powders AL-2, AL-6, AL-7 and AL-8, of varying particle sizes, into the parent powder AL-5 is suspected to have aided the powder packing efficiency of the blended powders, thereby eliminating the shortcomings of the deposition mechanism in this instance. Therefore, it may be argued that the optimisation of the average bed density with the lowest possible variation could only be achievable when additive powders of appropriate particle sizes are blended with the parent powder AL-5. The effect of blending additive powders of varying particle sizes and distribution with powder AL-5 will be discussed in detail in chapters six and seven of this thesis.

.

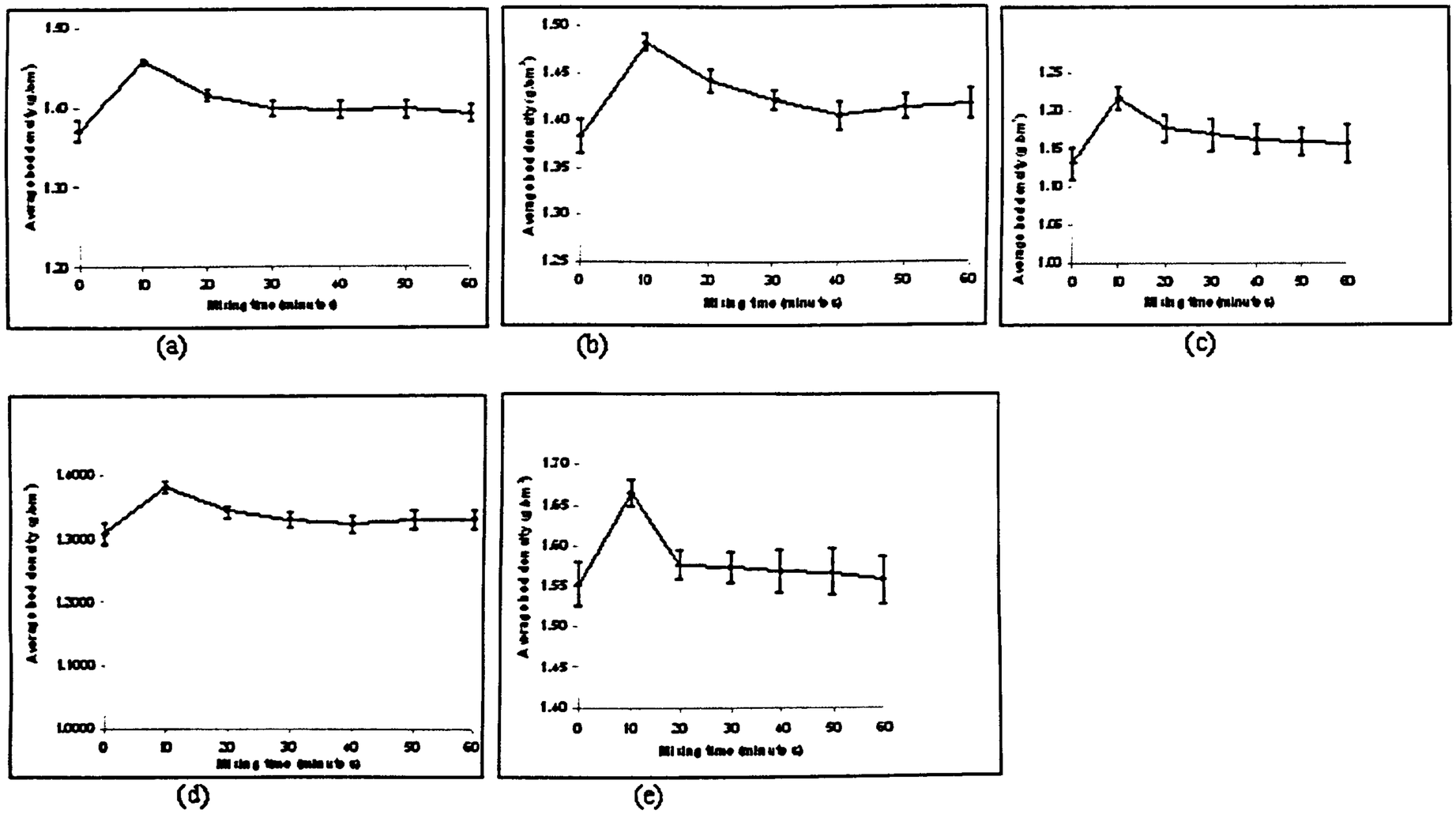

Figure 4.6: Average powder bed density as a function of mixing time for monosized powder batches (a) AL-1 (b) AL-2 (c) AL-3 (d) AL-4 (e) AL-5.

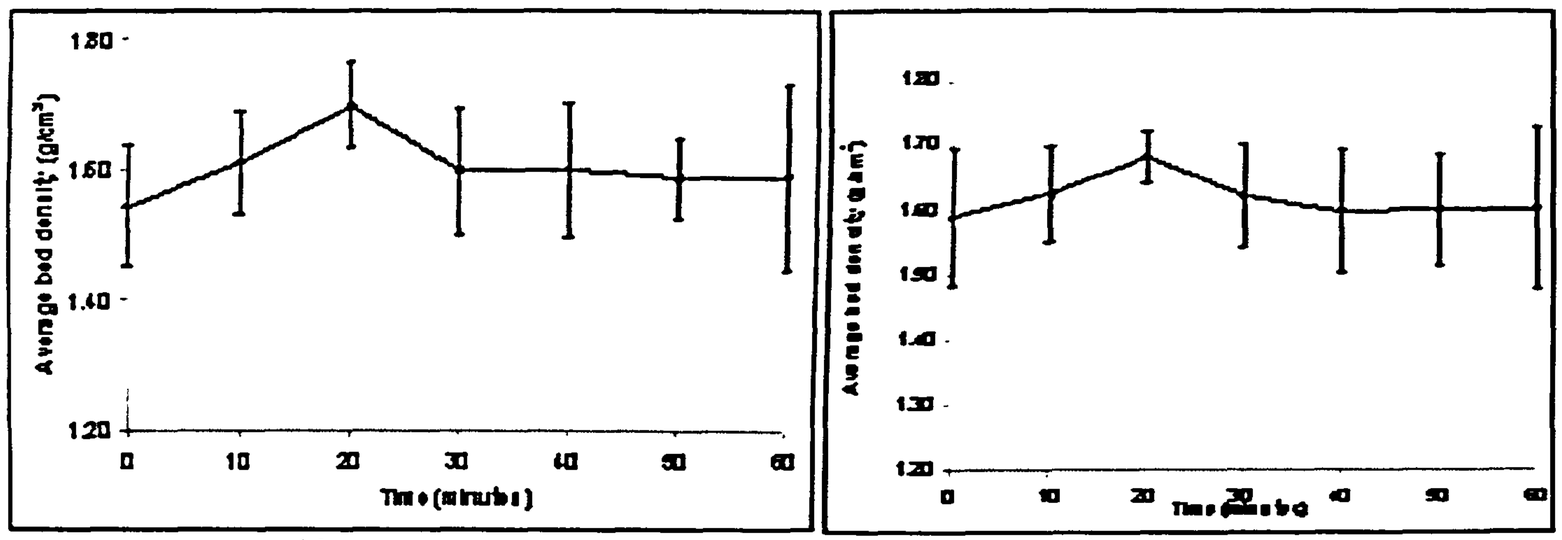

Figure 4.7: Average powder bed density as a function of mixing time for the blended powder batches (a) 50%AL-5/50AL-2 (b) 50%AL-5/50AL-6 (c) 50%AL-5/50AL-7 (d) 50%AL-5/50AL-8.

As noted in section 3.2.4, the basis of the findings from these powder mixing time experiments, monosized powder samples of AL-1, AL-2, AL-3, AL-4 and AL-5 were mixed for ten minutes before processing in the sinter station while twenty minutes mixing duration was adopted for all bimodal and tri-modal powders, irrespective of component ratio. These choices were made in order to give the least variability between the deposited powder layers. The choice of these powder mixing durations was not made on the premise of the highest bed density because this is largely indeterminate during the SLS/SLM process, as pointed out by Hauser (2003).

4.4 Results of Single Layers Experiments on SLS of As-received Powders

The results of the sintering response of the AL-1, AL-2, AL-3, AL-4, and AL-5 powders under argon atmosphere as a function of process parameters (laser power, scanning rate, and scan spacing) are presented in this section.

4.4.1 Macrostructure of Layer Surfaces

Figures 4.8, 4.10, 4.12, 4.14, and 4.16 show the images of single layer specimens as-sintered on the sintering plates for powdered samples AL-1, AL-2, AL-3, AL-4, and AL-5, respectively. Layer surfaces for AL-1, AL-2, AL-3 and AL-4 were noted to be grey in colour irrespective of the processing parameters adopted whereas those of AL-5 appeared yellowish in colour. For AL-5, it was noted that the intensity of "yellowishness" of the surfaces increases as more material appeared to have been melted. For AL-1 through AL-5, it was noted that the surface quality of sintered specimens varied across the regions on the sintering plates as the processing parameters varied. For example, when scan rates of 80 mm/s or less was adopted at high laser powers, surface quality were noted to be very poor and characterised with balls formation resulting from molten particles. Moreover, the degree of protrusion of "first line scan balling" (FLSB) effects over the layer surface was observed to be very high for this range of processing parameters. Evidence of molten particles abound in the sintered specimens and accompanied by improved surface quality of the sintered specimens as the scan rates were increased from 80 mm/s to 250 mm/s. In addition, the degree of protrusion of FSLB over layer surface in this range of processing

parameters was noted to have reduced significantly such that it is at the same level with the surface of the sintered specimen. As the laser power reduced from 200 W to 50 W at high scan rates, it was noted that the preponderance of unmelted particles occurred in the sintered specimens with the surface qualities appearing to be finer and the FSLB effect was not noticeable. As the laser power is less than 50 W, and the scan rate is increasing, it was evident that a most of the particles in the sintered specimens had not been melted and the surface quality of specimens remained finest over the same range of laser power with no formation of FSLB effect.

4.4.2 Processing Maps for Single Layer Fabrication of As-received Powders

The results of the images obtained on the sintering plates of AL-1, AL-2, AL-3, AL-4 and AL-5, are transferred onto processing maps in Figures 4.9, 4.11, 4.13, 4.15 and 4.17, respectively. The regions in the processing maps are categorised and described qualitatively. The nodal arrays on each processing map are the experimental points used in the construction of the processing maps. A comparison of the processing windows developed for each of the as-received monosized aluminium powders reveals that their sintering responses appear to have followed a similar trend but the optimum processing window for each powder is different. Four regions of behaviour could be identified for all powders: no marking, partial marking, minimal balling, and excessive balling. These regions are discussed in more detail in the following sections.

4.4.2.1 Region of No Marking

The region of no marking appeared on each of the processing maps (Figures 4.9, 4.11, 4.13, 4.15 and 4.17) and is separated by diagonal f-a from the region of partial marking to the right. The boundary f-a indicates that a critical value of energy density of 2 J/mm^2 must be attained for all powder samples AL-1, AL-2, AL-3, AL-4, and AL-5 before their particles will react with impinging laser beam. In all the processing maps, (Figures 4.9, 4.11, 4.13, 4.15 and 4.17), it evident that the minimum laser power required for the powder particles to react with the laser beam is 50 W. Although, the processing maps do not reveal the sintering responses of the powders for scanning rates greater than 250 mm/s at the range of laser powers (20-240 W) studied, it was noted during the experiments that this region broadens as scan rates increase from 200 to 500 mm/s for all laser power studied.

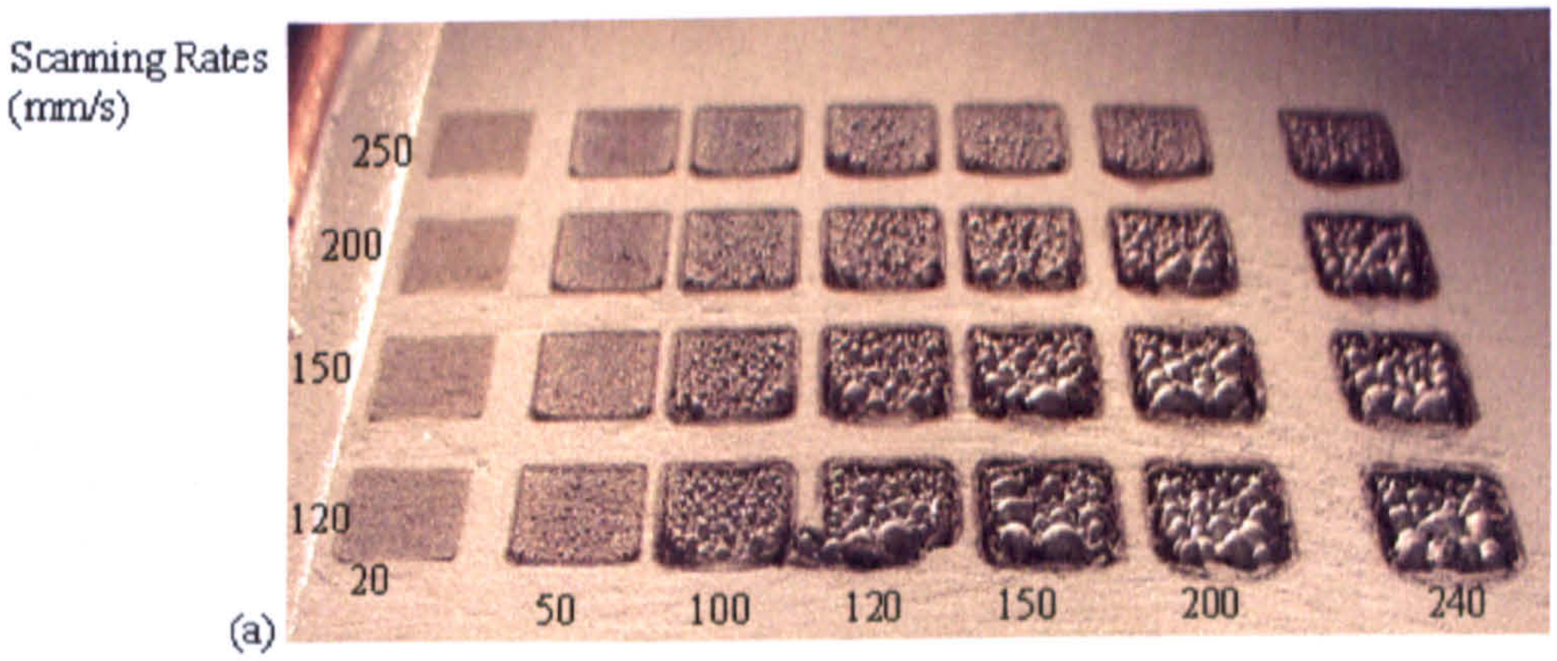

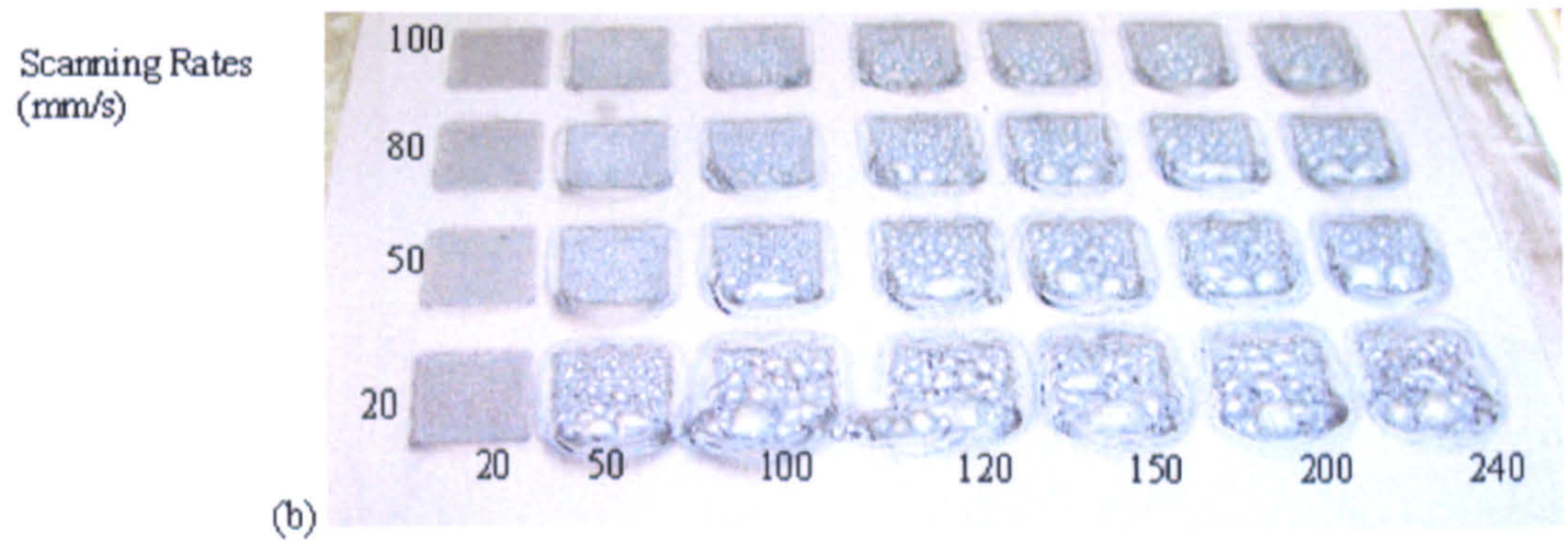

Figure 4.8: Images of single layers, as sintered on the plates, made in AL-1 powder with varying processing conditions (a) Single layer scanning at 120-250mm/s over 20-240W laser power range and scan spacing 0.1mm. (b) Single layer scanning at 20-100mm/s over 20-240W laser power range and scan spacing 0.1mm.

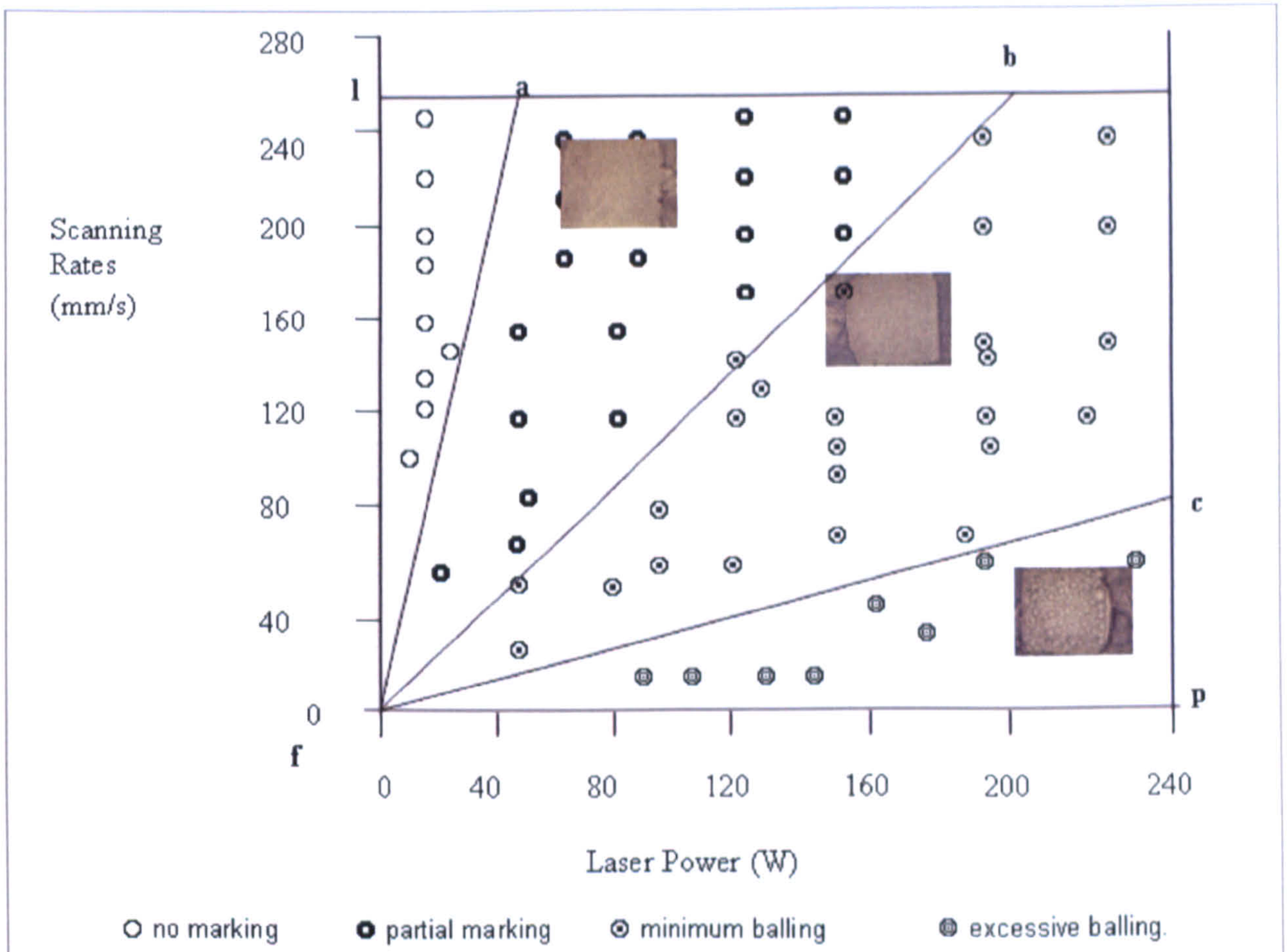

Figure 4.9: Processing window for single layer parts made in AL-1 developed from Figure 4.8.

(Note: Reciprocals of slopes f-a, f-b, and f-c, were computed and multiplied by the reciprocal of scan spacing (0.1 mm) in order to obtain the applied energy density).

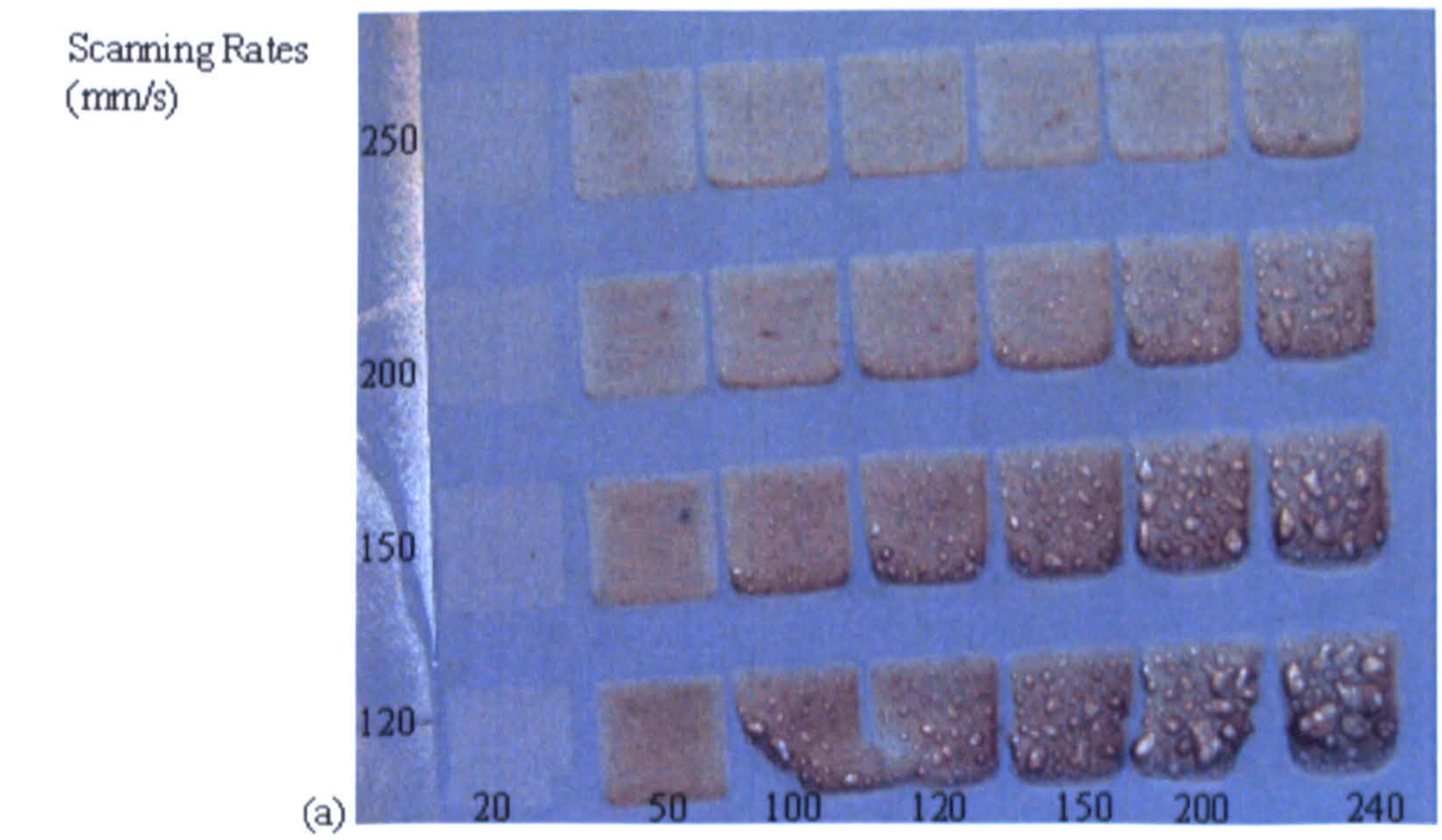

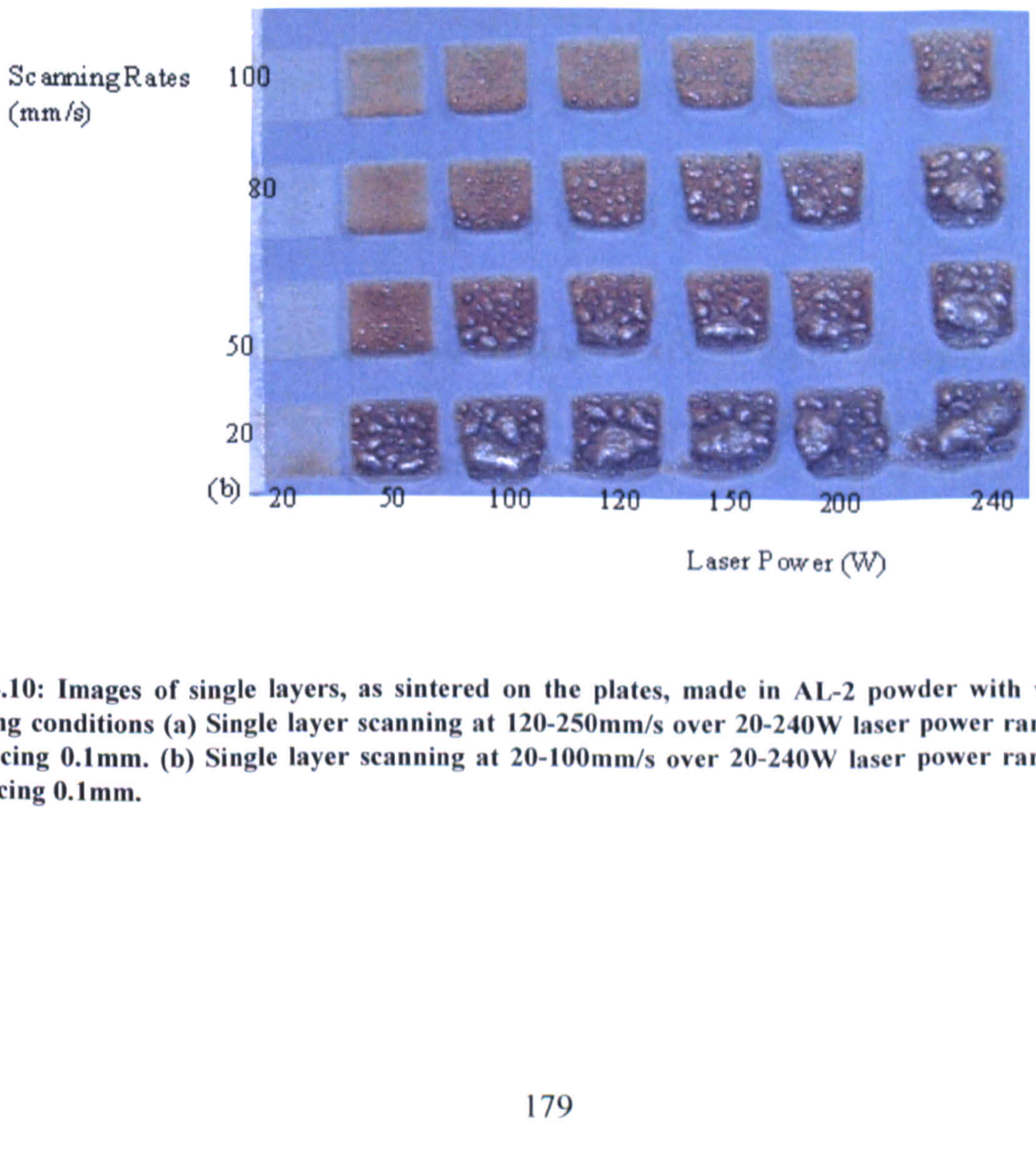

Figure 4.10: Images of single layers, as sintered on the plates, made in AL-2 powder with varying processing conditions (a) Single layer scanning at 120-250mm/s over 20-240W laser power range and scan spacing 0.1mm. (b) Single layer scanning at 20-100mm/s over 20-240W laser power range and scan spacing 0.1mm.

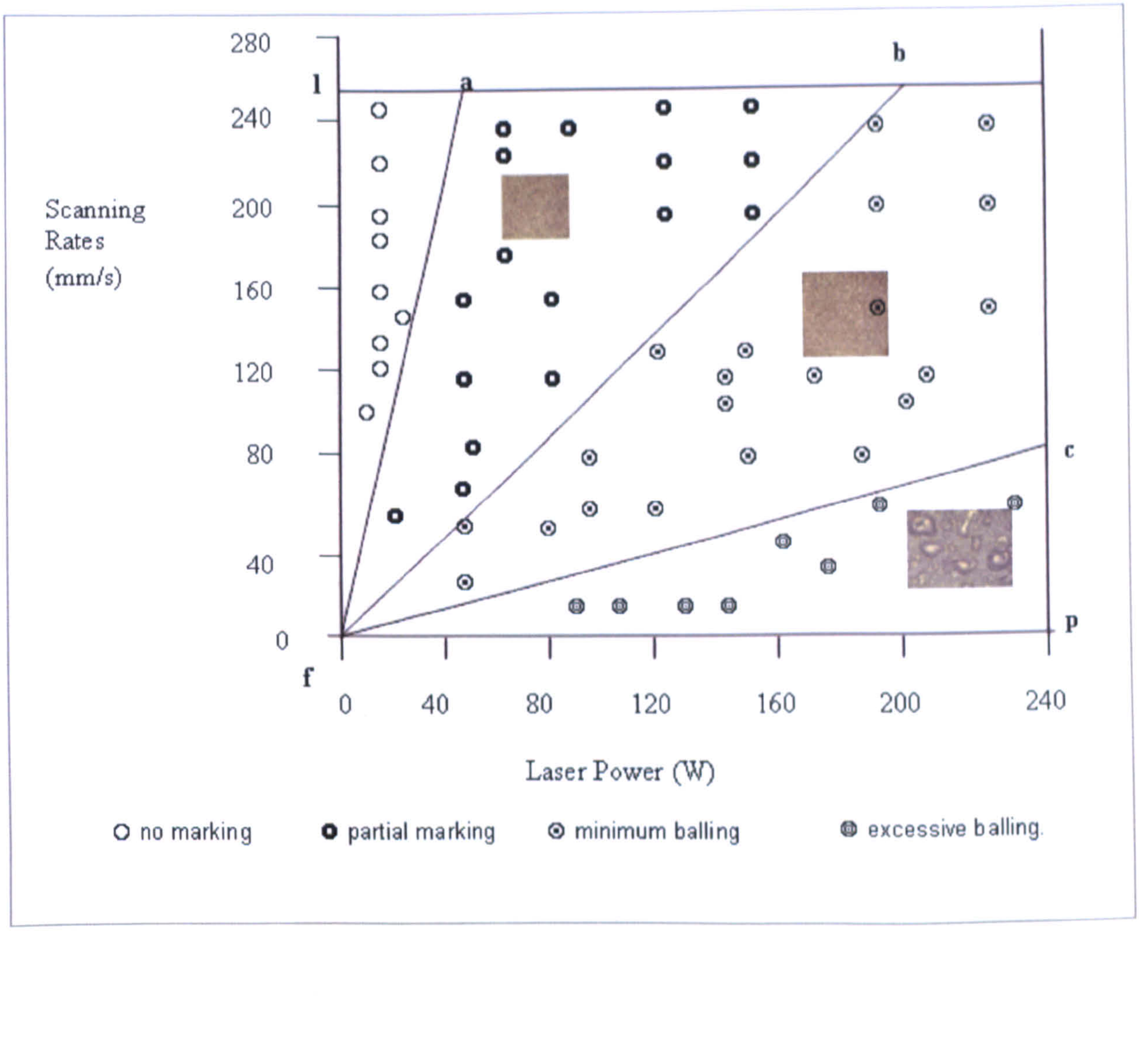

Figure 4.11: Processing window for single layer parts made in AL-2 developed from Figure 4.10.

(Note: Reciprocals of slopes f-a, f-b, and f-c, were computed and multiplied by the reciprocal of scan spacing (0.1 mm) in order to obtain the applied energy density).

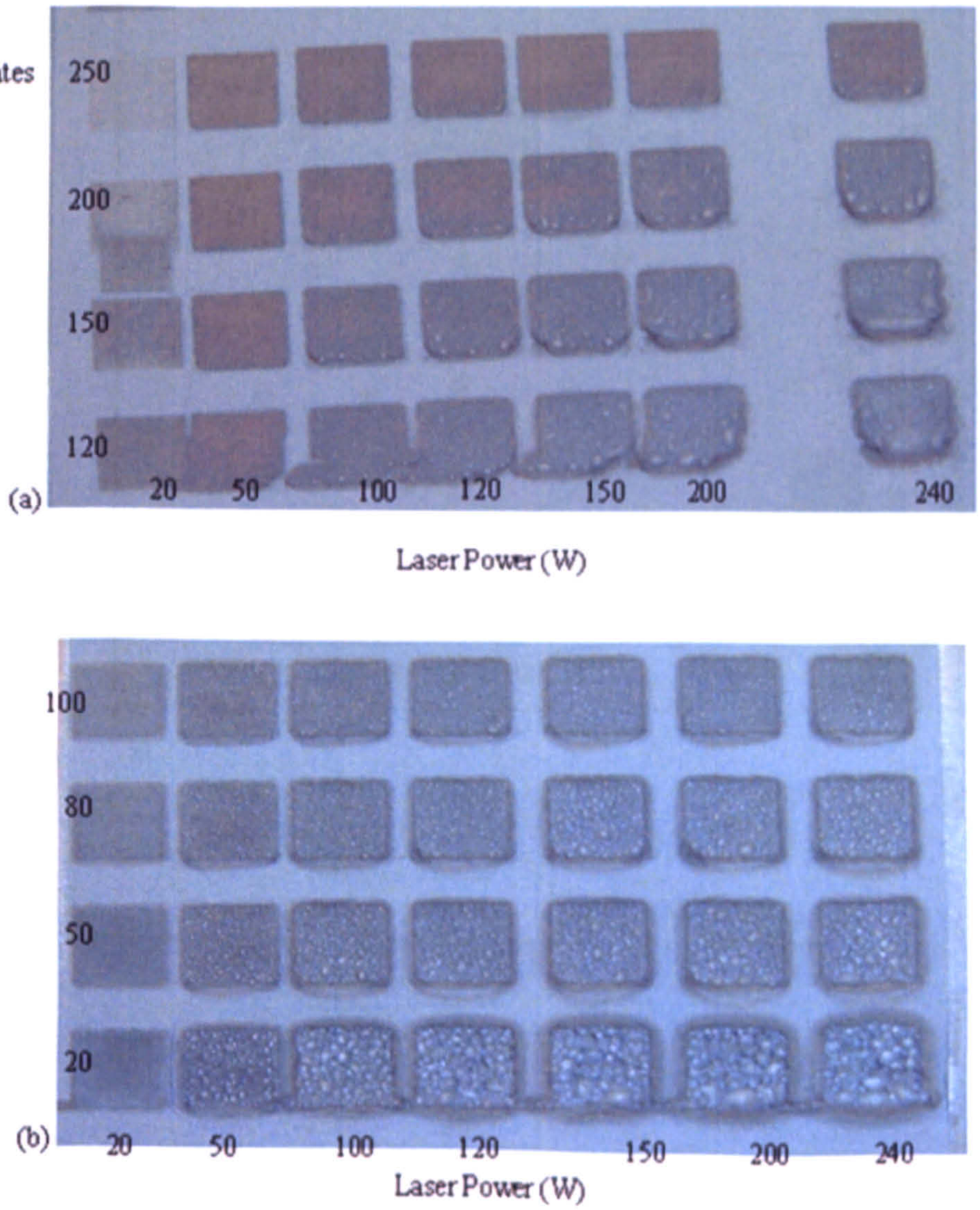

Figure 4.12: Images of single layers, as sintered on the plates, made in AL-3 powder with varying processing conditions (a) Single layer scanning at 120-250mm/s over 20-240W laser power range and scan spacing 0.1mm. (b) Single layer scanning at 20-100mm/s over 20-240W laser power range and scan spacing 0.1mm.

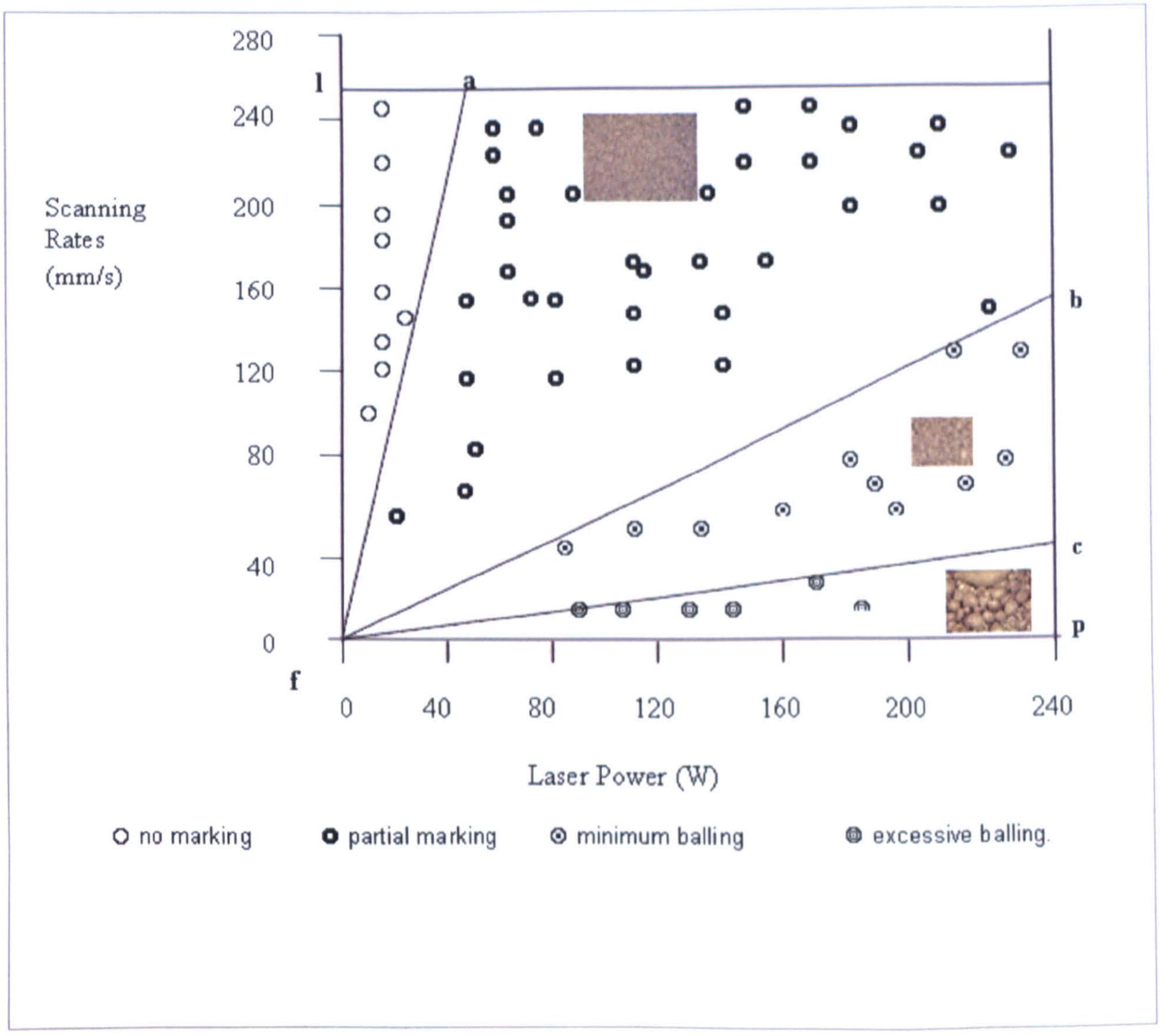

Figure 4.13: Processing window for single layer parts made in AL-3 developed from Figure 12.

(Note: Reciprocals of slopes f-a, f-b, and f-c, were computed and multiplied by the reciprocal of scan spacing (0.1 mm) in order to obtain the applied energy density).

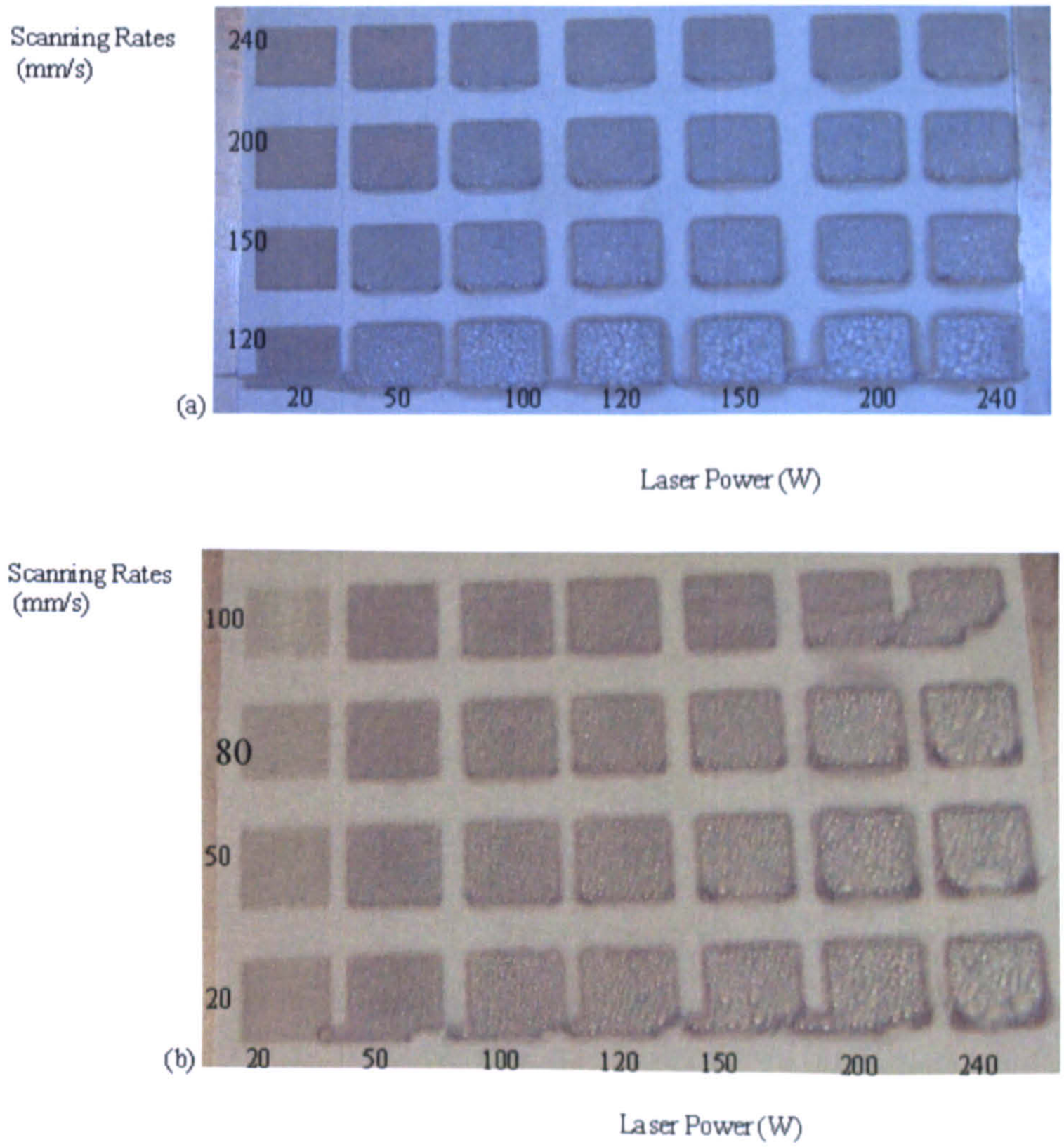

Figure 4.14: Images of single layers, as sintered on the plates, made in AL-4 powder with varying processing conditions (a) Single layer scanning at 120-250mm/s over 20-240W laser power range and scan spacing 0.1mm. (b) Single layer scanning at 20-100mm/s over 20-240W laser power range and scan spacing 0.1mm.

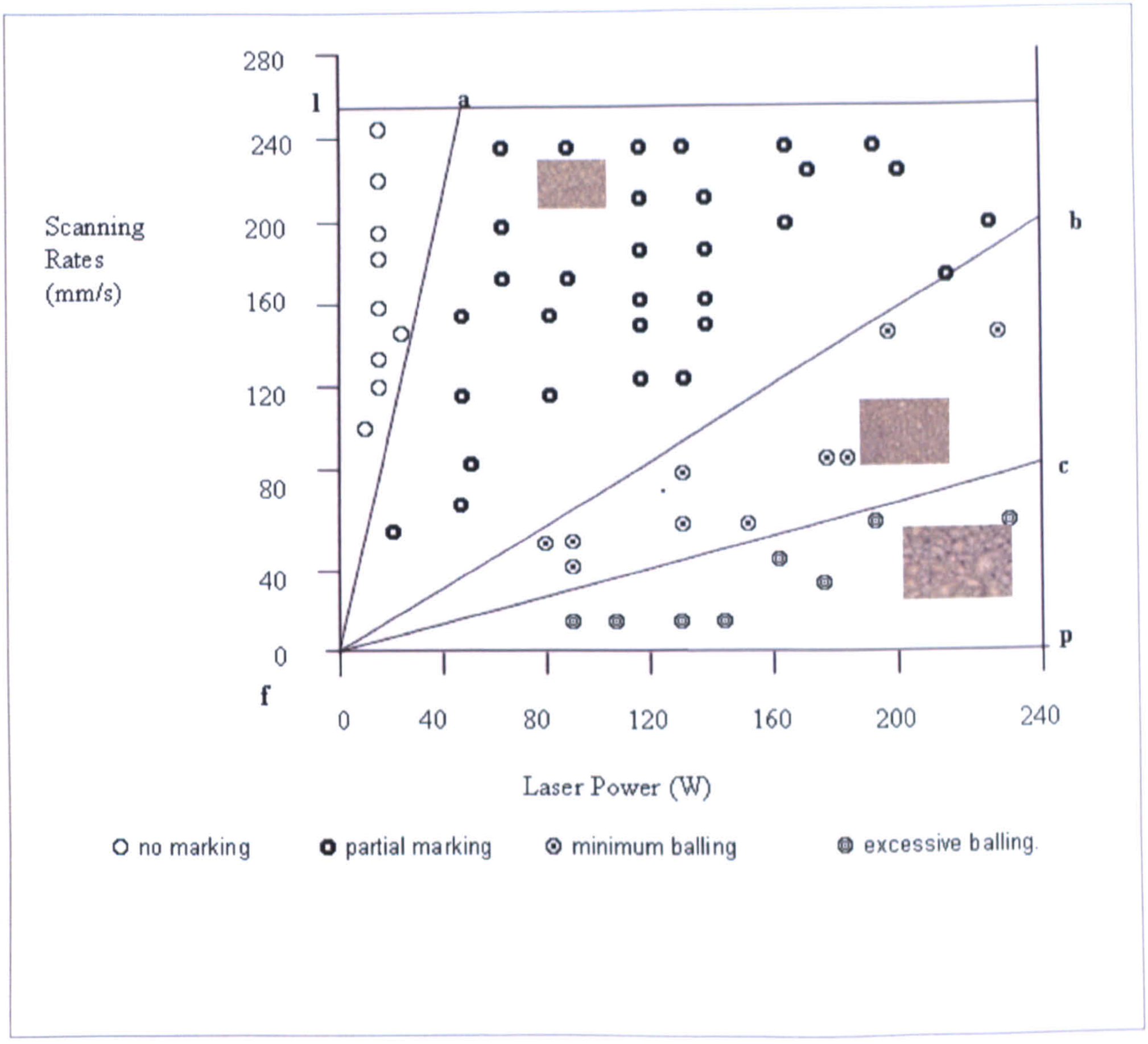

Figure 4.15: Processing window for single layer parts made in AL-4 developed from Figure 4.14.

(Note: Reciprocals of slopes f-a, f-b, and f-c, were computed and multiplied by the reciprocal of scan spacing (0.1 mm) in order to obtain the applied energy density).

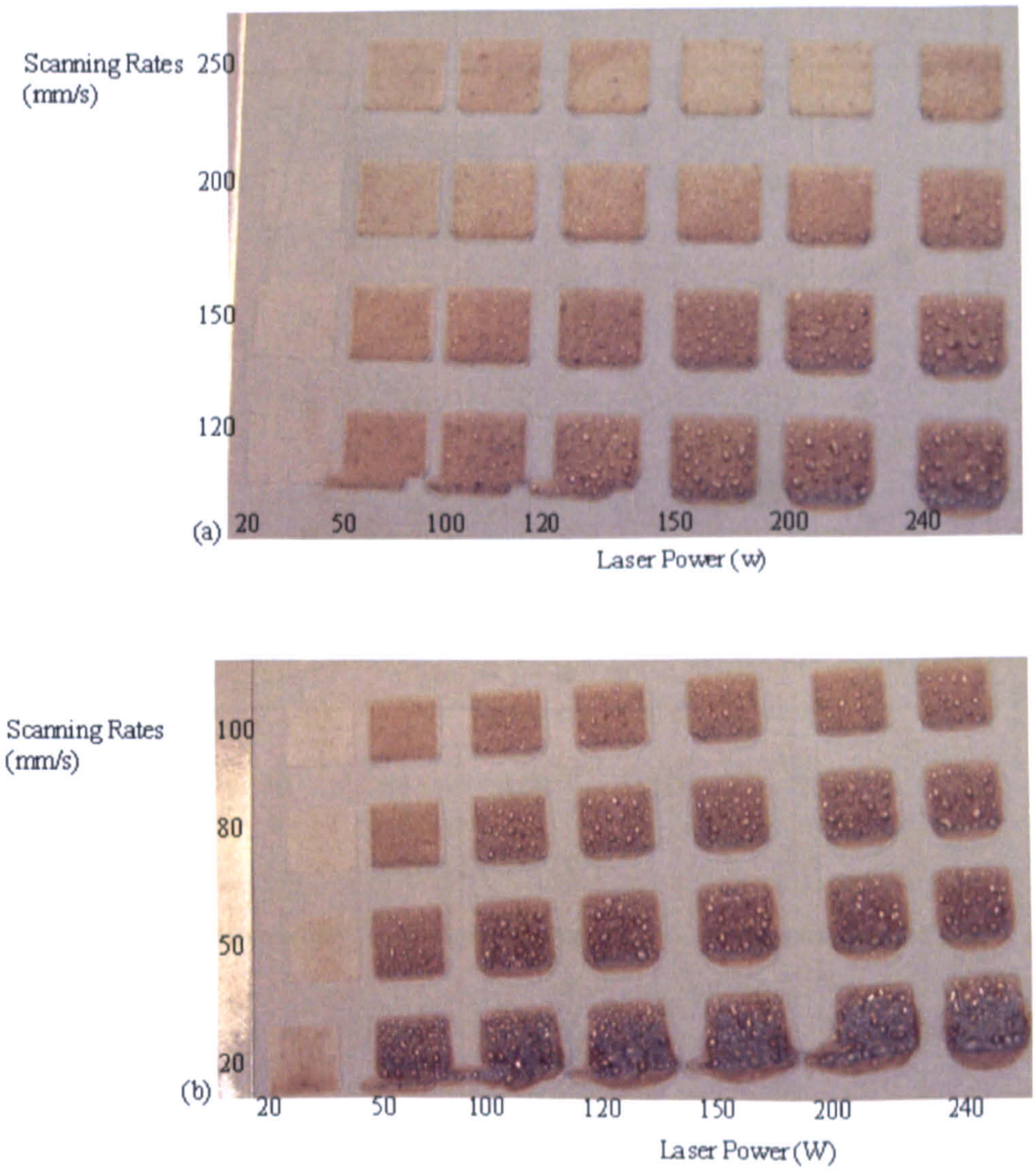

Figure 4.16: Images of single layers, as sintered on the plates, made in AL-5 powder with varying processing conditions (a) Single layer scanning at 120-250mm/s over 20-240W laser power range and scan spacing 0.1mm. (b) Single layer scanning at 20-100mm/s over 20-240W laser power range and scan spacing 0.1mm.

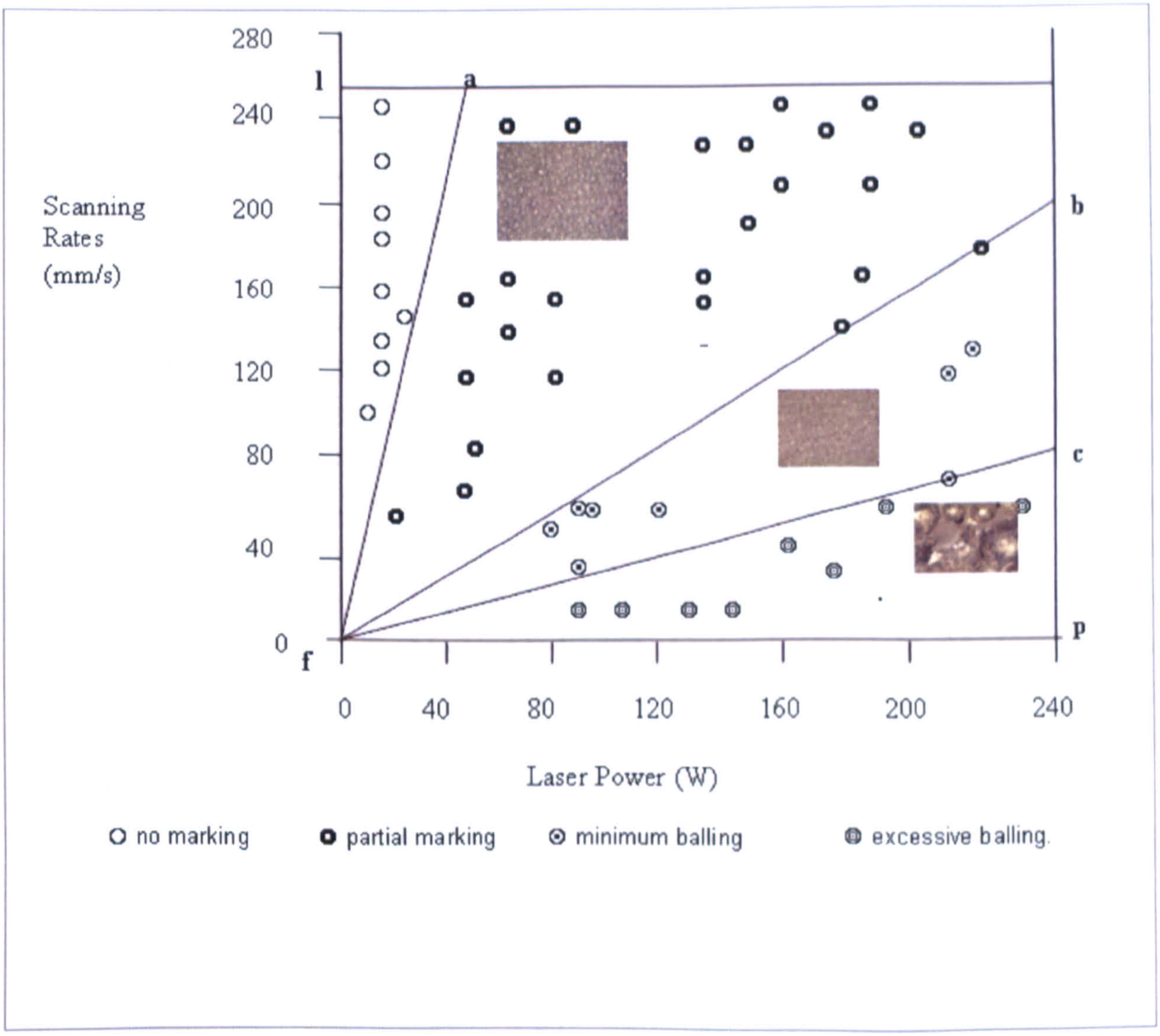

Figure 4.17: Processing window for single layer parts made in AL-5 developed from Figure 4.16.

(Note: Reciprocals of slopes f-a, f-b, and f-c, were computed and multiplied by the reciprocal of scan spacing (0.1 mm) in order to obtain the applied energy density).

In this region, the duration of laser-material interaction is too short to allow liquid phase to form and bond the powder particles together. The absence of liquid phase for inter-particulate bonding results in a very low strength of the single layer samples such that the samples could not be held by hand without fracture occurring.

4.4.2.2 Region of Partial Marking

The region of partial marking appeared on each of the processing maps (Figures 4.9, 4.11, 4.13, 4.15 and 4.17), and is separated by the boundary line f-b from the region of minimal balling to the right. It worth noting that the boundary region is less distinct in all the processing maps, most especially at higher laser powers and scan rates. Observation of the surfaces of the sintered samples from this region reveals a small number of agglomerated particles. It is evident that full melting of the particles had not occurred in this region. Energy density with the range of 2 J/mm^2 to 15 J/mm^2 is required for the formation of this region. This estimate is taken to be a reasonable assumption because there exists a critical value of energy density that minimal balling commences during laser scanning of the powders. The range of values of energy density required for the formation of this region is the same for both AL-1 and AL-2, (2 J/mm^2 to 8 J/mm^2); while it is higher for the pre-alloyed aluminium powders AL-3, AL-4, and AL-5 (2 J/mm^2 to 15 J/mm^2). The occurrence of this region could be ascribed to the presence of a very small amount of liquid phase with low viscosity which, nevertheless, is insufficient to impart adequate interparticulate bonding to the single layer samples. This results from a low energy density as a result of very high scanning speeds at high laser powers or low laser powers scanned at higher scan speeds.

4.4.2.3 Region of Minimal Balling

The region of minimal balling appeared on each of the processing maps (Figures 4.9, 4.11, 4.13, 4.15 and 4.17) and is separated by boundary line f-c from the region of excessive balling. Observation of the surfaces of the sintered samples from this region reveals that continuous melting of the particles had occurred in this region. Energy density with the range of 8 J/mm^2 to 30 J/mm^2 is required for the formation of this region. The range of values of energy density required for the formation of this region is the same for both AL-1 and AL-2, (8 J/mm^2 to 30 J/mm^2); while for the pre-alloyed aluminium powders AL-3, AL-4, and AL-5, it is 12 J/mm^2 to 30 J/mm^2. It is clear that continuous melt pool is maintained by reducing the scan rates from 200 mm/s to 80 mm/s in all the powders' processing maps with the exception of AL-3 (150mm/s to 50 mm/s). The increase in the minimum scanning speed of the processing window when the laser power was increasing could be elucidated as the compensation for the effect of increased laser power which

could have resulted in balling if the scanning rate had not been adjusted upward. The area of minimal balling should be a favourable region for the construction of multiple layers in direct SLS. The amount of liquid phase in this region is optimised to generate a component which neither has the problem of excessive balling nor insufficient liquid phase to promote sintering.

4.4.2.4 Region of Excessive Balling

The region of excessive balling appeared on each of the processing maps (Figures 4.9, 4.11, 4.13, 4.15 and 4.17) and is separated by line f-c to the right of the region of minimal balling. Energy density required for the initiation of excessive balling is estimated to 30 J/mm^2 or more. This region becomes predominant in all powders at scan rates of 80 mm/s or less with the exception of AL-3 (50 mm/s or less) at high laser powers. This region of excessive balling is undesirable. The phenomenon of excessive balling has been explained as the basis of excessive amount of liquid phase with very low viscosity arising as a result of longer laser-material interaction.

Observation of the processing maps reveals that the solidified melt balls are noted to be uniform in shape, equi-distant between its neighbours and increased in diameter and reduced in number as the energy density increases. Significant breakage of agglomerates is noted to have occurred over the scanning conditions that promote the formation of the regions of minimal balling and partial marking The four regions identified in this study are similar to the regions noted in the processing maps for other direct SLS studies on high speed steel (Dewidar *et al.* 2003) and stainless steel (Hauser 2003). These researchers had also attributed the occurrence of these regions on the processing maps to the variation in the duration of laser-material interaction.

4.4.2.5 Effect of Powder Properties on the Processing Maps

As noted earlier on, whilst the processing windows show similar trend for all powders investigated, there were differences in the location of boundaries of the different regions between powders. In order to understand the reasons underlying this observation, it is necessary that the processing map of each powder is analysed with respect to the different powder properties, variations in the surface oxide film, and the alloying elements present

in the powders. Oxide present at the powder surface would be expected to inhibit the initiation of inter-particulate bonding/melting during laser sintering/melting. Comparison of the processing maps for AL1 and AL-2 (Figures 4.9 and 4.11) reveals that they are both identical. This is exemplified by the occurrence of the region of minimal balling for both AL-1 and AL-2 when scanning rates were varied between 80 mm/s to 250 mm/s. Although, oxide content (Table 4.2) in AL-1 (15.9%) is higher than that of AL-2 (6.5%), and the bed densities (Figure 4.6a and b) for both powders are similar. It may be inferred from this analysis that predominant differences in the oxide contents of pure aluminium powders AL-1 and AL-2 appear to have little or no effect on the nature of processing maps obtained for them. It may therefore be argued that the identical processing maps obtained for these powders could be linked to their similar tapping densities which are expected to determine their thermal conductivities. Therefore, powders having similar tapping densities may possibly have identical processing maps because of similar thermal conductivities of their particles.

The processing maps for AL-3 and AL-4 (Figures 4.15 and 4.17) reveal significant differences in their features. For example, the processing condition for obtaining the region of minimal balling was at scan rates varying between 50 mm/s to 150 mm/s for AL-3 whereas the same region was obtained in AL-4 when scan rates from 80 mm/s to 200 mm/s were adopted. A cursory look through the powder properties shows slight differences in the magnesium contents (Table 4.2) and significant variation in bed densities (Figures 4.6c and d), but similar oxide contents (Table 4.2) for the powders. In line with the analysis from the last paragraph that differences in oxide contents of powders have little or no influence on their processing maps, it may be suggested that the similarity in the oxide contents of AL-3 and AL-4 has little or no influence of their processing maps. Therefore, significant differences noted in the processing maps of AL-3 and AL-4 could be attributed to the variations encountered in their bed densities. It is hereby reasoned that the degree of sphericity of AL-3 particles is significantly lower than that of AL-4 (Figures 4.3 and 4.4). In line with German's (1989) observation that irregularly shaped particles characterised by high surface area per unit volume have the tendency to absorb more laser energy. Therefore, it is suggested that higher irregularity of particles' shape in AL-3, than is found in AL-4, is responsible for the occurrence of the minimal balling region at lower boundary of the scan rates (50mm/s to 150 mm/s). Moreover, the processing map obtained for AL-4 is noted to be similar to those obtained for AL-1 and AL-2 powders. Again, a study of their packing densities (Figures 4.4, 4.6a, b, and d) indicates a striking similarity in their values.

This confirms further that the similarity in the packing densities of AL-1, AL-2 and AL-4 is also responsible for identical processing maps obtained for them, thereby, affirming that the determining factor that controls the processing maps of SLS aluminium powders is the packing density.

The processing map of AL-5 (Figure 4.17) shows the occurrence of the region of minimal balling when scan rates of 80mm/s to 200 mm/s were adopted. AL-5 is characterised by high packing density (Figure 4. 4 and 4.6e), and lower oxide content (Table 4.2). Moreover, its processing map appears similar to those of AL-1 and AL-2, although the partial marking regions in AL-1 and AL-2 are narrower horizontal along the laser power axis than that obtained in AL-5 and AL-4. Nevertheless, it may be concluded that it is the packing densities of powders that predominantly influence their processing map. Moreover, the similarities existing in the processing maps of AL-1, AL-2, AL-4 and AL-5 as a consequence of similarities in their packing densities suggest that alloying additions of magnesium and silicon to aluminium powders have no effect on the processing maps of these powders.

4.4.3 Microstructure and Agglomerate Development of Single Layered Monosized Aluminium Powder Specimens Processed by SLS

The surface morphologies of single layer laser sintered samples using varying energy densities are presented in Figures 4.18 to 4.22 for AL-1, AL-2, AL-3, AL-4 and AL-5 powders respectively. At a low the energy density of 3.3 J/mm^2 (Figures 4.18a, 4.19a, 4.20a and 4.21a), the sintered surfaces of samples AL-1, AL-2, AL-3, and AL-4 consisted of a network of agglomerates with a large amount of small, open, and deep pores, leading to a equiaxed structure. Powder sample AL-5, consisting of spherical particles, give surface structures which consist of spherical particles connected by necks suggesting initial stages of sintering at the same laser power (Figure 4.22a). Such structures also contained some remaining unsintered starting powder particles indicating insufficient densification.

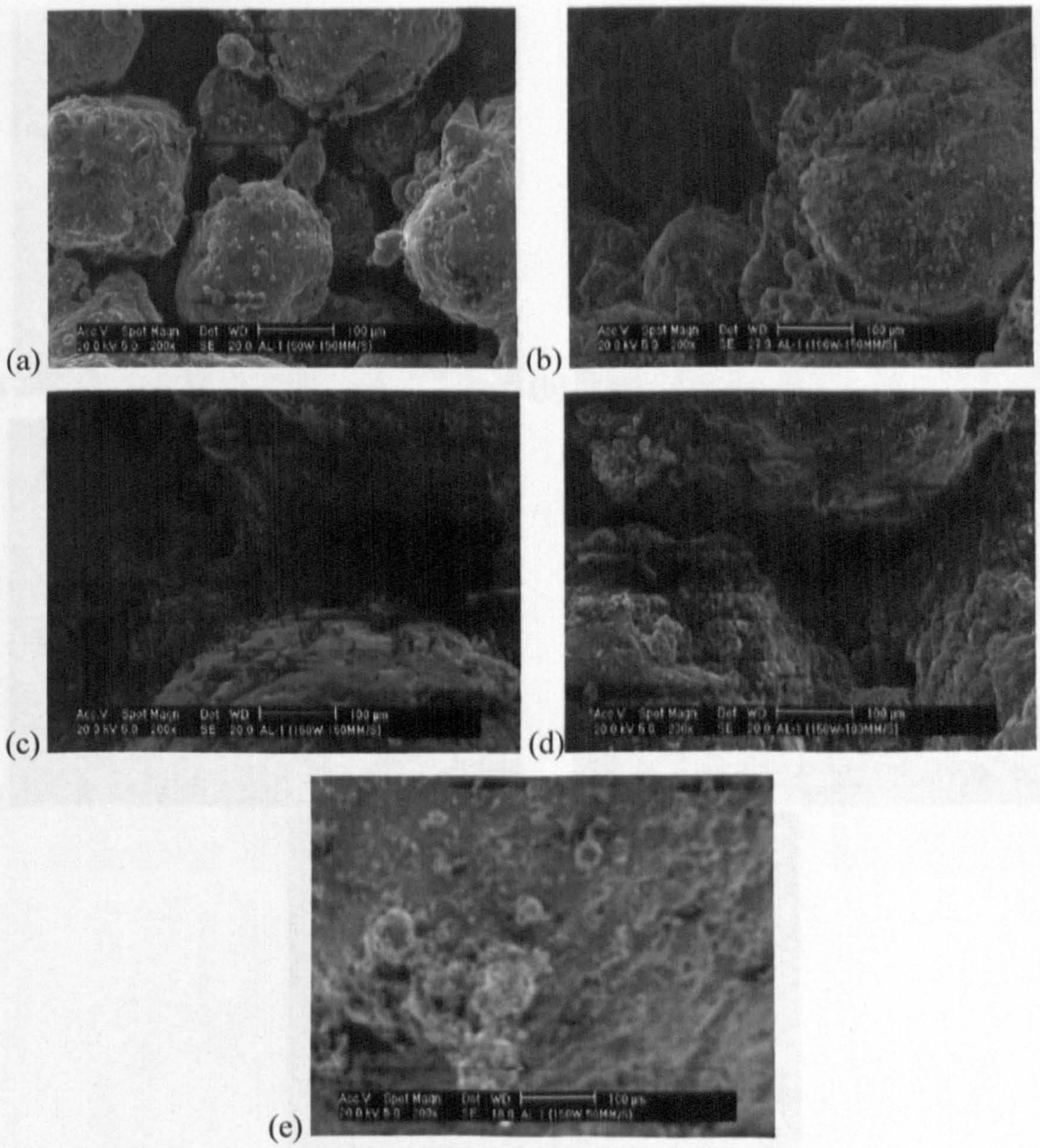

Figure 4.18: SEM images of the surface of laser sintered pure aluminium (AL-1) powder produced at varying energy densities of: (a) 3.3 J/mm^2 (b) 6.6 J /mm^2, (c) 10 J/mm^2, (d) 15 J/mm^2, (e) 30 J/mm^2 (Scan direction ↔).

When the energy density was increased to 6.6 J/mm^2 (Figures 4.18b, 4.19b, 4.20b, and 4.21b), the agglomerates of samples AL-1, AL-2, AL-3, and AL-4 coarsened significantly with the inter-agglomerate pores increasing in size.

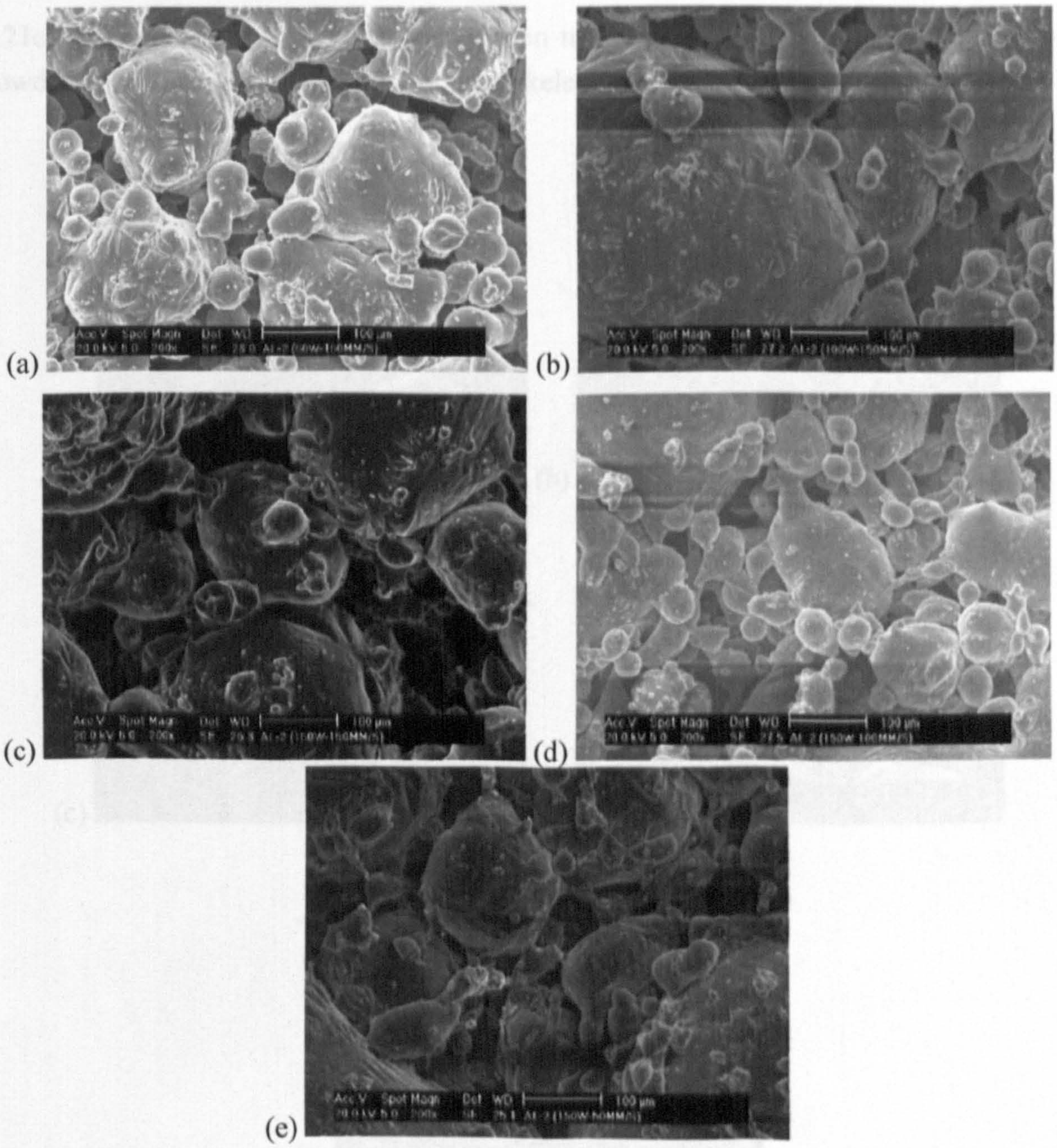

Figure 4.19: SEM images of the surface of laser sintered pure aluminium (AL-2) powder produced at varying energy densities of: (a) 3.3 J/mm^2 (b) 6.6 J /mm^2, (c) 10 J/mm^2, (d) 15 J/mm^2, (e) 30 J/mm^2. (Scan direction ↔).

In addition, the pores around the agglomerates began to merge and appear interconnected. Figure 4.22b reveals that with the same amount of energy density, AL-5 gives structures of randomly oriented, dense and equiaxed agglomerates with inter-connected pores. The sintered surfaces of AL-5 appeared to have a finer structure than those of AL-1, AL-2, AL-3 and AL-4. At a higher energy density of 10 J/mm^2 (Figures 4.18c, 4.19c, 4.20c, and

4.21c), the agglomerates were no longer seen in samples AL-1, AL-2, AL-3, and AL-4 powders, but were replaced by a continuous skeleton structure.

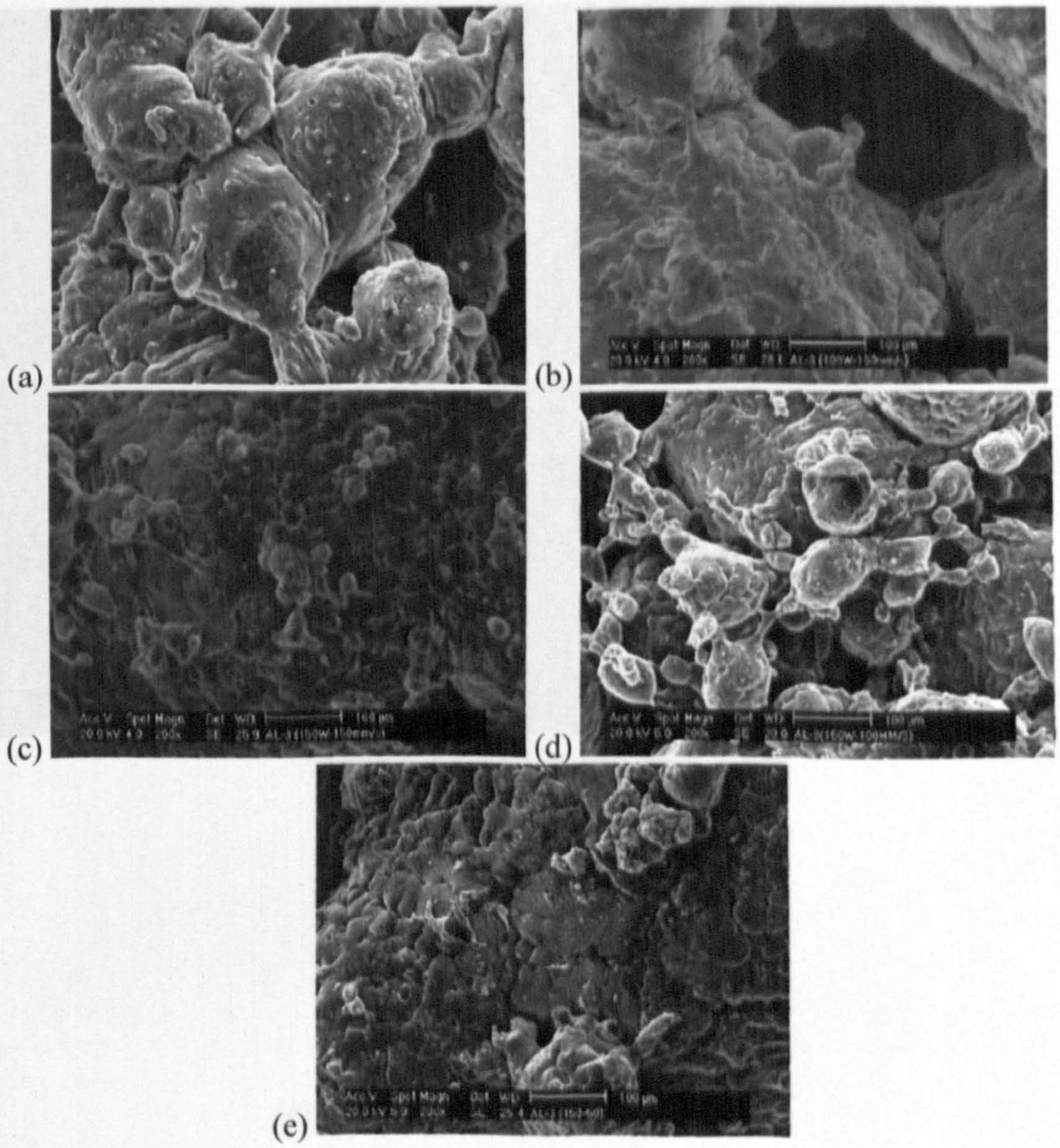

Figure 4.20: SEM images of the surface of laser sintered pure aluminium (AL-3) powder produced at varying energy densities of: (a) 3.3 J/mm^2 (b) 6.6 J /mm^2, (c) 10 J/mm^2, (d) 15 J/mm^2, (e) 30 J/mm^2. (Scan direction ↔).

This produced a fairly dense structure with closed pores whereas a relatively smooth and almost fully dense sintered surface was obtained for AL-5 as shown in Figure 4.22c. When the energy density was further increased to 15 J/mm^2, the surface morphology of the laser sintered AL-1, AL-2, AL-3, and AL-4 powders was noted to have remained porous and consisted of a network of agglomerates now aligned parallel to the scan direction (Figures

4.18d, 4.19d, 4.20d, and 4.21d) whereas SLS imparted a fully dense surface (Figure 4.22d) devoid of pore formation, for powder AL-5.

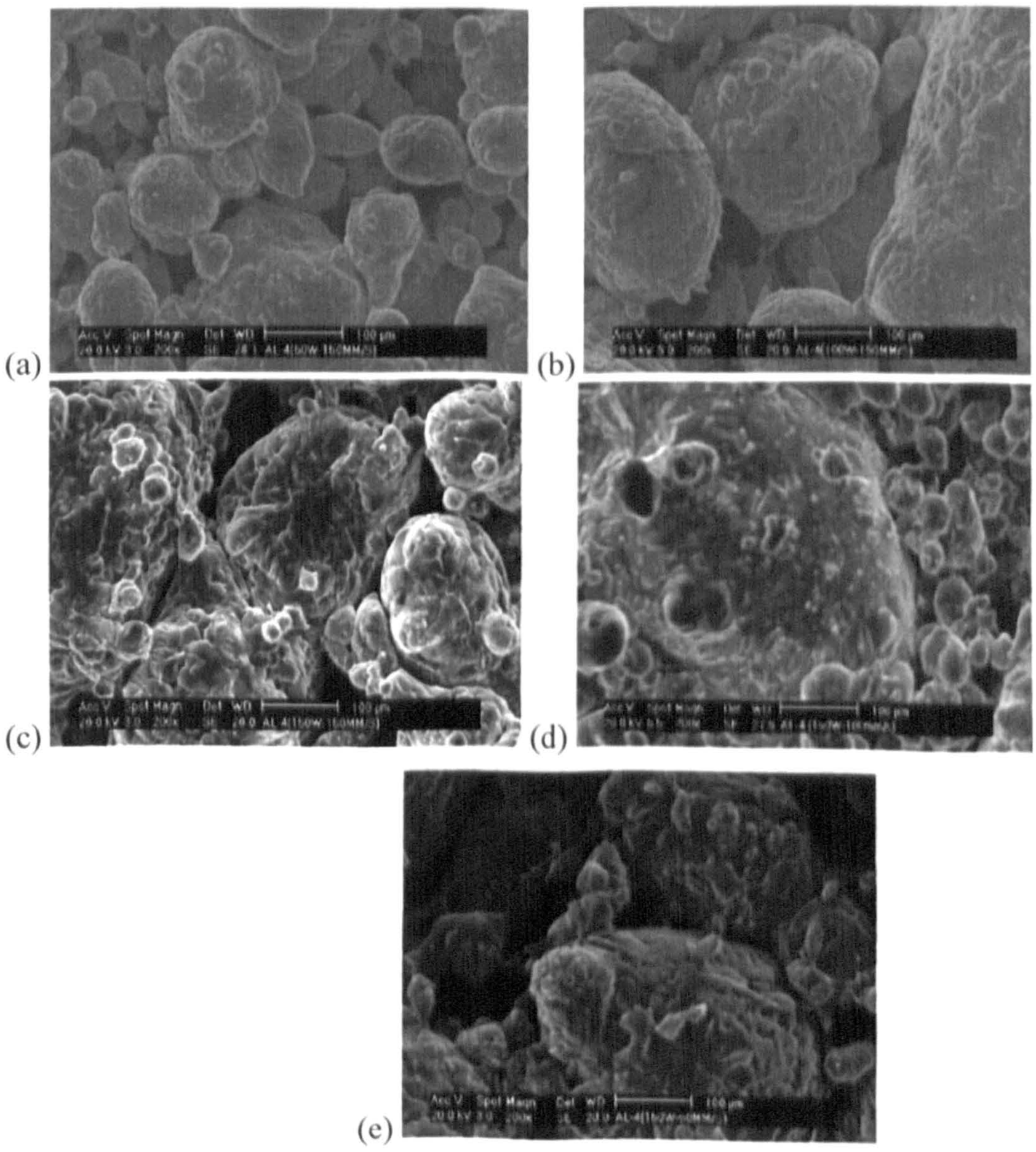

Figure 4.21: SEM images of the surface of laser sintered pure aluminium (AL-4) powder produced at varying energy densities of: (a) 3.3 J/mm^2 (b) 6.6 J /mm^2, (c) 10 J/mm^2, (d) 15 J/mm^2, (e) 30 J/mm^2. (Scan direction ↔).

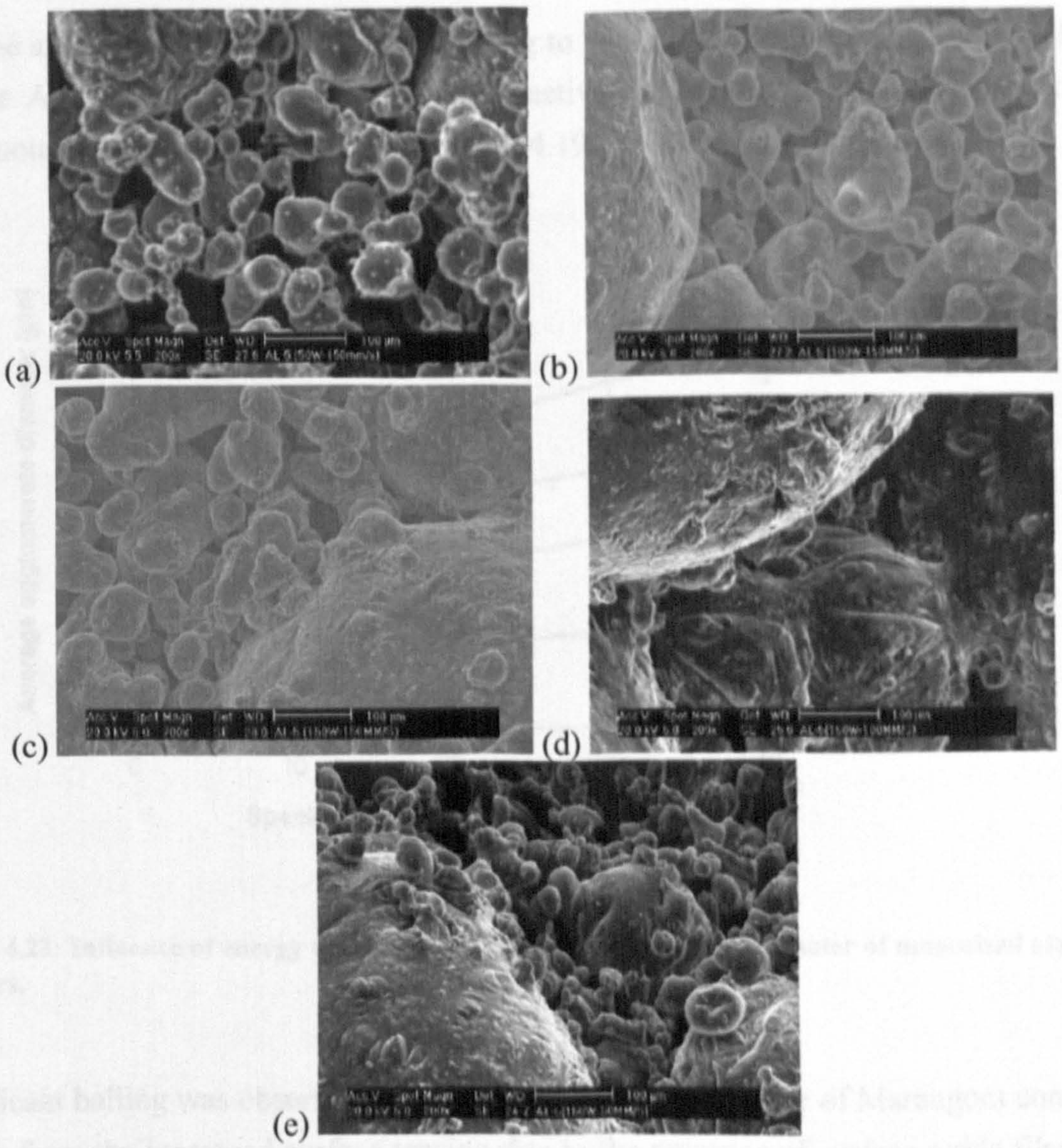

Figure 4.22: SEM images of the surface of laser sintered pure aluminium (AL-5) powder produced at varying energy densities of: (a) 3.3 J/mm^2 (b) 6.6 J /mm^2, (c) 10 J/mm^2, (d) 15 J/mm^2, (e) 30 J/mm^2. (Scan direction ↔).

Furthermore, Figure 4.23 confirms that the agglomerate diameter of all the laser sintered aluminium samples continuously increase as the applied energy density increases. For example, at an energy density of 15 J/mm^2, agglomerate formation was in the average diameter of 595 μm, 153 μm, 435 μm, and 455 μm for samples AL-1, AL-2, AL-3, and AL-4, respectively (Figures4.23). Necking was observed for several aluminium powder particles (Figures 4.18d, 4.19d, 4.20d and 4.21d). The same observation was noted in the sintered samples of AL-5 (Figure 4.23) with average agglomerate sizes at 305 μm at an energy density of 15 J/mm^2. Laser sintering of AL-1, AL-2, AL-3, and AL-4 using an energy density of 30 J/mm^2 resulted in the formation of a rough and fully dense surface

with the average agglomerate sizes increasing to 754.3 μm, 215.3μm, 588.7 μm, and 579.5 μm for AL-1, AL-2, AL-3 and AL-4 respectively (Figures 4.23) and connected by a continuous network of solid (Figures 4.318e, 4.19e, 4.320e and 4.21e).

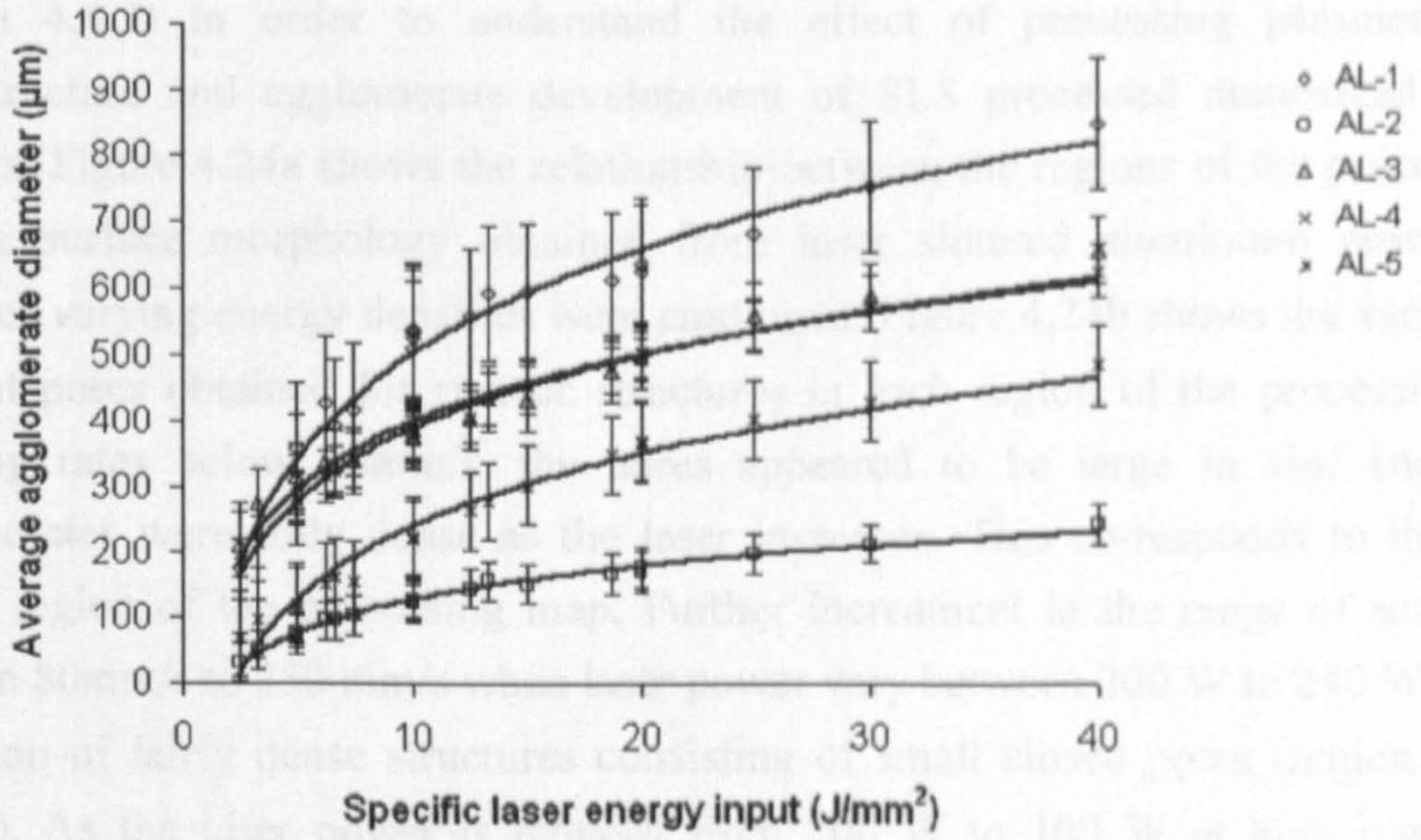

Figure 4.23: Influence of energy density on the average agglomerate diameter of monosized aluminium powders.

Significant balling was observed in the samples as a consequence of Marangoni convection arising from the increased surface tension due to the presence of surface oxide film on the powders. This eventually resulted in high thermal gradients which led to residual stresses relieved by shape change in the form of curl or balling. The internal density of the agglomerates (fraction of solid region) was noted to be increasing as the energy density increases from 3.3 J/mm^2 to 30 J/mm^2. A closer observation of the sintered surfaces from Figures 4. 4.22a, to 4.22e indicates that the surfaces of laser sintered AL-5 samples were found to have consisted of a relatively homogeneous structure at both low and high energy densities.

4.4.4 Effect of Processing Parameters and Powder Properties on the Microstructure and Agglomerate Development of SLS Processed Single Layer Aluminium Powders

This first part compares the process maps (section 4.4.2) and the surface morphologies (section 4.4.3) in order to understand the effect of processing parameters on the microstructure and agglomerate development of SLS processed monosized aluminium powders. Figure 4.24a shows the relationship between the regions of the processing maps and the surface morphology obtained from laser sintered aluminium powders at the instances varying energy densities were employed. Figure 4.24b shows the variation in the types of pores obtained for surface structures in each region of the processing map. At scanning rates below 80mm/s, the pores appeared to be large in size and the inter-agglomerates were fully dense as the laser increases. This corresponds to the excessive balling region of the processing map. Further increament in the range of scanning rates between 80mm/s to 250 mm/s when laser power vary between 200 W to 240 W, resulted in formation of fairly dense structures consisting of small closed pores (region of minimal balling). As the laser power is reduced from 200 W to 100 W at high scanning rates, surface morphology appeared smooth, but less dense while it was characterised with lateral pores (region of partial marking). Meanwhile, the formation of open or interconnected pores were found to be associated with the use of high scanning rates at laser powers varying between 50 W to 100 W. At this instance, the sample density was very low at these scan rates. These observations conform to discoveries made by Niu & Chang (2000) in their studies on the SLS of M2 high speed steels (see Figure 2.42).

It may be inferred from these comparisons that the occurrence of different morphologies associated with various regions of the processing window is dependent on the relationship between laser power and scan rate which in turn may yield high or low laser energy density that generates adequate or insufficient liquid phase for interparticulate bonding. For example, the formation of structures characterised by a network of agglomerates with a large amount of small, open, and deep pores at the given process parameters could be explained by the generation of lowest energy density (2 J/mm^2 to 4 J/mm^2) resulting from the adoption of low laser powers (50 W to 100 W) at high scan rates (Figures 4.24a, b). This condition leads to the generation of inadequate liquid phase that consequently produce low interparticulate bonding evident in the microstructures (Figure18a to 4.22a)

.

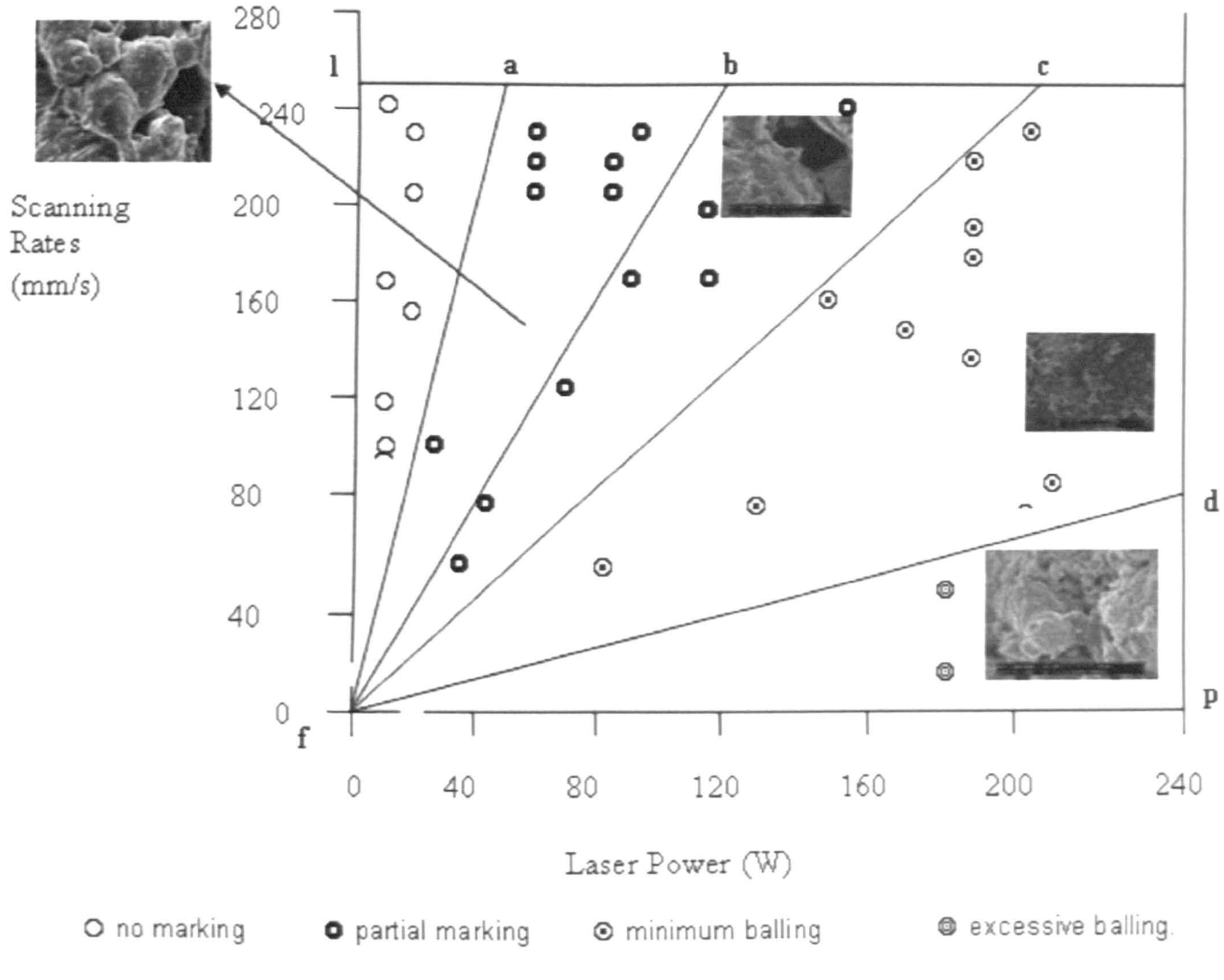

(a)

Figure 4.24: (a) Relationship between the various regions of processing map and the surface morphology at a laser power of 150 W and varying scanning rates and

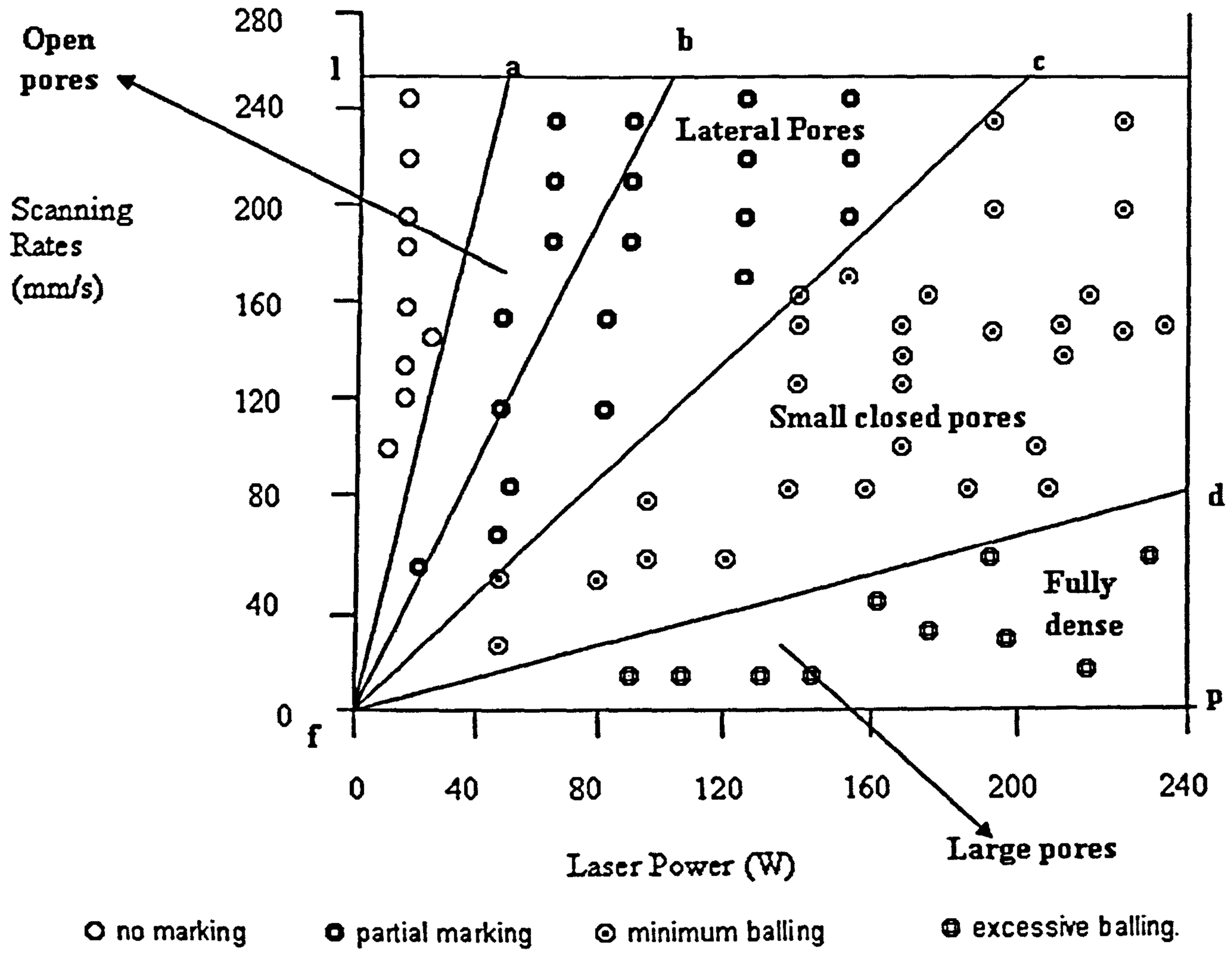

(b)

Figure 4.24: (b) Processing map showing change in porosity of laser sintered aluminium powders in each region of the processing map.

Moreover, lateral pores (Figures 4.18b to 4.22b) were discovered to have formed as a result of employing increased laser power (100 W to 200 W) at high scan rates which generated energy density range of 4 J/mm^2 to 8 J/mm^2. Occurrence of two types pore morphologies in the region of partial marking should be noted due to variation in processing parameters. Further increament in the laser power (100W to 240 W) at the scan rates (80 mm/s to 250 mm/s) leads to increased energy density, (8 J/mm^2 to less than 30 J/mm^2), (Figures 4.24a, b) which results in the formation of almost or fairly dense structures characterised by closed pores (Figures 4.18c, d to 4.22c, d). This could be attributed to the resultant high energy density which leads to the formation of adequate amount of liquid phase that promotes full melting. High energy density in SLS/SLM increases the powder bed temperature, while reducing the viscosity of molten aluminium and facilitating more efficient densification with the solid aluminium particles. The formation of surface morphologies having almost or fairly dense structures and characterised by closed pores is relevant in the construction of multiple layer samples.

The occurrence of rough and fully dense structures associated with the region of excessive balling could be ascribed to higher energy density resulting from the combined effect of higher laser powers at the lower scan rates (80 mm/s or less). Energy density from 30 J/mm^2 or more generated at this instance is believed to have lead to the formation of excess amount of liquid phase that result in the formation of balling (Figures 4.18e to 4.22e, 4.24a, b). This analysis suggests that it is the energy density, not laser power or scanning rates in isolation, that influence the processing map and the microstructure obtained for the SLS/SLM of aluminium powders.

In order to further investigate the independence of the effects of laser power and scan speed, Figures 4.23 was constructed which shows the agglomerate size as a function of energy density for a range of different laser power and scanning rates. These findings reveal clearly that it is energy density which controls the agglomerate size for all the materials studied. This suggests that the particle shape, oxygen content, and alloying element present in each of the materials define the extent to which the energy delivered will be translated into molten material, but that in all cases an increase in energy density will result in more molten material and larger sized agglomerates. These results agree with the findings by Zhu *et al.* (2005) and Niu & Chang (1998) who had investigated the sintering mechanism for Cu–based and high speed steel powders respectively.

Furthermore, this section shall account for the discernible differences observed in the surface morphologies of AL-1, AL-2, AL-3 and AL-4 on one hand as well as AL-5 on the other hand, during the various stages of the SLS process. For example, the formation of a network of agglomerates and pores in the surface morphologies of AL-1, AL-2, AL-3 and AL-4 (Figures 4.18a to 4.18e, 4.19a to 4.19c, 4.20a to 4.20c, 4.21a to 4.21c) and relatively homogeneous structures in AL-5 (Figures 4.22a and 4.22c) could be attributed to the sintering kinetics of the powders which Niu & Chang (1999a) noted was dependent on the particle shape and chemical composition. The degree of sphericity of the particles of the powders increase in the following order: AL-3 < AL-1 < AL-4 < AL-2 < AL-5 (Figures 4.1 and 4.3). It is on this basis that the powders were grouped at the beginning of this paragraph. In agreement with Niu & Chang (1999a), at a low energy density of 3.3 J/mm^2, it is clear that the dominant mechanism in the SLS of aluminium powders is the partial sintering (Figures 4.18a to 4.22a). Irregularly shaped particles of AL-1, AL-3, AL-4 and near spherical particles of AL-2 are characterised by higher surface area per unit volume, therefore, they tend to absorb additional laser energy which influence the sintering process. German (1989) observed that non-spherical particles give a lower random packing density and co-ordination than spherical particles. Monosized aluminium powder bed densities presented in Figures 4.4 and 4.6a, b, c and d lend credence to German's (1989) observation. This inhibits the densification process and consequently results in the formation of large pores around the agglomerates of AL-1, AL-2, AL-3, and AL-4 as shown in Figures 4.18a to 4.21a due to the applied low laser energy density. Moreover, liquid phase sintering (LPS) becomes predominant in the SLS process of aluminium as the energy density increases from 6.6 J/mm^2 to 10 J/mm^2. For the irregular particles of AL-1, AL-2, AL-3 and AL-4; mis-allignment of the particle center occurs during the particle re-arrangement stage of the LPS as a result of the torque which tends to rotate the particles (Niu & Chang 1999a). This torque causes the particles to move towards the centre of the laser beam where the temperature is maximum (Niu & Chang 1999a). This mechanism results in what Niu & Chang (1999a) described as the formation of a regular array of agglomerates situated at the center of the melt pool and the larger inter-agglomerate pores in samples AL-1, AL-2, AL-3 and AL-4 (Figures 4.18b, 4.18c, 4.19b, 4.19c, 4.20b, 4.20c 4.21b, and 4.21c). These agglomerates were found to have developed a specific growth direction which is at random to the direction of the laser beam scan. With the increament of energy density to 15 J/mm^2 particulate melting (Figures 4.18d, 4.19d, 4.20d, and 4.21d) was noted to have occurred due to increasing energy density (Niu & Chang 199a).

Meanwhile, as the surface tension is a function of temperature, the presence of a temperature gradient causes a corresponding variation of the surface tension ($d\gamma_{LV}/dT$) between the center (γ_C) and the edges (γ_A, γ_B) of the melt pool of AL-1, AL-2, AL-3 and AL-4, thus initiating Marangoni thermocapillary forces for fluid flow (Niu & Chang, 1999a). For pure metals having low oxygen content, Niu & Chang (1999a) noted that as the Marangoni flows occur from a region of increasing temperature (low surface tension) to a region of low temperature (high surface tension), radial outward flow is initiated in the melt pool consequently, thus, resulting in the formation of wide and shallow scan track (Figure 4.24c). However, when metal powders have high oxygen content, Niu & Chang pointed out that surface tension increases with temperature and radial inward flow occurs in the melt pool which consequently leads to the formation of deep and narrow scan track (Figure 4.24d). Powders AL-1, AL-2, AL-3, and AL-4 have higher oxygen content than powder AL-5 (Table 4.2). Therefore, SLS melt pools of samples AL-1, AL-2, AL-3, and AL-4 could be said to have been distributed around the center of melt pool as a consequence of the fluid flow from the edge to the center (see arrow directions in Figure 4.24d), thereby imparting large pores in between the scan tracks, whereas, in the case of samples AL-5, the fluid flow is from the center of the laser beam to the edge of the melt pool (see arrow directions in Figure 4.24c).

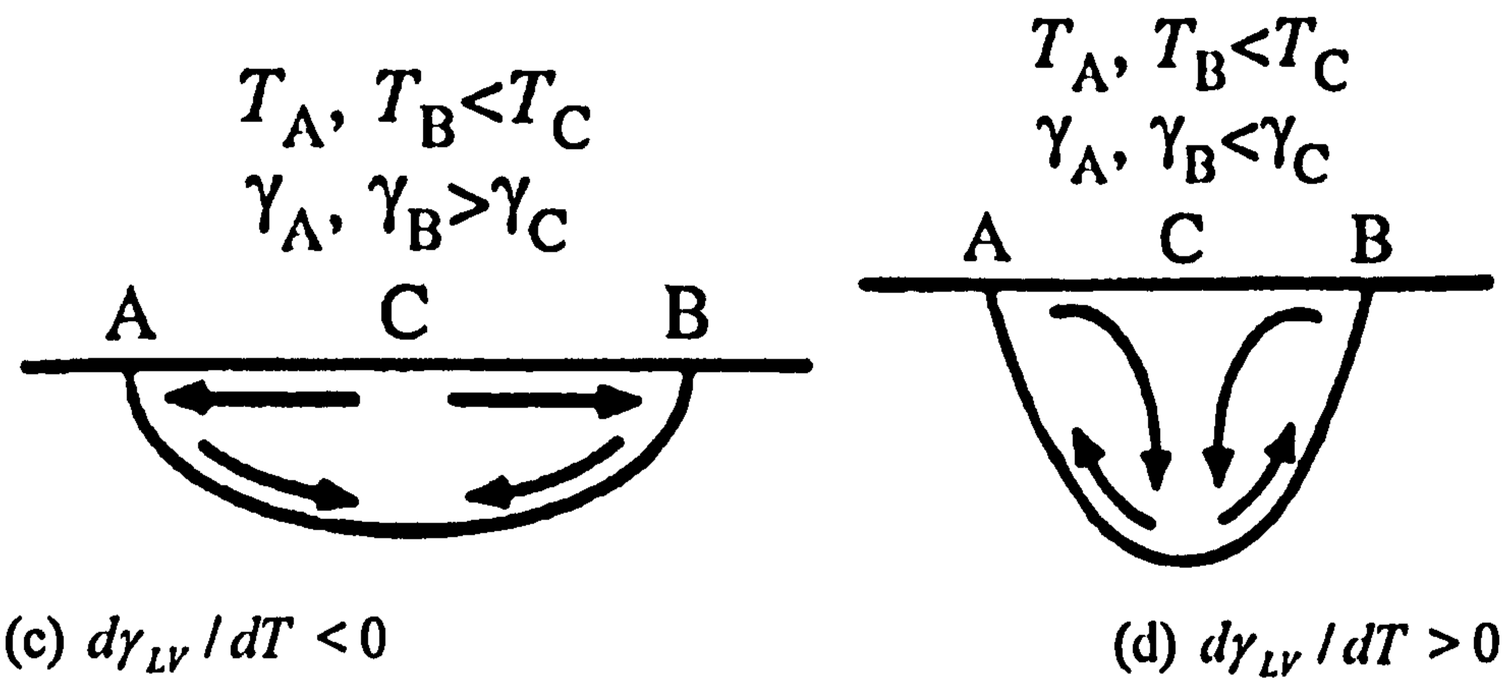

Figure 4.24c and d: Schematic representation of Marangoni convection in a melt pool showing occurrence of (c) negative surface tension gradient ($d\gamma_{LV}/dT < 0$) resulting in broad melt pool and shallow pores due to spherical particles and low oxygen content in powders; and (d) positive surface tension gradient ($d\gamma_{LV}/dT > 0$) resulting in narrow melt pool and deep pores due to irregular particles and high oxygen content in powders. (after Mills et al. 1998).

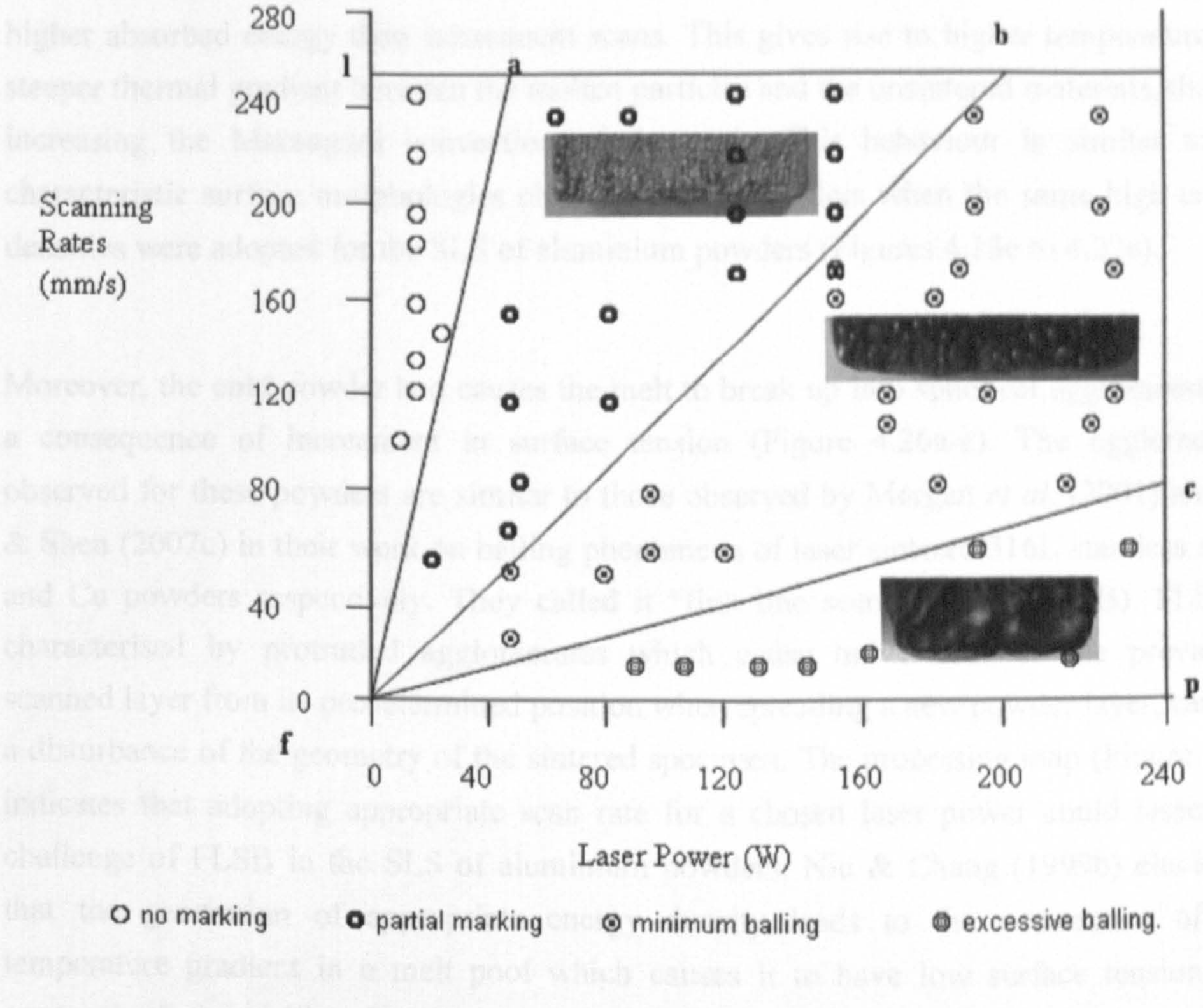

Figure 4.25: Processing map showing the initiation of first line scan balling process in SLS/SLM processed aluminium powders.

This section describes in detail, the balling process during the SLS/SLM of aluminium powders under varying processing conditions obtained. Figure 4.25 presents the processing map describing the characteristic first line scan track obtained for an aluminium powder sample at varying laser power and varying scan rates that yield corresponding energy densities whereas Figure 4.26 describes the characteristic microstructures of the first line tracks for each aluminium powder samples AL-1, AL-2, AL-3, AL-4, and AL-5 when processed at the laser power of 150 W and scan rates of 50 mm/s (30 J/mm^2). All the samples (Figure 4.26) are characterised by significantly coarsened isolated agglomerates between which only a poor bond is formed. First line scan tracks formed, when laser power of 150W and scan rates of 50 mm/s were adopted for processing, are similar in structure and sizes to the surface morphologies obtained in the excessive balling region of the process map developed for aluminium powders (Figures 4.24a, 4.25 and 4.26). Unsintered powder particles are noted to be distributed over the surfaces of the agglomerates. It is suggested that the high energy density generated by the impingement of the laser beam onto the cold powder bed, having a low thermal conductivity, has lead to a significantly

higher absorbed energy than subsequent scans. This gives rise to higher temperature and steeper thermal gradient between the molten particles and the unsintered materials, thereby increasing the Marangoni convection of the melt. This behaviour is similar to the characteristic surface morphologies obtained for all powders when the same high energy densities were adopted for the SLS of aluminium powders (Figures 4.18c to 4.22c).

Moreover, the cold powder bed causes the melt to break up into spherical agglomerates as a consequence of increament in surface tension (Figure 4.26a-c). The agglomerates observed for these powders are similar to those observed by Morgan *et al.* (2001) and Gu & Shen (2007c) in their work on balling phenomena of laser sintered 316L stainless steels and Cu powders respectively. They called it "first line scan balling" (FLSB). FLSB is characterised by protruded agglomerates which cause movements of the previously scanned layer from its predetermined position when spreading a new powder layer, causing a disturbance of the geometry of the sintered specimen. The processing map (Figure 4.25) indicates that adopting appropriate scan rate for a chosen laser power could lessen the challenge of FLSB in the SLS of aluminium powders. Niu & Chang (1999b) elucidated that the generation of appropriate energy density leads to the occurrence of low temperature gradient in a melt pool which causes it to have low surface tension, and consequently controlling the Marangoni flow and the capillary instability effect.

.

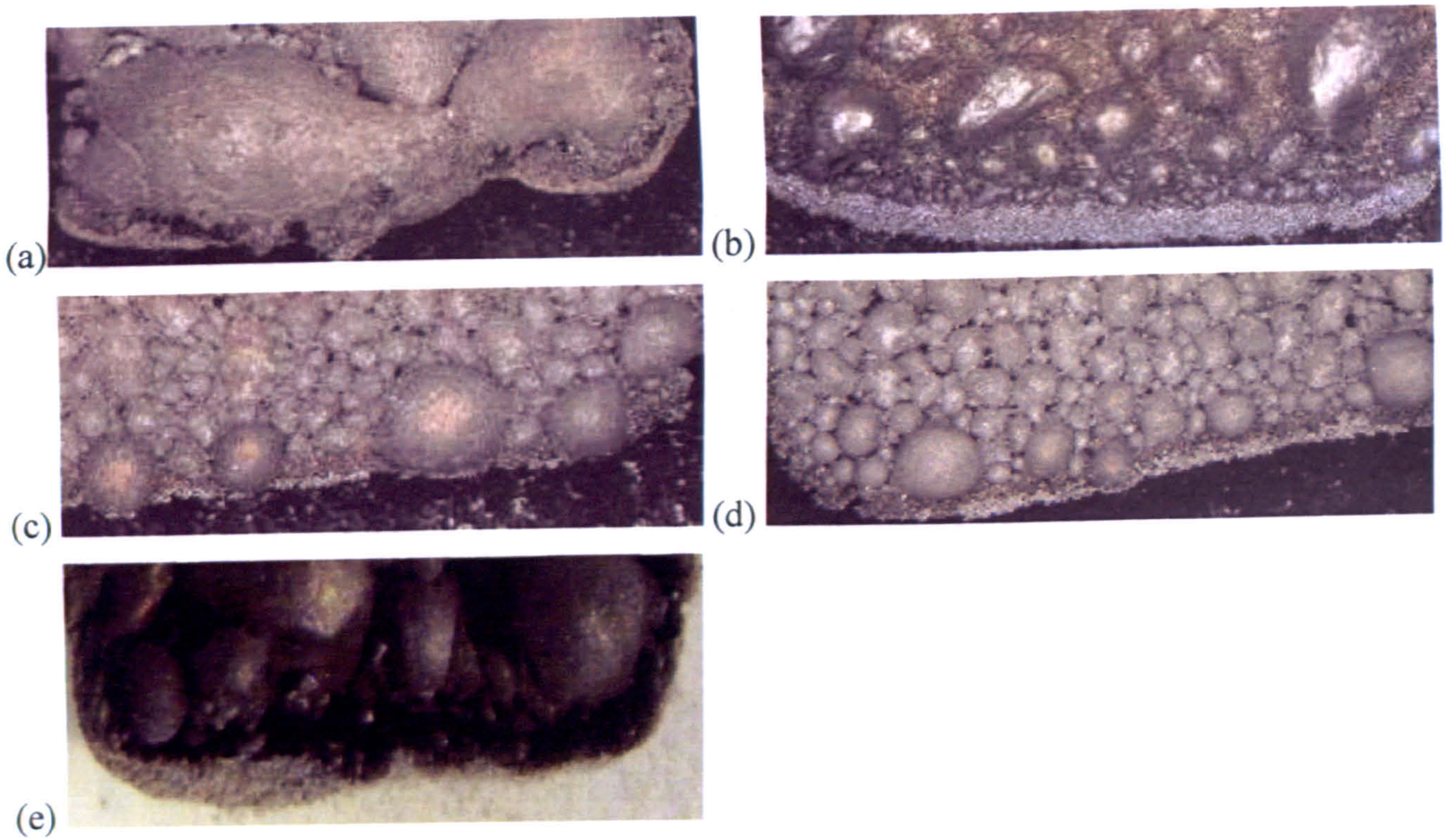

Figure 4.26: First line scanning balling phenomenon in aluminium powders (a) AL-1 (b) AL-2 (c) AL-3 (d) AL-4 (e) AL-5.

Eventually, this condition reduces the propensity for the occurrence of FLSB. The region of minimal balling in the processing map (Figure 4.25) shows the first line track obtained when energy density of 15 J/mm^2 was applied It is evident that a continuous and smooth scan track, characterised by stronger interparticle bond was attained, and showing no apparent balling phenomena. This is quite similar to the structure obtained surface morphologies of samples fabricated with similar energy densities (Figure 4.18c, d to 4.22c, d). Reducing the energy density to a range of 3.3 J/mm^2 to 6.6 J/mm^2, resulted in the break up of the scan track into a series of coarsened metal balls similar to the surface morphologies obtained in the partial marking region of the processing map (Figures 4.18a, b to 4.22a, b, and 4.25).

Findings from Figure 4.25 confirm that the applied energy density has a significant influence on the initiation of balling. During SLS/SLM, line by line scanning results in the melting of powder particles, thereby, forming a melt track which is cylindrical in shape. At a moderate energy density (10 J/mm^2 to 15 J/m^2), the liquid cylinder tends to break up into a row of spheres as a consequence of enhancement of capillary instability effect. This leads to fast collection of liquid at the contact points between the solid particles, where, considerable stresses are generated. As a result, Gu & Shen (2007c) pointed out that a significant transverse shrinkage distortion occurred in interparticle regions due to reduced non-deformability of the liquid along the molten track, thus causing the breakage in the molten track. Furthermore, they elucidated that the radial contraction of the liquid cylindrical track occurred to alter the direction of fluid flow from radially outward to radially inward flow, thereby resulting in balling. In agreement with Gu & Shen (2007c), it is hereby proposed that balling mechanism, termed "shrinkage-induced balling" occurring at moderate energy density is as a consequence of excessive shrinkage of the liquid track in both transverse and radial directions.

Figure 4.25 (the excessive balling region) also indicates that "shrinkage-induced balling" occurred in samples fabricated high energy density (30 J/mm^2 or more). This observation suggests that an increased energy density results in higher sintering temperature and eventually an excessive amount of liquid phase accompanied by a long liquid lifetime. This leads to lower melt viscosity, higher degree of superheat and an enhanced Marangoni flow which form a large amount of individual small balls with the reducing surface energy (Raleigh instability). This causes balling phenomenon observed here and previously in the SLS processing of Cu-based powder (Gu & Shen, 2007c), M3/2 high speed steel (Niu & Chang 1998), 316L steel (Morgan et al. 2001) and iron powder (Simchi & Pohl, 2003).

Analysis of the instability of the liquid cylinder reveals that provided wavelength $\lambda < \Pi D$ (where D is the initial diameter of the unperturbed cylinder), the liquid cylinder is stable against any perturbation (Niu & Chang 1998, 1999b). The mechanism of breakup of the laser sintered aluminium liquid cylinder into agglomerates is such that the diameter of the agglomerates varies directly with the diameter of aluminium liquid cylinder which has been found to increase with increasing applied energy density (Figure 4.23). It can be inferred from this analysis that increasing the energy density through the combination of high laser power and reducing scan rates inhibits the breakup of aluminium liquid cylinder into smaller agglomerates in order to attain sintered surfaces with minimal balling. Again, this is consequent upon the initiation of Marangoni convection and surface tension as a result of high thermal gradient generated at high energy density. Therefore, it is now evident that it is virtually impossible to achieve sintered surfaces with minimal balling only by increasing energy density which produces "self balling phenomenon". In order obtain a significant reduction in the diameter D of the agglomerate, an employment of appropriate energy density together with an increament in λ will counteract the effect of large D. Under this condition, aluminium liquid is bound to break up more readily. Moreover, continuous and smooth sintered surface will result from the usage of moderate or appropriate energy density to maintain the instantaneous liquid cylinder of $\lambda < \Pi D$.

An examination of the surface quality for each of the laser sintered aluminium samples (Figure 4.27) reveals that the agglomerate sizes for AL-1 are much larger than the agglomerate sizes obtained for other aluminium samples at comparable energy density. For instance, at an energy density of 10 J/mm^2 the average agglomerate size for AL-1 was found to be 536 μm whereas for AL-2, AL-3, AL-4 and AL-5, the average agglomerate sizes were found to be 129 μm, 379 μm, 382 μm and 221 μm respectively (Figures 4.23). Figure 4.23 reveals a wider range of agglomerate size for AL-1 compared to the other samples.

The most obvious difference between AL-1 and the other powders is the higher oxygen content determined by EDS (Table 4.2). This is particularly true when AL-1 is compared with AL-2, both powders being pure aluminium. It would seem, therefore, that the increased agglomerate diameter in AL-1 is associated with a higher oxygen content. This observation seems to be in agreement with the findings from the work of Niu & Chang (1999b) who noted that high speed steel powders with 0.10wt % oxygen has a greater propensity towards spheroidisation or balling phenomenon during SLS process than those with an oxygen content of only 0.02wt%.

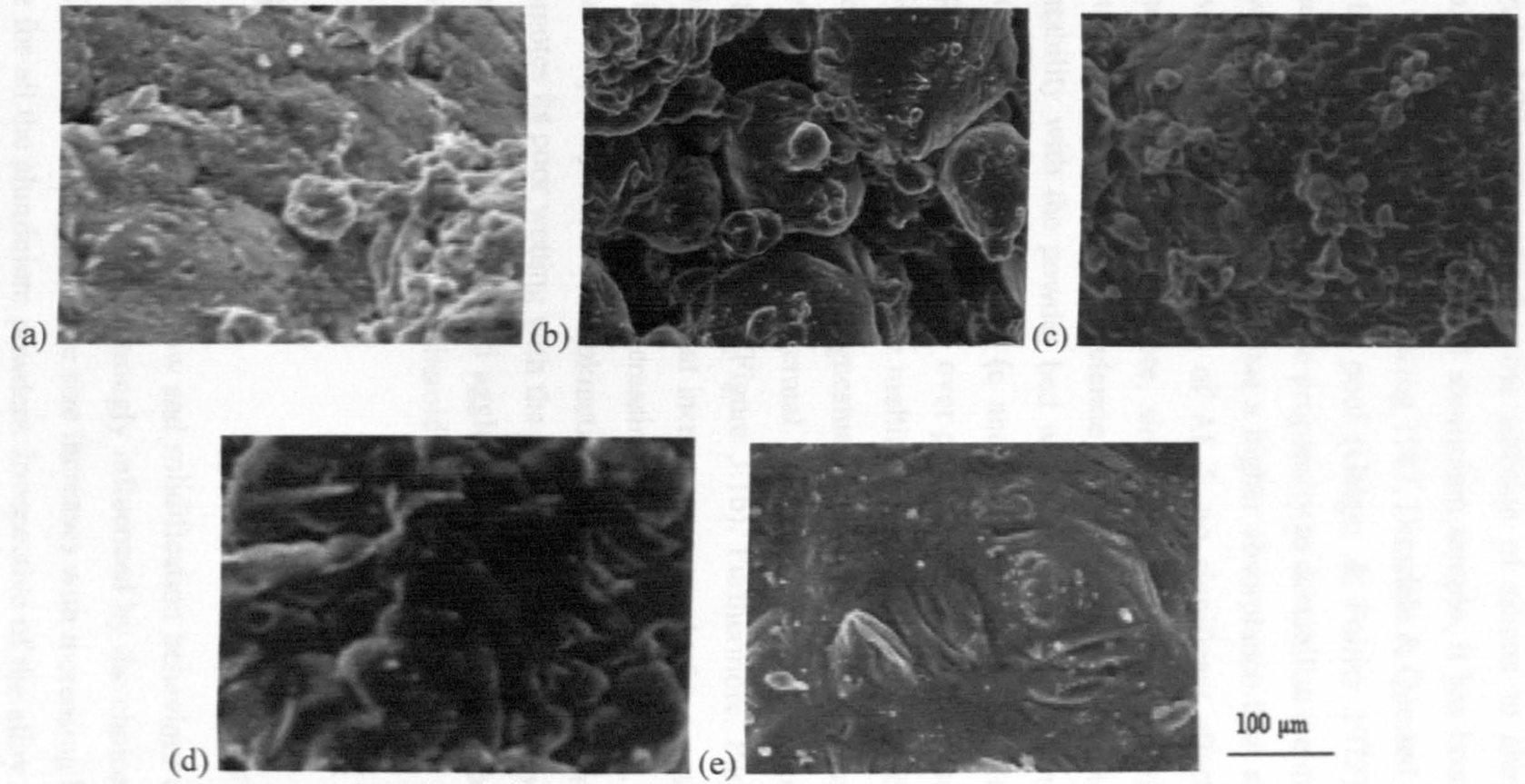

Figure 4.27: SEM images of sintered aluminium powders processed at laser power of 150W, scan speed of 150mm/s, scan spacing of 0.1mm: (a) AL-1 (b) AL-2 (c) AL-3 (d) AL-4 (e) AL-5

The surface quality of laser sintered samples AL-3, AL-4 and AL-5 will now be explained in the contexts of the role of the alloying elements (magnesium and silicon). For example, Figure 4.27e suggests that the addition of silicon to aluminium improves the surface quality direct SLS processed aluminium sample. It has been reported that silicon reduces the viscosity of aluminium (King 1987, Dinsdale & Quested 2004) and has no effect on the surface tension of its melt pool (Geiger & Poirier 1973). On this basis, it is hereby speculated that silicon has the propensity to destabilise the melt pool of laser sintered AL-5 powders. Although, silicon has a higher absorptance than aluminium for CO_2 continuous wave radiation, in the case of AL-5, no significant effect is expected due to the low concentration of Si. Therefore, since silicon reduces the viscosity of the melt pool, this would be expected to accelerate the development of Raleigh instability through its wettability with the powder bed which reduces increament in agglomerate diameter. An observation of Figure 4.27 (c and d) reveals that pre-alloying addition of magnesium improves the surface quality over pure aluminium but not so much as silicon. Magnesium (650°C) has nearly the same melting point as aluminium (660°C) and lower absorptance. Therefore, the effect of magnesium, in varying contents in the aluminium powders, has substantial effect on the thermal properties of aluminium as indicated by the melting ranges of AL-3 and AL-4 (Figure 3.1b). Furthermore, Park *et al.* (2002) and Geiger & Poirier (1973) established that increasing content of magnesium in aluminium reduced the surface tension while increasing the melt viscosity. Therefore, the competing thermocapillary and thermokinetic effects of magnesium on aluminium melt which promotes its poor wetting with the powder bed could be responsible for the formation of an irregular layer and increased agglomerate diameter as a consequence of high inclination towards the occurrence of spheroidisation phenomenon.

4.5 Conclusion

It is now established that flow and solidification behaviour of the aluminium powder melt during single layer scan is strongly influenced by the choice of laser power and scan rates This implies that agglomerate size increases with increasing laser power or decreasing scan rate for all the aluminium powders. Irrespective of the alloy composition of the aluminium powders, the processing window for each powder was noted to have fallen reasonably within the same range of laser power and scanning rates. The presence of surface oxide film as well as irregularly shaped particles in the powders exacerbated the agglomerate development, and formation of porous surfaces which was found to be undesirable for the

development of multiple layer parts. Laser sintering of aluminium powders with spherically shaped particles resulted in the formation of a homogeneous and dense layer.

CHAPTER FIVE FABRICATION OF MULTIPLE LAYER SAMPLES FROM MONOSIZED POWDERS

5.1 Introduction

Details of the sintering response of the monosized aluminium powders AL-1, AL-2, AL-3, AL-4 and AL-5 fabricated as multiple layer coupons are reported in this chapter. The impact of powder properties and SLS/SLM processing conditions on the density and microstructural characteristics of processed parts is described and discussed. The aim of this chapter is to present an understanding of the laser sinterability of the as-received aluminium powders in order to select a suitable alloy and appropriate processing conditions to develop a high sintered density and desirable microstructure in a multiple-layer sample. Section 5.2 presents results of multi-layer sintering experiments of the five as-received powders using the optimum processing conditions described in section 3.4.3.2. Thereafter, the effect of the powder's properties (particle's shape, powder densities, and chemical composition) on the sintered density, oxide disruption, and microstructure of the direct SLS processed aluminium powders are described and analysed in Section 5.3. Appropriate processing parameters for the suitable direct SLS aluminium powder AL-5 were determined and optimised with a view to obtaining enhancement in its sintered density and microstructural properties in Section 5.4. The presented results included records of sintered density and microhardness measurements as well as optical and SEM images taken to observe sample's microstructure when material properties and processing conditions were varied. The implications of the findings in section 5.4 are discussed in section 5.5.

5.2 Determination of Suitable Candidate Aluminium Alloy Powder for Direct Laser Sintering

In order to determine which of the monosized aluminium powders is the most suitable candidate material for the direct selective laser sintering process, multiple layer parts were developed for each powder. To select an appropriate set of process parameters for each

powder, reference was made to the single layer process maps presented in section 4.4.2 (Figures 4.9, 4.11, 4.13, 4.15, and 4.17). A range of laser power and scanning rate was identified which had given a small agglomerate size. This would be expected to provide for strong metallurgical bonding between multiple layers. The processing conditions chosen for further investigation were:

AL-1: Scanning rates (100-200 mm/s); laser power (100-200 W);

AL-2: Scanning rates (80-200 mm/s); laser power (100-200 W);

AL-3: Scanning rates (50-150 mm/s); laser power (80-200 W);

AL-4: Scanning rates (80-200 mm/s); laser power (80-200 W);

AL-5: Scanning rates (80-200 mm/s); laser power (80-200 W).

From within these ranges, a uniform, narrower range of processing parameters was adopted such that this could be used for all the powders. Therefore, the range of processing parameters chosen to be investigated for multi-layer deposition of the as-received powders was as follows: scanning rates (80-200 mm/s), laser power (150 W), scan spacing 0.1 mm, and layer thickness 0.25 mm. The adoption of these processing parameters would assist in the assessment of the role of powder properties (apparent and tapping densities, flowability, and chemical composition) in the development of sintered density and the microstructural evolution of the laser sintered powders.

The results of this preliminary investigation into the response of SLS/SLM processed monosized aluminium powders AL-1 to AL-5 are presented in Figure 5.1 whilst the individual density data may be found in Appendix C1. Figure 5.1 shows that as the specific laser energy input increases, density of the direct laser sintered/melted samples increases marginally over the entire range of specific laser energy input investigated (30-75 J/mm^3), with the exception of AL-3. Although, the rate of increase in density becomes less pronounced as the specific laser energy input increases, this means that there is little potential to increase density of the SLS/SLM processed parts beyond an energy density of 60-75 J/mm^3. Moreover, the range of values of percentage sintered density obtained for samples AL-1, AL-2, AL-3 and AL-4 (1.17 g/cm^3 to 1.62 g/cm^3) is found to be significantly lower than that of sample AL-5 (1.68 g/cm^3 to 1.94 g/cm^3).

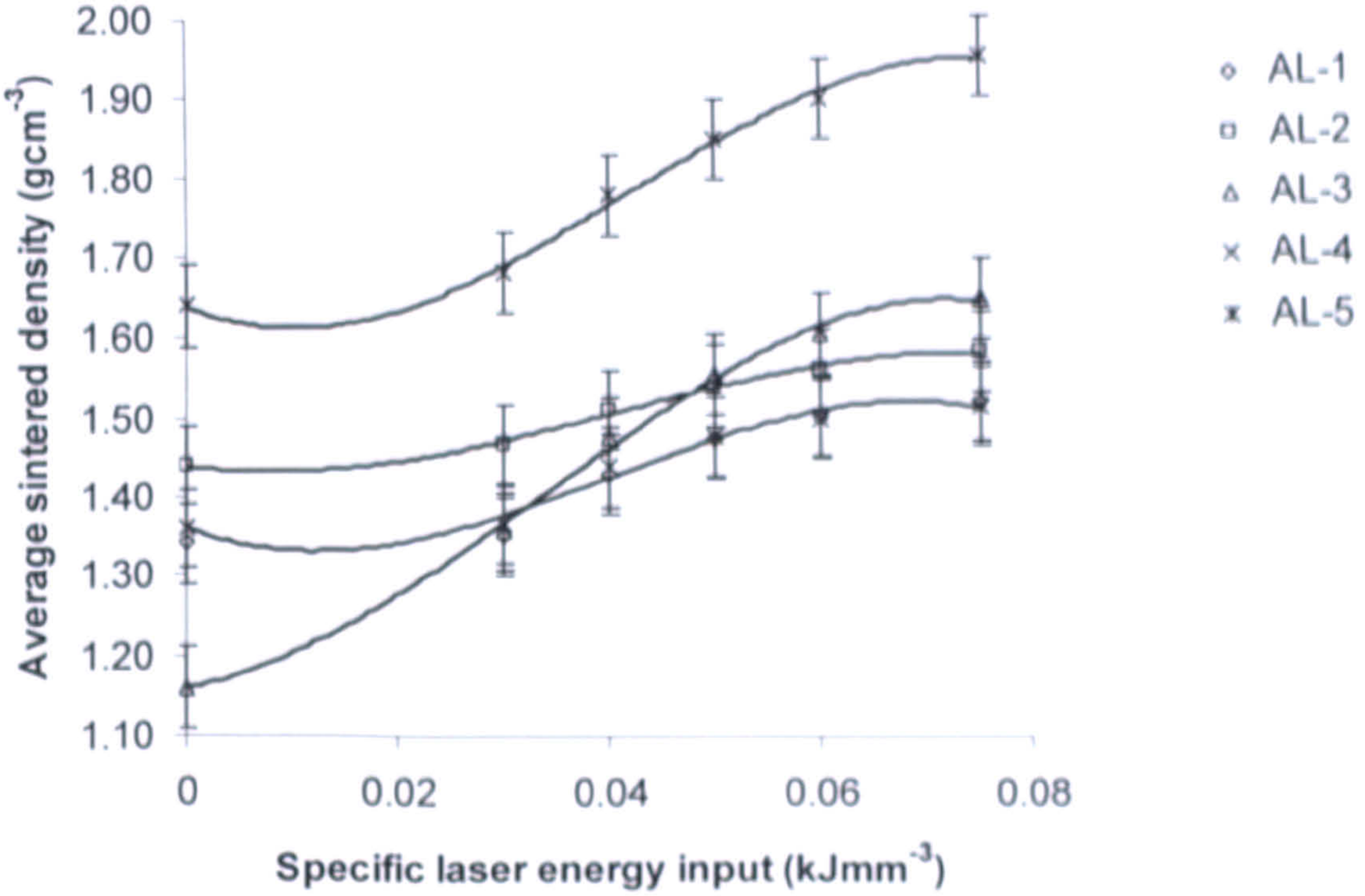

Figure 5.1: Graph of average sintered density versus the specific laser energy input for the aluminium powders. The solid lines are the result of a least squares fit as-received of the data to equation 2.18.

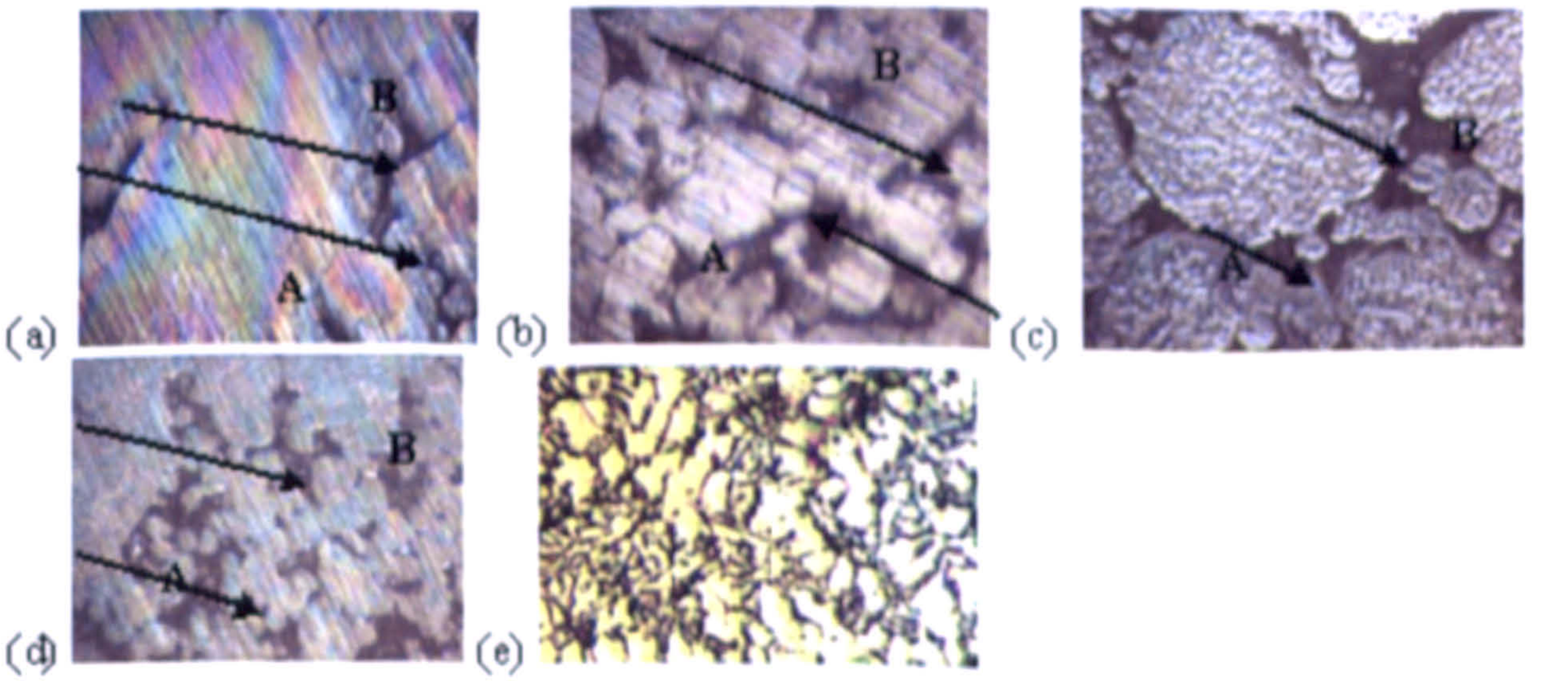

Figure 5.2: Microstructure of laser sintered multiple layers samples of (a) AL-1 and (b) AL-2 (c) AL-3 (d) AL-4 and (e) AL-5 powders showing the differential sintering response as a consequence of the non-uniform layer of oxide covering the particles and varying thermal properties of the oxide film fabricated at 75 J/mm^3.

The differential responses of the SLS/SLM processed powders are presented in Figures 5.2, while 5.3, 5.4, 5.5, 5.6, and 5.7, show the microstructures and macrostructures of monosized AL-1, AL-2, AL-3 AL-4, and AL-5 powder respectively. Black zones (B) in

the micrographs are indication of the presence of pores while the grey regions (Λ) illustrate the sintered mass. The pores are found to be responsible for a significant decrease in density of the sintered parts. An observation of Figures 5.2 and 5.3 to 5.6 reveal the occurrence of sintering only in the isolated regions. A preponderance of irregularly shaped and inter-connected porosities is common to all these samples. Unsintered powders can be seen clearly in all the micrographs. The sintered regions could be seen to have formed as agglomerates. Figure 5.7 shows the microstructure of sintered AL-5 powder. Although pores exist in the microstructure, they are much smaller than those observed in the microstructures of the other alloys. These smaller pores occurred partly due to the influence of the spherical shaped powder particles which packed much better than those of AL-1 to AL-4 having irregular particles. Furthermore, particles were melted and the liquid duplets coalesced before freezing across the layers in AL-5. The formation of clearly large, spherical regions which are much bigger than the particle size of AL-5 powders are noted in Figure 5.7. This suggests the occurrence of full melting in AL-5, thereby, leading to the formation of balling due to increased lifetime of the melt pool.

The results of the average microhardness of the direct laser sintered monosized aluminium powders are presented in Figure 5.8a. Average value of microhardness are 78 kgf/mm^2, 44 kgf/mm^2, 72 kgf/mm^2, 85 kgf/mm^2, and 59 kgf/mm^2 for AL-1, AL-2, AL-3, AL-4, and AL-5 respectively. For sample AL-5, the average microhardness value obtained was found to be higher than that of common Al-12Si castings (36-45 kgf/mm^2). Figure 5.8b shows the variation of microhardness across etched sections of direct laser sintered aluminium powders. This variation is clearly not systematic. Furthermore, the variation of microhardness across the surfaces of sample AL-2 and AL-5 could be described as similarly uniform.

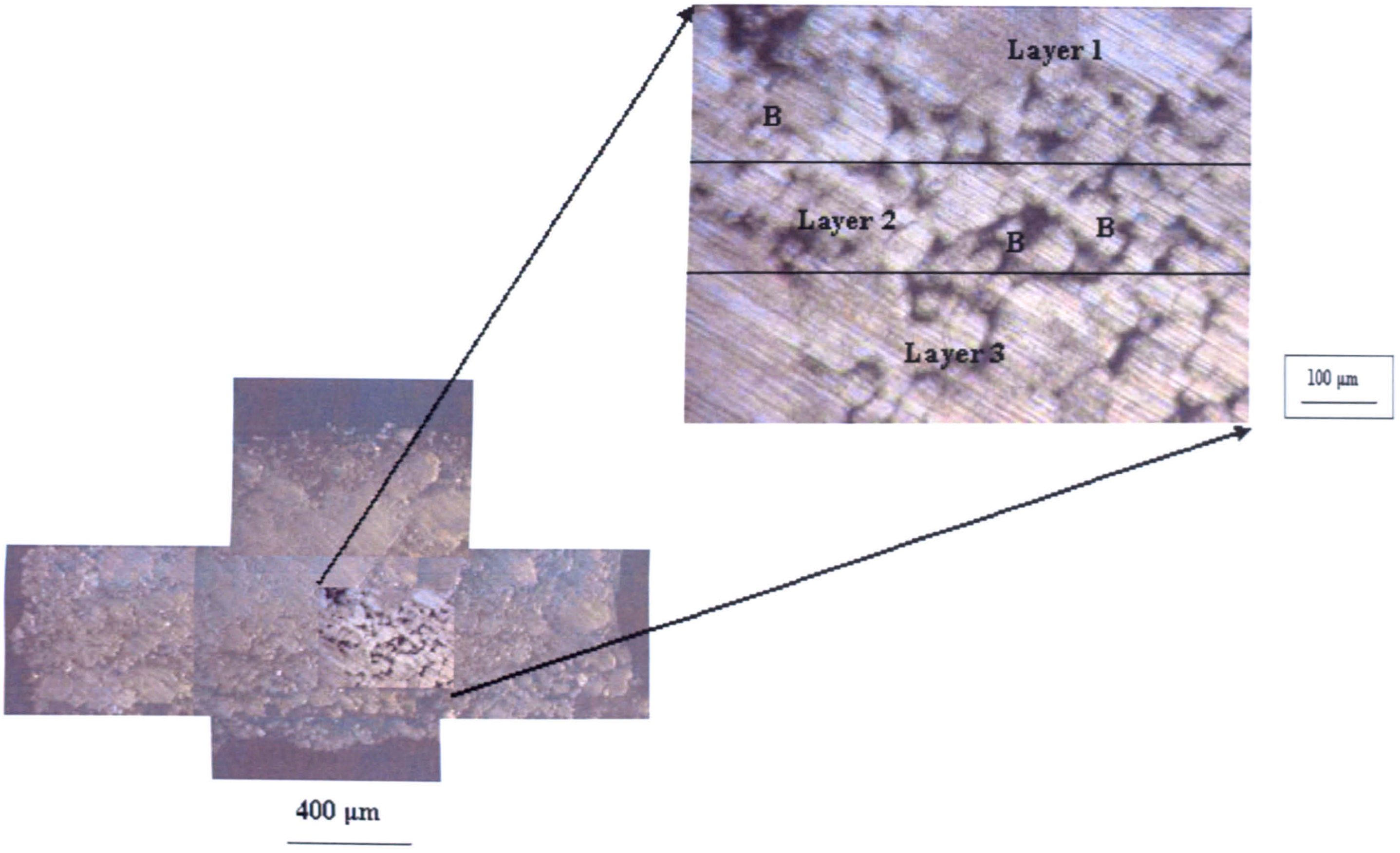

Figure 5.3: Macrostructure of laser sintered AL-1 fabricated at 150 W, 80 mm/s (75 J/mm3) revealing lack of inter-particulate bonding across the layers as well as presence of unsintered particles in regions B.

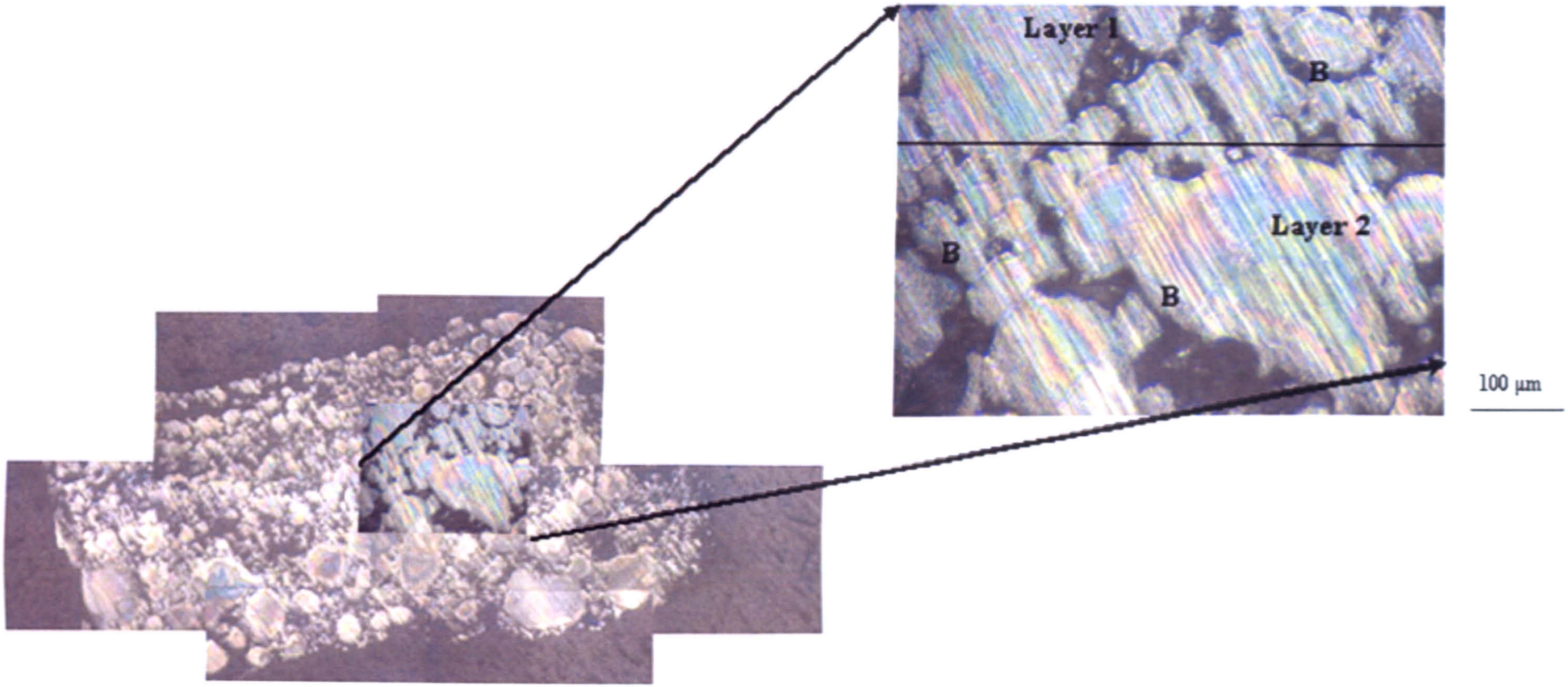

Figure 5.4: Macrostructure of laser sintered AL-2 fabricated by 150W-80mm/s (75 J/mm^3) revealing lack of inter-particulate bonding across the layers as well as presence of unsintered particles in regions B.

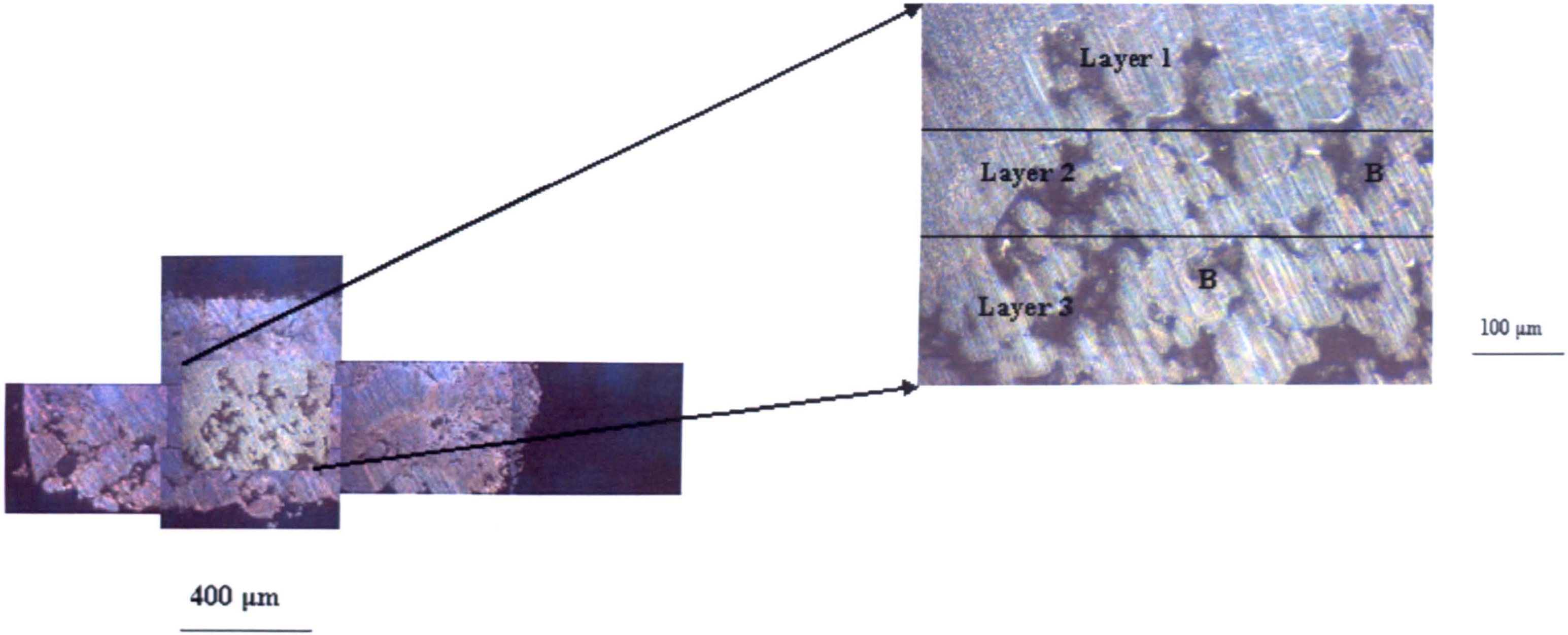

Figure 5.5: Macrostructure of laser sintered AL-3 fabricated by 150 W, 80 mm/s (75 J/mm^3) revealing lack of inter-particulate bonding across the layers as well as presence of unsintered particles in regions B.

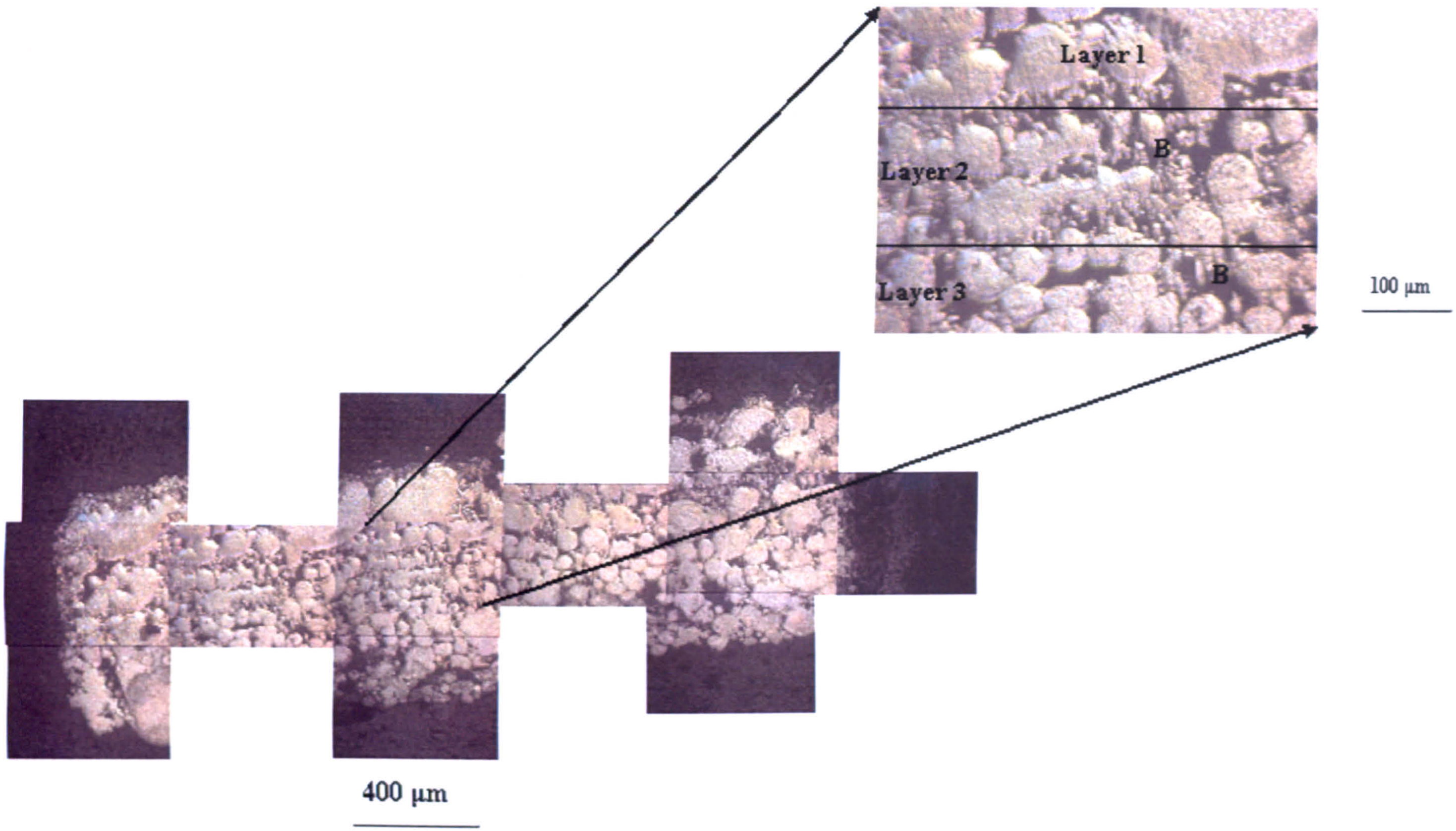

Figure 5.6: Macrostructure of laser sintered AL-4 fabricated by 150 W, 80 mm/s (75 J/mm^3) revealing lack of inter-particulate bonding across the layers as well as presence of unsintered particles in regions B.

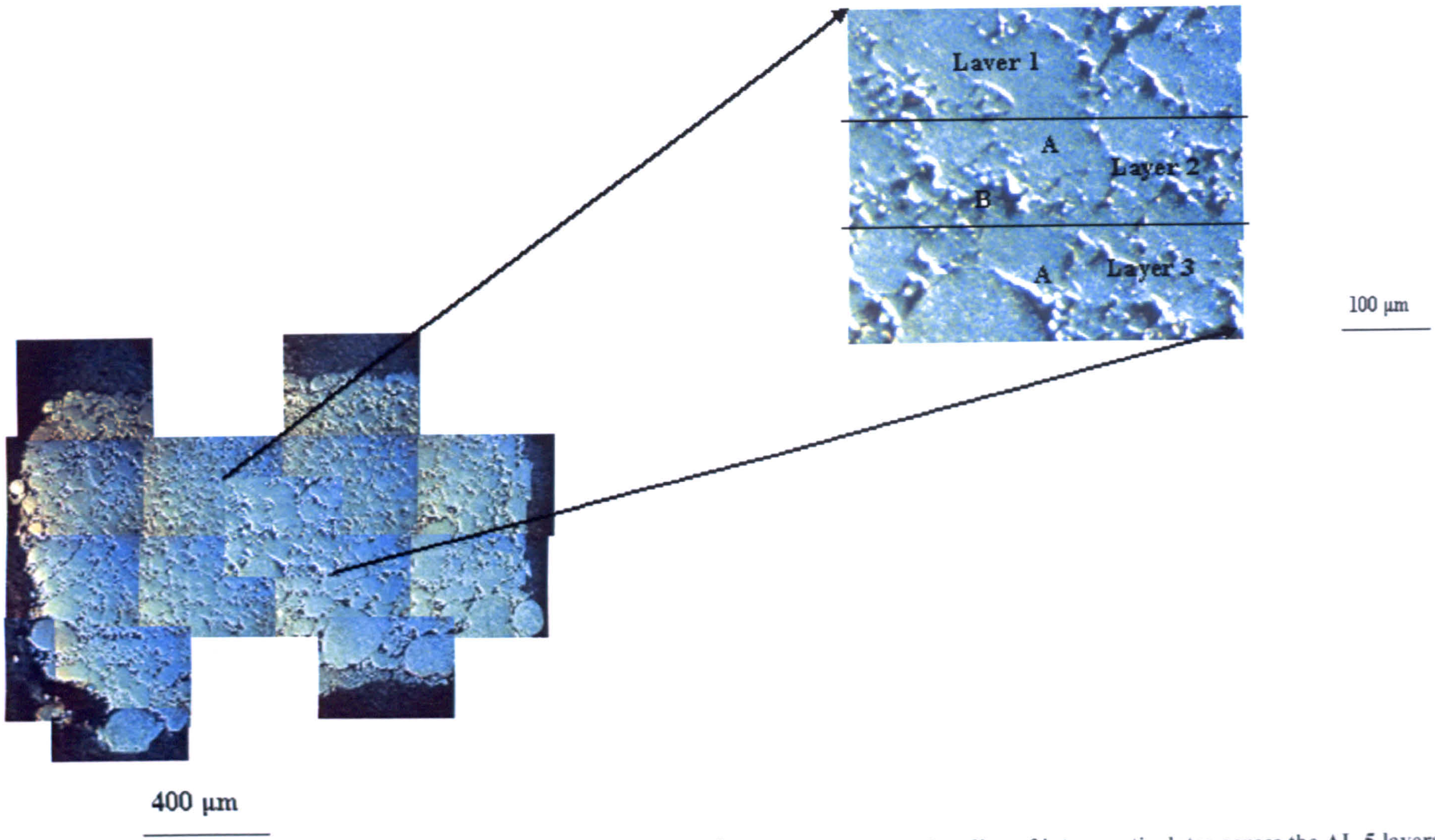

Figure 5.7: Macrostructure of laser sintered AL-5 fabricated by 150 W-80 mm/s (75 J/mm^3) revealing coherent bonding of inter-particulates across the AL-5 layers as well as evidence of melt back in regions A.

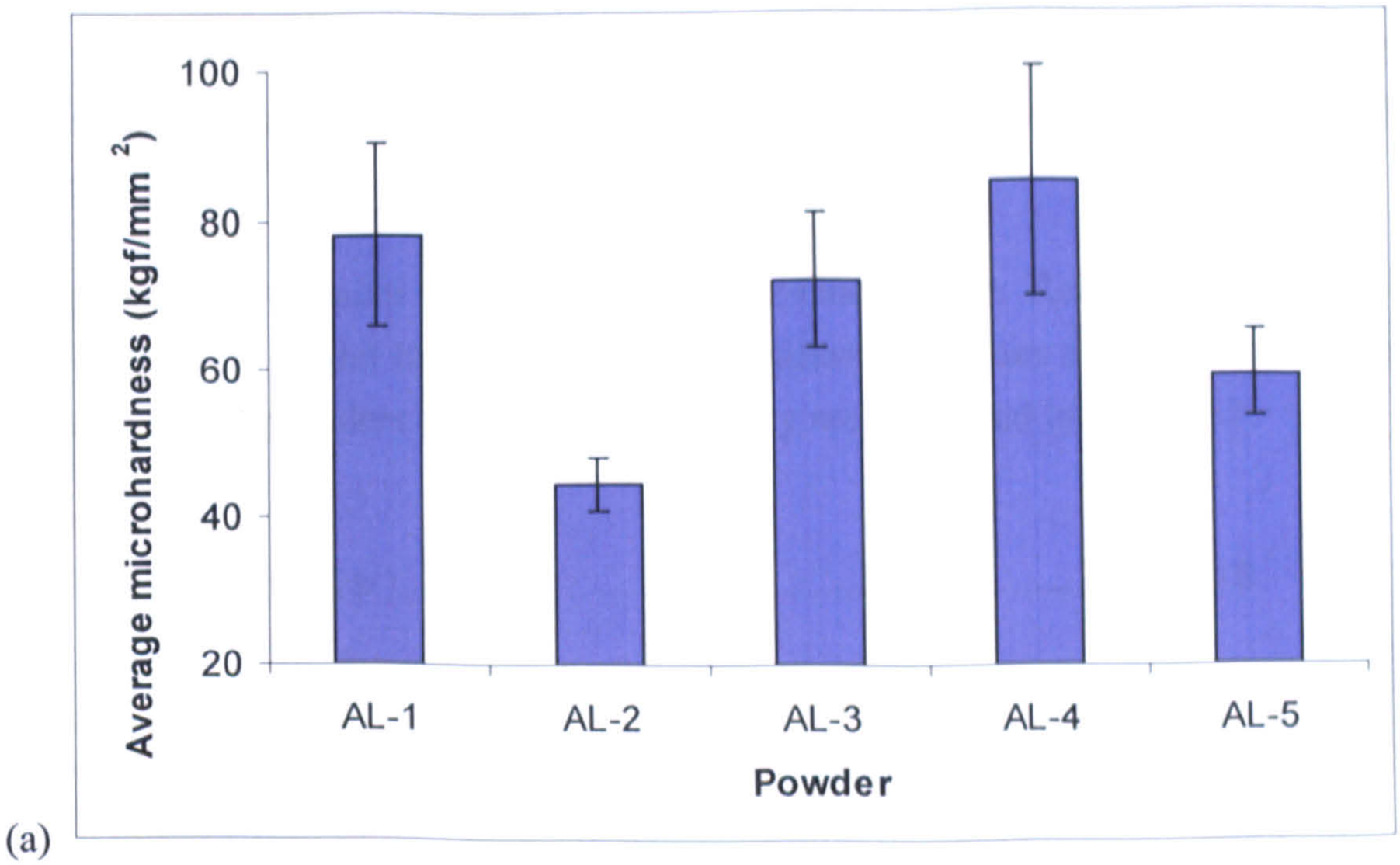

(a)

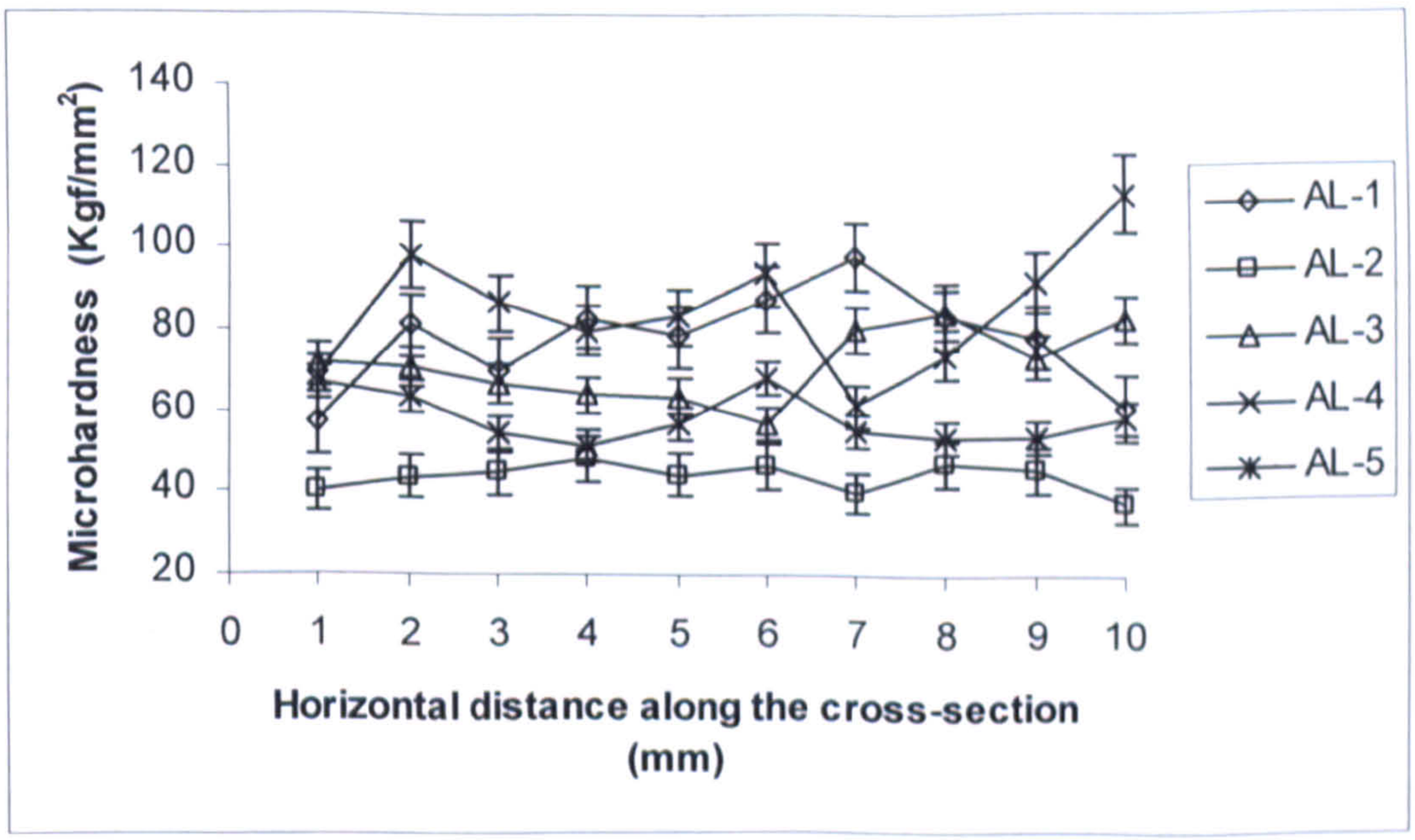

(b)

Figure 5.8: Microhardness of direct laser sintered monosized aluminium powders: (a) Average values across section; (b) Microhardness variation along the horizontal cross-section.

5.3 Effect of Powder Properties on the Density and Microstructural Characteristics of Direct Laser Sintered/Melted Monosized Aluminium Powders

Equation 2.18 (Simchi & Pohl 2003, Sanz-Guerrero & Ramos-Grez 2007) has been employed to fit/model the experimental data allowing values of C_1, C_2, and K for each of the as-received powders to be determined: they are presented in Table 5.1.

$$\rho = C_1 - C_2 \exp(-K\psi) \quad \text{.....2.18}$$

Table 5.1: Densification parameters obtained from Figure 5.1 for direct SLS/SLM processed original powders AL-1, AL-2, AL-3, AL-4 and AL-5

Powder	C_1	C_2	K	ρ_{st} (gcm^{-3})	Exp. ρ_{bed} (gcm^{-3})	ρ_{tap} (gcm^{-3})	$\alpha^* = \rho_{tap} / \rho_{bed}$	ρ_{st}/C_1
AL-1	1.537	0.989	55.6	1.531	1.335	1.593	0.84	0.997
AL-2	1.614	0.411	35.6	1.582	1.442	1.662	0.87	0.980
AL-3	1.692	1.277	44.5	1.618	1.156	1.296	0.89	0.956
AL-4	1.525	0.985	60.9	1.510	1.362	1.609	0.85	0.990
AL-5	2.030	0.910	31.9	1.947	1.642	1.732	0.95	0.959

Interestingly, Figure 5.1 reveals that at an energy density of 30 J/mm^3, SLS of the powdered particles occurred as evident by the values of the sintered density which are more or less equal to the experimental bed density of each powder. This suggests that the specific laser energy input must be greater than 30 J/mm^3 to cause significant densification. Application of the energy conservation rule, as employed by Simchi & Pohl (2003) and Sanz-Guerrero & Ramos-Grez (2007), to SLS/SLM of aluminium powders and depicted by Figure 5.1 and Table 5.1 suggest that the densification of monosized aluminium powders is controlled by the combined effects of laser power (P), scanning rates (u), scan line spacing (h), and layer thickness (d) which were unified into specific laser energy input (ψ) according to equation 2.18. Furthermore, it can be deduced from Table 5.1, that

powder shape, amount of oxide present in the powder, and alloy composition may influence the densification kinetics of laser sintered aluminium powders.

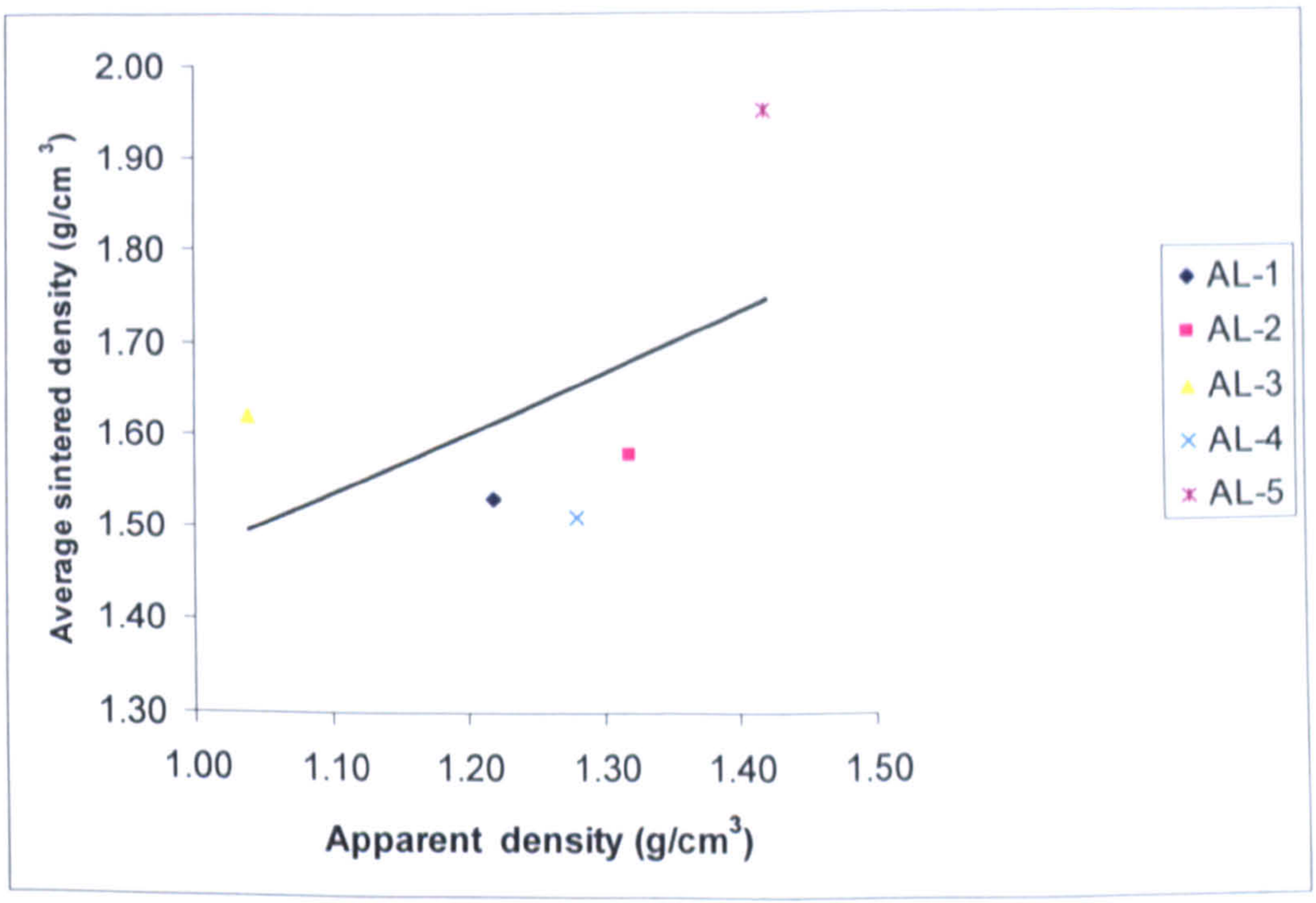

(a)

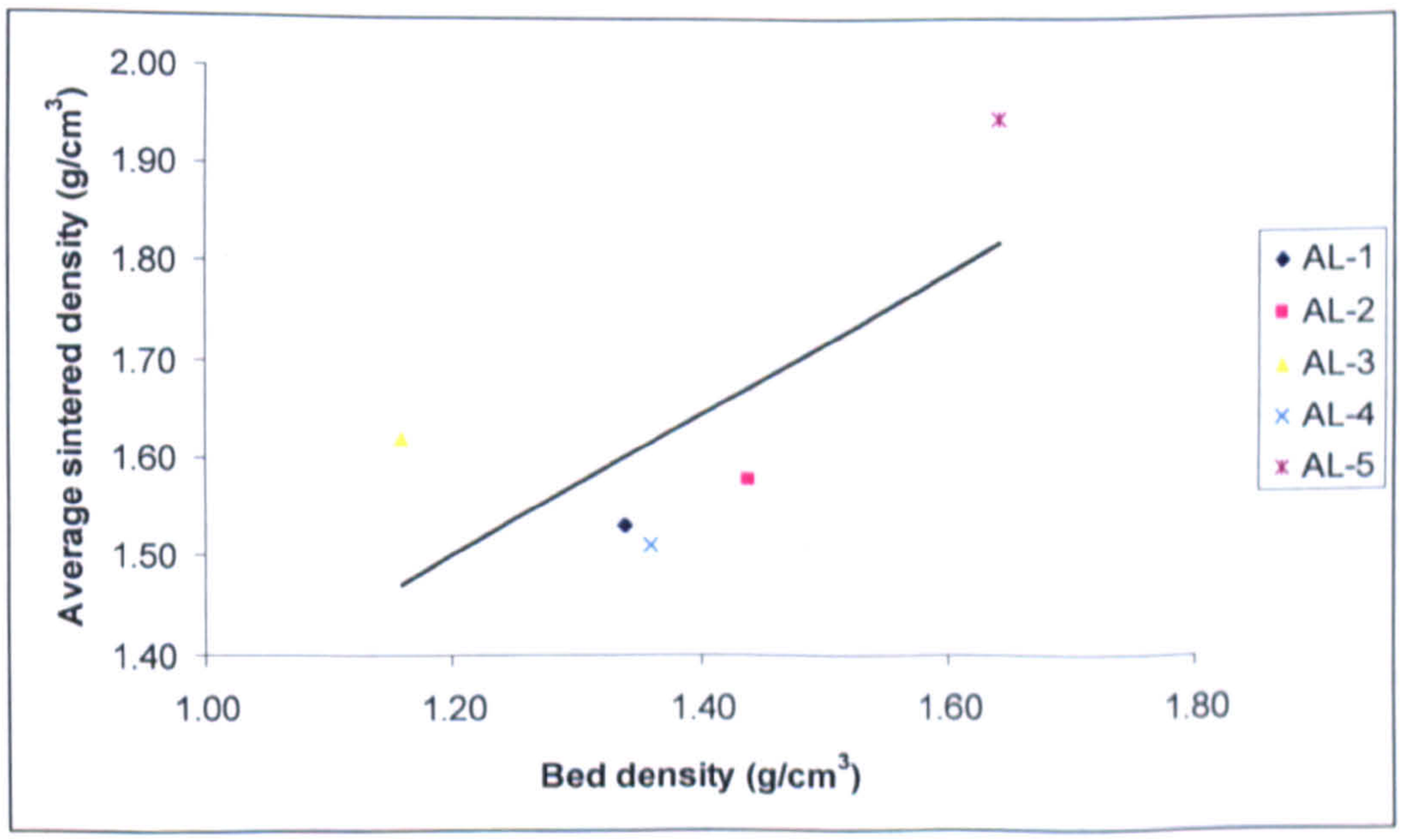

(b)

Figure 5.9: Comparison of sintered density of monosized aluminium powder with (a) apparent density and (b) bed density at the specific laser energy input of 75 J/mm^3.

Table 5.1 presents values of K, a densification co-efficient defined by equation 2.18, for each powder. K determines the relative energy density required to achieve a given maximum attainable sintered density (C_1) for a particular powder. High values of K suggest lesser degree of densification as indicated by the experimental saturation sintered density (ρ_{st}) and C_1 obtained during the SLS process (Table 5.1).

Figure 5.1 indicates that as the specific laser energy input (ψ) tends towards zero, the sintered density approaches the powder bed density (ρ_{bed}) during the SLS process. Equation 2.18 predicts that as the specific laser energy input approaches infinity, the saturation density (ρ_{st}) for each SLM processed powder approaches a maximum attainable density C_1. This observation is especially true for samples AL-1, AL-2, AL-3, AL-4, and AL-5 (see the last column of Table 5.1). The implication of C_1 which is always less than the theoretical density of wrought aluminium is that the SLS/SLM of powdered aluminium cannot attain full density even at very high energy density. These outcomes are in agreement with Simchi (2004, 2006) who demonstrated that excellent laser sinterability of a powder is indicated by lower values of densification co-efficient K. The reasons behind the difference in the responses of these SLS/SLM processed powders as exemplified by varying values of K are examined, on the basis of powders' properties in the next section.

SEM images of the as-received aluminium powders presented in Figure 4.1 revealed that samples AL-1, AL-3, and AL-4 (Figures 4.1a, c, and d) had irregular powder particle shapes, AL-2 powder had nearly spherical particles (Figure 4.1b) while sample AL-5 (Figures 4.1e) consisted of mainly spherically shaped particles. Since the powders were sieved before being supplied, all the monosized aluminium powders have the same particle size distribution (Table 4.1). Moreover, all the powdered samples could be described as free flowing with the exception of sample AL-1 (Figure 4.2). Figures 5.9a and b show that, generally, sintered density of powders increase with their apparent and bed densities when the same processing parameters are employed. For instance, at a laser power of 150 W, scanning rate of 80 mm/s, scan spacing of 0.1 mm, and layer thickness of 0.25 mm (75 J/mm^3), sintered densities are found to be 56 %, 59 %, 60 %, 59 %, and 73 % for AL-1, AL-2, AL-3, AL-4, and AL-5, respectively. Other results are found to follow the same trend. The implication of the presence of the irregular or near spherical particles in samples AL-1, AL-2, AL-3 and AL-4 is that they disturb and hinder the SLS/SLM process and lead to the formation of inferior products, as evident in the lower values of density obtained

(Figures 5.1, 5.9a, b). This occurs through significant inter-particle friction which makes particle packing less effective during powder spreading, thereby resulting in lower values of bed density (Figure 5.1 and Table 5.1). Moreover, the second to the last column in Table 5.1 shows the values of the ratio of the experimental bed density to the experimental tap density of the aluminium powder, as an agglomeration factor designated α^*. The values of α^* reveal that the spherical particles of AL-5 do not agglomerate during the SLM process, unlike the AL-1, AL-2, AL-3 and AL-4 powder with irregular and nearly spherical particles which have greater tendency towards agglomeration. It is hereby suggested that the agglomeration factor for irregularly or nearly spherically shaped powder particles that are more susceptible to agglomeration or segregation will be less than those of the spherically shaped particles. Therefore, the nearer the agglomeration factor of a powder is to a unity, the greater the tendency for such a powder bed not to be susceptible to agglomeration during SLM. Simchi (2004) established that agglomeration results in poor particle packing on the powder bed thereby causing lower values of the density of SLM processed parts. This explains the powder particle shape effect on the densification kinetics of monosized aluminium powders. In contrast, the presence of spherically shaped particles in sample AL-5 which pack together very effectively to yield high apparent, tapping and bed densities of 1.42 g/cm^3 and 1.73 g/cm^3, 1.64 g/cm^3 respectively (Tables 4.3 and 5.1, Figures 5.9a and b) could be said to have contributed to the highest density (1.94 g/cm^3) obtained during its SLM processing. The findings reported in this section are well supported by the results obtained by Sustarsic *et al.* (2005) and Simchi (2004) in their work investigating the effect of powder properties on SLM processed iron powders. It also reflects, in part, the works of Liu *et al.* (2007) who emphasised that particle shape contributed to the sintering response of P/M aluminium powder. While, the pure aluminium powders AL-1, and AL-2 contain varying amount of surface oxide and pre-alloyed AL-3, AL-4, and AL-5 have different alloying elements and oxygen contents in their compositions, it was thought that the particle shape effect could not give wholly explanation of the sintering behaviour of the monosized aluminium powders in this context. Therefore, other mechanisms governed by powder properties such as the nature and the constitution of the surface oxide film present in aluminium powders need to be explored. On this basis, it was decided that the finding from this section is not definitive because of varying composition of the as-received powders. Therefore, the role of chemical composition of the powders in their densification mechanism will be explored in the next section.

The surface oxide film is known to inhibit the densification mechanism by initiating the surface tension in liquid aluminium which promotes balling and disrupts inter-particulate coalescence/wetting across the laser sintered/melted layers. The semi-quantitative EDS analysis of the powdered samples presented in Table 4.2 will be related to Table 5.1 in order to explore the effect of the amount of oxide present in an aluminium powder on the laser sintered density and microstructure. Although, little confidence may be placed in the quantitative oxygen content determined, the relative values should indicate the relative oxide thickness on the particle surface. The presence of 16 % oxygen, according to EDS analysis, in AL-1 is an indication that it has a very thick surface oxide film (see section 4.2.3, Figure 4.1a). As pointed out earlier on in Table 5.1 from the last section, a higher value of K indicates greater energy density requirement (poor densification). It can be seen that K is influenced by the amount of oxide present in the powders and bed densities. For example, a reduction in the oxygen content of a pure aluminium powder going from AL-1 to AL-2 (see Table 4.2), as well as increased bed density of AL-2 over that of AL-1 resulted in a significant reduction of K, from 55 (AL-1) to 36 (AL-2) and a smaller increase in C_1 from 1.54 to 1.61. Besides the amount of oxide present in a powder, the nature and the distribution of the surface oxide also determines its response during SLS/SLM processing (Figure 4.1). For example, considering the specific laser energy input between 60 J/mm^3 to 75 J/mm^3, (sufficient to initiate complete melting of the particles), low values of density (50 % to 59 %) obtained for the SLS processed AL-1 and AL-2 could be explained as a consequence of the thermal properties and the presence of non-uniform thickness of oxide film covering these aluminium particles. Figure 4.1a indicates the presence of oxide islands (see arrows) of uneven thickness covering the unsintered particles of AL-1 as revealed by EDS analysis of the powders (Table 4.2). Moreover, in the multiple-layer samples, the unsintered powder particles developed into the porosity (see arrow B in Figure 5.2a and b). Evidence of non-uniform inter-particulate bonding across the layers can be seen in Figure 5.2a and b. Areas marked with arrow A suggest interparticulate bonding whereas areas marked with arrow B indicate the unsintered regions containing non-bonded particles suspected to have thin layer of oxide films. Unlike in powder metallurgy, oxide disruption could not have occurred as a result of shear because no powder compaction was undertaken so the particles could not have been mechanically deformed by an external load. Oxide disruption could not have been initiated via a chemical reaction as no alloying element was added to both AL-1 and AL-2. Thus, un-even rupturing of the oxide film across the layers in both AL-1 and AL-2 has to have been initiated and sustained by some different mechanism. It has been noted earlier on that there was slight difference in the saturation sintered density of irregular particles of AL-1

and nearly spherical particles of AL-2 (Table 5.1), so it is hereby proposed that un-even oxide thickness and the resultant variation in film fracture might have exercised a critical influence on the sintering response of the two powders (Figure 5.2a and b).

Harper (2001) noted that the thermal expansion co-efficient of alumina (α_{Al2O3} = 7.4 x 10^{-6}/°C) is only around one-quarter that of aluminium (α_{Al} = 27.4 x 10^{-6}/°C). During laser scanning, a circumferential stress, σ, is generated in the layer of oxide film covering the aluminium particles as a consequence of the disparity in thermal expansion of the oxide film and aluminium particle. According to Hooke's law, the circumferential stress generated in a thin oxide shell of modulus E, subjected to temperature change ΔT, is given by:

$$\sigma_{cirm.stress} = E(\alpha_{Al} - \alpha_{Al2O3}) \quad \text{.....5.1}$$

A temperature change of 620 °C is expected to accompany the SLS/SLM of aluminium powders, thus giving maximum tensile stress of approximately 4,700 MPa on an alumina surface film (Table 5.2). The un-even layer thickness of oxide films covering the aluminium particles in both AL-1 and AL-2 is hereby conjectured to be responsible for the uneven sintering observed (Figures 5.3 and 5.4). For a thin layer of oxide shell designated as half crack length a, the generated stress of 4,700 MPa by laser scanning could be said to be several times higher than the required fracture stress of 330 MPa for the effective disruption of the shell of alumina (Accuratus 2002).

Table 5.2: Mechanical and thermal properties of interfacial aluminium oxide films.

Oxide	E (GPa)	ΔT (°C)	α (x10^{-6}/°C)	$\sigma_{circumferential\ stress}$ (MPa)	$\sigma^*_{fracture\ stress}$ (MPa)
Alumina	379	620	7.40	4,700	330
Spinel	238	620	9.50	2,640	11000
Mullite	69	620	5.40	940	180

Therefore, powders with thick oxide films on the surface might be seen as being easily susceptible to thermal cracking leading to covalescence of particles (see regions A in Figures 5.2a and b). In contrast, when thinner layers of oxide are present, powders may

have remained "unsintered" in spite of the application of a sufficiently high specific laser energy input to melt the aluminium. Considering the fracture mechanics of the oxide film, the stress required for brittle fracture is given approximately by equation (5.1). The analysis of the equation 5.2 implies that as the thickness of the oxide film covering the aluminium particles gets smaller, the stress required for thermal cracking tends towards infinity. Putting some data into equation 5.2, (K_{IC} = 4 $MPam^{1/2}$) (MatWeb 2008) and assuming the maximum circumferential stress in the oxide layer is 4,700 MPa, a value of around 0.25 μm for the critical half length is obtained. Therefore, films thicker than this should fracture whereas thinner films should just deform elastically. This explanation helps in gaining insight as to why aluminium powders with thicker oxide film might be better in yielding desirable sintered density when laser sintered even at a reasonably high energy density.

$$\sigma_{cirm\ stress} \approx K_{IC} / (\sqrt{(\pi * a_c)}) \quad \text{.....5.2}$$

where K_{IC} is the fracture toughness, a_c is half crack length.

$a_c \approx (1/\Pi) * (K_{IC} / \sigma_{cirm\ stress})^2$

$a_c \approx (1/\Pi) * (4 / 4700)^2$

$a_c \approx 2.3 \times 10^{-7}$ m

This implies that oxide films ≥ 0.2-0.3 μm thick should fracture.

Furthermore, the amount of specific laser energy input dissipated on the powder bed also influences the fracture behaviour of the oxide film in a direct SLS/SLM processed aluminium powder. For example, if the specific laser energy input is insufficient (e.g. 30 J/mm^3) to reduce the surface tension because adequately high temperature could not be generated for disrupting the oxide film, the sintered density is reduced significantly as a consequence lack of generation of significant melting pool. This occurs because the applied laser energy is not high enough to fracture the surface oxide film covering the aluminium powdered particles. In this case, it may be proposed that fewer amounts of aluminium powder particles are bonded together. On the basis of findings presented in the last paragraph, it could be suggested that the presence of lower amount of surface oxide film in a powder does not significantly affect the sintered density of a powder. What may be thought of as considerably influencing the density of a SLS/SLM processed aluminium powder is the typical layer thickness as well as the nature of its oxide film as pointed out earlier on. If the amount of oxide does significantly affect the sintered density of a laser

sintered aluminium powder, it is expected that with the oxide content of AL-2 which is about two-fifth that of AL-1, substantial increase in the density and non-porous microstructure of the latter over the former would have been achievable. Finally, it is hereby suggested that fracture occurs in thicker oxide regions but not as a reason underlying the behaviour of AL-1 and AL-2.

An observation of Figure 5.1 also reveals that samples AL-3 and AL-4 exhibit very marginal increase in sintered density over that of AL-1 and AL-2, even though both AL-3 and AL-4 contain a lower amount of oxide than AL-1 and AL-2 (see Table 4.2). Again, it is now evident that it is not amount of the surface oxide film content in an aluminium powder that influences its laser sintered density but the nature and the thickness of the oxide film (its distribution over the aluminium particle's surface) which affects its sintering response. To understand why there has been significant increament in the density of SLM processed sample AL-5 over those of other aluminium powders, especially SLS processed AL-3 and AL-4, the next section will assess how alloy composition do affect the density and microstructure of laser sintered aluminium powders.

The pre-alloying of magnesium in the aluminium powders AL-3 and AL-4 raised the values of K to 45 and 61 respectively (see Table 5.1). By comparison with AL-2, this indicates that the addition of magnesium to aluminium worsens the densification kinetics. On the other hand, the addition of silicon to aluminium lowered K considerably to 32 suggesting that silicon is beneficial to the densification kinetics of AL-5. To understand the role of magnesium and silicon in the development of the density of SLS/SLM processed aluminium powders, their effect on the oxide film disruption and wettability will be discussed. Addition of Mg or Si to the aluminium alloy prior to atomisation might be expected to change the nature of the oxide film. Specifically, Mg promotes the formation of spinel ($MgAl_2O_4$) in thin layers and Si, the formation of mullite (Al_2O_3 SiO_2) (Dunkley 1998). Table 5.2 also presents the thermal properties calculated values of the thermal stresses and reported fracture strengths for these oxides. The maximum circumferential stress, σ, generated in a surface layer of spinel as a consequence of the thermal expansion mismatch is 2,640 MPa, significantly less than the reported fracture stress of spinel of 10,800 MPa, (Singh *et al.* 2007). Moreover, observation of the particle's surface of the Al-Mg (Figure 4.1c and d) powders reveals the presence of uneven layer of oxides films. As noted earlier on, areas containing thicker oxide shells will be easier to fracture thermally

and the Al-Mg particles in such areas can easily melt and coalesce. Portions of the Al-Mg powder bed containing thinner layers of oxide films are speculated to be much more difficult to sinter because the generated thermal stress for a thinner layer of spinel film is far less than the required thermal fracture stress which approaches infinity. Observation of the Ellingham diagram and comparisons of the reported fracture stress (Table 5.2) suggest that the oxide film on Al-Mg powders are the most stable at very high processing temperatures. This behaviour suggests that oxide films of Al-Mg powders have the highest fracture toughness of the pure aluminium powders (AL-1 and AL-2) and Al-12Si (AL-5) powders. On this basis, by considering equation 5.2, it is hereby speculated that regions having thinner layers of oxide films in AL-3 and AL-4 powders are likely to be many. Generally, variability in film thickness and effect on location of fracture as well as the relative value of maximum circumferential stress which is lower than the fracture stress suggest that fracture of oxide film is less likely. Figures 5.2c and d show the areas where coalescence or sintering of particle occurs (see arrow A) whereas portions containing porosities (see Arrow B) have not experienced sintering at all. On the other hand, Park *et al.* (2002) and Geiger & Poirier (1973) established that increasing content of magnesium in an aluminium melt pool reduced the surface tension while increasing the melt viscosity. Eventually, this inhibits the wettability between the layers of SLM processed Al-Mg samples and consequently reduces the sintered density, thereby exacerbating the microstructure (Figure 5.2c and d).

In the case of AL-5, observation of Figure 4.1e reveals even distribution of oxide over the surface of its particles. From Table 5.2, the maximum circumferential stress of 940 MPa is again greater than the fracture stress of mullite, (180 MPa) (Accuratus 2002). On this basis, the oxide film present in AL-5 is thought to be much more susceptible to cracking thereby causing inter-particulate melting at lower temperature. An examination of Figure 5.2c shows uniform melting across the powder's particles. This could be attributed to the uniform thickness of oxide layers across the AL-5 particles, leading to more widespread fracture of the oxide film. Moreover, as pointed out in section 4.4.4, pre-alloying silicon into aluminium powders reduces its viscosity (King 1987, Dinsdale & Quested 2004), and has no effect on the surface tension of aluminium melt pool (Geiger & Poirier 1973). Consequently, this improves the wettability between the deposited layers, by destabilising the melt pool of laser sintered AL-5 powders. Eventually, silicon promotes particle melting across layers and increases the sintered density (Figures 5.1 and 5.2c).

The lowest average value of microhardness recorded for sample AL-2 is indicative of the poor densification noted earlier while that of AL-1 is considered to be very high due to high oxide content (16 wt%) and the uneven distribution of oxide layer over the aluminium particles in AL-1. It is speculated that these factors tend to promote compression of particles during testing thereby raising the microhardness of AL-1. Average values of microhardness obtained for AL-3 and AL-4 are consistent with strengthening due to magnesium additions, as is the case for conventionally processed alloys. The variation of microhardness across etched sections of samples suggests that the microstructures of these samples are heterogeneous and reflects the fact that they contain large, irregularly shaped pores and substantially aggregated particulates as shown in Figures 5.2, and 5.3 to 5.7.

From the available evidence, it is now clear that a suitable aluminium powder for the direct SLS/SLM must not only contain lower amount of oxides in order to prevent the challenge of balling, but the distribution of the thickness of its oxide film must be uniform in order to avoid differential sintering of the aluminium particles. Moreover, the thermal properties of the oxide film of the alloying elements has significant role to play in influencing the properties of SLS/SLM processed powders. It can be suggested that when the thermal co-efficient of expansion of the oxide of an alloying element in aluminium is much lower that of aluminium and the oxide layer thickness is evenly distributed, higher values of density will be obtained, as seen in SLM processed AL-5.

A careful analysis of the results obtained so far suggests the possibility of producing aluminium alloys via SLS/SLM process with desirable microstructural features and properties, provided a suitable aluminium alloy powder can be identified. This evidence suggests that SLM processed samples made in AL-5 powder show the most promising behaviour which can be taken further to improve properties. The best sample made in this powder had 73 % sintered density, a Vicker's hardness of 59 kg/fmm^2 and showed coherent interparticulate bonding across the layers. These properties were obtained using the same set of processing parameters for all the powders studied, these being derived from single layer experiments. Optimisation of the processing parameters for fabricating multiple layer parts in AL-5 will allow a more thorough investigation of the influence of

the processing parameters on the density and microstructural properties while optimising sintered density and mechanical properties.

5.4 Optimisation of Processing Parameters for the Direct Laser Sintered AL-5

The most important entity that affects the density and microstructure of direct laser sintered materials is the energy density (section 2.7.2.1).

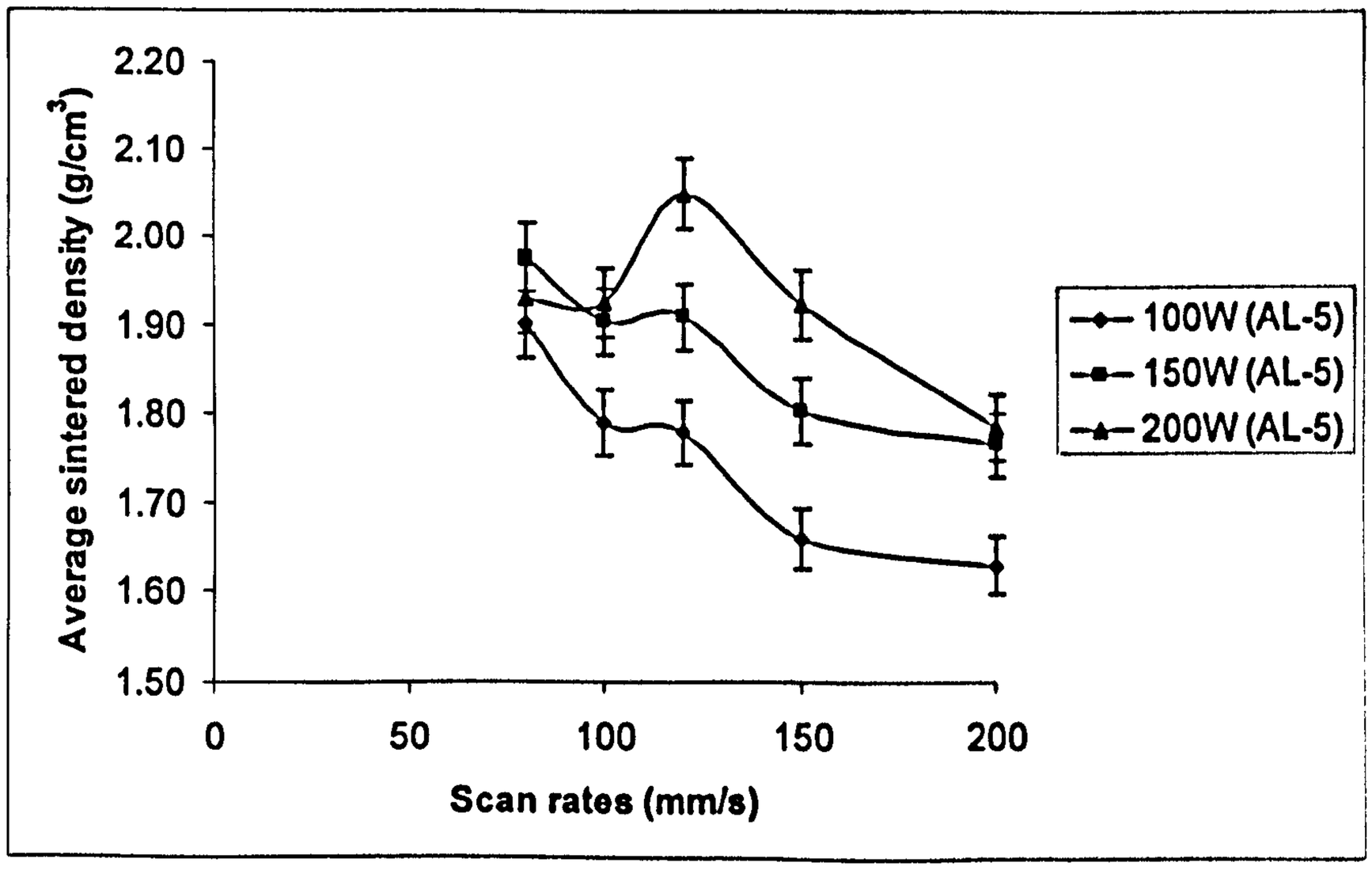

Figure 5.10: Variation of the density of SLM processed AL-5 powder with scanning rates at different laser powers.

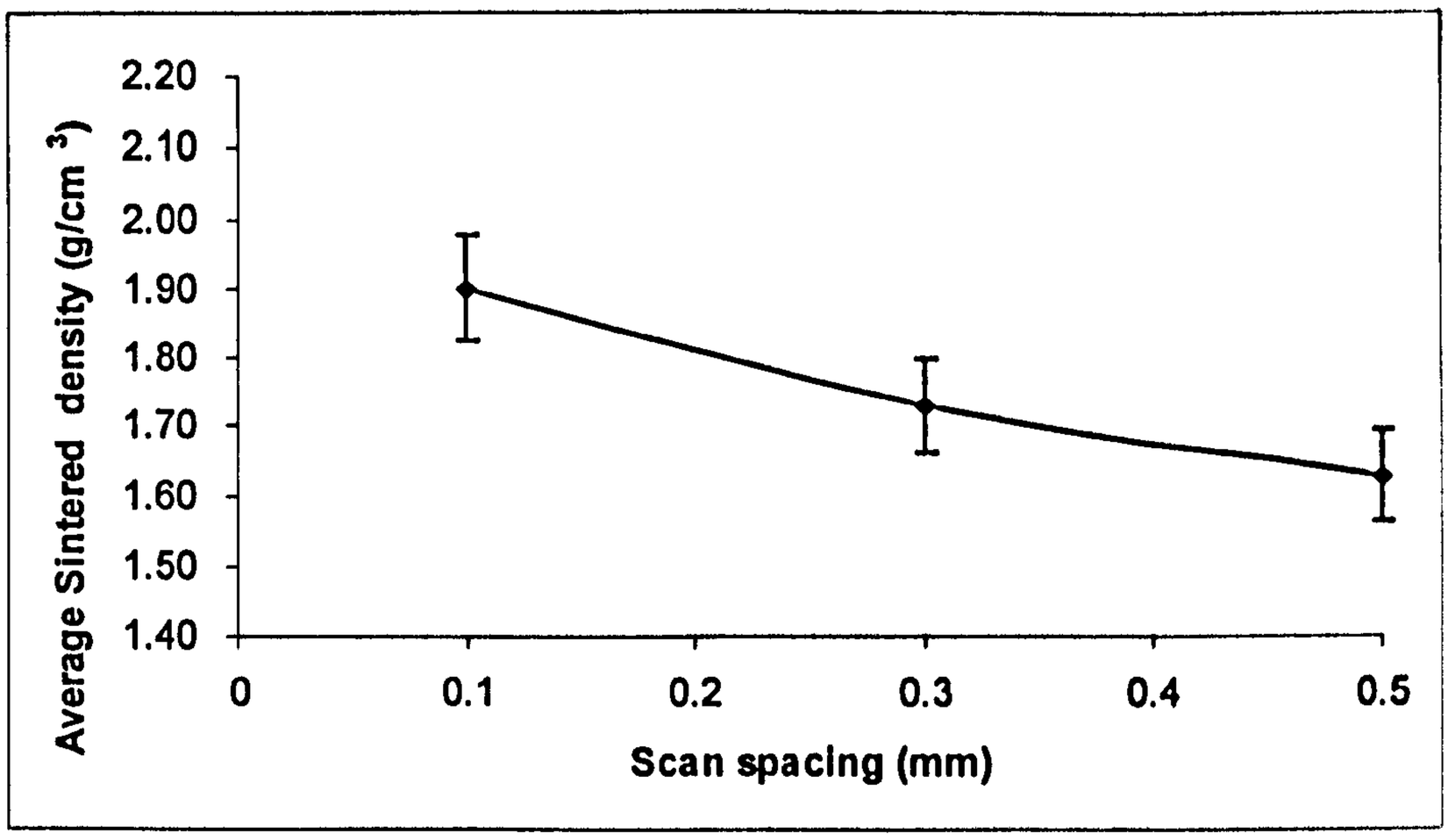

Figure 5.11: Variation of the density of SLM processed AL-5 powder with scan spacing at fixed laser power (240 W), scan spacing (0.1 mm) and layer thickness (0.25 mm).

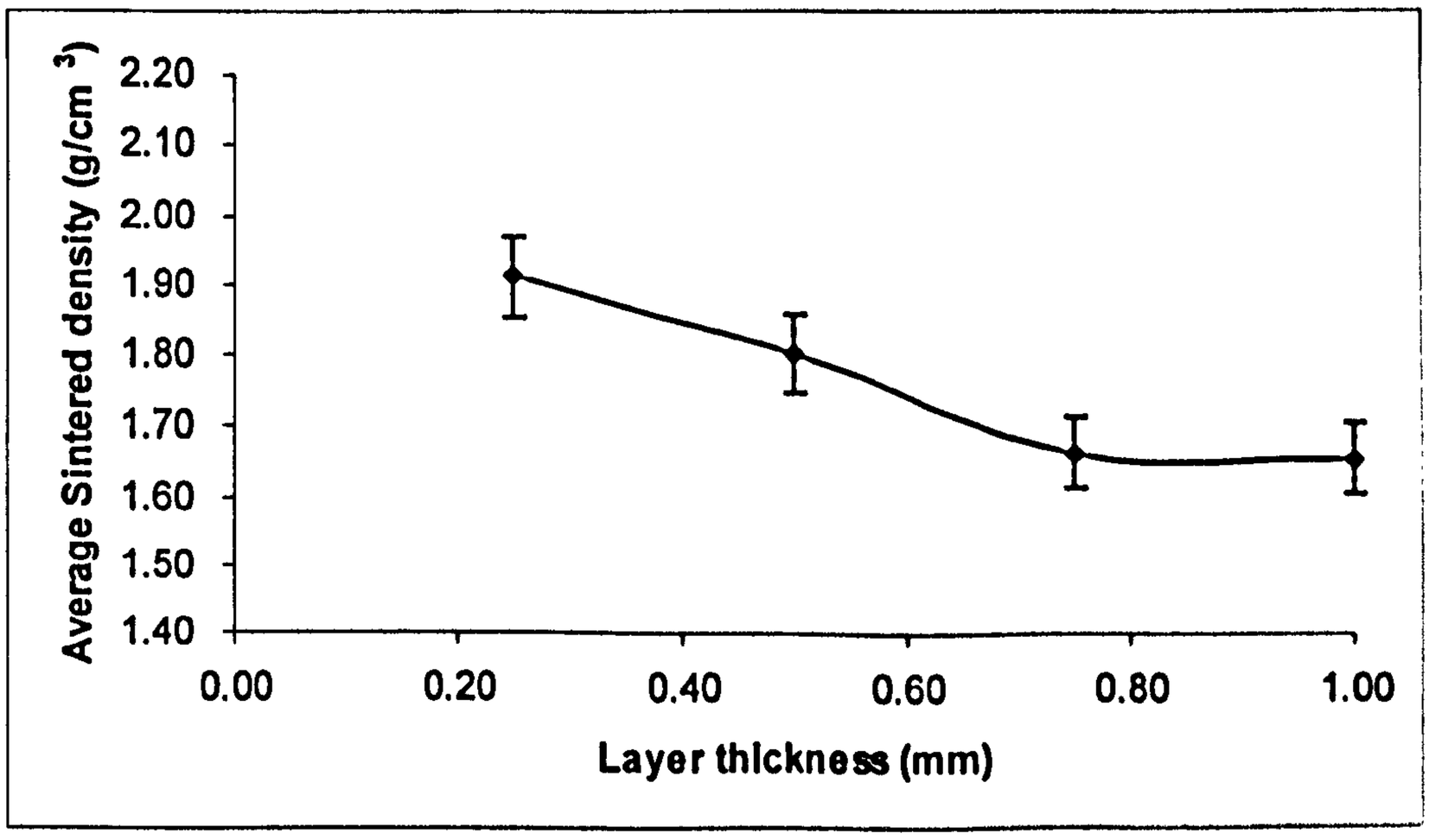

Figure 5.12: Variation of the density of SLM processed AL-5 powder with layer thickness at fixed laser power (240 W), scanning rate (120 mm/s); and scan spacing (0.1 mm).

Experiments were carried out to investigate the effects of laser power and scan rate (Figure 5.10), scan spacing (Figure 5.11), layer thickness (Figure 5.12) on the density of SLM processed AL-5. These results were then consolidated onto a single figure showing the variation of sintered density with specific laser energy input (Figure 5.13). An increase in

the laser scanning speeds consequently results in the reduction of the sintered density of AL-5 (Figure 5.10,) whereas, there exists a direct variation relationship between the sintered density and the laser power (Figure 5.10). Furthermore, Figures 5.11 and 5.12 reveal that there exists an inverse relationship between the scan spacing and layer thickness on one hand and density of laser sintered samples made in AL-5 on the other hand.

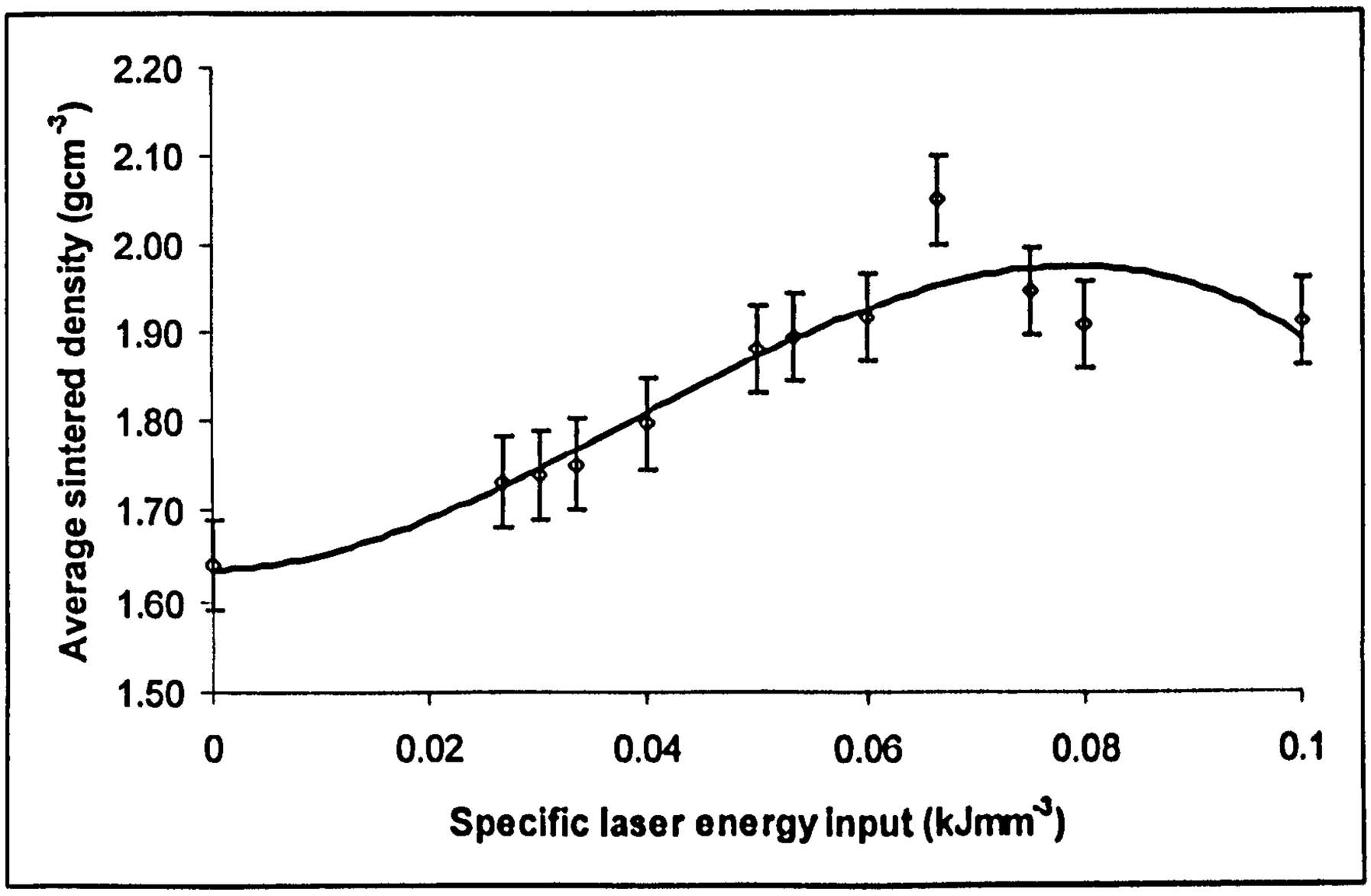

Figure 5.13: Variation of the density of SLM processed AL-5 powder with the applied energy density.

Figure 5.13 shows that the density of SLM processed sample AL-5 increases as the quantity of specific laser energy delivered to the powder bed increases until a maximum density (2.05 g/cm^3) was attained at a saturated specific laser energy input of 67 J/mm^3 after which a reduction in sintered density is observed until a constant value lying between 1.90 and 1.95 g/cm^3 was achieved. The manufacturing of functional engineering components by the SLS/SLM technique requires the appropriate choice of powder layer thickness and processing parameters. This is because the thinner the powder layer chosen for a specified range of specific laser energy input, the greater the degree of interlayer bonding and the lower the incidence of balling.

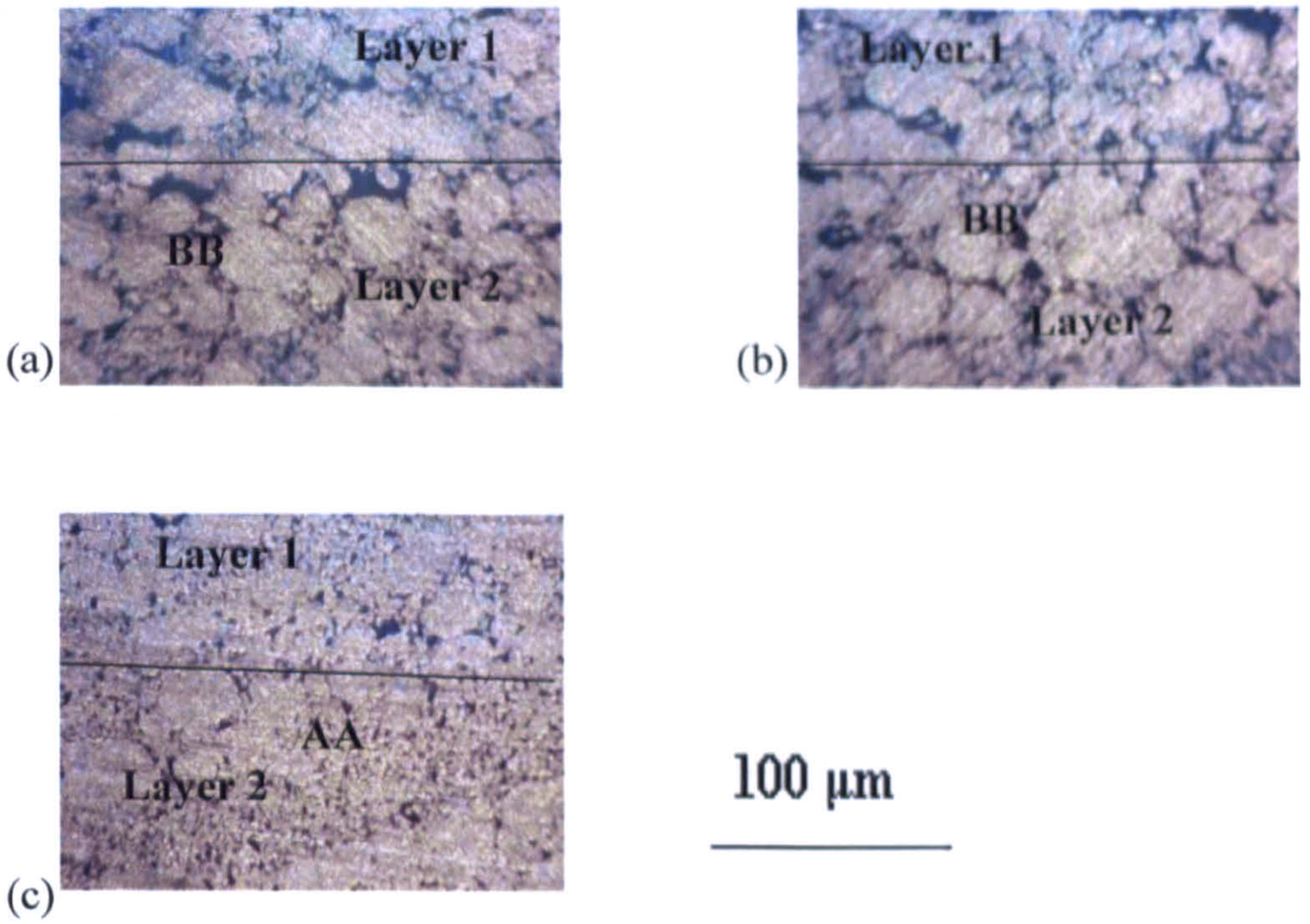

Figure 5.14: Effect of variation in layer thickness on the microstructure of laser sintered AL-5 powder at laser power of 200 W, scan rates of 120 mm/s; and scan spacing of 0.1 mm: (a) 1.0 mm (b) 0.5 mm (c) 0.25 mm.

For example, if the layer thickness is very high (1.00 mm), large and interconnected pores will be formed in the AL-5 microstructure (see region BB in Figure 5.14a). This occurs because the powder layer, in this instance, has not completely melted as a result of the insufficient energy penetration of the laser beam. In order words, the available quantity of materials for sintering is much more than the intensity of the available laser power. The result obtained from this research indicates that the sintered density decreases with increasing layer thickness (Figure 5.12). At a layer thickness of 0.25 mm, inter-layer densification could be seen to have increased. Here, the available specific laser energy input is sufficient to re-melt the top of the previous layer in order to achieve coherent bonding (see region AA in Figure 5.114c). Chatterjee *et al.* (2003) established that the remelting of the deposited layer does not contribute to balling effect, whereas melting of the powder particles may lead to spheroidisation if it does not wet the substrate. It is pertinent to note that the minimum layer thickness is determined by the maximum particle size in the powder system and the precision of the powder delivery mechanism employed in the sintering equipment (Agarwala *et al.* 1995). In the context of this work, it was discovered that lowering the layer thickness below 0.25 mm for AL-5 powder system resulted in difficulty in spreading a homogeneous layers of the fresh powders without

displacing the SLS/SLM processed substrate layers which resulted in a decline in the quality of the SLM processed AL-5 specimens.

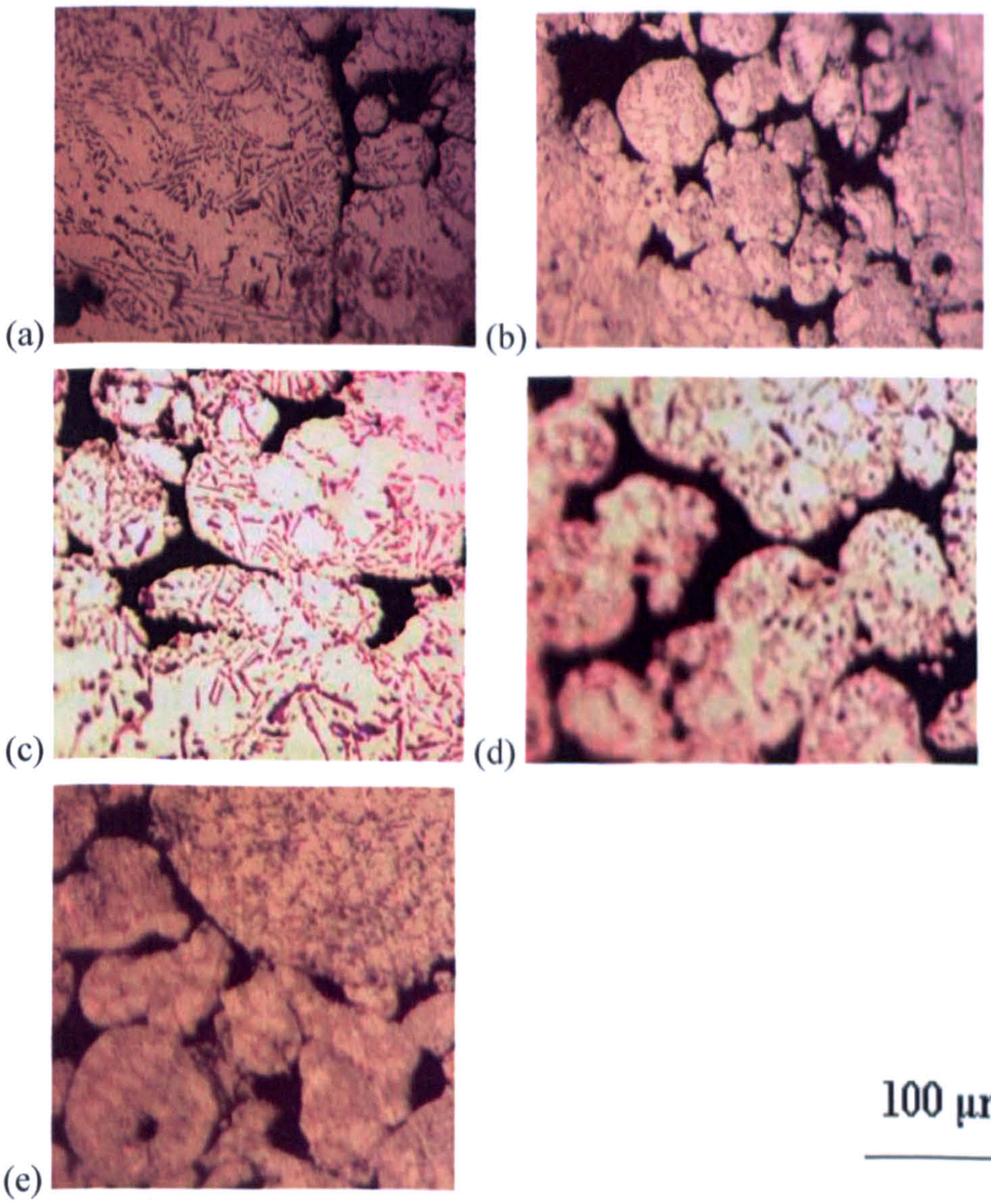

Figure 5.15: Optical micrographs of etched, polished sections parallel to the build directions at different energy density: (a) 100 J/mm^3 (b) 75 J/mm^3 (c) 67 J/mm^3 (d)40 J/mm^3 (e)13 J/mm^3

Figure 5.15 shows the representative inter-agglomerate structures in SLS/SLM processed AL-5 specimens as a function of the processing conditions. Figure 5.15 shows that, though the microstructures consist of small pores, the connectivity and orientation of pores are largely dependent on the choice of processing parameters which determines the quantity of specific laser energy dissipated to the powder bed. For instance, elongated pores which are nearly perpendicular to the building direction were found in a sample fabricated with laser

power of 200 W; scan rates of 120 mm/s; scan spacing of 0.1 mm and layer thickness of 0.25 mm which generated specific laser energy input of 67 J/mm^3 (Figure 5.15c). The inter-agglomerates are fully dense and consist of dendrite grains which are oriented nearly perpendicular to the build direction (Figure 5.15b). Comparison of the inter-agglomerate pores obtained at specific laser energy input of 100 J/mm^3 and 75 J/mm^3 (Figure 5.15a, b) with that produced by 67 J/mm^3 shows that sizes of inter-agglomerates pores are larger and appear less dense for the former. Furthermore, the inter-agglomerates obtained when specific laser energy inputs are reduced to of 40 J/mm^3, and 13 J/mm^3 are observed not to have been as fully dense as the sample made with specific laser energy input of 67 J/mm^3. It is evident that decreament or increament in specific laser energy input of 67 J/mm^3 leads to increament in pore sizes, less dense inter-agglomerates and less oriented pores (Figure 5.15a to e).

Figures 5.16, 5.17, and 5.18 show the overall macrostructure and microstructural evolution of samples produced at specific laser energy inputs between 50 and 100 J/mm^3. In order to attempt to quantify the microstructural changes resulting from changes in the specific laser energy input, measurements of secondary arm spacing and primary phase fraction were made (see Appendix S for the details of these measurements). The results are presented in Figures 5.20 and 5.21 respectively. Figure 5.20 shows that there is an increase in secondary dendrite arm spacing as energy density increases, with no significant variation in measurements when errors bars are considered. Similarly, there is a small but barely significant decrease in primary phase present. At the highest energy density (100 J/mm^3), there is the potential for greater melt superheat so it takes longer for the initiation of solidification. A lower temperature gradient may result giving rise to a lower cooling rate and coarser dendrite arm spacing (Figure 5.19a and d). In AL-5, rather than the continuous network of pores seen in AL-1 and AL-2; irregular shaped pores with no preferred orientation surrounded by a fully dense aluminium-silicon matrix are seen, accompanied by small, pin-hole pores. As the specific laser energy input is reduced by one-third to 67 J/mm^3, superheating is not so pronounced giving a higher average interfacial temperature gradient leading to a faster cooling rate and slightly finer microstructure as shown in Figures 5.17 and 5.19b. The pin hole porosity found could be attributed to the shrinkage which occurs during solidification. As the specific laser energy input is reduced to 50 J/mm^3, the heat is just enough to sinter the powder and the dendritic microstructure can be seen to have become finer whilst the interconnectivity of the porosity increases (Figures 5.24 and 5.19c). Figure 5.20 shows that the average dendritic arm spacing at the top of the

sintered samples (14.3 μm, 16.5 μm, 19 μm) are smaller than that obtained at the bottom of each sintered sample (31.2 μm, 35.2 μm, and 42 μm) at specific laser inputs of 50 J/mm^3, 67 J/mm^3 and 100 J/mm^3 respectively. Meanwhile, the average fraction of primary phase obtained with laser energy densities of 50 J/mm^3, 67 J/mm^3 and 100 J/mm^3 are 8.8wt%, 7.2wt% and 5.6wt% respectively (Figure 5.21).

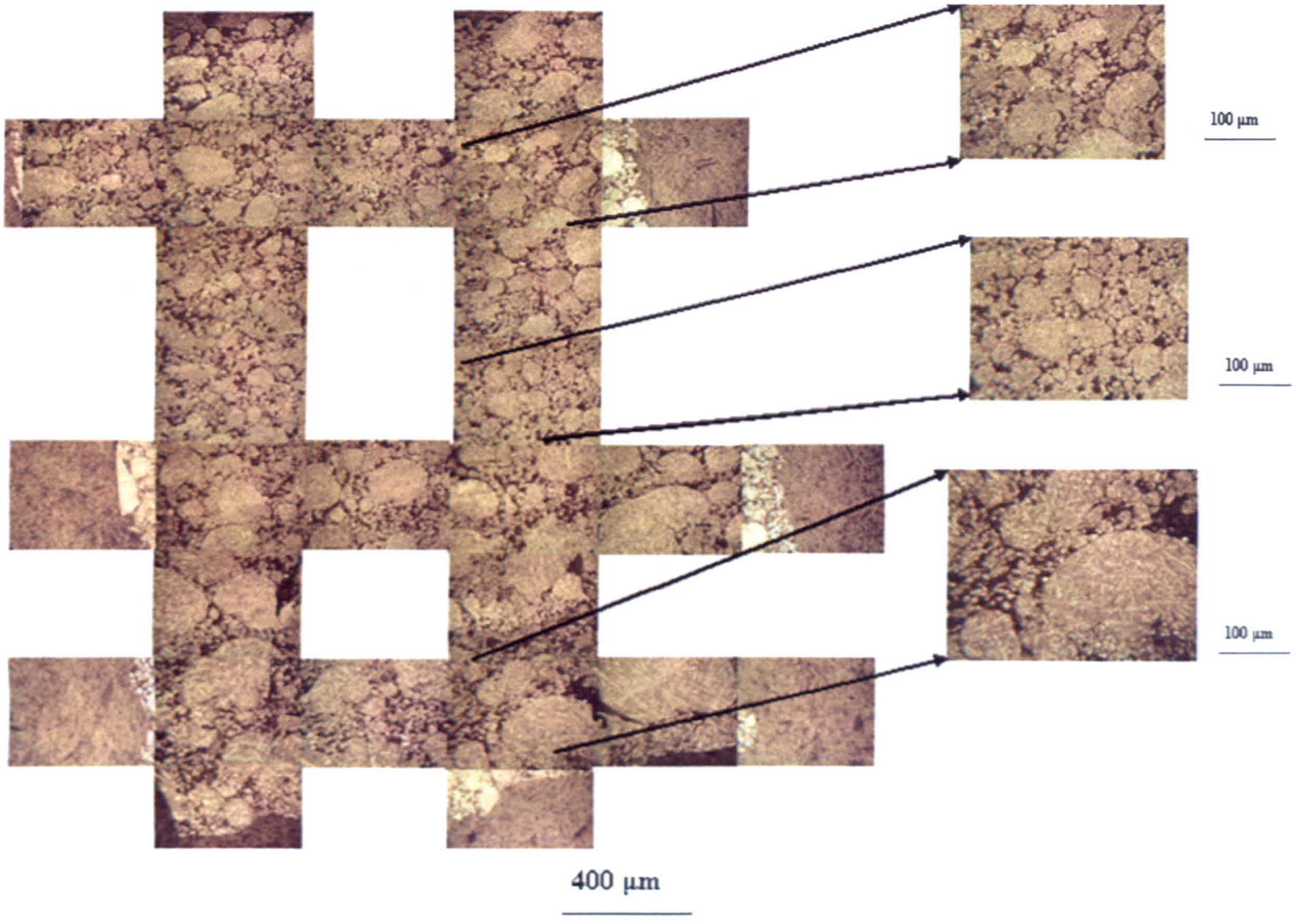

Figure 5.16: Sections through the micrograph of AL-5 (200W-80mm/s) generated by 100J/mm^3.

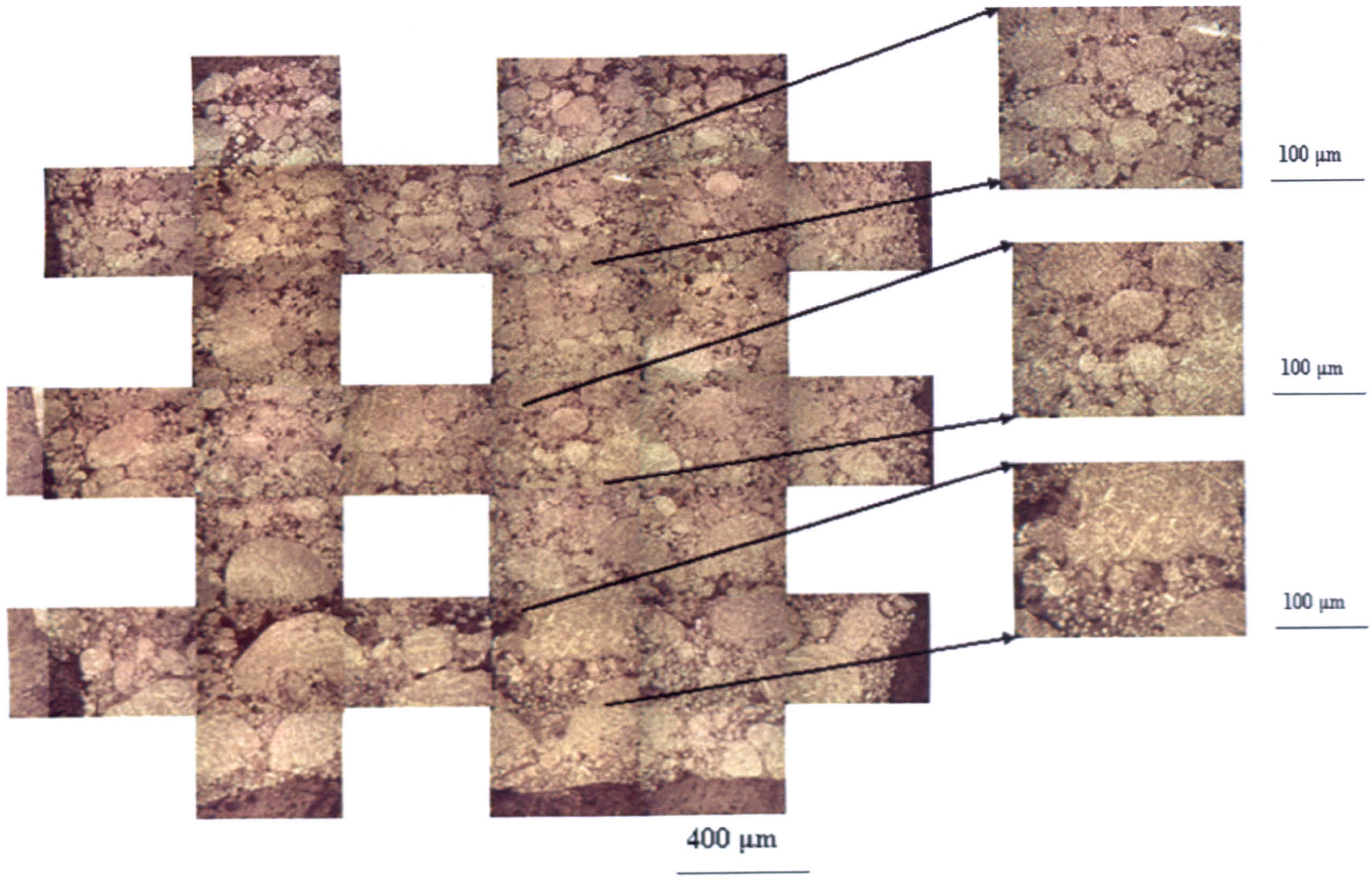

Figure 5.17: Sections through the micrograph of AL-5 (200W-120mm/s) generated by 67 J/mm^3.

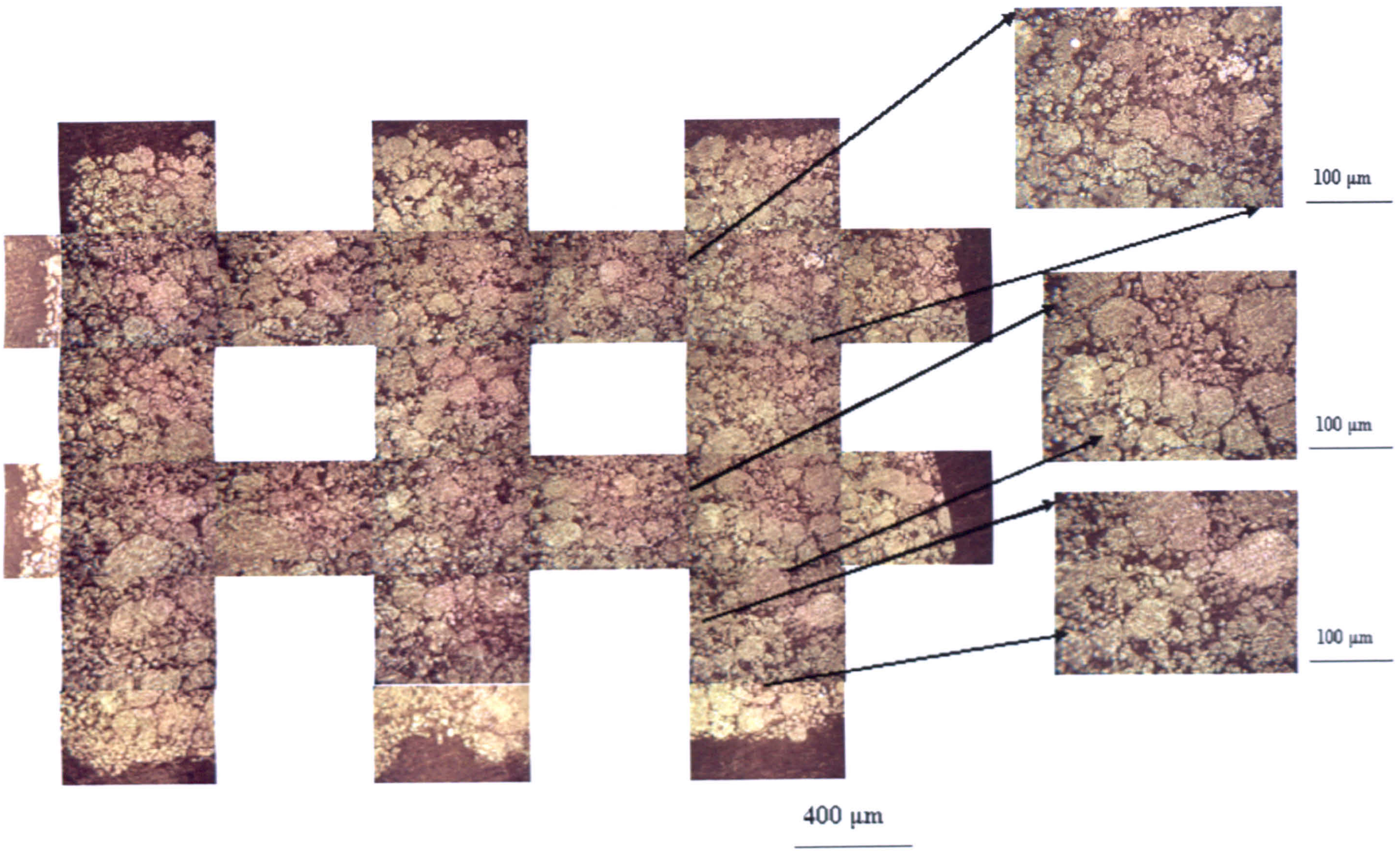

Figure 5.18: Sections through the micrograph of AL-5 (150W-120mm/s) generated by 50J/mm^3.

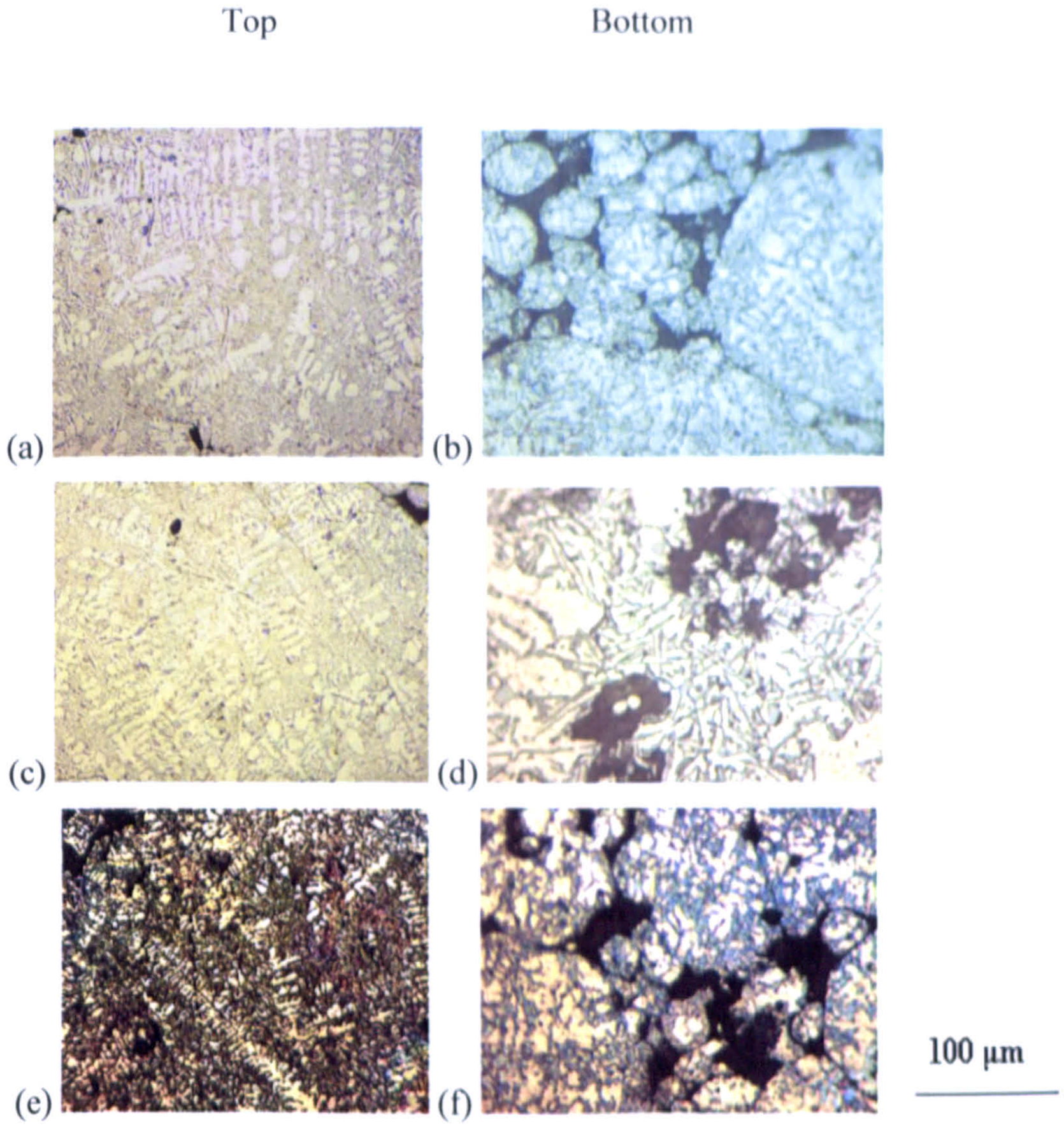

Figure 5.19: Characteristic microstructures of SLM processed AL-5 powder with varying processing conditions: (a, b) 100 J/mm^3; (c, d) 67 J/mm^3; (e, f) 50 J/mm^3.

It can be seen that the growth of the secondary dendritic arm spacing is in direct relationship with the energy density irrespective of the depth of measurement because the dissipation of high energy density on the powder bed is accompanied by lower thermal gradient and slow undercooling which results in coarse "broomlike" dendritic microstructure. On this basis, the fraction of primary phase in a laser sintered AL-5 might be adjudged to be indirectly proportional to the applied energy density, but, the variation in both dendritic arm spacing and fraction of primary phase could be said to be marginal and largely insignificant.

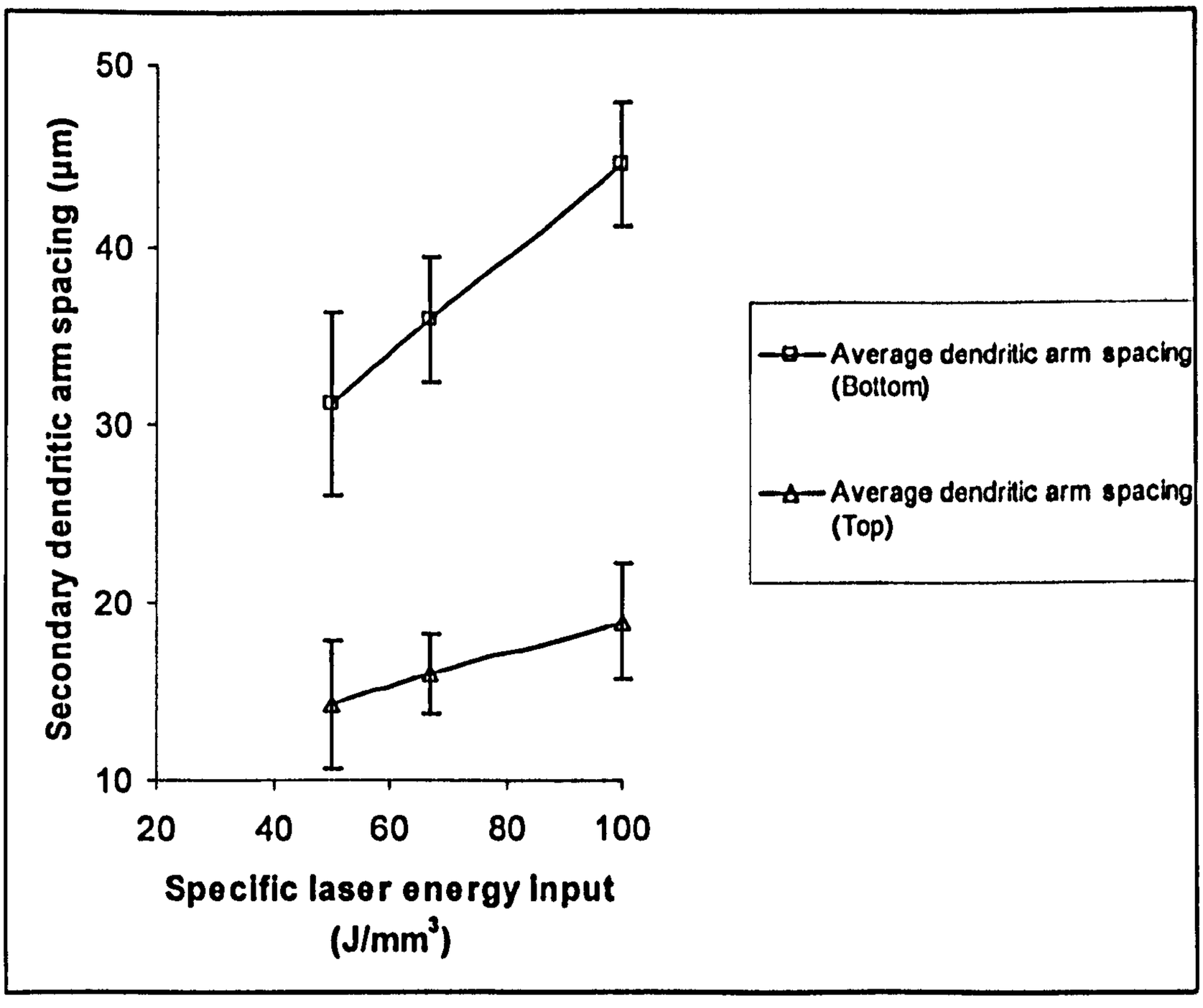

Figure 5.20: Relationship between the energy density and the average dendritic arm spacing of the SLM processed AL-5 powders across the depth of the laser sintered AL-5 samples

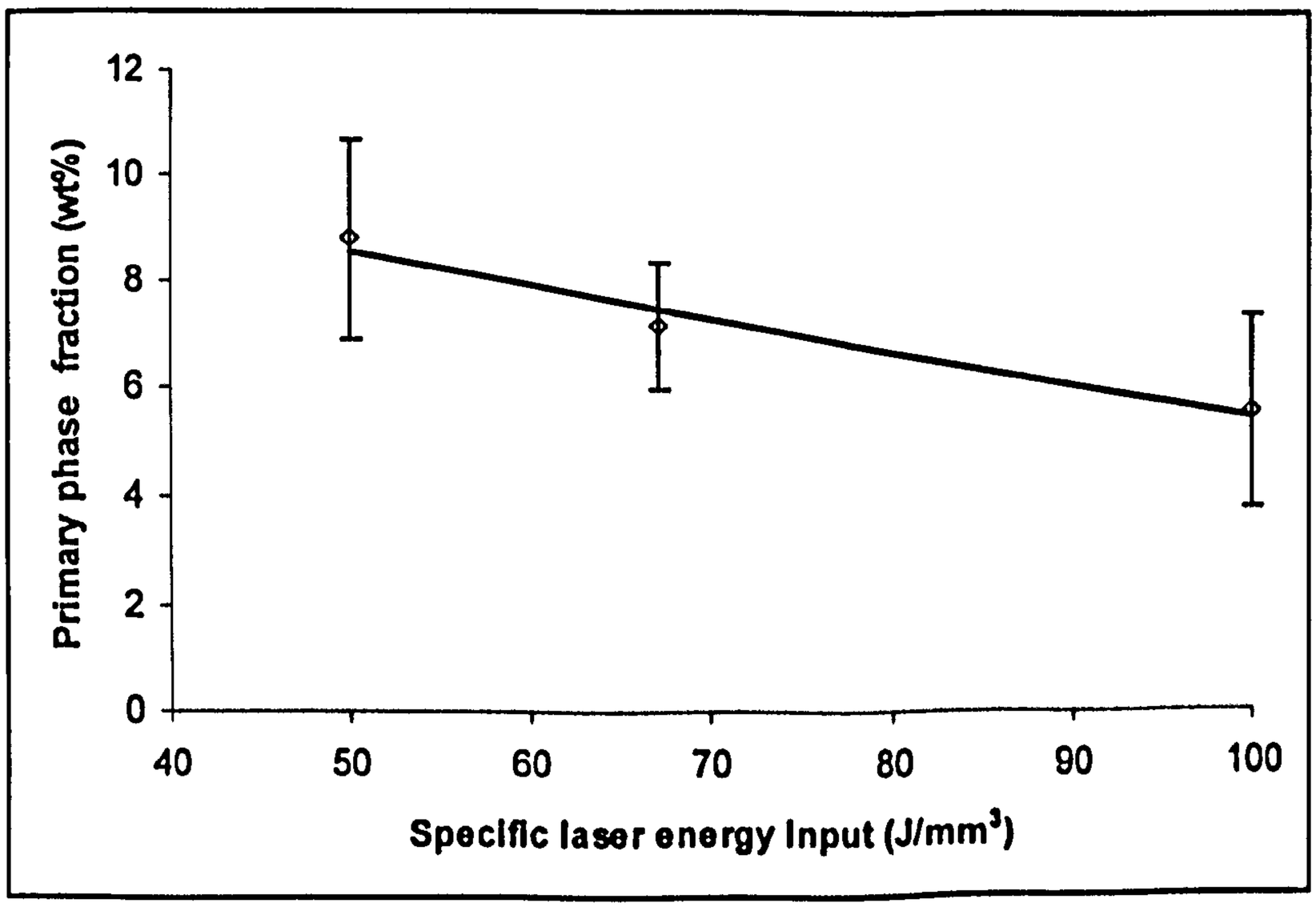

Figure 5.21: Effect of energy density on the fraction of primary phase in SLM processed AL-5 powder.

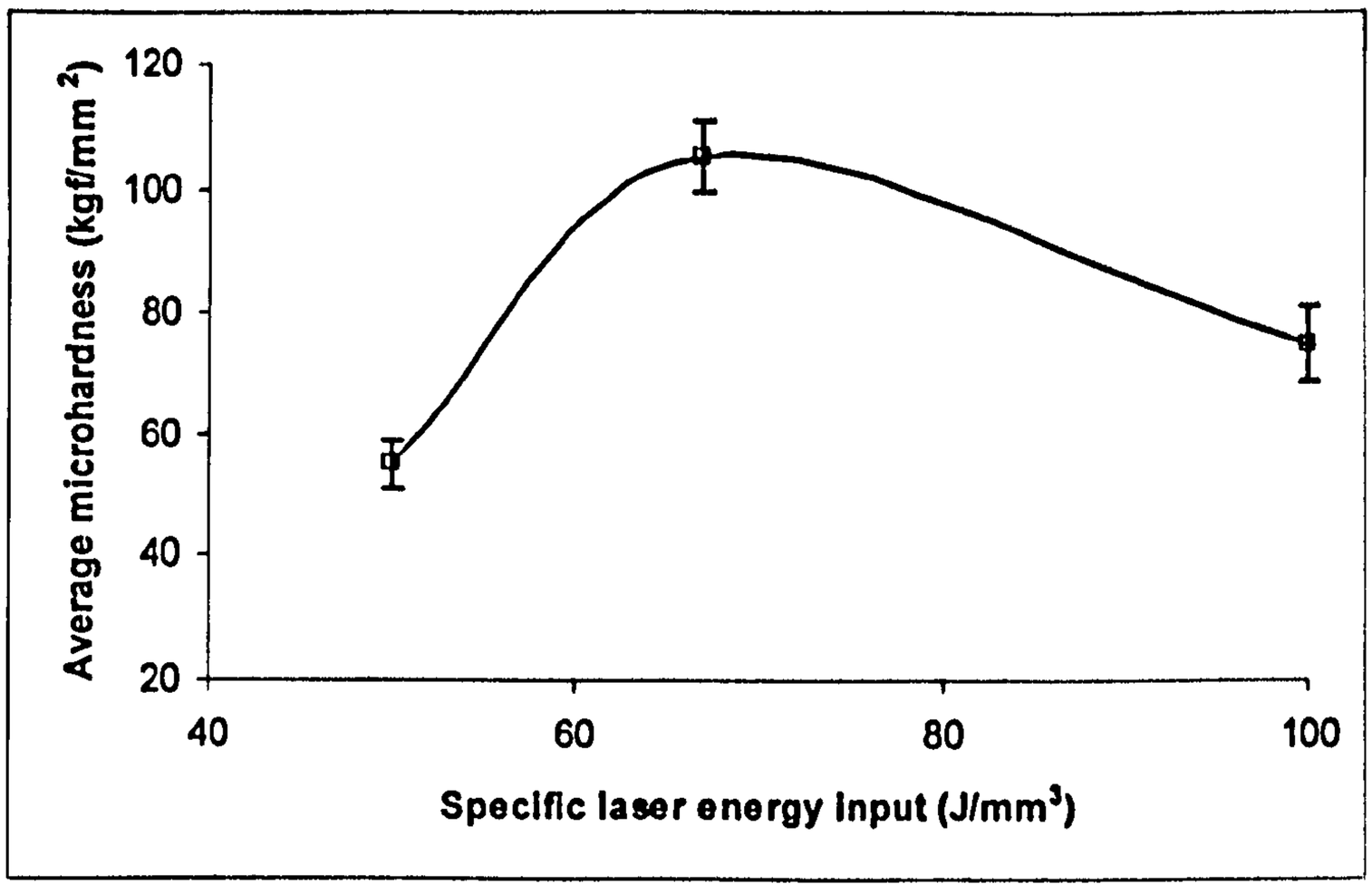

Figure 5.22: Effect of specific laser energy input on the microhardness of SLM processed AL-5 powder.

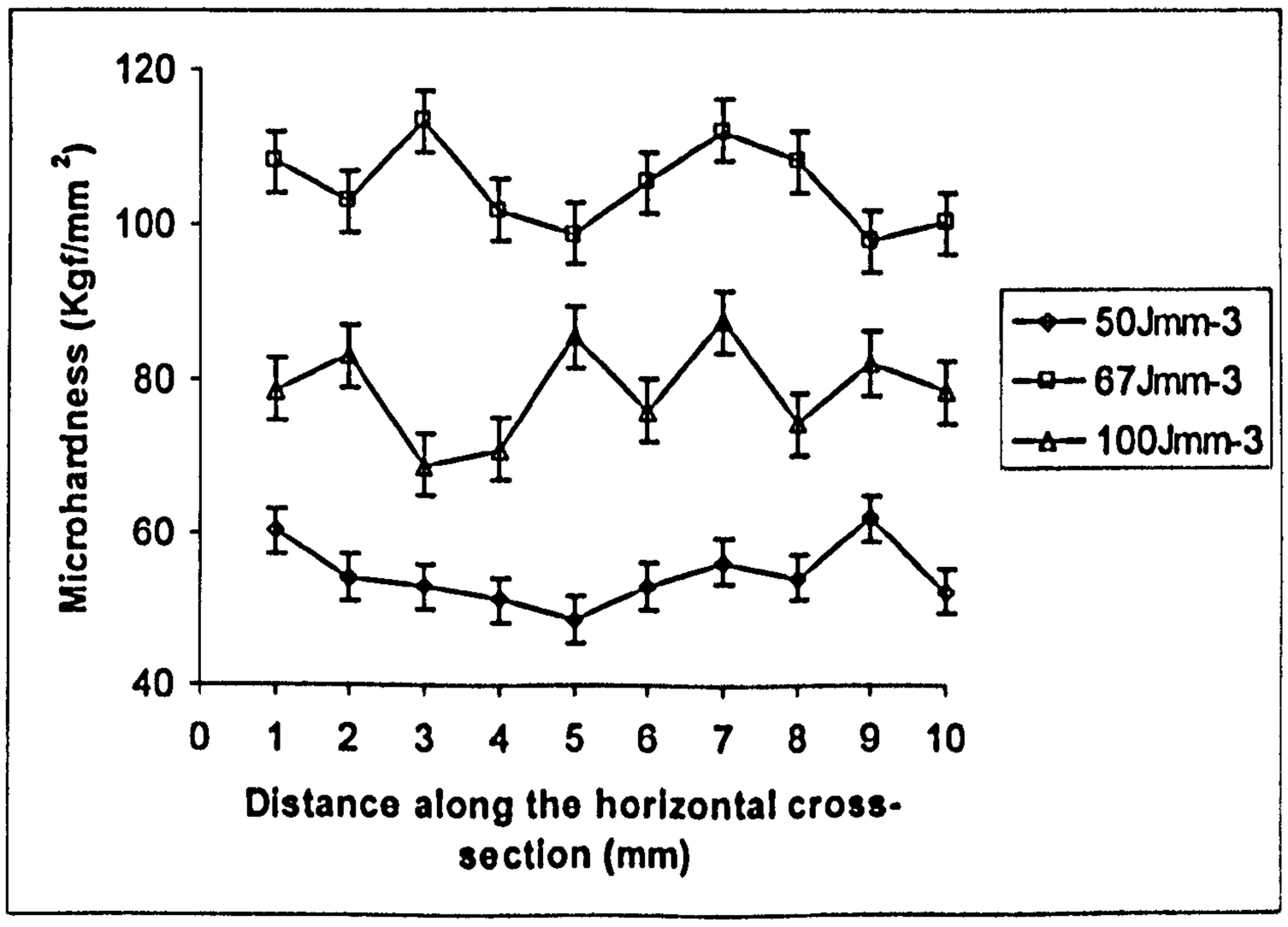

Figure 5.23: Effect of specific laser energy input on the variation of microhardness across the sections of the SLM processed AL-5 powder.

Figure 5.22 shows the effect of specific laser energy input on the average microhardness of SLM processed AL-5 powders. The maximum microhardness of 105 kgf/mm^2 is found at specific laser energy input of 67 J/mm^3, the same energy input at which the density (2.11

g/cm^3) of SLM processed AL-5 is a maximum. Figure 5.23 shows the variation of microhardness across the horizontal sections of the SLM processed AL-5 powder for each of these specific energy inputs.

5.5 Effect of Processing Parameters on the Density and Microstructure of SLM Processed AL-5 Powder.

Equation 2.18 was fitted to the experimental data (Table C1, Appendix C) giving improved values of the densification parameters, as shown in Table 5.3, over the values of densification parameters obtained in section 5.2.

Table 5.3: Densification parameters obtained from Figure 5.13 for the optimisation of process parameters for direct SLS processed AL-5 powder.

Powder	C_1	C_2	K	ρ_{st} (gcm^{-3})	Theor. ρ_{bed} (gcm^{-3})	Exp. ρ_{bed} (gcm^{-3})	ρ_{tap} (gcm^{-3})	$\alpha^* = \rho_{bed}/\rho_{tap}$	ρ_{st}/C_1
AL-5	2.25	0.65	15	2.05	1.60	1.64	1.73	0.95	0.91
AL-5 ($)	2.03	0.91	31.9	1.95	1.12	1.64	1.73	0.95	0.96

$ Initial densification parameters obtained from Figure 5.1

This illustrates that the optimisation of the processing parameters is able to improve densification kinetics for AL-5 powder. Furthermore, the reduction in the density of SLM processed AL-5 observed between 75 and 100 J/mm^3 coincided with the onset of spheroidisation, presumably as a result of increased lifetime of the liquid phase formation under these processing conditions (Figures 5.7 and 5.16).

The increament in inter-agglomerate pores and reduction in the density of SLM processed AL-5 samples as the specific laser energy input is less than 67 J/mm^3 could be explained by the reduction in the energy density applied to the powder bed as the laser power reduces and scan rates, scan spacing and layer thickness increase according to equation 2.17.

Therefore, the lesser the energy density applied, the amount of liquid phase available for sintering which enhances densification mechanism becomes largely insufficient, thus, the microstructural pore channels become bigger and inter-agglomerates become less dense. Furthermore, there seems to be a significant change in microstructure obtained with 67 J/mm^3 (Figure 5.15b) as a consequence the occurrence of re-melting. At specific laser energy input greater than 67 J/mm^3, inter-agglomerate pore increases in size and reduces in sintered density due to the increased lifetime of the melt pool which causes spheroidisation as a result of reduced scan rates when laser power increases, as well as scan spacing and layer thickness also decreasing (Figures 5.7, 5.15a, and 5.16). These findings are similar to the results obtained by Simchi and Pohl (2003) in the SLM of iron powders in that they identified a critical specific laser energy input at which the sintered density was saturated. Above this energy input, sintered microstructure was characterised by horizontal elongated pores while the sintered density remained almost constant (Figures 5.7, 5.15a, and 5.16).

Furthermore, during SLM of AL-5, cooling of the molten pool occurs via the heat loss to the substrate and the surrounding atmosphere at rates of between 10^3 to 10^{11} K/s (Basu & Date 1992a, 1992b; Steen 2003; and Ion 2005). Initially, heat loss through the substrate culminates in rapid cooling via conduction rather than through convection and radiation. The consequence of this is directional growth of grains counter to the cooling direction (Figures 5.16 to 5.18). As noted previously in section 2.6.2 (comparison of the fusion welding process to SLS/SLM processing of metallic powders), since the base and weld metals are of similar composition, it can be argued that there is little or no free-energy barrier to the phase transformation from liquid to solid due to complete wetting of the substrate by the molten weld metal, and the nearly ideal substrate/interface provided by the partially melted HAZ grains at the fusion boundary from which the solid can nucleate and grow. From the analysis carried out by Savage *et al.* (1976), it is hereby contemplated that the growth of a solid in the SLM molten pool evolved as atoms in the molten pool arrange themselves on the partially melted HAZ grains at the fusion boundary. Therefore, HAZ grains at the fusion boundary are thought to have been extended at the expense of the liquid in the SLM molten pool as it cools down. Just as it occurs in fusion welding of homogeneous metals, the crystallographic structure and orientation of the HAZ grains can be said to have been maintained without alteration across the fusion boundary of SLM processed AL-5 powders (Figure 5.16 to 5.18, and 5.24).

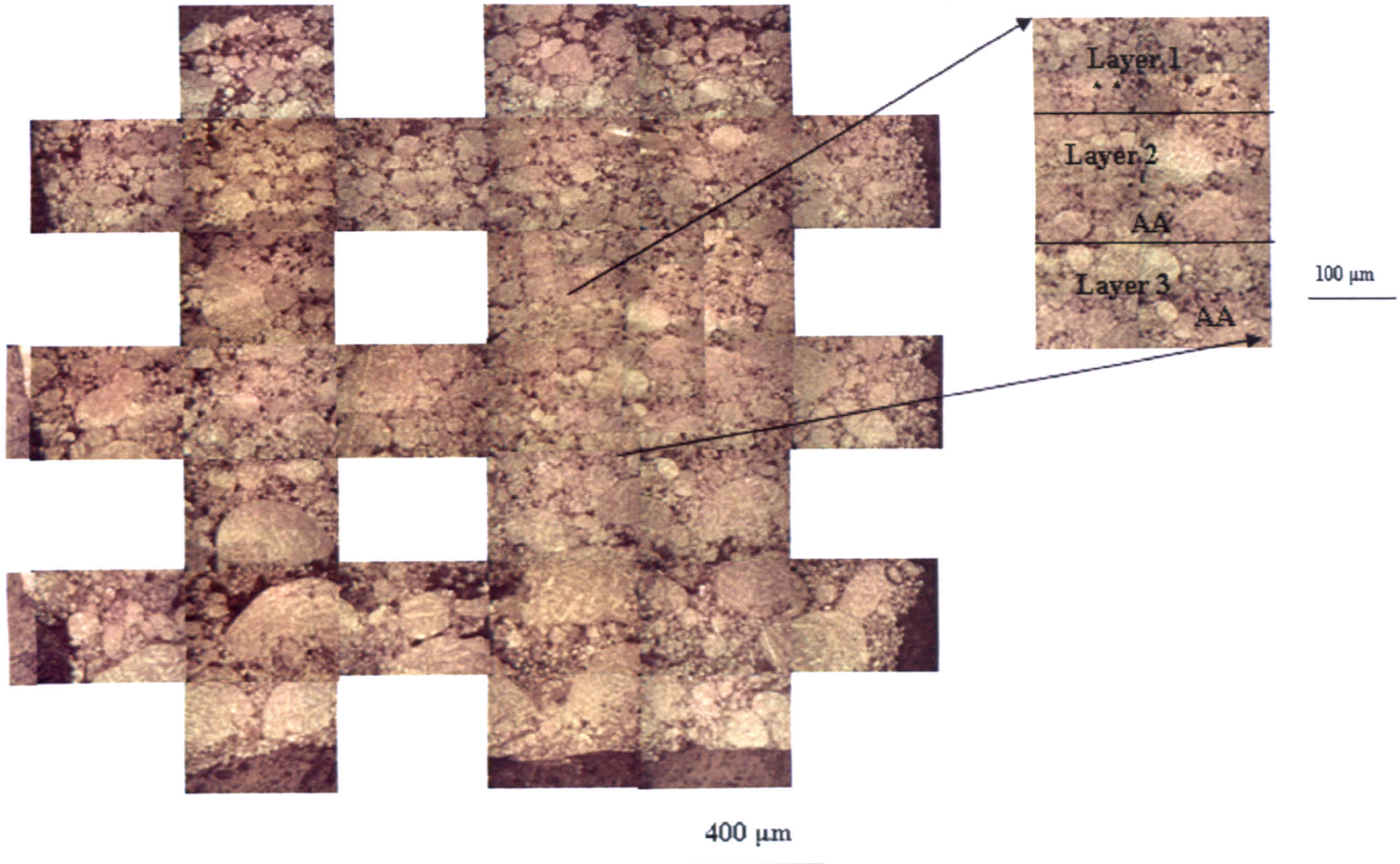

Figure 5.24: Evidence of melt-back in the SLM processed AL-5 powder produced using specific laser energy input of 67 J/mm^3 (↑ layer direction). (Note: Region AA indicates meltback across the layers).

Meanwhile, it must be emphasised that the exact nature of the fusion boundary at the onset of solidification in the SLM processing of AL-5 powders is difficult to ascertain possibly due to its occurrence at high temperatures, coupled with the non-equilibrium conditions associated with the SLM process and the on-cooling transformations in materials.

Figure 5.24 appears to show that the tops of the grains in the previous layer are partially re-melted and then undergo epitaxial growth in the next layer (Steen 2003; Ion 2005) where the HAZ grain boundaries and SGBs are continuous along the fusion boundary. It is hereby reasoned that as the first solid forms on the partially melted HAZ grains, the crystal structures of base and weld metal are the same. Likewise, lattice parameters between the base and weld metals in the SLM of AL-5 are very similar, because they are both the same composition. Once the latent heat of fusion has been liberated during SLM, the atoms in the weld metal arrange themselves on the substrate provided by the partially melted HAZ grains without altering the crystallographic structure or orientation. Thus, the HAZ grains and grain boundaries are extended across the fusion boundary without alteration, similar to that observed in the fusion welding of homogeneous metals. Re-heating of the previously solidified layers give rise to re-growth in this part of the SLM processed sample. This process is repeated for many consecutive layers until heat loss via the substrate is no longer dominant due to poor thermal conductivity of the powder bed. As the sample height increases, heat conduction through the built layers to the substrate becomes very poor and the build temperature increases uncontrollably (Figures 5.16 to 5.18) (Steen 2003; Ion 2005) thereby causing significant heating to a greater depth with microstructural changes to a larger part of the build (Figures 5.19 and 5.20). As a result, the microstructure in the bottom part of the build (Figure 5.19b, d, and f, 5.20) becomes coarse as evident by the occurrence of larger dendritic arm spacing which implies slower solidification rates. The occurrence of coarse structure at the bottom portion of the build could be attributed to the lower thermal conductivity of the powder bed at the first instance laser beam was impinged on it. This initiates low cooling rates at the bottom portion of the build. As the build height increases, subsequent layers being deposited solidify on solid metal substrates which initiates high cooling rates, thus finer dendritic microstructures are found at the top portion of the build. The disappearance of layer bands in the Figures 5.16, 5.17, and 5.18 when the energy density varies between 50-100J/mm^3 could be attributed to the same reason. Figures 5.16 to 5.20 again confirm the earlier assertion that as the sample height increases, heat conduction through the built layers to the substrate (bottom portion of build) becomes very poor (due to poor thermal conductivity of the powder bed), and the build temperature

increases uncontrollably (Steen 2003; Ion 2005) thereby causing significant re-heating to a greater depth with microstructural changes to a larger part of the build. The observations made here are similar to those reported by Loretto *et al.* (1998) and Srivastava *et al.* (1999, 2001) in their studies of direct laser fabricated TiAl-based alloys. Given that the higher the specific laser energy input, the lower the cooling rates generated across the depth of the samples during laser scanning. It can be inferred that the variation in dendritic arm spacing and fraction of primary phase in laser sintered AL-5 is marginal with variation in specific laser energy input (Figures 5.20 and 5.21). Arnberg *et al.* (1993) reported that the primary dendrite fraction in some Al foundry alloys decreased with increasing cooling rate whereas Veldman *et al.* (2001) reported the opposite behaviour, a slight increase with cooling rate. It must be emphasised that the processing technique employed by these researchers is quite different from the SLS/SLM under investigation in this research. Nevertheless, it must be pointed out that the finding from this work in respect of the influence of the cooling rates on the fraction of primary dendrite phase in SLS/SLM processed AL-5 agrees with the findings of Veldman *et al.* (2001). Moreover, the differences in the method of measurement of the fraction of primary dendrite phase as well as the chemical composition of the materials investigated by various groups of investigators should be noted as this may be responsible for the different findings of their work. Finally, the variation of microhardness (Figure 5.23) across all the samples in a non-systematic manner is indicative of the microstructural heterogeneity noted earlier.

5.6 Conclusion

AL-5 powder was found to be the most suitable candidate aluminium alloy powder for the SLS/SLM process due to its constituent spherical particles which packs effectively, thermal properties and uniform distribution of its surface oxides films. SLS/SLM conditions for the fabrication of multiple-layer parts made in pure aluminium and its alloyed powders revealed that eutectic AL-5 alloy has been found to have desirable sintering response with the optimum sintered density of 2.11 g/cm^3 achieved at laser power 200W, scanning rates 120mm/s, scan spacing 0.1mm and layer thickness 0.25mm.

CHAPTER SIX EFFECT OF BLENDING OF PURE ALUMINIUM POWDERS WITH AL-5 POWDER ON DENSIFICATION AND MICROSTRUCTURE

6.1 Introduction

It has been established that the densification mechanisms, microstructural characteristics, and the attendant mechanical properties of laser sintered components depend on the laser processing parameters (laser power, scan speed, scan spacing, and layer thickness) and the powder properties (composition of the constituent powders, particle size and its distribution, and particle shape) (Simchi *et al.* 2003, Gu & Shen 2006, 2007). In order to produce laser sintered Al-Si alloys samples with desirable physical, microstructural and mechanical characteristics, an attempt was made to optimise processing parameters and powder properties. Since it was not possible to obtain a range of pre-alloyed Al-Si compositions, a decision was made to blend Al-12wt%Si powder (AL-5) with different amounts of pure aluminium powder to study a range of hypoeutectic composition. This chapter describes the effect of this on the sintered characteristics. In addition, pure aluminium powders are available in a range of size fractions. This study also presented the opportunity to make up the same alloy composition but employing different Al powder sizes in the blend to independently investigate the effect of packing density on the microstructure and properties. Thus, four different pure Al powders AL-2 (45-75μm), AL-6 (10-45μm), AL-7 (17-30μm), and AL-8 (10-14μm) were blended with AL-5 at the same concentration of 10wt%, 25wt%, 30wt%, 40wt%, and 50wt%. Initially, the optimum processing conditions developed for fabricating multiple layers samples in AL-5 were adopted initially for the blended powder samples. This procedure was adopted with the aim of determining the optimum component ratio for each of the blended powders. Once these had been identified, the process conditions were optimised for blended powders containing 10wt%, 25wt% and 50wt% AL-7. The AL-7 powder was chosen because it was found to give the most desirable sintered characteristics.

From the foregoing discourse, it is now clear that the blending of larger sized powder's particles with smaller sized powder's particles could lead to the emergence of competing

effects. These competing effects make it difficult to gain an understanding of the relationship existing between the laser sintered properties of a powdered sample with a non-ideal distribution. For this reason, the relationship existing between the particle size distribution and direct laser sintered properties of four different blends of AL-5 powders with varying particle size distributions is hereby investigated. The direct laser sintered samples were made from each powder blend under a new processing regime developed. A new processing regime had been developed because the blending of AL-5 powder with the additive powders of varying particle sizes and distribution was expected to alter the particles packing arrangement as well as the heat conductivity of the powder bed which would have effectively modified the sintering behaviour of AL-5 powder (German 1993, 1996). The physical and microstructural properties of each powder blend are compared and related to the particle size and distribution.

The first part of this chapter (section 6.2) describes the results of the microscopic observation of the additive powders, in as-supplied state, and the blended powders. Section 6.3 presents the results of the measurement of the physical properties of these powders. Thereafter, the implications of the findings from the measurement of the physical properties of the powders are also discussed. Finally, the results of the sintered densities, microstructural properties of the multiple layer samples made from the blended powders and the analysis of results are presented in section 6.4.

6.2 Microscopic Observation of the Additive and Blended Aluminium Powders

Figure 6.1 presents SEM images of the as-received powders. Particles of AL-7 and AL-8 comprise spherical particles, similar to those of AL-5, whereas additive powder AL-2 has both irregular and spherical particles and additive powdered sample AL-6 has a preponderance of irregularly shaped particles. Figure 6.2 presents evidence of homogeneous mixing when 10wt%, 25wt%, and 50wt% AL-7 were blended with AL-5 powder whereas Figure 6.3 shows the homogeneous dispersion of the additive powders AL-2, AL-6, AL-7, and AL-8 in the matrix AL-5 powder with no observation of internal porosity or agglomerates when mixed for 20 minutes in a V-shape mixing device (Section

4.3). The SEM images reveal preponderance of spherically shaped particles in all the blended mixes.

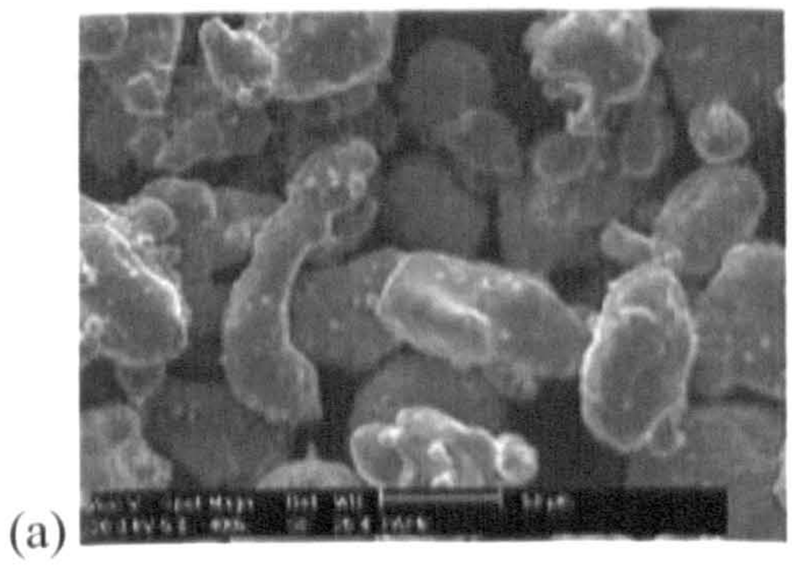
(a)

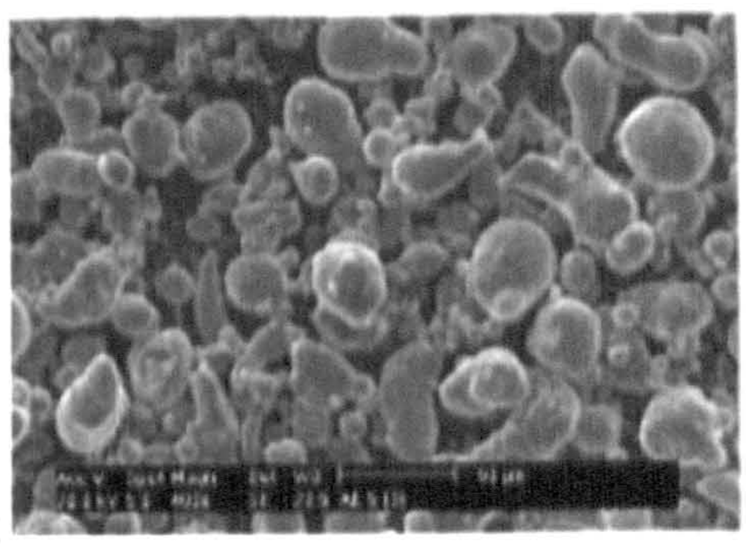
(b)

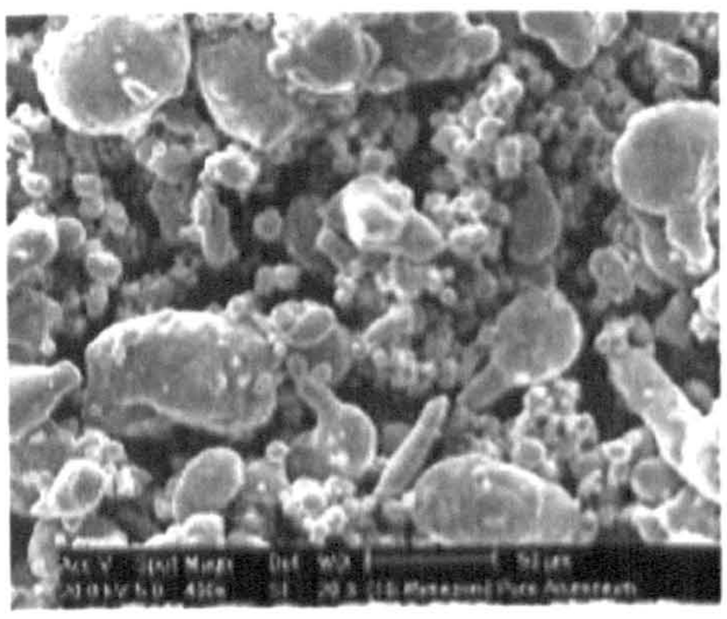
(c)

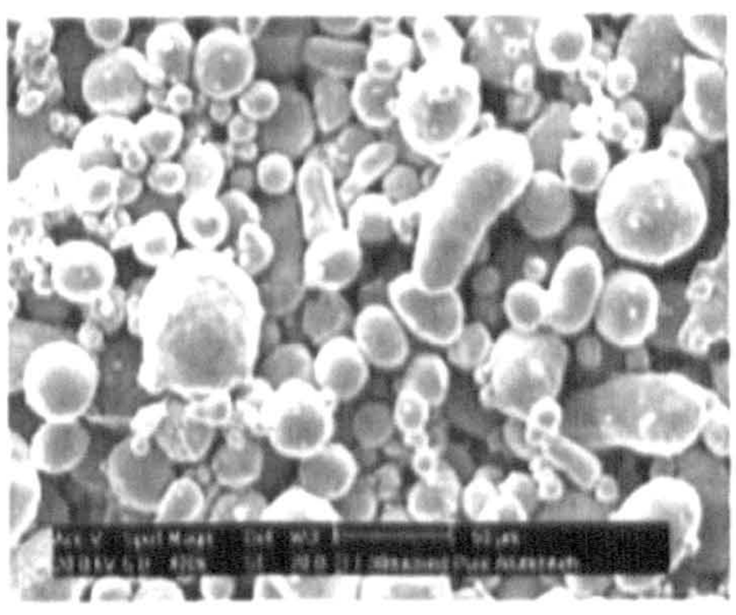
(d)

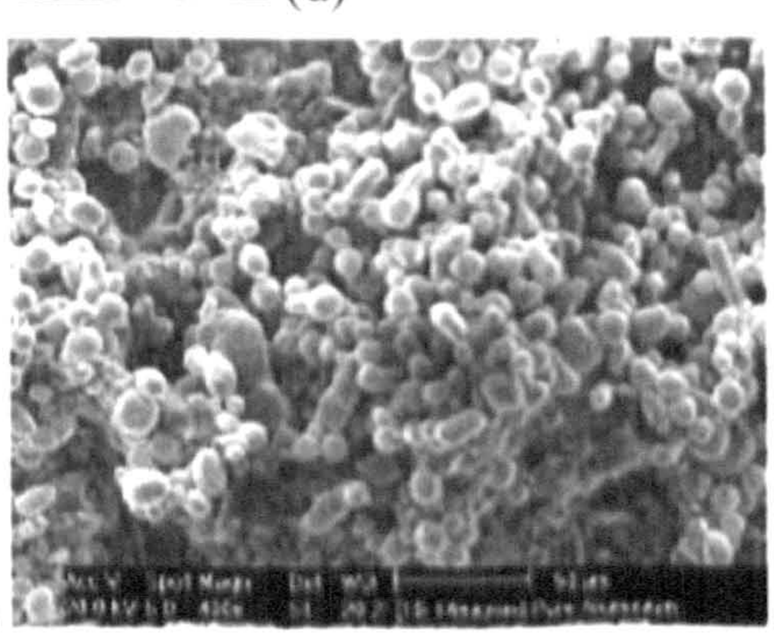
(e)

Figure 6.1: SEM images of the powders revealing their particle shape: (a) 45-75 micron (AL-2); (b) 45-75 micron (AL-5); (c) 10-45 micron (AL-6); (d) 17-30 micron (AL-7); (e) 10-14 micron (AL-8) powders.

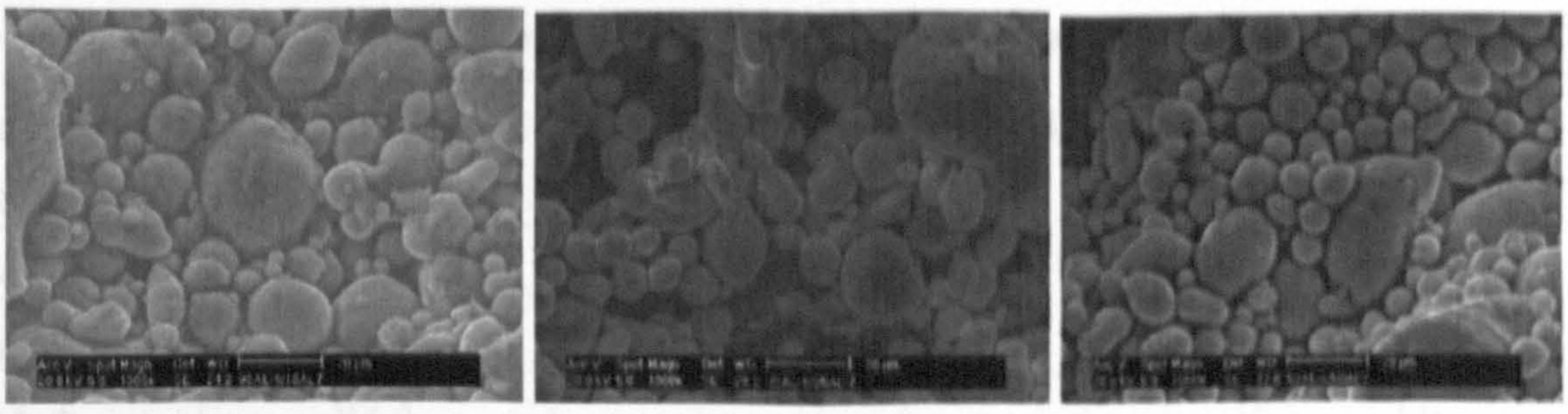

(a) (b) (c)

Figure 6.2: SEM images of blended powders illustrating homogeneous mixing of bi-modal blended powders containing (a) 10% AL-7; (b) 25% AL-7; (c) 50% AL-7.

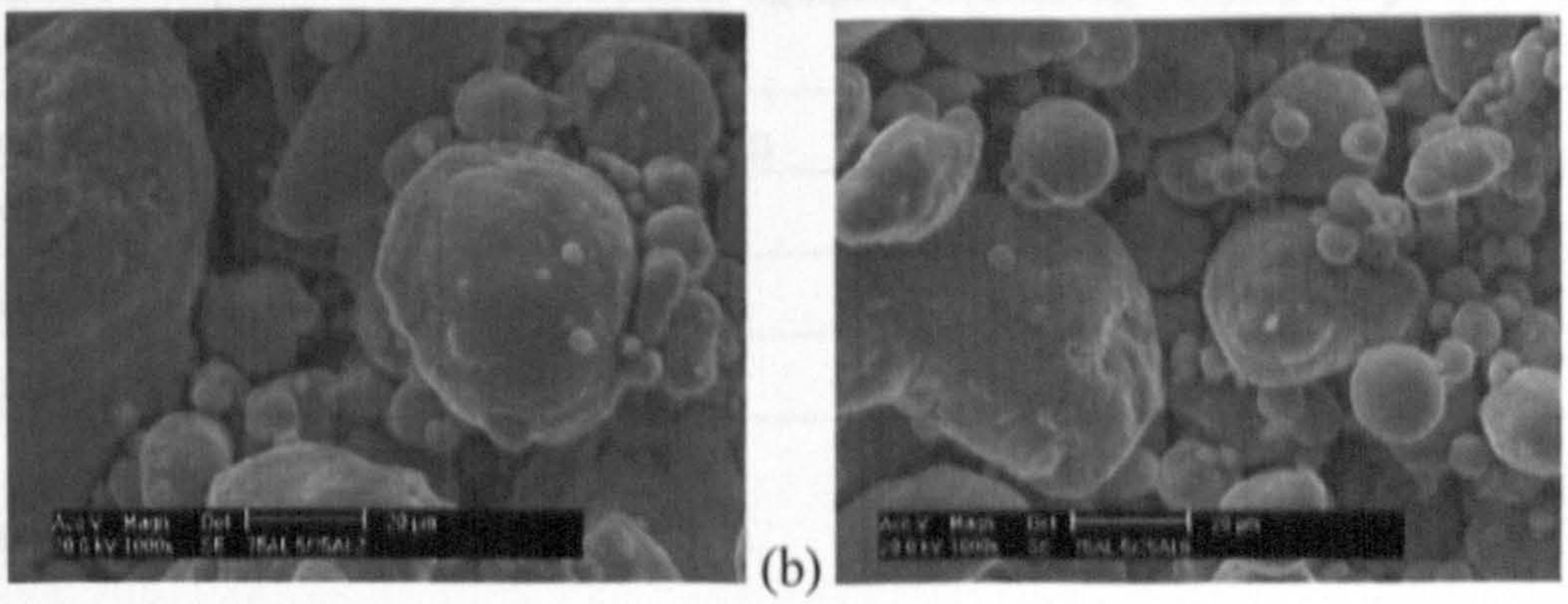

(a) (b)

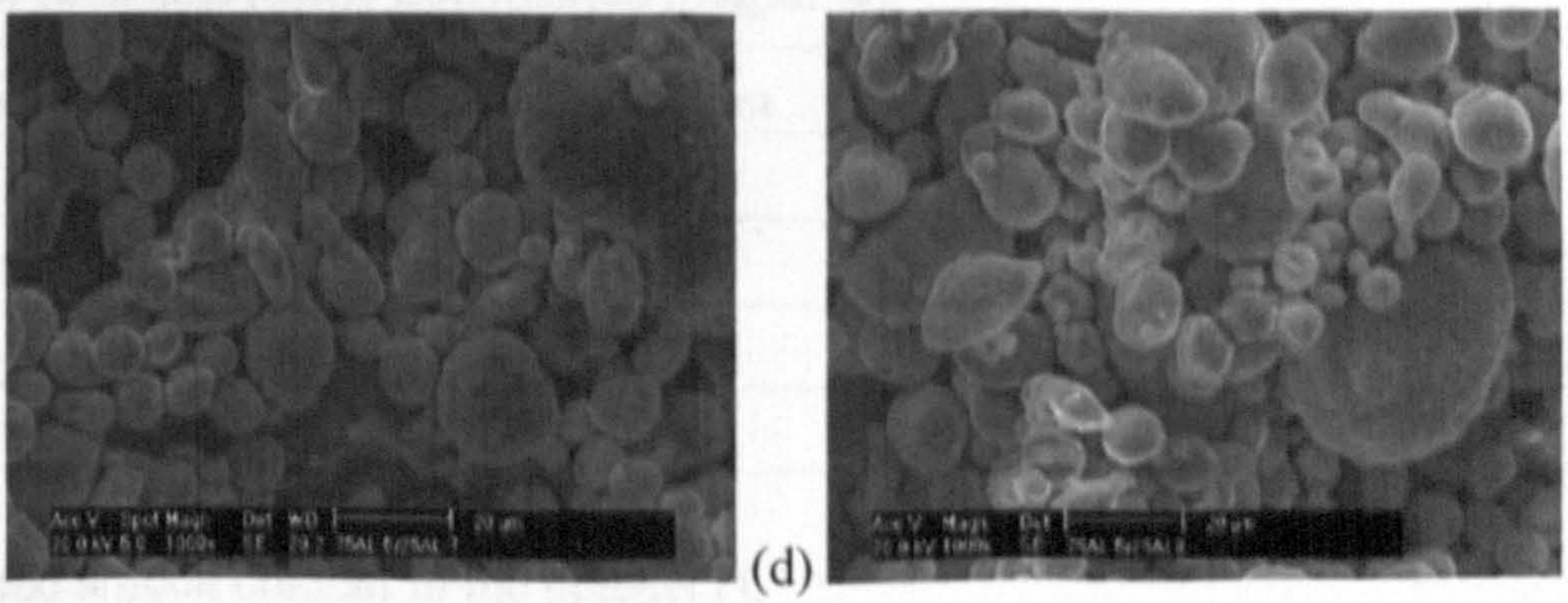

(c) (d)

Figure 6.3 SEM images of the blended powders after mixing for 20 minutes (a) 75% AL-5/25% AL-2 (b) 75% AL-5/25% AL-6 (c) 75% AL-5/25% AL-7 (d) 75% AL-5/25% AL-8

The elemental compositions of the unmixed additive powders, blended powders containing varying contents of AL-7, and additive powders of different particle sizes were determined by semi-quantitative EDS analysis (wt%) and presented in Tables 6.1, 6.2 and 6.3 respectively.

Table 6.1: Elemental Composition of the Powders by Semi-quantitative EDS (wt%).

Powdered Samples	Aluminium	Magnesium	Silicon	Oxygen
AL-2	93.5	-	-	6.5
AL-5	85.1	-	12.1	2.8
AL-6	97.4	-	-	2.6
AL-7	97.1	-	-	2.9
AL-8	97.0	-	-	3.0

Table 6.2: Elemental Composition of Blended Powder Samples, Containing Varying Proportion of AL-7, by Semi-quantitative EDS Analysis (weight. %).

Powdered Samples (wt%) AL-7	Aluminium	Silicon	Oxygen
10% AL-7	86.3	11.6 (10.8)	2.1
25% AL-7	89.3	8.7 (9.0)	2.0
50% AL-7	91.5	6.0 (6.0)	2.5

Note: Calculated silicon content in the bracket ().

Table 6.3: Elemental Composition of the Powdered Samples, Containing Additive Powders of Varying Particle Sizes, by Semi-quantitative EDS Analysis (weight. %).

Powdered Samples	Aluminium	Silicon	Oxygen
75% AL-5 + 25% AL-2	88.9	8.7 (9.0)	2.5
75% AL-5 + 25% AL-6	89.3	8.7 (9.0)	2.0
75% AL-5 + 25% AL-7	89.3	8.7 (9.0)	2.0
75% AL-5 + 25% AL-8	89.5	8.6 (9.0)	1.9

Note: Calculated silicon content in the bracket ().

The energy-dispersive spectra acquired for the unmixed additive powders, blended powders containing varying contents of AL-7, and additive powders of different particle sizes and all the blended samples (Tables 6.2 and 6.3) are shown in Appendix II. Only elemental aluminium, and oxygen, were detected in the unmixed additive powders AL-2 and AL-6, AL-7, and AL-8 whereas aluminium (Al), silicon (Si), and oxygen (O) were detected in unmixed AL-5 and all the blended powders. The EDS spectra for the major elements in each of the powder correlate with the major elemental composition indicated by the suppliers. Upon comparison of Table 6.1 with Table 3.2, it is instructive to note that

the failure to detect Fe and Cu in the energy-dispersive spectrum taken from the entire region for each powder is because the total amount of these elements over each EDS is below the detection limit. The same reason is responsible for the non detection of minor elements indicated by the manufacturer in each sample. The discrepancies noted in the chemical composition of the powders as supplied to the EDS semi-quantitative chemical analysis had been attributed to the wet method of analysis adopted by the manufacturers (section 4.2.3).

Although, great caution needs to be exercised with the quantitative oxygen values as explained in section 3.3.2.3 due to ZAF correction factor of ±16wt%, all the additive powders, with the exception of AL-2 could be said to contain nearly the same amount of oxygen. Earlier work on single and multiple layer samples (section 5.3) suggested that uneven distribution of oxide films in powders AL-2 and AL-6 might influence the sintering response of the blended powders. A careful observation of the particles in powders AL-2 and AL-6 (Figure 6.1) reveals the presence of islands or uneven distribution of oxide films on the surface which is absent in samples AL-5, AL-7 and AL-8. Proportions of aluminium and silicon in the blended powders containing varying proportion of AL-7 are noted to be significantly different whereas there appears to be little variation in their oxygen content (Table 6.2). Meanwhile, silicon constitution in the all the blended powders are comparable to the calculated values with the exception of the blended powder containing 10wt% AL-7. For the blended powders containing additive powders of varying particle sizes, the percentage of elemental aluminium, silicon, and oxygen in all the blended samples lie within the same ranges of 89.3-89.9wt%, 8.6-8.7wt% and 1.9-2.5wt%, respectively (Table 6.3). Comparison of the oxygen contents in the pure aluminium powders (Table 6.1) to that of the blended powders (Tables 6.2 and 6.3) shows that the effect of the lower oxygen content of AL-5 was predominant in the blended powders as their oxygen contents were reduced compared to those of the pure powders . Moreover, it was noted that oxygen content of the blended powders increases proportionally with that of the pure aluminium powders blended with AL-5.

The particle size range of the unmixed additive powders was presented in Table 3.1. Powders AL-2 and AL-5 have the same particle sizes and are coarser than powders AL-6, AL-7 and AL-8. The blending of coarse powders with fine particles had been undertaken in an attempt to fill up the interstices present in the coarse AL-5 with a view to improving the initial powder density and thus, the sintered microstructure (Simchi *et al.* 2003).

Average particle sizes of each of the additive powders estimated by SEM measurements are 62.9 μm, 35.8 μm, 23.6 μm, and 12.7 μm for AL-2, AL-6, AL-7, and AL-8 respectively. The fine particles increase the surface area of the powder, thereby, increasing the absorption of laser energy, and consequently affecting the processing window.

6.3 Properties of Blended Powders

6.3.1 Density and Flowability of the Blended Powders

Figure 6.4 shows the apparent densities of the blended powders as a function of composition with no significant variation in measurements as indicated by the error bars. The apparent density of AL-5 powder containing no additive powder is 1.43 g/cm^3. It is also clear that the apparent density of pure Al powders varies: AL-7 gives the highest density of 1.37 g/cm^3, AL-6 the least at 1.26 g/cm^3, whilst AL-2 and AL-8 were comparable at 1.34 g/cm^3. When these powders were added to AL-5, the variation in apparent density was not simple. Rather, a maximum in apparent density was observed. The addition level corresponding to this was around 25wt% for most powders but the level of density enhancement was greatest for AL-7. Small enhancements were seen for AL-2 and AL-6 but the maximum density for blended powders containing AL-5 and AL-8 never exceeded that of pure AL-5. Indeed, small additions of AL-6 and AL-8 initially reduced the apparent density of the blended powders before this increased to the maximum value. In all cases, addition of more than 25wt% of the pure Al powder caused a continual decrease in apparent density to a minimum for the pure Al powder.

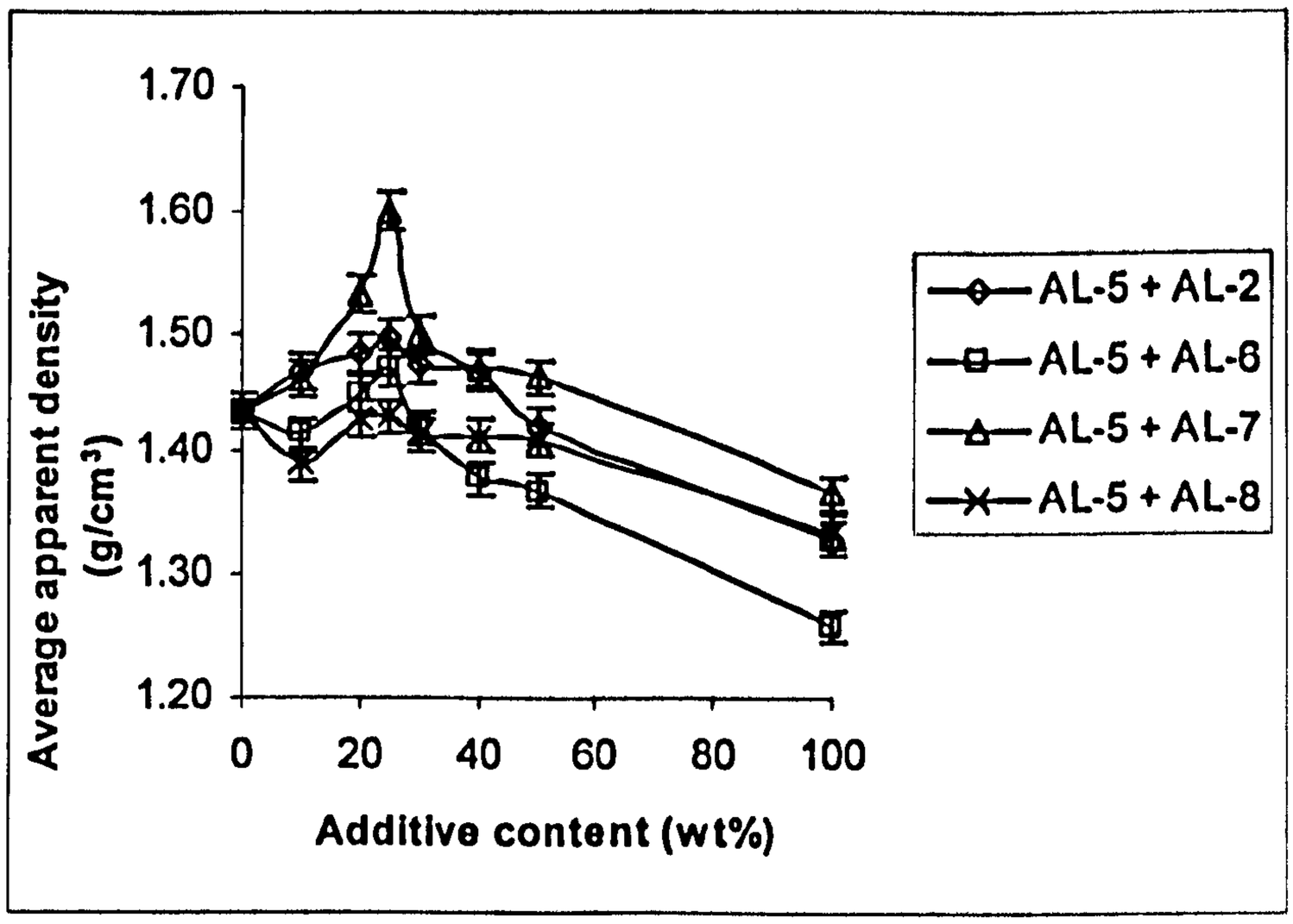

Figure 6.4: Effect of varying additive level on the apparent density of powders.

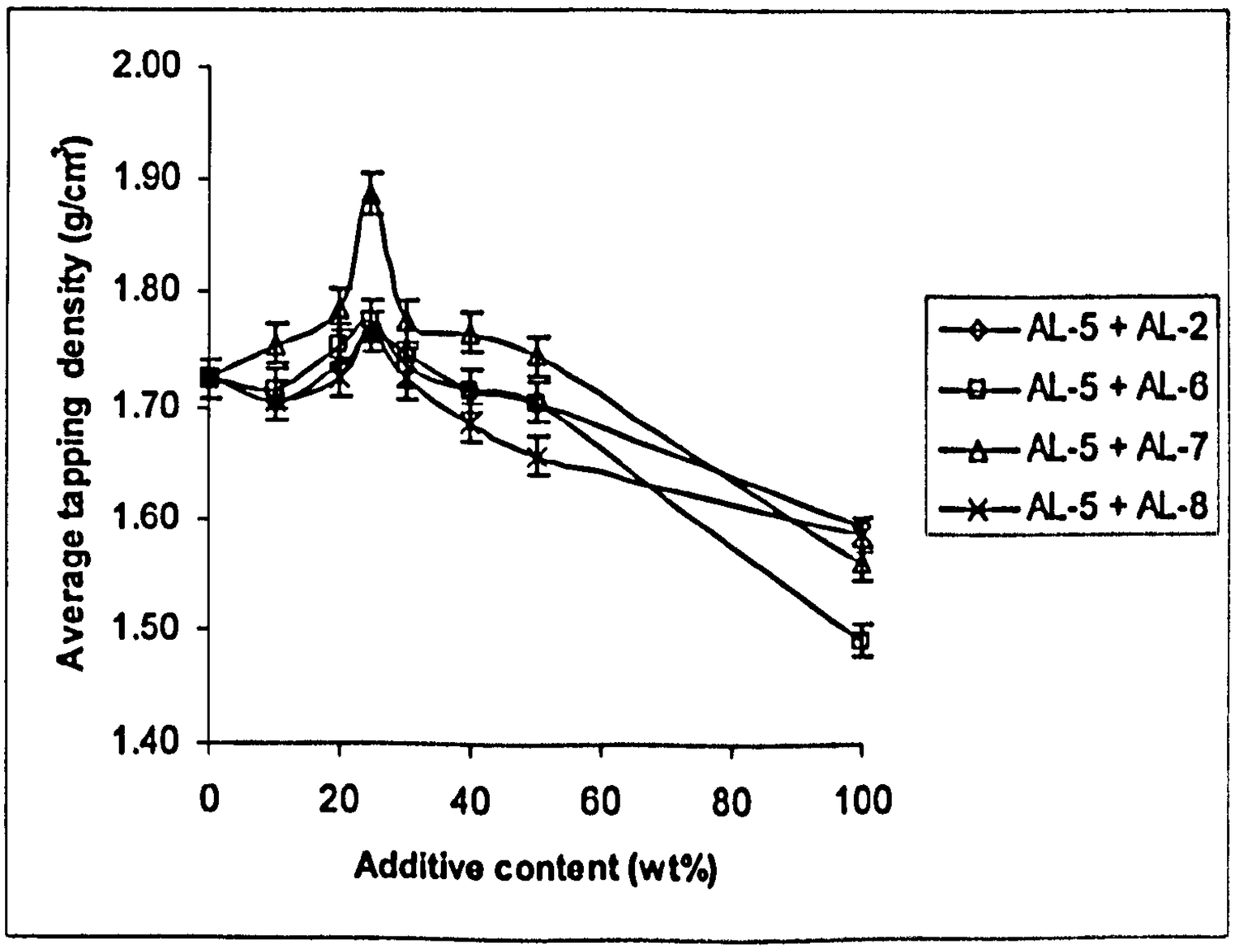

Figure 6.5: Effect of varying additive level on the tapping density of powders.

Figure 6.5 shows the effect of varying the contents of additive powders on the tapping density of blended powders, again, with no significant variation in measurements as indicated by the error bars. The behaviour is very similar to that observed for apparent

density with the maximum value seen at 25wt% of the pure Al powder addition: the maximum value of 1.89 g/cm^3 is again achieved with the AL-7 powder. However, all the additive powders produce an increase in density of the blended powder. The behaviour after the maximum is also more complex with the suggestion of a second maximum somewhere between 35wt% and 45wt%.

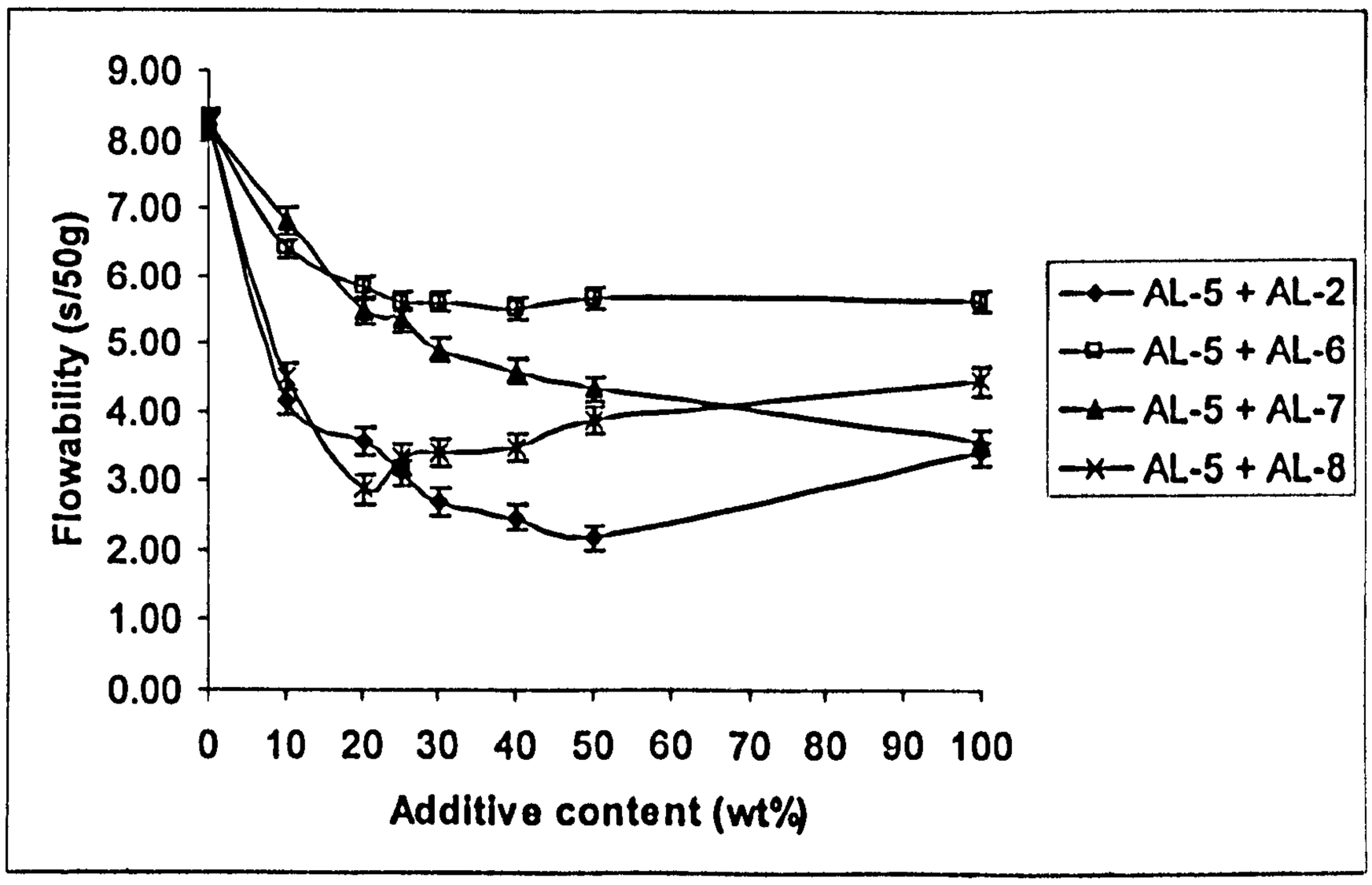

Figure 6.6: Effect of varying additive level on the flowability of powders.

Figure 6.6 shows the effect of the addition of pure Al powders on the flowability of blended powders with no significant variation in measurements as indicated by the error bars. The flowability of all the pure additive powders was better than that of AL-5: AL-6 gave best flowability, AL-8 the next best, whilst AL-2 and AL- 7 are comparable. A significant improvement was observed in the blended powders for all cases, suggesting that the additive powders had imparted their improved flowability to AL-5 upon mixing. This implies that the blending of AL-5 powder with the additive powders will enhance undisturbed powder transportation and deposition in the form of thin layer during the direct SLS/SLM process. While the relationship between variation in AL-7 content and flowability showed monotonic decreasing, slight increase at around 25wt % corresponding to maximum in density; samples AL-2, AL-6, and AL-8 all show a minimum (of different depths and at different weight fractions) and rather more complicated variations.

The blending together of aluminium powders of different particle sizes and distribution in varying proportions is expected to influence bulk powder properties such as apparent and packing densities; and flowability, with the aim of tailoring the sintered density and mechanical properties of parts towards achieving specific uses. (Thümmler & Oberacker 1993; German 1991). For the above stated aim to be met, it is essential that small-sized additive powders that are to be blended together with the large-sized powder particles must have a narrow range of particle sizes and distribution and be mixed in the appropriate proportion. This will ensure that small-sized additive particles in appropriate proportions are able to fill-up the interstices of the large sized particles. It is on this principle that powders of varying particle sizes and proportions were blended together in an attempt to attain improved bulk properties which are expected to yield improved sintered densities and mechanical properties for direct laser sintered aluminium powdered parts. Moreover, the particle shape of both small-sized and large-sized powder particles must be spherical in order to give room for the existence of little or no inter-particle friction during voids filling. Bimodal distributions of spherical powder were adopted in order to determine the appropriate combination of sizes and distribution that yields the best physical properties leading to optimum sintered characteristics. The AL-5 powder (45-75μm) was blended with pure aluminium powders AL-2 (45-75μm), AL-6 (10-45μm), AL-7 (17-30μm), or AL-8 (10-14μm). Figures 6.4, 6.5, and 6.6 show the influence which mixing of the additive powders with AL-5 powder has on the bulk properties of the blended powder. The effect of each additive powder on the properties of the blended powder can be explained on the basis of the influence of the particle shape and size distribution of the additive powder and its concentration.

Results presented in Figures 6.4 and 6.5 signify that the addition of AL-7 powder has impacted significantly and positively on the apparent and tapping densities of the blended powder. For AL-7, the increase in both apparent (1.46 to 1.60 g/cm^3) and tapping (1.70 to 1.89 g/cm^3) densities as the its content varies from 10wt% to 25wt% could be attributed to improved packing, with interstices in the spherical AL-7 powders fitting comfortably within the interstices in the spherical AL-5 powder. As the content of the spherical particle of AL-7 increases above 25wt%, the apparent density reduces to that of pure AL-7 powder. Therefore, it could be suggested that there exists a maximum content (25wt%) of AL-7 additive powder in AL-5 above which both the spherical particle and particle size and distribution of AL-7 have declining effect on its densities. This could be attributed to the particle packing arrangement of AL-7 in the interstices of AL-5 which becomes disturbed,

thereby resulting in the occurrence of porosities on the powder bed, as the content of AL-7 particles exceed 25wt%. Furthermore, the improved densities observed for the mixes containing AL-7 and AL-5 could be ascribed to the fact that the mixes meet up with the dual conditions that both powders contained spherical particle shape and that the smaller particle sizes of AL-7 are able to fill up the interstices contained in the larger particle sizes of AL-5 without the development of inter-particle friction and porosity. It can be summarised that spherically shaped particles present in AL-7 and AL-5 powders, and the smaller particle sizes of AL-7(17-30 micron) powder which are able to fill up the interstices contained in the larger particle sizes of AL-5 (45-75 micron) powders are the major factors contributing to the development of low or no inter-particle friction which enhances effective voids filling with smaller sized particles. It can be seen that the effective voids filling of AL-5 powder with the smaller sized particles of AL-7 promotes the development of improved apparent and tapping densities (Figures 6.4 and 6.5). In addition to having both finer and coarse powder particles in appropriate sizes and distribution, this outcome also highlights the importance of blending appropriate proportion of both fine and coarse powder particles together, with a view to obtaining desirable particle packing arrangement that enhances the bulk properties of blended powders.

The addition of AL-2 powder has resulted in marginal increase in the apparent (1.43 g/cm^3 to 1.50 g/cm^3) and tapping densities (1.70 g/cm^3 to 1.76 g/cm^3) over AL-5 powder as shown in Figures 6.4 and 6.5. This is despite the fact that, nominally, they have the same particle size. The increases in density are small, however, and probably not significant. It would be expected that adding AL-2 to AL-5, therefore, would have a marginal effect, if any, on the properties of AL-5. However, some effects are noted with a peak in apparent and tap densities at 25wt% and an improvement in flowability, peaking around a 50:50 mixture. This, presumably, must be due to either differences in size distribution with the 45-75 μm size fraction or to differences in shape and/or surface structure between the AL-2 and AL-5 powders (Figure 6.1).

The particle size of AL-6 powder is less than that of AL-5, therefore, it should be capable of filling up the interstitial voids in AL-5 as is the case for AL-7. This is because the particle packing arrangement of the blended powder containing AL-5 and AL-6 fulfils the bimodal powder particle packing arrangement in the aspect of interstitial filling principle

for particle sizes of both large and small-sized particles ($D_L >> D_S$) as proposed by Zhu *et al.* (2007). Meanwhile, it is noted from Figures 6.4 and 6.5 that this is less effective. Moreover, while the irregular particles of AL-6 are expected to improve the tapping density of the blended powder, the contrary was observed. Therefore, initial reduction in the densities of the blended powders obtained when 10wt% AL-6 was added could be attributed to poor particle packing arrangement resulting from insufficient quantity of AL-6 irregular particles which are unable to fill up completely the interstices of AL-5. Furthermore, marginal increament in the densities obtained when AL-6 content varies between 10wt% and 25wt% and further reduction in the densities attained as the content of AL-6 increases above 25wt% could be attributed the influence of broader size range of AL-6. The broader size range of AL-6 makes it unsuitable in filling up the interstices of AL-5 as it is likely the particles of AL-6 are larger than the available interstices of AL-5. In addition, the increasing content of the irregular particles of sample AL-6 could be said to have set up inter-particulate friction which reduces the apparent and tapping densities of the blended powder. This is exemplified with lower values of densities obtained for AL-5 and AL-6 blends when compared with blends containing AL-7 (Figures 6.4 and 6.5). This result indicates that if the particle size distribution and particle shape of AL-6 (10-45 micron) powder is not suitable in filling up the available interstices in 45-75 micron spherical AL-5 powder, then, variation in the content of AL-6 particles in the blended powder is of little or no effect on the bulk properties of the blended powder as seen in Figures 6.4 and 6.5.

For AL-8, its much smaller spherical particle size does not seem to have produced such significant benefits as the addition of coarser, wider size range spherical AL-7 particles to the blended powders. Despite the fact that both AL-5 and AL-8 contain spherical particles, low densities (Figures 6.4 and 6.5) reported for the blended powders with increasing content of AL-8 could be credited to the narrow size range of AL-8 particles which can not fill up the wider interstices in AL-5. Since the particle size of AL-8 is not sufficiently large, the variability to fill more than a few interstices could be said to be insufficient. Moreover, Figures 6.4 and 6.5 indicate that lower values of densities are obtained for AL-5 + AL-8 blends when compared with blends containing AL-7 (Figures 6.4 and 6.5). Therefore, the similarity in the values of densities obtained for the powder blends containing AL-2, AL-6 and AL-7 could be attributed to the inappropriateness of the choice of particle size and distribution for powder blending. The significance of this result is that, on its own, blending together both fine and coarse spherical powder particles does not give

the desirable particle packing arrangement that yields improved bulk powder properties, rather they must be blended in appropriate sizes and distribution that allows fine particles to fill up the interstices contained in the coarse particles. Moreover, they need to be blended in appropriate proportions in order to obtain the desirable bulk powder properties.

6.3.2 Effect of Additive Content, Particle Size Distribution and Shape on the Properties of Blended Powders

Evidence presented so far in this study points out that appropriate choice of additive powder's particle size distribution blended in appropriate proportions plays a dominant role in determining whether or not a mix of two powders of varying particle sizes will maximise its densities above the its original densities. Again, it is now clear that for a mix of powders of different particle sizes and distribution to pack effectively so as to obtain improved powder properties, the following conditions must be met: appropriate proportion of small sized additive particles must be blended with large sized AL-5 particles; the blended powders' particle packing arrangement should fulfil the particle size aspect of the proposals of Zhu and co-investigators (2007) ($D_L >> D_S$); powders of appropriate particle size and distribution must be blended together; and both additive and AL-5 particles must be spherical in shape. The results of this research suggest that the 25wt% AL-7 and 75wt% AL-5 mixes meet up with these conditions as attested to by the improved densities recorded for the mixes. Furthermore, it can be inferred from this study that for all the additive powders, with the exception of AL-7 (17-30 micron) powder, there exists a minimum quantity of the additive powder (10wt%) that must be added to the AL-5 (45-75 micron) powder in order to obtain an improvement over its apparent and tapping densities in unmixed state. Higher loose and tapping densities obtained for the mixes containing AL-7 suggests that it will be easier to achieve high laser sintered density for samples made from these blends.

The improved flowability obtained for all the blended powders suggests that it is not affected by particle shape, sizes and distribution, and the content of the additive powders. In line with the analysis carried out in section 4.2.6, the lower oxygen contents of the blended powders (Tables 6.2 and 6.3) could be said to be responsible for little or no inter-particulate friction that promotes the free flowing properties of the blended powders during deposition.

The studies of Carson & Pittenger (1998) and Reed (1988) showed that the addition of finer size additive powder which packs efficiently in the interstices of a coarse structural powder is necessary in order to obtain improvement in the bulk properties of powders. This is in agreement with the results obtained in this section. The optimisation of the blended powder densities at 25wt% AL-7 content is in conformity with the findings of Carson & Pittenger (1998) who state that, for atomised aluminium powders, the proportion of +45μm particle size should be at least 75% in order to attain an apparent density of 1.25 g/cm^3 when blended with aluminium powders of smaller particle size. The findings obtained in this section signify that increasing the content of irregular shaped additive powder particles reduce the tapping density because it prevents particle motion. The results obtained from the work of Carson & Pittenger (1998) and Reed (1988) strongly support this claim.

6.4 Sintered Properties of Blended Powders

The results of the effect of additive powders' component ratio in the blended AL-5 powdered samples, fabricated by direct SLS/SLM technique, on its sintered density, processing conditions, microstructural characteristics and surface morphology are hereby presented. Furthermore, the implications of the findings are also discussed.

6.4.1 Sintered density of bimodal powders

The sintered density of blended samples fabricated with the optimal processing conditions developed for AL-5 powders (section 5.4) are presented in Figures 6.7a and b. Figure 6.7a shows that increasing the additive content from 10 wt% to 25 wt% eventually results in an improvement in the sintered density from 1.93 to 2.03 g/cm^3; 1.96 to 2.07 g/cm^3; 2.05 to 2.18 g/cm^3; 1.89 to 1.99 g/cm^3; for the blended mixtures containing AL-2, AL-6, AL-7 and AL-8 respectively.

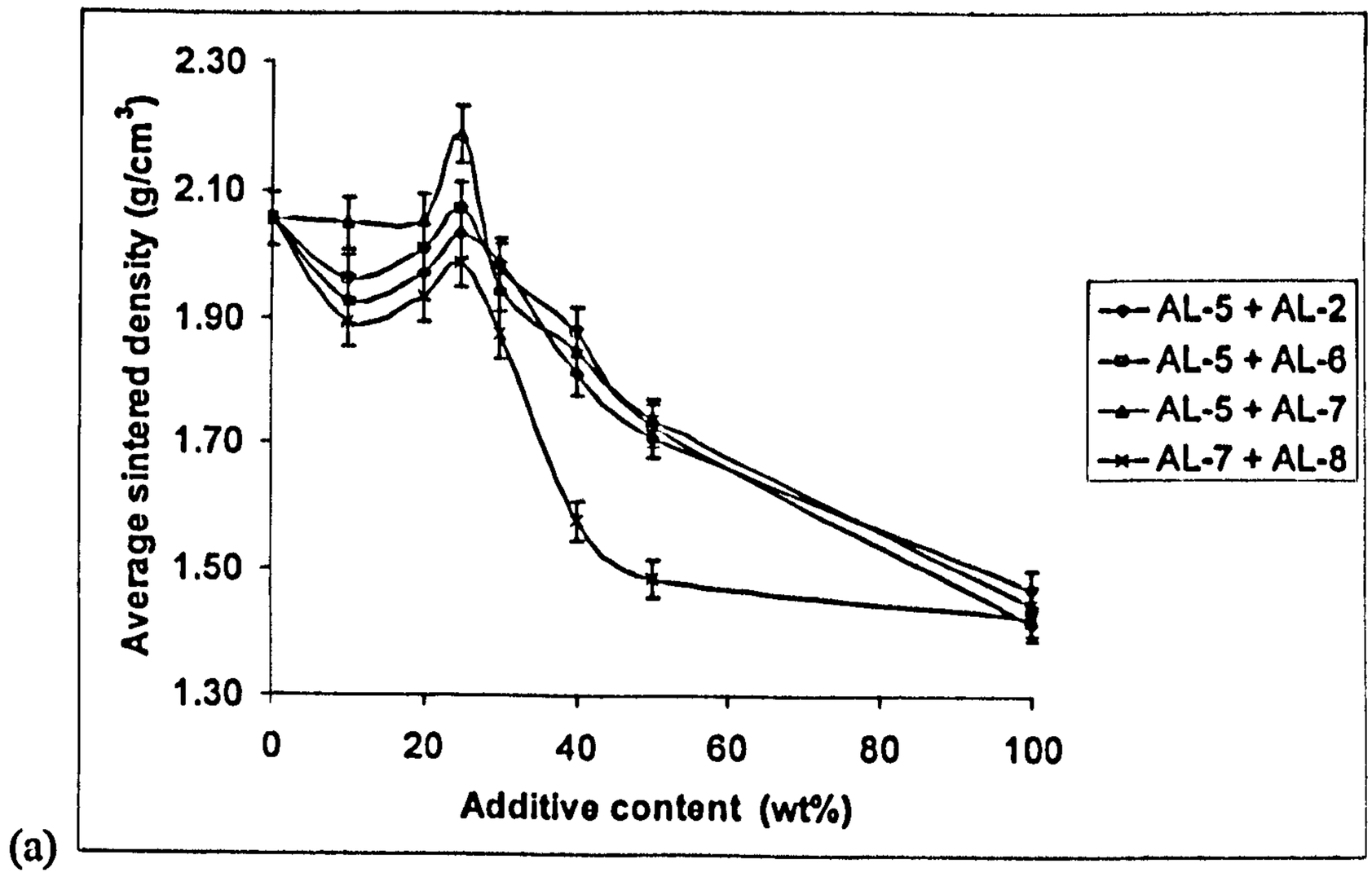

(a)

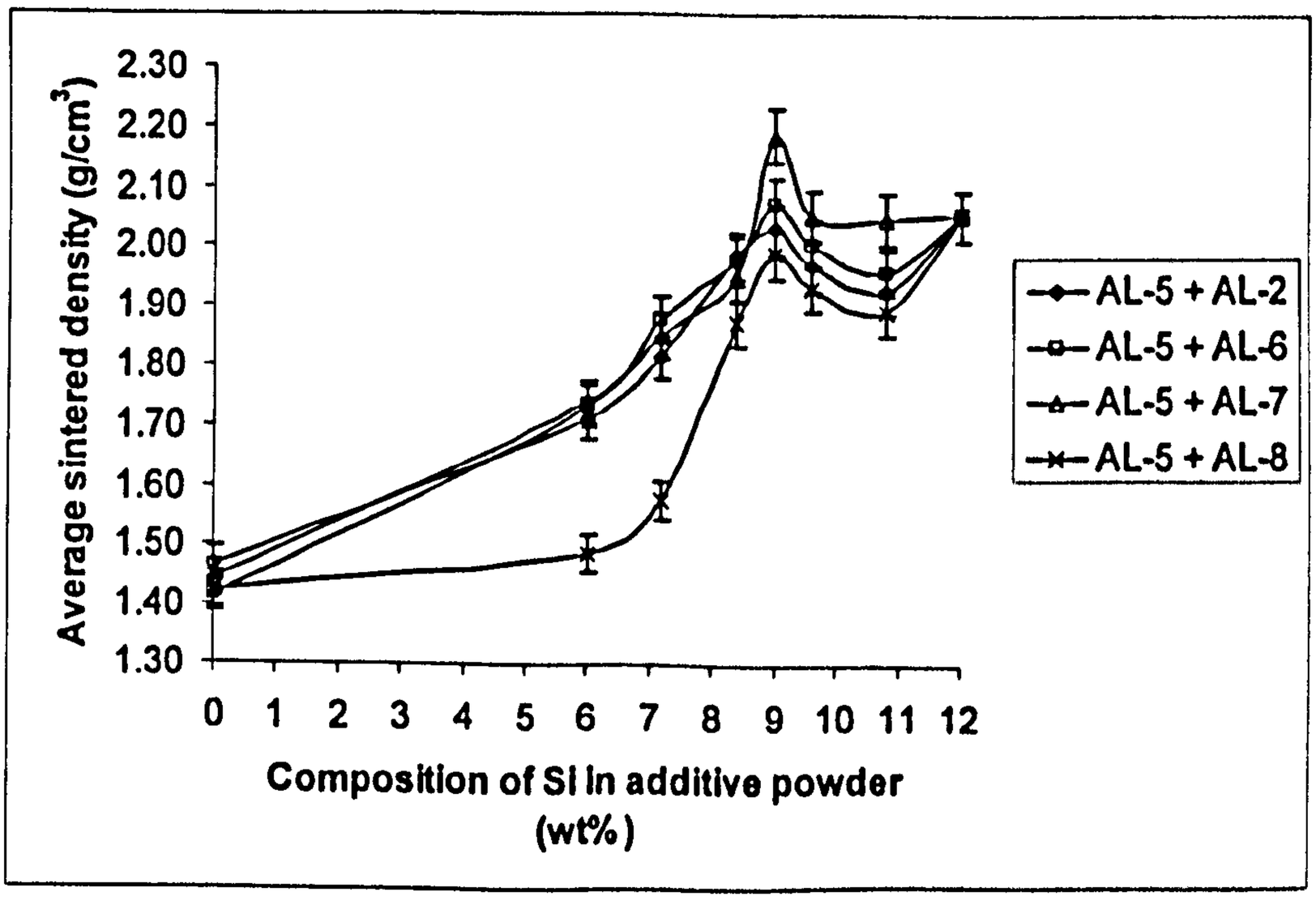

(b)

Figure 6.7: Effect of (a) additive powder content and (b) silicon constitution on the sintered density of SLS processed blended powders at specific laser energy input of 67 J/mm³. (Note: Theoretical values of silicon content have been plotted in Figure 6.7b.)

This shows that, despite differences in the apparent and tap densities between the pure aluminium powders AL-2, AL-6, AL-7, and AL-8, the sintered density of each of these pure powders is comparable, suggesting that powder size, shape, and packing is relatively

unimportant. Also of note is that only the blend of AL-7 with AL-5 results in an increase in sintered density above that of pure AL-5. The maximum sintered density in this blend is found at 25 % AL-7 (2.18 g/cm^3) corresponding to the peak observed in apparent and tap densities (Figures 6.4 and 6.5). Blends of AL-5 with the other three pure aluminium powders also show a peak in sintered density at 25wt% but this is always less than that for pure AL-5 (2.05 g/cm^3). The height of this peak decreases in the order AL-6 (2.07 g/cm^3) > AL-2 (2.03 g/cm^3) > AL-8 (1.99 g/cm^3). These results are somewhat surprising, given the packing properties of the powders. In all cases, the tap densities of the blended powders at 25 % addition exceeded that of the pure AL-5 powder which might be expected to lead to increased process bed density and thus sintered density. However, only in the case of AL-5 and AL-7 is this observed. Meanwhile, beyond the peak, sintered densities decrease smoothly to the value for the pure aluminium powder for all blends except for AL-5 + AL-8, there, the density drops sharply to an approximately constant value at and beyond 50wt% of AL-8. Again, this observation could be explained partly by the inappropriateness of the additive content present in AL-5 once it exceeds 25wt% such that particle packing arrangement in this context deteriorates, thereby impacting negatively on the sintered density.

Figure 6.7b shows the constitutive effect of silicon in the blended powders on the density of the sintered samples. The sintered density of the blended samples increases with silicon content and maximises its values at the silicon content of 9wt%. Further increament in the silicon content to 10.8wt% results in reduction of the sintered density of the samples to the minimal values of 1.93, 1.96, and 1.90 g/cm^3 for AL-2, AL-6 and AL-8 respectively. In the case of AL-7, the sintered density reduced to 2.05 g/cm^3 (density of unblended AL-5) and remains constant as silicon content varies between 9.6 and 12 wt%. For the blended samples containing AL-2, AL-6, and AL-8, Figure 6.7b reveals that increasing the silicon content from 10.8wt% to 12wt% increases the sintered density of the samples to that of unblended AL-5. According to Dinsdale & Quested (2004), the viscosity of the molten pool of aluminium alloys reduces with increasing silicon content. Therefore, increament observed in the sintered density of the samples could be attributed to the reduced viscosity of the molten pool due to increasing silicon content. This suggests that the maximisation of the sintered density of the samples could be credited to viscosity of the molten pool, at 9wt% silicon content, which is likely to have reduced sufficiently to a degree at which that the density of the sintered samples is maximised.

Furthermore, Figures 6.7a and b show that at the peak, only the blended powder containing AL-7 has its sintered density significantly greater than that of unmixed AL-5. Therefore, it is likely that the particle packing arrangement which is solely determined by the proportion and particle size distribution of the powders being blended together might have played a predominant role in determining the sintered density and microstructure of the blended samples in this context. Since only the blended sample containing AL-7 has a sinter density higher than that of pure AL-5, it is likely that the compositional effect of silicon becomes relevant in determining the sintering behaviour of SLS/SLM processed powders only in the event appropriate spherical powders of particle size distribution are blended together in appropriate proportion (Zhu *et al.* 2007). On the other hand, the increased silicon content which is likely to have reduced the viscosity of the molten pool much more than is necessary is thought to have contributed to the reduced sintered density when silicon content increases over 9wt%. The minimisation of sintered densities observed at 10.8wt% Si for AL-2, AL-6, and AL-8 could be explained in view of insufficient amount of additive particles which is unable to fill up the interstices of AL-5. It is likely that the particle packing arrangement in this context is poor, thereby, influencing the sintered density negatively. The role of particle packing arrangement in the determination of sintered density and microstructure will be explained on later in section 6.4.4.

6.4.2 Processing conditions of the bimodal powders

In an attempt to optimise the sintered properties of the blended AL-5 + AL-7 powders and to investigate whether the AL-5 + 25wt% AL-7 blend was the best choice irrespective of process conditions, the effect of process parameters was investigated. It was thought that this might be necessary because German (1993, 1996) had pointed out that the introduction of additive powders in varying component ratios to the base powders has the tendency to alter the processing regime of the base powder. Blends of AL-5 powders containing 10wt%, 25wt% and 50wt% of AL-7 were chosen in order to investigate the effect of component ratio on the processing regime of the mixed powders. This system alone was chosen based on the fact that it had shown the most desirable properties in all the experiments conducted so far and that time for further experiment was limited. The average sintered density as a function of specific laser energy input for those blends is presented in Figures 6.8. It is evident from Figures 6.8a that the maximum sintered density of each blended powder is found for a specific laser energy input of 150 J/mm^3. For

10wt%, 25wt% and 50wt% AL-7, these values are 2.14 g/cm^3, 2.32 g/cm^3, and 1.97 g/cm^3 respectively. The sintered density values only increase marginally (from 2.03 g/cm^3, 2.18 g/cm^3, and 1.83 g/cm^3) as the specific laser energy input is increased from 67 J/mm^3 to 150 J/mm^3. Figure 6.8 shows the impact of the ratio of the two powders on the maximum sintered density of the blended powder, the powder mixture containing 25%wt AL-7 having the highest sintered density. When equation 2.18 is fitted to the experimental data (Appendix C, Table C3), the values of C_1, C_2, and K given in Table 6.4 were found.

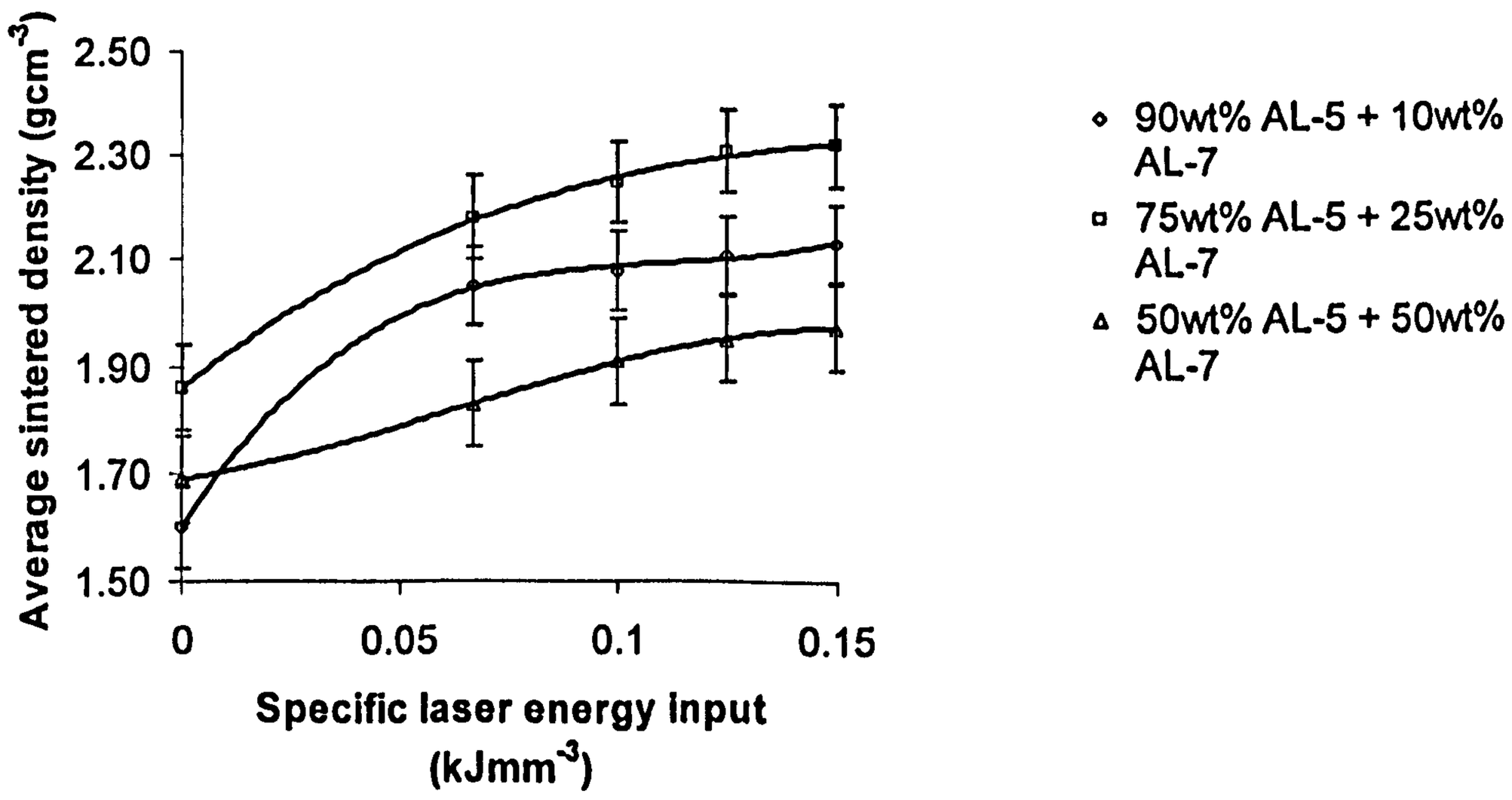

Figure 6.8: (a) Relationship between the sintered density and the specific laser energy input for different blends of AL-5/AL-7 powder- the lines show least-squares fitting to equation 2.18.

It can be seen from Table 6.4 that as more additive powders are introduced into the AL-5 powder, the agglomeration factor α^*, first tends close unity at 25wt% then decreases. This indicates that the introduction of 25wt% AL-7 into AL-5 powder gives minimum agglomeration. The effect of varying the percentage of AL-7 in the blended powder on the densification co-efficient K of powder mixes can be seen in Table 6.4. The value of K (13.4) coupled with the saturation sintered density (ρ_{st} =2.32 g/cm^3) obtained for the 25wt% AL-7 powder attests to its excellent sinterability. A reduction in the value of K for this blend is observed over that obtained for 100wt% AL-5 powder (21.8) which confirms that the choice of an appropriate ratio of SLS powders in the blend can improve sinterability.

Table 6.4: Densification parameters obtained from Figure 6.8 for AL-5 + AL-7 blended powders.

(wt% AL-7) Powder	C_1	C_2	K	ρ_{st} (g/cm^3)	ρ_{bed} (g/cm^3)	ρ_{tap} (g/cm^3)	$\alpha^* = \rho_{bed} / \rho_{tap}$
10% AL-7	2.15	0.55	23.16	2.14	1.60	1.70	0.94
25% AL-7	2.40	0.54	13.40	2.32	1.86	1.89	0.99
50% AL-7	2.07	0.46	10.48	1.97	1.69	1.74	0.92

Although, the lowest value of K (10.5) was obtained for the powder mixes containing 50% AL-7, the corresponding saturation sintered density (ρ_{st} =1.97 g/cm^3) was lower. The reason underlying this behaviour is unclear at this stage. Overall, powder blend containing 25wt% AL-7 has the best densification behaviour. Again, this finding confirms the excellent sinterability of the blended powder containing 25wt% AL-7.

Furthermore, the development of a new SLS/SLM processing regime for AL-5 powder blended with additive powders of varying particle sizes and distribution was thought to be a necessity at this stage because it was expected the introduction of additive powders of varying particle sizes and distribution would alter the particles packing arrangement as well as the heat conductivity of the powder bed (German 1993, 1996). This implies that the additive powders would effectively modify the sintering behaviour of AL-5 powder after blending. Powders consisting of a blend of AL-5 with 25wt% of each of the additive powders AL-2, AL-6, AL-7 and AL-8 were chosen in order to investigate the effect of variation of the additive powder particles sizes and distribution on the processing regime. The choice of mixed AL-5 powder containing 25wt% of each of the additive powder is founded on the basis that these blended compositions attained the most desirable properties in the results of the preliminary investigation reported in Figure 6.7. The sintering behaviour of the blended powders is presented in Figures 6.9. It is evident from Figure 6.9 that the maximum sintered density of each of the blended powders was 2.09 g/cm^3, 2.17 g/cm^3, 2.32 g/cm^3, and 2.08 g/cm^3 for blended powders containing 25wt% of each AL-2, AL-6, AL-7 and AL-8 respectively when a specific laser energy input of 150 J/mm^3 was employed.

These have increased marginally over the density values obtained, 2.03 g/cm^3, 2.07 g/cm^3, 2.18 g/cm^3, and 1.99 g/cm^3, when the specific laser energy input of 67 J/mm^3 was used. Values of C_1, C_2, and K obtained by fitting equation 2.18 to these data are given in Table 6.5. Again, these findings suggest that the introduction of additive powders affects the agglomeration factor, α^*, of the powder bed which approaches a value of unity with the exception of additive powder AL-8.

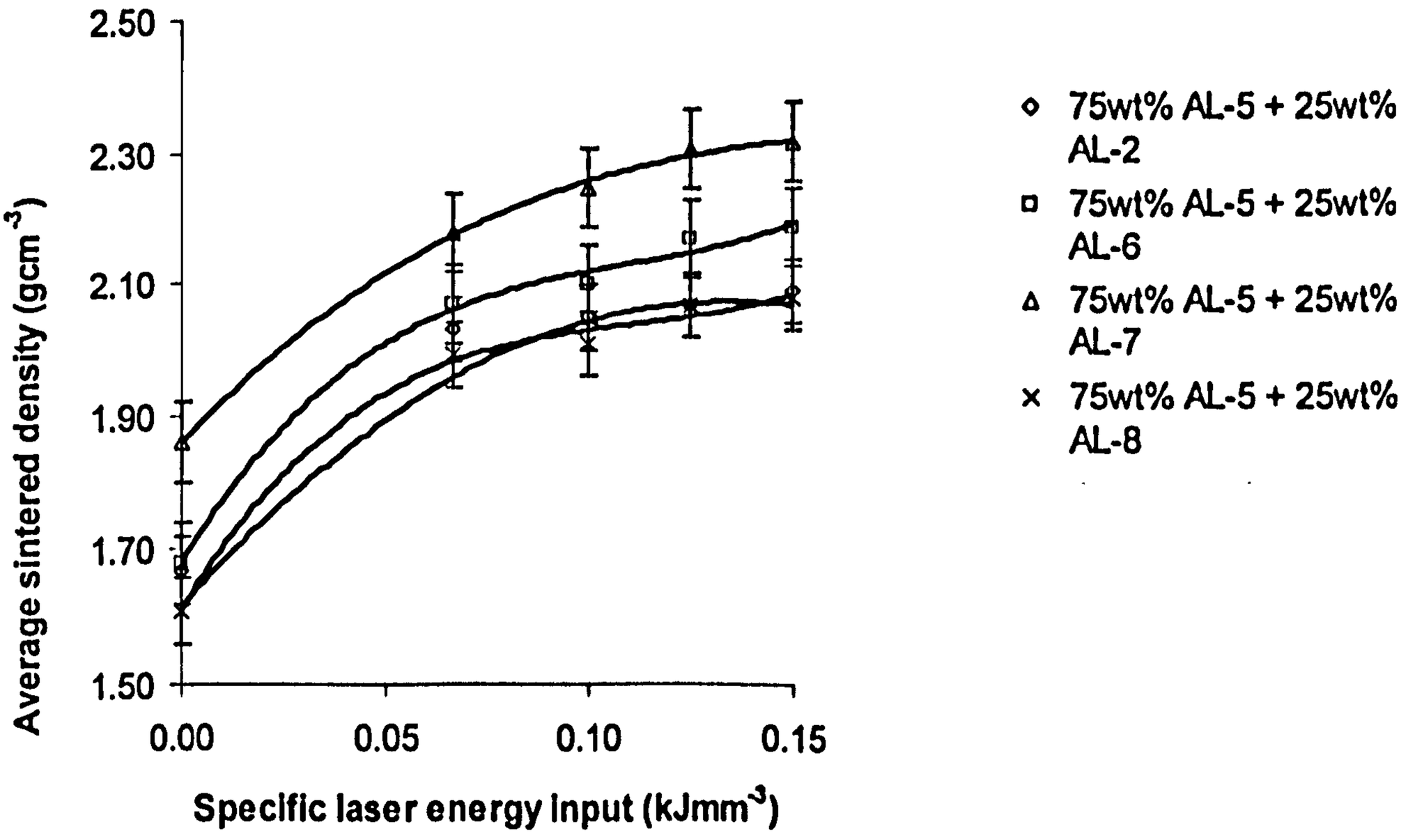

Figure 6.9: Relationship between the sintered density of the bimodal powders and the specific laser energy input.

This observation signifies that the addition of small-sized AL-8 particles to AL-5 powder has the propensity to aggravate the difficulty of agglomeration in the powder bed. The lowest value of densification co-efficient K (13.4) was obtained for the powder mix containing 17-30μm (AL-7) powder suggesting that this has the best densification kinetics. The sintering response of the blends obtained in this work is similar to that reported in sintering studies of ideal bimodal powder mixtures of iron powders (Simchi 2004, 2006).

Table 6.5: Densification parameters obtained from Figure 6.9 for direct SLS processed bimodal blended powders.

Powder .	C_1	C_2	K	ρ_{st} (g/cm^3)	ρ_{bed} (g/cm^3)	ρ_{tap} (g/cm^3)	$\alpha^* = \rho_{bed} / \rho_{tap}$
AL-2	2.12	0.45	18.08	2.09	1.67	1.76	0.95
AL-6	2.21	0.53	17.20	2.17	1.68	1.78	0.95
AL-7	2.40	0.54	13.40	2.32	1.86	2.00	0.99
AL-8	2.11	0.50	18.35	2.08	1.61	1.79	0.91

6.4.3 Microstructure of bimodal powders

6.4.3.1 Microstructure of bimodal powders containing varying proportions of AL-7

Polished but non-etched sections of the macrostructures and inset microstructures of SLS/SLM processed samples of AL-5 powder blended with various percentages of powder AL-7 are presented in Figures 6.10, 6.11 and 6.12. These macrographs and micrographs suggest that changes in microstructural characteristics such as amount of porosity, the size and shape of pores, and the shape and coherence of the sintered structure are dependent on the change in the content of AL-5. Regions labelled AA represent the occurrence of melt back from one layer to another. Melt back promotes coherence in inter-particulate melting across the layers of the samples, thereby improving the densification mechanism as well as microstructural characteristics of the SLS/SLM processed samples. Melt back had not successfully occurred in regions labelled BB where porosity is evident, reducing the sintered density.

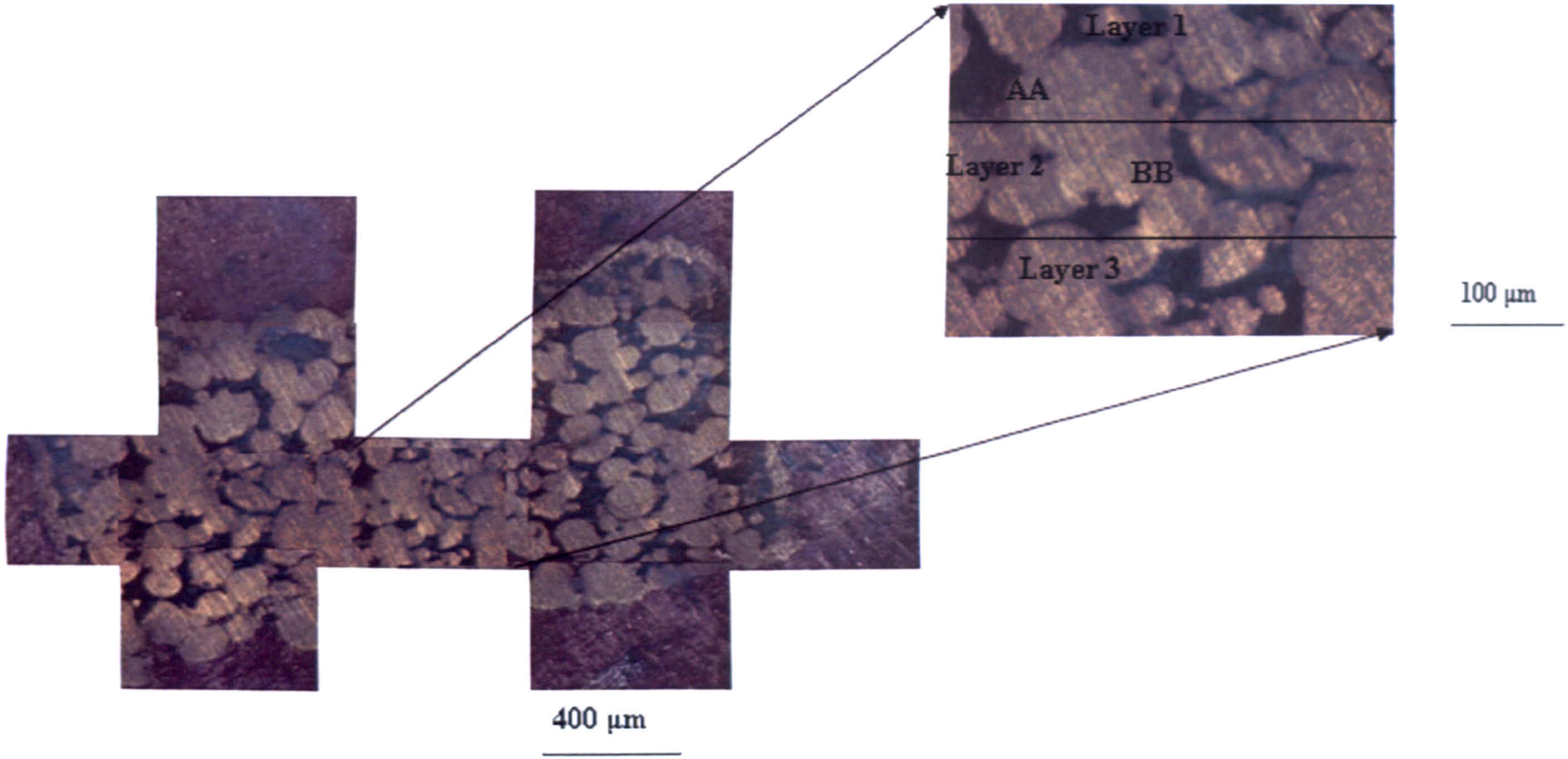

Figure 6.10: Sections through the sintered AL-5 (90wt%)-AL-7 (10wt%) blended powder at a specific laser energy input of 150 J/mm^3 showing the shape, size and distribution of pores as well as the particulate bonding across the layers.

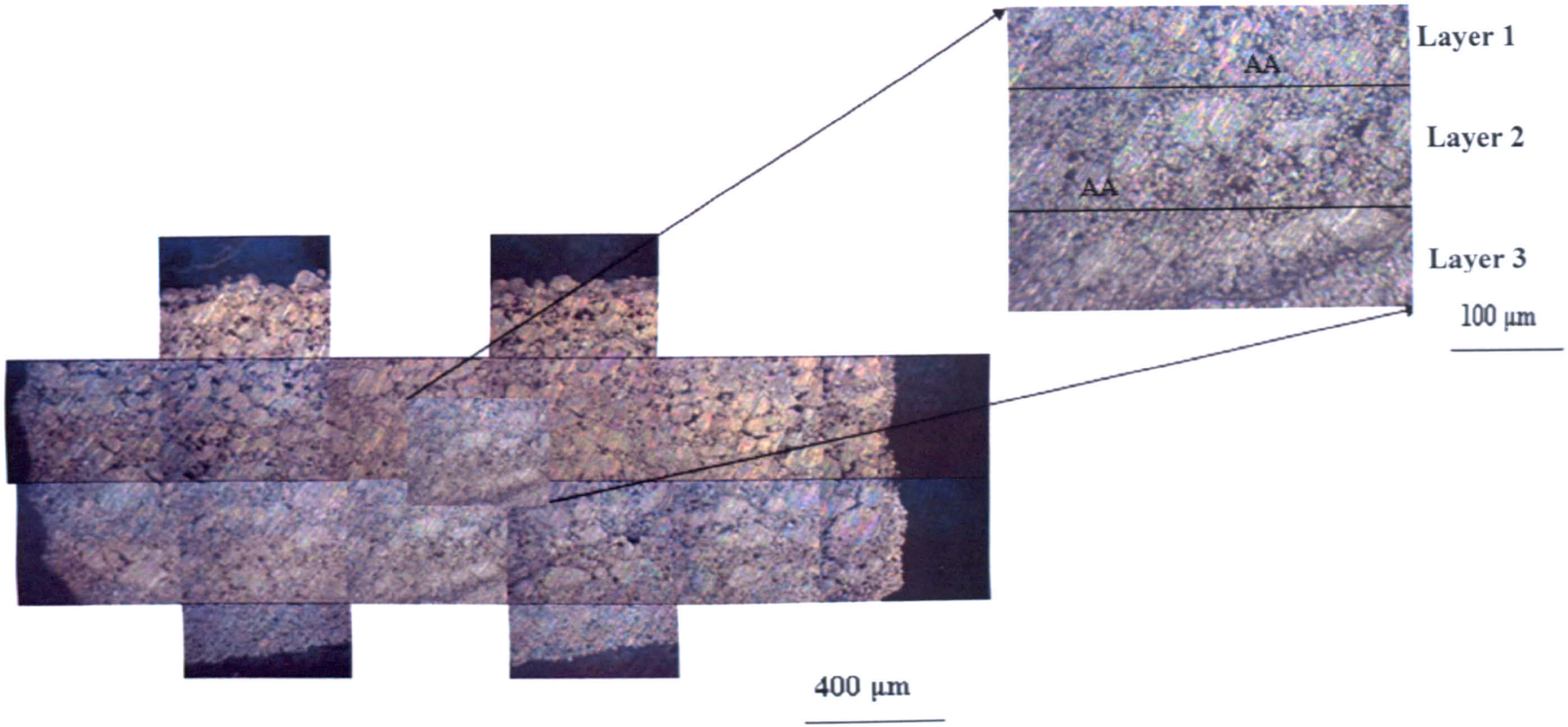

Figure 6.11: Sections through the sintered AL-5 (75wt%)-AL-7 (25wt%) blended powder at a specific laser energy input of 150 J/mm^3 showing the shape, size and distribution of pores as well as the particulate bonding across the layers.

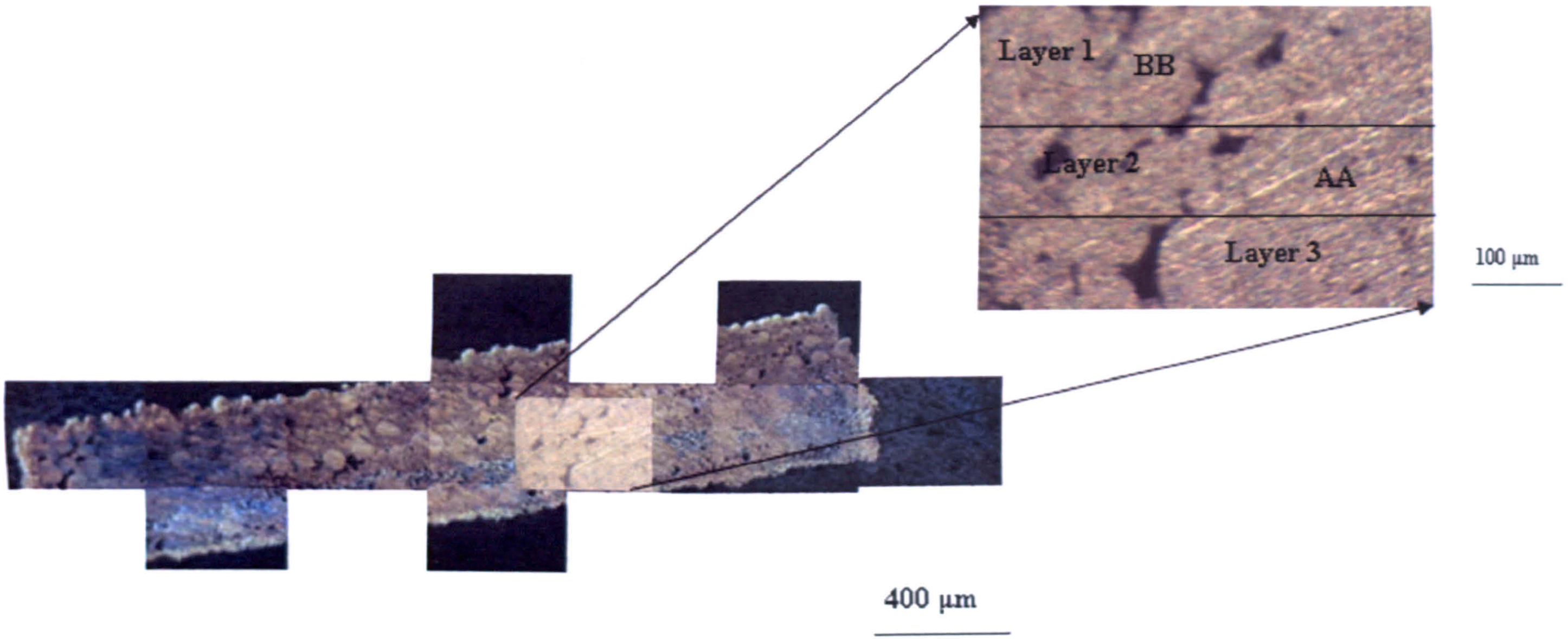

Figure 6.12: Sections through the sintered AL-5 (50wt%)-AL-7 (50wt%) blended powder at a specific laser energy input of 150 J/mm^3 showing the shape, size and distribution of pores as well as the particulate bonding across the layers.

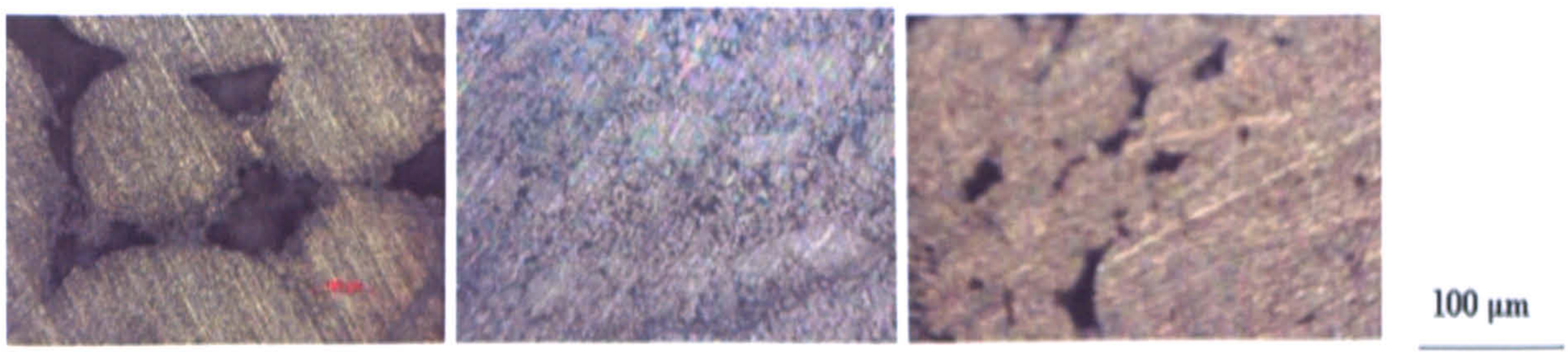

Figure 6.13: Optical microscopy images of the characteristic microstructures of direct laser sintered AL-5 powder containing varying contents of AL-7 additive powder, (a) 10% AL-7; (b) 25% AL-7; (c) 50% AL-7.

Comparison of the sintered macrostructure of unblended AL-5 (Figure 5.24) with those of the blended powders (Figures 6.10, 6.11 and 6.12) suggests that only the blended samples containing 25wt% of AL-7 had an improved macrostructure when compared to the unblended AL-5 powder (Figure 5.24). This is evident by lower porosity, fairly rounded, widely spaced pores and more coherent inter-particulate bonding across the layers (Figure 6.11).

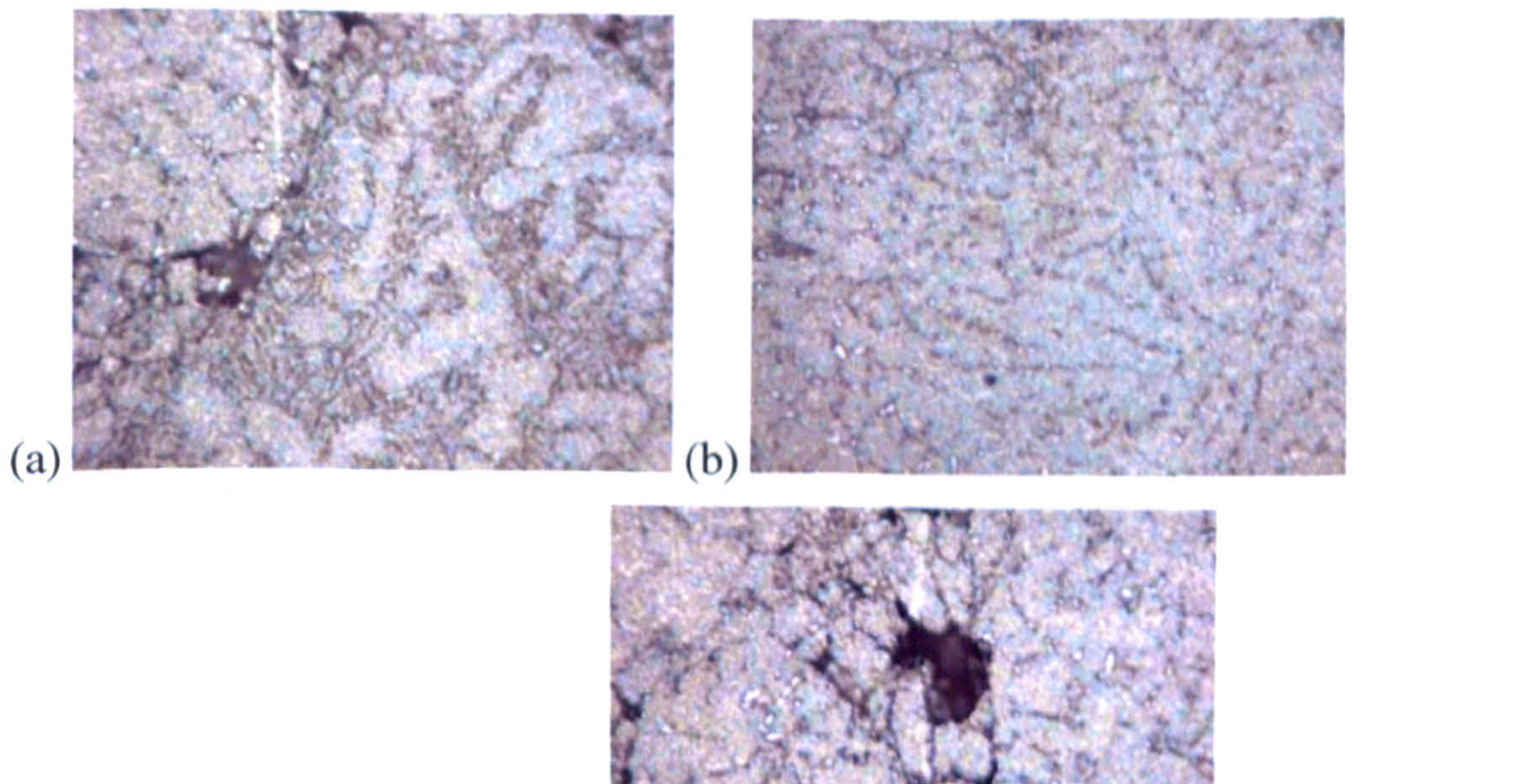

Figure 6.14: Microstructural heterogeneity and homogeneity in SLS/SLM processed blended AL-5 powder containing (a) 10wt% AL-7, (b) 25wt% AL-7 and (c) 50wt% AL-7.

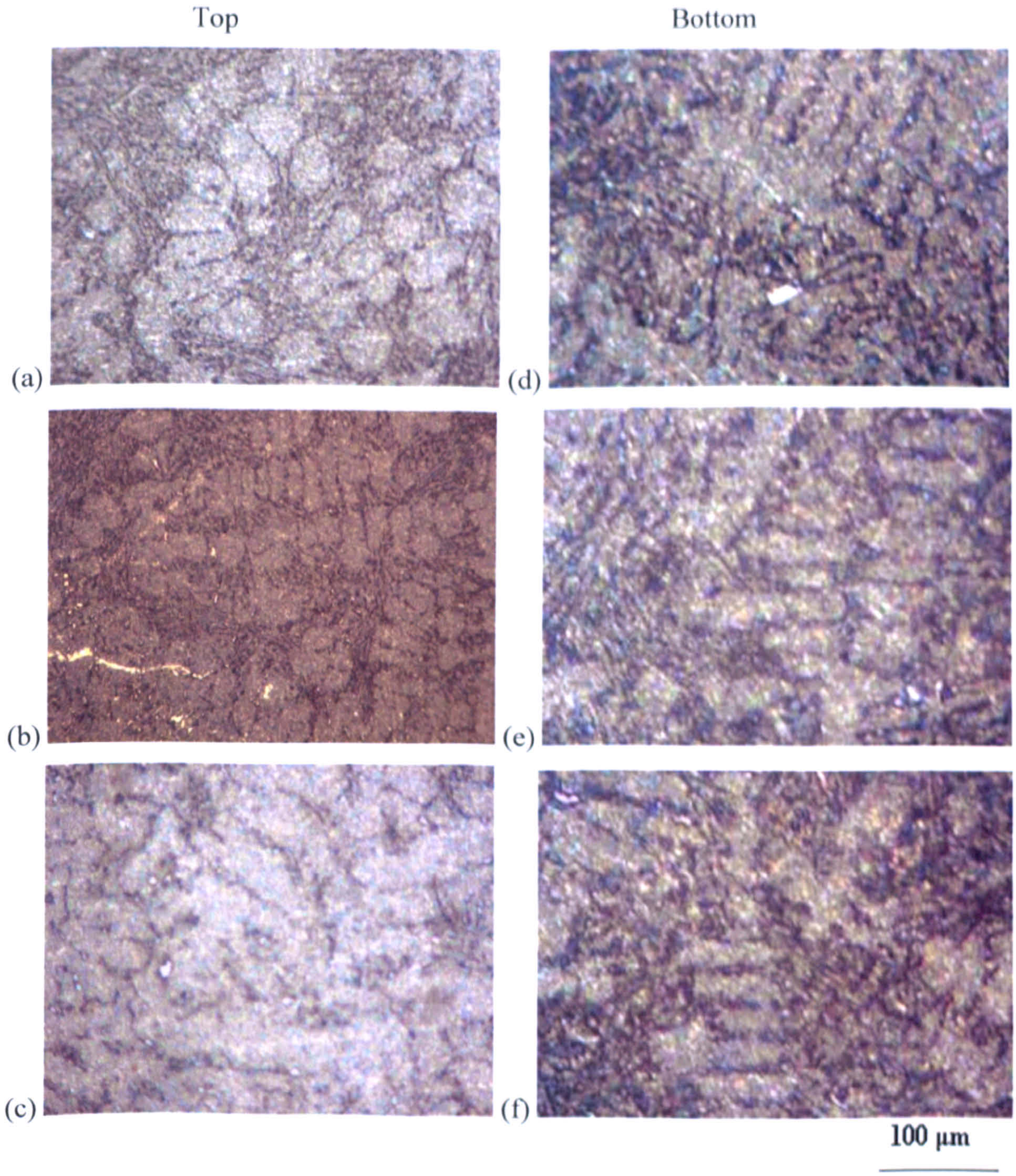

Figure 6.15: The nature of dendritic microstructure discovered in the SLS processed blended AL-5 powder containing varying content of AL-7: (a, d) 10wt%; (b, e) 25wt%; (c, f) 50wt%.

Figures 6.14a and 6.14c confirm the occurrence of heterogeneity in the microstructure of the blended samples containing 10wt% and 50wt% of AL-7 additive powder. The occurrence of porosity on the powder bed at these instances which is envisaged to have reduced the effective thermal conductivity of the powder bed is likely to be responsible for the occurrence of heterogeneity in the microstructure of the blended samples containing 10wt% and 50wt% of AL-7. In contrast, Figure 6.14b shows the formation of large melted regions consisting of dendrites where both 75wt% AL-5 and 25wt%

AL-7 particles appeared to have melted homogeneously. The formation of large melted homogeneous regions consisting of dendrites could be presumably attributed to the improved particle packing arrangement which is likely to have led to improved thermal conductivity of the powder bed which promotes formation of adequate melt pool for the densification mechanism in the blended sample.

The microstructures of the sintered samples revealed by etching are shown whilst the results of the quantitative metallography are presented in Figures 6.15, 6.16 and 6.17. Figure 6.15 shows that there appears to be a significant variation in the dendritic morphology from top to bottom of the SLS/SLM processed samples. The dendritic morphology at the bottom section (Figure 6.15 d, e, and f) of each sintered sample can be seen to be coarser than those at the top section of the sample (Figure 6.15a, b, and c). Observation of etched microstructure containing 75wt% AL-5 reveals a continuous network of finer dendrites in the sample (Figures 6.15b, and e) whereas samples containing 90wt% and 50wt% AL-5 have coarser and discontinuous network of dendrites across the depths of the samples (Figures 6.15a, c, d, and f).

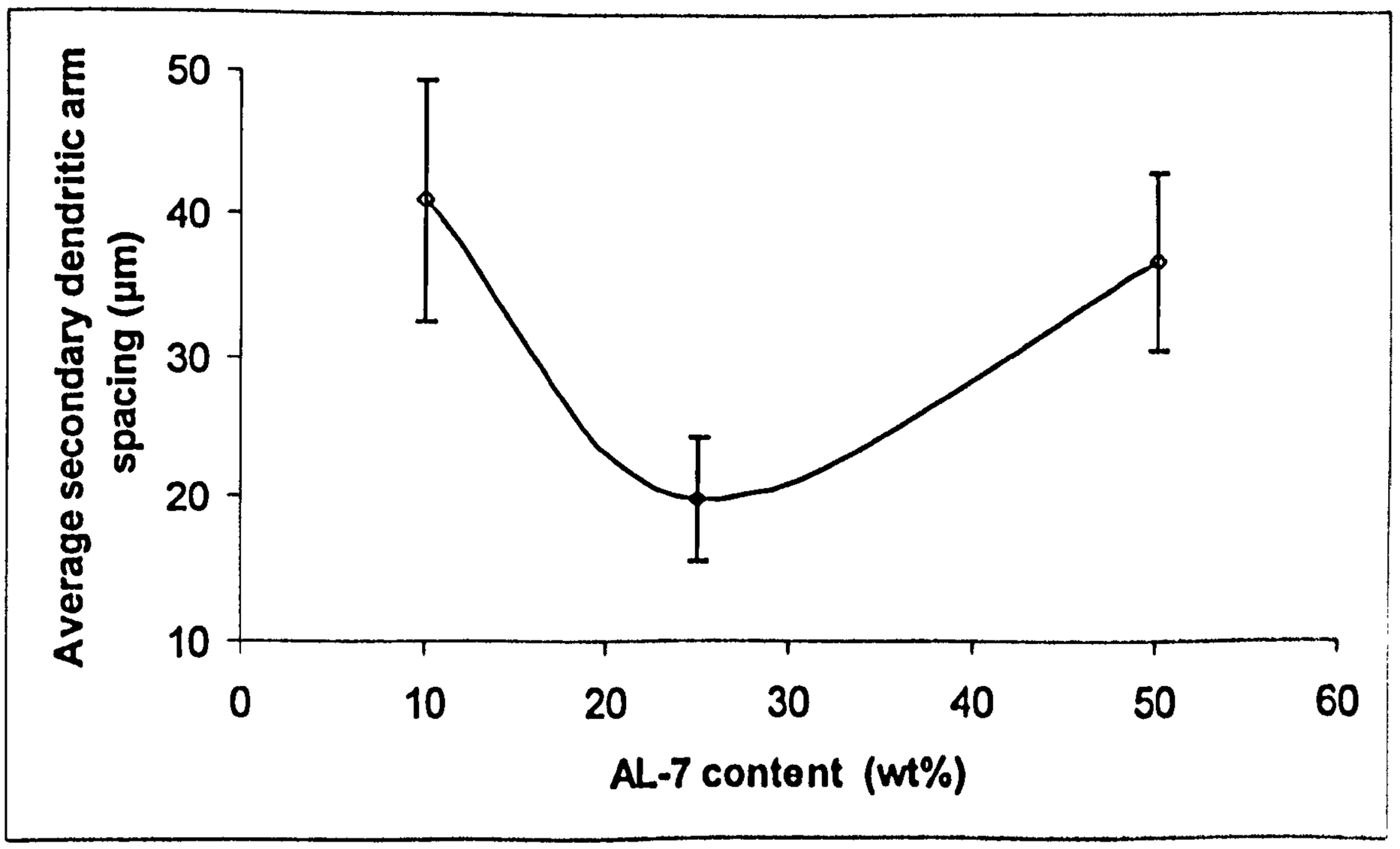

Figure 6.16: The relationship between the secondary dendritic arm spacing and the component ratio of additive powder AL-7 in the blended AL-5 powdered sample fabricated at the specific laser energy input of 150 J/mm^3.

Error bars in Figure 6.16 shows that there exists a slightly significant variation in measurements of dendritic arm spacing. Figure 6.16 shows that the secondary dendritic

to have resulted in change of the average compositions of the liquid and solid phases, and inhomogeneous distribution of the alloying elements in the microstructure of the blended samples. Meanwhile, error bars in Figure 6.17 establishes the existence of a significant variation in the measurements of fraction of primary phase in the blended samples.

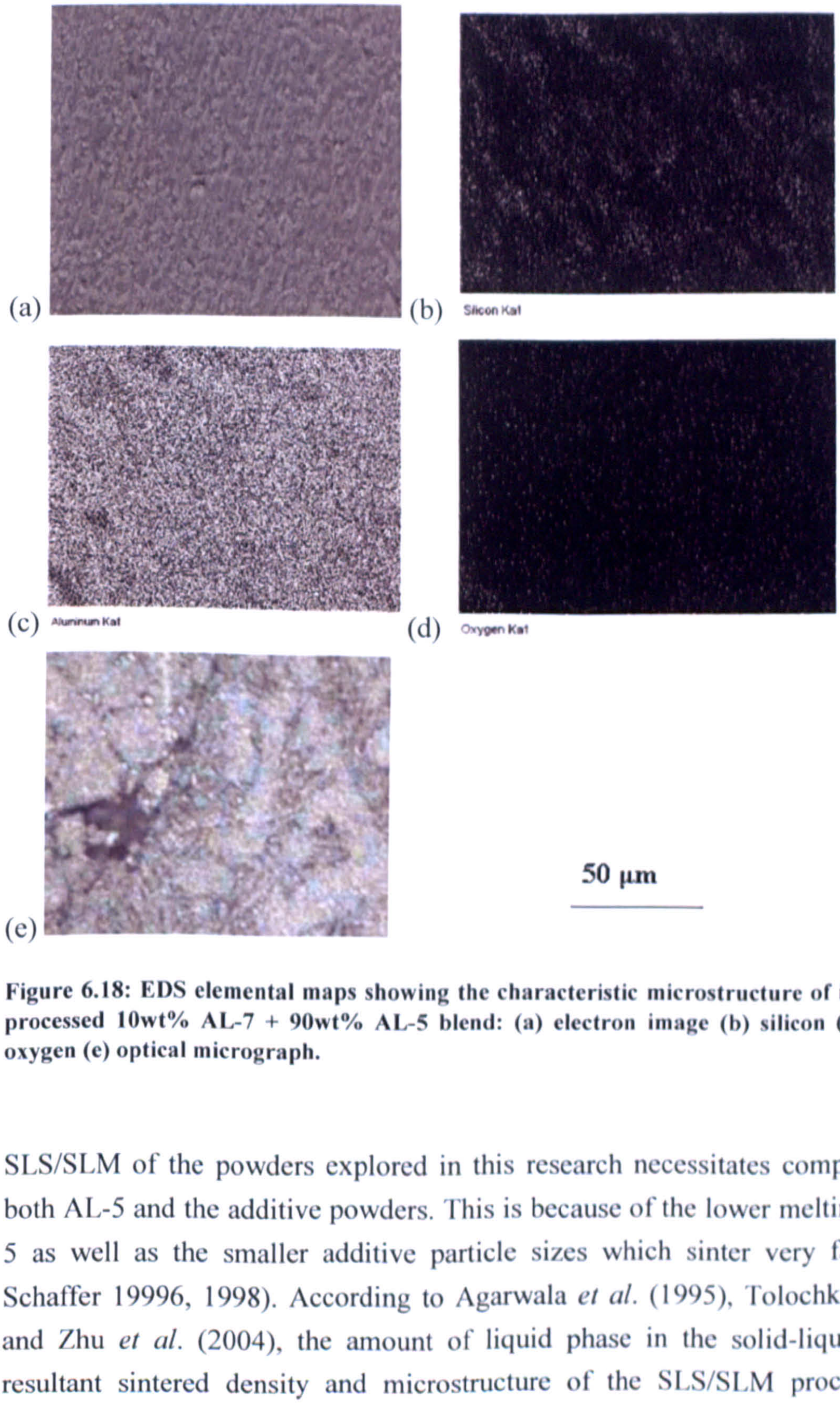

Figure 6.18: EDS elemental maps showing the characteristic microstructure of interfaces in SLM processed 10wt% AL-7 + 90wt% AL-5 blend: (a) electron image (b) silicon (c) aluminium (d) oxygen (e) optical micrograph.

SLS/SLM of the powders explored in this research necessitates complete melting of both AL-5 and the additive powders. This is because of the lower melting point of AL-5 as well as the smaller additive particle sizes which sinter very fast (Lumley & Schaffer 19996, 1998). According to Agarwala *et al.* (1995), Tolochko *et al.* (2003), and Zhu *et al.* (2004), the amount of liquid phase in the solid-liquid controls the resultant sintered density and microstructure of the SLS/SLM processed parts by

arm spacing is coarser for the blended powders containing 10wt% AL-7 (41 μm) and 50wt% AL-7 (37 μm) than that of 25wt% AL-7 (20 μm). With the measurements of the fraction of primary phase in each sample taking into consideration only well developed primary aluminium dendrites, it was discovered that the estimated fraction primary aluminium dendrite phase present in the SLS/SLM processed bimodal AL-5 powder containing 10wt%, 25wt%, and 50wt% AL-7 were 6.5wt%, 31.4wt%, and 22.2wt% respectively (Figure 6.17). The estimated weight fractions of primary phase also correspond to silicon contents of 11.6wt%, 8.7wt% and 6wt% (Table 6.2) in the blended powders being considered. The estimated fraction of primary phase obtained for all the blended samples are at variance with the theoretical values of 9.1wt%, 35wt% and 60wt% being expected from the Al-Si phase diagram (Figure 3.1a) using the lever rule. This outcome indicates that the powder packing arrangements in each of the blended powders differs and that it is thought to have initiated varying degrees of heat transfer or thermal conductivity across the packed layers on the powder bed.

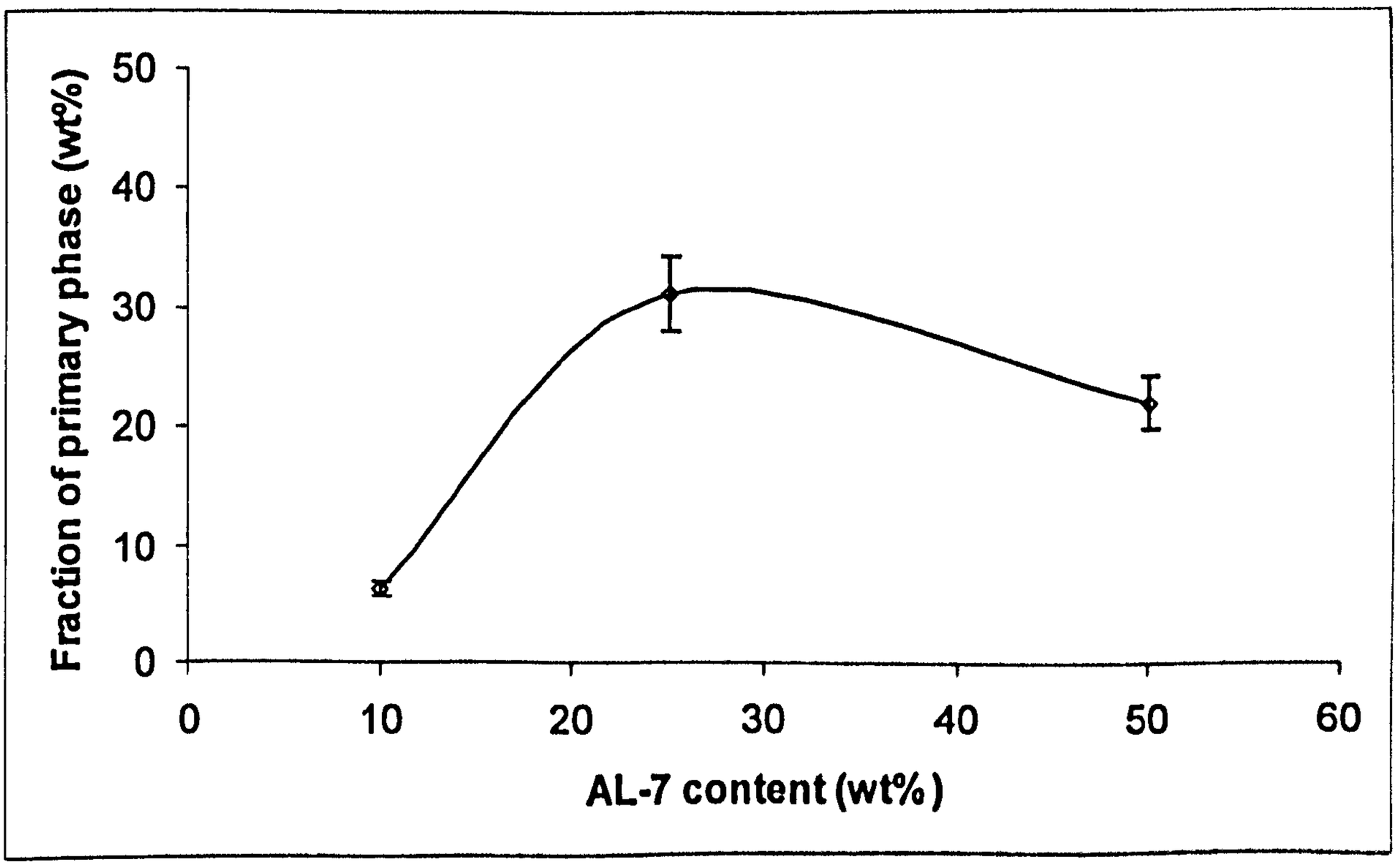

Figure 6.17: Relationship between fraction of primary phase and AL-7 content in the blended AL-5/AL-7 powder sample fabricated at a specific laser energy input of 150 J/mm^3.

Moreover, the variation in heat transfer across the packed layers in each blended powder is thought to have caused microsegregation or coring as a consequence of relatively low cooling rates which is thought to have occurred in all the blended powders. At the low relatively cooling rates, the diffusion processes are hereby considered incomplete to some extent. It is this incomplete diffusion which is thought

varying the thermodynamic and kinetic properties (e.g. solution, viscosity, wetting, and particle re-arrangement)of the molten pool. Therefore, when 10wt% AL-7 was added to AL-5 with corresponding 11.6wt% silicon content in its composition, excessive molten material with reduced melt viscosity was likely to have formed. This eventually results in the occurrence of "balling" phenomenon in the microstructure as shown in the inset microstructure of Figure 6.13a (Agarwala *et al.* 1995).

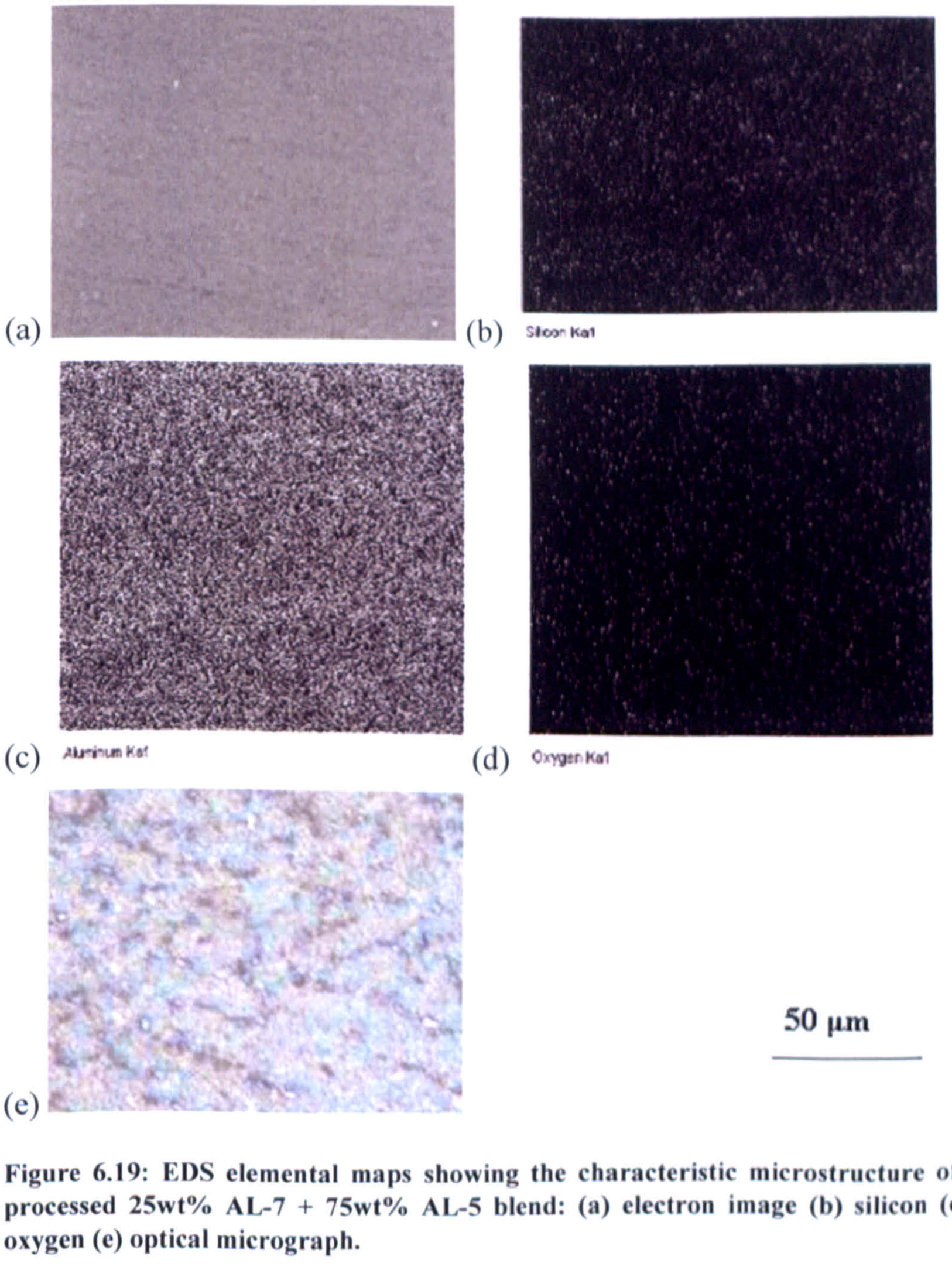

Figure 6.19: EDS elemental maps showing the characteristic microstructure of interfaces SLM processed 25wt% AL-7 + 75wt% AL-5 blend: (a) electron image (b) silicon (c) aluminium (d) oxygen (e) optical micrograph.

Moreover, Gusarov *et al.* (2003) and Gu & Shen (2007a), reported the initiation of repulsion forces between solid particles at the occurrence of high volume fraction of liquid which is presumed to have resulted in increased porosity and reduced sintered density observed in Figures 6.7a, b and 6.13a. Further increament in AL-7 content to

25wt% with corresponding silicon content of 8.7wt% was likely to have increased the viscosity of the melting pool sufficiently thereby improving the easiness of the flow of the melting pool (Figure 6.15b, c). In addition, the re-arrangement force of solid particles in the sintering pool could be said to have reduced sufficiently with the volume fraction of the liquid in this context (Zhu *et al.* 2004). This condition is thought to have promoted adequate wettability and re-arrangement of AL-7 particles which results in improved density and microstructure of the sintered sample (see the inset of Figures 6.11, 6.9b, and 6.19). By increasing the AL-7 content to 50wt% with the corresponding silicon content of 6wt%, it is envisaged that the amount of liquid phase being formed was just sufficient to bind the AL-7 particles, thereby resulting in the formation of discontinuous agglomerates with large and irregular pores (Figure 6.12, and 13c). In this condition, the viscosity of the molten pool is thought to have increased much more than is necessary such that the re-arrangement force which is induced by the capillary force of the liquid is speculated to be too high to re-arrange all AL-7 particles, hence, the reduced densification and heterogenous microstructure (Figure 6.14c).

The characteristic microstructures of the laser sintered blended powders are presented in term of the EDS elemental maps of silicon, aluminium and oxygen in Figures 6.18, 6.19, and 6.20. When 10wt% and 50wt% of AL-7 were added to AL-5 (45-75 micron) powder samples (Figures 6.18 and 6.20), there exist dark regions in the silicon and oxygen maps which are presumed to have sizes and shapes that approximate to the sizes and shapes of pores seen in Figures 6.18c and 6.20c. These dark regions are hereby speculated to be the porosities existing in the microstructure of the laser melted blended AL-5 powders. With the additive content of 25wt%, absence of isolated dark regions in the silicon and oxygen maps (Figure 6.19) suggest that the particles of additive powder were uniformly dispersed in the matrix of AL-5 and the microstructure could be described as dense and homogeneous (Figures 6.19c).

Figures 6.21 and 6.22 present the effect of blending AL-7 powder with AL-5 on the average sintered microhardness and the variation of microhardness measured across the horizontal cross-section of the samples respectively. The microhardness values obtained are generally lower than those reported for unblended SLM processed AL-5 (Figure 5.22). It can be inferred from Figure 6.21 that microhardness values obtained could be associated with variation in the additive particle component ratio in the blended AL-5 powder. Furthermore, the microhardness value of the blended powders containing 25% AL-7 has the most desirable microhardness upon comparison with

other blended powders. Error bars on Figure 6.18 indicate the existence of significant variation in measurements of microhardness on the samples. Meanwhile, the results obtained could be described as complex as one would expect that adding pure Al powders would decrease hardness whether mixed or not.

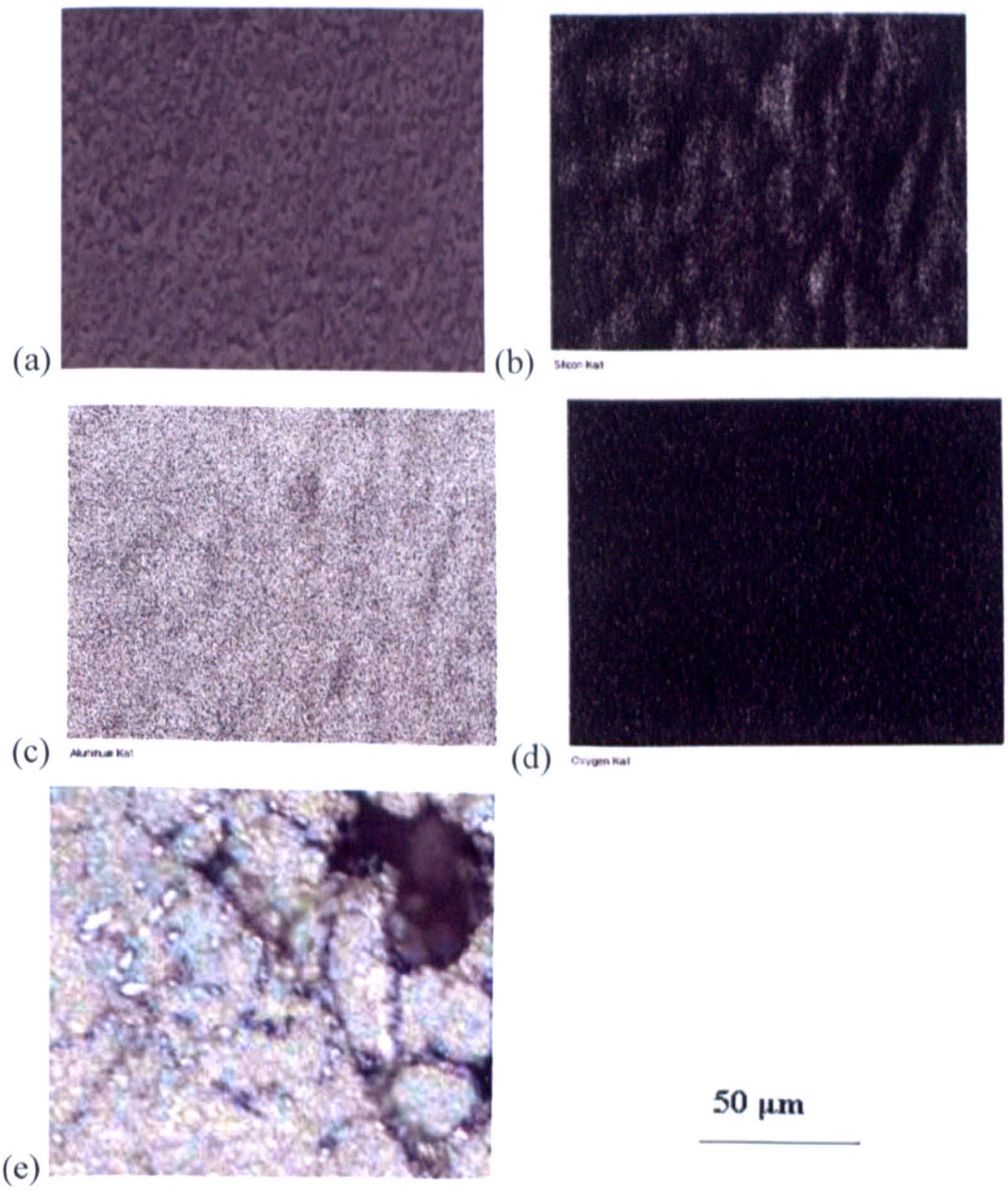

Figure 6.20: EDS elemental maps showing the characteristic microstructures of interfaces in SLM processed 50wt% AL-7 + 50wt% AL-5 blend: (a) electron image (b) silicon (c) aluminium (d) oxygen (e) optical micrograph.

Although, an increase observed at 25wt% suggests that the effect of porosity is superimposed on alloying. A relatively uniform microhardness distribution was obtained for the 25wt% AL-7 blend (Figure 6.21) compared to other blended powders where the values of microhardness are observed to fluctuate to a very great extent (Figures 6.22). Error bars on Figure 6.22 suggest that there is no significant variation in microhardness for each cross-section on which it was measured. Figure 6.23 shows the

surface morphology of laser sintered AL-5 powder blended with different amounts of AL-7. The formation of agglomerates joined together by small necks and interconnected pores could be seen in Figures 6.23a and c. It is clear that addition of 25wt% AL-7 produced a markedly lower surface roughness with high agglomerate interconnectivity and minimum interconnected pore size.

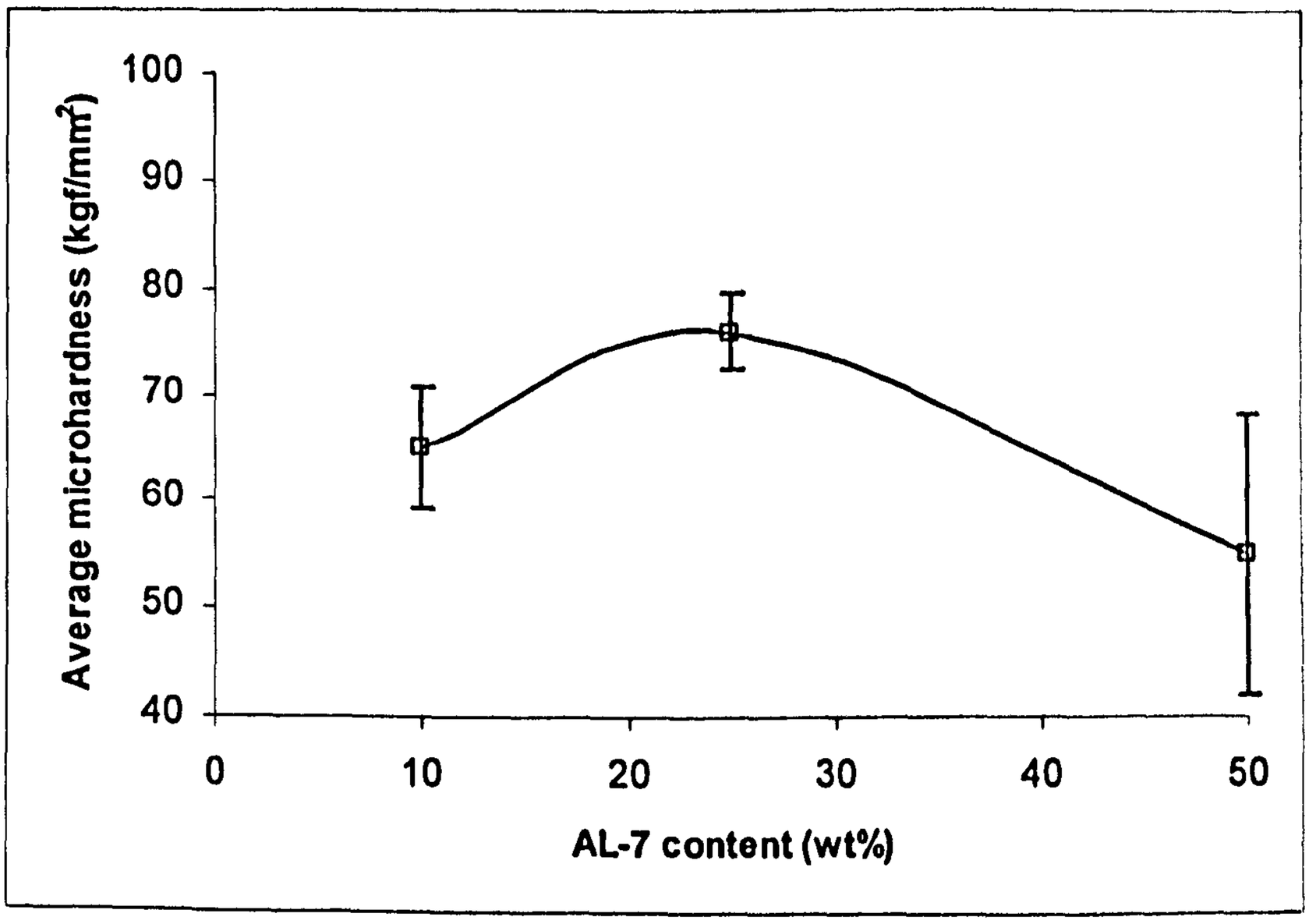

Figure 6.21: Effect of powder composition on the microhardness of the direct laser-sintered AL-5 + AL-7 blends (specific laser energy input 150 J/mm^3).

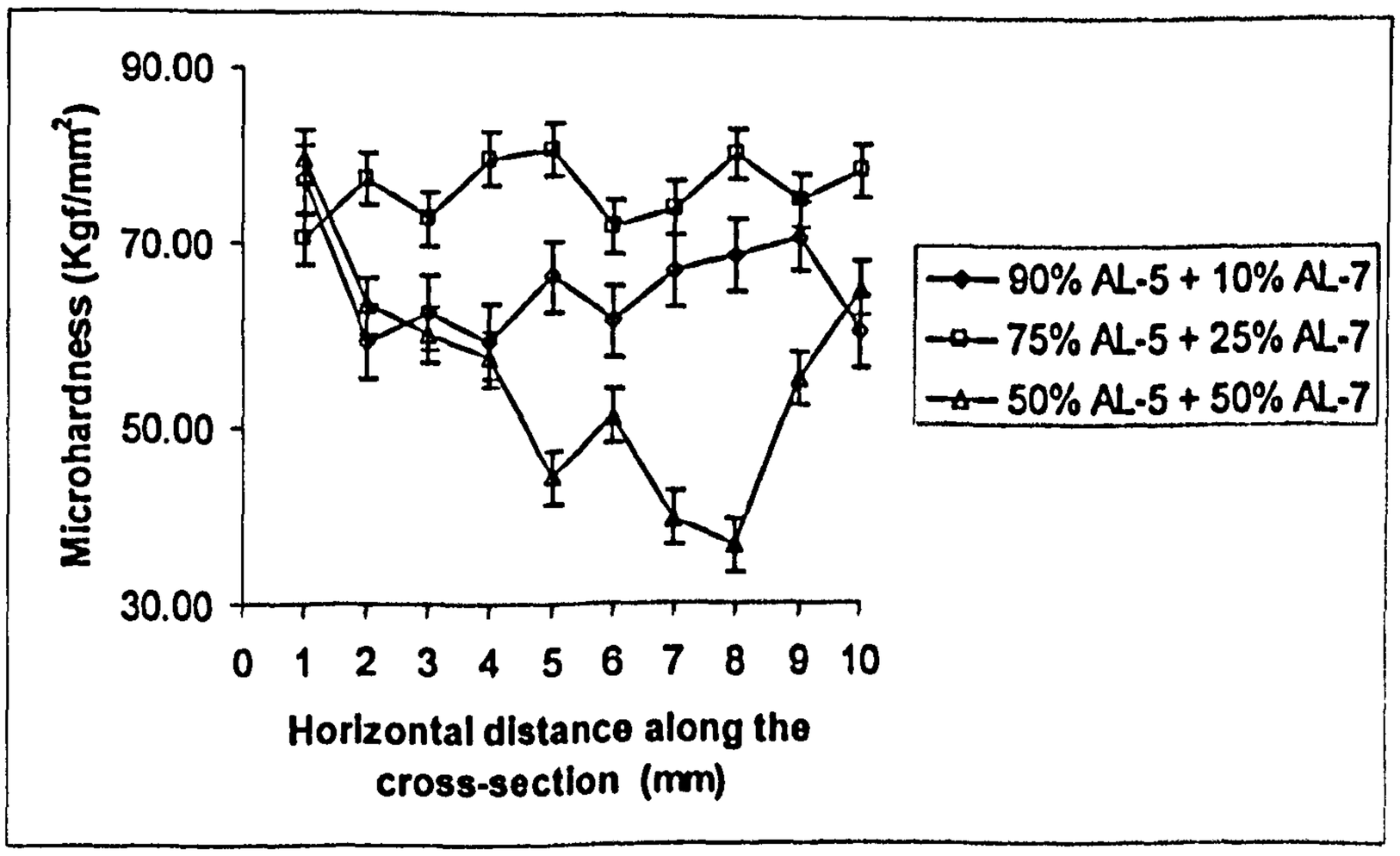

Figure 6.22: Variation in microhardness on the horizontal cross-sections of the direct laser-sintered AL-5/AL-7 blends (specific laser energy input of 150 J/mm^3).

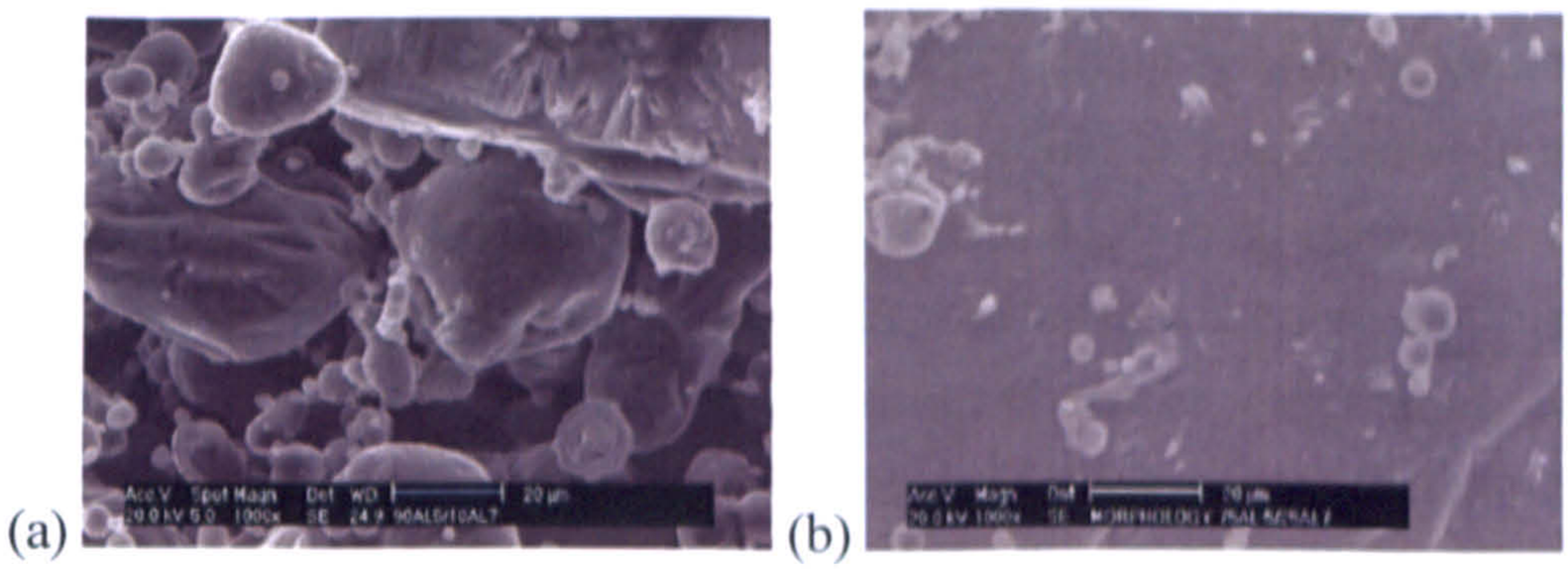

Figure 6.23: Surface morphologies of the laser sintered blended AL-5/AL-7 powders containing (a) 10wt% AL-7, (b) 25wt% AL-7, (c) 50wt% AL-7 (specific laser energy input of 150 J/mm^3).

6.4.3.2 Microstructures of Bimodal Powders Containing Additive Powders of Varying Particle sizes

The microstructure of the AL-5 powder blended with each of the additive powders of varying particle sizes is presented in Figures 6.24, 6.25, 6.26, and 6.27. As in Section 6.4.3.1, regions designated AA in Figures 6.24, 6.25, 6.26, and 6.27 represent the occurrence of melt back from one layer to another whilst melt back had not successfully occurred in regions designated BB. The microstructures of all samples, but that containing 25wt% AL-7, are characterised by large residual pores connected with short inter-pore spacing. The occurrence of inter-particulate diffusion, evident by the formation of necking in all the samples indicates that all samples appear to be well sintered (Figure 6.28). Agglomerate formation could be seen to be associated with the samples containing coarse additive powders AL-2 and AL-6. Fine additive powder AL-8 was expected to be beneficial in the SLS processing of AL-5 powder due to its tendency to increase densification and form smaller secondary pores. However, Figure 6.28 shows that the microstructure of the blended sample 25wt% AL-8 is not optimised.

Figures 6.29a, 6.29b and 6.29d confirm the occurrence of heterogeneity in the blended samples containing 25wt% of each of AL-2, AL-6 and AL-8 respectively. As noted

earlier on, sintered particles of AL-2, AL-6, and AL-8, could be seen to be coated with the melted particles of AL-5 whereas no distinction could be made between AL-5 and AL-7 particles in the microstructure containing 25wt% AL-7 upon comparison (Figures 6.29a to 6.29d). Again, this observation suggests that the microstructure of the blended samples containing 25wt% AL-7 is homogeneous. Moreover, observation of Figures 6.29a, 6.29b, and 6.29d suggests that the occurrence of heterogeneous microstructure in the blended samples containing AL-2, AL-6, and AL-8 respectively could be speculatively attributed to the presence of porosity in the powder bed which lowers its thermal conductivity. Meanwhile, the formation of homogeneous microstructure in the blended sample containing 75wt% AL-5 + 25wt% AL-7 is suspected to have been due to its improved particle packing arrangement which led to improved thermal conductivity of the powder bed.

The effects of the additive powder particle sizes and distribution on the microstructure of SLS/SLM processed blended powder are presented in Figures 6. 30, 6.31, 6.32, 6.33, 6.34 and 6.35. It is evident from Figure 6.30 that the introduction of additive powders of different particle sizes and distribution alters the dendritic morphology of laser sintered bimodal AL-5 powder. Finer dendritic microstructures are generally seen in the blended samples containing AL-7. In the case of the blended samples containing AL-2, AL-6 and AL-8, the dendrite structures are noted to be coarser. Meanwhile, it was observed that a coarse dendritic microstructure existed at the bottom parts of the samples, irrespective of additive particle size distribution contained in the bimodal AL-5 powder (Figure 6.31). Figures 6.32 and 6.33 reveal that dendritic arm spacing was finest for the blended samples containing additive particles having size distribution of 17-30 μm (AL-7) and average particle size of 23.6 μm respectively. Figures 6.34 and 6.35 reveal that the primary fraction in the blended samples was optimised at the instance the blended samples contain additive particles having size distribution of 17-30 μm (AL-7) and average particle size of 23.6 μm respectively. Observation of error bars reveals that variation in measurements is not significant for the dendritic arm spacing (Figures 6.32 and 6.33) whereas, significant variation occurs in the measurement of the primary fraction (Figures 6.34 and 6.35).

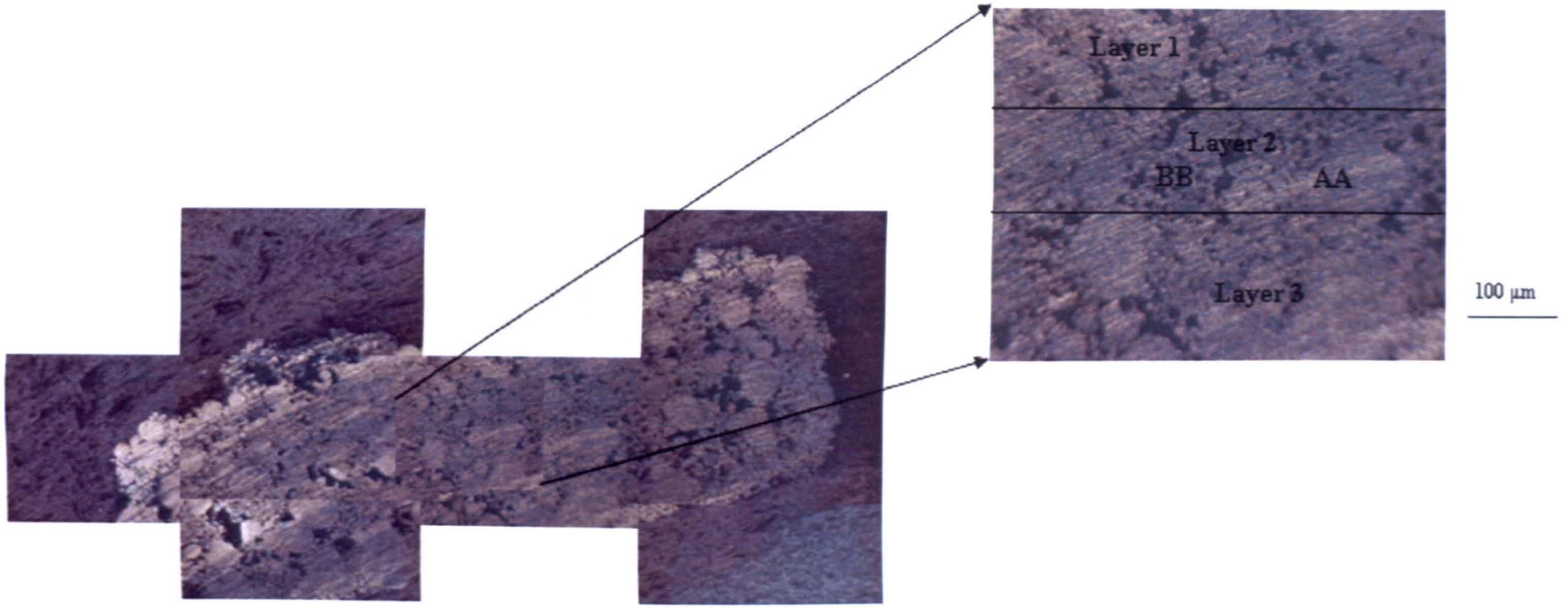

Figure 6.24: Macrostructure of sections through sintered AL-5/25wt% AL-2 showing the shape, size and distribution of porosity as well as the inter-particulate bonding across the layers.

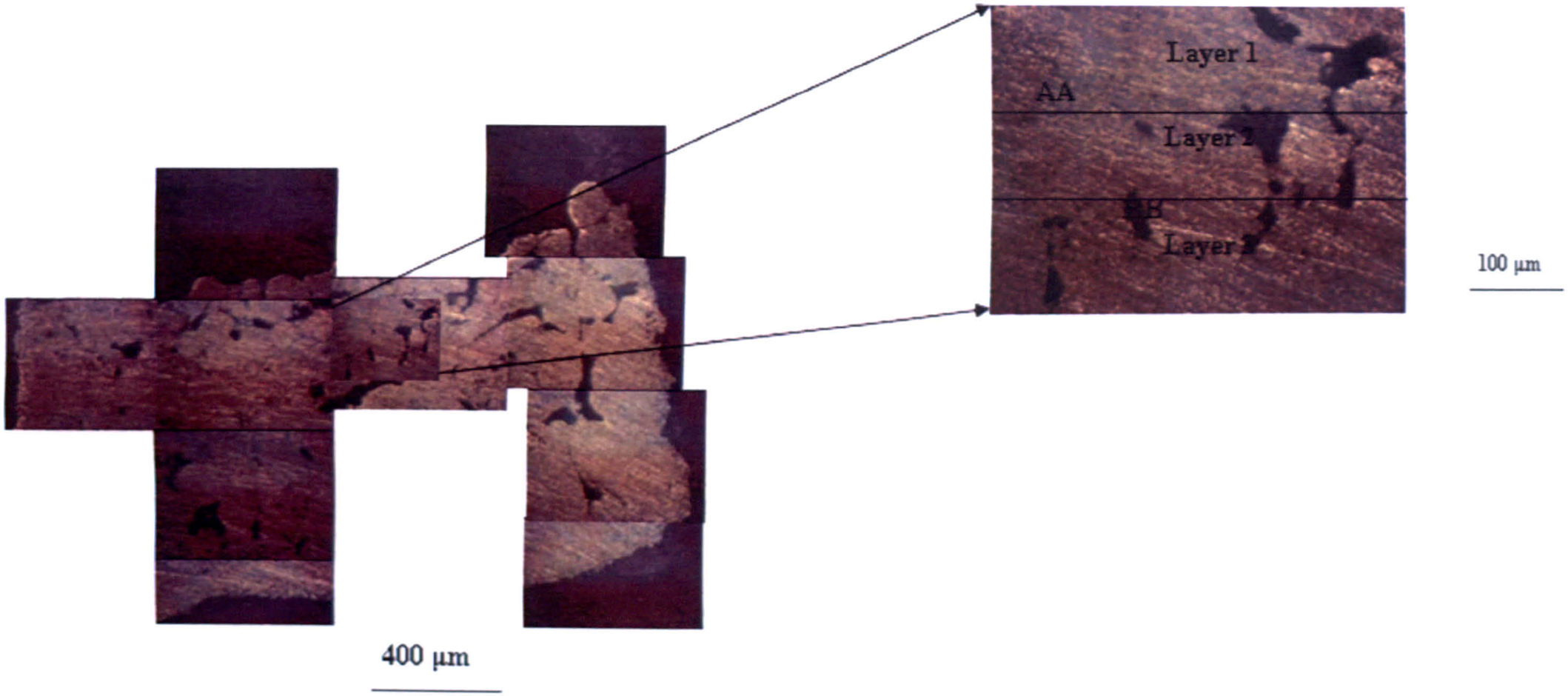

Figure 6.25: Macrostructure of sections through sintered AL-5/25wt% AL-6 fabricated showing the shape, size and distribution of porosity as well as the inter-particulate bonding across the layers.

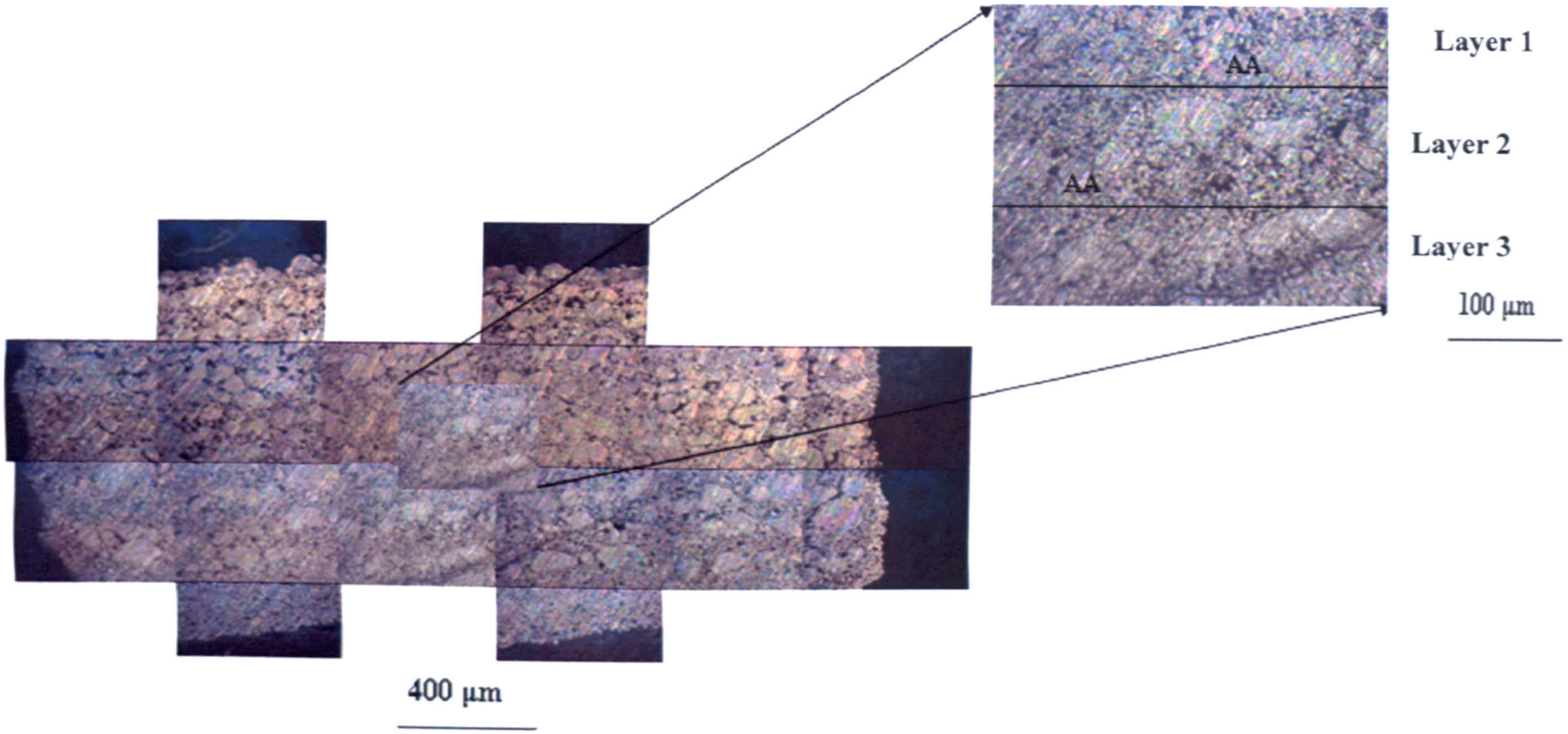

Figure 6.26: Macrostructure of sections through sintered AL-5/25wt% AL-7 showing the shape, size and distribution of porosity as well as the inter-particulate bonding across the layers.

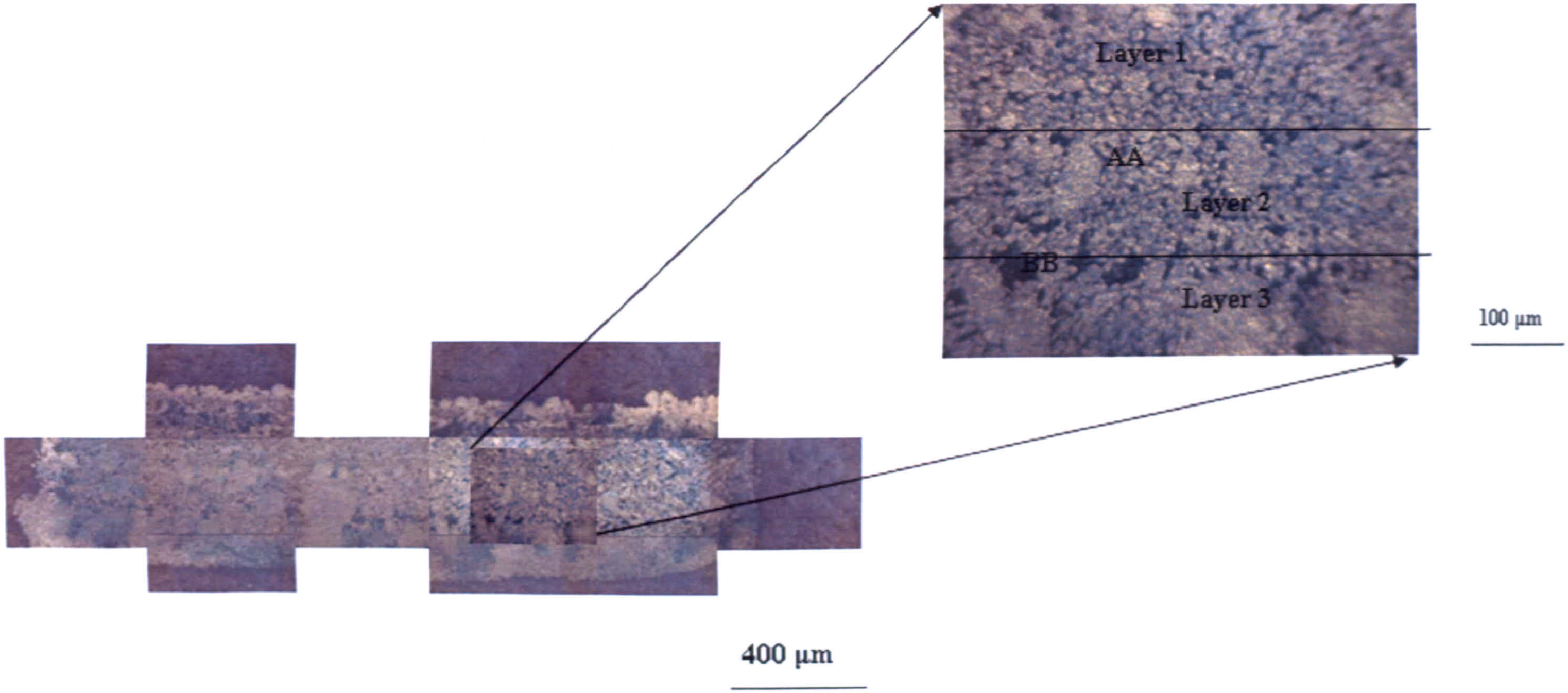

Figure 6.27: Macrostructure of sections through sintered AL-5/25wt% AL-8 showing the shape, size and distribution of porosity as well as the inter-particulate bonding across the layers.

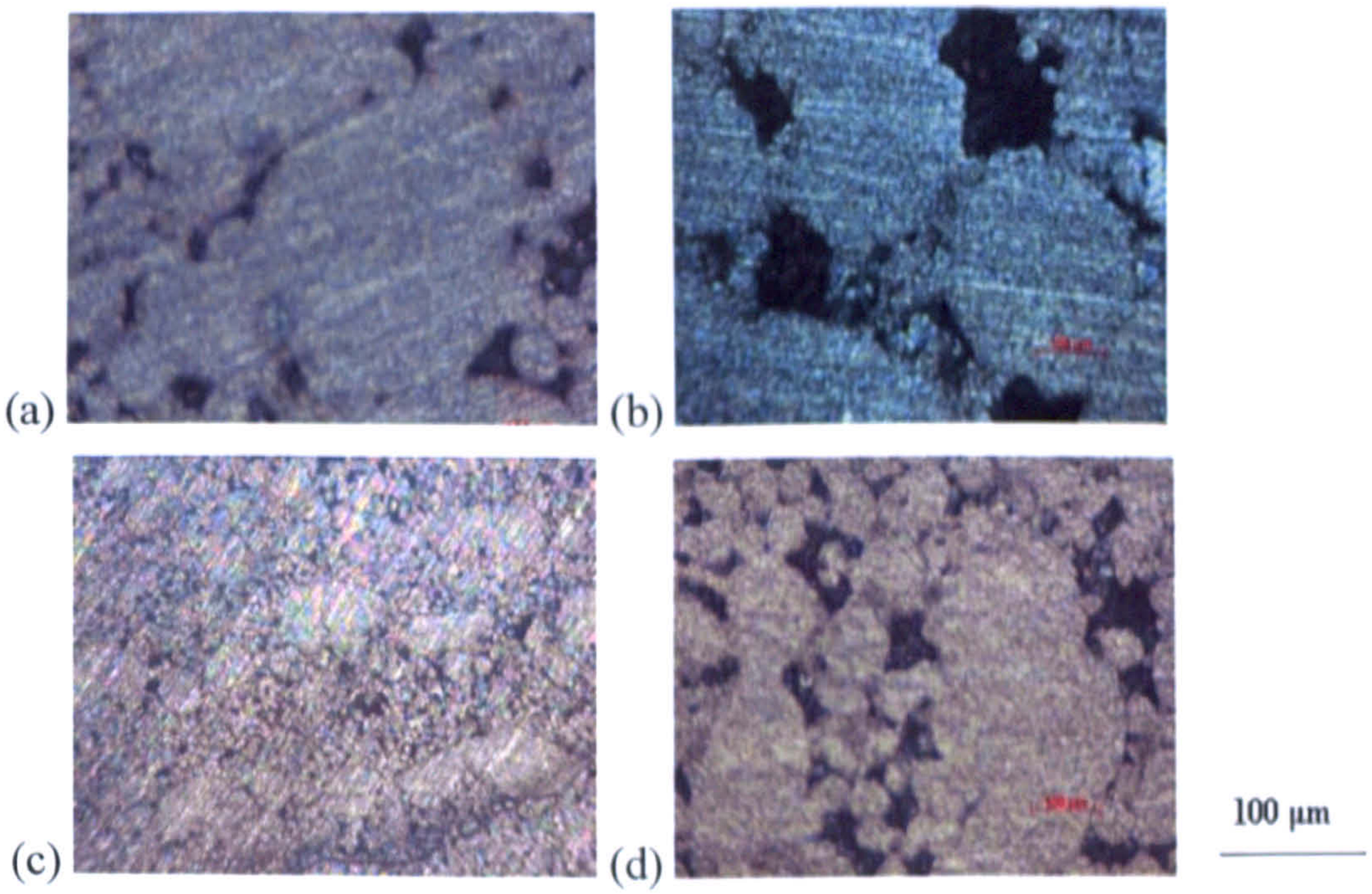

Figure 6.28: Optical microstructures through polished sections showing the effect of laser sintered AL-5 powder blends (a) AL-5/25wt% AL-2 (b) AL-5/25wt% AL-6 (c) AL-5/25wt% AL-7 and (d) AL-5/25wt% AL-8.

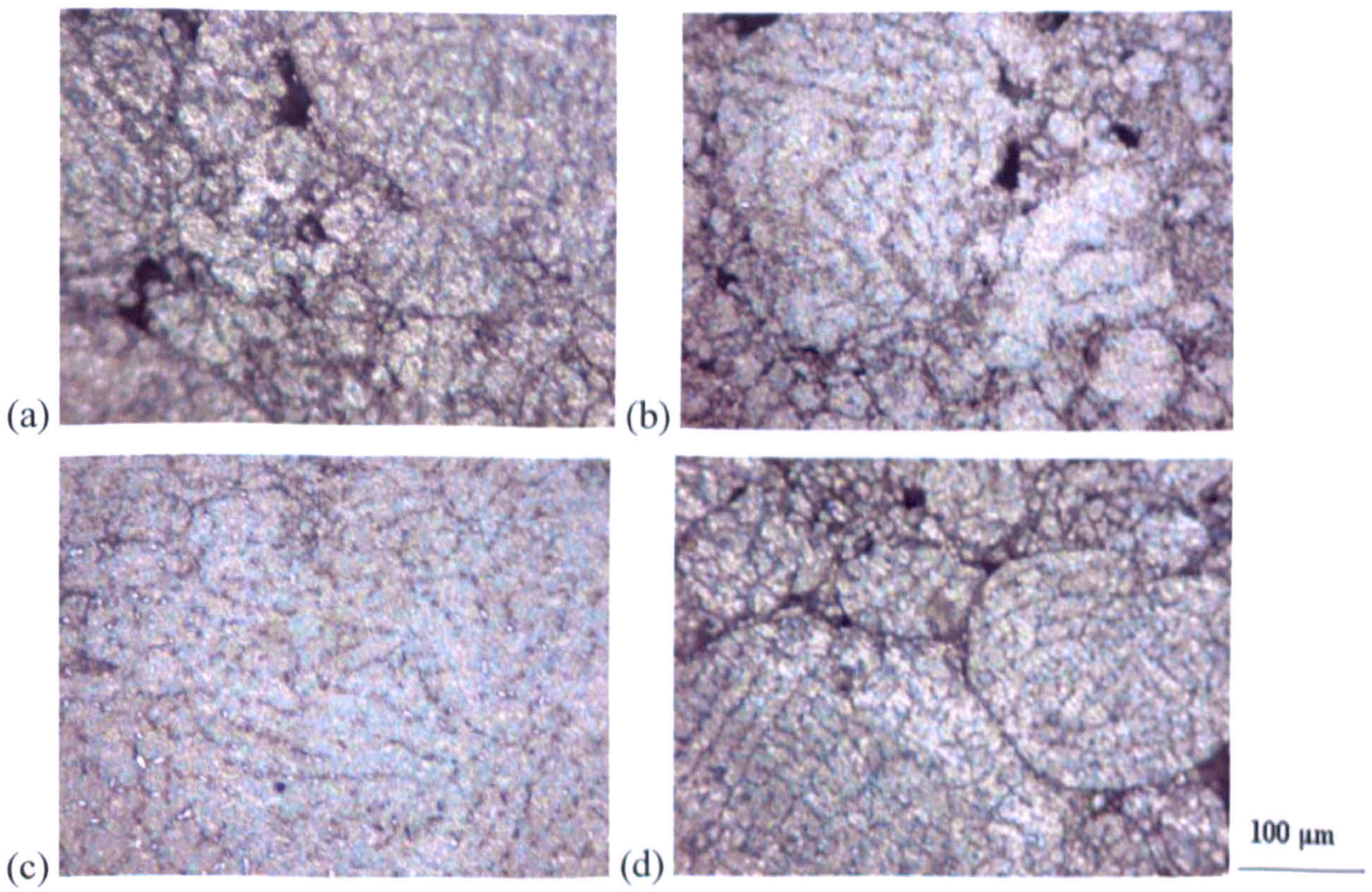

Figure 6.29: Microstructural heterogeneity and homogeneity in SLS/SLM processed blended AL-5 powder containing additive powders of varying particle sizes: (a) 25wt% AL-2, (b) 25wt% AL-6 and (c) 25wt% AL-7 and (d) .25wt% AL-8.

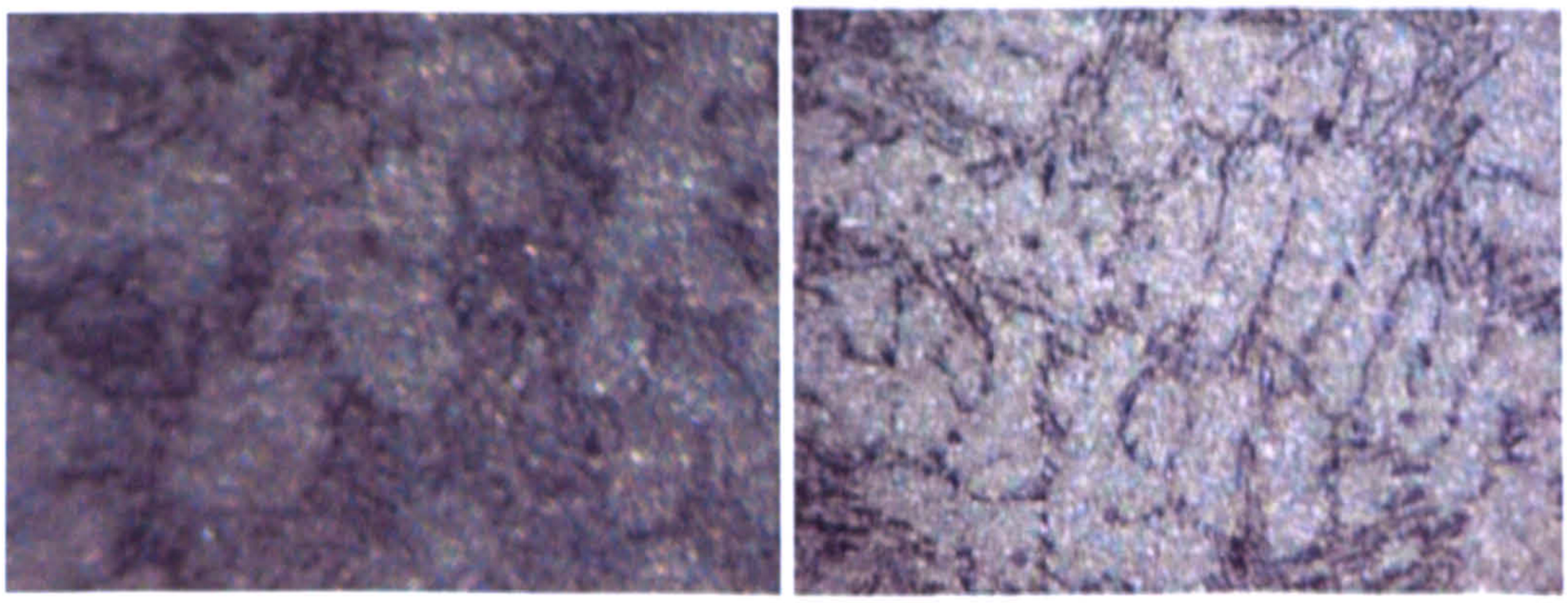

Figure 6.30: Effect of additive powder's particle size and distribution on the development of dendritic microstructure at the top portion of the SLS/SLM processed blended AL-5 powder (a) 25wt% AL-2, (b) 25wt% AL-6 (c) 25wt% AL-7 (d) 25wt% AL-8

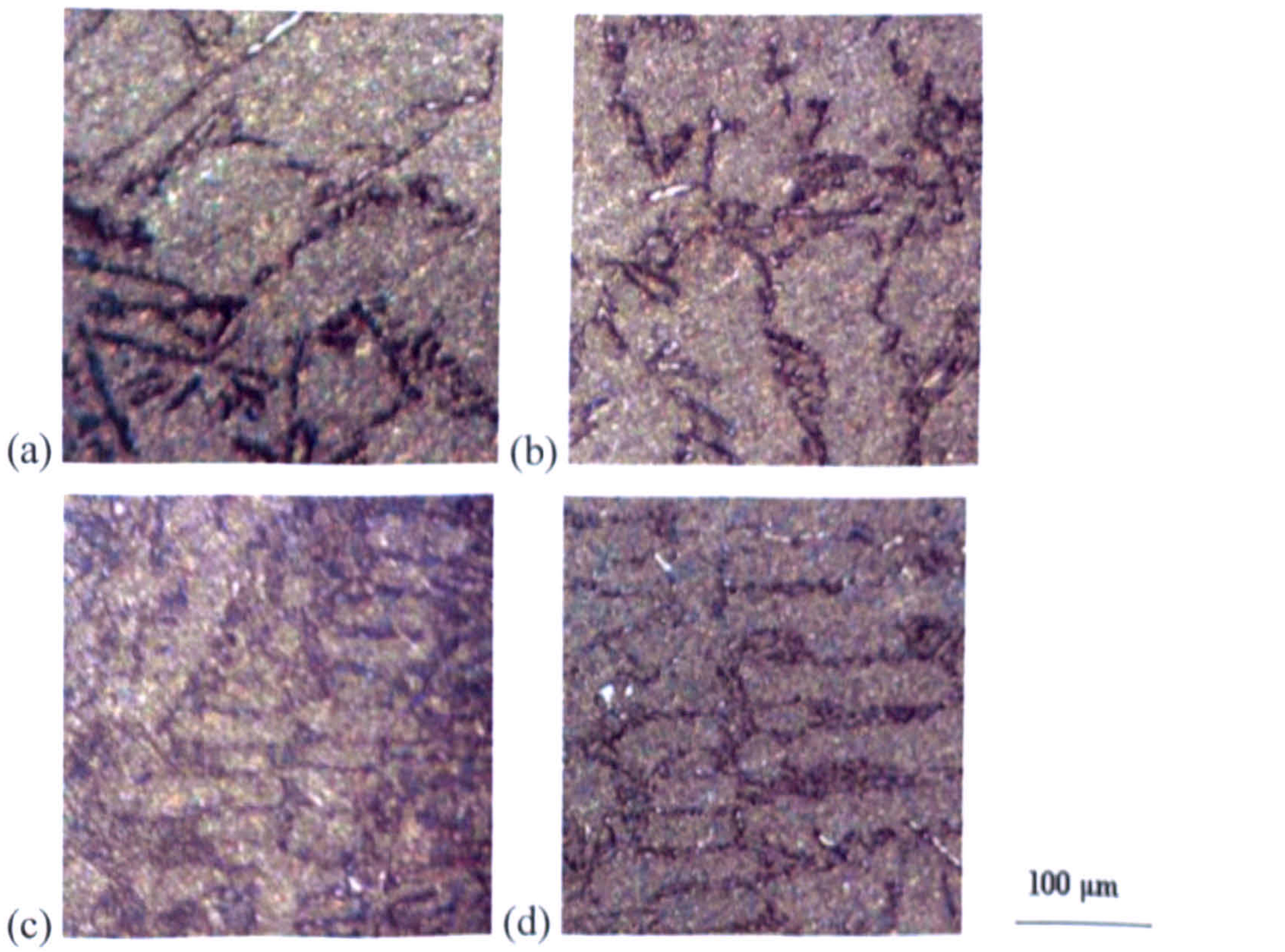

Figure 6.31: Effect of additive powder's particle size and distribution on the development of dendritic microstructure at the bottom portion of the SLS/SLM processed blended AL-5 powder (a) 25wt% AL-2 (b) 25wt% AL-6 (c) 25wt% AL-7 (d) 25wt% AL-8.

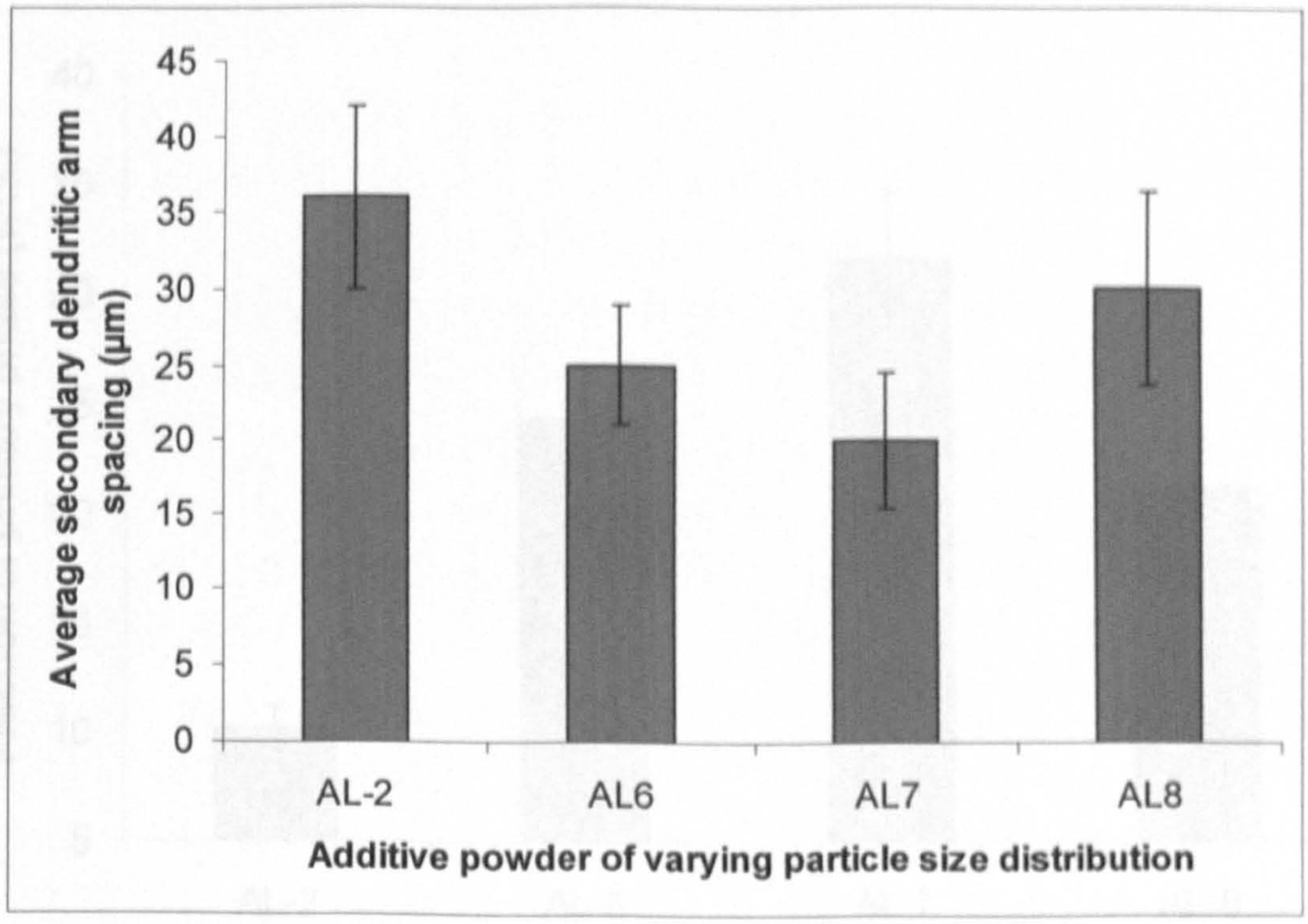

Figure 6.32: Effect of varying additive powders' particle size distribution on the dendritic arm spacings of the SLS processed blended powders.

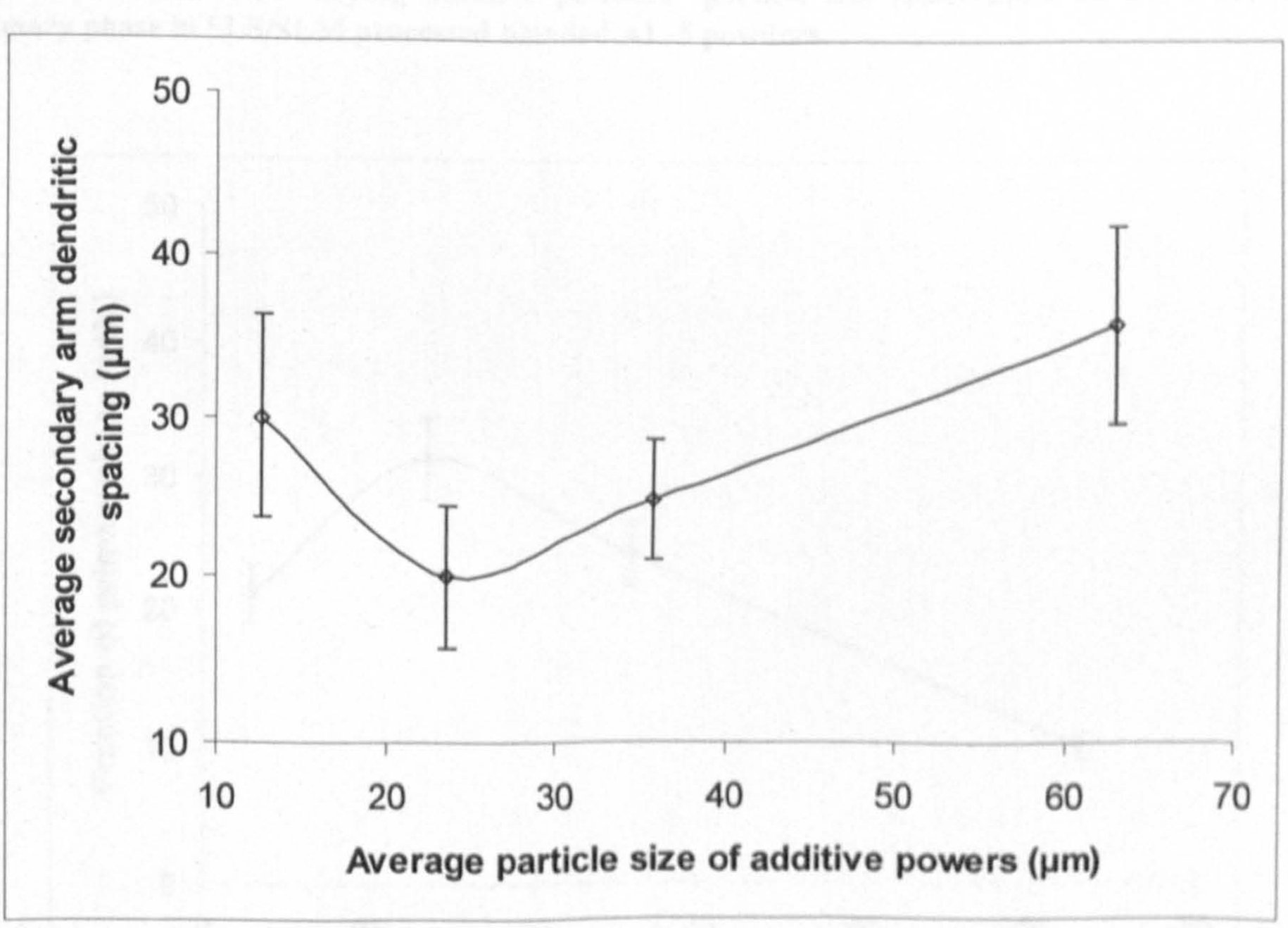

Figure 6.33: Effect of average particle size of the additive powders on the secondary dendritic arm spacing.

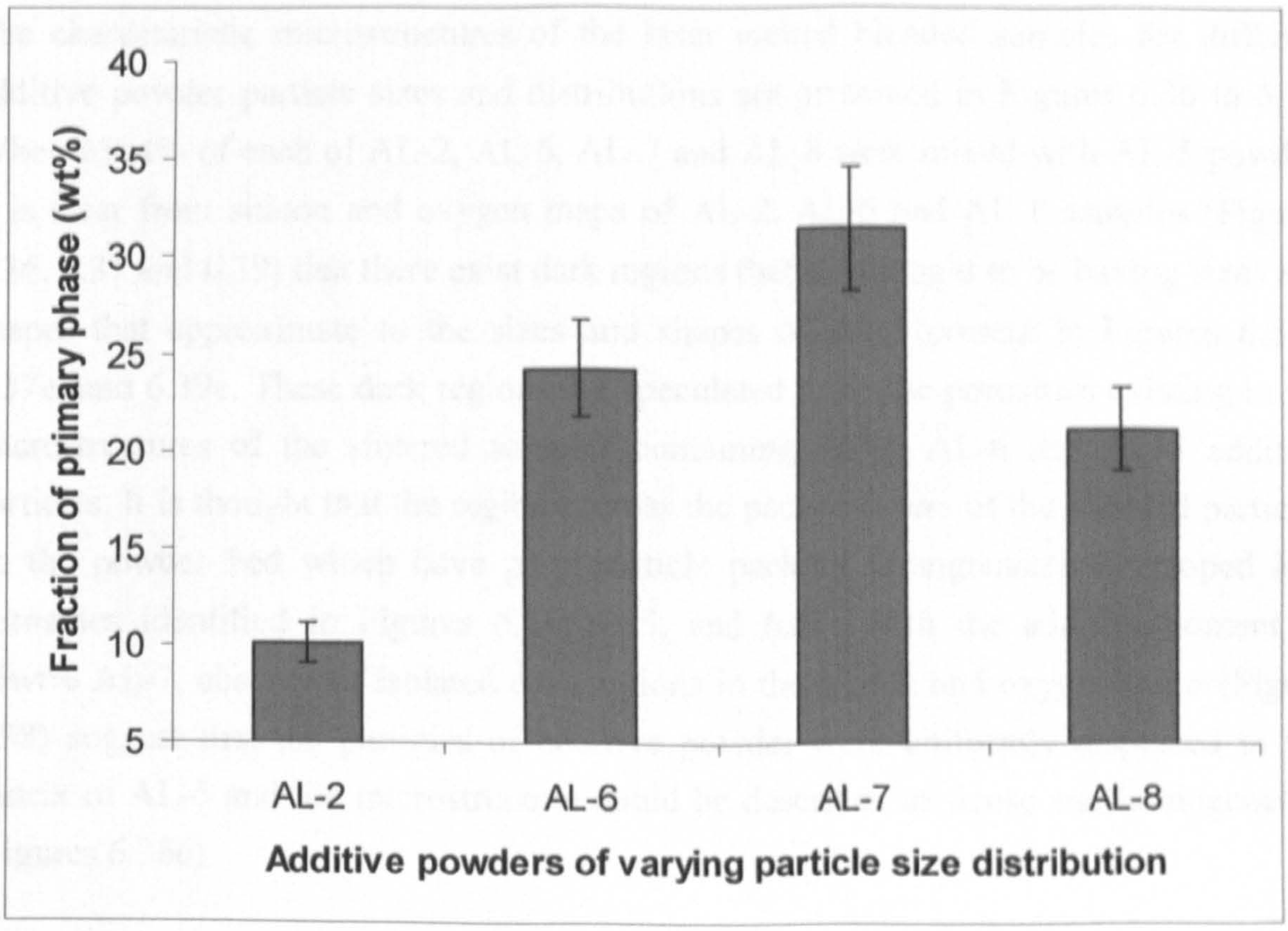

Figure 6.34: Effect of varying additive powders' particle size distribution on the fraction of primary phase in SLS/SLM processed blended AL-5 powders.

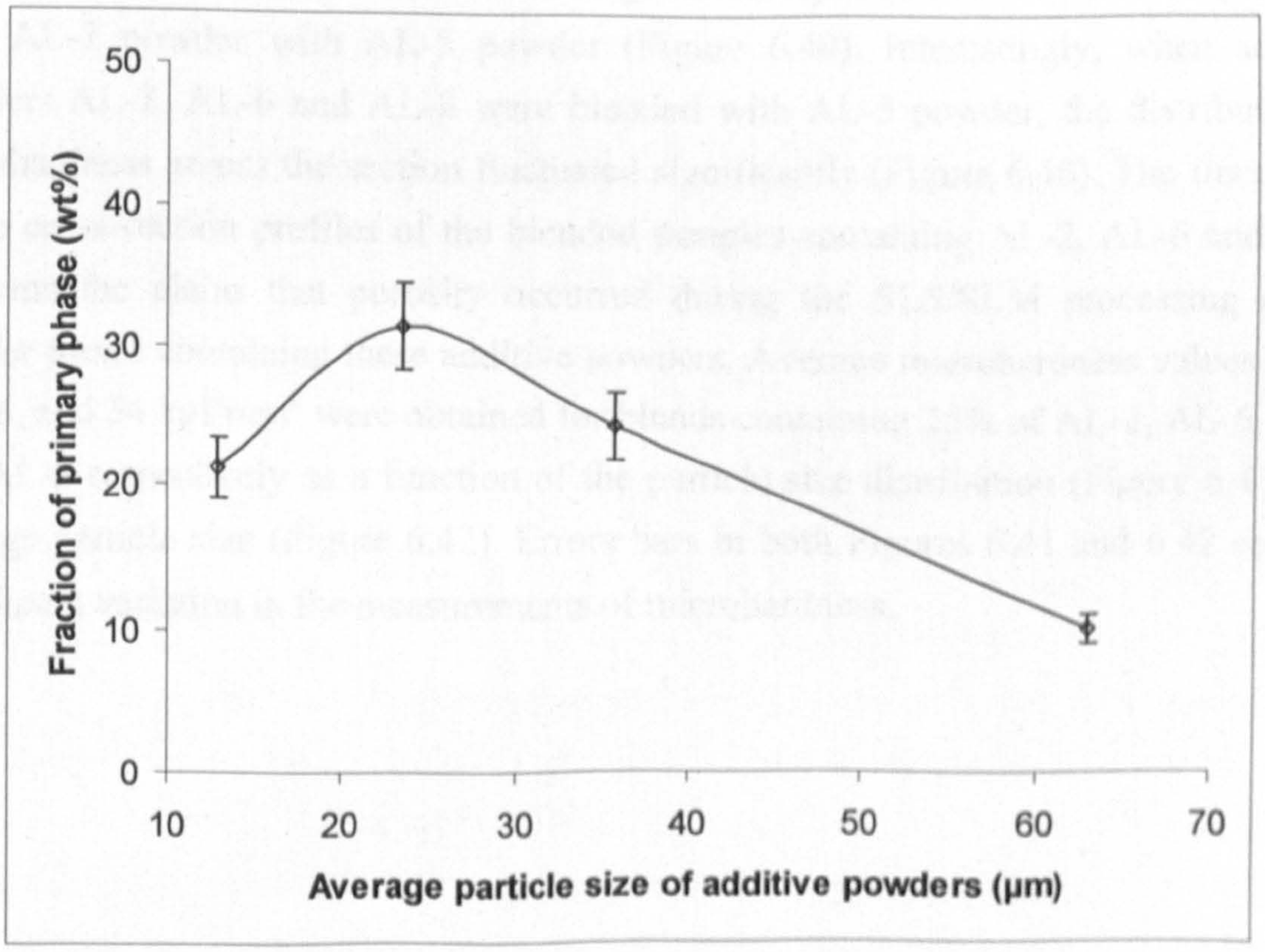

Figure 6.35: Effect of average particle size of the blended powders on the fraction of primary phase

The characteristic microstructures of the laser melted blended samples for different additive powder particle sizes and distributions are presented in Figures 6.36 to 6.39. When 25wt% of each of AL-2, AL-6, AL-7 and AL-8 were mixed with AL-5 powder, it is clear from silicon and oxygen maps of AL-2, AL-6 and AL-8 samples (Figures 6.36, 6.37 and 6.39) that there exist dark regions that are thought to be having sizes and shapes that approximate to the sizes and shapes of pores present in Figures 6.36e, 6.37e, and 6.39e. These dark regions are speculated to be the porosities existing in the microstructures of the sintered samples containing AL-2, AL-6 and AL-8 additive particles. It is thought that the regions across the packed layers of the blended particles on the powder bed which have poor particle packing arrangements developed into porosities identified in Figures 6.24, 6.25, and 6.27. With the additive content of 25wt% AL-7, absence of isolated dark regions in the silicon and oxygen maps (Figure 6.38) suggest that the particles of additive powder were uniformly dispersed in the matrix of AL-5 and the microstructure could be described as dense and homogeneous (Figures 6.38e).

Figure 6.40 reveals the profile of the microhardness measured on the horizontal sections of blended samples containing each additive powder. A uniform microhardness distribution with an average of 76 kgf/mm^2, was obtained by mixing 25% AL-7 powder with AL-5 powder (Figure 6.40). Interestingly, when additive powders AL-2, AL-6 and AL-8 were blended with AL-5 powder, the distribution of microhardness across the section fluctuated significantly (Figure 6.40). The fluctuation in the cross-section profiles of the blended samples containing AL-2, AL-6 and AL-8 confirms the claim that porosity occurred during the SLS/SLM processing of the powder mixes containing these additive powders. Average microhardness values of 67, 58, 76, and 54 kgf/mm^2 were obtained for blends containing 25% of AL-2, AL-6, AL-7 and AL-8 respectively as a function of the particle size distribution (Figure 6.41) and average particle size (Figure 6.42). Errors bars in both Figures 6.41 and 6.42 confirm significant variation in the measurements of microhardness.

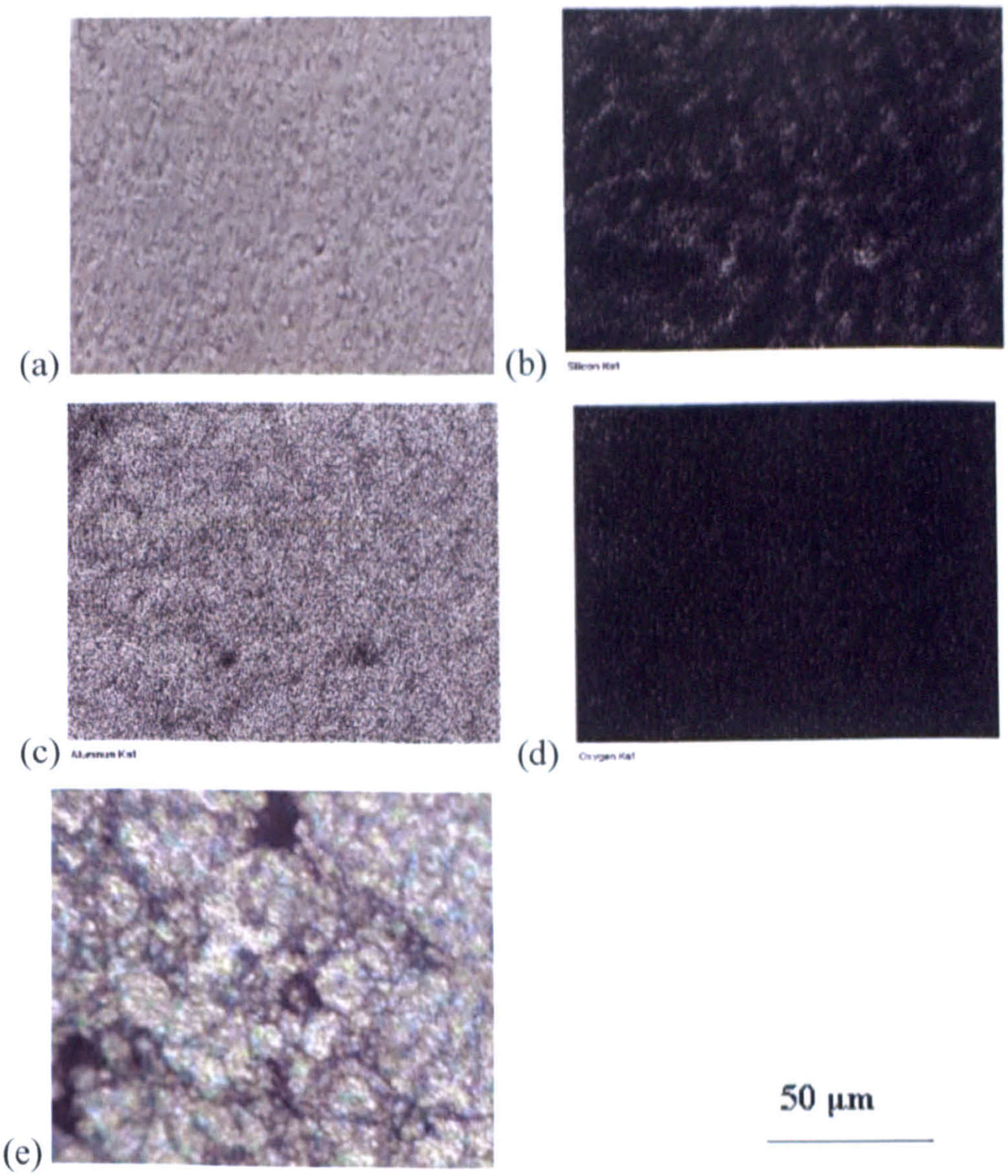

Figure 6.36: EDS elemental maps showing characteristic microstructure of the interfaces in SLM processed 25wt% AL-2+ 75wt% AL-5 blend: (a) electron image (b) silicon (c) aluminium (d) oxygen (e) optical micrograph.

High microhardness values obtained could be associated with variation in the additive particle sizes and distribution. Furthermore, the average microhardness values obtained for all the blended samples are considered to be generally less than that obtained for the optimised pure AL-5 powder (Figure 5.22). Figure 6.43 shows the surface morphology of laser sintered blended AL-5 powder containing additive powders of varying particle sizes. The formation of agglomerates joined together with by small necks and interconnected pores could be clearly seen in all samples (Figure 6.43a to d). This lends credence to the claim that consolidation occurred by sintering in all the powder mixes during SLS/SLM processing. It can be deduced from Figure 6.43 that when additive powder AL-7 was added to AL-5 powder, the lowest surface roughness was obtained, agglomerate interconnectivity was greatest, the size of the interconnected pores was minimised and the least metal splashes was formed.

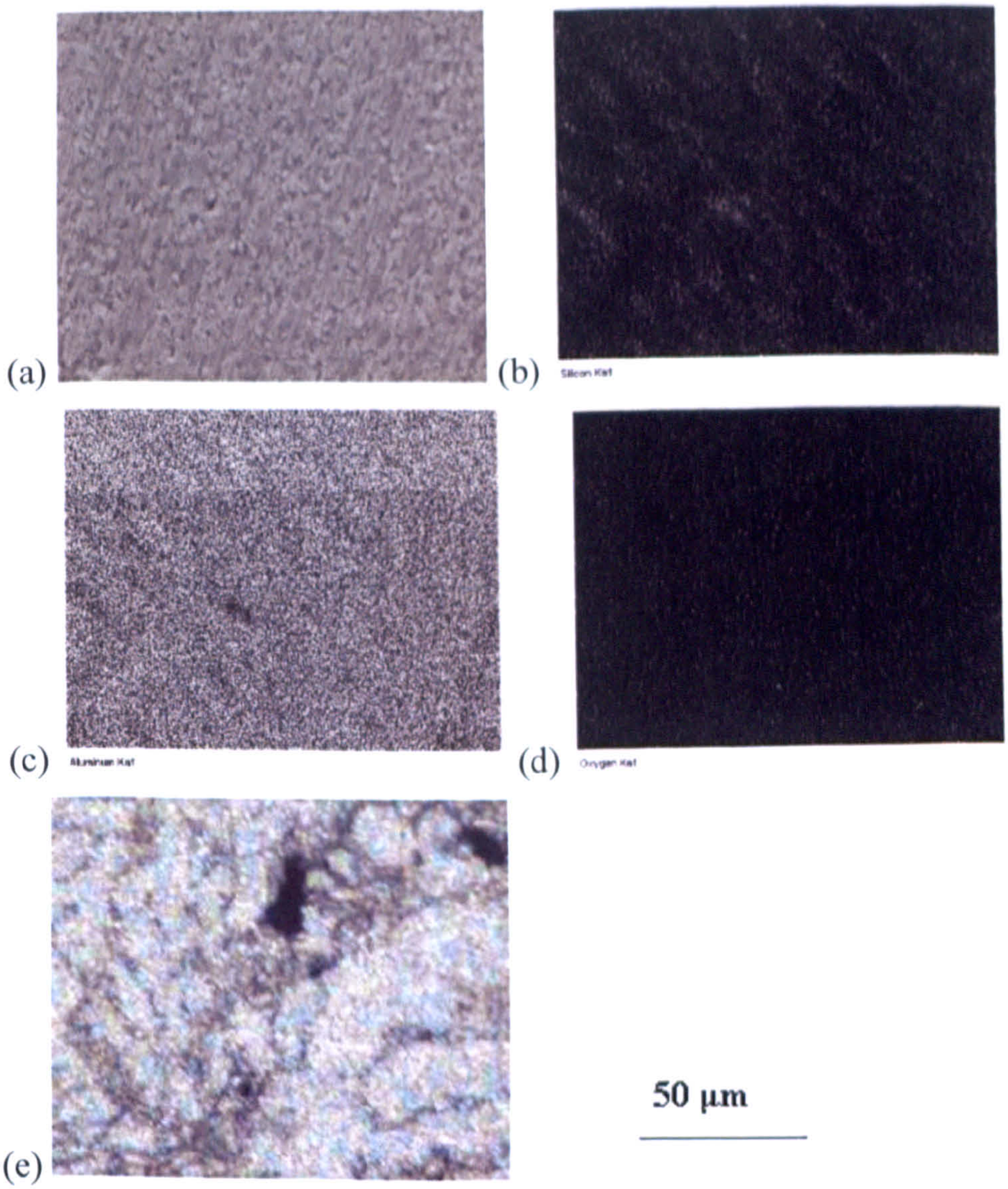

Figure 6.37: EDS elemental maps showing characteristic microstructure of the interfaces in SLM processed 25wt% AL-6 + 75wt% AL-5 blend: (a) electron image (b) silicon (c) aluminium (d) oxygen (e) optical micrograph.

Figure 6.38: EDS elemental maps showing characteristic microstructure of the interfaces in SLM processed 25wt% AL-7 + 75wt% AL-5 blend: (a) electron image (b) silicon (c) aluminium (d) oxygen (e) optical micrograph.

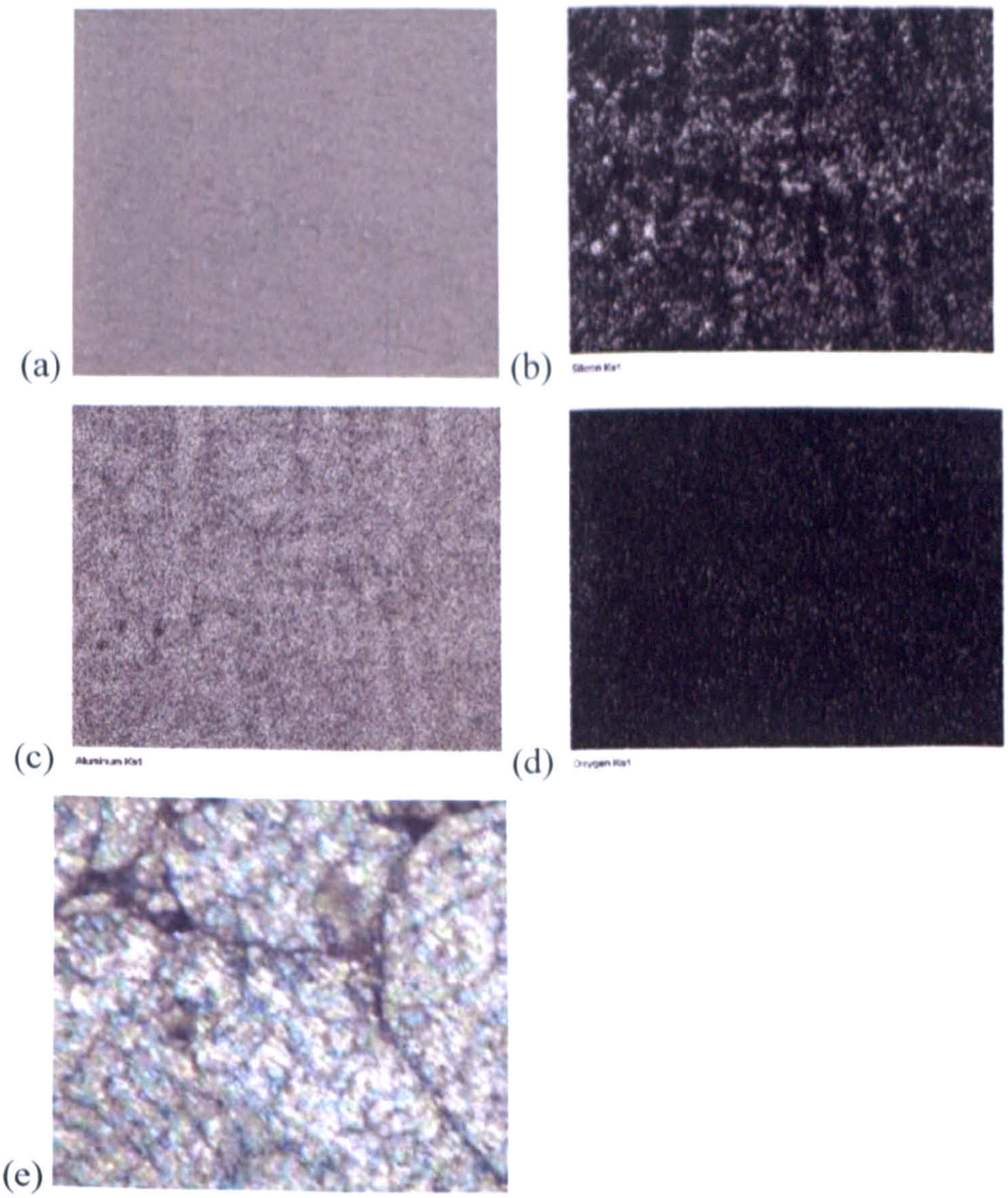

Figure 6.39: EDS elemental maps showing the characteristic microstructures of interfaces in SLM processed 25wt% AL-8 + 75wt% AL-5 blend: (a) electron image (b) silicon (c) aluminium (d) oxygen (e) optical micrograph.

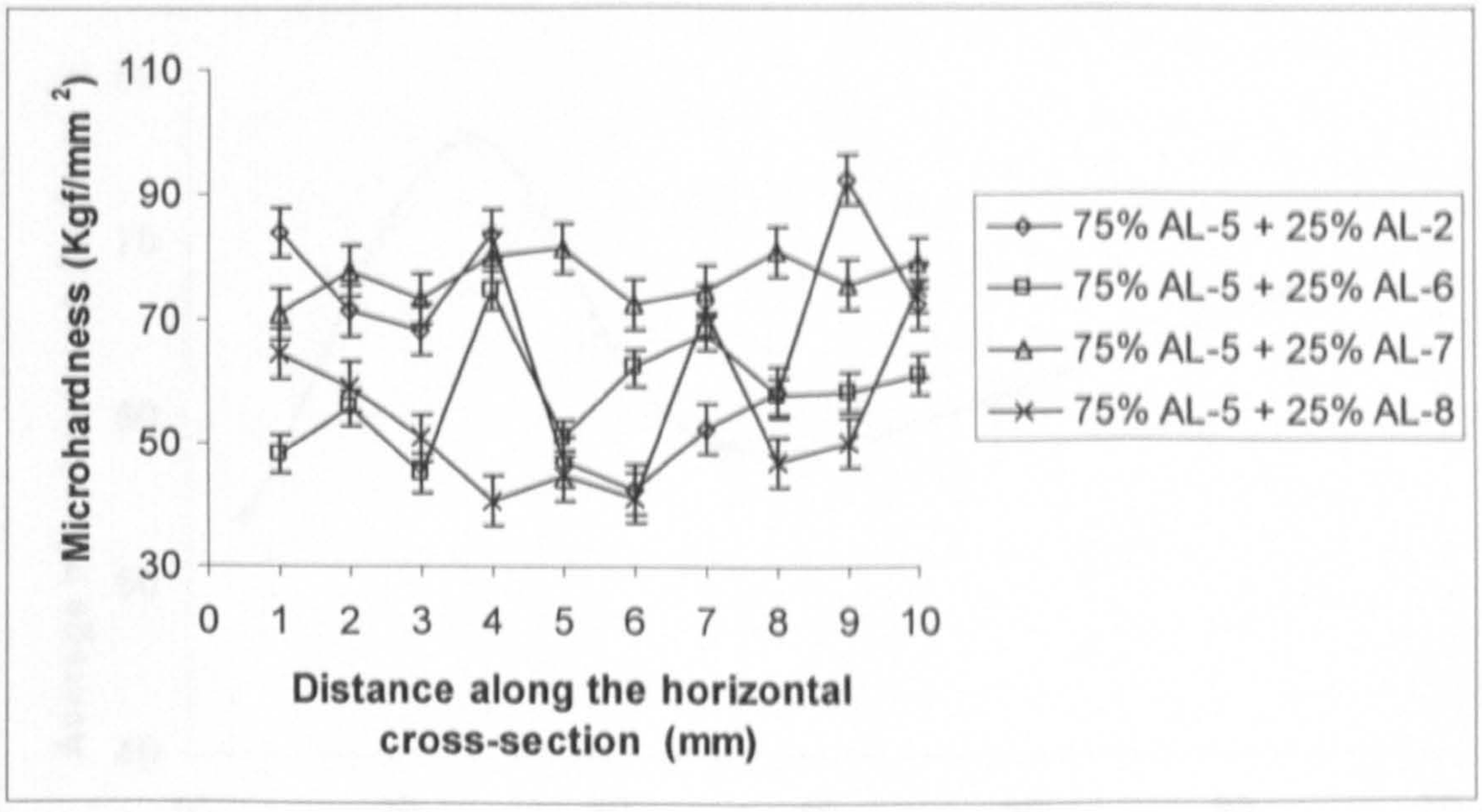

Figure 6.40: Variation in microhardness on the horizontal cross-sections of direct laser-sintered blended powders processed with a specific laser energy input of 150 J/mm^3.

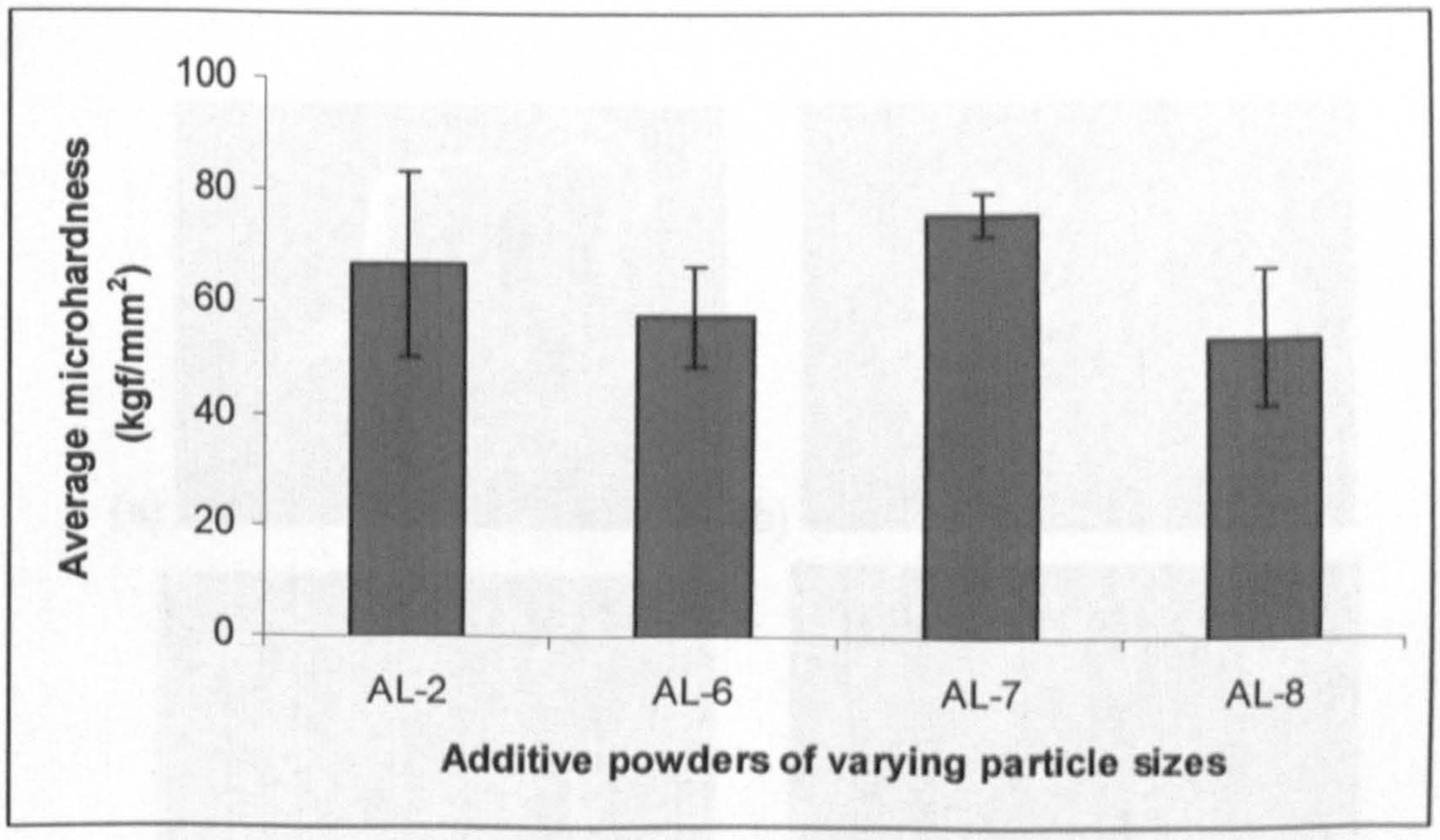

Figure 6.41: Average microhardness of direct laser-sintered blended powders processed with a specific laser energy input of 150 J/mm^3.

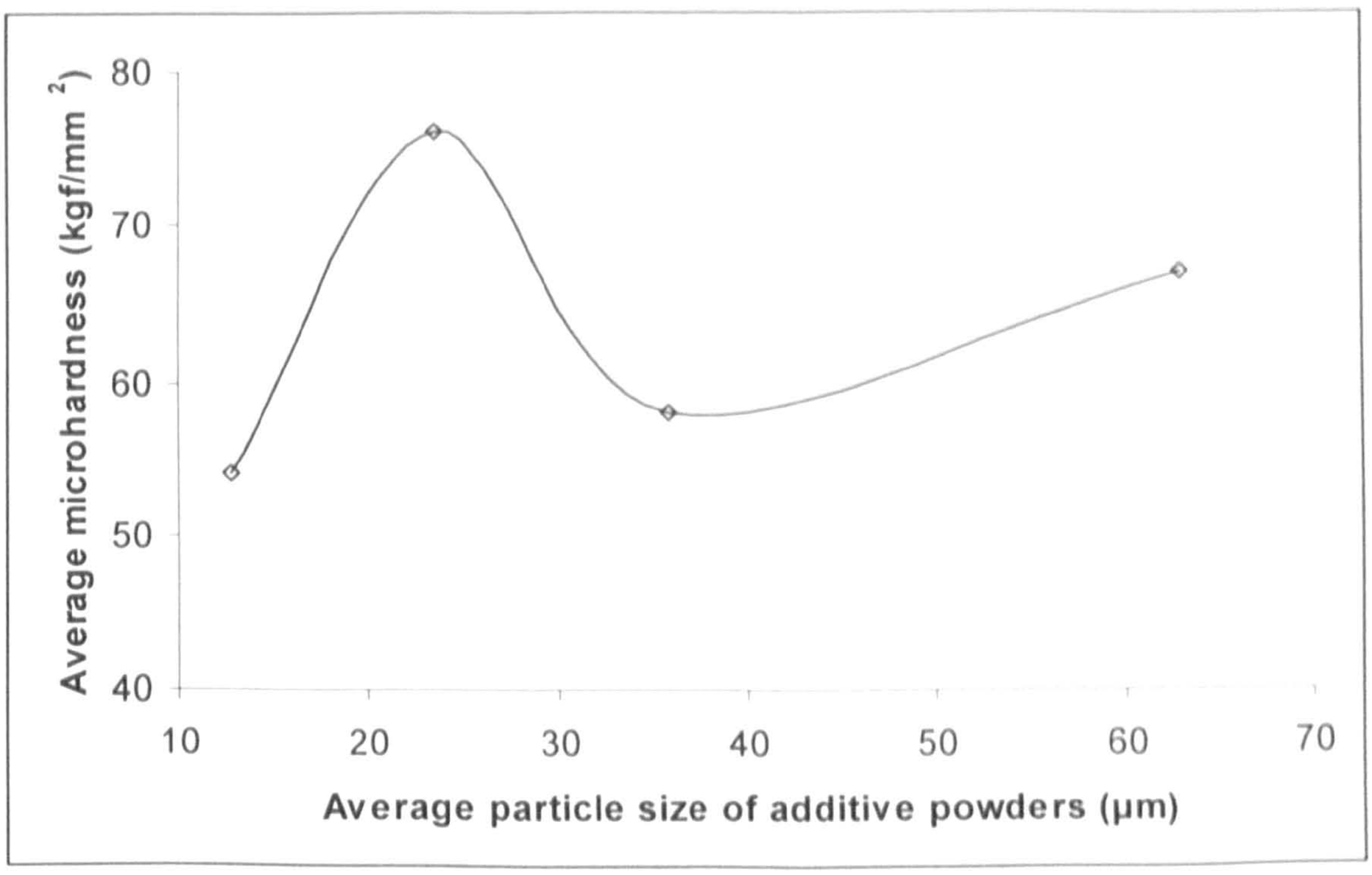

Figure 6.42: Effect of average particle size of the blended powders on the microhardness.

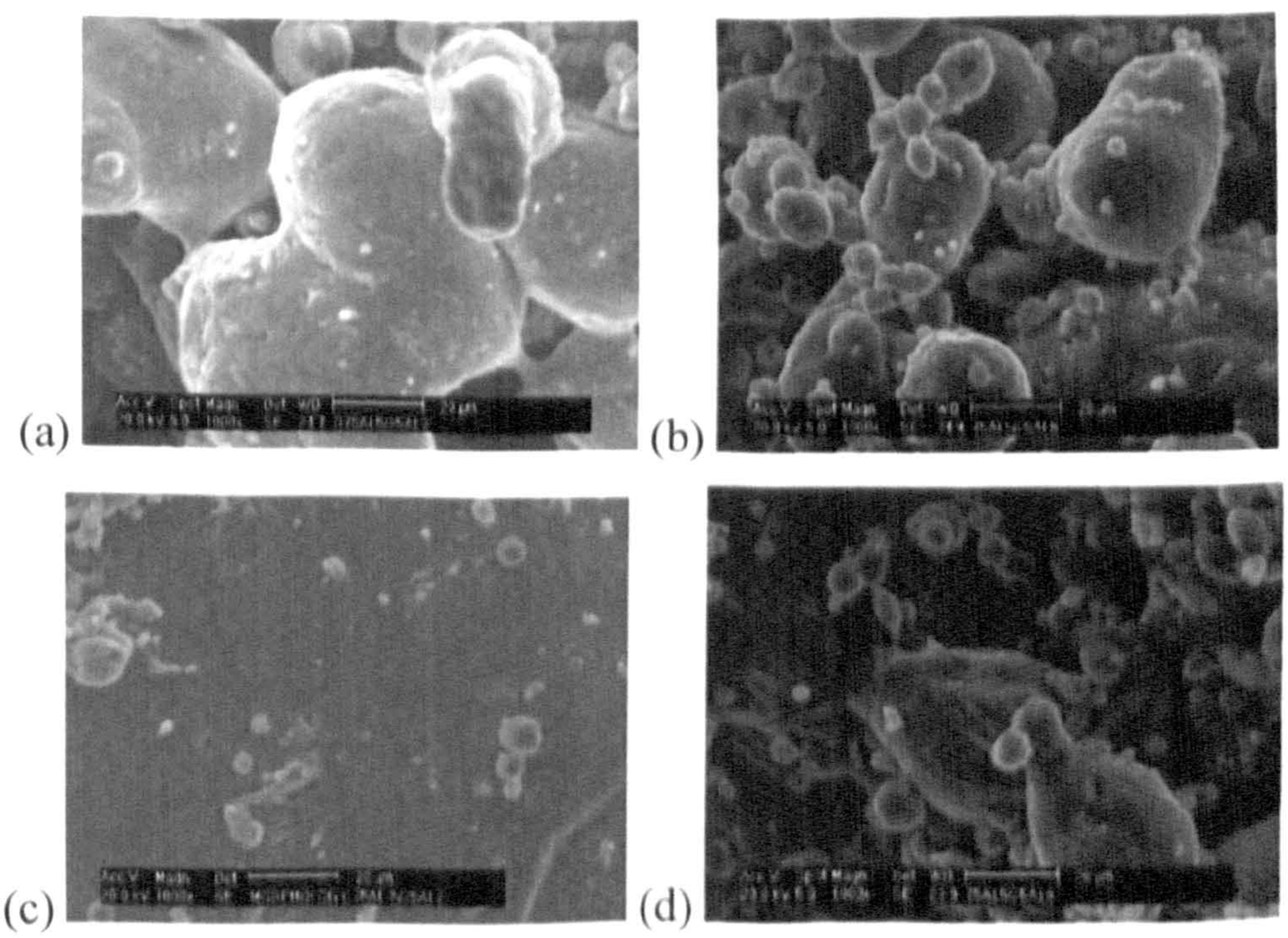

Figure 6.43: Surface morphologies of the laser sintered blended AL-5 powder containing 25wt% of additive powders of varying particle sizes: (a) AL-2, (b) AL-6, (c) AL-7 and (d) AL-8.

6.4.4 Effect of Additive Content, Particle Sizes and Chemical Constitution on the Sintered Density and Microstructure

The nature of particle packing arrangement determines to a very great extent, the degree of particle contacts in SLS/SLM processed blended powders (Gusarov *et al.* 2003). Consequently, this controls the effective thermal conductivity between the powder particles in a newly spread powder layer over a substrate and across the layers of the laser sintered sample. Again, the thermal conductivity across the layers of the laser sintered sample influences the amount of molten pool available for densification mechanisms of the material component system because it is a function of the powder properties and the process parameters. Therefore, the thermal conductivity is determined by the depth of penetration of heat flux to the core of a particle. Furthermore, the effective thermal conductivity of the constituent particles in a blended powder, which determines the depth of penetration to the core of a particle, is directly related to the contact size which is a function of powder density and the co-ordination number. Gusarov *et al.* 2003 established that at a given contact size, thermal conductivity increases with the powder density and co-ordination number of the particle packing arrangement of a blended powder. The direct correlation obtained between the powder and sintered densities of the blended samples in Figures 6.44 and 6.45 support the assertion made by Gusarov and co-investigators.

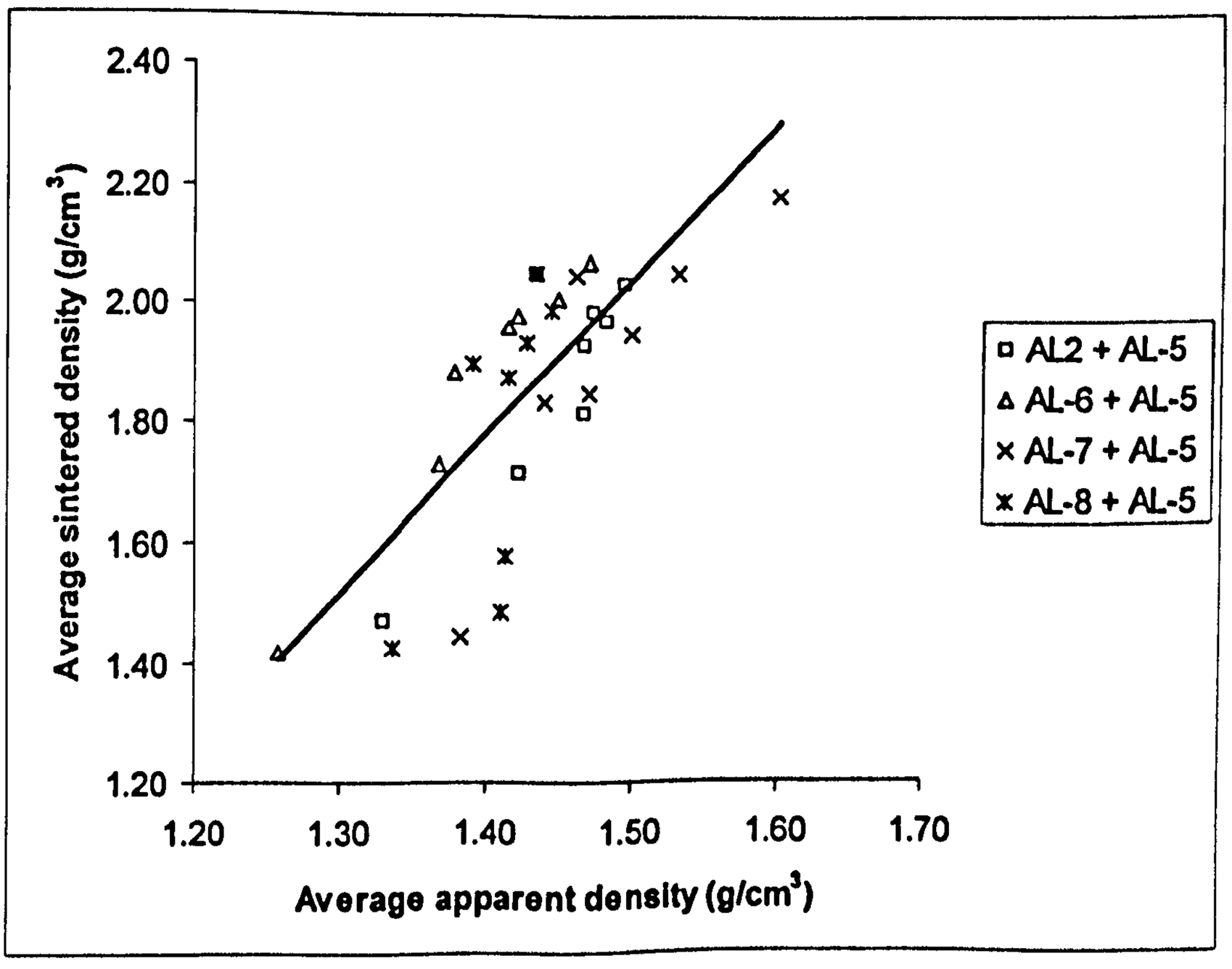

Figure 6.44: Correlational relationship between the sintered density and apparent density of blended samples fabricated using specific laser energy input of 150 J/mm³.

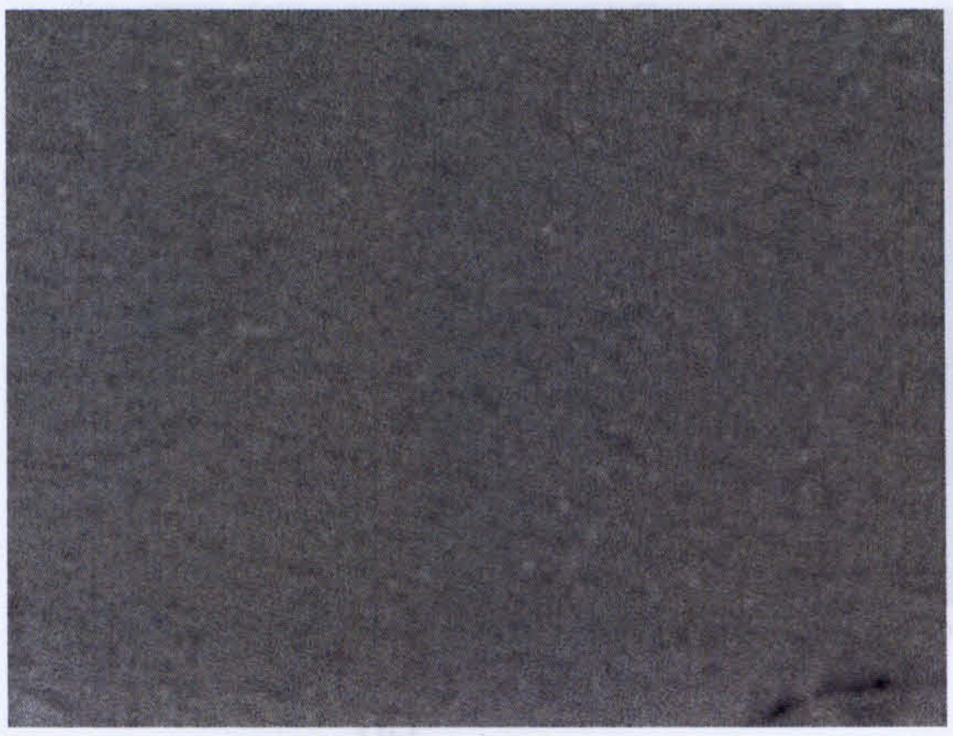

Silicon Ka1

(a)

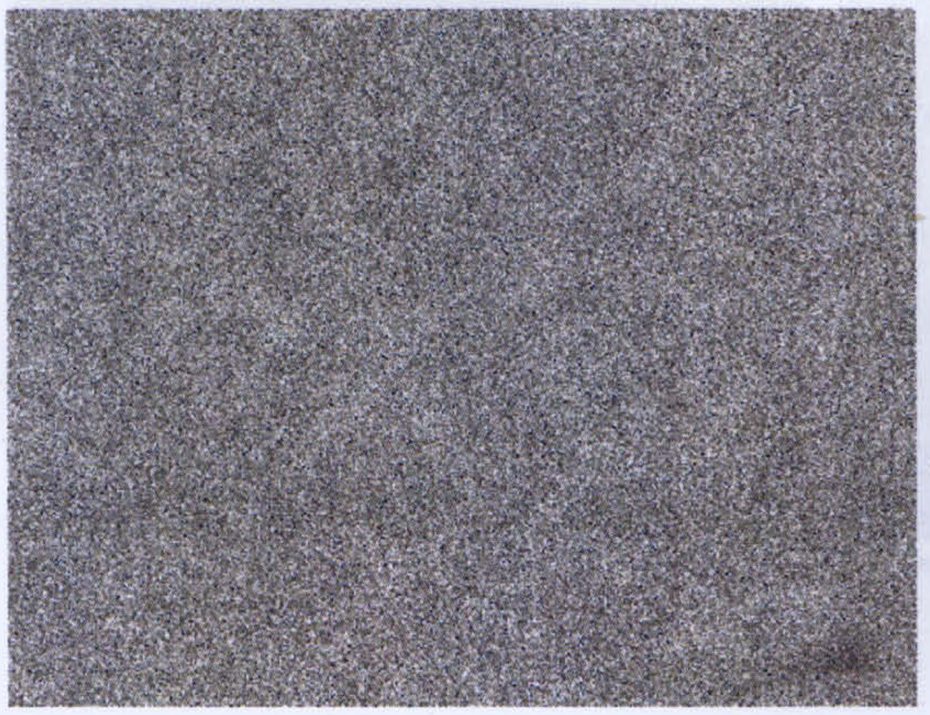

(b)

Aluminum Ka1

Oxygen Ka1

(c)

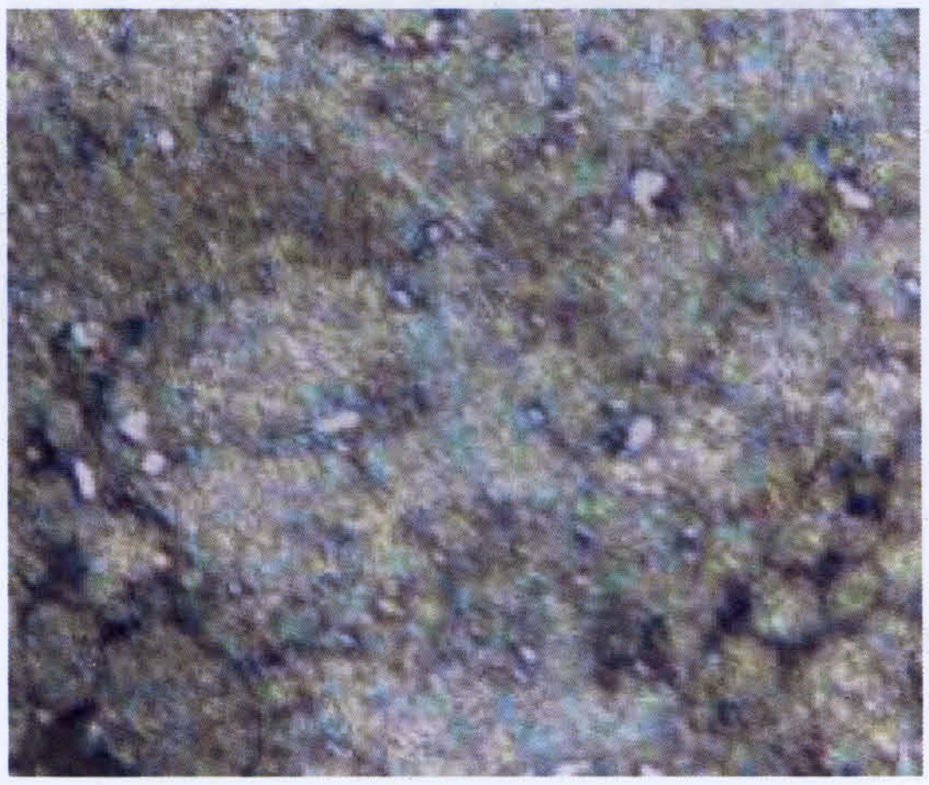

(d)

50 µm

(e)

Figure 7.17: EDS elemental maps showing characteristic microstructure of the interfaces in SLM processed 75wt% AL-5/10wt% AL-7/15wt% AL-8 blend: (a) electron image (b) silicon (c) aluminium (d) oxygen (e) optical micrographs.

increases the process time significantly since the molten pool can only loose heat via conduction of the heat into deeper layers of the loose powder bed and not by radiation or convection at the surface. This is due to the thermal conductivity of argon gas which is about three to four times lower than that of metals.

Meanwhile, the occurrence of porosity in the packed layers of powder particles during SLS/SLM introduces heterogenous sites that promote differential sintering mechanism across the packed layers on the powder bed. With regard to the results obtained in this work, it is now clear that greater amount of porosity occurred in the layers of packed particles of the blended powders having 25wt% AL-2, 25wt% AL-6, 10wt% AL-7, 50wt% AL-7, and 25wt% AL-8 as evident in Figures 6.14a, c, 6.29a, b, d, 6.44 and 6.45. This is suspected to have resulted in the formation of deeper sintering pool in the layers of powder particles and a longer processing time due to their reduced thermal conductivities. For SLS/SLM of blended powder containing these additive particles in varying sizes and proportions, sintered density obtained are not as high as that of the sintered blended powder containing 25wt%AL-7. It is hereby suggested that the lower thermal conductivity between the particles contained in the packed layers of these powders' particles keeps the heat flow at the surface of particles, therefore, full inter-particulate melting could not occur as they could not absorb sufficient amount of specific laser energy to form adequate molten pool necessary for attaining fully dense microstructure. Moreover, due to the porosity effect on the bed, the applied specific laser energy could not disrupt the oxide film on the additive particles, thus reduced sintered density and poor microstructure were obtained. In summary, in the porously packed layers of particles on the powder beds, particles existing within the vicinity of voids remain unmelted and are thought to have sintered or coated with the sintering pool (Figures 6.14a, c, 6.18, 6.20, 6.29a, b, d, 6.36, 6.37, and 6.39). Therefore, in the porous regions across the packed layers on the powder bed, it is presumed that the blended particles only sinter rather than melting. With regard to the blended powder containing 25wt% AL-7, it could be argued that the particles contained in its layers were more densely packed upon comparison with other blended powders as evident in Figures 6.29c, 6.38, 6.44 and 6.45. Therefore, inter-particulate melting occurred probably due to the increased thermal conductivity of the densely packed layers of the powder particles, since it is thought that the depth of penetration of heat flux across individual particles increases more than that of the porous powder bed.

In order to understand the effect of the variation in additive contents, particle size and chemical constitution of the blended powders on the sintered density and

microstructure, the degree of interfacial bonding in the laser sintered blended AL-5 powder, the influence of the thermodynamic and kinetic properties of the additive powders and the matrix AL-5 powder on the interfacial chemistry of the sintered samples will be examined. These properties include the surface energy, viscosity and wettability. In the context of this research, the spread of the liquid phase is thought to have occurred probably upon full melting of AL-5 and the additive particles as explained earlier on. The melt pool is contemplated to have wetted both unmelted AL-5 and additive particulates at the initial stages of sintering. This eventually leads to the formation of sintering pool, in the porous regions of packed layers of particles on the powder bed, in which unmelted or partially melted particles are speculated to have been coated (Figures 6.14a, c, 6.29a, b and d). Meanwhile, the interfacial characteristics between the particulates of the additive powders and the matrix AL-5 powder are noted to rely on the variation in the additive particle's content as well as additive particle sizes (Figures 6.14a, c, 6.18, 6.20, 6.29a, b, d, 6.36, 6.37, and 6.39) in the blended powders. With regard to the effect of additive content on sintered density and microstructure, the results obtained so far showed that the they were maximised as evident by the excellent coherence across the interfacial bonding at 25wt% additive content (Figures 6.7, 6.11, 6.19 and 6.38) but decreased when 10wt% and 50wt% (Figures 6.7, 6.10, 6.12, 6.14a, c, 6.18 and 6.20) of each of the additive powder was introduced into AL-5 matrix. When the particle sizes and distribution of additive powders were varied, sintered density and microstructure were maximised again as evident by the excellent coherence obtained across the interfacial bonding when AL-7 was added (Figures 6.7, 6.11, and 6.38) but decreased when AL-2, AL-6, and AL-8 were introduced into AL-5 matrix (Figures 6.24, 6.25, 6.27, 6.29a, b, d, 6.36, 6.37, and 6.39).

These results could be explained by the occurrence of poor particle packing arrangement in the blended powders at the instances it contained 10wt% and 50wt% AL-7, 25wt% AL-2, 25wt% AL-6, and 25wt% AL-8. Previous results (Figures 6.4, 6.5, 6.46 and 6.47) obtained at these instances established that the additive particles are not suitable for SLS either due to inappropriateness of their particle sizes, non-sphericity of their shapes, or incorrectness of their composition in the blended powders (sections 6.3.1 and 6.3.2). Therefore, it is seen that their apparent and tapping densities are not maximised as they could not completely fill up the interstices of AL-5. Moreover, Figures 6.46 and 6.47 lend credence to the observations made in Figures 6.30 and 6.34 that the blending of 25wt% AL-7 with AL-5 resulted in the formation of finest dendritic arm spacing and maximisation of the fraction of primary phase respectively, due to improved particle packing arrangement. It is clear from Figures 6.46 and 6.47

that the most desirable powder packing arrangement in this context (indicated by the highest tapping density of 1.90 g/cm^3) most improves the thermal conductivity across the layers of blended particles on the powder bed, thereby increasing the cooling rates of the molten pool which result in the formation of the finest dendrites and highest amount of primary phase fraction (31.4 wt%). Moreover, the occurrence porosity (indicated by reduced tapping density) in the packed layers of the particles of these blended powders suggests that the particles of the additive powders having component ratios and particle sizes and distributions at these instances could not comfortably fit in the interstices of AL-5, thereby, leaving out some voids unfilled and thereby lowering the thermal conductivity of the SLS processed blended AL-5 powder bed at these instances. In this context, due to poor particle arrangement (indicated by reduced tapping density), porosity in the powder bed reduces the efficiency of the applied specific laser energy in disrupting the oxide film on the surfaces of additive particles.

As pointed out earlier, the introduction of 25wt% AL-7 into AL-5 powder is contemplated to have initiated the finest dendritic microstructure (Figure 6.30c) of all the samples. This could be attributed to the speculative improvement in thermal conductivity of the layers of the packed powder particles through which the depth of penetration of the heat flux into the core of an aluminium particle is thought to have increased, thereby resulting in lower thermal gradient across the powder bed as well as the high cooling rates. Figure 6.46 lends credence to the speculation that increased tapping density of blended powders leads to improved thermal conductivity of the powder bed. It is evident that an inversely direct relationship occurs between the tapping density of the blended powders and the resultant dendritic arm spacing. Again, this supports the earlier assertion that a blended powder containing densely packed layers of the powder particles promote a more rapid heat transfer than the one in which layers of poorly packed particles exist on the powder bed. It is hereby speculated that the occurrence of high cooling rates that promotes undercooling advanced partial melt back that enhances growth from the prior grains of the substrate (Figures 6.14b). Moreover, it is hereby suggested that densely packed layers of powder particles enabled the applied specific laser energy to disrupt the surface oxide film of the additive particles more efficiently due the heat flux which is thought to have penetrated into core of particles. This is thought to have caused uniform melting of densely packed particles which eventually promoted homogeneity in the microstructure of the blended sample containing 25wt% AL-7.

(a)

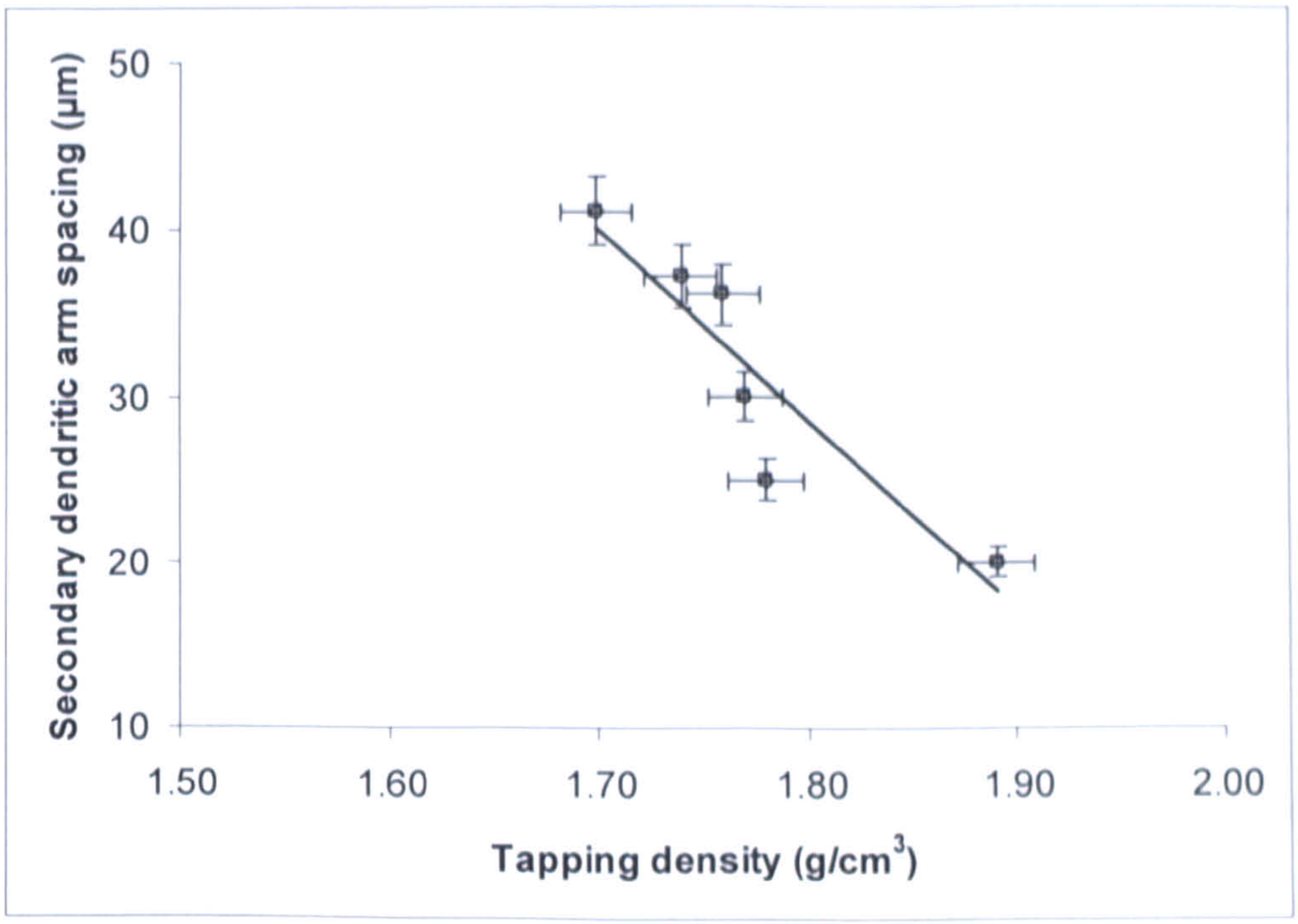

(b)

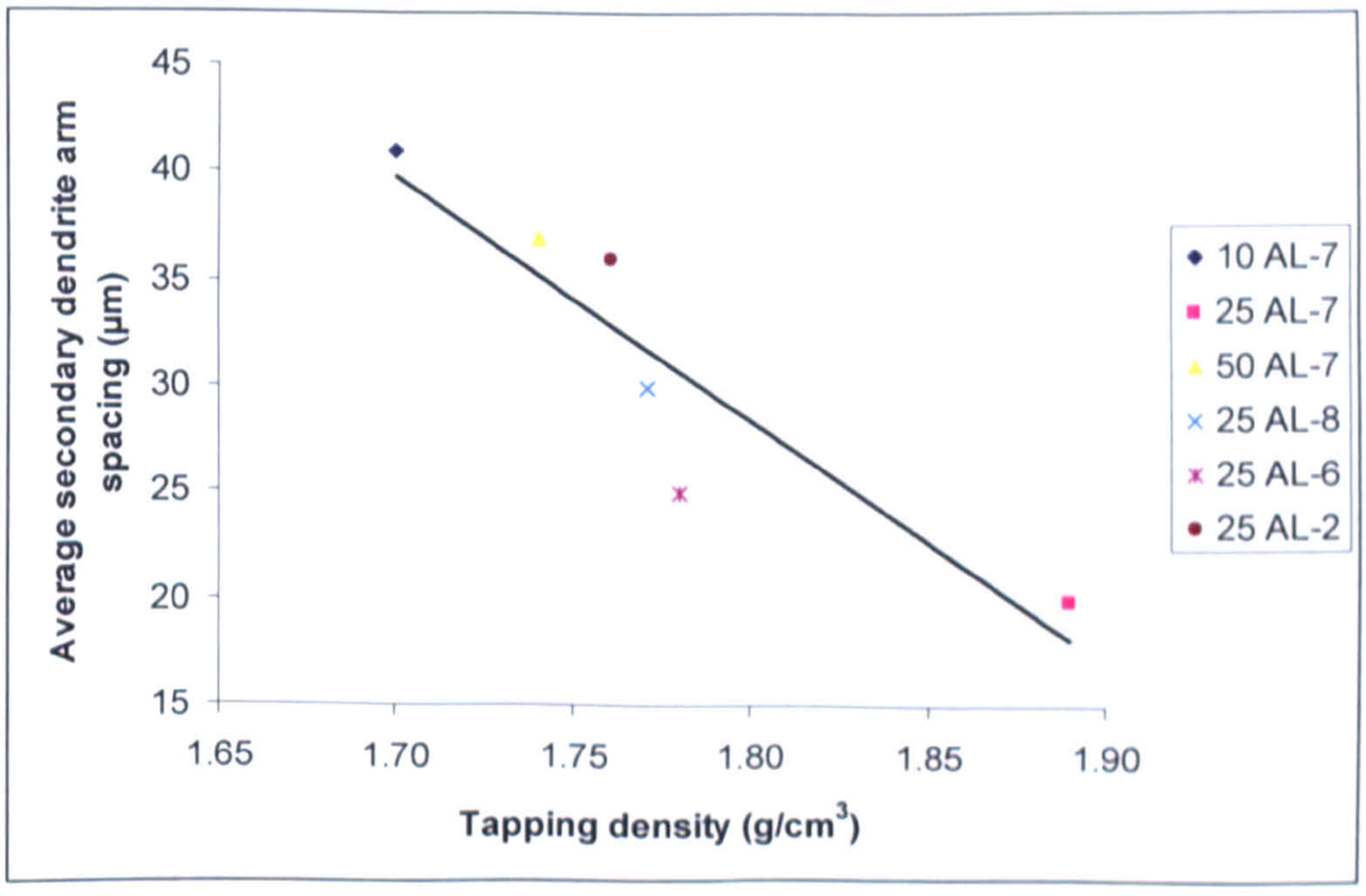

Figure 6.46: (a) Correlational relationship between the dendritic arm spacing of blended powders and the tapping density (b) Variation between dendritic arm spacing and tapping density for SLS/SLM processed bimodal containing additive powders in varying composition and particle size distribution fabricated using 150 J/mm^3.

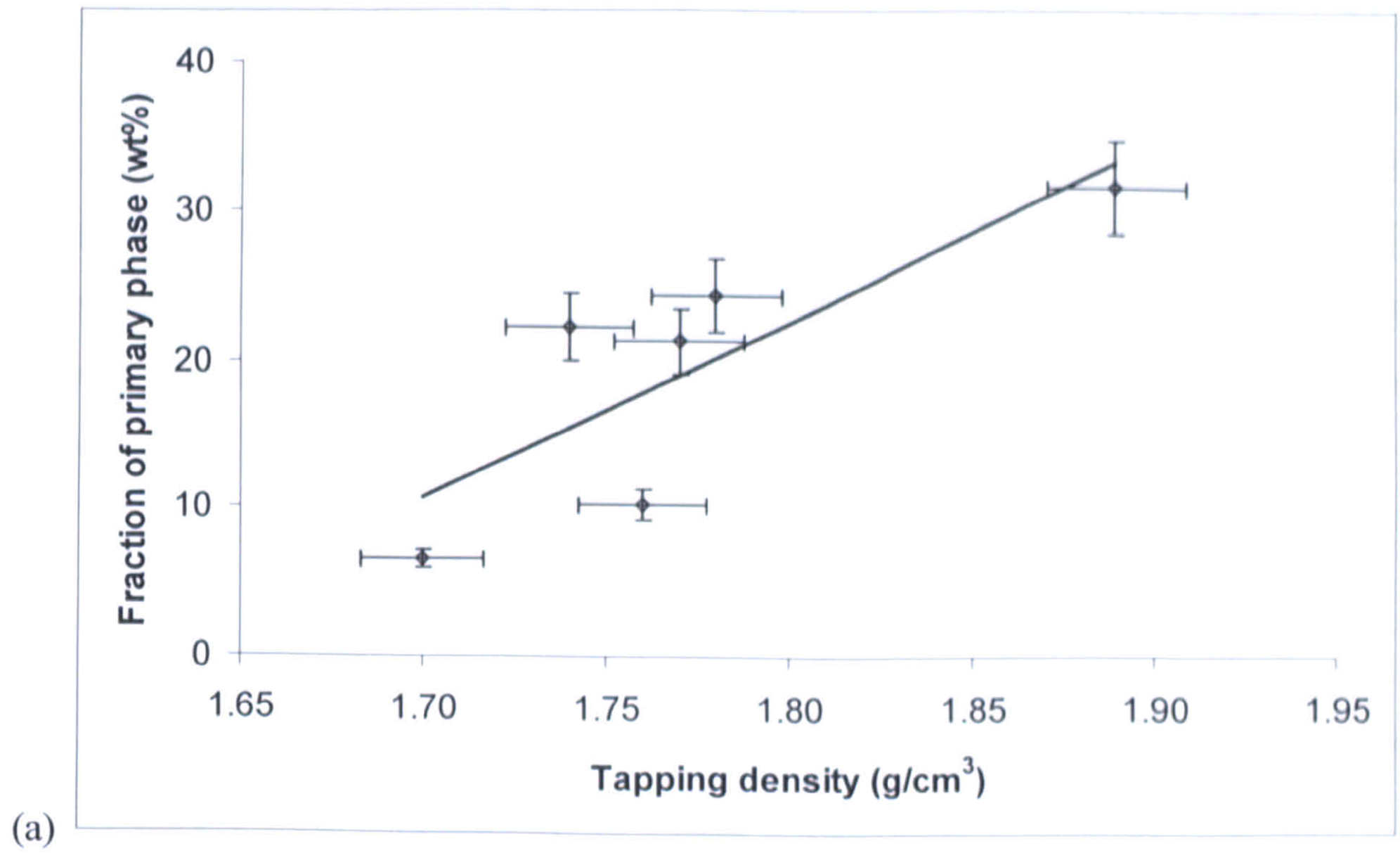

(a)

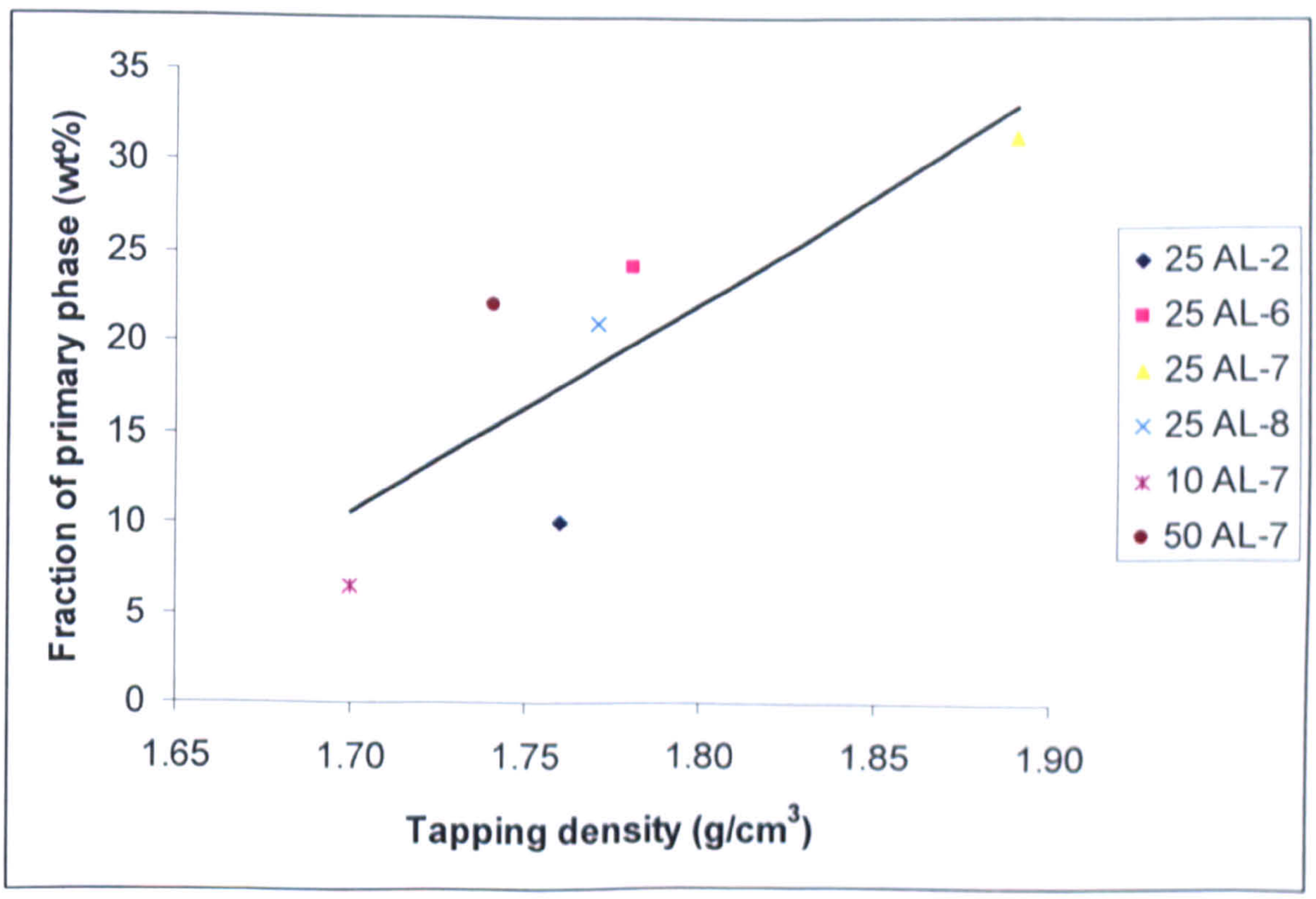

(b)

Figure 6.47: (a) Correlational relationship between the fraction of primary phase of blended powders and the tapping density. (b) Variation between fraction of primary phase and tapping density for SLS/SLM processed bimodal powders containing additive powders in varying composition and particle size distribution fabricated using 150 J/mm^3.

Consideration of the errors bars in Figures 6.32 suggests significant variation in the dendritic arm spacing for each blended powder. Moreover, the occurrence of coarse dendritic microstructure at the bottom parts of each sample could be attributed to the

poor thermal conductivity of the powder bed and directional solidification which initiates low thermal gradient (high thermal mass of the build) in these areas. It is the initiation of low thermal gradients in the bottom parts of the samples that consequently results in the formation of coarse dendritic structure (Steen 2003, Ion 2005). Coring, (a micro-level segregation of alloying elements that occur during solidifications of the blended powders employed in this study) will be now be explained in the next paragraph.

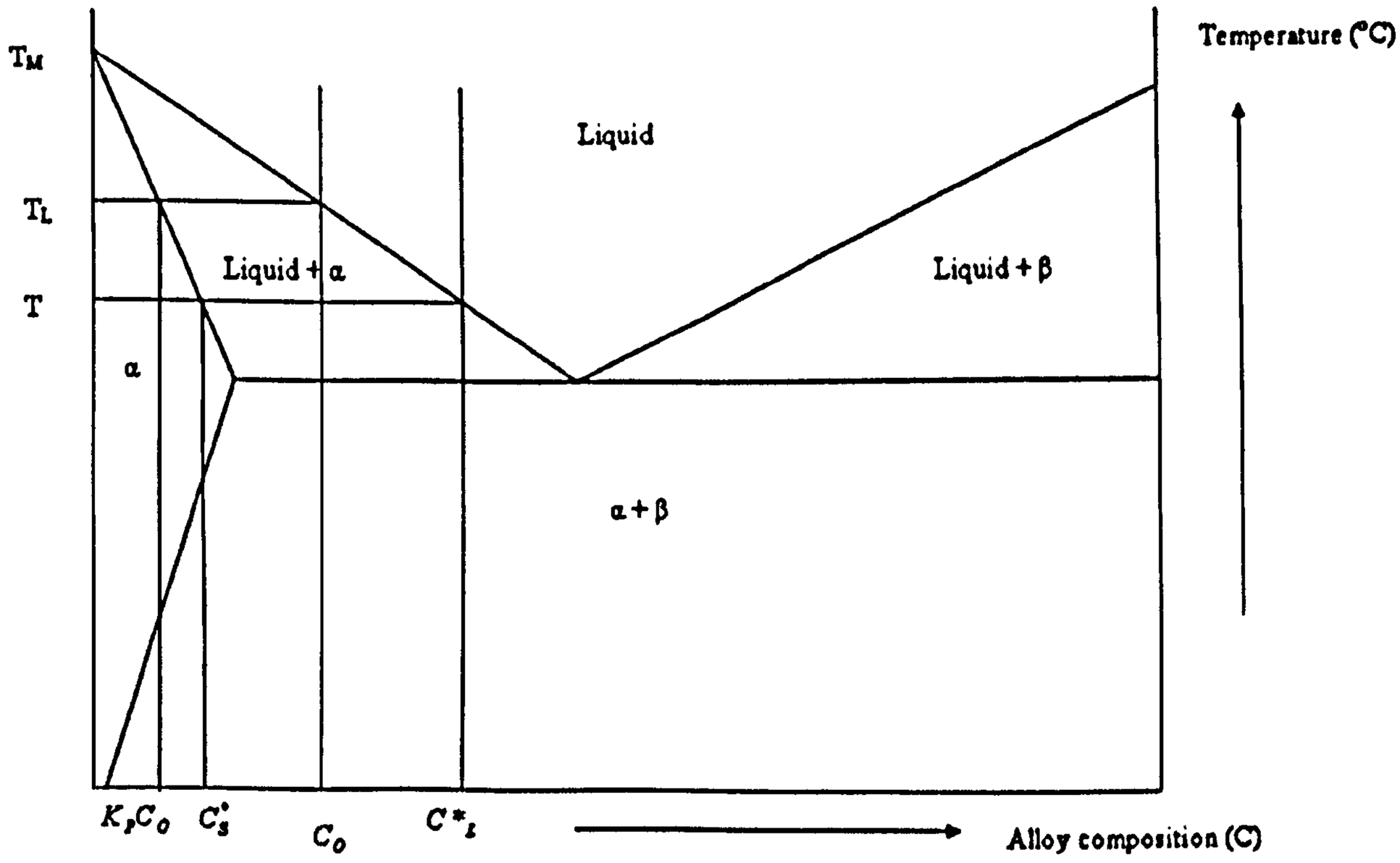

Figure 6.48: Section of a hypoeutectic region of a binary eutectic phase diagram showing the solidification process under the equilibrium condition. The solute composition in the solid, C_S^*, and the liquid C_L^*, vary along the solidus and liquidus lines, as shown. $C_S^*/C_L^* = K_p$ (partition co-efficient). Ideal diffusion in the solid and complete mixing in the liquid also exists (i.e. $D_S^* = \infty, D_L^* = \infty$) in the equilibrium solidification such that a liquid with a nominal concentration C_O solidifies at $T = T_L$ with a solid fraction of $K_p C_O$.

Under SLS/SLM equilibrium condition of solidification, in agreement with Eskin (2008), it is hereby proposed that the degree of accomplishment of phase transformations is determined by the following diffusion processes namely:

(a) Diffusion of alloying element in the bulk liquid toward and from the solid-liquid interface in order to create the equilibrium difference of concentrations according to the difference in concentrations in the liquid and solid phases reflected by the liquidus and solidus lines in the equilibrium phase diagram (Figure 6. 48).

(b) Diffusion in the liquid close to the solid-liquid interface in order to dissipate the solute (partition co-efficient $K_p < 1$) or solvent ($K_p > 1$) pile-up at the solidification front.

(c) Diffusion in the solid phase in order to equilibrate the solute concentration within the solid grain.

Provided these three diffusion processes proceed accordingly during solidification by SLS/SLM, it is expected that solidification mechanism proceed in consonance with the equilibrium phase diagram with the average compositions of solid and liquid changing according to the solidus and liquid lines respectively. Meanwhile, if these three diffusion processes are incomplete, microsegregation is deemed to have occurred. With respect to the variation in the content of AL-7, increasing the effective silicon constitution of the blended powder (Table 6.2.) is expected to reduce the fraction of primary phase in the SLS/SLM processed bimodal AL-5. Expected theoretical values of primary phase in the blended bimodal AL-5 containing 11.6wt% Si, 8.7wt% Si and 6wt% Si are 9.1wt%, 35wt% and 60wt% respectively. Results obtained so far indicate none of the SLS/SLM processed bimodal powder containing varying proportions of AL-7 has its primary phase fraction equal to its expected theoretical value. Moreover, fraction of the primary phase determined for the blended AL-5 powder containing AL-2, AL-6, AL-7 and AL-8 are 10.2wt%, 24.3wt%, 31.4wt%, and 21.2wt% respectively (Figure 6.34). Since all these blended powders containing almost the same silicon content of 8.7wt% (Tables 6.3), the theoretical weight fraction of primary phase expected to be formed in each blended sample is approximately 35wt%. Again, none of these is seen to have primary phase fraction which is equal to the theoretical value. These results indicate occurrence of microsegregation or coring in all the blended samples.

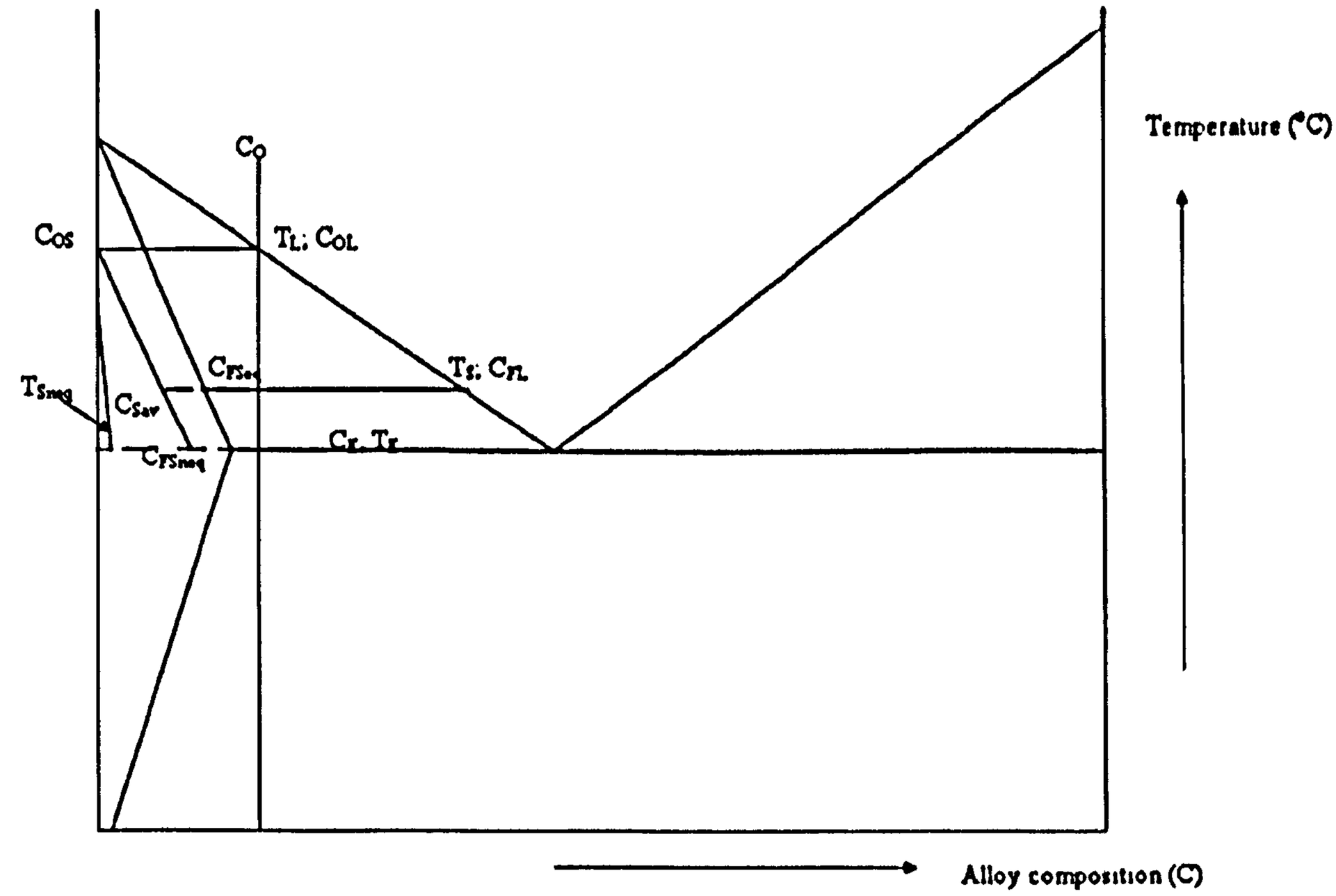

Figure 6.49: A scheme of non-equilibrium solidification as applicable to a typical binary eutectic alloy (e.g Al-xSi). C_O is the nominal composition of the eutectic alloy, T_L^* is the equilibrium liquidus temperature; T_S^* is equilibrium solidus temperature; T_E is the equilibrium eutectic temperature; C_{OS} is the initial concentration of solid ($C_{OS} = K_P C_{OL}$); C_{FL} and C_{FSeq} are the equilibrium liquid and solid concentration at the end of equilibrium solidification and the liquid and solid concentrations at the interface at T_S^*; C_{FSeq} is the average concentration of the solid phase at the eutectic temperature T_E; C_{Sav} is the line of average solid concentration; and T_{Sneq} is the actual non-equilibrium solidus (Adapted from Eskin 2008).

The occurrence of microsegregation in the blended microstructure will now be explained by Gulliver-Scheil approximation represented in equation 6.1 below:

$$C_L = C_O(1 - f_s)^{(K_p - 1)} \quad \text{.....6.1}$$

where C_L^* is the composition of the liquid phase, C_O is the nominal alloy composition, f_s is the fraction of solid and K_p is the partition co-efficient ($K_p = C_S^* / C_L^*$). In accordance with the proposal of Eskin (2008), it is presumed that solidification by SLS/SLM occurs within Gulliver-Scheil approximation as follows (Figure 6.49):

(a) The liquid phase changes its composition during primary solidification according to the liquidus line, from C_{OL} to C_{FL} and eventually to the eutectic composition C_E.

(b) The composition of the solid phase at the interface with the liquid is according to the equilibrium solidus at each temperature in the primary solidification range and is locally preserved at lower temperatures.

(c) Consequently, the solute distribution in the solid phase changes from C_{OS} in the center of the grain (dendrite) to C_{Fsneq} and, eventually, to $C_{\lim it}$ (which is the limit solubility of the solute in the matrix) at the periphery of the grain (dendrite).

(d) The average composition of the solid phase C_{Sav} changes with the decreasing temperature from C_{OS} to C_{Fsneq}.

As a consequence of the non-equilibrium solidification, the solid phase at the moment when the alloy reaches the equilibrium solidus contain less solute than the nominal alloy composition C_O. Therefore, liquid still exists in the system to accommodate the remaining solute as the liquid continue to solidify according to the equilibrium liquidus. This may result in the difference between the alloy composition and the actual average composition of the solid phase becoming so large that the solidification process will continue until the eutectic temperature is reached. Gulliver-Scheil approximation shows the amount of the remaining liquid phase of the eutectic composition (Figure 2.8) at the instance just described above. The liquid will therefore solidified as the "non-equilibrium eutectic".

Meanwhile, it had been established that the reality of solidification is more complicated than as depicted by the Gulliver-Scheil approximation (Eskin 2008). Measurable diffusion of solute in the solid phase during and after solidification, hindrance to diffusion in the liquid phase at high cooling rates, evolution of dendritic grains during solidification with dissolution of some finer arms, thermo-solutal convection resulting in changes in the composition with correspondingly accelerated or slowed-down local

solidification, and the temperatures of liquidus and solidus (eutectic reaction) being lower than the equilibrium ones as a result of undercooling during solidification are physical phenomena which occur simultaneously and in different proportions in SLS/SLM solidification, which can alter the distribution of the solute in the solid grain and the ratio of phase fractions (Eskin 2008). For the purpose of study, cooling rates, one of the most important parameters that controls microsegregation during solidification will be investigated. However, Eskin (2008) noted that experimental results on the effect of cooling rates on the extent of microsegregation appeared to be unclear as evident in the variation in the amount of non-equilibrium eutectics in Al-Cu alloys. In regard to this study, it can be inferred that the heat transfer in the solidification regime at each of these blended powders differ due to the varying particles' packing arrangement engendered across their packed layers. This speculation is supported by the evidences obtained from Figures 6.46 and 6.47 which indicate that the rate of cooling is fastest in the bimodal powder containing 25wt% AL-7 whereas cooling rates in the other blended powders are slower. Therefore, the lower cooling rates solidification regime occurring in the bimodal powders containing 25wt% AL-2, 25wt% AL-6, 10wt% AL-7, 50wt% AL-7, and 25wt% AL-8, is thought to have resulted in coarse dendritic structures and reduced fraction of primary aluminium dendrite phase. Again, the initiation of lower cooling rates had been attributed to the occurrence of porosity in the powder beds due to the introduction of these additive powders into AL-5. Increased cooling rates generated by the addition of 25wt% AL-7 into AL-5 could be said to have culminated in increasing the fraction of the primary phase and formation of finer dendrites. If the finding in this section is compared to the presented result in section 5.5, it can be inferred that it is the change in additive content as well as variation in particle sizes and distribution that influence the variation in cooling rates which in turn determines the nature and the size of dendrite arm spacing in the microstructure. This is also consequent upon the poor particle packing arrangements which results when the proposals of Zhu *et al* (2007) are not strictly adhered to in powder blending. The existence of slightly coarse dendritic structure at the bottom part of each sample could be ascribed to the poor thermal conductivity of the substrate powder bed at the moment laser beam was incident on the powder bed. Subsequent deposited layers solidify on a solid metal substrate increases the cooling rate at the top portion of the build while as a result of directional solidification, heat transfer at the powder bed substrate is very slow, thus coarse dendrite structure results.

Fisher *et al.* (2003) described the absorption of laser energy by the powder's solid particle through both bulk coupling and powder coupling phenomena. They noted that the absorbed energy consequently increases the local temperature across the scanned layers on the powder bed. In the context of this work, it is likely the first liquid formation was attained by the melting of AL-5 and the additive particles due to the lower melting point of AL-5 as well as the smaller particles sizes which are thought to have promoted rapid sintering rates (Lumley & Schaffer 1996, 1998). Meanwhile, partial or complete melting of both AL-5 and the additive powders is a function of the working temperature which also depend on the quantity of specific laser energy input into the blended powders. It is likely the liquid phase was formed at heterogenous regions of the powder bed, such as the inter-particulate contact sites, as a consequence of the existence of porous regions on the powder bed. With increase in the amount of specific energy absorbed by the particles during SLS/SLM, localised temperature increases and formation of larger molten pool results. In this context, the powder layer is thought to have lost its rigidity and hence, it shrinks rapidly. As the working temperature is increased, complete melting of both AL-5 and the additive particles occurs and the consequence of this is the formation of a "melting pool" shown in Figures 6.14a, 6.14c, 6.18, 6.20, 6.29a, b, d, 6.36, 6.37, and 6.39.

The employment of the Gaussian laser beam for the sintering process initiates a significant temperature gradient between the centre and the edge of the sintering pool. This consequently results in the existence of surface tension gradient and Marangoni convection. According to Niu & Chang (1999b, 2000), the surface tension gradients and Marangoni effects inducing capillary forces for liquid flow and particle re-arrangement are responsible for promoting an efficient densification of solid particles with the wetting liquid. As pointed out earlier in section 2.5, the amount of available liquid phase in the sintering pool controls the densification mechanism and the resultant microstructure of the SLS/SLM processed parts by altering the thermokinetic and thermocapillary properties such as viscosity, wettability, and rheological properties (Agarwala *et al.* 1995, Zhu *et al* 2004). The degree of interfacial bonding is a function of the amount and viscosity of the melt. The viscosity μ of the solid-liquid mixture had been is defined as shown below according to Agarwala *et al.* (1995), and Tolochoko *et al.* (2003).

$$\mu = \mu_o (1 - (\varphi / \varphi_M))^{-2} \quad \text{.....2.9}$$

where μ_o is a base viscosity that contains no solid particles, φ, the volume fraction of solids in the liquid, and φ_M, a critical volume fraction of solids above which the

mixture has essentially infinite viscosity. The inter-particulate bonding across layers is controlled by the base viscosity, μ_o, which decreases with increasing temperature across the packed layers. For the liquid phase to completely wet the unmelted powder particulates in order to achieve sufficient densification and improved microstructure, the mixture viscosity, μ, must be low enough. Moreover, the viscosity of the mixture must be sufficiently high to prevent balling and this condition can best be attained by manipulating an appropriate solid-liquid ratio (Agarwala *et al.* 1995, Zhu *et al* 2004). This can be achieved by the combination of low μ_o and regulated μ if parts having desirable sinterability are to be obtained. According to Zhu *et al.* (2004), in LPS, the relative shrinkage of the powder bed is described mathematically by equation 6.--.

$$(\Delta L / L_o) = (k\gamma_{lv} t) / D\mu \quad \text{.....2.10}$$

where γ_{lv} is the liquid-vapour surface energy, t, the sintering time, D the particle diameter, and k is a constant.

The sintered density ρ for a powder bed having initial tapping density ρ_t is described in equation 2.11 by German (1990).

$$\rho = \rho_t (1 - (\Delta L / L_o))^{-3} \quad \text{.....2.11}$$

Defining a non-dimensional parameter α according equation 2.12,

$$\alpha = ((k\gamma_{lv} t) / D\mu_o) \quad \text{.....2.12}$$

The final sintered density ρ is obtained by combining equations 2.10 to 2.12 according to German (1990):

$$\rho = \rho_t (1 - \alpha(1 - (\varphi / \varphi_M))^2)^{-3} \quad \text{.....2.13}$$

The interpretation of equation 2.13 confirms earlier findings from this research that the sintered density of the SLS/SLM processed blended AL-5 is directly proportional to its tapping density (ρ_t) (Figures 6.45). Hence, the outcomes of this work lend credence to the claim that the sintered density, which is a function of the tapping density of blended

powders, is dependent upon the powder characteristics and can be maximised by adopting the following:

(a) Blending of AL-5 (45-75 μm) with AL-7 having appropriate particle size and distribution (17-30 μm) that sits comfortably within the interstices of large sized AL-5 powder.

(b) Using spherical powders.

(c) Blending the large-sized particles with small-sized particles in appropriate proportion of 75wt% to 25wt% respectively.

As the tapping density of blended powders increases, it can be inferred that thermal conductivity increases, until the optimum tapping density corresponding to the highest thermal conductivity is attained (Figures 6.46 and 6.47). Moreover, equation 2.13 shows that the sintered density of SLS/SLM processed blended AL-5 powder is dependent upon the amount of liquid phase available. At the optimum powder packing arrangement at which the thermal conductivity is optimised, adequate molten pool with sufficient degree of viscosity is likely to have formed with a view to maximising the sintered density (Figure 6.7a). Above or below the optimum tapping density, it is thought that thermal conductivity of the powder bed is likely to have deteriorated, thereby resulting in the sintering of particles rather than melting. Consequently, sintered density and microstructure are not optimised at these instances. For instance, in the case of the additive powder AL-7, the formation of balling at a low content (10%) of the additive powder AL-7 (Figures 6.7b, 6.10 and 6.13a) suggests an excess amount of liquid phase formation from AL-5 (a low μ) due to its high content of silicon (11.6wt%) which reduces viscosity (Dinsdale & Quisted 2004). The unmelted particulates severely aggregate in the process of balling, and subsequently segregate from the AL-5 matrix (Figures 6.14a) thus resulting in low sintered density (Figure 6a, b). The reduced sintered density obtained when 50% of the additive powder AL-7 was blended with AL-5 binder powder is mainly attributable to an increased μ_o, which results from small amount of melt in this context as evident by porosity (Figures 6.7a, 6.12, and 6.13c) and reduced silicon content (6wt%) (Figure 6.7b). Due to the reduced content of AL-5 in the blend, it is likely that the amount of resultant liquid phase had reduced drastically and the viscosity of melt has increased much more than is necessary. Figures 6.7a, 6.11, and 6.13b) show that the combination of desirable μ and μ_o which is attainable by adding 25% additive powders (8.7wt% Si), produces sound sinterability for the blended mixtures of AL-5 and AL-7 with little or no balling and minimal porosity (Figure 6.7b).

These findings are in agreement with the results obtained from the works of Gu & Shen (2007a) in which the tapping density of the blended powders, employment of spherical powders for SLS/SLM, amount of CuSn binder's liquid volume fraction were found to have influenced the densification mechanism and microstructures of direct SLS processed multi-component Cu-based powders. With regard to this work, it is hereby argued that Gu & Shen. (2007a) had not optimised the binder content in the powder mixture that could yield the highest sintered density. This research highlights the relevance of the optimisation of both processing parameters and the powder properties in order to attain sound sinterability for direct laser sintered parts.

6.5 Conclusions

The results obtained in this chapter reveal significant variation in the properties of the blended powders which subsequently influence the laser sintered microstructures and properties. The pronounced differences observed in the properties of the blended powders and their sintered microstructure could be traced to the variation in the contents of additive powders in the AL-5 powder, additive particle sizes and distribution, and silicon constitution of the blended powders. The variation in the contents of additive powders in the blended powders as well as the particle sizes and distribution are responsible for the changes observed in the porosity of the powder bed. These effectively influence the thermal conductivity of the powder bed, which in turn influences the amount of liquid phase available for the interparticulate bonding/melting during the SLS/SLM process. Moreover, the silicon constitution in the additive powder influences the fraction of primary phase and determines whether or not balling occurs by controlling the melt viscosity. In conclusion, aluminium powder with composition and particle sizes and distribution 75wt% AL-5 (45-75 μm) / 25wt% AL-7 (17-30 μm) was found to have 1.89 g/cm^3 packing density, 2.32 g/cm^3 sintered density, and 76.2 kgf/mm^2 microhardness via processing condition employing 150J/mm^3. The component ratio and particle sizes and distribution were noted to have influenced the densification kinetics of the blended powder with the optimum composition having K = 13.4. The microstructure of the optimised sample was found to be devoid of excessive porosity. The outcomes of this investigation indicate the role play by the component ratio and particle size distribution in the SLS/SLM of aluminium powders and provides a basis for process control.

CHAPTER SEVEN DEVELOPMENT OF TRIMODAL ALUMINIUM POWDER BLENDS FOR DIRECT SLS PROCESSING

7.1 Introduction

This chapter aims to take further the improvement already achieved in the powder and sintered properties of the bi-modal powders by blending two additive powders AL-7 and AL-8 with the AL-5 powder in varying proportions. Applying the proposition of Carson & Pittenger (1998) that the proportion of aluminium powder having + 45μm particle distribution should be at least 75% in order to attain an apparent density of 1.25 g/cm^3, the proportion of AL-5 was held constant at 75% while the remainder consisted of AL-7 and AL-8, each component being allowed to vary between 5% to 25% through four different blends of powders. Due to the consequential influence of improved particle packing on the thermal conductivity of the powder bed which modifies the sintering behaviour powder (German 1993, 1996); the four different powders were fabricated for testing with a specific laser energy input of 150 J/mm^3. In this case, three point-bend test specimens, tensile test specimens and unnotched impact test specimens were also fabricated using the same processing regime. The physical, sintered and microstructural properties of each tri-modal powder blend were compared and related to the results of the 75% AL-5/25% AL-7 bimodal powder blend.

Microscopic observation of the trimodal powders is presented section 7.2. The effect of blending the trimodal powder on their physical properties and sintered properties, including density, microstructural properties and surface morphology are presented in Section 7.3 and 7.4. Section 7.5 describes the difficulties associated with the fabrication and preliminary investigation of the mechanical test specimens as well as the results of the three-point bend testing.

7.2 Microstructural Observation of the Trimodal Powders

Figure 7.1 presents the evidence of homogeneous mixing of the additive powders AL-7 and AL-8 with AL-5 after 20 minutes in a V-shape mixing device (see Section 4.3). The SEM images reveal a preponderance of spherically shaped particles in all the blended powders. The elemental composition of the trimodal powders and the bimodal AL-7 and AL-8 are presented in Table 7.1 for comparative analysis. The concentration of aluminium, silicon and oxygen in all the blended samples fall within the ranges of 89.0-90.2 %, 8.5-9.0 % and 1.3-2.0 % respectively. Meanwhile, all the powders are designated as shown on the first column by the left hand side of Table 7.1. The designations shall be used to refer to these powders in plotting graphs.

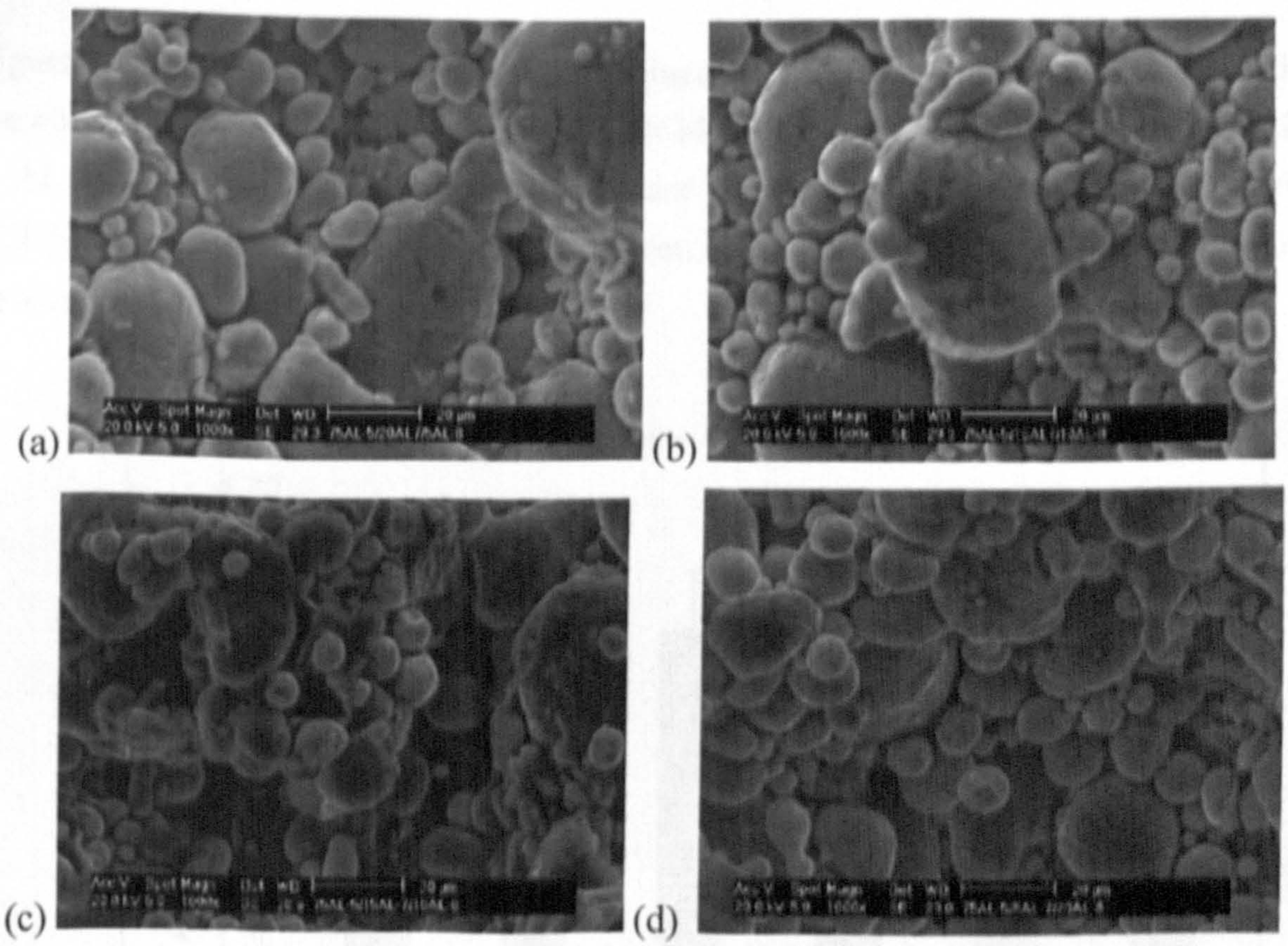

Figure 7.1: SEM images of the tri-modal blended powders: (a) 75% AL-5/20% AL-7/5% AL-8 (b) 75% AL-5/15% AL-7/10% AL-8 (c) 75% AL-5/10% AL-7/15% AL-8 (d) 75% AL-5/5% AL-7/20% AL-8.

Table 7.1: Elemental Composition of the Powdered Samples by Semi-quantitative EDS Analysis (Weight %).

Designation	Powdered Samples	Al	Si	O
I	75wt% AL-5 + 25wt% AL-7	89.3	8.7	2.0
II	75% AL-5 + 20% AL-7 +5%AL-8	89.7	8.9	1.5
III	75% AL-5 + 15% AL-7 +10%AL-8	89.0	9.0	2.0
IV	75% AL-5 + 10% AL-7 +15%AL-8	89.8	8.6	1.6
V	75% AL-5 + 5% AL-7 +20%AL-8	90.2	8.5	1.3
VI	75wt% AL-5 + 25wt% AL-8	89.5	8.6	1.9

7.3 Physical Properties of Tri-modal Powder Blends

Figure 7.2 shows the apparent density obtained for the tri-modal powder blends. When the apparent density of the tri-modal powder blends is compared with those of the AL-5 + AL-7 and AL-5 + AL-8 bimodal powder blends, with the exception of the AL-5/20%AL-7/5%AL-8 blend, they can be seen to lie between those of the two bimodal powder blends (Figure 7.2).

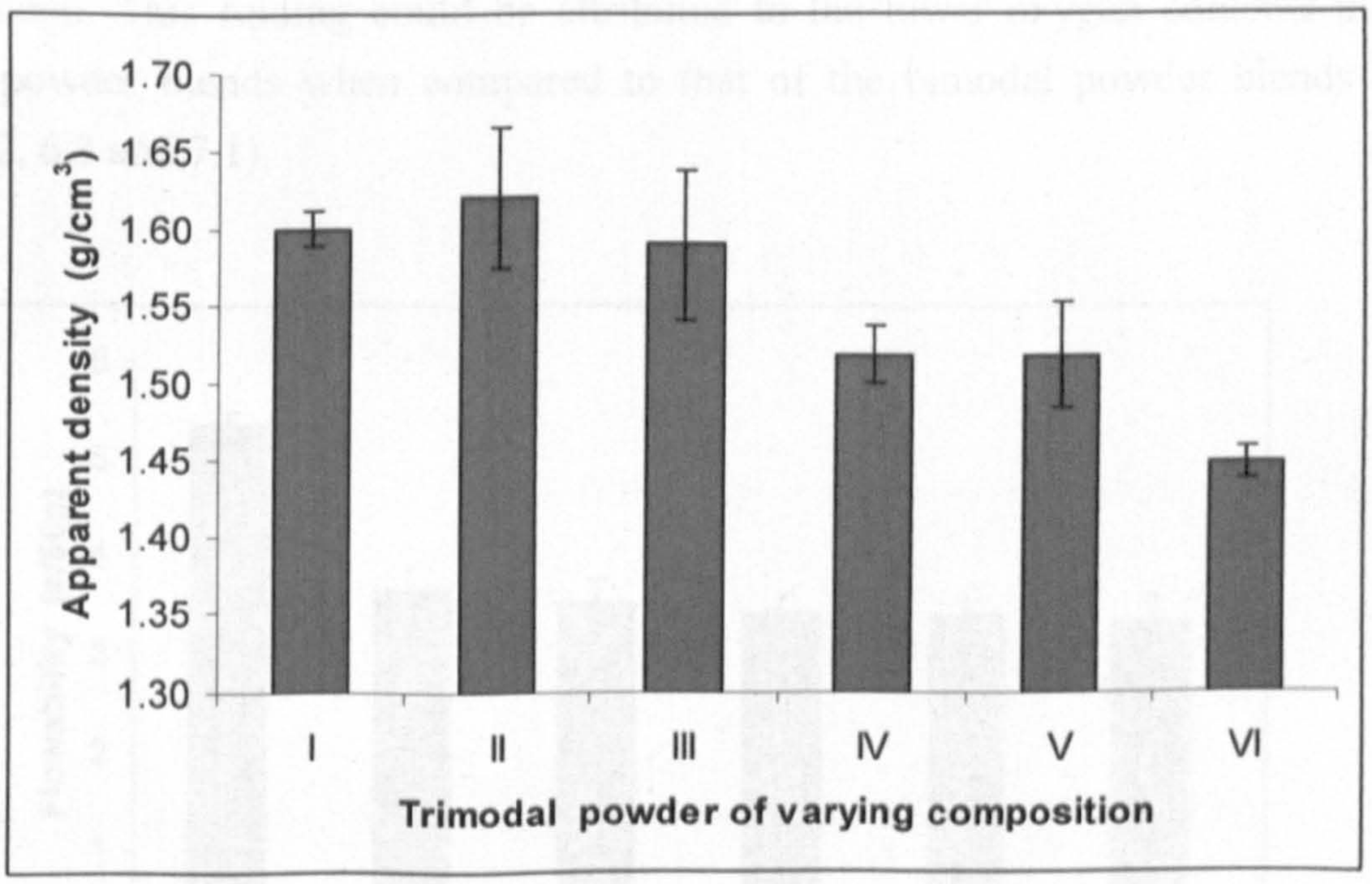

Figure 7.2: Apparent density of the trimodal powder blends.

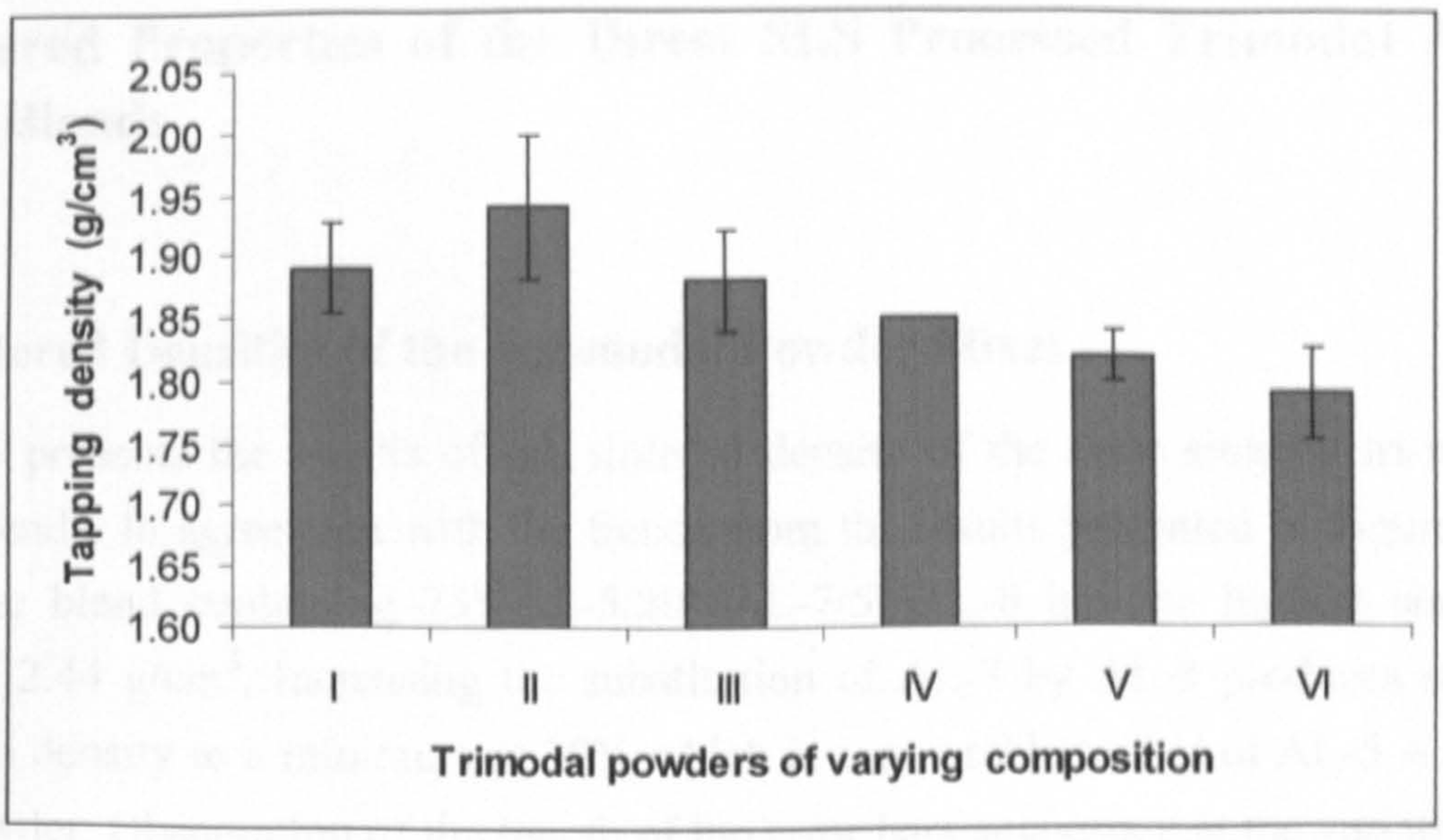

Figure 7.3: Tapping density of the trimodal powder blends.

A similar behaviour is observed in the tapping densities (Figure 7.3). Although all the powder blends fulfil the trimodal packing condition proposed by Zhu *et al.* (2007), ($D_L >> D_M >> D_S$), it is now evident the component ratio of additive powder also plays a significant role in determining tapping density via the particle arrangement. Figure 8.4 presents the flowability of the trimodal powders. All the tri-modal powder blends are found to be of comparable flowability and this is rather better than that of the binary powder blend. This finding could be attributed to the lower oxygen contents in the trimodal powder blends when compared to that of the bimodal powder blends (see Tables 6.2, 6.3 and 7.1).

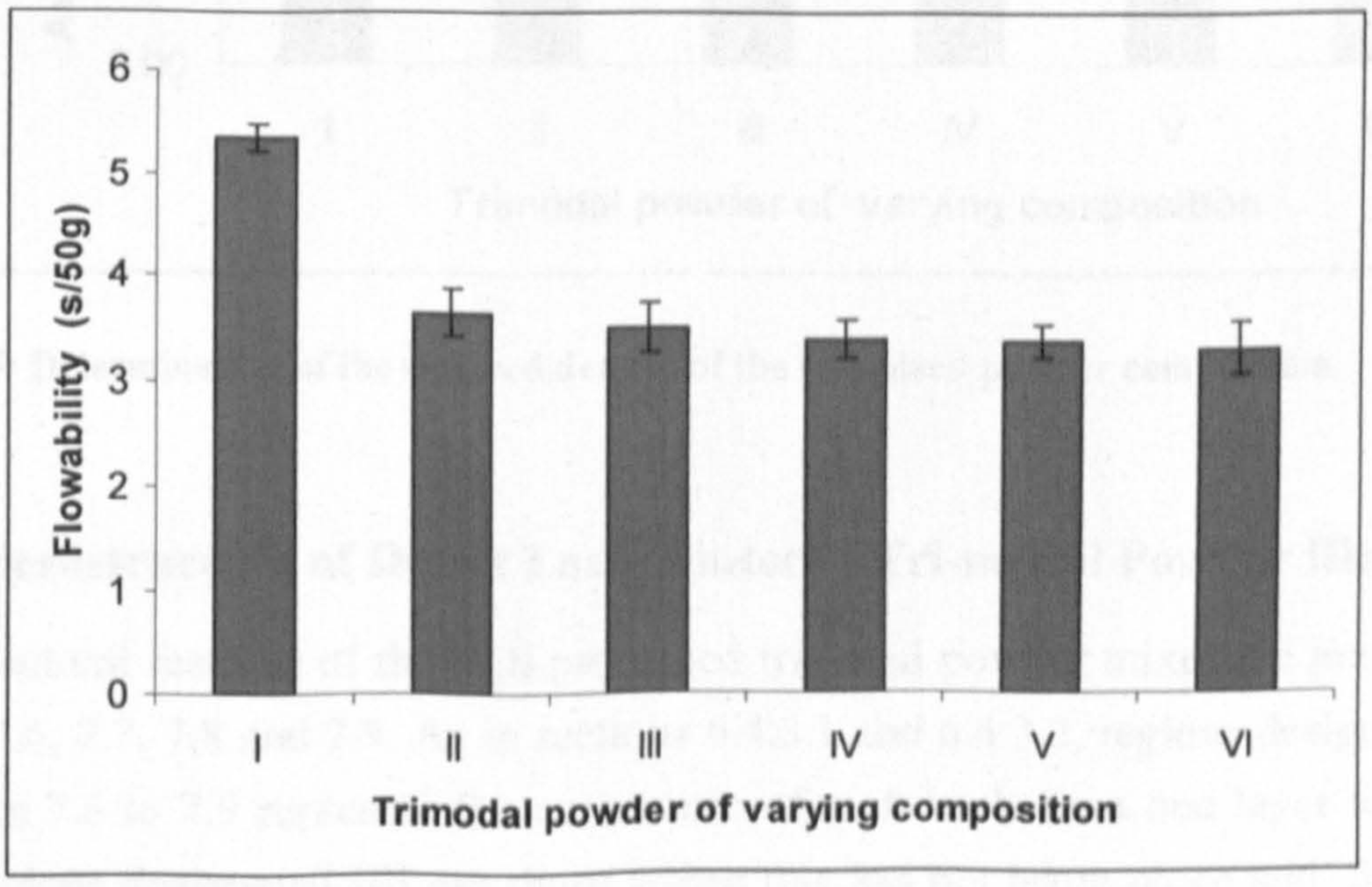

Figure 7.4: Flowability of the trimodal powder blends.

7.4 Sintered Properties of the Direct SLS Processed Trimodal AL-5 Powder Blends

7.4.1 Sintered Densities of the Tri-modal Powder Mixes

Figure 7.5 presents the results of the sintered density of the laser sintered tri-modal powder blends. In agreement with the trends from the results presented in Figure 7.3, the powder blend containing 75%AL-5/20%AL-7/5%AL-8 has the highest sintered density of 2.44 g/cm^3. Increasing the substitution of AL-7 by AL-8 produces steady decrease in density to a minimum at 20% which is comparable to that of AL-5 + AL-8 binary powder. Observation of the length of the error bars suggests that the variation of the sintered density is significant across the samples.

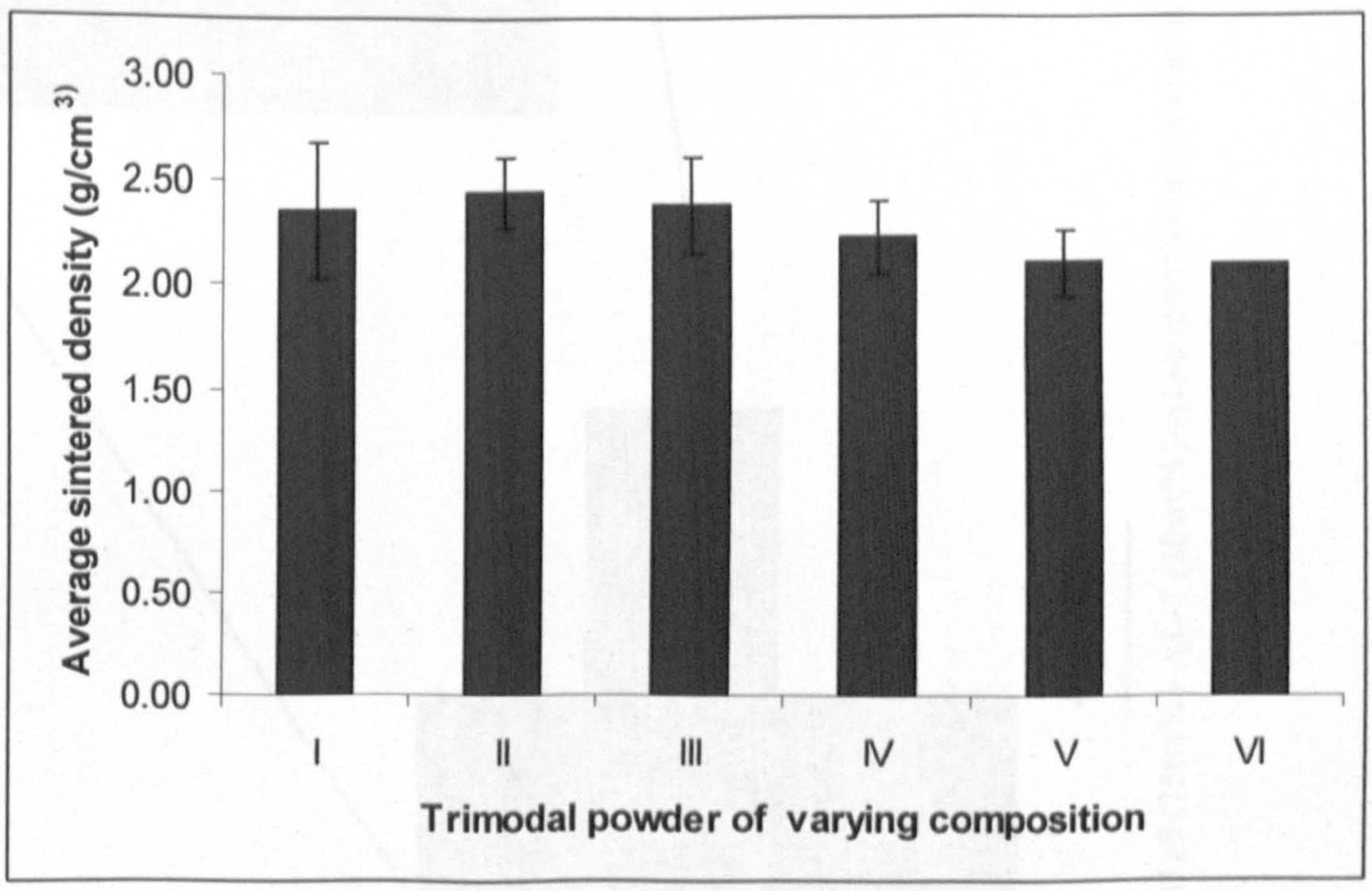

Figure 7.5: Determination of the sintered density of the optimised powder composition.

7.4.2 Microstructure of Direct Laser Sintered Tri-modal Powder Blends

Microstructural features of the SLS processed trimodal powder mixes are presented in Figures 7.6, 7.7, 7.8 and 7.9. As in sections 6.4.3.1 and 6.4.3.2, regions designated AA in Figures 7.6 to 7.9 represent the occurrence of melt back from one layer to another whilst regions designated BB are those where this has not taken place and, thus, have high porosity which reduces the sintered density.

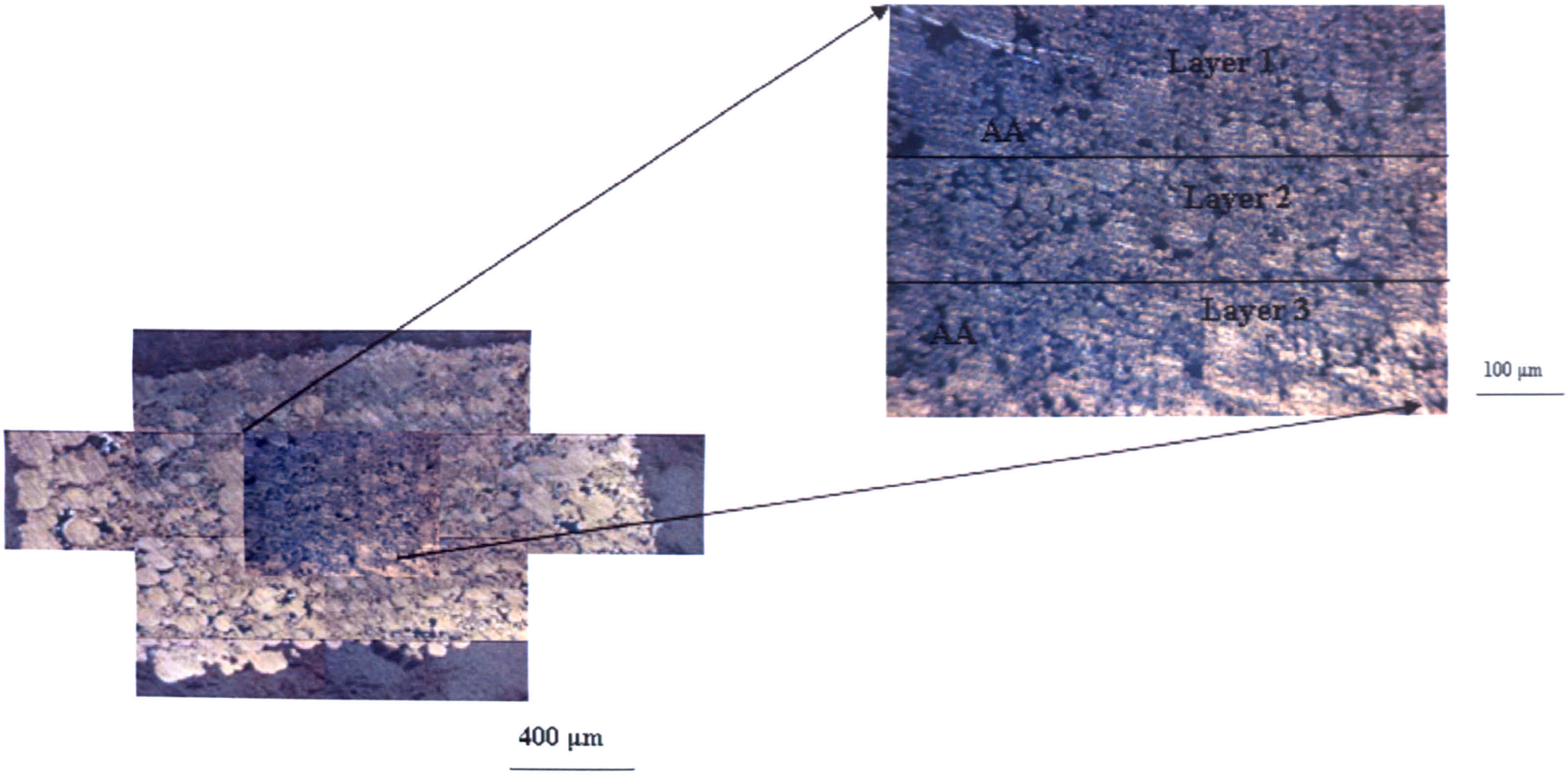

Figure 7.6: Microstructure of sections through AL-5 (75wt%)-AL-7 (20wt%)-AL-8 (5wt%) fabricated at a specific laser energy input of 150 J/mm^3.

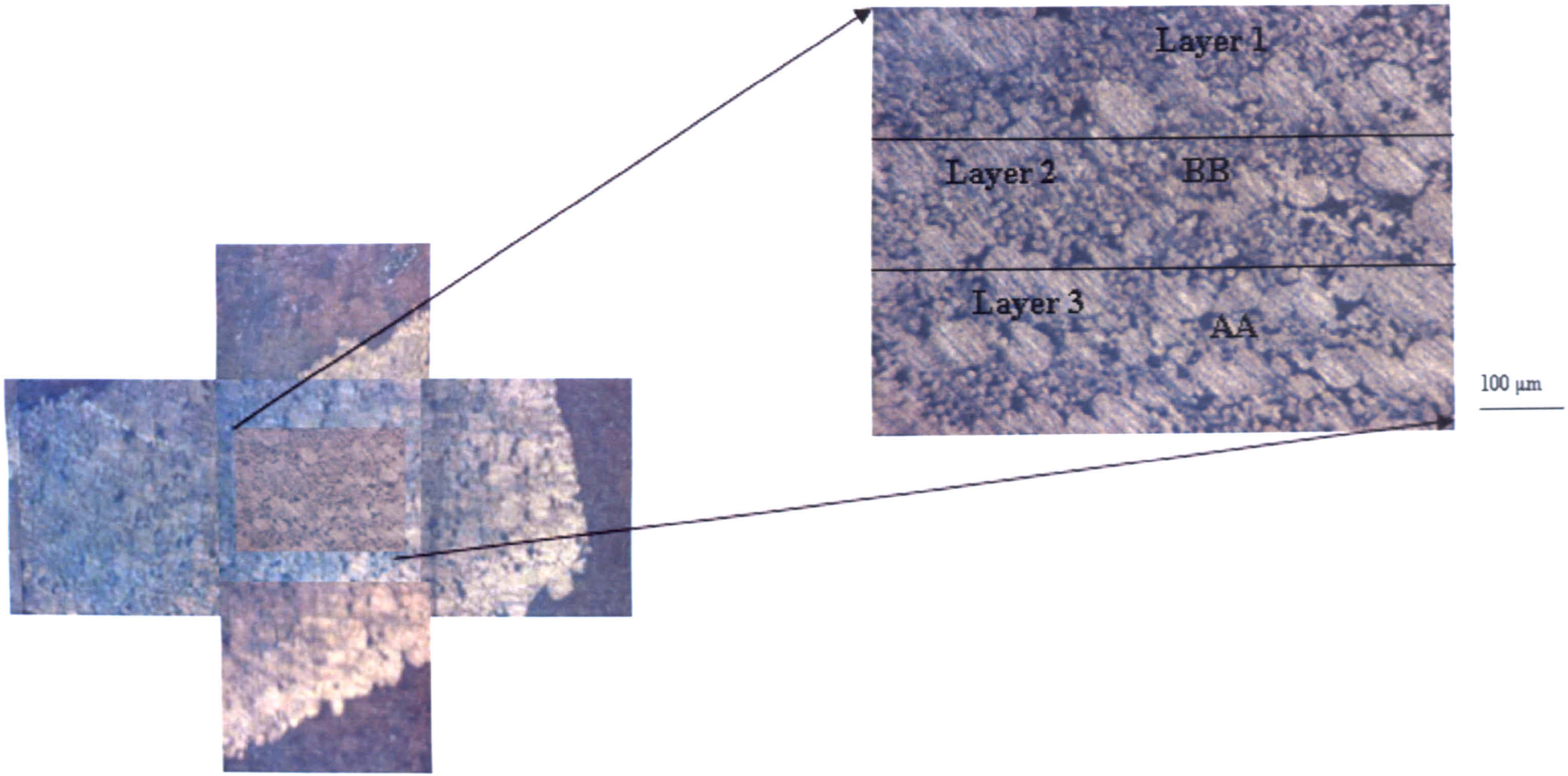

Figure 7.7: Microstructure of sections through AL-5 (75wt%)-AL-7 (15wt%)-AL-8 (10wt%) fabricated at a specific laser energy input of 150 J/mm^3.

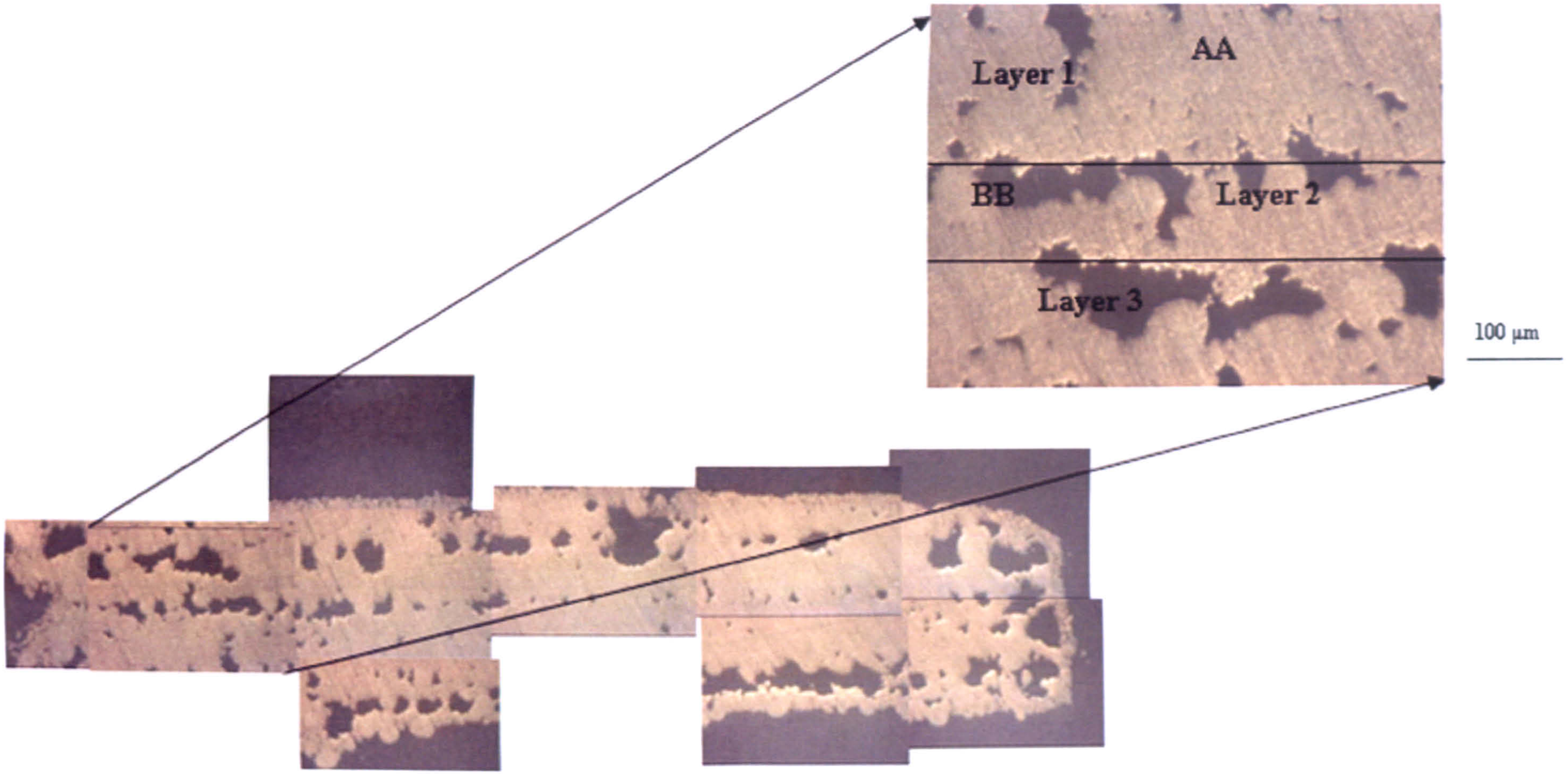

Figure 7.8: Microstructure of sections through AL-5 (75wt%)-AL-7 (10wt%)-AL-8 (15wt%) fabricated at a specific laser energy input of 150 J/mm^3.

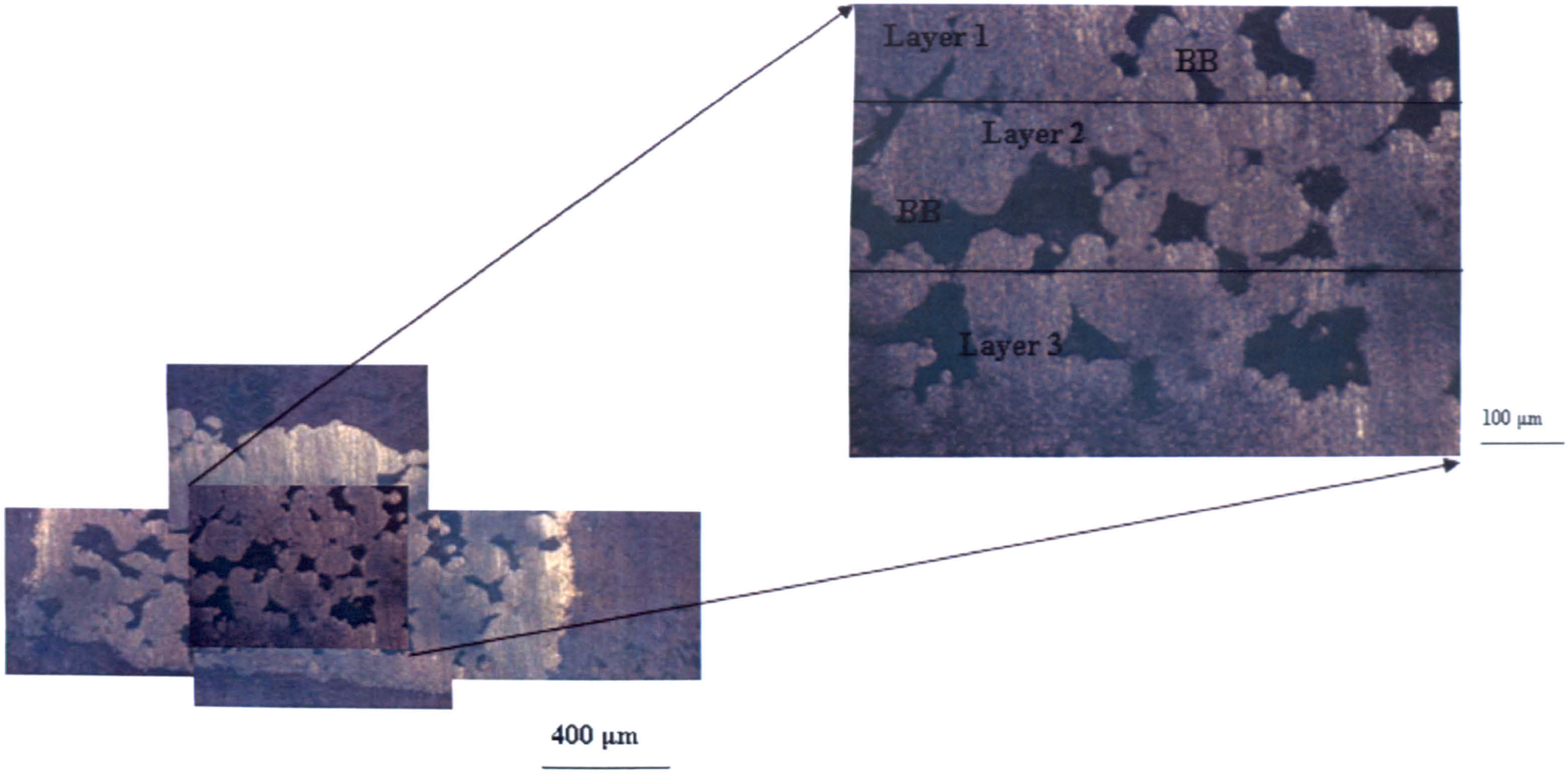

Figure 7.9: Microstructure of sections through AL-5 (75wt%)-AL-7 (5wt%)-AL-8 (20wt%) fabricated at a specific laser energy input of 150 J/mm^3.

Comparison of the optical micrographs (Figures 7.6 to 7.10) indicates that inter-particulate bonding and coherence across the layers appears to be declining in the following order: 75wt% AL-5/10wt%AL-7/15wt%AL-8 > 75wt% AL-5/5wt%AL-7/20wt%AL-8 >75wt%AL-5/20wt%AL-7/5wt%AL-8 > 75wt%AL-5/15wt%AL-7/10wt%AL-8. The microstructures of all the samples are characterised with the existence of residual pores connected with short inter-pore spacing. This observation is expected to impact on the mechanical properties of the specimens during testing. The occurrence of inter-particulate diffusion, evident by the formation of necking in all the samples, indicates that these appear to be well sintered. Agglomerate formation seems to be more prominent in the samples containing more AL-8. This could be ascribed to the oxidation tendency of small sized AL-8 particles which promotes the formation of porous structure via incomplete wetting (Niu & Chang 2000)

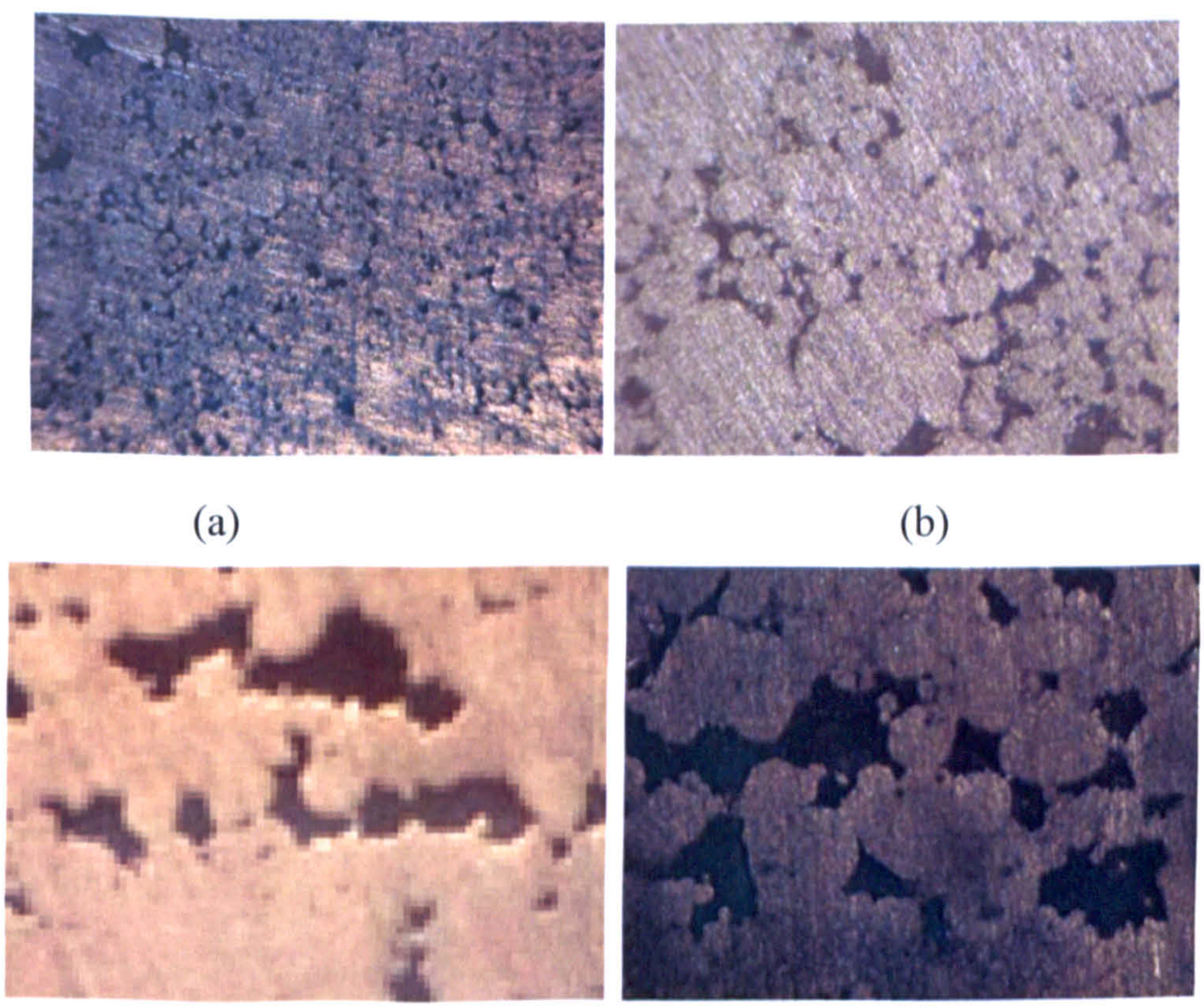

Figure 7.10: Optical microstructures of polished sections showing the pore size and distribution in laser sintered (a) 75%AL-5/20%AL-7/5%AL-8, (b) 75% AL-5/15%AL-7/10%AL-8, (c) 75% AL-5/10%AL-7/15%AL-8, and (d) 75% AL-5/5%AL-7/20%AL-8.

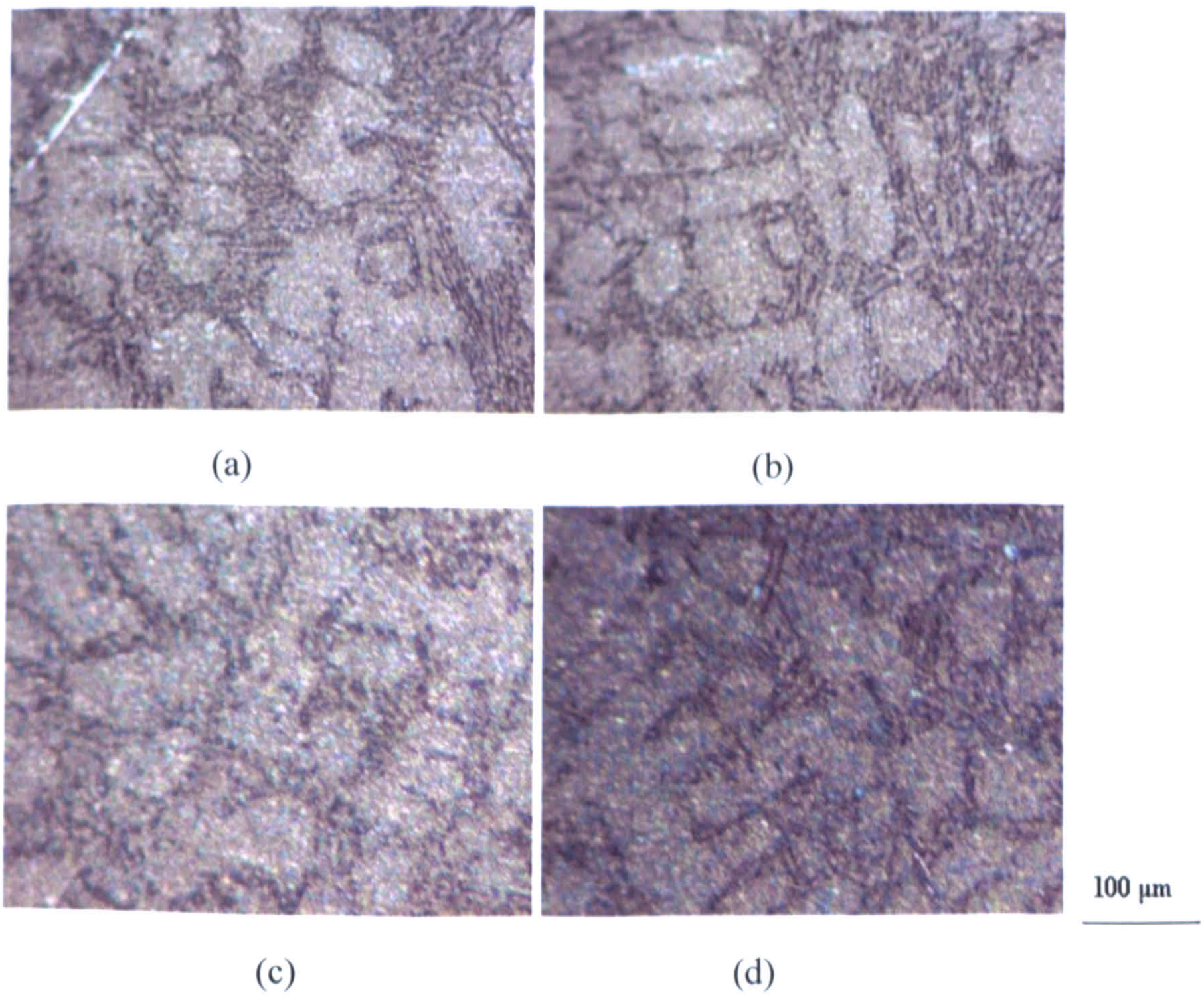

Figure 7.11: Dendritic microstructure in the SLS processed tri-modal powder blends: (a) 75wt%AL-5/20wt%AL-7/5wt%AL-8 (b) 75wt%AL-5/15wt%AL-7/10wt%AL-8 (c) 75wt% AL-5/10wt%AL-7/15wt%AL-8 and (d) 75wt% AL-5/5wt%AL-7/20wt%AL-8.

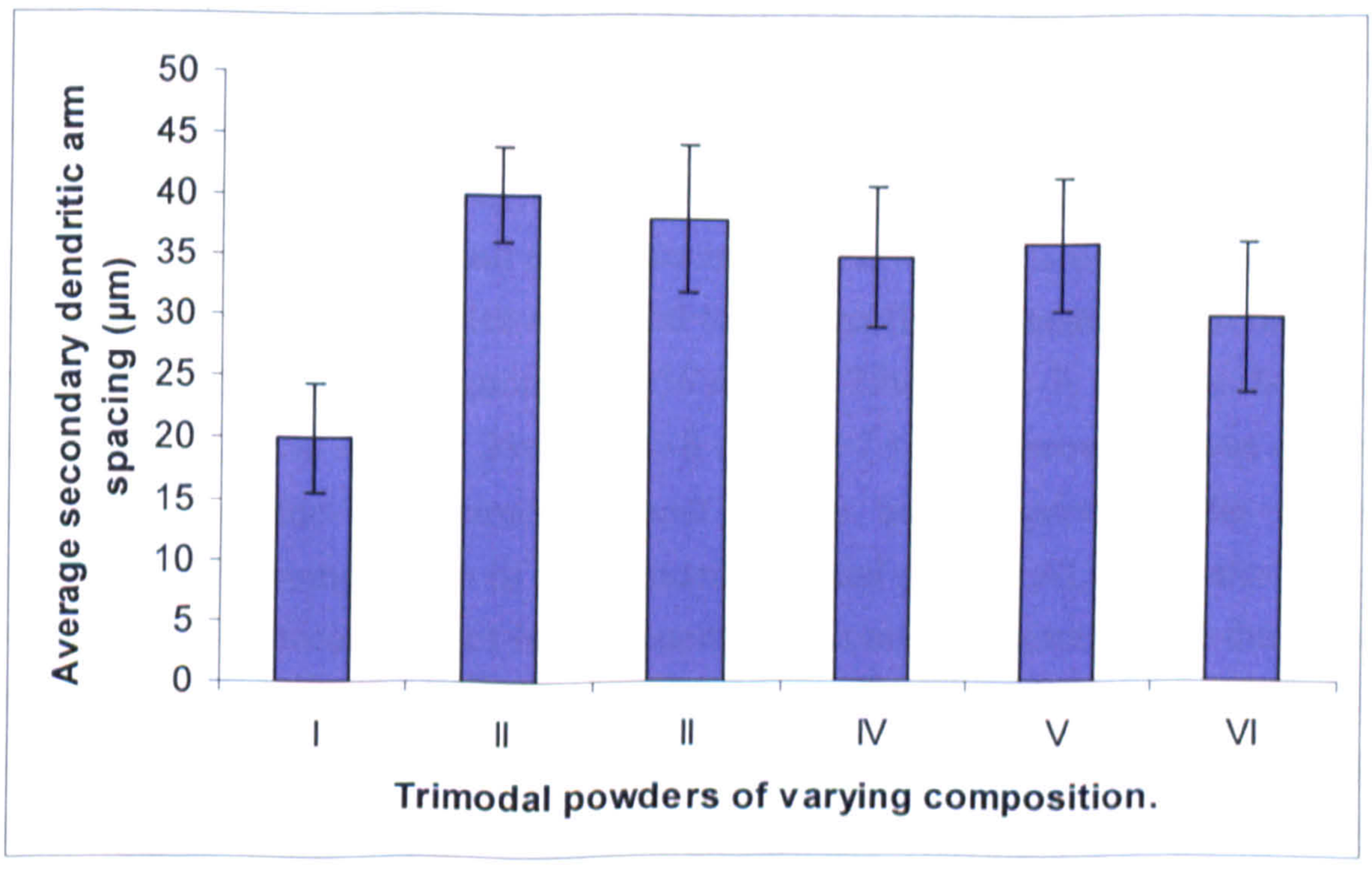

Figure 7.12: Dendrite arm spacing in SLS processed trimodal powders.

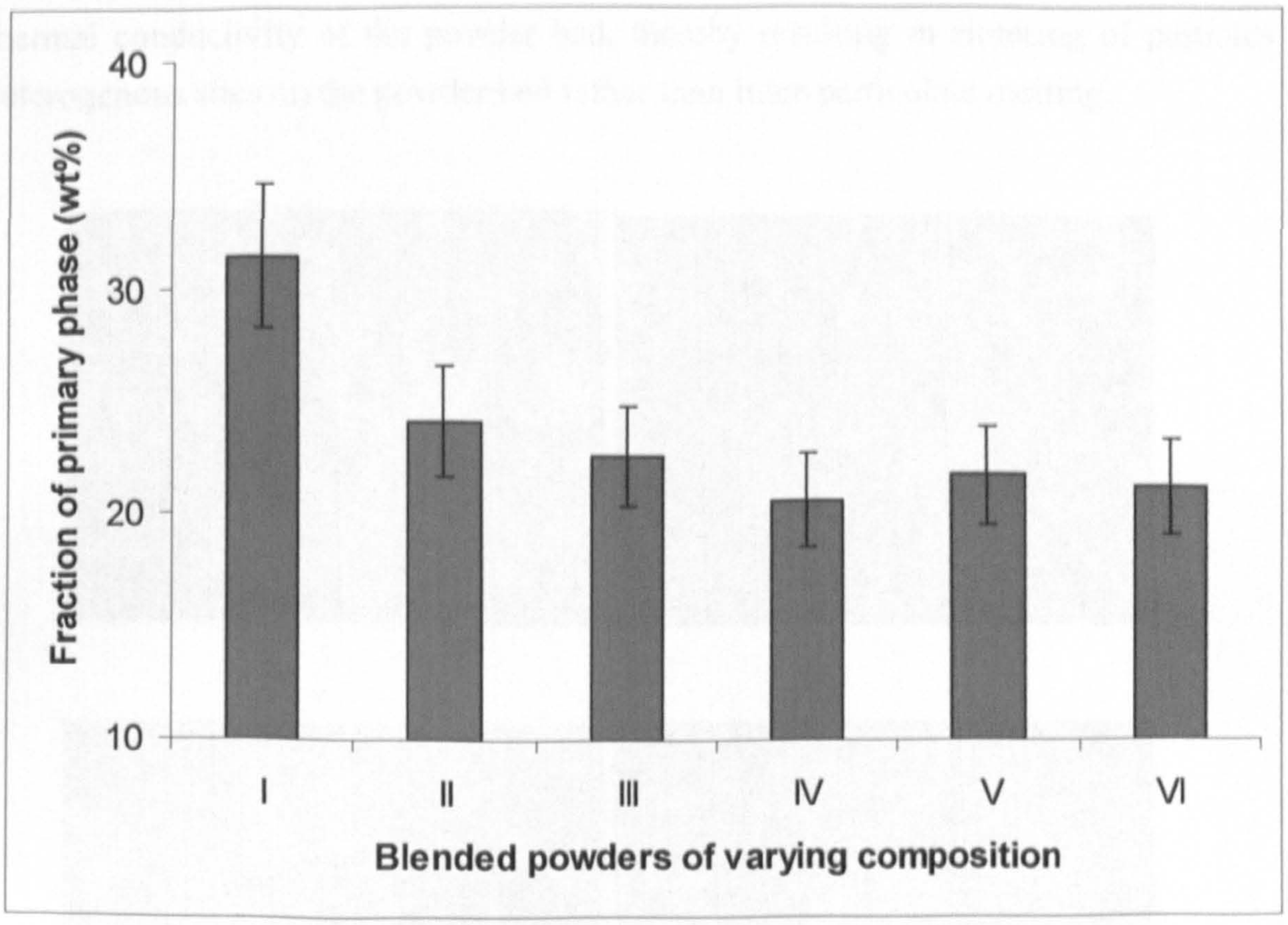

Figure 7.13: Fraction of primary phase in the SLS processed trimodal powders.

The microstructures, measurements of dendrite arm spacing, and fractions of primary dendrite phase in the SLS/SLM processed trimodal powder blends are presented in Figures 7.11 to 7.13. Comparison of the tapping (Figure 7.3) and sintered (Figure 7.5) densities of the trimodal powders confirm the earlier claim (Figures 6.45) that enhanced particle packing arrangement indicated by increased tapping density tend to increase the thermal conductivity of the powder. This consequently is expected to lead to improved sintered density and microstructure. Meanwhile, the dendritic structure of all the trimodal blended samples are noted to be significantly coarser than that of the bimodal blended powder containing 75wt% AL-5 + 25wt% AL-7, whereas they are as coarse for the 75wt% AL-5 + 25wt% AL-8 (Figure 7.12). Moreover, it was observed that coarse dendritic microstructure exist at the bottom parts of the samples, irrespective of the composition of the blended trimodal powder AL-5. Figures 7.14a to 7.14d confirm the occurrence of heterogeneity in the microstructure of all the blended trimodal samples. This is evident by the occurrence of unmelted particles of AL-7 and AL-8. Furthermore, it is clear that heterogeneity of the blended trimodal microstructure increases as the content of AL-8 increases. The occurrence of porosity on the powder bed and the increasing tendency of AL-8 particles to oxidise during SLM/SLM are likely to be responsible for the occurrence of unmelted particles in the microstructure of all the trimodal blended samples. Consequently, both factors reduce the effective

thermal conductivity of the powder bed, thereby resulting in sintering of particles in heterogenous sites on the powder bed rather than inter-particulate melting.

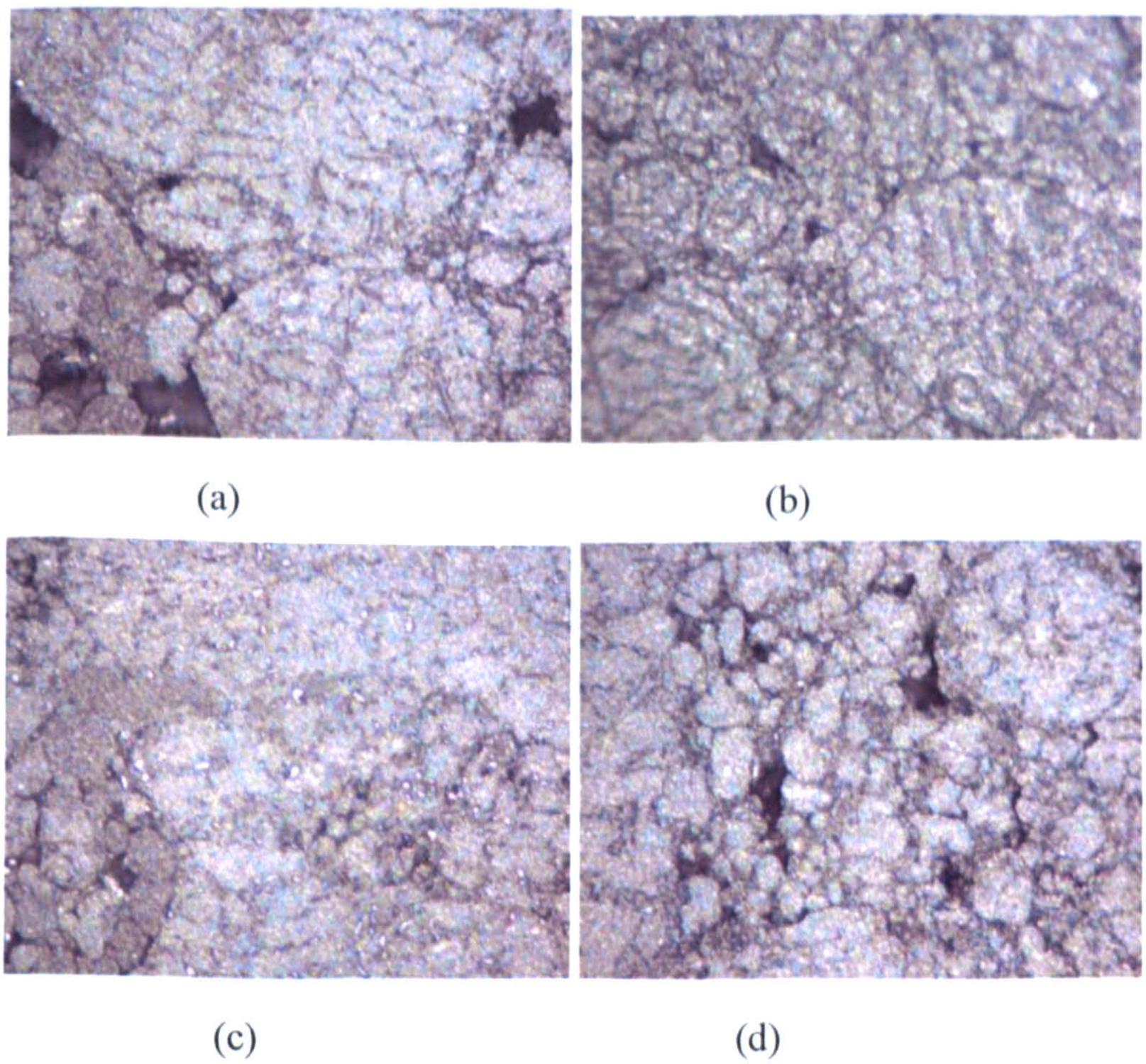

Figure 7.14: Microstructural heterogeneity and homogeneity in SLS/SLM processed trimodal powder of varying composition: (a) 75wt% AL-5/20wt% AL-7/5wt% AL-8 (b) 75wt% AL-5/15wt% AL-7/10AL-8 (c) 75wt% AL-5/10wt% AL-7/15wt% AL-8 (d) 75wt% AL-5/5wt% AL-7/20wt% AL-8

The characteristic microstructures of the laser sintered/melted trimodal blended samples are presented in Figures 7.15 to 7.18. As AL-8 content increases, it is evident from silicon and oxygen maps that there exist dark regions having sizes and shapes that approximate to the sizes and shapes of pores present in Figures 7.15e to 7.18e. These dark regions are speculated to be the porousities existing in the microstructure of the SLS/SLM blended trimodal powders. It is speculated that it is the porosity existing across the packed layers of these powders' particles that develop into porosities identified in Figures 7.6 to 7.9. Upon comparison of the trimodal microstructures with those of bimodal powders (Figures 6.29a and 6.29d), Figure 7.12 lends credence to observations made in Figure 7.11 through high values of dendritic arm spacing obtained for all the samples.

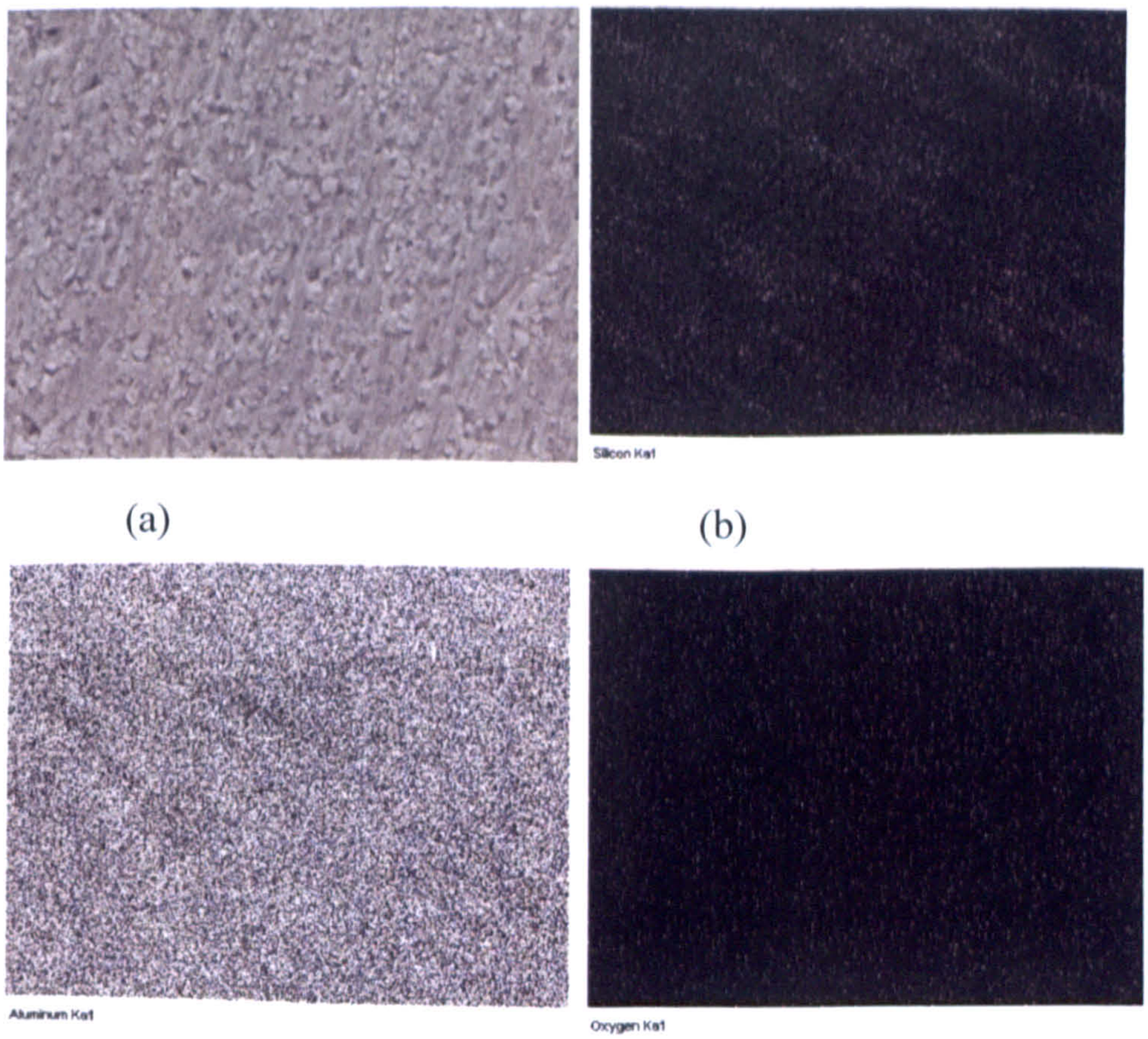

Figure 7.15: EDS elemental maps showing characteristic microstructure of the interfaces in SLM processed 75wt% AL-5/20wt% AL-7/5wt% AL-8 blend: (a) electron image (b) silicon (c) aluminium (d) oxygen (e) optical micrograph.

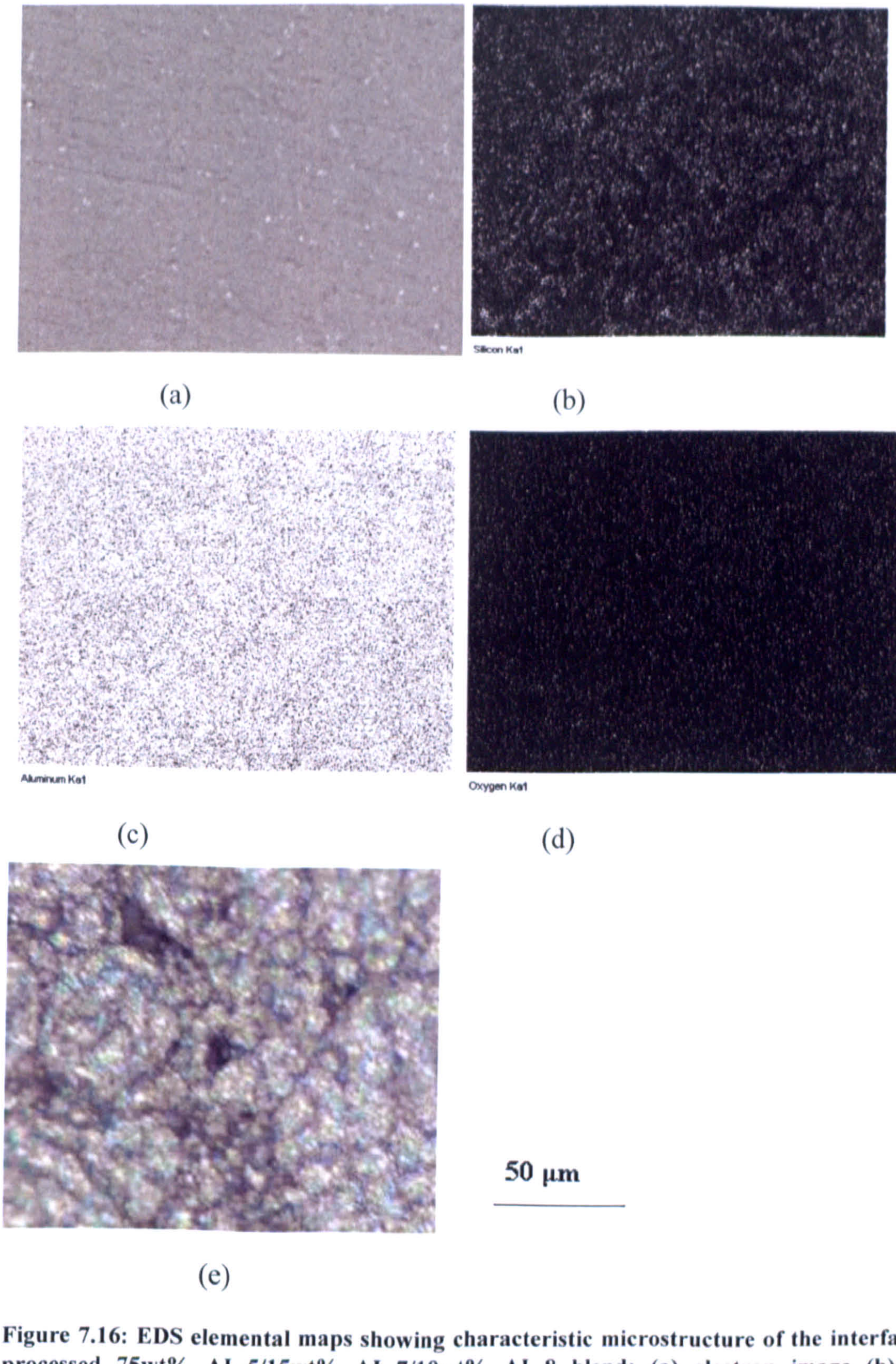

Figure 7.16: EDS elemental maps showing characteristic microstructure of the interfaces in SLM processed 75wt% AL-5/15wt% AL-7/10wt% AL-8 blend: (a) electron image (b) silicon (c) aluminium (d) oxygen (e) optical micrograph.

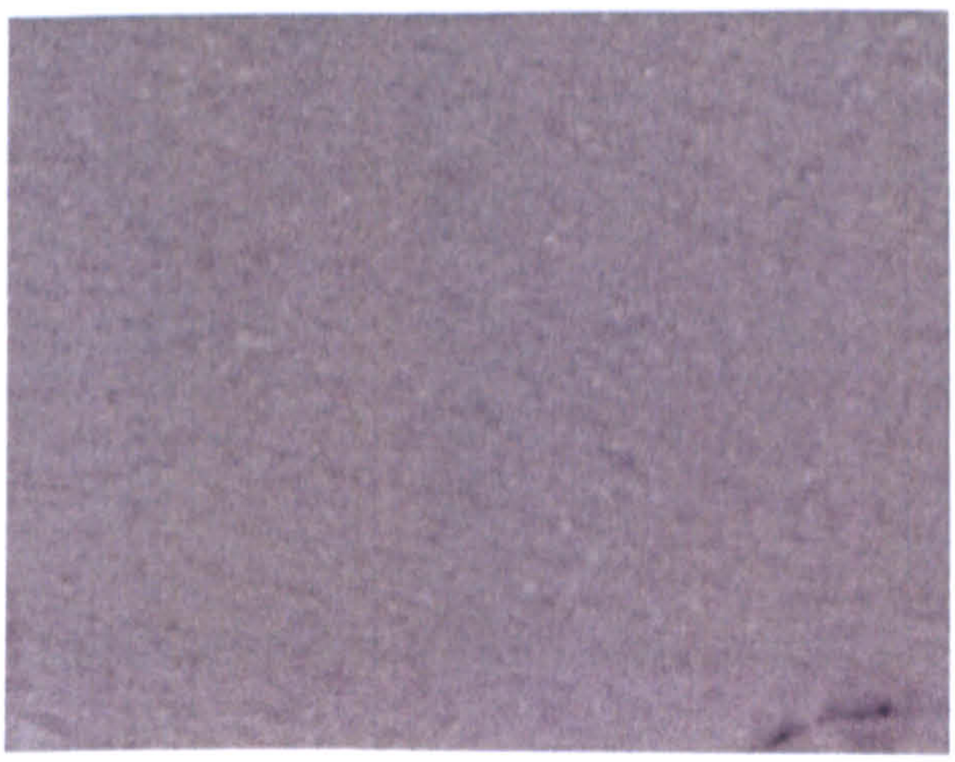

(a)

(b)

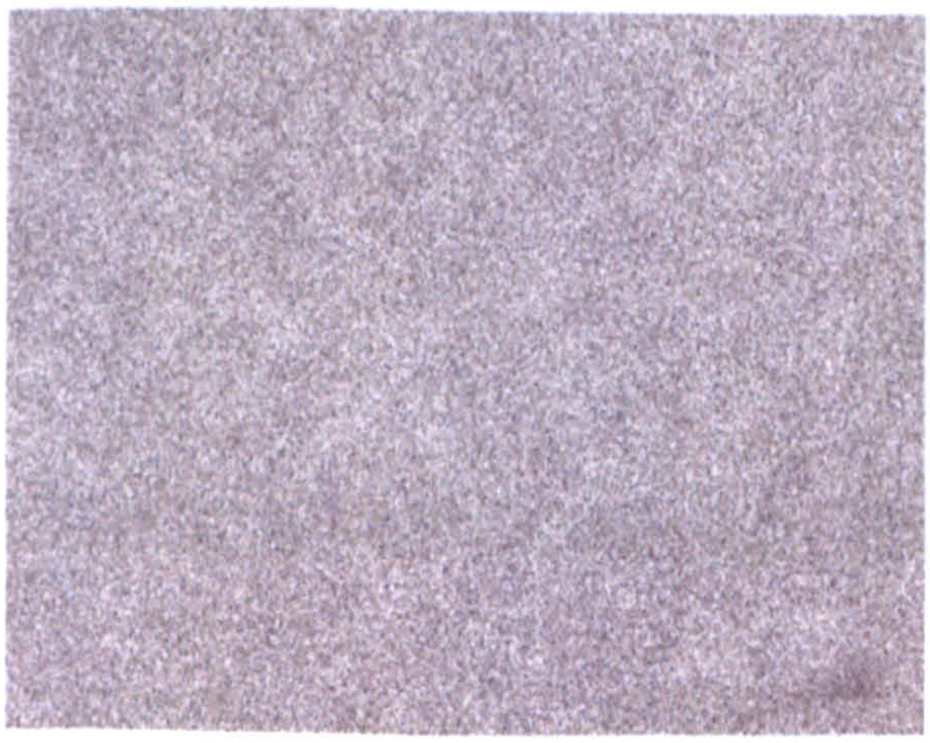

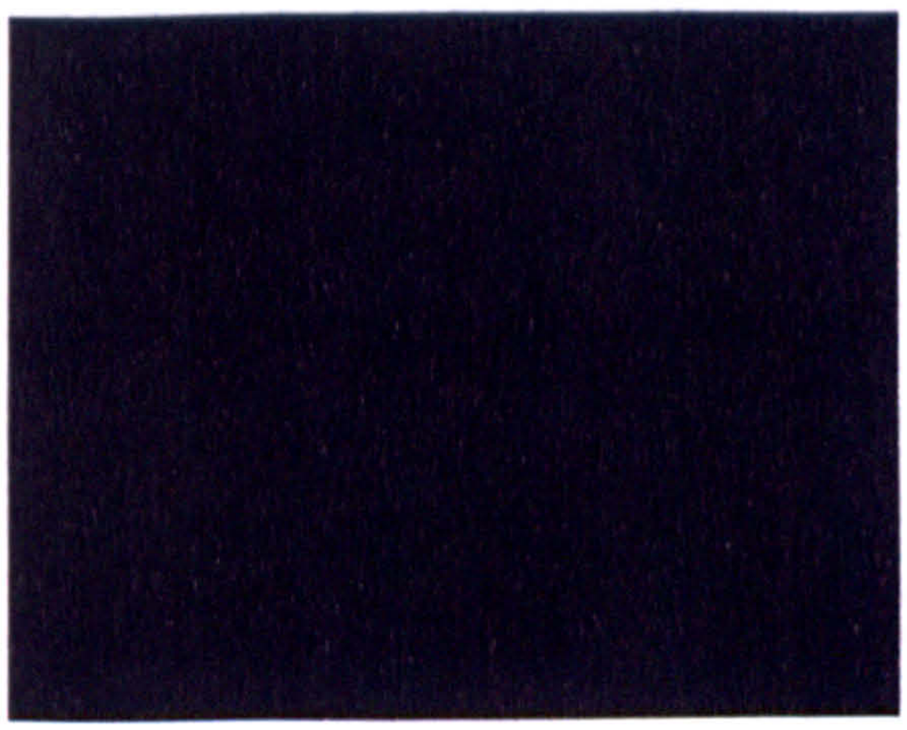

(c)

(d)

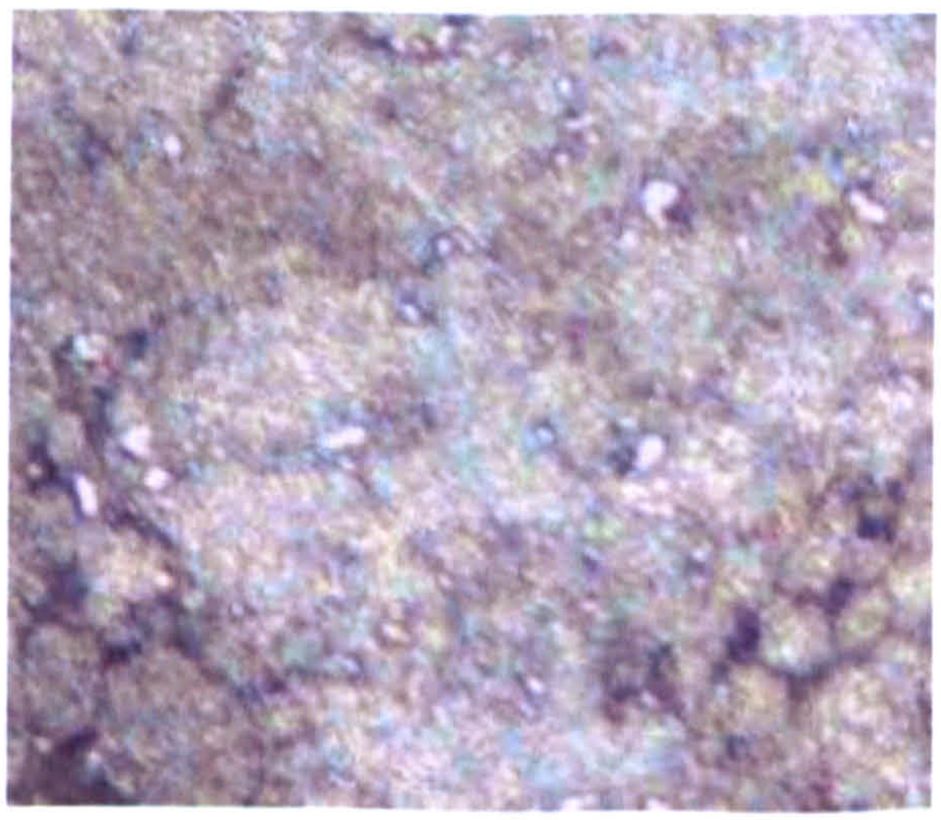

50 μm

(e)

Figure 7.17: EDS elemental maps showing characteristic microstructure of the interfaces in SLM processed 75wt% AL-5/10wt% AL-7/15wt% AL-8 blend: (a) electron image (b) silicon (c) aluminium (d) oxygen (e) optical micrographs.

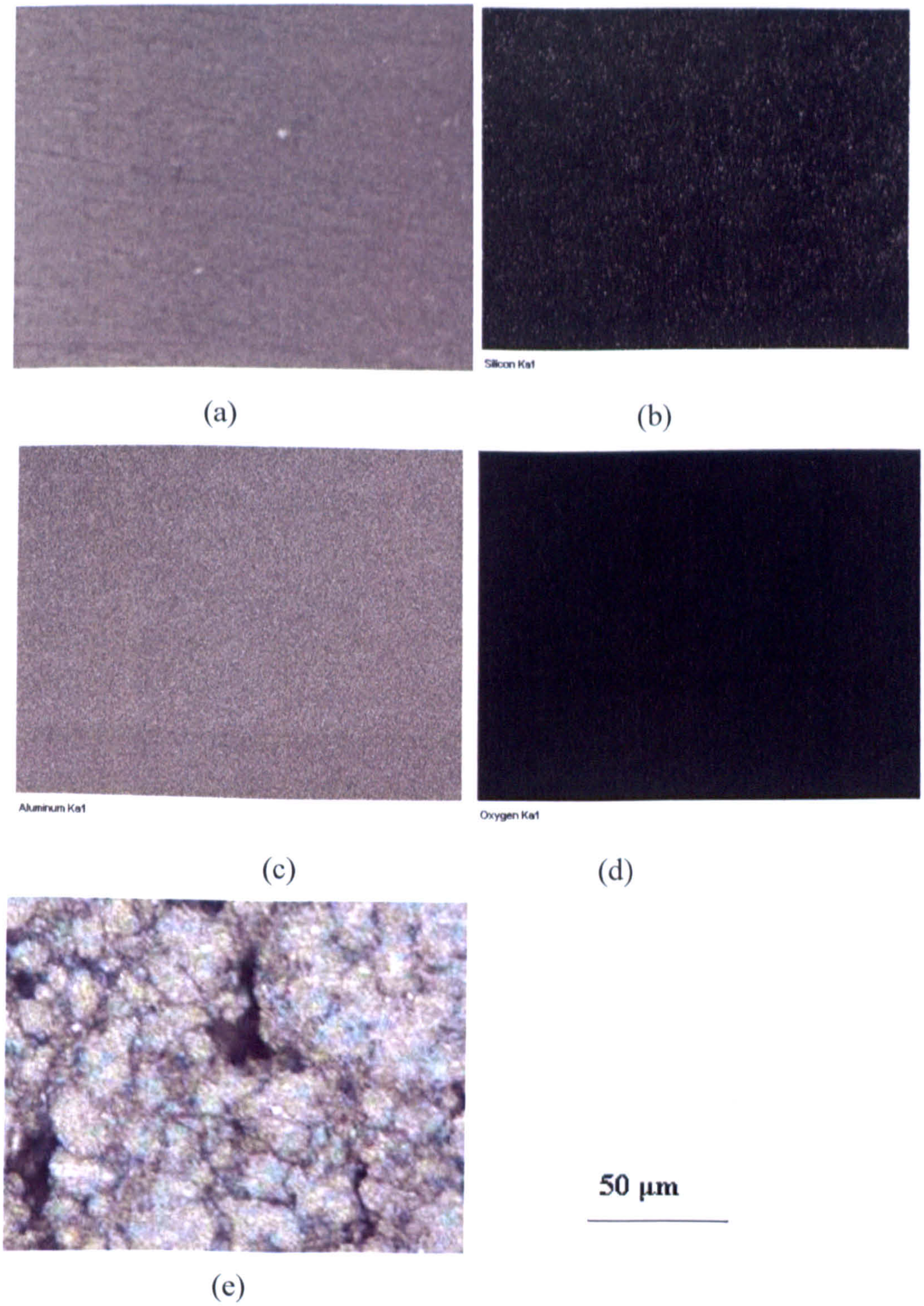

Figure 7.18: EDS elemental maps showing characteristic microstructure of the interfaces in SLM processed 75wt% AL-5/5wt% AL-7/20wt% AL-8 blend: (a) electron image (b) silicon (c) aluminium (d) oxygen.

Dendritic arm spacing obtained for 75%AL-5/20%AL-7/5%AL-8; 75% AL-5/15%AL-7/10%AL-8; 75% AL-5/10%AL-7/15%AL-8; and 75% AL-5/5%AL-7/20%AL-8 are 40 µm, 38 µm, 35 µm and 36 µm respectively. It could be inferred that the combined introduction of AL-8 in varying amount into the trimodal powder blend initiates a poor particle packing arrangement which consequently exacerbates the thermal conductivity of the powder bed, hence, culminating in the formation of coarse dendritic

microstructure with irregular morphology. From the previous analysis carried out in section 5.3, it had been speculated that the thin layer of oxide film covering small-sized particles in AL-8 are difficult to disrupt probably due to its oxide layer thickness being less than 0.25 μm. Consequently, as noted in section 5.3, it is likely the applied specific laser energy input could not generate adequate circumferential stress to disrupt the thin layer of oxide film in AL-8. On this basis, the undisrupted thin surface oxide film covering particles in AL-8 powders is likely to have contributed to the poor thermal conductivity of the packed layers of the trimodal powders' particles which results in the occurrence of sintering of particles in the microstructure. Moreover, fraction of the primary phase (Figure 7.13) determined for the tri-modal blends of AL-5 powder are 24.1wt%, 22.6wt%, 20.6wt%, and 21.7wt% for 75%AL-5/20%AL-7/5%AL-8; 75% AL-5/15%AL-7/10%AL-8; 75% AL-5/10%AL-7/15%AL-8; and 75% AL-5/5%AL-7/20%AL-8 respectively. It could be inferred from these results that there has been no positive change in the effect of the particle packing arrangement of the trimodal powders on the thermal conductivity of its bed due to change in the powder composition. Consequently, no significant variation in the fraction of primary phase occurring as a result of the variation in the blended powder composition that would have resulted in significant change in the fraction of primary phase. Rather, as a consequence of low cooling rate initiated by the introduction of AL-8 into the bimodal AL-5 + AL-7, it is likely that the particle packing arrangement deteriorated.

Figure 7.19 reveals the results of microhardness measured along the etched horizontal cross-sections of the SLS/SLM processed trimodal powder samples. A relatively uniform microhardness distribution, with an average of 81 kgf/mm^2 was obtained by mixing 20wt% AL-7 and 5wt% AL-8 powders with AL-5 powder. Furthermore, as the content of AL-8 increases above 5%, the microhardness fluctuation increases significantly to a very great extent with average values falling to 66, 56, and 55 kgf/mm^2 for 75wt% AL-5/15wt% AL-7/10wt% AL-8; 75wt% AL-5/10wt% AL-7/15wt% AL-8; and 75wt% AL-5/5wt% AL-7/20wt% AL-8 respectively (Figure 7.20). The fluctuation in the cross-section profiles of the blended samples containing 75% AL-5/15%AL-7/10%AL-8; 75% AL-5/10%AL-7/15%AL-8; and 75% AL-5/5%AL-7/20%AL-8 lends credence to the claim that porosity occurred during the SLS/SLM processing of the tri-modal powder mixes as the content of additive powders AL-8 increases above 5%. Average microhardness values obtained could be associated with variation in the additive particle sizes and distribution as there occurs wide error limits seen to lie between 75wt% AL-5 + 25wt% AL-7 and 75wt% AL-5 + 25wt% AL-8. Again, the results in this section emphasises the relevance of mixing powders of

appropriate particle sizes and distribution in the correct proportion in order to obtain improved properties for the direct SLS processed materials.

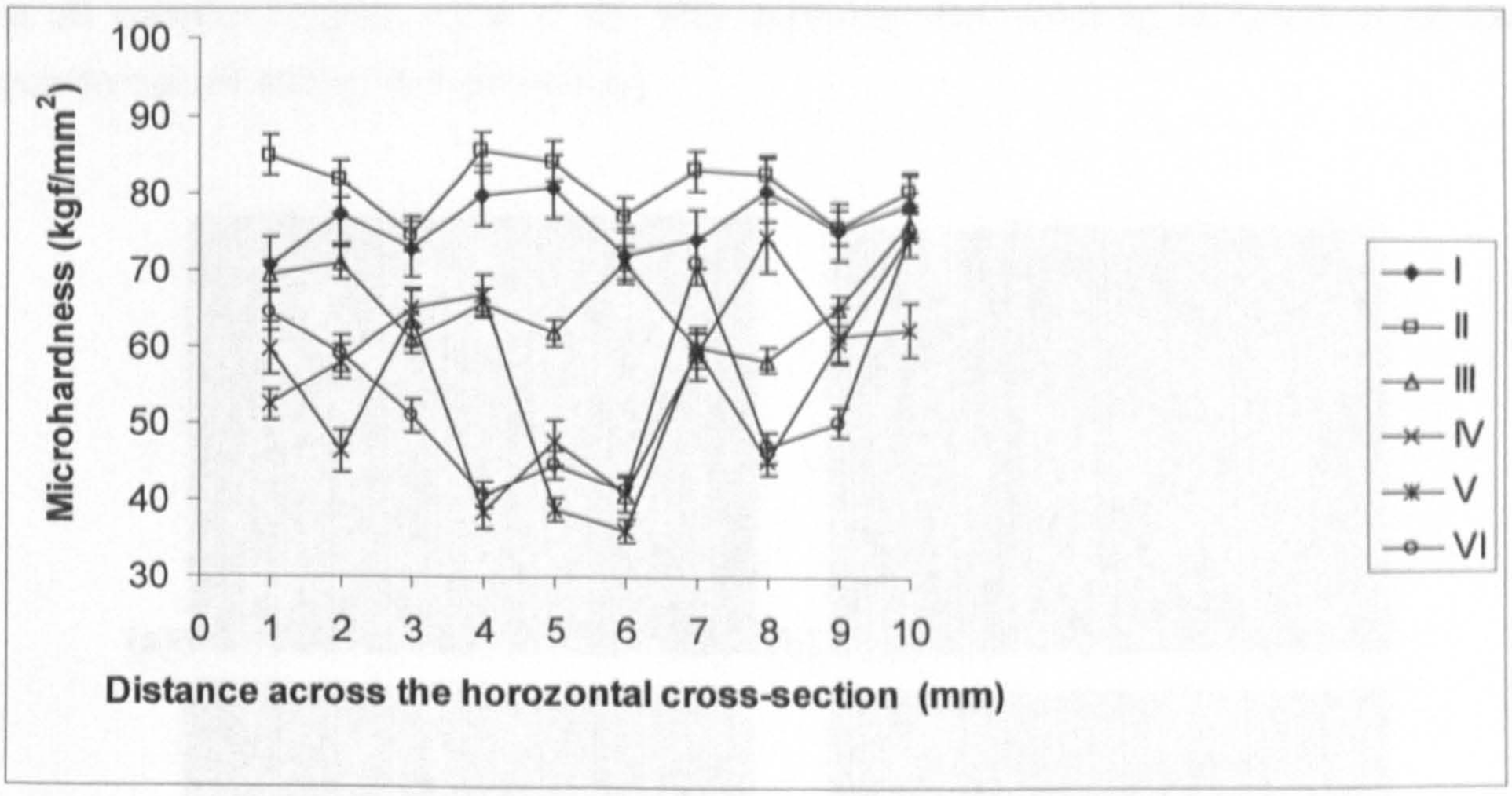

Figure 7.19: Variation in microhardness on the cross-sections of the direct laser-sintered trimodal powders.

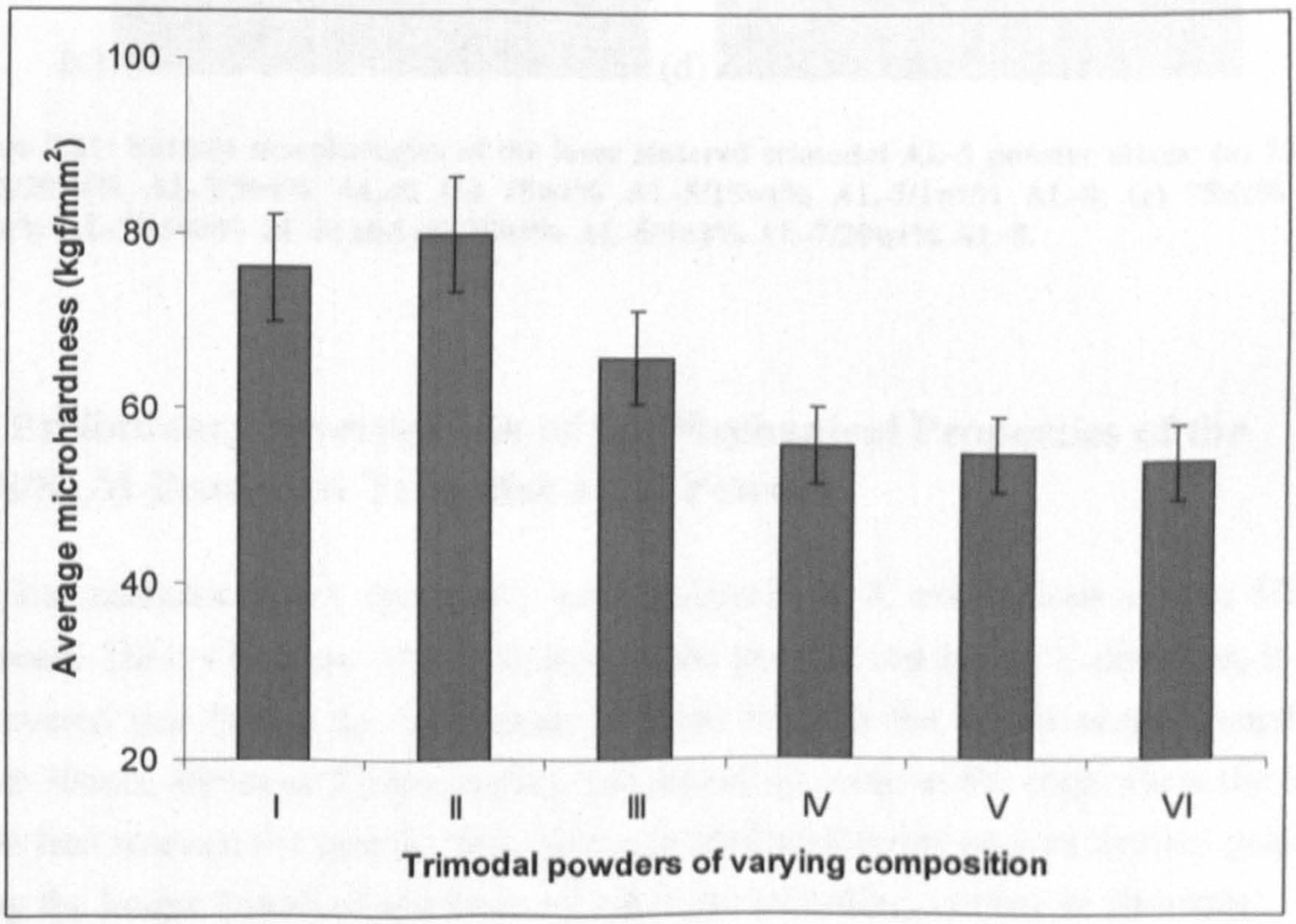

Figure 7.20: Average microhardness of the direct laser-sintered trimodal powders

7.4.3 Surface Morphology of the Laser Sintered Trimodal Powder Mixes

The surface morphology of direct SLS processed tri-modal Al-Si powder blend is presented in Figure 7.21. Agglomerates connected by small necks could be clearly seen in all samples (Figure 7.21a to d). This confirms that sintering occurred in all the powder mixes during SLS processing

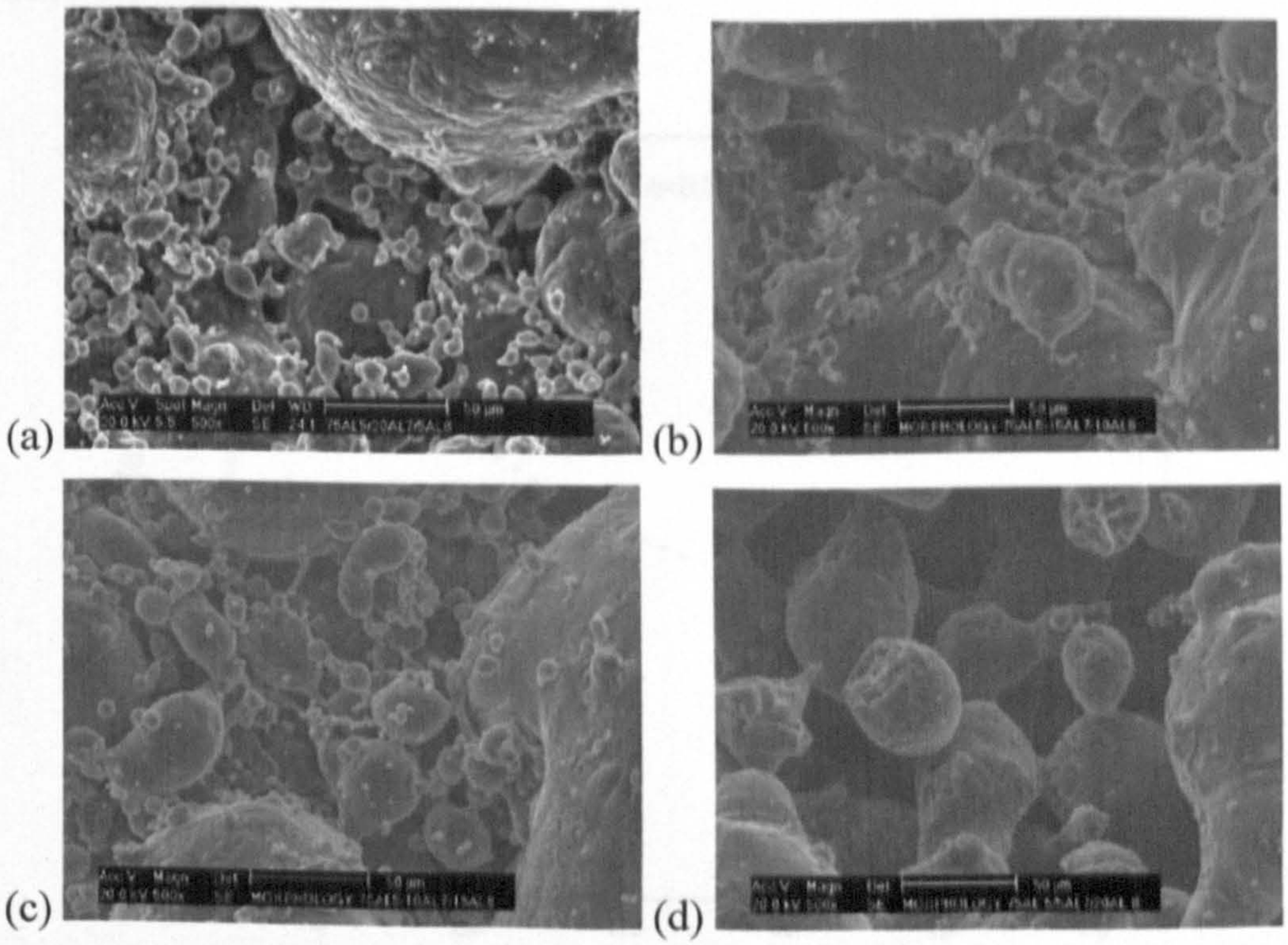

Figure 7.21: Surface morphologies of the laser sintered trimodal AL-5 powder mixes: (a) 75wt% AL-5/20wt% AL-7/5wt% AL-8; (b) 75wt% AL-5/15wt% AL-7/1wt% AL-8; (c) 75wt% AL-5/1wt% AL-7/15wt% AL-8; and (d) 75wt% AL-5/5wt% AL-7/20wt% AL-8.

7.5 Preliminary Investigation of the Mechanical Properties of the SLS/SLM Processed Trimodal AL-5 Powder

All the mechanical test specimens were designed in X orientations on the HPGL software. This is because upon scanning of the powder bed in the Y-direction, it was discovered that before the laser beam scanned through the whole sample length of either 30mm, 45mm or 55mm, curling had started to occur at the edge where the laser beam first scanned the powder bed. This was attributed to the uneven thermal gradient along the longer length of specimen which initiates balling, curling or shrinkage. This results from the successively scanned tracks having more time to cool down resulting in a lower temperature scanned test specimen (Agarwala *et al*. 1995, Simchi & Pohl 2003, Kruth *et al*. 2004). During attempts to fabricate the mechanical test specimens, it was discovered that the maximum length of specimen that could be produced on the

sinter station at a specific laser energy input of 150 J/mm^3, for which inter-particulate consolidation across the layers would occur, was 30 mm. For lower values of energy density, the maximum length was lower. The difficulty encountered in fabricating large sized test specimens via SLS/SLM in aluminium powder could also be attributed in part to the machine limitation. It is likely this factor became more predominant as the scan vector length increases such that the laser energy input could not be effect full consolidation in the powder bed.

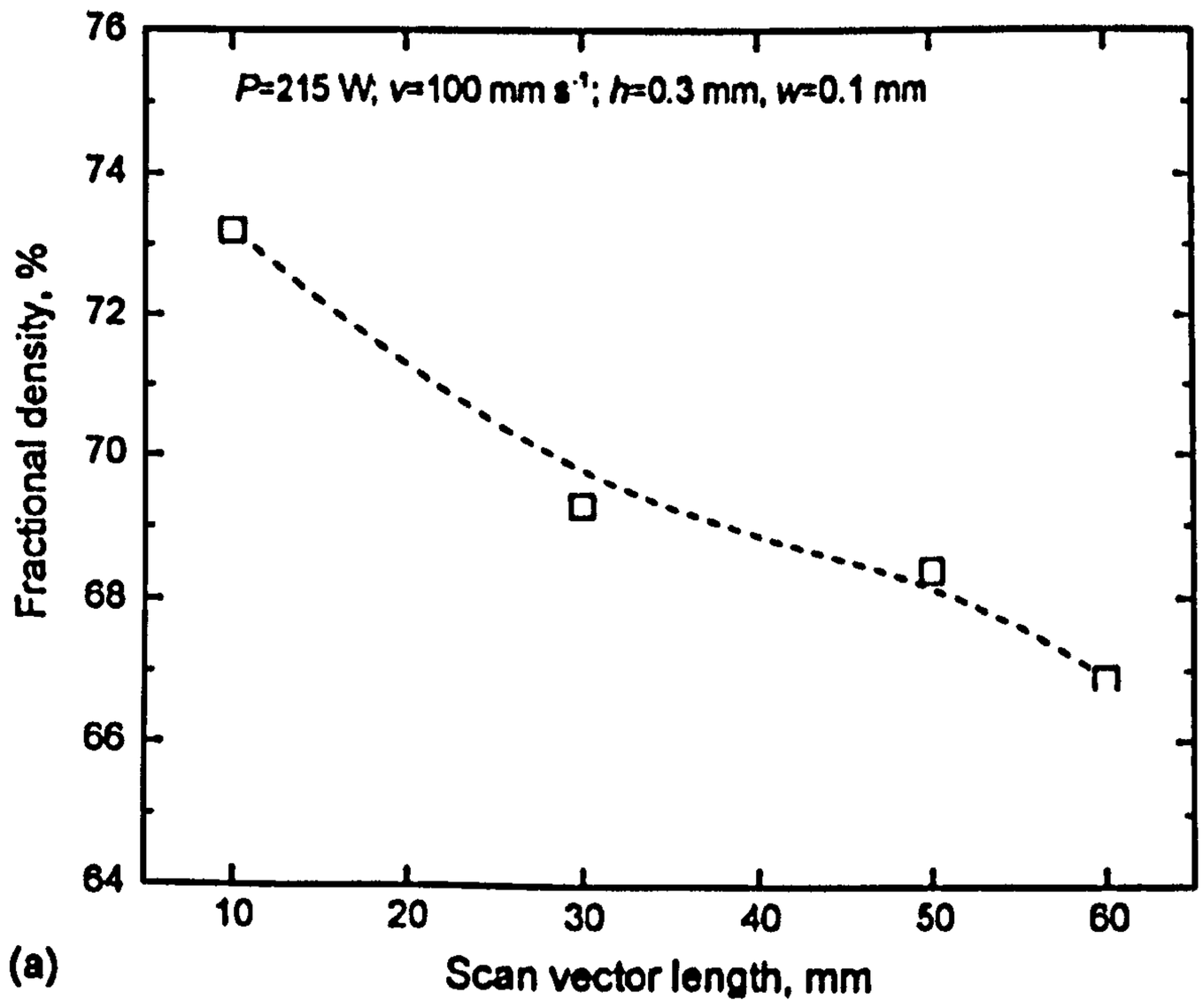

Figure 7.22: Effect of scan vector length on the fractional density of laser sintered iron (after Simchi, 2006).

This finding is supported by the work of Simchi (2006) (Figure 7.22) who noted that the density of laser sintered parts reduces as the scan vector length increases for reasons discussed above.

Furthermore, the standard length of 100mm required for impact testing could not be fabricated on the sinterstation as the diameter of the powder bed could not accommodate this length. A 55mm impact test sample length was produced (Figure 7.23), the maximum possible length, but again, the particulate consolidation along the full length was noted to be very poor. Moreover, the modification of the impact test machine which this length required was found to be impossible. As a consequence of this particular difficulty encountered, no impact test data could be generated.

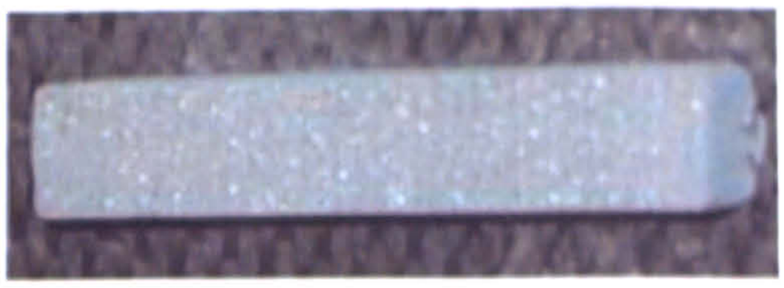

Figure 7.23: Fabrication of Charpy impact test specimen.

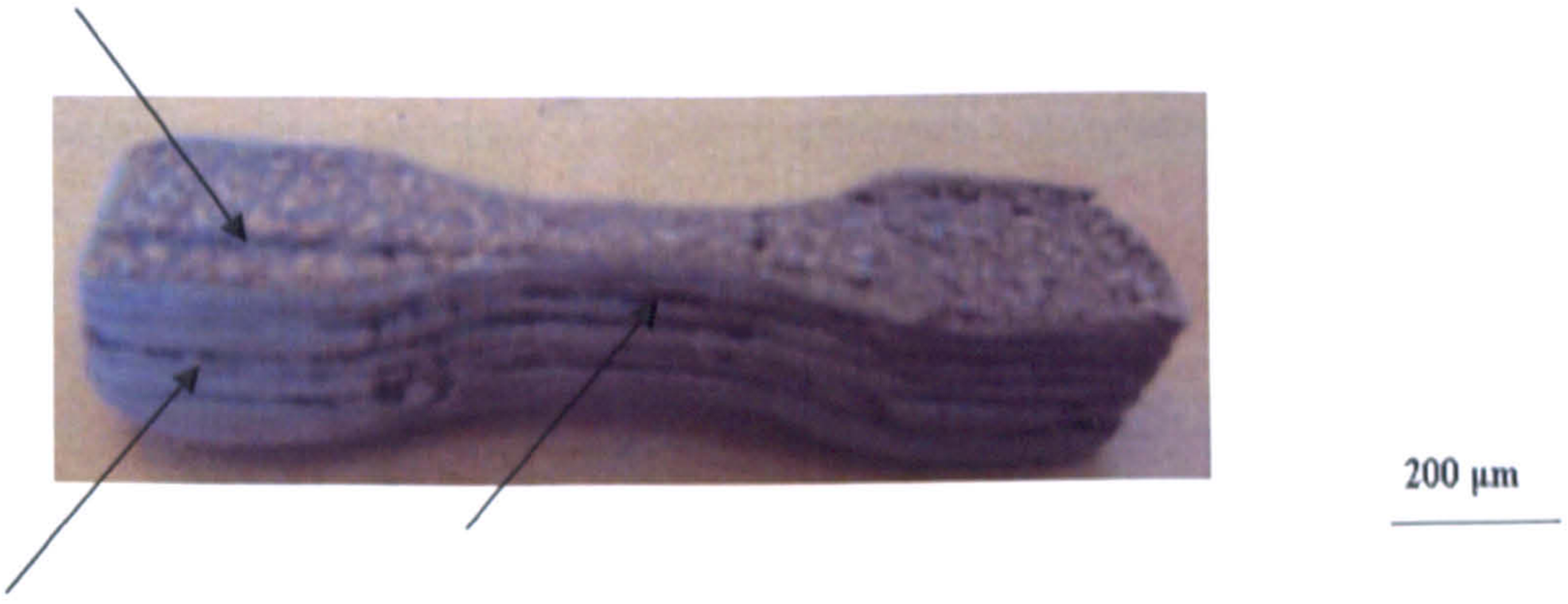

Figure 7.24: Images of 7 layer tensile test specimen showing the initiation or development of cracks or delamination in a trimodal powder (arrowed).

As noted above, cracks, delamination and balling were observed on the tensile test specimens produced on the sinter station. The initiation of defects (arrowed in Figure 7.24) which weakened the mechanical test sample could be ascribed to the uneven thermal gradient developing along the non-uniform cross section of the test specimen. To attempt to compensate this, other processing parameters such as laser power, scanning speed and layer thickness were varied. However, it was discovered that this still had a negative effect on the thermal gradient during production of the part and the problems of cracks, delamination and balling kept on re-occurring. Obtaining results for the tensile strength of the fabricated samples was therefore, not possible as the test samples were discovered to be very weak. Solving this problem is of process design could not be tackled due to time constraints in this project.

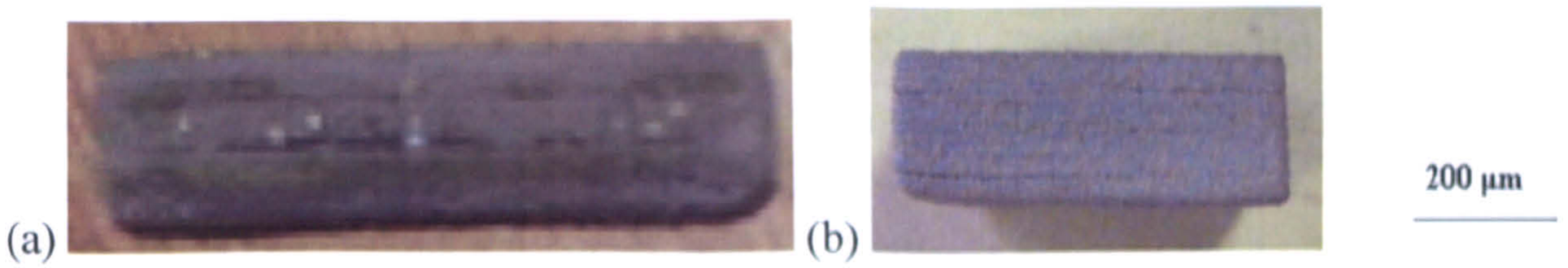

Figure 7.25: (a) Initiation of cracks and delamination in a trimodal powder (75wt% AL-5 + 10wt% AL-7 + 15wt% AL-8) three-point bend test specimen having a dimension of length of 30mm, breadth of 6mm, and height of 4mm. (b) Absence of delamination in trimodal powder test sample of dimension of length of 15mm, breadth of 15mm, and height of 2mm (of the same composition as (a).

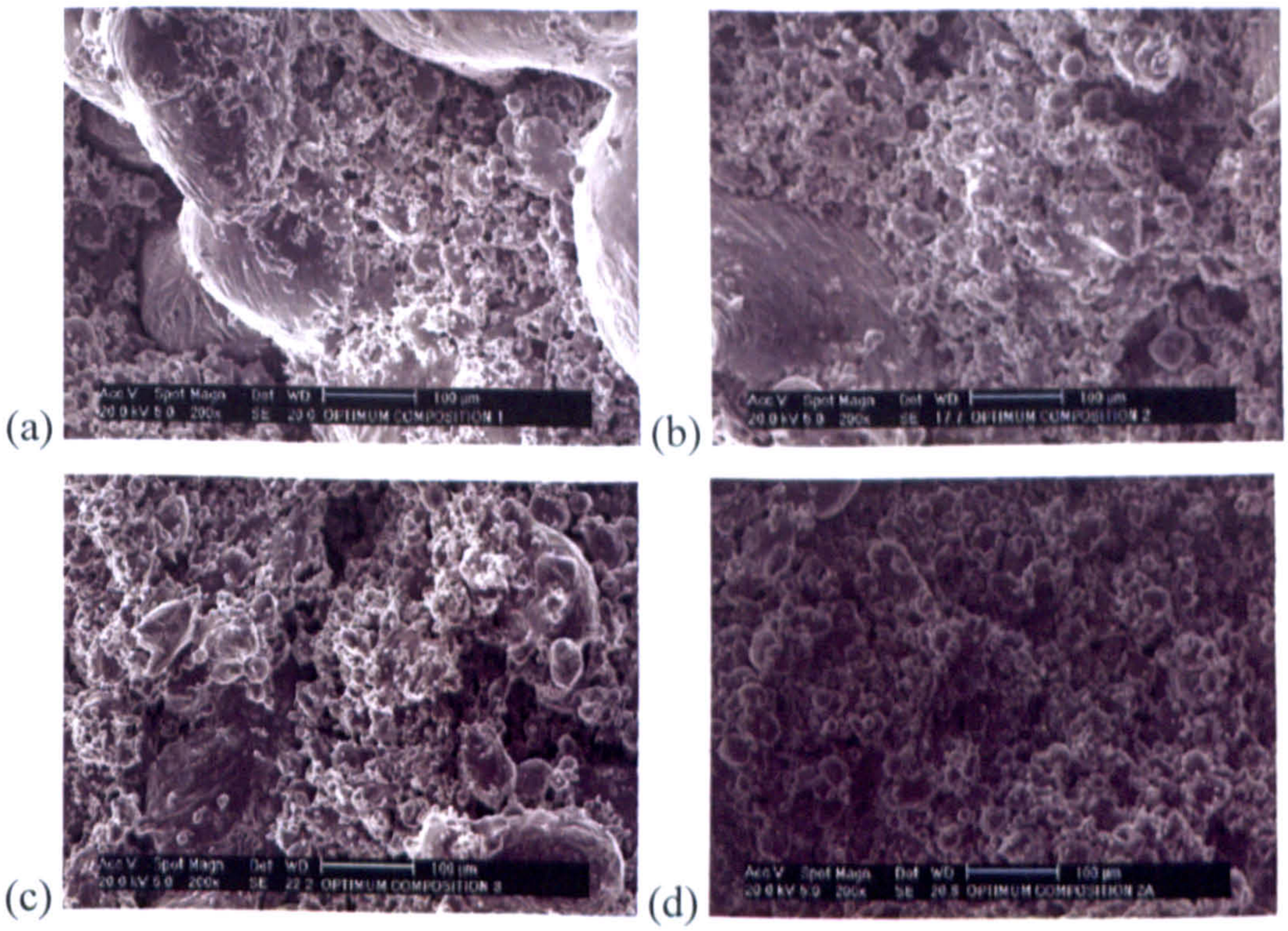

Figure 7.26: SEM of fracture surfaces of the laser sintered trimodal samples: (a) 75wt% AL-5/20wt% AL-7/5wt% AL-8; (b) 75wt% AL-5/15wt% AL-7/10wt% AL-8; (c) 75wt% AL-5/10wt% AL-7/15wt% AL-8; and (d) 75wt% AL-5/5wt% AL-7/20wt% AL-8.

During the fabrication of three-point bend test specimens, initiation of cracks and delamination were observed again in the test sample (see the arrows in Figure 7.25a). These were expected to affect the bend strength results significantly. By contrast, Figure 7.25b shows the absence of cracks and layer delamination in a eight layer test sample employed for density measurements and microstructural characterisation. This difference in behaviour could be attributed to the shorter vector length travelled by the laser beam during scanning which produced an even thermal gradient across the layers for interparticulate consolidation. Despite these problems, the results of the preliminary tests carried out showed that the test specimens were too weak and no reasonable results could be obtained.

Figure 7.26 shows the fracture surfaces of SLS/SLM processed trimodal powder blends obtained via three-pint bend tests. Observation of the fractured surfaces indicates absence of dimples in the SLS/SLM processed trimodal AL-5 powders. Preponderance of unsintered particles similar to AL-8 particle sizes is noted in Figure 7.26a to d. This confirms the earlier speculation that AL-8 particles did not mix with AL-5 + AL-7 bimodal powders. On one hand, this could be attributed to oxidising tendency of AL-8 particles which inhibited interparticulate bonding during SLS/SLM. Moreover, the low laser absorptivity of aluminium powder which is speculated to have become more predominant on the structure of SLS/SLM processed materials as the area of scan increases is also thought to have exacerbated the structures of these parts. It is also likely that the processing regimes employed for fabricating the test specimens are not the most suitable, hence, the need to investigate this further.

Analysis of the fractured surfaces suggests that crack was instigated at the surfaces or subsurface pores and pore clusters. Therefore, it can inferred from this study that the microstructures and mechanical properties of the SLS processed trimodal AL-5 powders significantly vary from those of extruded, cast and sintered materials as a result of differences encountered in types and distribution of intermetallic phase and porosity. These differences could be attributed to the transient nature of the laser-material interaction which results in the formation of liquid phase that could not impart sufficient inter-particulate strength, but it was able to attain high density for the particulates. Furthermore, it is now clear that the size of a component to be fabricated by SLS/SLM may also alter the processing regime in addition to the blending of powders of different particle sizes in varying composition.

7.6 Conclusion

The implication of the findings from this investigation is that trimodal powder mixes improves marginally the powder properties and the sintered density of SLS processed AL-5 powders over those of bimodal powders. The mechanical properties of the tri-modal powder mixes as indicated by the three-point bend test were found to be very poor. Analysis of the fractured samples suggests the presence of the veins of oxide phase, on the fracture surfaces, which are thought to have instigated fatigue crack at the surfaces or subsurface pores and pore clusters. It can inferred from this study that the microstructures and mechanical properties of the SLS processed trimodal AL-5 powders significantly vary from those of extruded, cast and sintered materials as a result of differences encountered in types and distribution of intermetallic phase and

porosity. The poor mechanical property obtained for the trimodal powders could be attributed to the need to re-investigate the processing regime as the size of parts to be fabricated increases, the machine limitation which is to thought to have influenced the structure of the parts being made, and the oxidising tendency of small-sized particle AL-8 which inhibits inter-particulate melting.

CHAPTER EIGHT DISCUSSION OF RESULTS

8.1 Summary

The implications of the key findings of this work are here discussed.

8.2 Discussions

Evidence gathered from single layer studies (sections 4.4.3 and 4.4.4) and preliminary investigation of the suitable aluminium powders (section 5.3) suggest that the particle shape, oxygen content, and alloying element presents in aluminium powders define the extent to which laser energy input will be translated into molten material, but that in all cases an increase in energy input (Figure 4.23) will result in more molten materials, and larger sized agglomerates. Observation of the processing maps indicates that the nature of porosity (Figure 4.24b), the surface morphology (Figures 4.24a), and first line scan balling (FSLB) (Figures 4.25) are dependent on the energy density incident on the powder bed. It was also confirmed that the elimination of FSLB, leading to a surface with minimal balling and enhanced sintered density, are made possible by controlling the energy density (Figures 4.24a, b and 4.25). According to Dinsdale & Quested (2004), the efficacy of silicon in reducing the melt viscosity is inferred to have promoted wettability between the single layer and the powder bed, this could be said to have resulted in reducing the agglomerate diameters during single layer scanning (Figure 4.23).

Powder properties such as particle shape, oxide contents, and alloying composition are noted to have influenced the densification mechanism and microstructural features of SLM processed pure aluminium and pre-alloyed aluminium powders. The densification co-efficient, (K = 32), was found to be the lowest for pre-alloyed Al-12Si powder of all the as-received powders. Examination of the microstructures of both pure and pre-alloyed aluminium powders (Figure 5.2) suggests that inter-particulate melting is a function of the oxidic constitution of the surface oxide film present in these powders, the degree of thermal mismatch, the thickness of the oxide film and the alloying element present in the powder. It is proposed that if the circumferential stress generated by laser scanning in an oxide film is lower than the reported fracture stress, oxide disruption will not be able to occur: this is consistent with the behaviour of pre-alloyed

Al-Mg powders (Figures 5.2b, c and Table 5.2). Moreover, it was proposed that oxide disruption occurred when the oxide film thickness was greater than or equal to 0.2 to 0.3 μm for pure aluminium powders. While silicon reduces viscosity and has no effect on the surface tension of aluminium melt pool, microstructural evidence suggest that silicon promotes wettability between layers whereas magnesium inhibits inter-layer wettability of particles because it increases the viscosity and lowers the surface tension (Dinsdale & Quested 2004).

The densification mechanism and microstructural evolution of AL-5 (Al-12Si) were discovered to have been predominantly controlled by the specific laser energy input to the powder bed. The densification co-efficient, K, was found to have reduced from 32 to 15, evidence that the densification of laser melted AL-5 has improved as a result of optimising the processing parameters. Furthermore, both the sintered density and microstructure of AL-5 were found to have been optimised at a specific laser energy input of 67 J/mm^3 (Figure 5.13). Increasing the specific laser energy beyond 67 J/mm^3 led to the occurrence of spheroidisation, reduced sintered density and increased porosity in the microstructure. The occurrence of spheroidisation is consequent upon an increased lifetime of the AL-5 melt pool. That increased specific laser energy input gives rise to this is supported by an increased coarseness of the dendrites and reduction in the weight fraction of primary dendrites. Again, this supports the earlier claim that the specific laser energy input delivered into the powder bed controls both the densification mechanism and microstructural development in laser melted AL-5 powder.

In order to improve the sintered density and microstructure of AL-5 powder, it was blended with pure aluminium powders of varying particle sizes and component ratio with a view to assessing their influences on its densification and microstructure. It was observed that the introduction of the additive powders of different particle sizes in varying component ratios altered the sintering behaviour of AL-5 (Figures 6.8 and 6.9). Moreover, the powder densities were discovered to have had a positive correlation with the sintered density and fraction of primary phase, whereas, a negative correlation was obtained for the secondary dendritic arm spacing (Figures 6.44, 6.45, 6.46, and 6.47). This suggests that the degree of effectiveness of particle packing arrangement in a blended powder determines the effective thermal conductivity of the powder bed. It was discovered that the blending of appropriate small-sized spherical powders with appropriate large-sized spherical powders in the right component ratio will effectively improve the powder bed thermal conductivity, thus resulting in formation of an adequate molten pool which increased the sintered density and improves the

microstructure. This occurs as a result of deeper penetration of heat flux into the aluminium particles, thus causing more molten pool to form rather than sintering of particles. Furthermore, it was speculated that the introduction of additive particles into AL-5 powder which may be inappropriate in terms of component ratio, particle size distribution and shape, initiated heterogenous sites of poor packing arrangements across the packed layers of blended powders on the powder bed. It is thought that at these sites that thermal conductivity should be lower, leading to sintering of powder particles rather than inter-particulate melting. At the heterogenous sites across the layers on the powder bed, it is presumed additive particles could not sit comfortably in the interstices of AL-5, thus introducing the occurrence of porosity which were observed in the blended microstructures containing 25wt% AL-2, 25wt% AL-6, 10wt% AL-7, 50wt% AL-7 and 25wt% AL-8 25wt% (Figures 6.14a, c, 6.29a, b, and d). At the porous regions across the layers of blended particles on the powder bed, it is clear that particles of both AL-5 and additive particles sintered rather than melting. Moreover, the surface oxide film of the particles of the additive powders, which inhibit their disruption, could be said to be responsible for their sintering. Only in the bimodal blended sample containing 75wt% AL-5 + 25wt% AL-7 it could be speculated that the highest degree of contact occur between the particles of AL-5 and additive powders, thus resulting in homogenous melted structure (Figure 6.14b, and 6.29a) possibly due to improved thermal conductivity of the particles across the layers (Figure 6.44, 6.45, 6.46, and 6.47). The fraction of primary phase in all the blended samples was not equal to the expected theoretical values from the Al-Si phase diagram. This suggested that the solidification regime in the SLS/SLM processing of these powders resulted in varying degrees of microsegregation in the microstructure of the blended powders due to different regime of cooling rates occasioned by the different particle packing arrangement in each blended powder. Meanwhile, the attainment of the highest fraction of primary phase in the blended sample containing 25wt% AL-7 suggested that it has the highest degree of inter-particulate contact and by implication, the highest thermal conductivity.

The introduction of AL-8 into the bimodal AL-5 and AL-7 was expected to increase the sintered density, the microstructure, and the mechanical properties. While the sintered density and microhardness were noted to be good, the bend strength was noted to be very poor due to the occurrence of delamination along the length of the bend test specimens. This outcome is a surprise. Moreover, it is contemplated that this was consequent upon the longer vector length travelled by the laser beam during the scanning of bend test specimens which produced an uneven thermal gradient across the layers, thereby resulting in inter-particulate consolidation among some layers to

become stronger than the bonds among other adjoining layers. On the other hand, it is thought that the blending of AL-8 with the bimodal AL-5 + AL-7 powder has reduced the porosity of the powder bed, therefore, it is more likely that smaller sized AL-8 particles gives greater fraction of oxide as this is more difficult to fracture and blend during SLS/SLM as a result of the tendency of the powder bed to oxidise during laser scanning. These two factors are speculated to have reduced the thermal conductivity of the powder bed, thereby resulting in the inter-particulate bonding (sintering) rather than melting. The poor results obtained from the preliminary investigation into the mechanical properties of the trimodal blended powders suggest that either a new set of processing conditions ought to have been developed which was not possible due to time constraints or a different powder blend need to be formulated. Again, it is believed that pre-alloyed Al-Si powders of wider range of particle sizes should be used such that it could be sieved into various fractions and these could be blended together. This suggestion should present little or no problem of oxidation as it had been established in section 5.3 that Al-Si powders are suitable SLS/SLM candidates.

CHAPTER NINE CONCLUSIONS AND RECOMMENDATIONS FOR FUTURE WORK

9.1 Conclusions

On the basis of this study, the following conclusions may be drawn about the SLS/SLM of aluminium alloy powders.

(1) The flow and solidification behaviour of molten aluminium powders during single layer scanning is strongly influenced by specific laser energy input which is the combined effect of laser power and scanning rates. Agglomerate sizes of the SLS/SLM processed aluminium powders increase with increasing specific laser energy input.

(2) Irrespective of the composition of the aluminium alloy powders investigated, the processing window seems to fall within the same range of laser power and scanning rates. The presence of surface oxide film and irregularly shaped particles in the powders exacerbate the agglomerate development and formation of porous surfaces which was found to be undesirable for the development of multiple layer parts. Laser sintering of aluminium powders with spherically shaped particles resulted in the formation of homogeneous and dense layers.

(3) Balling occurred in the single layer specimens due to the lower thermal conductivity of the bed and, possibly, the difference in wettability of the powder bed and sintered layers.

(4) The processing maps suggest that adopting an appropriate scan rate for a chosen laser power could lessen the challenges of balling, FSLB, and porous structures in the laser melting of aluminium powders.

(5) The existence of a high degree of thermal expansion mismatch between the oxide film and the parent metal and a uniform oxide layer thickness are believed to favour the disruption of the oxide shell promoting inter-particulate melting across the layers. This

establishes that oxide film can be disrupted and liquid droplets mix to give consolidation.

(6) Microstructural evidence suggests that SLM occurs in pure and pre-alloyed aluminium as inter-particulate melting at regions where the layer thickness of oxide film is greater than or equal to 0.2 to 0.3 μm.

(7) AL-5 (Al-12wt% Si) powders were found to be the most suitable candidate aluminium alloy powder for the direct SLS/SLM process as a consequence of their low thermal expansion and uniform distribution of its surface oxide films as well as the mullite phase presumed to be in its oxide film. All these factors seem to promote oxide film disruption that enhances coalescence across the layers.

(9) A densification co-efficient K, determined for all the powders, affirmed that the Al-12wt% Si powder possessed the most desirable sintering behaviour reflected in the lowest value of K (32) when compared to the other powders investigated. This densification co-efficient could be reduced further to 15 when the processing parameters were optimised to give specific laser energy input of 67 J/mm^3. The sintered density achieved in this instance was 2.1 g/cm^3.

(10) The degree of porosity and its orientation, the degree of densification of the inter-agglomerates of powders were found to be controlled by the choice of processing parameters. At energy density lower or higher than the optimum value of 67 J/mm^3, the sintered microstructure was heterogenous and characterised by large and irregularly shaped pores. The microstructural evolution of direct SLS processed AL-5 was found to be dependent on the applied energy density. As this was increased, the dendritic morphology was found to be increasing in its coarseness and the fraction of the available primary phase was decreasing.

(11) Powder properties such as apparent and tapping densities as well as flowability, could be controlled by blending aluminium powders, having different particle size and distribution, in varying proportions. Irrespective of the particle size distribution of the additive powders, apparent and tapping densities were optimised at 25wt% additive content of each powder blend. Powder blends containing 25wt% of AL-7 had the highest apparent and tapping densities. The flowability of all the blended powders

improved above that of monosized AL-5 powder probably due to their reduced oxide contents.

(12) Optimum specific laser energy input was found to have increased to 150 J/mm^3 when AL-5 was blended with different amount of pure aluminium additive powders of varying particle sizes and distribution. The blending of 25wt% of 17-30μm powder was found to have improved sintered density to 2.32 g/cm^3 by further reducing the densification co-efficient to 13.4.

(13) The positive correlation existing between the powder and sintered densities suggest that appropriate choice of particle sizes distribution, particle shape and component ratios of the powders to be blended together could result in improving the thermal conductivity of the powder bed. Negative correlation between the tapping density and dendritic arm spacing on one hand and positive correlation between tapping density and fraction of primary phase seems to confirm this speculation. Therefore, it is now clear that the blending together of powders having either inappropriate particle sizes distribution, irregular shape and incorrect component ratios will lead to occurrence of porous in powder beds which causes heterogeneity in microstructure.

(14) It was discovered that the introduction of additive powders of varying particle sizes and distribution altered the powder packing arrangement that which was inferred to have resulted in variation in the powder bed thermal conductivity. This influences the microstructural evolution of the sintered sample. It was discovered that better particle packing arrangement reduced the dendrite arm spacing. The dendritic morphology becomes coarser with the fraction of primary phase reducing as the powder bed became porous due to reduced thermal conductivity of the powder bed.

(15) It was discovered that the variation in the component ratio of the additive powderAL-7 in the bimodal AL-5 powder altered the particle packing arrangement which was inferred to have influenced the thermal conductivity of the powder bed. This is evident in the optimisation of the amount of liquid phase available for sintering when 25wt% AL-7 was blended with AL-5. The variation of sintered density with silicon content in the blended powders was inferred to have reduced the melt viscosity. Therefore, at the instance silicon content was 9wt% Si, the melt viscosity was deemed to have sufficiently reduced so that the sintered density and microstructure were optimised. The dendritic morphology was finest when 25wt% AL-7 was blended with

AL-5: this was speculated to have been as a consequence of maximisation of the thermal conductivity of the powder bed.

(16) The fraction of primary phase in all the blended samples was not equal to the expected theoretical values from the Al-Si phase diagram. This suggested that the solidification regime in the SLS/SLM processing of these powders was not at equilibrium because complete inter-particulate mixing did not occur between AL-5 and the additive powders. Meanwhile, the attainment of the highest fraction of primary phase in the blended sample containing 25wt% AL-7 suggested that it has the highest degree of inter-particulate mixing and by implication, the highest thermal conductivity.

(17) The development of the trimodal powder containing 75wt% AL-5/20wt% AL-7/5wt% AL-8 was discovered to have yielded the highest sintered density of 2.44 g/cm^3. The microstructures of the trimodal powders were noted to have deteriorated when compared with the bimodal powder containing 75wt% AL-5/25wt%A L-7. The introduction of the additive powder AL-8 alongside AL-7 into AL-5 could be said to be responsible for poor microstructures obtained from the trimodal powders due to its increasing tendency to oxidise and increase porosity during laser scanning.

(18) The bending strength properties of all the sintered trimodal powders were found to be very poor in contrast to the microhardness of all the samples which was fairly good. By implication, fairly good microhardness values suggest that compression was so weak that interfaces might be hidden during testing, but this was not so in tension bending. Moreover, the lack of consistency between the densities, hardness, and bend test properties could also be attributed to the machine limitation, design problem, and the material properties. It was discovered that layer delamination occurred during the fabrication of the tensile and bend tests specimens. The layer delamination is as a consequence of poor inter-layer bonding arising from uneven thermal gradient along the longer length of specimen which initiated balling, curling or shrinkage as a result of the successively scanned tracks having more time to cool down, thereby, lowering temperature of the scanned area.

9.2 Recommendation for Further Work

In order to advance the feasibility of taking the direct SLS of aluminium powders to commercialisation stage, the following are hereby recommended:

In order to improve the bonding in the SLS/SLM of Al-Si powders, it is hereby suggested that pre-alloyed Al-Si powders of different sizes should be blended together in varying composition with a view to optimising the bed density and consequently, the sintered density and the microstructure. Moreover, adoption of high laser power machines (Nd: YAG lasers) will ensure that laser absorption improves and laser scanning could be carried out at high scanning speeds which generate higher laser energy density. This is expected to promote higher cooling rates across the layers. The automation of the powder delivery mechanism in such machines will also go a long way in improving consistent powder compaction on the bed such that effective melt-back across the layers can be more pronounced.

In conclusion, proper manipulation of the processing and powder parameters and the adoption of higher power SLS machine could ultimately result in the feasibility of making aluminium parts via direct SLS process.

REFERENCES

Abe, F., Osakada, K., Shiomi, M., Uematsu, K., and Matsumoto, M. (2001). "The manufacturing of hard tools from metallic powders by selective laser melting." Journal of Materials Processing Technology 111: pp.210-213.

Accuratus (2002). "Materials." Retrieved 2 June, 2008, from http://www.accuratus.com/mullite.html

Agarwala, M., Bourell, D., Beaman, J., Marcus, H., and Barlow, J. (1995). "Direct selective laser sintering of metals." Rapid Prototyping Journal 1(1): pp.26-36.

Arnberg, L., Chai, G., and Backerud, L. (1993). "Determination of dendritic coherency in solidifying melts by rheological measurements " Materials Science and Engineering A173(1-2): pp. 101-103.

Asgharzadeh, H., and Simchi, A. (2005). "Effect of sintering atmosphere and carbon content on the densification and microstructure of laser-sintered M2 high-speed steel powder." Materials Science and Engineering A, 403(1-2): pp.290-298.

Basu, B., and Date, A.W. (1992a). "Rapid solidification following laser melting of pure metals—I. Study of flow field and role of convection." International Journal of Heat and Mass Transfer 35(5): pp. 1049-1058.

Basu, B., and Date, A.W. (1992b). "Rapid solidification following laser melting of pure metals—II. Study of pool and solidification characteristics." International Journal of Heat and Mass Transfer 35(5): pp. 1059-1067.

Bayer, A. M., Vasco, T., and Walton, L.R. (1998). Wrought Tool Steels (9th edition). ASM Handbook Vol. 1. Metal Park, OH, ASM: p. 752.

Beaman, J. J., Barlow, J.W., Bourell, D.L., Crawford, R.H., Marcus, H.L., and McAlea,

K. (1997). Solid Freeform Fabrication: A new Direction in Manufacturing, Kluwer Academic Publishers, U.S.A.

Bertrand, P., Bayle, F., Combe, C., Goeuriot, P., and Smurov, I. (2007). "Ceramic components manufacturing by selective laser sintering." Applied Surface Science **254**: pp. 989-992.

Beuth, J., and Klingbeil, N. (2001). "The role of process variables in laser-based direct metal solid freeform fabrication." JOM **53**(9): pp.36-39.

Birmingham, B., Jakubenas, K., Manthiram, A., Bourell, D.L., and Marcus, H.L. (1995). Solid Freeform Fabrication Processing Using In-Situ Reactive Sintering. Proceedings of the In-situ Reactions for Synthesis of Composites, Ceramics, and Intermetallics, The Minerals, Metals & Materials Society, Warrendale, PA. pp. 25-34.

Bishop, D. P., Cahoon, J.R., Chaturvedi, M.C., and Kipouros, G.J. (1998). "Diffusion-based microalloying of aluminium alloys by powder metallurgy and reaction sintering." Journal of Materials Science **33**: pp.3927-3934.

Bishop, D. P., Cahoon, J.R., Chaturvedi, M.C., Kipouros, G.J., and Caley, W.F. (2000). "On enhancing the mechanical properties of aluminium P/M alloys." Materials Science and Engineering A. **290**: pp.16-24.

Boivie, K. (2000). SLS application of the Fe-Cu-C system for liquid phase sintering. Proceedings of the 11th Solid Freeform Fabrication Symposium The University of Texas at Austin, Austin, TX pp. 141-149.

Boivie, K. (2001). Limits of loose metal powder density in the sinterstation. Proceedings of the 12th Solid Freeform Fabrication Symposium, University of Texas at Austin, Austin, USA.: pp. 264-275.

Bourell, D. L., Marcus, H.L., Barlow, J.W., and Beaman, J.J. (1992). "Selective laser sintering of metal and ceramics." The International Journal of Powder Metallurgy **28**(4

): pp. 369 - 381.

Brandon, D., and Kaplan, W.D. (1999). Microstructural Characterisation of Materials. Chichester, John Wiley & Sons.

Brewin, P., Ed. (1991). PM High Speed Steels. Selected Case Studies in Powder Metallurgy. London, The Institute of Metals.

Callister, W. D. (2007). Materials Science and Engineering: An Introduction. New York, John Willey & Sons, Inc.

Carson, J. W., and Pittenger, B.H. ,Ed. (1998). Bulk properties of powders. Powder Metal Technologies and Applications. Materials Park, OH, ASM International.

Chatterjee, A. N., Kumar, S., Saha, P., Mishra, P.K., Choudhury, A.R. (2003). "An experimental design approach to selective laser sintering of low carbon steel." Journal of Materials Processing Technology **136**(1-3): pp.151-157.

Chen, X. C., Xie, J.W., and Fox, P. (2004). "Direct laser remelting of iron with addition of boron." Materials Science and Technology **20**: pp.715719.

Childs, T. H. C., Hauser, C., and Badrossamay, M. (2004). "Mapping and modeling single scan track formation in direct metal selective laser melting." Annals of the CIRP, STC E, **53**(1): pp. 191–194.

Childs, T. H. C., and Hauser, C. (2005). "Raster scan selective laser melting of the surface layer of a tool steel powder bed." Proceedings of the Institution of Mechanical Engineers, Part B: Journal of Engineering Manufacture **219B** (4): pp. 379–384.

Childs, T. H. C., Hauser, C., and Badrossamay, M. (2005). "Selective laser sintering (melting) of stainless and tool steel powders: experiments and modelling,." Proceedings of the Institution. of Mechanical Engineers, Part B: Journal of Engineering

Manufacture 219B (4): pp. 339–357.

Dalgarno, K. W., and Wright, C.S. (2001). "Approaches to processing metals and ceramics through the laser scanning of powder beds- A review." Powder Metallurgy Progress. 1(1): pp.70-79.

Das, S., Wohlert, M., Beaman, J.J., and Bourell, D.L. (1998a). "Producing metal parts with selective laser sintering/hot isostatic pressing." JOM 50(12): pp.17-20.

Das, S., Harlan, N., Lee, G., Beaman, J. J., Bourell, D.L., and Barlow, J.W. (1998b). "Direct SLS Processing for Production of Cermet Composite Turbine Sealing Components." Materials and ManufIU:turing Processes 13(2): pp. 241-261.

Das, S., Wohlert, M., Beaman, J. J., and Bourell, D.L. (1999). "Processing of titanium net shapes by SLS/HIP." Materials & Design 20: pp.115-121.

Das, S., Fuesting, T.P., Danyo, G., Brown, L.E., Beaman, J. J., and Bourell, D.L. (2000). "Direct laser fabrication of superalloy cermet abrasive turbine blade tips." Materials & Design 21: pp. 63-73.

Das, S. (2001). On some physical aspects of process control in direct selective laser sintering of metals part III Proc. of the 12th Annual SFF Symposium, University of Texas at Austin, Austin, Texas.: pp 102-109

Das, S. (2003). "Physical aspects of process control in selective laser sintering of metals." Advanced Engineering Materials 5(10): pp.701-711.

Deckard, L., and Dennis, C.T. (1993). Fabrication of ceramic and metal matrix composites from selective laser sintered preforms. Proceedings of the 4th Solid Freeform Fabrication Symposium, University of Texas at Austin, Austin,: pp. 215-222.

Delannay, F., Froyen, L., and Deruyttere, A. (1987). "The wetting of solids by molten

metals and its relation to the preparation of metal-matrix composites composites." Journal of Materials Science 22(1): pp. 1-16.

Delgado, M. L., Ruiz-Navas, E. M., Gordo, E., and Torralba, J.M. (2005). "Enhancement of liquid phase sintering through Al-Si additions to Al-Cu systems." Journal of Materials Processing Technology **162-163**: pp.280-285.

Dewidar, M. M. (2002). Direct and indirect laser sintering of metals. School of Mechanical Engineering. Leeds, University of Leeds. **PhD**

Dewidar, M. M., Dalgarno, K.W., and Wright, C.S. (2003). "Processing conditions and mechanical properties of high-speed steel parts fabricated using direct selective laser sintering." Journal of Engineering Manufacture **217 Part B** (Proceedings of the Institution of Mechanical Engineers, ImechE): pp.1651-1662.

Dinsdale, A. T., and Quested, P. N. (2004). "The viscosity of aluminium and its alloys-A review of data and models." Journal of Materials Science 39(24): pp. 7221-7228.

Dunkley, J. J., Ed. (1998). Atomisation. Powder Metal Technologies and Applications. Materials Park, OH, ASM International.

Dunne, P., Soe, S.P., Byrne, G., Venus, A., and Wheatley, A. R. (2004). "Some demands on rapid prototypes used as master patterns in rapid tooling for injection moulding." Journal of Materials Processing Technology 150(3): pp. 201-207.

Eane, R. B. (2002). Metal Powder Effects on Selective Laser Sintering. School of Mechanical Engineering. Leeds, University of Leeds. **PhD**: pp. 214.

Eskin, D. G. (2008). Physical Metallurgy of Direct Chill Casting of Aluminium Alloys Boca Raton, CRC Press/Taylor & Francis.

Exener, H. E., and Weinbruch, S., Ed. (2004). Scanning Electron Microscopy. Metallography and Microstructures. Materials Park ,Ohio, ASM International.

Fischer, P., Roman, V., Weber, H.P., Karapatis, N. P., Boillat, E., and Glardon, R. (2003). "Sintering of commercially pure titanium powder with a Nd:YAG laser source." Acta Materialia **51**: pp. 1651-1662.

Fischer, P., Roman, V., Weber, H.P., and Kolossov, S. (2004a). "Pulsed laser sintering of metallic powders." Thin Solid Films **453-454**: pp.139-144.

Fischer, P., Locher, M., Romano, V., Weber, H.P., Kolossov, S., and Glardon, R. (2004b). "Temperature measurements during selective laser sintering of titanium powder." International Journal of Machine Tools and Manufacture **44**: pp.1293-1296.

Fischer, P., Roman, V., Blatter, A., and Weber, H. P. (2005). "Highly precise pulsed selective laser sintering of metallic powders." Laser Physics Letters **2**(1): pp.48-55.

Flewitt, P. E. J., and Wild, R.K. (2001). Grain Boundaries: Their Microstructure and Chemistry. Chichester, John Wiley & Sons Ltd.

Fritz, B., and Noorani, R. (1999). "Form sheet metal with RP tooling." Advanced Materials & Processes ASM International **155**(4): pp 37-39.

Gåård, A., Krakhmalev, P., and Bergström, J. (2006). "Microstructural characterisation and wear behaviour of (Fe,Ni)-TiC MMC prepared by DMLS." Journal of Alloys and Compounds **421**(1-2): pp.166-171.

Geiger, G. H., and Poirier, D. R. (1973). Transport Phenomena in Metallurgy. Wesley, USA, Pearson Addison

German, R. M. (1985). Liquid phase sintering. London, Plenum Press.

German, R. M. (1989). Particle packing characteristics. Princeton, NJ, Metal Powder

Industries Federation.

German, R. M. (1990). "Supersolidus liquid phase sintering part II: densification theory." International Journal of Powder Metallurgy 26(1): pp. 35-43.

German, R. M., and Bulger, M. (1992). "A model for densification by sintering of bimodal particle size distribution." International Journal of Powder Metallurgy 28(3): pp.301-311.

German, R. M. (1993). "The importance of particle characteristics in powder injection moulding." Reviews in Particulate Materials 1: pp.109-160.

German, R. M. (1994). Powder Metallurgy Science New Jersey, Metal Powder Industries Federation.

German, R. M. (1996). Sintering Theory and Practice. New York, John Wiley & Sons, Inc.

German, R. M. (1998). Powder Metallurgy of Iron and Steel, Chichester, John Wiley & Sons, Inc.

German, R. M. (1999). Particle Packing Characteristics. New Jersey, Metal Powder Industies Federation.

German, R. M. (2001). Liquid phase sintering: Metals. Encyclopedia of Materials: Science and Technology: pp.4601-4603.

German, R. M. (1991). Metal Powder Injection Moulding Powder Metallurgy: An Overview. Jenkins I. and J. V. Wood. London, The Institute of Metals p.102-113.

Gibson, I., and Shi, D. (1997). "Material properties and fabrication parameters in selective laser sintering process." Rapid Prototyping Journal 3(4): pp.129-136.

Gokhale, A. M., Ed. (2004). Quantitative characterisation and representation of global microstructural geometry. Metallography and Microstructures. Materials Park, OH, ASM International.

Gomes, M. A., Wronski, A. S., and Wright, C.S. (1995). "Fracture behaviour of a highly alloyed high speed steel." Fatigue Fracture Engineering of Material Structure 18 (1): pp. 1-18.

Goodridge, D. R. (2003). Indirect selective laser sintering of an apatite-mullite glass-ceramic School of Mechanical Engineering. Leeds, University of Leeds. PhD: pp. 211.

Grayson, G. N., Schaffer, G.B., and Griffiths, J.R. (2004). "On the fatigue of sintered aluminium alloys." Materials Forum 28: pp. 981-985.

Gremaud, M., Allen, D. R., Rappaz, M., and Perepezko, J.H. (1996). "The development of nucleation controlled microstructures during laser treatment of Al-Si alloys." Acta Materialia 44(7): pp.2669-2681.

Grong, Ø., Ed. (1997). Metallurgical Modelling of Welding (2nd Edition) Materials Modelling Series. London, The Institute of Materials.

Grugel, R., and Kurz, W. (1987). "Growth of interdendritic eutectic in directionally solidified Al-Si alloys." Metallurgical Transactions A 18: pp.1137-1142.

Grugel, R. N. (1993). "Secondary and tertiary dendrite arm spacing relationships in directionally solidified Al-Si alloys." Journal of Materials Science 28: pp.677-683.

Gu, D., and Shen, Y. (2006a). "WC-Co particulate reinforcing Cu matrix composites produced by direct laser sintering." Materials Letters 60(29): pp.3664-3668.

Gu, D., and Shen, Y. (2006b). "Processing and microstructure of submicron WC-Co

particulate reinforced Cu matrix composites prepared by direct laser sintering." Materials Science and Engineering A, **435-436**: pp.54-61.

Gu, D., and Shen, Y. (2007a). "Effect of dispersion technique and component ratio on densification and microstructure of multi-component Cu-based metal powder in direct laser sintering." Journal of Materials Processing Technology **182**: pp.564-573.

Gu, D., and Shen, Y., Fang, S., and Xiao, J. (2007a). "Metallurgical mechanisms in direct laser sintering of Cu-CuSn-CuP mixed powder." Journal of Alloys and Compounds **438**: pp.184-189.

Gu, D., Shen, Y., Zhao, L., Xiao, J., Wu, P., and Zhu, Y. (2007b). "Effect of rare earth oxide addition on microstructures of ultra-fine WC-Co particulate reinforced Cu matrix composites prepared by direct laser sintering." Materials Science and Engineering A, **445-446**: pp.316-322.

Gu, D., and Shen, Y. (2007b). "Influence of reinforcement weight fraction on microstructure and properties of submicron WC-Cop/Cu bulk MMCs prepared by direct laser sintering." Journal of Alloys and Compounds **431**: pp.112-120.

Gu, D., and Shen, Y. (2007c). "Balling phenomena during direct laser sintering of multi-component Cu-based metal powder." Journal of Alloys and Compounds **432**: pp.163-166.

Gu, D., Shen, Y., and Wu, X. (2008). "Formation of a novel W-rim/Cu-core structure during direct laser sintering of W-Cu composite system." Materials Letters **62**: pp. 1765-1768.

Gu, D., and Shen, Y. (2008b). "Direct laser sintered WC-10Co/Cu nanocomposites." Applied Surface Science **254** (13): pp 3971-3978.

Gu, D., and Shen, Y. (2008c). "Influence of Cu-liquid content on densification and microstructure of direct laser sintered submicron W-Cu/micron Cu powder mixture."

Materials Science and Engineering A, 489 (1-2): pp 169-177.

Guha, A., Ed. (2004). Bending Strength Tests (ASTM E 855). Mechanical Testing and Evaluation. Materials Park, OH, ASM International.

Gunduz, M., and Cardirli, E. (2002). "Directional solidification of aluminium-copper alloys." Materials Science and Engineering A, 327: pp.167-185.

Guo, R. Q., Rohatgi, P.K., and Nath, D. (1997). "Preparation of aluminium-fly ash particulate composite by powder metallurgy technique." Journal of Materials Science 32(15): pp. 3971-3974

Gusarov, A. V., Laoui, T., Froyen, L., and Titov, V. I. (2003). "Contact thermal conductivity of a powder bed in selective laser sintering." International Journal of Heat and Mass Transfer 46(6): pp. 1103-1109.

Hall, B. J. and G. B. Schaffer (2002). "Statiscal experimental design of Al-Cu-Mg-Si P/M alloys." Journal of Light Metals 2(4): pp.229-238.

Harper, C. A. (2001). Handbook of Ceramics, Glasses and Diamond. New York NY, McGraw-Hill.

Hauser, C., Childs, T.H.C., and Dalgarno, K. W. (1999a). Selective laser sintering of stainless steel 314S HC processed using room temperature powder beds Proceedings of the 10th Solid Freeform Fabrication Symposium. University of Texas at Austin, Texas., : pp.273-280.

Hauser, C., Childs, T.H.C., Dalgarno, K.W., and Eane, R.B. (1999b). Atmospheric control during selective laser sintering of stainless steel 314S powder Proceedings of the 10th Solid Freeform Fabrication Symposium, University of Texas at Austin, TX.: pp.265-272.

Hauser, C., Childs, T.H.C., Taylor, C.M., and Badrossamay, M. (2003). Direct Selective Laser Sintering of Tool Steel Powders to High Density: Part A - Effects of Laser Beam Width and Scan Strategy Proceedings of the 14th Solid Freeform Fabrication D. L. Bourell, R. H. Crawford, J. J. Beaman, K. L. Wood and H. L. Marcus. The University of Texas at Austin, Texas: pp.644-655.

Hauser, C. (2003). Selective Laser Sintering of a Stainless Steel Powder School of Mechanical Engineering Leeds, University of Leeds PhD: p.1-270.

Hayashi, T., Maekawa, K., Tamura, M., and Hanyu, K. (2005). "Selective laser sintering method using titanium powder sheet toward fabrication of porous bone substitutes." JSME International Journal, Series A 48(4): pp. 369-375.

Hegge, H. J., and De Hosson, J.T.M. (1990a). "Solidification structures during laser treatment." Scripta Materialia 24: pp.593-599.

Hegge, H. J., and De Hosson, J.T.M. (1990b). "Microstructure of laser treated Al alloys." Acta Materialia 38(12): pp.2471-2477.

Henriques, V. A. R., Bellinati, Cesar. E., and da Silva, Cosme. R.M. (2001). "Production of Ti-6%Al-7%Nb alloy by powder metallurgy (P/M)." Journal of Materials Processing Technology 118: 212-215.

Hertzberg, R. W. (1989). Deformation and Fracture Mechanics of Engineering Materials. New York, John Willey & Sons.

Higgins, P. K., and Munir, Z. A. (1982). "Application of the surface oxide model in the sintering of metallic particles." Powder Metallurgy International 14(1): pp. 26-29.

Hollander, D. A., von Walter, M., Wirtz, T., Sellei, R., Schmidt-Rohlfing, B., Paar, O., and Erli, H-J. (2006). "Structural, mechanical, and in vitro characterisation of individually structured Ti-6Al-4V produced by direct laser forming." Biomaterials 27: pp. 955-963.

Ion, J. C. (2005). Laser Processing of Engineering Materials: Principles, Procedures and Industrial Applications, London, Elsevier Butterworth Heinemann.

Ip, S. W., Kucharski, M., and Toguri, J. M. (1993). "Wetting behaviour of aluminium and aluminium alloys on Al_2O_3 and CaO." Journal of Materials Science Letters 12(21): pp. 1699-1702.

Kalay, Y. E., Chumbley, L.S., Anderson, I. E., and Napolitano, R.E. (2007). Characterization of hypereutectic Al-Si powders solidified under far-from equilibrium conditions." Metallurgical and Materials Transactions A 38: pp.1452-1457.

Kalpakjian, S., and Schmid, S. R. (2001). Manufacturing Engineering and Technology. Upper Saddle River, NJ, Prentice Hall.

Kang, L. S.-J. (2005). Sintering: Densification, Grain Growth & Microstructure. London, Elsevier Butterworth Heinemann.

Karapatis, N. P., van Griethuysen, J.-P.S., and Glardon, R. (1998). "Direct rapid tooling: a review of current research " Rapid Prototyping Journal 4(2): pp. 77-89.

Kathuria, Y. P. (1999). "Microstructuring by selective laser sintering of metallic powder." Surface and Coatings Technology 116-119: pp.643-647.

Kent, D., Schaffer, G. B., and Drennan, J. (2005). "Age hardening of a sintered Al-Cu-Mg-Si(Sn) alloy." Materials Science and Engineering A. 405(1-2): pp.65-73.

Khaing, M. W., Fuh, J.Y.H., and Lu, L. (2001). "Direct metal laser sintering for rapid tooling: processing and characterisation of EOS parts." Journal of Materials Processing Technology 113: pp.269-272.

Kobryn, P. A., and Semiatin, S.L. (2003). "Microstructure and texture evolution during solidification processing of Ti-6Al-4V." Journal of Materials Processing Technology

135: pp.330-339.

Konrad, C., Zhang, Y., and Xiao, B. (2005). "Analysis of melting and resolidification in a two-component metal powder bed subjected to temporal Gaussian heat flux." International Journal of Heat and Mass Transfer 48(19-20): pp. 3932-3944.

Kou, S. 1987. Welding Metallurgy. New York, N.Y.: John Wiley & Sons, Wiley Interscience.

Kruth, J.-P., Leu, M.C., and Nakagawa, T. (1998). "Progress in Additive Manufacturing and Rapid Prototyping " CIRP Annals - Manufacturing Technology 47(2): pp.525-540.

Kruth, J.-P., Peeters, P., Smolderen, T., Bonse, J., Laoui, T., and Froyen, L. (1998b). "Comparison of CO2 and Nd-YAG lasers for use with selective laser sintering of steel-copper powders " Int. Journal of CADCAM and Computer Graphics, 13(4-6): pp.95-110.

Kruth, J.-P., Froyen, L., Van Vaerenbergh, J., Mercelis, P., Rombouts, M., and Lauwers, B. (2004). "Selective laser melting of iron-based powder." Journal of Materials Processing Technology 149: pp.616-622.

Kruth, J.-P., Mercelis, P., Van Vaerenbergh, J., Froyen, L., and Rombouts, M. (2005). "Binding mechanisms in selective laser sintering and selective laser melting." Rapid Prototyping Journal 11(1): pp.26-36.

Kruth, J.-P., Levy, G., Klocke, F., and Childs, T. H. C. (2007). "Consolidation phenomena in laser and powder-bed based layered manufacturing" CIRP Annals - Manufacturing Technology 56(2): pp. 730-759.

Kruth, J.-P., Leu, M. C., and Nakagawa, T. (1998a). "Progress in additive manufacturing and rapid prototyping." Annals of the CIRP 47 (2): pp.525-40. .

Kruth, J.-P. F., L; Rombouts, M; Van Vaerenbergh, J; and Mercelis, P. (2003). "New ferro powder for selective laser sintering of dense parts." Annals of the CIRP 52(1): pp. 139-142.

Kruth, J.-P. V. d. S., B; Bonse, J.E; and Morren, B. (1996). "Basic powder metallurgical aspects in selective metal powder sintering." Annals of the CIRP 45(1): pp.183-186.

Kumar, S. and J.-P. Kruth (2007). "Effect of bronze infiltration into laser sintered metallic parts." Materials & Design 28(2): pp.400-407.

Laoui, T., Froyen, L., and Kruth, J.-P. (1999). "Effect of mechanical alloying on selective laser sintering of WC-9Co powder." Powder Metallurgy 42(3): pp.203-205.

Lauwers, B., Kruth, J.P., Froyen, L., and Laoui, T. (1999). Comparison between Nd:YAG and CO2 laser for use with selective laser sintering of metal powders. Proceedings of the PHOTOMEC'99-ETE'99, European Workshop, Leige, Belgium.

Lee, S.-J. J., Sachs, E., and Cima, M. (1995). "Layer position accuracy in powder-based rapid prototyping " Rapid Prototyping Journal 1(4): pp. 24-37.

Leong, C. C., Lu, L., Fuh, J.Y.H., Wong, Y. S. (2002). "In-situ formation of copper matrix composites by laser sintering." Materials Science and Engineering A, 338: pp.81-88.

Levy, G. N., Schindel, R., and Kruth, J.P. (2003). "Rapid manufacturing and rapid tooling with layer manufacturing (LM) technologies, state of the art abnd future perspectives." Annals of the CIRP 52(2): pp.589-607.

Lewis, G. K. (1995). "Direct laser metal deposition process fabricates near-net-shape components rapidly." Materials Technology 10: pp.3-4.

Lippold, J. C., Clark, W. A. T., and Tumuluru, M. (1992). An investigation of weld metal interfaces. *The Materials Science of Joining*. Edited by M. J. Cieslak, J. H. Perepezlo, and M. E. Glicksman, The Minerals, Metals & Materials Society, pp. 141–145.

Liu, Y., He, Z., Yu, S., Dong, G., and Li Q. (1992). "The effect of cerium on the wettability of Al2O3/Al-4.5Cu alloy " Journal of Materials Science Letters 11(12): 896-898.

Liu, Y., Chen, L.F., Tang, H.P., Liu, C.T., Liu, B., and Huang, B.Y. (2006). "Design of powder metallurgy titanium alloys and composites." Materials Science and Engineering A. **418**: pp.25-35.

Liu, Z. Y., Sercombe, T.B., and Schaffer, G.B. (2007). "The effect of particle shape on the sintering of aluminium." Metallurgical and Materials Transactions A **38A**: pp. 1351-1357.

Loretto, M. H., Godfrey, A.B., Hu, D., Blenkinsop, P. A., Jones, I. P., and Cheng, T.T. (1998). "The influence of composition and processing on the structure and properties of TiAl-based alloys." Intermetallics 6(7-8): pp. 663-666.

Lumley, R. N., and Schaffer, G.B. (1996). "The effect of solubility and particle size on liquid phase sintering." Scripta Materialia **35**(5): pp.589-595.

Lumley, R. N. and G. B. Schaffer (1998). "The effect of additive particle size on the mechanical properties of sintered aluminium-copper alloys." Scripta Materialia **39**(8): pp.1089-1094.

Lumley, R. N. and G. B. Schaffer (1999). "Anomalous pore morphologies in liquid-phase -sintered Al-Zn alloys." Metallurgical Transactions A **30** (6): pp. 1682-1685.

Lumley, R. N., Sercombe, T.B., and Schaffer, G.B. (1999). "Surface oxide and the role

of magnesium during sintering of aluminium." Metallurgical and Materials Transaction A: Physical Metallurgy and Materials Science. 30 (2) pp. 457-463.

Maeda, K. and T. H. C. Childs (2004). "Laser sintering (SLS) of hard metal powders for abrasion resistant coatings." Journal of Materials Processing Technology 149(1-3): pp. 609-615.

Martin, J. M. and F. Castro (2003). "Liquid phase sintering of P/M aluminium alloys: effect of processing conditions." Journal of Materials Processing Technology 143-144: pp.814-821.

Massalski, T. B. (1990). Binary alloy phase diagrams. Metals Park Ohio, American Society for Metals.

MatWeb (2008). "Spinel, $MgAl_2O_4$ ". Retrieved 30th August, 2008, from http://www.matweb.com/search/DataSheet.aspx?MatGUID=c8c56ad547ac4cfabad15977bfb537f1&ckck=1

McGeary, R. K. (1961). "Mechanical packing of spherical particles." Journal of American Ceramic Society 44(10): pp.513-522.

McPhee, W. A. G., Schaffer, G.B., and Drennan, J. (2003). "The effect of iron on liquid film migration and sintering of an Al-Cu-Mg alloy." Acta Materialia 51(13): pp.3701-3712.

Merklein, M., Hennige, T., and Geiger, M. (2001). "Laser forming of aluminium and aluminium alloys - microstructural investigation." Journal of Materials Processing Technology 115: pp.159-165.

Miller, D., Deckard, C., and Williams, J. (1997). "Variable beam size SLS workstation and enhanced SLS model." Rapid Prototyping Journal 3(1): pp.4-11.

Mills, K.C., Keene, B.J., Brooks, R.F., and Shirali, A. (1998) Marangoni effects in welding. In Marangoni and interfacial phenomena in materials processing (Eds. E. D. Hondros, M. McLean and K. C. Mills). London. Institute of Materials, Minerals and Mining.

Minkoff, I. (1986). Solidification and Cast Structure, Chichester, John Wiley & Sons.

Mondolfo, L. F. (1976). Aluminium Alloys: Structure and Properties, London, Butterworths.

Morgan, R., Papworth, A., Sutcliffe, C., Fox, P., and O'Neill. (2001). Direct metal laser re-melting of 316L stainless steel powder Part2: analysis of cubic primitives. 12th Solid Freeform Fabrication Symposium, Austin, TX.

Morgan, R., Papworth, A., Sutcliffe, C., Fox, P., and O'Neill. (2002). "High density net shape components by direct laser re-melting of single-phase powders." Journal of Materials Science **37**: pp.3093-3100.

MPIF (1995). Standard Test Methods for Metal Powders and Powder Metallurgy Products. Princeton, New Jersey., Metal Powder Industries Federation.

Mumtaz, K. A., Erasenthiran, P., and Hopkinson, N., (2008). "High density selective laser melting of Waspaloy®." Journal of Materials Processing Technology **195 (1-3)**: pp. 77-87.

Munir, Z. A. (1981). "The electrical conductivity of doped and undoped uranium oxide " International Journal of Thermophysics **2**(2): pp. 177-186.

Murali, K., Chatterjee, A.N., Saha, P., Palai, R., Kumar, S., Roy, S.K., Mishra, P.K., and Choudhury, A.R. (2003). "Direct selective laser sintering of iron-graphite powder mixture." Journal of Materials Processing Technology **136**: pp.179-185.

Narashiman, K. S. (2001). Powder characterisation. Encyclopedia of Materials: Science

and Technology, Elsevier: pp. 7781-7788.

Nelson, T. W., Lippold, J. C., and Mills, M. J. (1999). "Nature and evolution of the fusion boundary in ferritic-austenitic dissimilar weld metals, Part I – Nucleation and growth." Welding Journal, 78(10): pp. 329-337.

Niu, H. J., and Chang, I.T.H. (1998). "Liquid phase sintering of M3/2 high speed steel by selective laser sintering." Scripta Materialia 39(1): pp.67-72.

Niu, H. J., and Chang, I.T.H. (1999a). "Selective laser sintering of gas and water atomized high speed steel powders." Scripta Materialia 41(1): pp.25-30.

Niu, H. J., and Chang, I.T.H. (1999b). "Instability of scan tracks of selective laser sintering of high speed steel powder." Scripta Materialia 41(11): pp.1229-1234.

Niu, H. J. a. C., I.T.H. (2000). "Selective laser sintering of gas atomized M2 high speed steel powder." Journal of Materials Science 35: pp.31-38.

ODonnchadha, B., and Tansey, A. (2004). "A note on rapid metal composite tooling by selective laser sintering." Journal of Materials Processing Technology 153: pp.28-34.

Olakanmi, E. O., Cochrane, R.F., and Dalgarno, K.W. (2006). Direct selective laser sintering of aluminium powders. 7th Rapid Design, Prototyping and Manufacture, C. F. Bocking, A. E. W. Rennie and D. M. Jacobson. Buckinghamshire Chilterns University College, UK.: pp. 1-8.

O'Neill, W., Sutcliffe, C. J., Morgan, R., Landsborough, A., and Hon, K.K.B. (1999). "Investigation on Multi-Layer Direct Metal Laser Sintering of 316L Stainless Steel Powder Beds " Annals CIRP 48(1): pp.151-154.

Park, S.-H., Hur, B-H., Kim, S-Y., Ahn, D-K., and Ha, D-I. (2002). A study on the viscosity and surface tension for Al foaming and the effects of addition elements. 65th

World Foundry Congress. Gyeongju, Korea: pp. 515 -524.

Peng, L., Taiping, Y., Sheng, L., Dongsheng, L., Qianwu, H., Weihao, X., and Xiaoyan, Z. (2005). "Direct laser fabrication of nickel alloy samples." International Journal of Machine Tools and Manufacture 45(11): pp.1288-1294.

Pham, D. T., Dimov, S., and Lacen, F. (1998). "Techniques for Firm Tooling using Rapid Prototyping." Proceedings of the I MECH E Part B: Journal of Engineering Manufacture 212(4): pp. 269-277.

Pinnow, K. E. and W. Stasko (1998). P/M Tool Steels ASM Handbook Vol. 7 (10th edition). Metals Park, OH, ASM: p. 780.

Pogson, P., Fox, P., Sutcliffe, C. J., and O'Neill, W. (2003). "The production of copper parts using DMLR." Rapid Prototyping Journal 9(5): pp.334-333.

Powell, M. J. (1980). "Computer simulated random packing of spheres." Powder Technology 25: pp.45-52.

Reed, J. S. (1988). Introduction to the Principles of Ceramic Processing. New York, John Wiley & Sons.

Rombouts, M., Froyen, L., Bourell, D., and Kruth, J.-P. (2005). Surface roughness after laser melting of iron based powders. Proceedings of the 2nd International Conference on Virtual Modelling and Rapid Manufacturing: Advanced Research in Virtual and Rapid Prototyping. Portugal: pp. 329-335.

Rombouts, M., Kruth, J.-P., Froyen, L., and Mercelis, P. (2006). "Fundamentals of selective laser melting of alloyed steel powders." CIRP Annals 55(1): pp. 187-192.

Salak, A. (1995). Ferrous Powder Metallurgy. Cambridge, Cambridge International Science Publishing.

Sands, R. L., and Shakespeare, C. R. (1966). Powder Metallurgy: Practice and Applications. London, George Newnes Limited.

Santos, E. C., Abe, F., Kitamura, Y., Osakada, K., and Shiomi, M., (2002). Mechanical properties of pure titanium models processed by selective laser melting. Proceedings of the 13th Solid Freeform Fabrication Symposium, University of Texas at Austin, Austin: pp. 180-186.

Santos, E. C., Shiomi, M., Osakada, K., and Abe, F. (2004). "Microstructure and mechanical properties of pure titanium models fabricated by selective laser melting." Journal of Mechanical Engineering Science Part C(Proceedings of the Institution of Mechanical Engineers, ImechE 217): pp. 210-213.

Santos, E. C., Shiomi, M., Osakada, K., and Laoui, T. (2006). "Rapid manufacturing of metal components by laser forming." International Journal of Machine Tools and Manufacture 46(12): pp.1459-1468.

Sanz-Guerrero, J., and Ramos-Grez, J. (2008). "Effect of total applied energy density on the densification of copper–titanium slabs produced by a DMLF process." Journal of Materials Processing Technology 202(1-3): pp. 339-346.

Savage, W. F., Lundin, C. D., and Aronson, A. H. (1965). "Weld metal solidification mechanisms." Welding Journal 44(4): pp. 175-181.

Savage, W. F., and Aronson, A. H. (1966). "Preferred orientation in the weld fusion zone." Welding Journal 45(2): pp. 85-89.

Savage, W. F., and Hrubec, W. J. (1972). "Synthesis of weld solidification using crystalline organic materials." Welding Journal 51(5): pp. 260-271.

Savage, W. F., Nippes, E. F., and Erickson, J. S. (1976). "Solidification mechanisms in fusion welds." Welding Journal 55(8): pp. 213-221.

Savage, W. F. (1980). "Solidification, segregation and weld imperfections." Welding in the World 18(5-6): pp. 89–114.

Schaffer, G. B., and Apelian, D. (2000). Aluminium Powder Metallurgy: Process, Properties, and Design Solutions. Washington, DC, The Aluminium Association Inc.

Schaffer, G. B., Huo, S.H., Drennan, J., and Auchterlonie, G.J. (2001a). "The effect of trace elements on the sintering of an Al-Zn-Mg-Cu alloy." Acta Materialia 49(14): pp. 2671-2678.

Schaffer, G. B., Sercombe, T.B., and Lumley, R.N. (2001b). "Liquid phase sintering of aluminium alloys." Materials Chemistry and Physics 67(1-3): pp.85-91.

Schaffer, G. B., and Hall, B.J. (2002). "The influence of atmosphere on the sintering of aluminium " Metallurgical Transactions A 33(10): pp. 3279-3284.

Schaffer, G. B., Hall, B.J., Bonner, S. J., Huo, S.H., and Sercombe, T.B. (2006). "The effect of the atmosphere and the role of pore filling on the sintering of aluminium." Acta Materialia 54(1): pp.131-138.

Schiaffino, S., and Sonin, A. A. (1997a). "Motion and arrest of a molten contact line on a cold surface: An experimental study. " Physics of Fluids 9(8): pp. 2217-2226.

Schiaffino, S., and Sonin, A. A. (1997b). "On the theory for the arrest of an advancing molten contact line on a cold solid of the same material." Physics of Fluids 9(8): pp.2227-2233.

Schiaffino, S., and Sonin, A. A. (1997c). "Molten droplet deposition and solidification at low Weber numbers." Physics of Fluids 9(11): pp. 3172-3187.

Sercombe, T. B., and Schaffer, G.B. (1999a). "Freeform fabrication of functional aluminium prototypes using powder metallurgy " Journal of Materials Science 34 pp.

4245 - 4251.

Sercombe, T. B., and Schaffer, G.B. (1999b). "The effect of trace elements on the sintering of Al-Cu alloys." Acta Materialia 47(2): pp.689-697.

Sercombe, T. B., and Schaffer, G. B. (1999c). "On the use of trace additions of Sn to enhance sintered 2xxx series Al powder alloys" Materials Science and Engineering A, 268(1-2): pp. 32-39.

Sercombe, T. B., and Schaffer, G.B. (2003). Rapid manufacturing of aluminium components. Science. **301:** pp.1225-1227.

Sercombe, T. B. (2003a). "On the sintering of uncompacted, pre-alloyed Al powder alloys." Materials Science and Engineering A, **341**(1-2): pp.163-168.

Sercombe, T. B. (2003b). "Sintering of freeformed maraging steel with boron additions." Materials Science and Engineering A, **363**: pp.242-252.

Sercombe, T. B., and Schaffer, G.B. (2004a). "On the role of magnesium and nitrogen in the infiltration of aluminium by aluminium for rapid prototyping applications." Acta Materialia **52**(10): pp.3019-3025.

Sercombe, T. B., and Schaefer, G.B. (2004b). "On the role of tin in the infiltration of aluminium by aluminium for rapid prototyping applications." Scripta Materialia **51**(9): pp.905-908.

Sercombe, T. B., and Hopkinson, N. (2006). "Process shrinkage and accuracy during indirect laser sintering of aluminium." Advanced Engineering Materials 8(4): pp. 260-264.

SGTE (2008). "Alloy Phase Diagrams." Retrieved August 25, 2008, from http://www.crct.polymtl.ca/FACT/documentation/BINARY/BINARY_Figs.htm.

Shapiro, E., Ed. (2000). Bend Testing. Mechanical Testing and Evaluation. Materials Park, Ohio, ASM International.

Shellabear, M., and Nyrhilä, O. (2007). "Advances in materials and properties of direct metal laser-sintered parts ". Retrieved January 18, 2008, from http://www.rm-platform.com/index.php?option=com_docman&task=cat_view&gid=24&Itemid=38.

Shi, Y., Chen, S., Lu, X., and Huang, S. (2004). "Study on self-heating metallic powder for the selective laser sintering process." Journal of Engineering Manufacture Proceedings of the Institution of Mechanical Engineers, ImechE, 218: pp.1239-1247.

Simchi, A., Pohl, H., and Petzoldt, F. (2001a). A novel steel powder for rapid tooling using direct metal laser sintering. International User's Conference on Rapid Prototyping & Rapid Tooling & Rapid Manufacturing (uRapid) Amsterdam: pp.292-298.

Simchi, A., Pelzoldt, F., and Pohl, H. (2001b). "Direct metal laser sintering: materials considerations and mechanisms of particle bonding." International Journal of Powder Metallurgy. 37(2): pp.49-61.

Simchi, A., and Pohl, H. (2003). "Effect of laser sintering processing parameters on the microstructure and densification of iron powder." Materials Science and Engineering A. 359(1-2): pp.119-128.

Simchi, A., Petzoldt, F., and Pohl, H. (2003). "On the development of direct metal laser sintering for rapid tooling." Journal of Materials Processing Technology 141: pp.319-328.

Simchi, A., and Pohl, H. (2004). "Direct laser sintering of iron-graphite powder mixture." Materials Science and Engineering A, 383(2): pp.191-200.

Simchi, A. (2004). "The role of particle size on the laser sintering of iron powder." Metallurgical and Materials Transactions B, 35B: pp.937-948.

Simchi, A. (2006). "Direct laser sintering of metal powders: Mechanism, kinetics and microstructural features." Materials Science and Engineering A, 428(1-2): pp.148-158.

Simchi, A., and Godlinski, D. (2008). "Effect of SiC particles on the laser sintering of Al-7Si-0.3Mg alloy." Scripta Materialia 59(2): pp. 199-202.

Singh, G., Yu, Y., Ernst, F and Raj, R. (2007). "Shear strength and sliding at a metal–ceramic (aluminum–spinel) interface at ambient and elevated temperatures." Acta Materialia 55 (9): pp. 3049 - 3057.

Slocombe, A., and Li, L. (2001). "Selective laser sintering of TiC-Al2O3 composite with self-propagating high-temperature synthesis." Journal of Materials Processing Technology 118: pp.173-178.

Song, Y., Yan, Y., Zhang, R., Xu, D., and Wang, F. (2002). "Manufacture of the die of an automobile deck part based on rapid prototyping and rapid tooling technology." Journal of Materials Processing Technology 120(1-3): pp 237-242.

Srivastava, D., Hu, D., Chang, I. T. H., and Loretto, M.H. (1999). "The influence of thermal processing route on the microstructure of some TiAl-based alloys." Intermetallics 7(10): pp. 1107-1112.

Srivastava, D., Chang, I.T.H., and Loretto, M.H. (2001). "The effect of process parameters and heat treatment on the microstructure of direct laser fabricated TiAl alloy samples." Intermetallics 9: pp.1003-1013.

Steen, W. M. (2003). Laser Materials Processing. London, Springer.

Stephens, M. D., MacDonald, S.A., Levoy, N. F., and Miller, S. A. (1999). Influence of particle size distribution on sintering behaviour of fine titanium powders. Advances in P/M and Particulate Materials. C. L. Rose and M. H. Thibodeau.

Stoodley, M. A., Abbott, J.R., and Simpson, A. (1996). "Titanium cranioplaty using 3-D computer modelling of skull defects." Journal of Clinical Neuroscience 3(2): pp. 149-155.

Storch, S., Nellessen, D., Schaefer, G., and Reiter, R. (2003). "Selective laser sintering: qualifying analysis of metal based powder systems for automotive applications." Rapid Prototyping Journal 9(4): pp.240-251.

Su, W. N., Erasenthiran, P., and Dickens, P. M. (2003). "Investigation of fully dense laser sintering of tool steel powder using a pulsed Nd:YAG laser." Proceedings of the I MECH E Part C Journal of Mechanical Engineering Science 217 (1): pp. 127–138. .

Sustarsic, B., Godec, M., Jenko, M., Drglin, T., and Dolinsek, S. (2005). "Bulk and surface characterisation of metal powders for direct laser sintering." Vacuum 80(1-3): pp.29-34.

Tandon, R., and Johnson, J., Ed. (1998). Liquid-Phase Sintering. Powder Metal Technologies and Applications. Materials Park, OH, ASM International.

Tang, Y., Loh, H. T., Wong, Y.S., Fuh, J.Y.H., Lu, L., and Wang, X. (2003). "Direct laser sintering of a copper-based alloy for creating three-dimensional metal parts." Journal of Materials Processing Technology 140(1-3): pp.368-372.

Technologies, P. A. D. (2008). "Selective Laser Sintering (SLS)." Retrieved 17th February, 2008, from http://www.padtinc.com/rm/sls/default.htm.

Thummler, F., and Oberacker, R., Ed. (1993). Introduction to Powder Metallurgy. The Institute of Materials Series on Powder Metallurgy. London, The Institute of Materials.

Tolochko, N. K., Khlopkov, Y. V., Mozzharov, S. E., Ignatiev, M.B., Laoui, T., and Titov, V.I. (2000). "Absorptance of powder materials suitable for laser sintering." Rapid Prototyping Journal 6(3): pp.155-161.

Tolochko, N. K., Mozzharov, S.E., Laoui, T., and Froyen, L. (2003). "Selective laser sintering of single- and two-component metal powders." Rapid Prototyping Journal 9(2): pp.68-78.

Toloui, B., and Hellawell, A. (1976). "Phase separation and undercooling in Al-Si eutectic alloy - the influence of freezing rate and temperature gradient." Acta Metallurgica 24: pp.565-573.

Tontowi, A. E. (2000). Selective laser sintering of crystalline polymers School of Mechanical Engineering. Leeds, University of Leeds. PhD: pp. 279.

Upadhyaya, G. S. (2000). Sintered Metallic and Ceramic Materials: Preparations, Properties and Applications. Chichester, John Wiley & Sons, Limited.

Uzunsoy, D., and Chang, I.T.H. (2005). "The effect of infiltrant choice on the microstructure and mechanical properties of Rapidsteel*2.0 " Materials Letters 59(22): pp. 2812-2817

Van der Schueren, B., and Kruth, J. P. (1995). "Powder deposition in selective metal powder sintering." Rapid Prototyping Journal 1(3): pp. 23 - 31.

Vaucher, S., Paraschivescu, D., Andre, C., and Beffort, O. (2002). Selective laser sintering of aluminium-silicon carbide metal matrix composites. Proc. Materials Week. Munich, Germany, ICM

Vaucher, S., Carreno-Morelli, E., Andre, C., and Beffort, O. (2003). "Selective laser sintering of aluminium- and titanium-based composites: processing and characterisation." Physica Status Solidi 199(3): pp.11-13.

Veldman, N. L. M., Dahle, A. K., StJohn, D.H., and Arnberg, L. (2001). "Dendrite coherency of Al-Si Cu alloys." Metallurgical and Materials Transactions A 32A.

Wang, C. Y. (2002). "Rapid Manufacturing: Overview ". Retrieved 31/05/2008, from http://www.csa1.co.uk/discoveryguides/rapidman/overview.php.

Wang, X. (1999). "Calibration of shrinkage and beam offset in SLS process." Rapid Prototyping Journal 5(3): pp. 129-133.

Wang, X. C., Laoui, T., Bonse J., Kruth, J.-P., Lauwers, B., and Froyen, L. (2002). "Direct Selective Laser Sintering of Hard Metal Powders: Experimental Study and Simulation " The International Journal of Advanced Manufacturing Technology 19(5): pp. 351-357.

Wang, Y., Bergstrom, J., and Burman C. (2006a). "Characterisation of an iron-based laser sintered material." Journal of Materials Processing Technology 172: pp.77-87.

Wang, Y., Bergstrom, J., and Burman C. (2006b). "Four-point bending fatigue behaviour of an iron-based laser sintered material." International Journal of Fatigue 28(12): pp.1705-1715.

Weiss, L. E. (1997). "Process overview." Retrieved August 30, 2008, from http://www.wtec.org/loyola/rp/02_01.htm.

Williams, J. D., and Deckard, C. R. (1998). "Advances in modelling the effects of selected parameters on the SLS process." Rapid Prototyping Journal 4(2): pp.90-100.

Worldwide Guide to Rapid Prototyping (2002). "Selective laser sintering." Retrieved January 10, 2008, from http://home.att.net/~castleisland/sls.htm

Wright, C. S., Ogel, B., Lemoisson, F., and Bienvenu, Y. (1995). "Supersolidus sintering of high speed steels Part 2: sintering of tungsten based alloys." Powder Metallurgy 38(3): pp. 221-229

Wu, X., Sharman, R; Mei, J., and Voice, W. (2002). "Direct laser fabrication and microstructure of a burn-resistant Ti alloy." Materials and Design 23: pp.239-247.

Wu, X., and Mei, J. (2003). "Near net shape manufacturing of components using direct laser fabrication technology." Journal of Materials Processing Technology 135: pp.266-270.

Wu, X., Sharman, R., Mei, J., and Voice, W. (2004a). "Microstructure and properties of a laser fabricated burn-resistant Ti alloy." Materials & Design 25: pp.103-109.

Wu, X., Liang, J., Mei, J., Mitchell, C., Goodwin, P. S., and Voice, W. (2004b). "Microstructures of laser-deposited Ti-6Al-4V." Materials & Design 25: pp.137-144.

Wu, X. L., and Chen, G.N. (1999). "Microstructure and wear resistance of in situ TiCp composite coating by laser cladding." Journal of Materials Science and Technology 15, (3): pp. 233-238.

Xiao, K. (2007). Indirect selective laser sintering of Apatite-Wollastonite glass-ceramic. School of Mechanical Engineering. Leeds, University of Leeds. PhD: pp.248.

Xie, G., Ohashib, O., Songa, M., Mitsuishia, k., and Furuyaa, K. (2005a). "Reduction mechanism of surface oxide films and characterization of formations on pulse electric-current sintered Al–Mg alloy powders." Applied Surface Science 241, (1-2): pp. 102-106.

Xie, G., Ohashi, O., Song, M., Furuya, K., and Noda, T. (2003). "Behavior of oxide film at the interface between particles in sintered Al powders by pulse electric-current sintering " Metallurgical and Materials Transactions A 34(3): pp. 699-703.

Xie, W., Fox, P., O'Neill, W., and Sutcliffe, C.J. (2005b). "Effect of direct laser re-melting processing parameters and scanning strategies on the densification of tool steels " Journal of Materials Processing Technology 170 (3): pp. 516-523.

Xu, F., Loh, H., and Wong, Y. S. (1999). "Considerations and selection of optimal orientation for different rapid prototyping systems." Rapid Prototyping Journal 5(2): pp.54-60.

Yokoyama, T. (1991). Fluidity of Powder. Powder Technology Handbook. K. Linoya, K. Gotoh and K. Higashitani. New York, Marcel Dekker, Inc.

Zheng, H., Zhang, J., Shiqiang, L., Wang, G., and Xu, Z. (2006). "Effect of core-shell composite particles on the sintering behaviour and properties of nano-Al2O3/polystrene composite prepared by SLS." Materials Letters 60: pp. 1219-1223.

Zhou, G. L., and Wood, J.V. (1995). "Influence of alloying elements on mechanical properties of sintered high speed steel powders diluted with highly compressible powders." Powder Metallurgy 38(3): pp. 230-236.

Zhu, H. H., Lu, L., and Fuh, J.Y.H. (2003a). "Development and characterisation of direct laser sintering Cu-based metal powder." Journal of Materials Processing Technology 140: pp.314-317.

Zhu, H. H., and Fuh, J.Y.H. (2003b). "Formation of Fe-Cu metal parts using direct laser sintering." Proceedings of the I MECH E Part C Journal of Mechanical Engineering Science, 217(1): pp. 139-147.

Zhu, H. H., Lu, L., and Fuh, J. Y. H. (2004). "Influence of binder's liquid volume fraction on direct laser sintering of metallic powder." Materials Science and Engineering A, 371: pp.170-177.

Zhu, H. H., Fuh, J. H., and Lu, L. (2005). "Microstructural evolution in direct laser sintering of Cu-based metal powder." Rapid Prototyping Journal 11(2): pp.74-81.

Zhu, H. H., Lu, L., Fuh, J.Y.H., and Wu, C. C. (2006). "Effect of braze flux on direct laser sintering Cu-based metal powder." Materials & Design 27(2): pp.166-170.

Zhu, H. H., Fuh, J. Y. H., and Lu, L. (2007). "The influence of powder apparent density on the density in direct laser-sintered metallic parts." International Journal of Machine Tools and Manufacture 47(2): pp.294-298.

Zhuoxing, G., Jiandong, H., and Zhenfeng, Z. (1999). "Laser sintering of Cu-Sn-C system P/M alloys." Journal of Materials Science 34: pp.5403-5406.